



UNIVERSITAT DE  
BARCELONA

## High Energy Processes in Active Galaxies

Núria Torres i Albà

**ADVERTIMENT.** La consulta d'aquesta tesi queda condicionada a l'acceptació de les següents condicions d'ús: La difusió d'aquesta tesi per mitjà del servei TDX ([www.tdx.cat](http://www.tdx.cat)) i a través del Dipòsit Digital de la UB ([diposit.ub.edu](http://diposit.ub.edu)) ha estat autoritzada pels titulars dels drets de propietat intel·lectual únicament per a usos privats emmarcats en activitats d'investigació i docència. No s'autoritza la seva reproducció amb finalitats de lucre ni la seva difusió i posada a disposició des d'un lloc aliè al servei TDX ni al Dipòsit Digital de la UB. No s'autoritza la presentació del seu contingut en una finestra o marc aliè a TDX o al Dipòsit Digital de la UB (framing). Aquesta reserva de drets afecta tant al resum de presentació de la tesi com als seus continguts. En la utilització o cita de parts de la tesi és obligat indicar el nom de la persona autora.

**ADVERTENCIA.** La consulta de esta tesis queda condicionada a la aceptación de las siguientes condiciones de uso: La difusión de esta tesis por medio del servicio TDR ([www.tdx.cat](http://www.tdx.cat)) y a través del Repositorio Digital de la UB ([diposit.ub.edu](http://diposit.ub.edu)) ha sido autorizada por los titulares de los derechos de propiedad intelectual únicamente para usos privados enmarcados en actividades de investigación y docencia. No se autoriza su reproducción con finalidades de lucro ni su difusión y puesta a disposición desde un sitio ajeno al servicio TDR o al Repositorio Digital de la UB. No se autoriza la presentación de su contenido en una ventana o marco ajeno a TDR o al Repositorio Digital de la UB (framing). Esta reserva de derechos afecta tanto al resumen de presentación de la tesis como a sus contenidos. En la utilización o cita de partes de la tesis es obligado indicar el nombre de la persona autora.

**WARNING.** On having consulted this thesis you're accepting the following use conditions: Spreading this thesis by the TDX ([www.tdx.cat](http://www.tdx.cat)) service and by the UB Digital Repository ([diposit.ub.edu](http://diposit.ub.edu)) has been authorized by the titular of the intellectual property rights only for private uses placed in investigation and teaching activities. Reproduction with lucrative aims is not authorized nor its spreading and availability from a site foreign to the TDX service or to the UB Digital Repository. Introducing its content in a window or frame foreign to the TDX service or to the UB Digital Repository is not authorized (framing). Those rights affect to the presentation summary of the thesis as well as to its contents. In the using or citation of parts of the thesis it's obliged to indicate the name of the author.

HIGH ENERGY PROCESSES IN  
ACTIVE GALAXIES

NÚRIA TORRES I ALBÀ

DIRECTORS:

Dr Valentí Bosch Ramon

Dr Kazushi Iwasawa



UNIVERSITAT DE  
BARCELONA

Departament de Física Quàntica i  
Astrofísica  
Facultat de Física  
Universitat de Barcelona



Núria Torres i Albà , *High Energy Processes in Active Galaxies*,  
PhD Thesis  
Barcelona , June 2019

Cover Image: -

UNIVERSITAT DE BARCELONA  
DEPARTAMENT DE FÍSICA QUÀNTICA I  
ASTROFÍSICA  
Programa de doctorat en física  
Línia de recerca en astronomia i astrofísica

# High Energy Processes in Active Galaxies

Memòria presentada per  
Núria Torres i Albà  
per optar al grau de  
*Doctor en física per la Universitat de Barcelona*

Directors de la tesi:  
Dr Valentí Bosch Ramon  
Dr Kazushi Iwasawa  
Tutor de la tesi:  
Dr Alberto Manrique Oliva

Barcelona , June 2019



## DECLARATION

---

This thesis is presented following the regulations of the University of Barcelona (Aprovada pel CdG en sessió del 16 de març de 2012 i modificada pel CdG de data 9 de maig i 19 de juliol de 2012, 29 de maig i 3 d'octubre de 2013, 17 de juliol de 2014, 16 de juliol de 2015, 15 de juny i 21 de novembre de 2016, 5 de desembre de 2017 i 4 de maig de 2018). The listed regulations allow for the presentation of a PhD thesis as a "compendia of published articles". According to the regulations, the thesis must contain a minimum of four published or accepted articles. This thesis contains the published version of four articles, which is sufficient to allow its presentation. It also contains two additional articles, not yet accepted for publication at the moment of thesis presentation.

*Barcelona , June 2019*

---

Núria Torres i Albà



## ABSTRACT

---

This thesis has as an objective the study of very energetic phenomena in the central regions of active galaxies. Intense star formation is triggered by mergers of galaxies, and the funneling of large quantities of gas toward the inner regions is thought to also cause accretion onto the central black hole. Whether the two processes necessarily take place together as a step of galaxy evolution is still debated.

Regardless of the origin of their connection, star formation and strong AGN activity often coexist in the nuclei of galaxies. Even after star formation is no longer ongoing, the nuclear starburst in a merger results in the formation of galactic bulges. Therefore, stellar densities in the inner kiloparsecs of a galaxy are typically high. As stars, or star forming regions, are close to the AGN, interaction between the two is expected to be frequent, and it can result in a multitude of phenomena worthy of study.

In particular, the goal of the thesis is to study the emission produced by these phenomena, in the range of X-rays to gamma-rays, whether to disentangle their individual contributions or to detect emission resulting from their interaction. The thesis intends to provide data to continue the study of the starburst-AGN connection, and new models to explain the production of gamma rays in other galaxies.

The first part focuses on the X-ray analysis of a local sample of luminous infrared galaxies (LIRGs). In this part we analyze data for 84 sources which span a wide range of activity types and merger stages. We provide X-ray images, fluxes, luminosities and radial profiles, as well as comparison with IR data and information on the AGN presence within their nuclei.

The central part of the thesis focuses on the interaction of AGN jets with stellar populations. We consider the interaction caused by stars being within the jet, penetrating it, or exploding as supernovae within it. We study whether their dynamical evolution and impact on the jet, and estimate if their gamma-ray emission is detectable.

The last part estimates the possible contribution of AGN jets to the reionization of the Universe, given how their interaction with cosmic microwave background radiation can result in the production of ionizing photons.



## ACKNOWLEDGMENTS

---

In the first place, I would like to thank my supervisors Dr. Valentí Bosch i Ramon and Dr. Kazushi Iwasawa for their teachings and their guidance along these past four years. This thesis would not have been possible without their knowledge and willingness to share it. I would also like to thank Dr. Josep M. Paredes, who introduced me to the group and helped me throughout the first stages of my scientific career.

Part of the research presented in this thesis has been carried out in other institutions. I thank Dr. Andrea Comastri and Dr. Christian Vignali for their warm reception in Osservatorio Astronomico di Bologna, where I learnt both X-ray astronomy and properties of AGN at all wavelengths. I thank Dr. Manel Perucho, who kindly welcomed me to Valencia, and taught me about hydrodynamical simulations. I also thank Dr. Gustavo Romero, Dr. Daniela Pérez and Dr. Santiago del Palacio for welcoming me to Instituto Argentino de Radioastronomía in La Plata. In particular, I want to thank Dr. Florencia Vieyro, who has taught me all she knows about relativistic jets and who has become a very dear friend.

I would also like to thank the GOALS people; in particular Dr. Tanio Díaz Santos, Dr. Claudio Ricci and Dr. Vassilis Charmandaris, who helped improve the C-GOALS paper and gave me valuable advice. Tanio taught me all I know about infrared astronomy, and without him my understanding of U/LIRGs would be much poorer.

I would like to thank Benito, Xavi, Victor and Dani, my first office mates, who were always present when I struggled and never refused to help me when I asked. Their knowledge of programming and observational astronomy has been invaluable. Likewise, I want to thank Edgar, with whom I've shared MAGIC shifts, stays abroad and teaching duties, and who has always been reliable.

I also need to thank Nico and Jose, who have been there with me from the very beginning, and were always willing to lend me a hand. Special thanks to Laia, who was the friend I needed most and who is missed dearly. I thank also Roger, Lluís, Ignasi, Alfred, Pau, Samuel, Ali, Juan, David, Dani and everyone else who shares our everyday lives and helps make the PhD a truly enjoyable experience.

And of course, I thank JR, Rosa, Jordi and all the personnel in secretaries and informatics, who help us make science possible.



Aquesta tesi té com a objectiu l'estudi dels fenòmens altament energètics a les regions centrals de les galàxies actives. Les galàxies actives són aquelles que tenen una emissió molt intensa a les regions més centrals, i que és clarament diferent de l'emissió de la majoria de galàxies. Tant un episodi de formació estel·lar especialment intens (galàxia "starburst", de l'anglès per a "explosió estel·lar") com accreió de material sobre el forat negre supermassiu central (AGN, de l'anglès per a "nucli actiu de galàxia") poden donar lloc a aquesta activitat.

L'origen d'ambdós fenòmens es podria trobar en una fusió entre galàxies, que ocasiona que el gas sigui transportat a les regions centrals, facilitant la formació d'estrelles i l'accreió. Si els dos processos es troben íntimament lligats, i constitueixen un estadi necessari en l'evolució de les galàxies, és motiu de debat. L'estudi d'aquesta relació, per tant, és interessant en l'actualitat.

Independentment de l'origen de la seva connexió, el que és clar és que tant la formació estel·lar intensa com l'activitat AGN sovint coexisteixen en les regions centrals de les galàxies. Fins i tot quan la formació d'estrelles s'ha acabat, els starbursts als nuclis resulten en la formació dels bulbs galàctics. Per tant, els kiloparsecs centrals de les galàxies típicament tenen densitats estel·lars elevades. Com que les estrelles, o la formació estel·lar, són properes a l'AGN, l'interacció entre els dos és freqüent, i pot donar lloc a una multitud de fenòmens interessants d'estudiar.

Aquesta tesi, doncs, s'enfoca en l'estudi dels processos altament energètics que tenen lloc en regions on la formació estel·lar i l'activitat AGN són especialment intenses. En particular, l'objectiu és l'estudi de l'emissió produïda per aquests fenòmens, sobretot en raigs X i raigs gamma, bé per tal de distingir les seves contribucions individuals, o per detectar l'emissió resultant de la seva interacció. La tesi pretén proporcionar dades per a continuar l'estudi de la relació starburst-AGN, i nous models per a explicar la producció de raigs gamma en altres galàxies.

Aquesta tesi està dividida en cinc parts, després del capítol introductori.

La primera part se centra en l'estudi en raigs X d'una mostra local de galàxies lluminoses en infraroig (LIRGs, de les sigles en anglès), publicat com a Torres-Albà et al. (2018). GOALS (sigles en anglès de "mostra de LIRGs a tot el cel usant grans observatoris") és un projecte que té com a objectiu estudiar les galàxies més brillants en infraroig a redshift (o desplaçament al roig)  $z < 0.1$ , en totes les longituds d'ona

possibles. L'estudi en raigs X de les galàxies més brillants dins la mostra es va publicar en Iwasawa et al. (2011). En el nou article analitzem dades de 63 LIRGs en el rang de menor lluminositat de GOALS. Proporcionem imatges, fluxos, lluminositats i perfils radials per a 84 galàxies individuals, amb tipus d'activitat i estadis d'interacció molt diversos. També proporcionem informació sobre la presència d'AGN en elles, mitjançant dades de raigs X i infraroig, i comparem els resultats obtinguts amb els de la mostra d'alta lluminositat.

La segona part se centra en l'interacció de jets d'AGN, feixos col·limats de partícules altament relativistes, amb poblacions estel·lars. El primer treball és publicat com Vieyro, Torres-Albà, and Bosch-Ramon (2017), i té com a objectiu l'estudi de l'emissió en raigs gamma i la càrrega de massa del jet deguda a la presència d'estrelles dins el jet. Primer de tot, modelem les poblacions estel·lars amb grans pèrdues de massa en els centres de les galàxies; estrelles OB en el nucli de LIRGs i estrelles gegants vermelles en el bulb de galàxies el·líptiques. Després estimem quantes d'aquestes estrelles, estadísticament, es troben dins el jet en tot moment. Les estrelles són impactades pel jet i es desenvolupen xocs, on les partícules poden ser accelerades a velocitats relativistes. Estimem l'emissió gamma que pot donar a lloc aquest procés, i la càrrega de massa al jet, per als dos tipus de galàxia mencionats.

En el segon treball de la segona part, publicat com Torres-Albà et al. (2018), considerem la interacció que té lloc no quan les estrelles són dins el jet, sinó en el moment en què hi penetren. Quan les estrelles es mouen a través del medi interestel·lar (ISM, de les sigles en anglès), els seus vents l'impacten i es forma un xoc en què tant material del vent com de l'ISM s'acumulen (bombolles). Aquest material pot ser expulsat dins el jet després de la penetració, i és accelerat cap amunt degut al moment adquirit en l'impacte amb el jet. En el xoc que es forma, de nou, es poden accelerar partícules que emetin de manera no tèrmica. Usem la població estel·lar prèviament desenvolupada per modelar galàxies el·líptiques per estimar el ritme en que entren al jet, i després modelem l'evolució dinàmica i emissió de les bombolles.

La tercera part se centra en la interacció d'un sol objecte amb el jet; un residu de supernova (SNR, de les sigles en anglès). Dos treballs, el primer publicat com a Vieyro, Bosch-Ramon, and Torres-Albà (2019) i el segon enviat a A&A per a publicar, estudien aquest procés en LIRGs i galàxies el·líptiques, respectivament. Modelem l'evolució dinàmica del SNR i calculem l'emissió generada en el xoc. Després estimem la freqüència dels esdeveniments i el nombre esperat de fonts detectables. Vieyro, Bosch-Ramon, and Torres-Albà (2019) inclou simulacions hidrodinàmiques de la interacció, que mostren com s'espera que afecti el jet.

La quarta part s'enfoca en l'interacció dels jets d'AGN amb el medi, però en aquest cas a gran escala, considerant-los possibles fonts de reionització a  $z \sim 6$ . Inclou un article, enviat a A&A, en el que es-

timem el nombre de fonts amb jet presents en l'època de la reionització mitjançant deteccions en òptic d'AGN. Després corregim la densitat de fonts observada per efectes d'obscuriment usant dades en raigs X. Els jets a alt redshift interactuen molt fortament amb la radiació del fons còsmic de microones, augmentant l'energia dels seus fotons a longituds d'ona ionitzants a través del procés de Compton invers. Per tant, poden significar una contribució significativa a la reionització de l'Univers.

La cinquena part inclou un resum i discussió dels resultats obtinguts en la tesi, així com de les conclusions derivades i perspectives futures de continuar la feina feta.



## PUBLICATIONS

---

Complete list of publications at the moment of thesis deposit.

### Articles in this thesis

- Torres-Albà, N. et al. (2018). “C-GOALS. II. Chandra observations of the lower luminosity sample of nearby luminous infrared galaxies in GOALS.” In: *A&A* 620, A140, A140. DOI: [10.1051/0004-6361/201834105](https://doi.org/10.1051/0004-6361/201834105). arXiv: [1810.02371](https://arxiv.org/abs/1810.02371) [astro-ph.GA].
- Torres-Albà, Núria and Valentí Bosch-Ramon (2019). “Gamma rays from red giant wind bubbles entering the jets of elliptical host blazars.” In: *A&A* 623, A91, A91. DOI: [10.1051/0004-6361/201833697](https://doi.org/10.1051/0004-6361/201833697). arXiv: [1902.05008](https://arxiv.org/abs/1902.05008) [astro-ph.HE].
- Vieyro, F. L., V. Bosch-Ramon, and N. Torres-Albà (2019). “Non-thermal emission resulting from a supernova explosion inside an extragalactic jet.” In: *A&A* 622, A175, A175. DOI: [10.1051/0004-6361/201833319](https://doi.org/10.1051/0004-6361/201833319). arXiv: [1901.09003](https://arxiv.org/abs/1901.09003) [astro-ph.HE].
- Vieyro, Florencia L., Núria Torres-Albà, and Valentí Bosch-Ramon (2017). “Collective non-thermal emission from an extragalactic jet interacting with stars.” In: *A&A* 604, A57, A57. DOI: [10.1051/0004-6361/201630333](https://doi.org/10.1051/0004-6361/201630333). arXiv: [1704.01919](https://arxiv.org/abs/1704.01919) [astro-ph.HE].

### Conference Proceedings

- MAGIC Collaboration et al. (2019a). “A fast, very-high-energy  $\gamma$ -ray flare from BL Lacertae during a period of multi-wavelength activity in June 2015.” In: *A&A* 623, A175, A175. DOI: [10.1051/0004-6361/201834010](https://doi.org/10.1051/0004-6361/201834010). arXiv: [1901.01733](https://arxiv.org/abs/1901.01733) [astro-ph.HE].
- MAGIC Collaboration et al. (2019b). “Deep observations of the globular cluster M15 with the MAGIC telescopes.” In: *MNRAS* 484.2, pp. 2876–2885. DOI: [10.1093/mnras/stz179](https://doi.org/10.1093/mnras/stz179). arXiv: [1901.04367](https://arxiv.org/abs/1901.04367) [astro-ph.HE].
- MAGIC Collaboration et al. (2019c). “Discovery of TeV  $\gamma$ -ray emission from the neighbourhood of the supernova remnant G24.7+0.6 by MAGIC.” In: *MNRAS* 483.4, pp. 4578–4585. DOI: [10.1093/mnras/sty3387](https://doi.org/10.1093/mnras/sty3387). arXiv: [1812.04854](https://arxiv.org/abs/1812.04854) [astro-ph.HE].
- Torres-Albà, N. and V. Bosch-Ramon (2018). “Emission from stellar wind bubbles interacting with an extragalactic jet.” In: *International Journal of Modern Physics D* 27.10, 1844018, p. 1844018. DOI: [10.1142/S0218271818440182](https://doi.org/10.1142/S0218271818440182).

- Torres-Albà, N., V. Bosch-Ramon, and F. L. Vieyro (2017). “Characterizing the stellar populations interacting with AGN jets.” In: *6th International Symposium on High Energy Gamma-Ray Astronomy*. Vol. 1792. American Institute of Physics Conference Series, p. 050031. DOI: [10.1063/1.4968977](https://doi.org/10.1063/1.4968977).
- Torres-Albà, N. and K. Iwasawa (2017). “An X-ray study of the lower-luminosity LIRGs from GOALS.” In: *Highlights on Spanish Astrophysics IX*, pp. 269–274.
- Vieyro, F. L., V. Bosch-Ramon, and N. Torres-Albà (2018). “Non-thermal emission produced by the interaction of a jet with a supernova remnant.” In: *International Journal of Modern Physics D* 27.10, 1844021–365, pp. 1844021–365. DOI: [10.1142/S0218271818440212](https://doi.org/10.1142/S0218271818440212).
- Vieyro, F. L., N. Torres-Albà, and V. Bosch-Ramon (2017). “Non-thermal emission from the interaction of extragalactic jets with stars.” In: *6th International Symposium on High Energy Gamma-Ray Astronomy*. Vol. 1792. American Institute of Physics Conference Series, p. 050012. DOI: [10.1063/1.4968958](https://doi.org/10.1063/1.4968958).

### Articles as part of the MAGIC collaboration

- Abeyssekara, A. U. et al. (2017). “A Search for Spectral Hysteresis and Energy-dependent Time Lags from X-Ray and TeV Gamma-Ray Observations of Mrk 421.” In: *ApJ* 834.1, 2, p. 2. DOI: [10.3847/1538-4357/834/1/2](https://doi.org/10.3847/1538-4357/834/1/2). arXiv: [1611.04626](https://arxiv.org/abs/1611.04626) [astro-ph.HE].
- Abeyssekara, A. U. et al. (2018). “Periastron Observations of TeV Gamma-Ray Emission from a Binary System with a 50-year Period.” In: *ApJ* 867.1, L19, p. L19. DOI: [10.3847/2041-8213/aae70e](https://doi.org/10.3847/2041-8213/aae70e). arXiv: [1810.05271](https://arxiv.org/abs/1810.05271) [astro-ph.HE].
- Acciari, V. A. et al. (2018). “Constraining dark matter lifetime with a deep gamma-ray survey of the Perseus galaxy cluster with MAGIC.” In: *Physics of the Dark Universe* 22, pp. 38–47. DOI: [10.1016/j.dark.2018.08.002](https://doi.org/10.1016/j.dark.2018.08.002). arXiv: [1806.11063](https://arxiv.org/abs/1806.11063) [astro-ph.HE].
- Acciari, V. A. et al. (2019a). “Measurement of the Extragalactic Background Light using MAGIC and Fermi-LAT gamma-ray observations of blazars up to  $z = 1$ .” In: *MNRAS*, p. 910. DOI: [10.1093/mnras/stz943](https://doi.org/10.1093/mnras/stz943). arXiv: [1904.00134](https://arxiv.org/abs/1904.00134) [astro-ph.HE].
- Acciari, V. A. et al. (2019b). “Measurement of the extragalactic background light using MAGIC and Fermi-LAT gamma-ray observations of blazars up to  $z = 1$ .” In: *MNRAS* 486.3, pp. 4233–4251. DOI: [10.1093/mnras/stz943](https://doi.org/10.1093/mnras/stz943). arXiv: [1904.00134](https://arxiv.org/abs/1904.00134) [astro-ph.HE].
- Ahnen, M. L. et al. (2017a). “A cut-off in the TeV gamma-ray spectrum of the SNR Cassiopeia A.” In: *MNRAS* 472.3, pp. 2956–2962. DOI: [10.1093/mnras/stx2079](https://doi.org/10.1093/mnras/stx2079). arXiv: [1707.01583](https://arxiv.org/abs/1707.01583) [astro-ph.HE].
- Ahnen, M. L. et al. (2017b). “First multi-wavelength campaign on the gamma-ray-loud active galaxy IC 310.” In: *A&A* 603, A25, A25. DOI: [10.1051/0004-6361/201630347](https://doi.org/10.1051/0004-6361/201630347). arXiv: [1703.07651](https://arxiv.org/abs/1703.07651) [astro-ph.HE].

- Ahnen, M. L. et al. (2017c). “MAGIC observations of the microquasar V404 Cygni during the 2015 outburst.” In: *MNRAS* 471.2, pp. 1688–1693. DOI: [10.1093/mnras/stx1690](https://doi.org/10.1093/mnras/stx1690). arXiv: [1707.00887](https://arxiv.org/abs/1707.00887) [astro-ph.HE].
- Ahnen, M. L. et al. (2017d). “Multiwavelength observations of a VHE gamma-ray flare from PKS 1510-089 in 2015.” In: *A&A* 603, A29, A29. DOI: [10.1051/0004-6361/201629960](https://doi.org/10.1051/0004-6361/201629960). arXiv: [1610.09416](https://arxiv.org/abs/1610.09416) [astro-ph.HE].
- Ahnen, M. L. et al. (2017e). “Observation of the black widow B1957+20 millisecond pulsar binary system with the MAGIC telescopes.” In: *MNRAS* 470.4, pp. 4608–4617. DOI: [10.1093/mnras/stx1405](https://doi.org/10.1093/mnras/stx1405). arXiv: [1706.01378](https://arxiv.org/abs/1706.01378) [astro-ph.HE].
- Ahnen, M. L. et al. (2017f). “Performance of the MAGIC telescopes under moonlight.” In: *Astroparticle Physics* 94, pp. 29–41. DOI: [10.1016/j.astropartphys.2017.08.001](https://doi.org/10.1016/j.astropartphys.2017.08.001). arXiv: [1704.00906](https://arxiv.org/abs/1704.00906) [astro-ph.IM].
- Ahnen, M. L. et al. (2017g). “Search for very high-energy gamma-ray emission from the microquasar Cygnus X-1 with the MAGIC telescopes.” In: *MNRAS* 472.3, pp. 3474–3485. DOI: [10.1093/mnras/stx2087](https://doi.org/10.1093/mnras/stx2087). arXiv: [1708.03689](https://arxiv.org/abs/1708.03689) [astro-ph.HE].
- Ahnen, M. L. et al. (2018a). “Extreme HBL behavior of Markarian 501 during 2012.” In: *A&A* 620, A181, A181. DOI: [10.1051/0004-6361/201833704](https://doi.org/10.1051/0004-6361/201833704). arXiv: [1808.04300](https://arxiv.org/abs/1808.04300) [astro-ph.HE].
- Ahnen, M. L. et al. (2018b). “Indirect dark matter searches in the dwarf satellite galaxy Ursa Major II with the MAGIC telescopes.” In: *Journal of Cosmology and Astro-Particle Physics* 2018.3, 009, p. 009. DOI: [10.1088/1475-7516/2018/03/009](https://doi.org/10.1088/1475-7516/2018/03/009). arXiv: [1712.03095](https://arxiv.org/abs/1712.03095) [astro-ph.HE].
- Ahnen, M. L. et al. (2018c). “Limits on the flux of tau neutrinos from 1 PeV to 3 EeV with the MAGIC telescopes.” In: *Astroparticle Physics* 102, pp. 77–88. DOI: [10.1016/j.astropartphys.2018.05.002](https://doi.org/10.1016/j.astropartphys.2018.05.002). arXiv: [1805.02750](https://arxiv.org/abs/1805.02750) [astro-ph.IM].
- Ahnen, M. L. et al. (2019). “MAGIC and Fermi-LAT gamma-ray results on unassociated HAWC sources.” In: *MNRAS* 485.1, pp. 356–366. DOI: [10.1093/mnras/stz089](https://doi.org/10.1093/mnras/stz089). arXiv: [1901.03982](https://arxiv.org/abs/1901.03982) [astro-ph.HE].
- IceCube Collaboration et al. (2018). “Multimessenger observations of a flaring blazar coincident with high-energy neutrino IceCube-170922A.” In: *Science* 361.6398, eaat1378, eaat1378. DOI: [10.1126/science.aat1378](https://doi.org/10.1126/science.aat1378). arXiv: [1807.08816](https://arxiv.org/abs/1807.08816) [astro-ph.HE].
- MAGIC Collaboration et al. (2017). “Constraining Lorentz Invariance Violation Using the Crab Pulsar Emission Observed up to TeV Energies by MAGIC.” In: *ApJS* 232.1, 9, p. 9. DOI: [10.3847/1538-4365/aa8404](https://doi.org/10.3847/1538-4365/aa8404). arXiv: [1709.00346](https://arxiv.org/abs/1709.00346) [astro-ph.HE].
- MAGIC Collaboration et al. (2018a). “Constraining very-high-energy and optical emission from FRB 121102 with the MAGIC telescopes.” In: *MNRAS* 481.2, pp. 2479–2486. DOI: [10.1093/mnras/sty2422](https://doi.org/10.1093/mnras/sty2422). arXiv: [1809.00663](https://arxiv.org/abs/1809.00663) [astro-ph.HE].

- MAGIC Collaboration et al. (2018b). “Constraints on particle acceleration in SS433/W50 from MAGIC and H.E.S.S. observations.” In: *A&A* 612, A14, A14. DOI: [10.1051/0004-6361/201731169](https://doi.org/10.1051/0004-6361/201731169). arXiv: [1707.03658](https://arxiv.org/abs/1707.03658) [astro-ph.HE].
- MAGIC Collaboration et al. (2018c). “Detection of persistent VHE gamma-ray emission from PKS 1510-089 by the MAGIC telescopes during low states between 2012 and 2017.” In: *A&A* 619, A159, A159. DOI: [10.1051/0004-6361/201833618](https://doi.org/10.1051/0004-6361/201833618). arXiv: [1806.05367](https://arxiv.org/abs/1806.05367) [astro-ph.GA].
- MAGIC Collaboration et al. (2018d). “Detection of the blazar S4 0954+65 at very-high-energy with the MAGIC telescopes during an exceptionally high optical state.” In: *A&A* 617, A30, A30. DOI: [10.1051/0004-6361/201832624](https://doi.org/10.1051/0004-6361/201832624). arXiv: [1801.04138](https://arxiv.org/abs/1801.04138) [astro-ph.HE].
- MAGIC Collaboration et al. (2018e). “Gamma-ray flaring activity of NGC1275 in 2016-2017 measured by MAGIC.” In: *A&A* 617, A91, A91. DOI: [10.1051/0004-6361/201832895](https://doi.org/10.1051/0004-6361/201832895). arXiv: [1806.01559](https://arxiv.org/abs/1806.01559) [astro-ph.HE].
- MAGIC Collaboration et al. (2018f). “Multi-wavelength characterization of the blazar S5 0716+714 during an unprecedented outburst phase.” In: *A&A* 619, A45, A45. DOI: [10.1051/0004-6361/201832677](https://doi.org/10.1051/0004-6361/201832677). arXiv: [1807.00413](https://arxiv.org/abs/1807.00413) [astro-ph.HE].
- MAGIC Collaboration et al. (2018g). “The broad-band properties of the intermediate synchrotron peaked BL Lac S2 0109+22 from radio to VHE gamma-rays.” In: *MNRAS* 480.1, pp. 879–892. DOI: [10.1093/mnras/sty1753](https://doi.org/10.1093/mnras/sty1753). arXiv: [1807.02095](https://arxiv.org/abs/1807.02095) [astro-ph.HE].

# CONTENTS

---

|       |   |     |
|-------|---|-----|
| 1     | INTRODUCTION  | 1   |
| 1.1   | Active Galactic Nuclei  | 2   |
| 1.1.1 | Spectral energy distribution of AGN   | 3   |
| 1.2   | Starbursts and their connection to AGN  | 5   |
| 1.2.1 | Spectral energy distribution of starbursts  | 6   |
| 1.3   | AGN jets  | 7   |
| 1.3.1 | Interaction with obstacles: mass loading and deceleration   | 9   |
| 1.3.2 | Particle acceleration and non-thermal emission  | 10  |
| 1.4   | Motivation, Goals and Structure of the Thesis   | 12  |
| I     | X-RAY STUDY OF LIRGS  | 15  |
| 2     | C-GOALS II. CHANDRA OBSERVATIONS OF THE LOWER LUMINOSITY SAMPLE OF NEARBY LUMINOUS INFRARED GALAXIES IN GOALS | 17  |
| II    | INTERACTION OF AGN JETS WITH STELLAR POPULATIONS  | 85  |
| 3     | COLLECTIVE NON-THERMAL EMISSION FROM AN EXTRAGALACTIC JET INTERACTING WITH STARS                              | 87  |
| 4     | GAMMA RAYS FROM RED GIANT WIND BUBBLES ENTERING THE JETS OF ELLIPTICAL HOST BLAZARS                           | 103 |
| III   | INTERACTION OF AGN JETS WITH A SNR  | 113 |
| 5     | NON-THERMAL EMISSION RESULTING FROM A SUPERNOVA EXPLOSION INSIDE AN EXTRAGALACTIC JET                         | 115 |
| 6     | TYPE IA SUPERNOVA EXPLOSION INSIDE AN EXTRAGALACTIC JET   | 131 |
| IV    | IMPACT OF AGN JETS IN REIONIZATION  | 141 |
| 7     | AGN JETS VERSUS ACCRETION AS REIONIZATION SOURCES   | 143 |
| V     | SUMMARY OF RESULTS, DISCUSSION AND CONCLUSIONS  | 151 |
| 8     | SUMMARY, DISCUSSION AND CONCLUSIONS   | 153 |
| 8.1   | Infrared and X-ray emission from nearby LIRGs   | 153 |
| 8.1.1 | AGN detection in the sample   | 153 |
| 8.1.2 | IR to X-ray luminosity correlation  | 154 |
| 8.1.3 | Soft-band emission  | 155 |
| 8.2   | Interaction of AGN jets with obstacles  | 156 |
| 8.2.1 | Non-thermal emission  | 157 |
| 8.2.2 | Observational distinctions between scenarios  | 158 |
| 8.2.3 | Usability of simplified models  | 159 |

|       |                                  |     |
|-------|----------------------------------|-----|
| 8.2.4 | Jet mass-loading                 | 160 |
| 8.2.5 | Modeling of stellar populations  | 160 |
| 8.3   | AGN jets as reionization sources | 161 |

|              |     |
|--------------|-----|
| BIBLIOGRAPHY | 163 |
|--------------|-----|

## INTRODUCTION

---

Active galaxies are those that have a distinct central emission, visibly different and superposed to that of an otherwise typical galaxy. The first evidence of such an additional, strongly emitting component was found by Carl Seyfert in the centre of six spiral galaxies (Seyfert, 1943). Their overall emission was intense, and particularly concentrated in the central regions. The spectra showed high-excitation emission lines, with widths of  $\sim 1000 \text{ km s}^{-1}$ , unlike those of any object previously detected.

It is now known that the lines observed by Seyfert have its origin in the presence of a supermassive, accreting black-hole (Salpeter, 1964; Zel'dovich and Novikov, 1964; Lynden-Bell, 1969). The high speeds in the orbits around the deep gravitational potential are responsible for the extreme broadening of the emission lines, which are emitted by the illuminated gas clouds orbiting the black hole. Accretion of nearby material onto the compact object can also account for the high luminosities.

Over the following decades, a large variety of subtypes of active galaxies was discovered, with bolometric luminosities in the range  $L_{\text{bol}} \sim 10^{41} - 10^{48} \text{ erg s}^{-1}$ . The wide range of luminosities and different observational properties resulted in a diverse and complex classification (e.g. Seyfert 1 and 2, radio-loud and radio-quiet, blazars, quasars...), which were difficult to unify into one single model (see Tadhunter, 2008, for a brief review on classification and unification of active galaxies). At the faintest end of the current classification stand low-ionization emission-line region (LINER) galaxies, which are assumed to be the link between galaxies with bright H II regions and Seyferts.

H II regions are prominent in starburst galaxies, those whose luminosity is dominated by an episode of star formation so intense that it cannot be sustained over their lifetimes (e.g. Moorwood, 1996). Their intense nuclear star formation is considered a type of activity, as H II regions also present intense emission lines, for which they are easily mistaken for Seyfert galaxies. The lines also arise from excitation of ambient gas, which is ionized by energetic photons. The ionizing sources in such a case are, however, hot, massive OB stars embedded within dense star-forming regions (see Shields, 1990, for a review on their properties).

## 1.1 ACTIVE GALACTIC NUCLEI

While activity in a galaxy can be associated both to the presence of an accreting black hole or of intense star formation, it is the former that is generally referred to as an active galactic nucleus (AGN).

AGN are one of the most luminous, persistent sources in the Universe; emitting intensely in the whole range of the electromagnetic spectrum. The large energy output has its origin in the accretion of nearby material onto a supermassive black hole (SMBH;  $M_{\text{SMBH}} \sim 10^5 - 10^{10} M_{\odot}$ ). Infalling gas settles around it in the form of an accretion disk and spirals inwards as it loses energy, heating up to extreme temperatures through friction (Shakura and Sunyaev, 1973). The disk emits thermally, through a superposition of black-body spectra, in the range of IR to UV.

A schematic representation of an AGN is depicted in Fig. 1. The SMBH, along with its accretion disk, lays within a dusty "torus", which obscures certain lines of sight. This configuration leads to some of the observational differences between AGN subtypes (see Sect. 1.1.1, and Antonucci, 1993). Gas clouds, responsible for the optical/UV line emission, orbit the central engine at different distances. A jet of relativistic charged particles is present in radio-loud AGN.

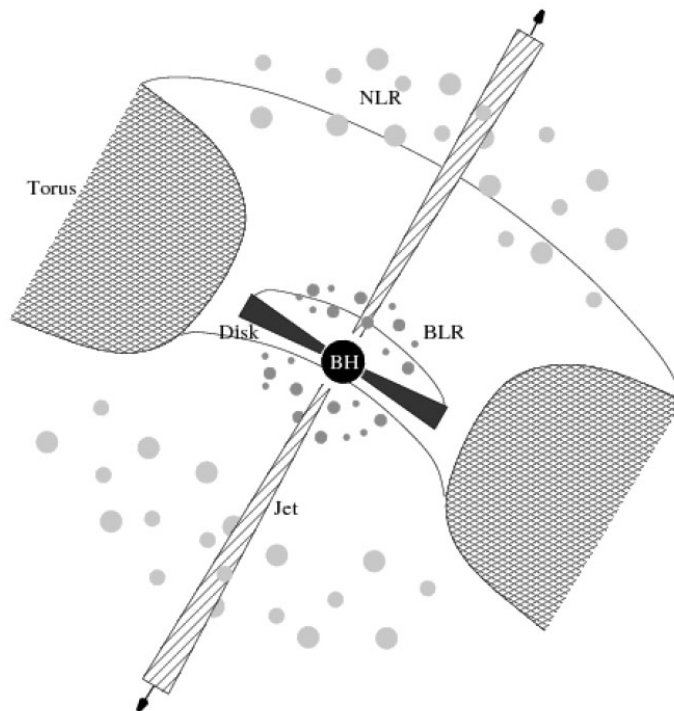


Figure 1: Representation of the inner structure of an AGN. Figure from Middelberg and Bach (2008), according to the unification model proposed by Antonucci and Miller (1985).

### 1.1.1 Spectral energy distribution of AGN

AGN spectra are notably different from those of normal galaxies; emitting from radio to TeV energies, and with a much higher energy output. A representation of the spectral energy distribution (SED) of the average AGN is shown in Fig. 2.

AGN continuum shows a broad infrared (IR) bump, raising from  $\sim 1 \mu\text{m}$  and peaking at  $\sim 60 \mu\text{m}$ , which rapidly decreases at lower energies. The IR spectrum is consistent with thermal emission from dust and gas, believed to form a torus around the SMBH, and which is heated by the ionizing radiation from the accretion disk (e.g. Efstathiou and Rowan-Robinson, 1995). Superposed to this continuum is molecular and atomic line emission, complex due to the large number of rotational and oscillatory modes associated to the molecules (e.g. Sturm et al., 2002).

Optical spectra of AGN are characterized by the presence of strong emission lines. If observing the source edge-on (type 2 AGN), the dusty torus obscures the disk emission as well as the broad line region (BLR). Then only the narrow line region (NLR) is visible, its lines being produced by gas clouds orbiting the blackhole at distances not obscured by the torus. The broad lines originate in faster clouds, which are closer to the central engine, hence the larger Doppler broadening (Antonucci and Miller, 1985). If the source is observed face-on (type 1 AGN), both narrow and broad line region lines are observed, as well as the "big blue bump", the thermal emission from the accretion disk (e.g. Shields, 1978). The Optical/UV emission can be even more prominent than IR when observable.

The ultraviolet (UV) spectrum includes the peak of emission of the big blue bump, as well as emission lines. However, UV wavelengths are often obscured by dust in the host galaxy or, in the case of the Extreme UV (EUV,  $100 - 1200 \text{\AA}$ ), even by the foreground interstellar medium (ISM) of our own galaxy. Therefore, UV emission from AGN often remains unobserved.

X-ray emission mostly arises from multiple inverse Compton (IC) upscatterings of accretion disk photons by hot electrons. These electrons are thought to form a hot plasma near the accretion disk, called the corona, though its exact configuration is presently unknown (Liang and Price, 1977; Liang, 1979). Multiple IC upscatterings yield a power-law spectrum, of photon-index in the range  $\Gamma = 1.7 - 2.0$  (Nandra and Pounds, 1994), with a high-energy cutoff at energies of the order of  $\sim 100 \text{ keV}$ .

A broad X-ray hump is seen at energies  $\sim 20 - 40 \text{ keV}$  due to reflection of the upscattered photons onto the cold material of the disk, which generally results in an overall hardening of the spectrum (e.g. George and Fabian, 1991). This reflection also produces intense emission lines, the most prominent of which is the  $\text{FeK}_{\alpha}$  at  $6.4 \text{ keV}$ , which

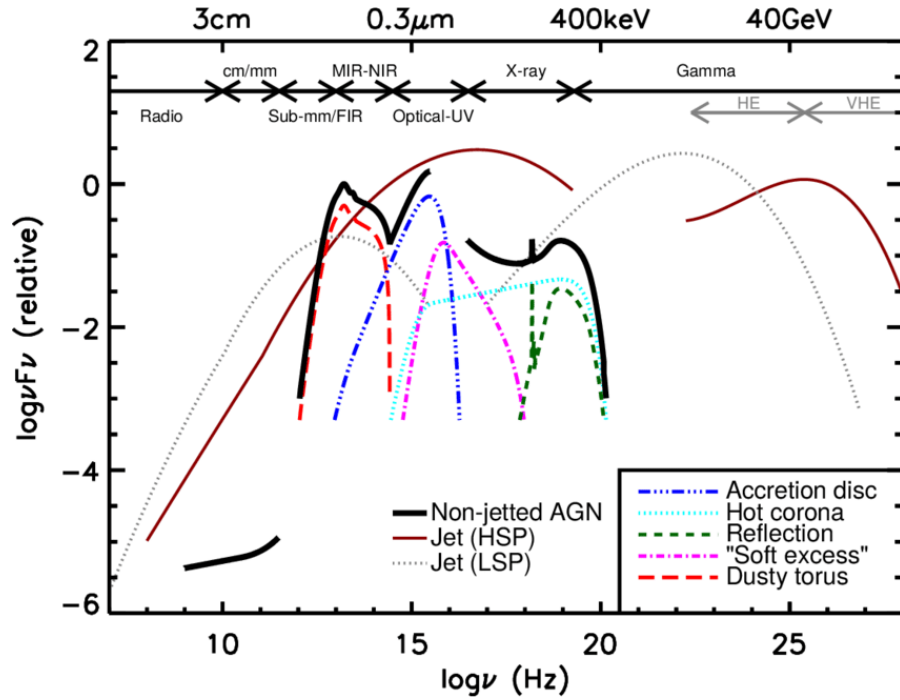


Figure 2: Representation of an AGN SED. The coloured curves correspond to the different components described in the text, while the black curve is the overall continuum (note the generally unobserved EUV emission). The SED is compared to those of high (HSP, red) and low (LSP, dotted grey) synchrotron peaked blazars, in which the a relativistic jet facing the observer dominates the emission. Figure from Padovani et al. (2017), adapted from Harrison (2014).

is often used as a clear indicator to diagnose the presence of an AGN (e.g. George and Fabian, 1991). Another X-ray component observed in AGN is the "soft excess", an emission excess at energies  $\leq 2$  KeV. Its origin is still debated, although it is frequently explained as Comptonized emission from warm electrons in the surface of the accretion disk (Rózańska et al., 2015; Petrucci et al., 2018), or reflection from ionized disk material (e.g. Fabian et al., 2009).

In a type 2 AGN, the softer X-ray emission (below  $\sim 10$  KeV) is obscured by the torus. If the column density is large enough (i.e.  $N_{\text{H}} \geq 1.5 \times 10^{24} \text{ cm}^{-2}$ , or a "Compton-thick" source) very little emission escapes below 10 KeV (see e.g. Gandhi, 2005, for a description of X-ray spectra of AGN).

Radio emission is of synchrotron origin and, in radio-quiet AGN, it is 5 – 6 orders of magnitude fainter than emission at other wavelengths. Its origin is not fully understood in this kind of AGN, though it is believed to be produced either by an unresolved compact jet (e.g. Smith et al., 1998), or by highly relativistic electrons in the corona (e.g. Laor and Behar, 2008).

Gamma-ray emission is not detected from AGN unless they present jets, in which case both gamma-ray and radio emission become prominent (see Sect. 1.3).

## 1.2 STARBURSTS AND THEIR CONNECTION TO AGN

AGN and star-formation activity are often found together in galaxies, although in highly variable proportions. The connection was first suggested by Sanders et al. (1988), who argued that a merger between two gas-rich galaxies could provide fuel for both an intense, nuclear starburst and an AGN.

Bursts of intense star formation were first proposed to explain IR luminosities that seemed too high for a galaxy to be sustained over long periods of time (i.e. the star formation rate, SFR, would exhaust all the available gas in less than the dynamical timescale of the galaxy; e.g. Harwit and Pacini, 1975). Starbursts can be of different magnitudes, from  $\text{SFR} \sim 10 M_{\odot} \text{ yr}^{-1}$  in nearby sources, to the extreme  $\text{SFR} \sim 100 - 1000 M_{\odot} \text{ yr}^{-1}$  of luminous and ultra-luminous infrared galaxies (LIRGs and ULIRGs).

U/LIRGs are characterized by large infrared luminosities, namely  $L_{\text{IR}} \geq 10^{12}/10^{11} L_{\odot}$ . The intense infrared emission is often the result of galaxy interactions, as mergers have been proved to funnel gas toward the innermost regions of galaxies, triggering extreme star formation (e.g. Sanders and Mirabel, 1996).

The scenario proposed by, for example, Sanders (1999) and Hopkins et al. (2005) places U/LIRGs at an important stage in galaxy evolution as the precursors of AGN. A merger provides large quantities of gas, which also triggers accretion onto the SMBH. Due to the abundance of material, its emission remains highly obscured, with the properties of a type 2 AGN (e.g. Di Matteo, Springel, and Hernquist, 2005). Feedback, both from starburst winds (i.e. supernova explosions and OB stellar winds) and the jet itself eventually clear up the gas surrounding the nucleus, giving rise to an exposed (or type 1) AGN (e.g. Hopkins, Quataert, and Murray, 2012; Fabian, 2012; Ishibashi and Fabian, 2016). Mergers are considered to eventually lead to the formation of an elliptical galaxy, and to account for the growth of the central supermassive black hole (e.g. Kormendy et al., 2009; Hopkins et al., 2009). In this scenario, the type 1–2 AGN dichotomy is the result of a combination between viewing angle and evolutionary stage.

Note, however, that some works find no direct relation between major mergers and AGN activity (see e.g. Marian et al., 2019, and references therein), and thus this topic is still subject to debate. What is true is that AGN and starburst activity are expected to frequently occur together, and that they are often difficult to disentangle.

### 1.2.1 Spectral energy distribution of starbursts

The starburst is brightest in IR wavelengths, contributing to galaxy the continuum as the UV photons from massive stars heat the dust (Soifer et al., 1986), and also responsible for line emission (most notably of polycyclic aromatic hydrocarbons, or PAH; e.g. Stierwalt et al., 2013). The IR emission can be difficult to differentiate from that of the AGN torus, as the number of lines is large and they merge together due to constraints in spectroscopy resolution. Generally, comparisons of line ratios in the IR are used to determine which phenomenon dominates the energetic output of the source (see e.g. Laurent et al., 2000; Díaz-Santos et al., 2017).

Optical and UV emission is dominated by starlight, although UV is highly absorbed by the large quantities of material present in the nuclear region. Optical line ratios are also often used to differentiate between star formation and AGN as the origin of the emission (Veilleux and Osterbrock, 1987).

The starburst can also be a prominent X-ray emitter, since given the enhanced star formation, phenomena related to the later stages of stellar evolution are abundant (see e.g. Persic and Rephaeli, 2002, for a detailed review).

The high supernova (SN) rate and the powerful winds of massive stars efficiently shock the ISM gas, which is heated up and emits thermally (with  $kT \lesssim 1$  keV) through bremsstrahlung radiation (e.g. Mewe, Gronenschild, and van den Oord, 1985; Cappi et al., 1999). The resulting spectrum, filled with emission lines superposed to a continuum, dominates the soft (0.5 – 2 keV) emission.

The hard band emission is thought to be non-thermal, and dominated by X-ray binaries. These systems are formed by stars with high mass-loss rates, which transfer material onto a compact object. The resulting spectrum has a thermal component (with  $kT \lesssim 1$  keV) originating in the accretion disk (e.g. Ebisawa et al., 1994), and a powerlaw component with photon index  $\Gamma = 1.5 - 2.5$  that extends up to several hundred keV (e.g. Wilson and Rothschild, 1983), and could be the result of IC scattering by corona electrons.

Radio emission is also composed by superposition of individual point sources, and generally dominated by synchrotron, mostly from electrons accelerated in SN remnants (SNR) shocks (e.g. Condon, 1992; Bressan, Silva, and Granato, 2002). A thermal component from free-free emission in HII regions can be important in the early phases of the starburst (e.g. Rubin, 1968).

The very high energy (VHE) electrons accelerated in SN explosions can upscatter FIR photons up to GeV and TeV energies, although models suggest that the dominant gamma-ray emission in starbursts is of hadronic origin (see Ohm, 2016, and references therein). The shocks that accelerate electrons also produce cosmic rays (CR, Bland-

ford and Eichler, 1987). Energetic protons and heavier nuclei undergo proton-proton interactions with ISM particles and produce neutral and charged mesons, of which  $\pi^0$  then decays into two gamma-rays. Only a handful of nearby starburst galaxies have been detected so far at gamma-ray wavelengths, due to their faint emission (in comparison with e.g. blazars or galactic sources). Among them, only NGC 253 (Acero et al., 2009) and M 82 (VERITAS Collaboration et al., 2009) have been detected at TeV energies.

A schematic representation of the SED of a starburst galaxy can be found in Fig. 3.

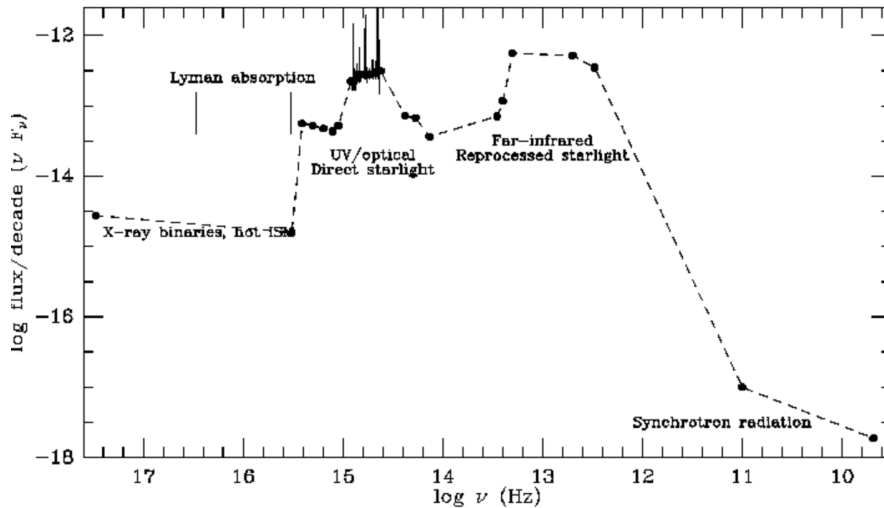


Figure 3: SED of NGC 7714, a typical starburst galaxy. The black points and emission lines correspond to data taken from NED. Image credit: William C. Keel.<sup>1</sup>

### 1.3 AGN JETS

AGN can emit relativistic jets; bipolar, extremely energetic plasma outflows that are produced near the central engine and can extend up to hundreds of kiloparsecs. The first image reported in the literature was of the optical jet of M87 (Curtis, 1918).

AGN with jets are called radio-loud (and those without, radio-quiet), since jets are particularly prominent radio emitters. The first powerful AGN at moderate redshift (i.e. quasars) were discovered, in fact, thanks to their radio emission (Schmidt, 1963; Greenstein, 1963).

Nearby AGN with jets not pointing toward the observer are generally referred to as radio galaxies. The morphology and power of the jet are used to classify them into two categories (Fanaroff and Riley, 1974). The first, or Fanaroff-Riley type I (FR-I) tend to be less luminous and have a compact morphology, with an emission close to

<sup>1</sup> <https://pages.astronomy.ua.edu/keel/galaxies/>

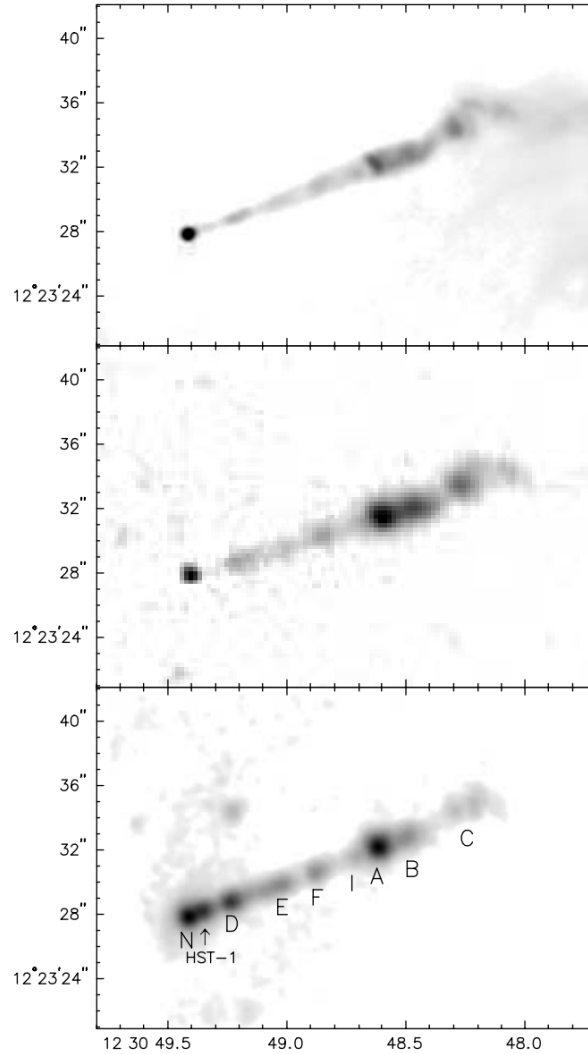


Figure 4: Composite image of the jet of M87. *Top*: 6-cm radio emission. *Middle*: Optical V band emission. *Bottom*: X-ray emission. Image from (Wilson and Yang, 2002). The letters are associated to visible knots, or intensity enhancements.

the core and jets that quickly fade at the edges. Fanaroff-Riley type II (FR-II) objects have powerful jets that remain tightly collimated up to hundreds of kiloparsecs and are particularly bright at the edges, or lobes.

Their radio emission is attributed to synchrotron radiation from the charged, relativistic particles comprising the jet (e.g. Burbidge, 1956; Shklovskii, 1961). Due to effects of relativistic beaming, FR-II jets often appear brighter on the side that moves toward the observer (jet) and much fainter on the side that faces the opposite direction (counter jet). If the jet is perfectly aligned with the line of sight (i.e. blazar) its emission can be dominant at all wavelengths up to TeV energies. As seen in Fig. 2, a blazar SED is characterized by the presence of two

peaks, one at low and one at high energies (e.g. Ghisellini et al., 2017). The synchrotron peak can extend up to IR (low synchrotron-peaking, LSP) or even X-rays (high synchrotron-peaking, HSP) (Abdo et al., 2010). A second component, at high energies (from X-rays up to TeV), is of IC origin in the case of leptonic jets, or due to processes such as  $\pi^0$  decay in hadronic ones. Fig. 4 shows the jet of M87 at three different wavelengths.

The composition of jets, whether hadronic or leptonic, is a current topic of debate. The observed emission can be explained with purely leptonic models (e.g. Mastichiadis and Kirk, 1997), although hadronic jets cannot be ruled out (e.g. Mücke and Protheroe, 2001; Aharonian, 2000). Up to date, hadrons (iron nuclei in particular) have only been detected with certainty in two galactic sources, SS433 (Migliari, Fender, and Méndez, 2002) and 4U1630C47 (Díaz Trigo et al., 2013).

Jets could be comprised of purely electron-positron plasma at the base (e.g. Laing and Bridle, 2002), but it is likely that hadrons will find their way into the flow through interactions with the ambient medium (e.g. De Young, 1986, and see Sect. 1.3.1). However, a jet of mixed plasma could have the bulk of the kinetic energy in the form of protons, and still have leptons be responsible for the observable emission (For a useful discussion on the topic, see e.g. Sikora et al., 2009; Böttcher et al., 2013).

Likewise, the mechanism of jet launching is uncertain. One of the most commonly invoked theories is the Blandford-Znajek mechanism (Blandford and Znajek, 1977), which assumes extraction of energy from a rotating black hole. Other theories involve extracting power from the accretion flow itself (Blandford and Payne, 1982).

For a review on the subject of relativistic jets, see e.g. Romero et al. (2017).

### 1.3.1 *Interaction with obstacles: mass loading and deceleration*

Jets are launched close to the central engine and extend up to distances of hundreds of kiloparsecs. In this process they must cross the host galaxy and, therefore, propagate through the ambient medium. As they advance, they inevitably interact with a variety of objects present in the galaxy, such as stars or gas clouds.

First evidences from jet interaction with the medium arise from two observational facts: the FR-I/FR-II dichotomy, and the presence of knots, or localized intensity enhancements, within the jet structure (see Fig. 4).

FR-II jets are brighter at the edges, point at which the density of the intergalactic material (IGM) is sufficient to stop their propagation. This collision leads to the formation of shocks, which are prominent non-thermal emitters (see Sect. 1.3.2).

FR-I jets are brighter in their inner regions, as well as slower and not as narrowly collimated as FR-II jets. This effect has since long been associated to entrainment of ISM, or the presence of strong shocks (e.g. Bicknell, 1984). As the jet propagates, the difference of velocity between its bulk motion and the surrounding medium gives rise to a shear layer, in which small instabilities can develop and grow, resulting in significant mixing. The exchange of momentum in this process forces the jet to decelerate significantly, and can even disrupt it (e.g. De Young, 1986). It has been shown that an FR-II powerful jet can become FR-I if sufficient material is entrained within the inner kiloparsecs of the host galaxy (e.g. De Young, 1993; Wang et al., 2009).

Mass entrainment can also occur through the presence of standing recollimation shocks. As the jet expands, its pressure decreases until, at some point, it becomes lower than that of the ambient medium. The jet is forced to recollimate when colliding with the ISM, which can produce inner shocks that result in deceleration and facilitate mixing of ambient material (Perucho and Martí, 2007).

Another possibility for jet mass-loading lies in stellar winds. As the jet crosses the galaxy, a great number of stars fall within the jet at all times, and the mass of their stellar winds is dragged downstreams, which can eventually result in deceleration (e.g. Komissarov, 1994; Bowman, Leahy, and Komissarov, 1996; Perucho et al., 2014).

Individual obstacles can also play a role in mass-loading the jet and slowing it down. For example, a supernova explosion taking place within it and loading the jet with its remnant (Vieyro, Torres-Albà, and Bosch-Ramon, 2017), or the winds of an individual asymptotic giant branch star (Perucho, Bosch-Ramon, and Barkov, 2017) may be sufficient to affect it dynamically.

### 1.3.2 Particle acceleration and non-thermal emission

Interaction with the environment not only leads to deceleration and disruption of the jet, but also to the production of non-thermal emission. As an obstacle finds its way into the jet (i.e. gas blob, star), it is impacted by its ram pressure and a double bow shock is formed. Fig. 5 depicts a stellar wind being impacted by a jet.

In a shock, particles can be accelerated to relativistic energies. The most commonly invoked mechanism at play is first-order Fermi acceleration (also known as diffusive shock acceleration) according to which particles are continuously scattered upstreams and downstreams the flow, reflected by magnetic inhomogeneities. The particles gain energy each time they cross the shock front, until they reach highly relativistic velocities (e.g. Bell, 1978; Blandford and Eichler, 1987). The accelerated particles then either escape the flow (e.g. cosmic rays), or radiate their energy non-thermally.

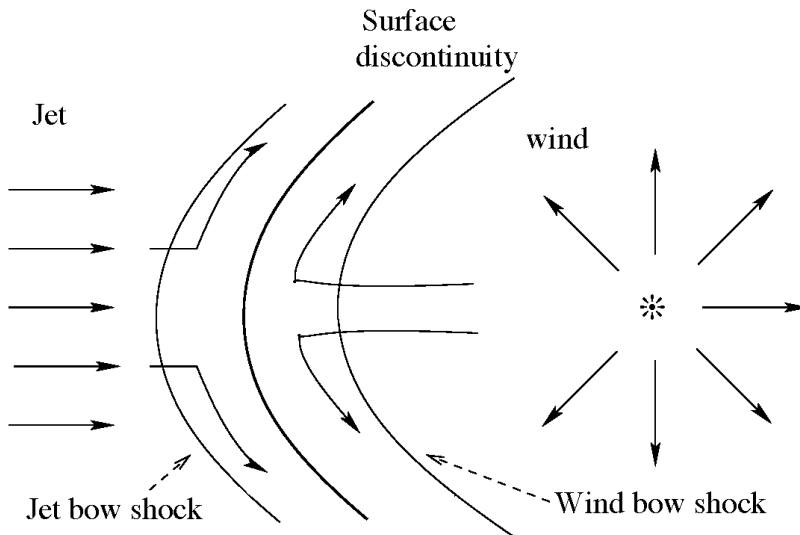


Figure 5: Sketch of a double bowshock formed by the collision between jet plasma and a stellar wind. Figure from Araudo, Bosch-Ramon, and Romero (2013).

Particle acceleration in shocks with obstacles has since long been proved capable of reproducing observational features. This phenomenon is believed to be responsible for the presence of knots in AGN jets (e.g. Blandford and Koenigl, 1979, see Fig. 6). Dar and Laor (1997) introduced interactions with BLR clouds to explain TeV variability in blazars, and Araudo, Bosch-Ramon, and Romero (2010) showed that the interaction can lead to variable gamma ray emission in radio galaxies. Steffen et al. (1997) showed how the jet impacting NLR clouds can affect their brightness and velocity distribution.

Interactions with single stars close to the jet base can also explain gamma ray variability in blazars, either through loading of their stellar winds (Bednarek and Protheroe, 1997), the envelope of a red giant being blown away by the jet (Barkov, Aharonian, and Bosch-Ramon, 2010), intense winds of a wolf-rayet star (Araudo, Bosch-Ramon, and Romero, 2013) or even tidal disruption of a red giant envelope by the central engine (Khangulyan et al., 2013). Supernova remnants within the jet have been suggested as possible explanations for the knots of M87 (e.g. Blandford and Koenigl, 1979). On the other hand, interactions with populations of stars can lead to persistent emission in X-rays (Wykes et al., 2015) and gamma-rays (Bosch-Ramon, 2015; de la Cita et al., 2016).

High resolution radio images may even provide direct evidence of the presence of obstacles within the jet (Hardcastle et al., 2003). Recently, interferometric imaging of the inner structure of the nearby radio galaxy Centaurus A shows substructure that strongly reminds of a bowshock shape (Müller et al., 2014, shown in Fig. 6, near J6).

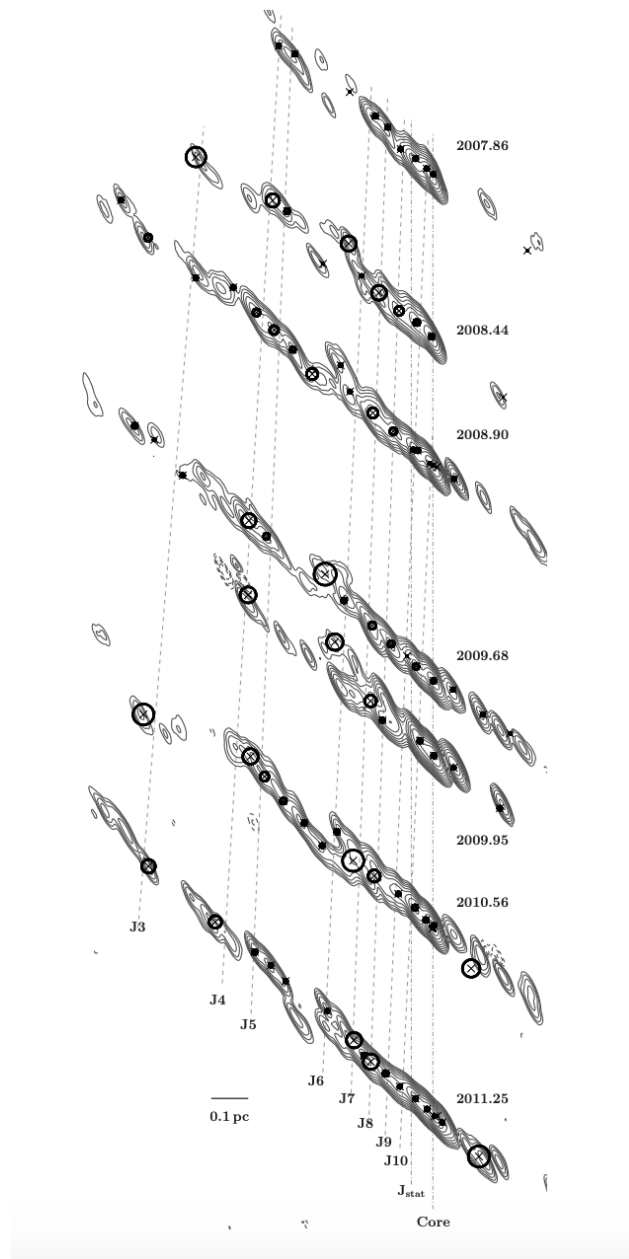


Figure 6: Time evolution at 8.4 GHz of the inner parsec of Centaurus A, the nearest radio-loud AGN. J1 – 10 are identified individual components. The flow appears to be interrupted by the presence of an obstacle, which gives rise to a possible bow-shock structure (near J6). Figure from (Müller et al., 2014).

#### 1.4 MOTIVATION, GOALS AND STRUCTURE OF THE THESIS

This thesis has as an objective the study of very energetic phenomena in the central regions of active galaxies. Intense star formation is triggered by mergers of galaxies, and the funneling of large quantities of gas toward the inner regions is thought to also cause accretion onto the SMBH. Whether the two processes necessarily take place together

as a step of galaxy evolution is still debated, making the study of related phenomena an interesting topic.

Regardless of the origin of their connection, star formation and strong AGN activity often coexist in the nuclei of galaxies. Even after star formation is no longer ongoing, the nuclear starburst in a merger results in the formation of galactic bulges. Therefore, stellar densities in the inner kiloparsecs of a galaxy are typically high. As stars, or star forming regions, are close to the AGN, interaction between the two is expected to be frequent, and it can result in a multitude of phenomena worthy of study.

The thesis thus focuses on high energy processes taking place in regions where AGN activity and stellar presence is likely important. In particular, the goal of the thesis is to study the emission produced by these phenomena, in the range of X-rays to gamma-rays, whether to disentangle their individual contributions or to detect emission resulting from their interaction. The thesis intends to provide data to continue the study of the starburst-AGN connection, and new models to explain the production of gamma rays in other galaxies.

This thesis is divided in five parts, after this first introductory chapter.

Part I focuses on the X-ray analysis of a local sample of LIRGs, published in Torres-Albà et al. (2018). The Great Observatories All-Sky LIRG survey (GOALS) is a project to study the brightest infrared galaxies at  $z < 0.1$ , in all possible wavelengths. The X-ray study of the IR-brightest galaxies within GOALS was published in Iwasawa et al. (2011). In this article we analyze data for 63 LIRGs in the lower luminosity range of GOALS. We provide arcsecond-resolution X-ray images, fluxes, luminosities and radial profiles for 84 individual galaxies, spanning a wide range of activity types and merger stages. We also provide information on AGN presence using X-ray and IR diagnostics, and compare the results to those derived for the brightest GOALS galaxies. The data provided in this part will help shine light into the importance of AGN presence in LIRGs, in the context of galaxy evolution.

Part II focuses on the interaction of AGN jets with stellar populations. The first work presented was published as Vieyro, Torres-Albà, and Bosch-Ramon (2017), and it aims to study the gamma-ray emission and jet mass-loading caused by the presence of stars within an AGN jet. In this work, we first model the populations of stars with high mass-loss rates present in galaxies; OB stars near the nucleus of a LIRG, and red giants in the bulge of an elliptical galaxy. Then we estimate how many of these stars are, statistically, present within the jet at all times. All these stars are impacted by the jet ram pressure and bow-shocks develop, in which particles can be accelerated to relativistic energies. We estimate the expected gamma-ray emission and mass loading both for elliptical galaxies and LIRGs.

The second work in Part II, published as Torres-Albà et al. (2018), considers the interaction that occurs not when stars are within the jet, but at the moment they penetrate it. As stars move through the ISM, their winds impact it and a shock is formed in which both ISM and stellar-wind material accumulate (bubbles). This material can be expelled into the jet after penetration, and it is accelerated upstreams due to the momentum gained by jet impact. In the shock that forms, particles can be accelerated and emit non-thermally. We use the previously modelled stellar population of M 87 to estimate the rate at which stars penetrate the jet, and then model the dynamical evolution and emission of their bubbles as they propagate upwards. The work includes dynamical simulations to illustrate the propagation of the bubbles within the jet.

Part III focuses on the interaction of one single object with the jet; a SNR. Two works, the first published as Vieyro, Bosch-Ramon, and Torres-Albà (2019) and the second sent to A&A for publication, study this process in LIRGs and elliptical galaxies, respectively. In them, we model the dynamical evolution of the remnant once expelled into the jet, and calculate the non-thermal radiation emitted in the shock. We then estimate the frequency of events and the expected number of detectable sources. Vieyro, Bosch-Ramon, and Torres-Albà (2019) also includes hydrodynamical simulations of the interaction.

Part IV focuses on the interaction of AGN jets with the environment at large scales, in this case considering them as possible sources of reionization at  $z \sim 6$ . It includes one article, sent to A&A for publication, in which we estimate the number of jetted sources at the epoch of reionization using rest-UV detections of AGN. We then correct the observed density of sources for effects of obscuration using X-ray data. Jets at high redshift interact strongly with the CMB, up-scattering its photons up to ionizing wavelengths through IC, and possibly ionizing the ambient medium significantly.

Part V includes a summary and discussion of the results obtained in this thesis, as well as the derived conclusions and future work perspectives. References to citations in the introduction and Part V can be found at the end of the thesis, while each individual publication enclosed has its own references listed at the end of its chapter.

Part I

X-RAY STUDY OF LIRGS



## C-GOALS II. CHANDRA OBSERVATIONS OF THE LOWER LUMINOSITY SAMPLE OF NEARBY LUMINOUS INFRARED GALAXIES IN GOALS

---

In this chapter we present our work "C-GOALS II. Chandra observations of the lower luminosity sample of nearby galaxies in GOALS" (Torres-Albà et al., 2018), in which we provide an X-ray analysis of 63 LIRGs and compare their X-ray and infrared properties to those of the LIRGs in the higher luminosity sample of Iwasawa et al. (2011).



## C-GOALS

### II. *Chandra* observations of the lower luminosity sample of nearby luminous infrared galaxies in GOALS

N. Torres-Albà<sup>1</sup>, K. Iwasawa<sup>1,2</sup>, T. Díaz-Santos<sup>3</sup>, V. Charmandaris<sup>4,5</sup>, C. Ricci<sup>3,6,7</sup>, J. K. Chu<sup>8</sup>, D. B. Sanders<sup>9</sup>, L. Armus<sup>10</sup>, L. Barcos-Muñoz<sup>11,12</sup>, A. S. Evans<sup>11,13</sup>, J. H. Howell<sup>10</sup>, H. Inami<sup>14</sup>, S. T. Linden<sup>13</sup>, A. M. Medling<sup>15,16</sup>, G. C. Privon<sup>17</sup>, V. U<sup>18</sup>, and I. Yoon<sup>11</sup>

<sup>1</sup> Institut de Ciències del Cosmos (ICCUB), Universitat de Barcelona (IEEC-UB), Martí i Franquès, 1, 08028 Barcelona, Spain  
e-mail: ntorresalba@icc.ub.edu

<sup>2</sup> ICREA, Pg. Lluís Companys 23, 08010 Barcelona, Spain

<sup>3</sup> Núcleo de Astronomía de la Facultad de Ingeniería y Ciencias, Universidad Diego Portales, Av. Ejército Libertador 441, Santiago, Chile

<sup>4</sup> Institute for Astronomy, Astrophysics, Space Applications & Remote Sensing, National Observatory of Athens, 15236 Penteli, Greece

<sup>5</sup> University of Crete, Department of Physics, 71003 Heraklion, Greece

<sup>6</sup> Kavli Institute for Astronomy and Astrophysics, Peking University, 100871 Beijing, PR China

<sup>7</sup> Chinese Academy of Sciences South America Center for Astronomy, Camino El Observatorio 1515, Las Condes, Santiago, Chile

<sup>8</sup> Gemini North Observatory, 670 N. A'ohoku Place, Hilo, HI 96720, USA

<sup>9</sup> Institute for Astronomy, University of Hawaii, 2680 Woodlawn Drive, Honolulu, HI 96822, USA

<sup>10</sup> Infrared Processing and Analysis Center, MC 314-6, Caltech, 1200 E. California Blvd., Pasadena, CA 91125, USA

<sup>11</sup> National Radio Astronomy Observatory, 520 Edgemont Road, Charlottesville, VA 22903, USA

<sup>12</sup> Joint ALMA Observatory, Alonso de Córdova 3107, Vitacura, Santiago, Chile

<sup>13</sup> Department of Astronomy, University of Virginia, PO Box 400325, Charlottesville, VA 22904, USA

<sup>14</sup> Univ Lyon, Univ Lyon1, ENS de Lyon, CNRS, Centre de Recherche Astrophysique de Lyon (CRAL) UMR5574, 69230 Saint Genis-Laval, France

<sup>15</sup> Cahill Center for Astronomy and Astrophysics, California Institute of Technology, MS 249-17, Pasadena, CA 91125, USA

<sup>16</sup> Research School of Astronomy & Astrophysics, Australian National University, ACT 2611 Canberra, Australia

<sup>17</sup> Department of Astronomy, University of Florida, 211 Bryant Space Sciences Center, Gainesville, FL 32611, USA

<sup>18</sup> Department of Physics and Astronomy, 4129 Frederick Reines Hall, University of California, Irvine, CA 92697, USA

Received 18 August 2018 / Accepted 2 October 2018

#### ABSTRACT

We analyze *Chandra* X-ray observatory data for a sample of 63 luminous infrared galaxies (LIRGs), sampling the lower-infrared luminosity range of the Great Observatories All-Sky LIRG survey (GOALS), which includes the most luminous infrared selected galaxies in the local Universe. X-rays are detected for 84 individual galaxies within the 63 systems, for which arcsecond resolution X-ray images, fluxes, infrared and X-ray luminosities, spectra and radial profiles are presented. Using X-ray and mid-infrared (MIR) selection criteria, we find AGN in  $(31 \pm 5)\%$  of the galaxy sample, compared to the  $(38 \pm 6)\%$  previously found for GOALS galaxies with higher infrared luminosities (C-GOALS I). Using MIR data, we find that  $(59 \pm 9)\%$  of the X-ray selected AGN in the full C-GOALS sample do not contribute significantly to the bolometric luminosity of the host galaxy. Dual AGN are detected in two systems, implying a dual AGN fraction in systems that contain at least one AGN of  $(29 \pm 14)\%$ , compared to the  $(11 \pm 10)\%$  found for the C-GOALS I sample. Through analysis of radial profiles, we derive that most sources, and almost all AGN, in the sample are compact, with half of the soft X-ray emission generated within the inner  $\sim 1$  kpc. For most galaxies, the soft X-ray sizes of the sources are comparable to those of the MIR emission. We also find that the hard X-ray faintness previously reported for the bright C-GOALS I sources is also observed in the brightest LIRGs within the sample, with  $L_{\text{FIR}} > 8 \times 10^{10} L_{\odot}$ .

**Key words.** infrared: galaxies – X-rays: galaxies – galaxies: active – galaxies: starburst

#### 1. Introduction

Luminous and ultra-luminous infrared galaxies (LIRGs and ULIRGs) are galaxies with infrared (IR) luminosities exceeding  $10^{11} L_{\odot}$  and  $10^{12} L_{\odot}$ , respectively. LIRGs and ULIRGs are normally found to be gas-rich galaxy mergers, as tidal torques can funnel material from kpc scales to the innermost regions of the galaxy and trigger intense star formation and/or AGN activity (e.g., Hernquist 1989; Sanders 1999; Di Matteo et al. 2005), the latter more significantly so with increasing IR luminosity (e.g.,

Valiante et al. 2009; Petric et al. 2011; Alonso-Herrero et al. 2012).

These objects, common at redshifts 1–3 where the peak of star formation in the Universe is observed, represent a very important stage in galaxy evolution (e.g., Casey et al. 2014). The scenario proposed by Sanders et al. (1988) and Hopkins et al. (2005), for example, indicates that after a complete obscuration phase of the merger, ULIRGs in a late stage of the interaction would later disperse or consume the gas and probably evolve into an obscured type II quasar (QSO), and eventually

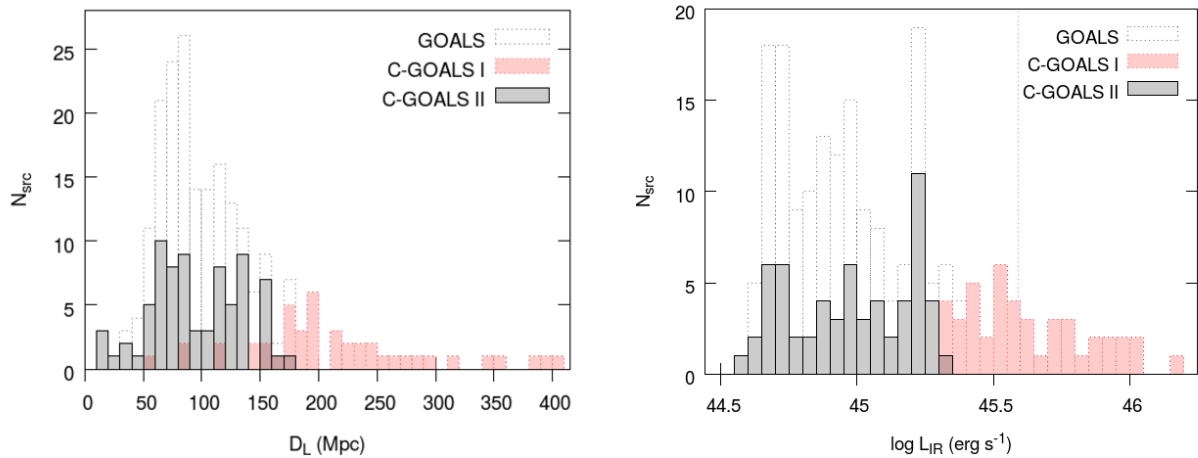


**Fig. 1.** Distribution of luminosity distance (*left panel*) and IR luminosity  $L_{\text{IR}}(8\text{--}1000\mu\text{m})$  (*right panel*) for the 44 objects of C-GOALS I (Iwasawa et al. 2011), the 63 objects of C-GOALS II, and the 201 systems of the full GOALS sample (Armus et al. 2009). The vertical dashed line represents  $L_{\text{IR}} = 10^{12} L_{\odot}$ , the boundary between LIRGs and ULIRGs.

into an exposed QSO. This process will ultimately lead to the formation of an elliptical galaxy, and accounts for the growth of the central supermassive black hole (e.g., Sanders et al. 1988; Hopkins et al. 2009).

In agreement with this scenario, recent studies of pairs of galaxies have found that the fraction of dual AGN grows with decreasing separation between companions (e.g., Ellison et al. 2011; Satyapal et al. 2014, 2017; Silverman et al. 2011; Koss et al. 2012). More specifically, in a sample of LIRGs and ULIRGs, Stierwalt et al. (2013) found an increase in the fraction of composite systems with merger stage. Satyapal et al. (2014) found larger fractions of IR-selected AGN with respect to optically selected AGN in mergers, which is likely due to the increase of obscuration. Evidence of an excess of AGN with high obscuring column densities in mergers are also found in recent works (e.g., Diaz-Santos et al. 2010; Kocevski et al. 2015; Del Moro et al. 2016; Lanzuisi et al. 2015; Ricci et al. 2017).

X-ray observations are an ideal tool for analyzing the properties of the inner regions of such obscured objects, because the gas and dust have a higher transparency than at larger wavelengths. Previous studies of small (e.g., Franceschini et al. 2003; Ptak et al. 2003; Teng et al. 2005) and larger (e.g., Teng & Veilleux 2010; Iwasawa et al. 2011; Ricci et al. 2017) samples of ULIRGs have highlighted the potential of X-rays in distinguishing the contribution of AGN and starburst and the ability to detect enshrouded AGN.

One of the recent works, C-GOALS I (*Chandra*-GOALS I, Iwasawa et al. 2011), is an X-ray study performed with the *Chandra* X-ray Observatory (*Chandra*, hereafter, Weisskopf et al. 2000) of a complete sample of LIRGs within the Great Observatories All-Sky LIRG Survey (GOALS, Armus et al. 2009). GOALS is a multi-wavelength study of the brightest IR galaxies in the local Universe, a low-redshift subsample of the  $60\mu\text{m}$  flux selected IRAS Revised Bright Galaxy Sample (RBGS, Sanders et al. 2003). The GOALS galaxies, all at  $z < 0.088$ , are perfect laboratories for multi-wavelength studies of LIRGs with a level of detail that only the observation of local galaxies allows. The arcsecond resolution provided by *Chandra* can offer information of individual galaxies within mergers, and help distinguish previously undetected or unresolved AGN, in particular, complementing studies of LIRGs and ULIRGs at harder X-rays (e.g. Ricci et al. 2017).

The C-GOALS I paper presents data obtained by us and others with *Chandra* and represents the X-ray component of the multi-wavelength survey for the most luminous IR GOALS sources. This work, C-GOALS II, extends the X-ray study to a subsample of the lower luminosity range of GOALS galaxies. These data were obtained during *Chandra* cycle 13 (PI: Sanders), combined with available archival data. The extension of the X-ray sample is motivated by the interest in reaching completeness in all wavelengths for the GOALS sample, and by the opportunity of comparing results derived at different IR luminosity ranges. The sample contains galaxies at earlier merger stages, contributing to the expansion of previous studies into the domain of the less luminous LIRGs. In particular, Iwasawa et al. (2011) observed a deviation in the correlation between IR and X-ray luminosities in nearby star-forming galaxies (e.g., Ranalli et al. 2003; Grimm et al. 2003; Mineo et al. 2014) for the galaxies in the C-GOALS I sample. The IR luminosities of galaxies in the C-GOALS II sample fall into the range where this change of behavior should occur, and are ideal to further study the reasons for and possible implications of such deviation.

The C-GOALS II sample is described and compared to the C-GOALS I sample in Sect. 2. The observations and data reduction are described in Sect. 3. Results, including all X-ray images, fluxes, spectra, and radial surface brightness profiles, are presented in Sect. 4, while derived properties and discussion of the X-ray and IR luminosity correlation are presented in Sect. 5. Finally, we summarize our conclusions in Sect. 6. Notes on individual objects can be found in Appendix A, and X-ray contours, detailed images in the 0.5–2 and 2–7 keV bands, along with radial surface brightness profiles for each source, can be found in Appendix B.

## 2. Sample

GOALS (Armus et al. 2009) is a comprehensive study of 201 of the most luminous IR-selected galaxies in the local Universe. The sample consists of 179 LIRGs and 22 ULIRGs, 85 of which are systems that contain multiple galaxies. GOALS is drawn from the IRAS RBGS (Sanders et al. 2003), with a luminosity threshold of  $L_{\text{IR}} \geq 10^{11} L_{\odot}$ . The RBGS is a complete sample of galaxies, covering the whole sky, that have IRAS  $60\mu\text{m}$  flux densities above 5.24 Jy and Galactic latitude  $|b| \geq 5^{\circ}$ .

**Table 1.** Basic parameters of the objects in the C-GOALS II sample.

| No. | IRAS Name   | Optical ID       | RA (NED)<br>(J2000) | Dec (NED)<br>(J2000) | $z$    | $D_L$<br>(Mpc) | $\log(L_{IR})$<br>( $L_\odot$ ) |
|-----|-------------|------------------|---------------------|----------------------|--------|----------------|---------------------------------|
| (1) | (2)         | (3)              | (4)                 | (5)                  | (6)    | (7)            | (8)                             |
| 45  | F13182+3424 | UGC 08387        | 13h 20m 35.34s      | +34d 08m 22.2s       | 0.0233 | 110.0          | 11.73                           |
| 47  | F01173+1405 | CGCG 436-030     | 01h 20m 02.72s      | +14d 21m 42.9s       | 0.0312 | 134.0          | 11.69                           |
| 49  | F01484+2220 | NGC 0695         | 01h 51m 14.24s      | 22d 34m 56.5s        | 0.0325 | 139.0          | 11.69                           |
| 50  | F12592+0436 | CGCG 043-099     | 13h 01m 50.80s      | +04d 20m 00.0s       | 0.0375 | 175.0          | 11.68                           |
| 51  | F11011+4107 | MCG+07-23-019    | 11h 03m 53.20s      | +40d 50m 57.0s       | 0.0345 | 158.0          | 11.62                           |
| 52  | F18329+5950 | NGC 6670         | 18h 33m 35.91s      | +59d 53m 20.2s       | 0.0289 | 129.5          | 11.65                           |
| 53  | F02512+1446 | UGC 02369        | 02h 54m 01.78s      | +14d 58m 24.9s       | 0.0312 | 136.0          | 11.67                           |
| 54  | F04315-0840 | NGC 1614         | 04h 33m 59.85s      | -08d 34m 44.0s       | 0.0159 | 67.8           | 11.65                           |
| 56  | F13497+0220 | NGC 5331         | 13h 52m 16.29s      | +02d 06m 17.0s       | 0.0330 | 155.0          | 11.66                           |
| 57  | F06076-2139 | IRAS F06076-2139 | 06h 09m 45.81s      | -21d 40m 23.7s       | 0.0374 | 165.0          | 11.65                           |
| 60  | F11231+1456 | IC 2810          | 11h 25m 47.30s      | +14d 40m 21.1s       | 0.0342 | 157.0          | 11.64                           |
| 63  | 18090+0130  | IRAS 18090+0130  | 18h 11m 35.91s      | +01d 31m 41.3s       | 0.0342 | 134.0          | 11.65                           |
| 64  | F01417+1651 | III Zw 035       | 01h 44m 30.45s      | +17d 06m 05.0s       | 0.0274 | 119.0          | 11.64                           |
| 65  | F10257-4339 | NGC 3256         | 10h 27m 51.27s      | -43d 54m 13.8s       | 0.0094 | 38.9           | 11.64                           |
| 67  | F16399-0937 | IRAS F16399-0937 | 16h 42m 40.21s      | -09d 43m 14.4s       | 0.0270 | 128.0          | 11.63                           |
| 68  | F16164-0746 | IRAS F16164-0746 | 16h 19m 11.79s      | -07d 54m 02.8s       | 0.0272 | 128.0          | 11.62                           |
| 69  | F18093-5744 | IC 4686/7        | 18h 13m 39.63s      | -57d 43m 31.3s       | 0.0173 | 81.9           | 11.62                           |
| 71  | F08354+2555 | NGC 2623         | 08h 38m 24.08s      | +25d 45m 16.6s       | 0.0185 | 84.1           | 11.60                           |
| 72  | F23135+2517 | IC 5298          | 23h 16m 00.70s      | +25d 33m 24.1s       | 0.0274 | 119.0          | 11.60                           |
| 73  | 20351+2521  | IRAS 20351+2521  | 20h 37m 17.72s      | +25d 31m 37.7s       | 0.0337 | 151.0          | 11.61                           |
| 75  | F16104+5235 | NGC 6090         | 16h 11m 40.70s      | +52d 27m 24.0s       | 0.0293 | 137.0          | 11.58                           |
| 79  | F13362+4831 | NGC 5256         | 13h 38m 17.52s      | +48d 16m 36.7s       | 0.0279 | 129.0          | 11.56                           |
| 80  | F03359+1523 | IRAS F03359+1523 | 03h 38m 46.70s      | +15d 32m 55.0s       | 0.0354 | 152.0          | 11.55                           |
| 81  | F04191-1855 | ESO 550-IG025    | 04h 21m 20.02s      | -18d 48m 47.6s       | 0.0322 | 135.8          | 11.51                           |
| 82  | F00085-1223 | NGC 0034         | 00h 11m 06.55s      | -12d 06m 26.3s       | 0.0196 | 84.1           | 11.49                           |
| 83  | F00506+7248 | MCG+12-02-001    | 00h 54m 03.61s      | +73d 05m 11.8s       | 0.0157 | 69.8           | 11.50                           |
| 85  | F17138-1017 | IRAS F17138-1017 | 17h 16m 35.79s      | -10d 20m 39.4s       | 0.0173 | 84.0           | 11.49                           |
| 95  | F12043-3140 | ESO 440-IG058    | 12h 06m 51.82s      | -31d 56m 53.1s       | 0.0232 | 112.0          | 11.43                           |
| 100 | F21453-3511 | NGC 7130         | 21h 48m 19.50s      | -34d 57m 04.7s       | 0.0162 | 72.7           | 11.42                           |
| 104 | F23488+1949 | NGC 7771         | 23h 51m 24.88s      | +20d 06m 42.6s       | 0.0143 | 61.2           | 11.40                           |
| 105 | F23157-0441 | NGC 7592         | 23h 18m 22.20s      | -04d 24m 57.6s       | 0.0244 | 106.0          | 11.40                           |
| 106 | F16577+5900 | NGC 6286         | 16h 58m 31.38s      | +58d 56m 10.5s       | 0.0183 | 85.7           | 11.37                           |
| 107 | F12590+2934 | NGC 4922         | 13h 01m 24.89s      | +29d 18m 40.0s       | 0.0236 | 111.0          | 11.38                           |
| 110 | F10015-0614 | NGC 3110         | 10h 04m 02.11s      | -06d 28m 29.2s       | 0.0169 | 79.5           | 11.37                           |
| 114 | F00402-2349 | NGC 0232         | 00h 42m 45.82s      | -23d 33m 40.9s       | 0.0227 | 95.2           | 11.44                           |
| 117 | F09333+4841 | MCG+08-18-013    | 09h 36m 37.19s      | +48d 28m 27.7s       | 0.0259 | 117.0          | 11.34                           |
| 120 | F15107+0724 | CGCG 049-057     | 15h 13m 13.09s      | +07d 13m 31.8s       | 0.0130 | 65.4           | 11.35                           |
| 121 | F02401-0013 | NGC 1068         | 02h 42m 40.71s      | -00d 00m 47.8s       | 0.0038 | 15.9           | 11.40                           |
| 123 | F02435+1253 | UGC 02238        | 02h 46m 17.49s      | +13d 05m 44.4s       | 0.0219 | 92.4           | 11.33                           |
| 127 | F13197-1627 | MCG-03-34-064    | 13h 22m 24.46s      | -16d 43m 42.9s       | 0.0165 | 82.2           | 11.28                           |
| 134 | F00344-3349 | ESO 350-IG038    | 00h 36m 52.25s      | -33d 33m 18.1s       | 0.0206 | 89.0           | 11.28                           |
| 136 | F23394-0353 | MCG-01-60-022    | 23h 42m 00.85s      | -03d 36m 54.6s       | 0.0232 | 100.0          | 11.27                           |
| 141 | F09437+0317 | IC 0563/4        | 09h 46m 20.71s      | +03d 03m 30.5s       | 0.0200 | 92.9           | 11.23                           |
| 142 | F13229-2934 | NGC 5135         | 13h 25m 44.06s      | -29d 50m 01.2s       | 0.0137 | 60.9           | 11.30                           |
| 144 | F13126+2453 | IC 0860          | 13h 15m 03.53s      | +24d 37m 07.9s       | 0.0112 | 56.8           | 11.14                           |
| 147 | F22132-3705 | IC 5179          | 22h 16m 09.10s      | -36d 50m 37.4s       | 0.0114 | 51.4           | 11.24                           |
| 148 | F03514+1546 | CGCG 465-012     | 03h 54m 16.08s      | +15d 55m 43.4s       | 0.0222 | 94.3           | 11.20                           |
| 157 | F12596-1529 | MCG-02-33-098/9  | 13h 02m 19.70s      | -15d 46m 03.0s       | 0.0159 | 78.7           | 11.17                           |
| 163 | F12243-0036 | NGC 4418         | 12h 26m 54.62s      | -00d 52m 39.2s       | 0.0073 | 36.5           | 11.19                           |
| 169 | F21330-3846 | ESO 343-IG013    | 21h 36m 10.83s      | -38d 32m 37.9s       | 0.0191 | 85.8           | 11.14                           |
| 170 | F06107+7822 | NGC 2146         | 06h 18m 37.71s      | +78d 21m 25.3s       | 0.0030 | 17.5           | 11.12                           |
| 174 | F14280+3126 | NGC 5653         | 14h 30m 10.42s      | +31d 12m 55.8s       | 0.0119 | 60.2           | 11.13                           |
| 178 | F12116+5448 | NGC 4194         | 12h 14m 09.47s      | +54d 31m 36.6s       | 0.0083 | 43.0           | 11.10                           |
| 179 | F23157+0618 | NGC 7591         | 23h 18m 16.28s      | +06d 35m 08.9s       | 0.0165 | 71.4           | 11.12                           |
| 182 | F00073+2538 | NGC 0023         | 00h 09m 53.41s      | +25d 55m 25.6s       | 0.0152 | 65.2           | 11.12                           |
| 188 | F23133-4251 | NGC 7552         | 23h 16m 10.77s      | -42d 35m 05.4s       | 0.0054 | 23.5           | 11.11                           |
| 191 | F04118-3207 | ESO 420-G013     | 04h 13m 49.69s      | -32d 00m 25.1s       | 0.0119 | 51.0           | 11.07                           |
| 194 | 08424-3130  | ESO 432-IG006    | 08h 44m 28.07s      | -31d 41m 40.6s       | 0.0162 | 74.4           | 11.08                           |
| 195 | F05365+6921 | NGC 1961         | 05h 42m 04.65s      | +69d 22m 42.4s       | 0.0131 | 59.0           | 11.06                           |
| 196 | F23444+2911 | NGC 7752/3       | 23h 47m 01.70s      | +29d 28m 16.3s       | 0.0162 | 73.6           | 11.07                           |
| 198 | F03316-3618 | NGC 1365         | 03h 33m 36.37s      | -36d 08m 25.4s       | 0.0055 | 17.9           | 11.00                           |
| 199 | F10196+2149 | NGC 3221         | 10h 22m 19.98s      | +21d 34m 10.5s       | 0.0137 | 65.7           | 11.09                           |
| 201 | F02071-1023 | NGC 0838         | 02h 09m 38.58s      | -10d 08m 46.3s       | 0.0128 | 53.8           | 11.05                           |

**Notes.** Column (1): Object number, also used in other tables. Column (2): Original IRAS source, where an “F” prefix indicates the Faint Source Catalog and no prefix indicates the Point Source Catalog. Column (3): Optical cross-identification, when available from NED. Columns (4)–(6): The best available right ascension (J2000), declination and heliocentric redshift from NED as of October 2008. Column (7): The luminosity distance derived by correcting the heliocentric velocity for the 3-tractor flow model of Mould et al. (2000) and adopting cosmological parameters  $H_0 = 73 \text{ km s}^{-1} \text{ Mpc}^{-2}$ ,  $\Omega_V = 0.73$ , and  $\Omega_M = 0.27$ , as provided by NED. Column (8): The total (8–1000)  $\mu\text{m}$  luminosity in  $\log_{10}$  Solar units as in (Armus et al. 2009).

Iwasawa et al. (2011) studied a subsample of GOALS, C-GOALS I (hereafter, also CGI), which is complete in the higher IR luminosity end of the GOALS sample ( $\log(L_{\text{IR}}/L_{\odot}) = 11.73\text{--}12.57$ ). It contains 44 systems in the redshift range  $z = 0.010\text{--}0.088$ . The new sample, C-GOALS II (hereafter, also CGII), is an incomplete subsample of the lower luminosity section of GOALS, and includes all sources in the  $\log(L_{\text{IR}}/L_{\odot}) = 11.00\text{--}11.73$  range with available *Chandra* data, as of January 2016. It is comprised of 63 systems, 30 of which contain multiple galaxies. The redshift range of the new sample is  $z = 0.003\text{--}0.037$ . The distribution of IR luminosities and distances of the two samples is shown in Fig. 1. Table 1 gives basic parameters for all the objects in the C-GOALS II sample. We note that names and positions refer to the IR detected systems. Decomposition into individual galaxies is taken into account in Sect. 4.

Figure 1 also shows the incompleteness of CGII, comparing it with the full GOALS distribution of distances and luminosities. Of the 63 systems within CGII, 31 were observed through the same proposal, which was drawn to be representative of all possible merger stages. For the remaining 32 systems, data were taken from the archive according to availability. The proposal for which observing time was awarded varies in each case, and all target different scientific goals (e.g., study of AGN, SFR, and X-ray binaries). For this reason, we do not expect our subsample to be biased toward a certain type of object, merger stage, or luminosity within the parent GOALS sample.

### 3. Observations and data reduction

Thirty-one systems were observed with *Chandra* in cycle 13 (PI: Sanders) with a 15 ks exposure on each target, carried out in imaging mode with the ACIS-S detector in VFaint mode (Garmire et al. 2003). For the remaining 32 objects studied in this work, *Chandra* data were obtained from the archive. Exposure times for these targets varied from 4.88 to 58.34 ks, all taken with the ACIS-S detector in either FAINT or VFaint mode. Table 2 shows the observation log for the whole CGII sample, as well as the total source counts in the 0.5–7 keV band for each object, obtained from the data analysis. The counts were derived for individual galaxies, and summed together when an object within the CGII sample contained more than one galaxy.

The data reduction was performed using the *Chandra* data analysis package CIAO version 4.7 (Fruscione et al. 2006), and HEASARC's FTOOLS (Blackburn et al. 1995). The cosmology adopted here is consistent with that adopted by Armus et al. (2009) and Iwasawa et al. (2011). Cosmological distances were computed by first correcting for the three-tractor flow model of Mould et al. (2000) and adopting  $H_0 = 70 \text{ km s}^{-1} \text{ Mpc}^{-1}$ ,  $\Omega_V = 0.72$ , and  $\Omega_M = 0.28$  based on the five-year WMAP results (Hinshaw et al. 2009), as provided by the NASA/IPAC Extragalactic Database (NED).

## 4. Results

Results of the X-ray analysis of the *Chandra* data are presented in Table A.1. For each galaxy we present the background-corrected ACIS-S X-ray soft band ( $S$ , 0.5–2 keV) count rate and X-ray hard band ( $H$ , 2–7 keV) count rate, the hardness ratio or X-ray color, estimated X-ray fluxes and luminosities in both soft and hard band, and the logarithmic ratio of each X-ray band to the IR luminosity listed in Table 1,  $L_{\text{IR}}(8\text{--}1000 \mu\text{m})$ . X-ray color, or hardness ratio, is computed as  $\text{HR} = (H - S)/(H + S)$ , using the bands defined previously.

Individual galaxies belonging to the same GOALS system (i.e., contributing to one single IRAS source) are identified by using the same GOALS number in the first column. Source names shown in the second column are used throughout this work; see Appendix A for a clarification on the identification of each component.

The hard X-ray flux ( $F_{\text{HX}}$ ) listed in Table A.1 is in the 2–7 keV band, where *Chandra* is more sensitive; and the listed hard X-ray luminosities ( $L_{\text{HX}}$ ) refer to the 2–10 keV band. Spectral fitting to derive the fluxes is performed in the 2–7 keV range as described in Sect. 4.4, and the fitted models are later used to estimate the luminosity up to 10 keV, in order to compare the derived results to those of previous works, in which the 2–10 keV band is used.

Although significant intrinsic absorption in dusty objects such as LIRGs is likely present, X-ray luminosities were estimated by correcting only for galactic absorption. The X-ray spectra of our galaxies are complex, containing multiple components, with different degrees of obscuration, as explained in Sect. 4.4. As the estimated absorbing column density values are heavily model dependent, we did not use them to correct the luminosities listed in Table A.1.

As mentioned in Sect. 2, many of the LIRGs in the CGII sample are composed of multiple galaxies, which are associated with a single GOALS object, as IRAS is unable to resolve them. All spatially resolved components in the *Chandra* data are presented separately, their count rates, fluxes, and luminosities were computed individually. In order to obtain the X-ray to IR ratios listed in Table A.1, the IRAS flux associated with each object must be appropriately separated into the corresponding contribution of each component. This separation was carried out according to the best possible estimate available for each source, as listed in Table 3. The most accurate estimation would be derived by obtaining the separate contribution of each component from the far-infrared (FIR) emission. When possible, this was done using *Herschel* photometric data (Chu et al. 2017). However, 14 of the multiple systems in the sample are unresolved by *Herschel*, and thus the MIR *Spitzer* MIPS 24 data were used for this purpose.

For four systems in the sample the individual components remain unresolved at MIR wavelengths, and other determinations were used, as specified in Table 3 and Appendix A.

Only objects that were detected in X-rays and contribute to at least 10% of the IR luminosity of the IRAS source were analyzed and are presented in this work. This cut means that out of the 63 GOALS systems in the sample, 84 individual galaxies are studied in CGII. No galaxy contributing <10% to the IR has a strong X-ray emission, but in cases in which the source is detected in the *Chandra* data, it is specified in Appendix A. For all galaxies in pairs that are not included in the analysis, their contribution to the IR luminosity of the bright component is taken into account.

### 4.1. X-ray images

We show how the X-ray radiation is related to the optical and IR emission, by comparing the 0.4–7 keV brightness contours with HST, SDSS, or IRAC images according to availability, in this order of preference. Appendix B shows X-ray contours overlaid on HST-ACS F814W ( $I$ -band) images (Evans et al. in prep.) for 27 objects, overlaid on SDSS DR-12  $i$ -band images (Alam et al. 2015) for 18 objects and overlaid on IRAC channel 1 images (Armus et al. 2009; Mazzarella et al., in prep.) for the remaining 18 objects.

The contours are taken from a 0.4–7 keV image, smoothed using a Gaussian filter with a dispersion of 1 arcsec, with the

**Table 2.** *Chandra* observation log for the objects in the CGII sample.

| No. | Galaxy           | Obs ID | Date       | Mode   | Exp. Time<br>(ks) | 0.5–7.0 keV <sup>a</sup><br>(cts) | $N_{\text{H,Gal}}^b$<br>( $10^{20} \text{ cm}^{-2}$ ) |
|-----|------------------|--------|------------|--------|-------------------|-----------------------------------|---|
| 45  | UGC 08387        | 7811   | 2007-02-19 | VFAINT | 14.07             | 277.9 ± 17.1                      | 1.0   |
| 47  | CGCG 436-030     | 15047  | 2012-11-24 | VFAINT | 13.82             | 168.6 ± 13.8                      | 3.4   |
| 49  | NGC 0695         | 15046  | 2013-01-01 | VFAINT | 14.78             | 312.9 ± 18.5                      | 6.9   |
| 50  | CGCG 043-099     | 15048  | 2012-11-23 | VFAINT | 14.78             | 71.9 ± 8.1                        | 1.9   |
| 51  | MCG+07-23-019    | 12977  | 2011-02-07 | VFAINT | 52.34             | 506.9 ± 26.8                      | 1.0   |
| 52  | NGC 6670         | 15049  | 2013-02-08 | VFAINT | 14.77             | 252.7 ± 16.8                      | 3.9   |
| 53  | UGC 02369        | 4058   | 2002-12-14 | FAINT  | 9.68              | 120.6 ± 12.0                      | 7.9   |
| 54  | NGC 1614         | 15050  | 2012-11-21 | VFAINT | 15.76             | 800.0 ± 28.9                      | 6.3   |
| 56  | NGC 5331         | 15051  | 2013-05-12 | VFAINT | 14.78             | 121.9 ± 12.4                      | 2.0   |
| 57  | IRAS F06076-2139 | 15052  | 2012-12-12 | VFAINT | 14.78             | 52.4 ± 8.2                        | 7.6   |
| 60  | IC 2810          | 15053  | 2013-10-27 | VFAINT | 14.78             | 93.2 ± 11.7                       | 2.5   |
| 63  | IRAS 18090+0130  | 15054  | 2013-02-10 | VFAINT | 14.77             | 98.9 ± 11.3                       | 20.2  |
| 64  | III Zw 035       | 6855   | 2006-02-24 | FAINT  | 14.98             | 81.4 ± 9.0                        | 4.8   |
| 65  | NGC 3256         | 835    | 2000-01-05 | FAINT  | 27.80             | 8117.2 ± 102.3                    | 9.1   |
| 67  | IRAS F16399-0937 | 15055  | 2013-06-30 | VFAINT | 14.87             | 161.9 ± 14.4                      | 13.0  |
| 68  | IRAS F16164-0746 | 15057  | 2013-01-19 | VFAINT | 14.78             | 99.2 ± 11.3                       | 11.3  |
| 69  | IC 4686/7        | 15056  | 2012-11-19 | VFAINT | 14.48             | 519.7 ± 23.8                      | 11.5  |
| 71  | NGC 2623         | 4059   | 2003-01-03 | FAINT  | 19.79             | 171.0 ± 14.1                      | 3.1   |
| 72  | IC 5298          | 15059  | 2013-02-04 | VFAINT | 14.78             | 222.8 ± 16.0                      | 5.7   |
| 73  | IRAS 20351+2521  | 15058  | 2012-12-13 | VFAINT | 13.56             | 146.8 ± 14.0                      | 13.1  |
| 75  | NGC 6090         | 6859   | 2006-05-14 | FAINT  | 14.79             | 347.5 ± 19.3                      | 1.6   |
| 79  | NGC 5256         | 2044   | 2001-11-02 | FAINT  | 19.69             | 1451.2 ± 43.5                     | 1.7   |
| 80  | IRAS F03359+1523 | 6856   | 2005-12-17 | FAINT  | 14.76             | 108.2 ± 11.4                      | 13.8  |
| 81  | ESO 550-IG025    | 15060  | 2012-11-24 | VFAINT | 14.78             | 72.2 ± 10.6                       | 3.2   |
| 82  | NGC 0034         | 15061  | 2013-06-05 | VFAINT | 14.78             | 329.0 ± 19.5                      | 2.1   |
| 83  | MCG+12-02-001    | 15062  | 2012-11-22 | VFAINT | 14.31             | 311.0 ± 19.3                      | 22.0  |
| 85  | IRAS F17138-1017 | 15063  | 2013-07-12 | VFAINT | 14.78             | 207-3 ± 15.4                      | 17.0  |
| 95  | ESO 440-IG058    | 15064  | 2013-03-20 | VFAINT | 14.78             | 187.0 ± 16.1                      | 5.6   |
| 100 | NGC 7130         | 2188   | 2001-10-23 | FAINT  | 38.64             | 3327.1 ± 59.3                     | 1.9   |
| 104 | NGC 7771         | 10397  | 2009-05-22 | VFAINT | 16.71             | 904.6 ± 34.6                      | 4.0   |
| 105 | NGC 7592         | 6860   | 2006-10-15 | FAINT  | 14.99             | 388.7 ± 21.9                      | 3.8   |
| 106 | NGC 6286         | 10566  | 2009-09-18 | FAINT  | 14.00             | 544.8 ± 27.9                      | 1.8   |
| 107 | NGC 4922         | 15065  | 2013-11-02 | VFAINT | 14.86             | 202.9 ± 17.2                      | 0.9   |
| 110 | NGC 3110         | 15069  | 2013-02-02 | VFAINT | 14.87             | 396.3 ± 22.3                      | 3.5   |
| 114 | NGC 0232         | 15066  | 2013-01-04 | VFAINT | 14.78             | 193.5 ± 15.7                      | 1.4   |
| 117 | MCG+08-18-013    | 15067  | 2013-06-03 | VFAINT | 13.79             | 101.7 ± 11.1                      | 1.7   |
| 120 | CGCG 049-057     | 10399  | 2009-04-17 | VFAINT | 19.06             | 30.2 ± 7.6                        | 2.6   |
| 121 | NGC 1068         | 344    | 2000-02-21 | FAINT  | 47.44             | 100828.1 ± 326.7                  | 2.9   |
| 123 | UGC 02238        | 15068  | 2012-12-02 | VFAINT | 14.87             | 132.1 ± 13.5                      | 8.9   |
| 127 | MCG-03-34-064    | 7373   | 2006-07-31 | FAINT  | 7.09              | 1029.3 ± 32.9                     | 5.0   |
| 134 | ESO 350-IG038    | 8175   | 2006-10-28 | VFAINT | 54.00             | 1794.5 ± 45.8                     | 2.4   |
| 136 | MCG-01-60-022    | 10570  | 2009-08-13 | FAINT  | 18.90             | 325.4 ± 21.7                      | 3.6   |
| 141 | IC 0563/4        | 15070  | 2013-01-19 | VFAINT | 14.96             | 252.5 ± 18.9                      | 3.8   |
| 142 | NGC 5135         | 2187   | 2001-09-04 | FAINT  | 29.30             | 3975.9 ± 68.0                     | 4.9   |
| 144 | IC 0860          | 10400  | 2009-03-24 | VFAINT | 19.15             | 25.9 ± 7.2                        | 1.0   |
| 147 | IC 5179          | 10392  | 2009-06-21 | VFAINT | 11.96             | 555.5 ± 32.2                      | 1.4   |
| 148 | CGCG 465-012     | 15071  | 2012-12-17 | VFAINT | 14.87             | 134.0 ± 13.4                      | 14.8  |
| 157 | MCG-02-33-098/9  | 15072  | 2013-05-08 | VFAINT | 14.87             | 141.0 ± 12.4                      | 3.7   |
| 163 | NGC 4418         | 4060   | 2003-03-10 | FAINT  | 19.81             | 59.6 ± 15.3                       | 1.9   |
| 169 | ESO 343-IG013    | 15073  | 2013-06-13 | VFAINT | 14.78             | 139.6 ± 13.9                      | 2.8   |
| 170 | NGC 2146         | 3135   | 2002-11-16 | FAINT  | 10.02             | 2144.2 ± 50.4                     | 7.1   |
| 174 | NGC 5653         | 10396  | 2009-04-11 | VFAINT | 16.52             | 387.1 ± 22.8                      | 1.3   |
| 178 | NGC 4194         | 7071   | 2006-09-09 | FAINT  | 35.50             | 2410.3 ± 51.4                     | 1.5   |
| 179 | NGC 7591         | 10264  | 2009-07-05 | FAINT  | 4.88              | 26.3 ± 6.1                        | 5.6   |
| 182 | NGC 0023         | 10401  | 2008-10-27 | VFAINT | 19.45             | 753.1 ± 31.9                      | 3.4   |
| 188 | NGC 7552         | 7848   | 2007-03-31 | FAINT  | 5.08              | 832.8 ± 30.2                      | 1.2   |
| 191 | ESO 420-G013     | 10393  | 2009-05-13 | VFAINT | 12.42             | 759.0 ± 29.2                      | 2.1   |
| 194 | ESO 432-IG006    | 15074  | 2013-06-24 | VFAINT | 16.05             | 280.7 ± 20.0                      | 19.3  |
| 195 | NGC 1961         | 10531  | 2009-05-08 | VFAINT | 32.83             | 723.3 ± 40.0                      | 8.1   |
| 196 | NGC 7752/3       | 10569  | 2009-08-30 | FAINT  | 11.99             | 96.0 ± 12.7                       | 5.4   |
| 198 | NGC 1365         | 6869   | 2006-04-20 | FAINT  | 15.54             | 4644.2 ± 72.7                     | 1.3   |
| 199 | NGC 3221         | 10398  | 2009-03-19 | VFAINT | 19.03             | 323.5 ± 28.3                      | 1.9   |
| 201 | NGC 0838         | 15667  | 2013-07-21 | VFAINT | 58.34             | 1996.0 ± 49.6                     | 2.6   |

**Notes.** <sup>(a)</sup>The source counts are background corrected and measured in the 0.5–7.0 keV band. The counts from separate components in a single system are obtained separately and then summed together. <sup>(b)</sup>The Galactic absorption column density is taken from the LAB HI map by Kalberla et al. (2005).

**Table 3.** IR fractions.

| No. | Galaxy in system<br>(1) | %<br>(2) | Ref.<br>(3) |
|-----|-------------------------|----------|-------------|
| 47  | CGCG 436–030 (W)        | 100      | 5           |
| 52  | NGC 6670 (W)            | 62       | 1           |
| 53  | UGC 02369 (S)           | 98       | 2           |
| 56  | NGC 5331 (S)            | 81       | 1           |
| 57  | IRAS F06076–2139 (N)    | 88       | 2           |
| 60  | IC 2810 (NW)            | 68       | 1           |
| 63  | IRAS 18090+0130 (E)     | 81       | 1           |
| 64  | III Zw 035 (N)          | 100      | 5           |
| 67  | IRAS F16399–0937 (N)    | 90       | 3           |
| 69  | IC 4687 (N,S)*          | 66,22    | 1           |
| 75  | NGC 6090 (NE)           | 90       | 4           |
| 79  | NGC 5256 (SW)           | 63       | 2           |
| 80  | IRAS F03359+1523 (E)    | 100      | 5           |
| 81  | ESO 550–IG025 (N)       | 59       | 1           |
| 83  | MCG+12–02–001 (E,W)*    | 90,10    | 2           |
| 95  | ESO 440–IG058 (S)       | 89       | 1           |
| 104 | NGC 7771                | 90       | 1           |
| 105 | NGC 7592 (E,S)*         | 63,0     | 2           |
| 106 | NGC 6286                | 87       | 1           |
| 107 | NGC 4922 (N)            | 99       | 2           |
| 110 | NGC 3110 (NE)           | 91       | 1           |
| 117 | MCG+08–18–013 (E)       | 97       | 1           |
| 127 | MCG–03–34–064           | 75       | 1           |
| 141 | IC 0564                 | 54       | 1           |
| 157 | MCG–02–33–098/9 (W)     | 69       | 2           |
| 163 | NGC 4418                | 99       | 1           |
| 169 | ESO 343–IG013 (N)       | 78       | 2           |
| 179 | NGC 7591                | 94       | 1           |
| 194 | ESO 432–IG006 (SW)      | 63       | 1           |
| 196 | NGC 7753                | 64       | 1           |

**Notes.** Column (1): Name of the galaxy (galaxies) that emits most of the IR luminosity in a double (triple) system. Column (2): Percentage of IR emission originating in the dominant component. Column (3): Reference from which the contribution to the IR luminosity is derived. 1: Derived from *Herschel* data (as in [Chu et al. 2017](#)). 2: Derived from MIPS 24 data (as in [Díaz-Santos et al. 2010](#)). 3: MIR determination from [Haan et al. \(2011\)](#). 4: Predicted IR emission from radio continuum in [Hattori et al. \(2004\)](#). 5: We refer to the notes on individual objects in Appendix A. (\*)Triple-component galaxy.

exception of NGC 5135, shown in Appendix B, for which a smoothing of 0.5 arcsec was used in order to preserve the two X-ray central peaks.

Eleven contour levels were defined, divided into ten equal logarithmic intervals, in the four different surface brightness ranges shown in Table 4. “Interval 1” was used for the majority of the sample. In order to outline lower surface brightness features in some sources, 11 contour levels starting at a lower surface brightness values were taken, as “Interval 2” or “Interval 3”. For a few systems, a higher lower surface brightness limit was taken in order to eliminate noisy features in the contours, defined as “Interval 4”. For the bright objects NGC 1068 and NGC 1365, 21 contour levels were used instead, in order to reflect the X-ray morphology appropriately. Appendix B contains information on which optical or IR image was used to overlay the X-ray contours on, and also on the Interval that we used for X-ray contour ranges.

As the hard-band emission from all objects is generally more peaked and less intense than the soft-band emission, the contours mostly trace soft X-ray emission from the sources. For

**Table 4.** X-ray contour ranges.

| Interval      | Low<br>(1)           | High<br>(2)          | Levels<br>(3) |
|---------------|----------------------|----------------------|---------------|
| 1             | $2.5 \times 10^{-5}$ | $7 \times 10^{-3}$   | 11            |
| 2             | $1.7 \times 10^{-5}$ | $7 \times 10^{-3}$   | 11            |
| 3             | $1.0 \times 10^{-5}$ | $7 \times 10^{-3}$   | 11            |
| 4             | $4.0 \times 10^{-5}$ | $7 \times 10^{-3}$   | 11            |
| <b>Galaxy</b> |                      |                      |               |
| CGCG 465-012  | $2.5 \times 10^{-5}$ | $2.0 \times 10^{-4}$ | 11            |
| NGC 1068      | $2.5 \times 10^{-5}$ | $4.0 \times 10^{-2}$ | 21            |
| NGC 5135      | $4.0 \times 10^{-5}$ | $1.0 \times 10^{-2}$ | 11            |
| NGC 1365      | $2.5 \times 10^{-5}$ | $2.0 \times 10^{-2}$ | 21            |
| NGC 0838      | $7.0 \times 10^{-6}$ | $4.0 \times 10^{-4}$ | 11            |

**Notes.** Columns (1) and (2): Lower and higher contour in [ $\text{counts s}^{-1} \text{arcsec}^{-1}$ ] for the given interval, respectively. (4): Number of logarithmic contour levels.

this reason, in sources for which one or more clear hard X-ray peaks are seen, these are marked with a green cross. We define a hard X-ray peak as point-source emission that clearly stands out from the rest of the photon distribution in the unsmoothed images. In cases where many point-like sources that are clearly not associated with any central source in the galaxy are present in an image, we opted not to mark them all individually. For a more detailed description of the X-ray emission in both bands, Appendix B also presents the smoothed and unsmoothed images in the 0.4–7 keV band, and smoothed images in the soft (0.5–2 keV) and hard (2–7 keV) bands, for all objects. An example of one of these images is shown in Fig. 2.

#### 4.2. X-ray spectra

Figure C.1 presents the X-ray spectra for all sources. Spectral data are shown separately for each object with more than one resolved component. Instead of showing the usual count rate spectra, which are data folded through the detector response, we present the *Chandra* ACIS spectra corrected for the detector response and converted into flux density units. This has the advantage of presenting the spectral properties without the need of spectral fitting, and facilitates comparison with other multi-wavelength data from GOALS. The flux density range for all spectra was set to be the same, two orders of magnitude, for consistent comparison. An example of one such spectrum is shown in Fig. 3.

This presentation introduces some uncertainty, particularly when a spectral bin is large enough, within which the detector response varies rapidly, for instance, for galaxies with only few counts. It should also be taken into account that even though these have been corrected for the detector effective area, the energy resolution of the detector is preserved, and therefore they are independent of any spectral model fitting; that is to say, they are not unfolded spectra.

It should also be noted that the spectra in Fig. C.1 are for display purposes only, and all physical quantities determined were obtained through spectral fitting of the count rate spectra, with the appropriate detector responses.

#### 4.3. AGN selection

The AGN classification in the sample was performed using different criteria in both X-rays and IR. Any galaxy that met any of

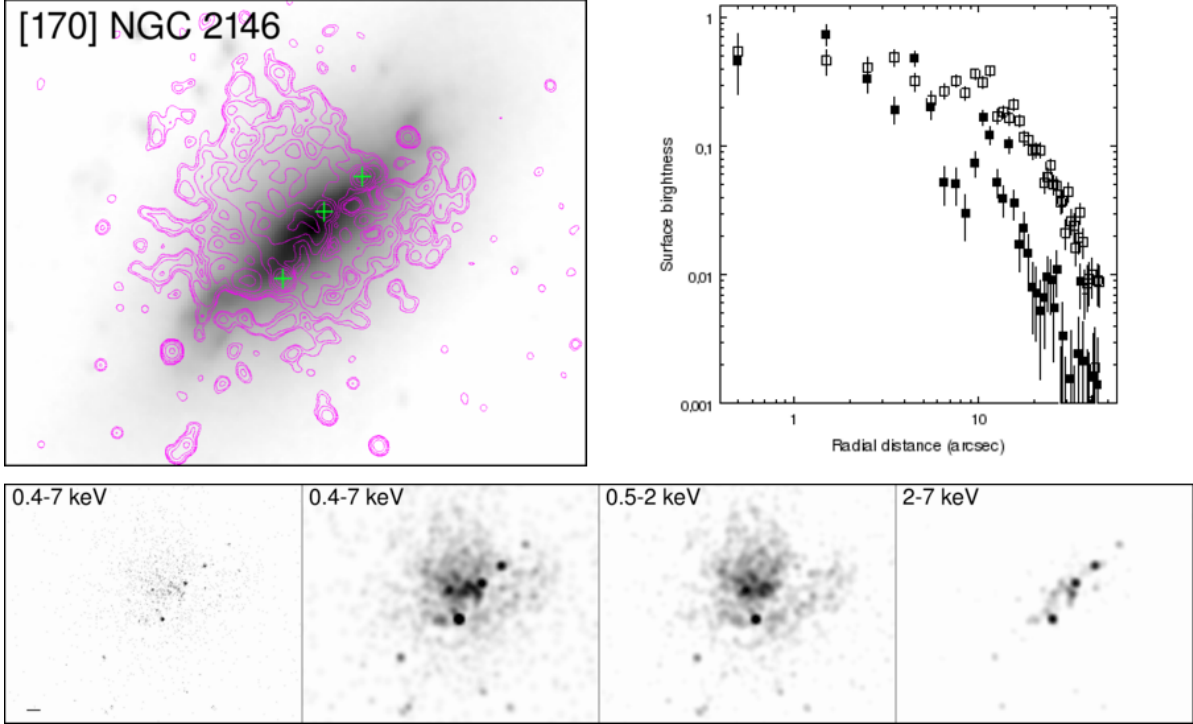


**Fig. 2.** X-ray images and surface brightness profiles for NGC 2146. North is up and east to the left. Similar figures for all 59 objects in the CGII sample are presented in Appendix B. *Upper left:* X-ray (0.4–7 keV) brightness contours (magenta) with marked hard X-ray peaks (green crosses) overlaid on optical/IR images. *Upper right:* Radial surface brightness profiles in the 0.5–2 keV band (open squares) and the 2–7 keV band (filled squares). Profiles have been centered using the brightness peak in the hard X-ray band, when clearly originating in the nucleus. We refer to Appendix A for ambiguous objects. *Bottom:* From left to right, unsmoothed and smoothed images in the 0.4–7 keV band, and smoothed images in the soft (0.5–2 keV) and hard (2–7 keV) bands. The pixel size is  $\sim 0.5'' \times 0.5''$ . The scale bar in the *bottom left* image represents  $5''$ .

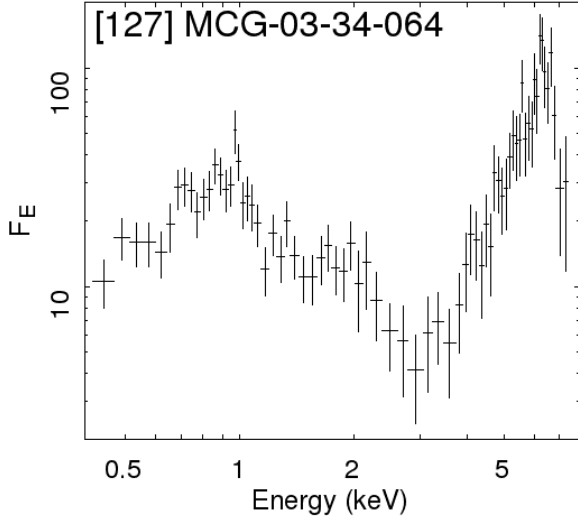


**Fig. 3.** X-ray flux density spectra for MCG-03-34-064, obtained from the *Chandra* ACIS. Flux density in units of  $10^{-14} \text{ erg s}^{-1} \text{ cm}^{-2} \text{ keV}^{-1}$ .

our selection criteria, described below, was classified as an AGN and is listed in Table 5.

The X-ray selection was performed using two different methods: an X-ray color selection, and detection of AGN spectral features.

The X-ray color, or hardness ratio, gives the relative intensity of emission in hard and soft bands (in counts). A high HR indicates strong emission above 2 keV, which is often associated with the presence of an obscured AGN, that is, column density,  $N_{\text{H}}$  in the range of  $10^{22} - 10^{24} \text{ cm}^{-2}$ . The threshold for AGN selection was chosen as  $\text{HR} > -0.3$ , as it was for the CGI sample (see Iwasawa et al. 2011).

Figure 4 shows the hardness ratio of all sources in the sample as a function of their hard X-ray luminosity. AGN selected through all criteria described in this section are plotted with filled squares, while all absorbed AGN are marked with open circles. Most AGN in the sample have an HR below the threshold, as many are absorbed or not selected through X-rays.

Some AGN are missed by this HR selection because absorption in the nucleus is significant and soft X-ray emission coming from external starburst regions is strong. Such galaxies can still show a hard-band excess in their spectra, and if fitting them with an absorbed power-law with a fixed 1.8 photon index yielded a high enough absorbing column density, we classified them as absorbed AGN (see Sect. 4.4.2). Each of these cases is listed in Table 5 and discussed individually in Appendix A.

When absorption is even stronger, only reflected radiation can be observed in the hard band, and therefore sources appear weak, their HR being even smaller. A clear signature of a highly obscured AGN is the detection of a strong Fe  $K\alpha$  line at 6.4 keV, which is also used as a criterion for AGN selection. We set a threshold of  $2\sigma$  for the detection of the iron line in order to classify a source as an AGN. Sources selected through this

**Table 5.** Sources with an AGN signature in IR or X-rays.

| No. | Galaxy               | AGN <sub>bol</sub><br>(1) | [Ne v]<br>(2) | PAH<br>(3) | X<br>(4) |
|-----|----------------------|---------------------------|---------------|------------|----------|
| 45  | UGC 08387            | 0.03 ± 0.01               | Y             | N          | N        |
| 57  | IRAS F06076–2139 (S) | –                         | N             | N          | C        |
| 68  | IRAS F16164–0746     | 0.05 ± 0.01               | Y             | N          | C        |
| 71  | NGC 2623             | 0.10 ± 0.03               | Y             | N          | C        |
| 72  | IC 5298              | 0.33 ± 0.05               | Y             | N          | A        |
| 79  | NGC 5256 (NE)        | 0.23 ± 0.07(u)            | Y(u)          | N          | A        |
| 79  | NGC 5256 (SW)        | 0.23 ± 0.07(u)            | Y(u)          | N          | L        |
| 82  | NGC 0034             | 0.04 ± 0.02               | N             | N          | A        |
| 85  | IRAS F17138–1017     | 0.07 ± 0.04               | N             | N          | C        |
| 100 | NGC 7130             | 0.22 ± 0.04               | Y             | N          | LA       |
| 105 | NGC 7592 (W)         | 0.20 ± 0.06               | Y(u)          | N          | N        |
| 106 | NGC 6286             | 0.11 ± 0.06               | N             | N          | A*       |
| 107 | NGC 4922 (N)         | 0.17 ± 0.05               | Y             | N          | A        |
| 114 | NGC 0232             | 0.09 ± 0.03               | Y             | N          | N        |
| 120 | CGCG 049–057         | 0.04 ± 0.02               | N             | N          | C        |
| 121 | NGC 1068             | 1.00 ± 0.01               | Y             | –          | L        |
| 127 | MCG–03–34–064        | 0.88 ± 0.04               | Y             | Y          | LA       |
| 136 | MCG –01–60–022       | 0.08 ± 0.06               | N             | –          | CA       |
| 142 | NGC 5135             | 0.24 ± 0.06               | Y             | N          | L        |
| 144 | IC 0860              | 0.06 ± 0.03               | N             | N          | C        |
| 163 | NGC 4418             | 0.48 ± 0.22               | N             | Y          | N        |
| 169 | ESO 343–IG013 (N)    | 0.09 ± 0.04               | N             | N          | C        |
| 191 | ESO 420–G013         | 0.25 ± 0.04               | Y             | N          | N        |
| 194 | ESO 432–IG006 (NE)   | 0.12 ± 0.04               | N             | N          | A        |
| 194 | ESO 432–IG006 (SW)   | 0.09 ± 0.05               | N             | N          | A        |
| 198 | NGC 1365             | 0.38 ± 0.03               | N             | N          | CLA      |

**Notes.** Column (1): Contribution of the AGN to the bolometric luminosity of the galaxy (Díaz-Santos et al. 2017). Column (2): Detection of the [Ne v] line (Petric et al. 2011). Column (3): EW of the 6.2 μm PAH feature < 0.1 μm (Stierwalt et al. 2013). Column (4): X-ray AGN selection criteria. C: X-ray color (HR > –0.3); L: Detection of 6.4 KeV line. A: Absorbed AGN feature. Y: Source meets the criterion. N: Source does not meet the criterion. (u) Unresolved detection in a multiple system. (\*) Only in the *NuSTAR* data (Ricci et al. 2016). See Appendix A for details on particular sources.

criterion are listed in Table 5, and details on the iron line fits can be found in Sect. 4.4, Table 6.

The IR selection was performed by means of the detection of the [Ne v] 14.32 μm line over kpc scales, which traces high-ionization gas. The ionization potential of [Ne v] is 96 eV, which is too high to be produced by OB stars. Therefore, detection of this line in the integrated spectra of galaxies is a good AGN indicator (see Petric et al. 2011, and references therein).

Another possible indicator is when the equivalent width of the 6.2 μm PAH feature is lower than 0.1 μm. Polycyclic aromatic hydro-carbons (PAHs) are either destroyed by the radiation originating from the AGN, or their features are diluted in the spectra by the strong MIR continuum it creates; this results in a low value of the EW (see Stierwalt et al. 2013, and references therein).

With the X-ray criteria alone, we found that 21 galaxies host an AGN. This represents (25 ± 5)% of our sample. With the addition of IR criteria, 5 other galaxies are classified as AGN, resulting in a total AGN fraction of (31 ± 5)% for the 84 individually analyzed galaxies in CGII. Galaxies selected as AGN are presented in Table 5, along with optical classifications and whether or not they meet our X-ray and IR selection criteria.

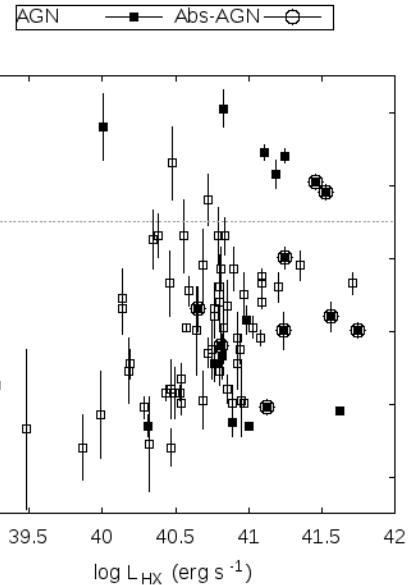


**Fig. 4.** Hardness ratio as a function of the 2–7 keV luminosity for all sources in the CGII sample. All AGN from Table 5 are plotted as filled squares, and those in which absorption features are fit (labeled A in the table) are marked with an open circle. The dashed line shows the –0.3 boundary, above which sources are selected as AGN (unless evidence points toward a lack of AGN presence, see Appendix A).

Two sources in the sample met the selection criteria, but we opted to not classify them as AGN, for reasons explained in Appendix A: IRAS F17138–1017 and IRAS F16399–0937 (S), which meet the HR criterion.

Table 5 also lists the contribution of the AGN to the bolometric luminosity for all sources classified as AGN. The contribution of the AGN to the MIR luminosity was derived by Díaz-Santos et al. (2017) for all GOALS galaxies, employing up to five *Spitzer*/IRS diagnostics. Applying corrections based on spectral energy distribution (SED) templates of pure starbursts and AGN sources, they derived the fractional contribution of the AGN to the overall bolometric luminosity (as in Veilleux et al. 2009).

Figure 5 shows the HR of all sources in the sample as a function of the fractional contribution of the AGN to the bolometric luminosity, AGN<sub>bol</sub>. Sources with a fraction larger than 0.2 can be considered to have an energetically significant AGN. X-ray selected AGN, through any of the three criteria mentioned above, are highlighted as filled symbols. All marked AGN below the HR = –0.3 threshold show signs of obscuration, as they have been selected through any of the other two X-ray criteria. In the full C-GOALS sample, 19 of 32 X-ray selected AGN lay below AGN<sub>bol</sub> < 0.2. Therefore, more than half of the AGN detected through X-rays are not easily selected through the described combination of MIR diagnostics.

#### 4.4. X-ray spectral fitting

The 0.4–7 keV *Chandra* spectra of the CGII galaxies present similar properties to those of the CGI sample, that was analyzed by Iwasawa et al. (2011): a mostly emission-line dominated soft X-ray band, and a hard X-ray power-law. As has been discussed by these authors, both the spectral shape and the morphology of the emission (see images in Appendix B) suggest a different

**Table 6.** Fe  $K\alpha$  line fits.

| No. | Galaxy        | $E$<br>(keV)           | $I$<br>( $10^{-6} \text{ s}^{-1} \text{ cm}^{-2}$ ) | EW<br>(keV)            |
|-----|---------------|------------------------|---|------------------------|
| 79  | NGC 5256 (SW) | $6.44^{+0.04}_{-0.05}$ | $1.4^{+0.9}_{-0.6}$                                 | $4.0^{+2.6}_{-1.8}$    |
| 100 | NGC 7130      | $6.42^{+0.03}_{-0.04}$ | $3.3^{+1.6}_{-1.3}$                                 | $0.8^{+0.4}_{-0.3}$    |
| 121 | NGC 1068      | $6.43^{+0.07}_{-0.04}$ | $32.2^{+12.6}_{-9.0}$                               | $0.9^{+0.3}_{-0.3}$    |
| 127 | MCG-03-34-064 | $6.43^{+0.10}_{-0.08}$ | $77.1^{+32.8}_{-25.4}$                              | $0.7^{+0.3}_{-0.2}$    |
| 142 | NGC 5135      | $6.41^{+0.03}_{-0.03}$ | $7.2^{+2.9}_{-2.5}$                                 | $1.1^{+0.4}_{-0.4}$    |
| 198 | NGC 1365      | $6.35^{+0.03}_{-0.04}$ | $40.3^{+15.0}_{-14.0}$                              | $0.14^{+0.07}_{-0.04}$ |

**Notes.** Iron  $K\alpha$  Line detections with a significance of  $2\sigma$  or higher. The line centroid energy is measured in the rest frame. Errors reported correspond to  $1\sigma$  for one parameter of interest, leaving five parameters free.

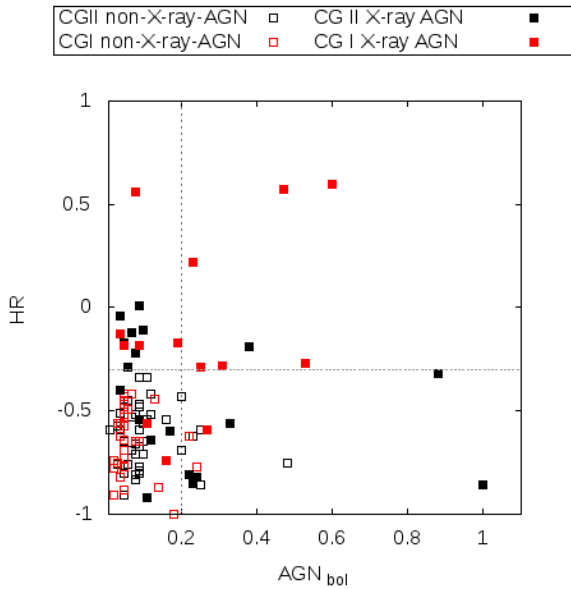


**Fig. 5.** Hardness ratio as a function of the fractional contribution of the AGN to the bolometric luminosity (as derived from MIR data, Díaz-Santos et al. 2017) of the source, in red for CGI sources and black for CGII. X-ray selected AGN from Table 5 are plotted as filled squares. The horizontal dashed line shows the  $HR = -0.3$  threshold. The vertical dashed line shows the value above which the AGN is energetically significant.

origin for the soft and hard X-rays, and therefore the two were analyzed separately.

A few objects in the sample (IRAS 18090+0130 (W), IRAS F06076-2139 (S), IC 0860, and NGC 7591) were not fit because they have an excessively low count number, of the order of  $\lesssim 25$  cts, in the full 0.4–7 keV band. For these sources, only the count rates and HR were computed, and results on fluxes and luminosities are not presented in Table A.1.

For the majority of our sources, which have few counts, we made the fit through C statistic minimization instead of  $\chi^2$  minimization.

#### 4.4.1. Soft band (0.4–2 keV) fitting

Starburst galaxies, when not dominated by a luminous AGN, have soft X-ray emission originating in hot interstellar gas

( $\sim 0.2$ – $1$  keV), which is shock-heated by supernovae explosions and stellar winds from massive stars. Emission from hot gas can generally be fit with a standard thermal emission model, with a solar abundance pattern, for instance, *mekal* (Mewe et al. 1985; Kaastra 1992; Liedahl et al. 1995). However, in our data, such a simple model does not agree with many of the observed emission line strengths and provides an unsatisfactory fit in most cases. A better fit can be obtained either with a modified abundance pattern that is richer in  $\alpha$  elements, or through the overlap of more than one *mekal* at different temperatures.

The hot gas within a starburst region is expected to be enriched by  $\alpha$  elements, which are produced in core-collapse supernovae. Metal abundances should deviate from a solar pattern, as has been found for star-forming knots in nearby galaxies, such as the Antennae (Fabbiano et al. 2004). At the same time, the extended soft X-ray emitting gas is expected to be multiphase: the shocked gas swept away by a starburst wind seen at outer radii is free from absorption, while the hotter gas at inner radii may have some absorption of the interstellar medium (e.g., Strickland & Stevens 2000). A temperature gradient can be approximated at first order as two *mekal* models with different temperatures. One model would fit the most external, colder gas component (at  $T = T_1$ ), which is located far away from the nucleus, and therefore is less strongly absorbed by the interstellar material. The other model would fit the inner, hotter gas (at  $T = T_2$ ), which is obscured by the denser material in the central region of the galaxy.

Ideally, the data should be modeled using more than one *mekal* component, with different temperatures and absorbing column densities, and with non-solar metal abundances. However, given the quality of the data, this would imply severe overfitting. As we are interested in probing the level of obscuration in the C-GOALS sources, we opted to model the data using two *mekal* models as defined above, which both have solar abundance patterns.

The results obtained through this fitting, the parameters of which are listed in Table A.2, show that it is possible to satisfactorily fit the sources with high enough number counts using this model, which is to be expected if part of the emission truly originates in a denser, inner region. However, we note that this model is not clearly superior to a single *mekal* component with non-solar abundances, as was used by Iwasawa et al. (2011) on the CGI sample; and that most of the analyzed sources do not have good enough data quality to determine a clear best fit between the two models.

The distributions of the obtained parameters for the full CGII sample are shown in the histograms presented in Fig. 6. The temperature associated with the colder *mekal* component ( $T_1$ ) used to model the 0.5–2 keV emission of each source presents a narrower distribution than that associated with the hotter component ( $T_2$ ). The distribution of  $T_1$  has a median value of  $0.38 \pm 0.03$  keV and an interquartile range of 0.32–0.63 keV. The distribution of  $T_2$  has, as expected, a higher median value of  $0.97 \pm 0.18$ . The interquartile range is 0.77–1.2 keV range, with a long tail extending up to  $T_2 \sim 4.5$  keV. We note that even though the two distributions overlap (i.e., some  $T_1$  values are higher than some  $T_2$  values), for each single source  $T_2 > T_1$ .

Figure 6 also shows the distribution of column densities,  $N_H$ , absorbing the hottest *mekal* component. The median of the distribution is  $(1.1 \pm 0.2) \times 10^{22} \text{ cm}^{-2}$ , with an interquartile range of  $(0.8$ – $1.4) \times 10^{22} \text{ cm}^{-2}$ .

A few sources, named in Sect. 4.4.2, were modeled in the full 0.4–7 keV band with a single power-law; and therefore no values for  $T_1$ ,  $T_2$ , and  $N_H$  were derived for them. In addition, NGC 6285

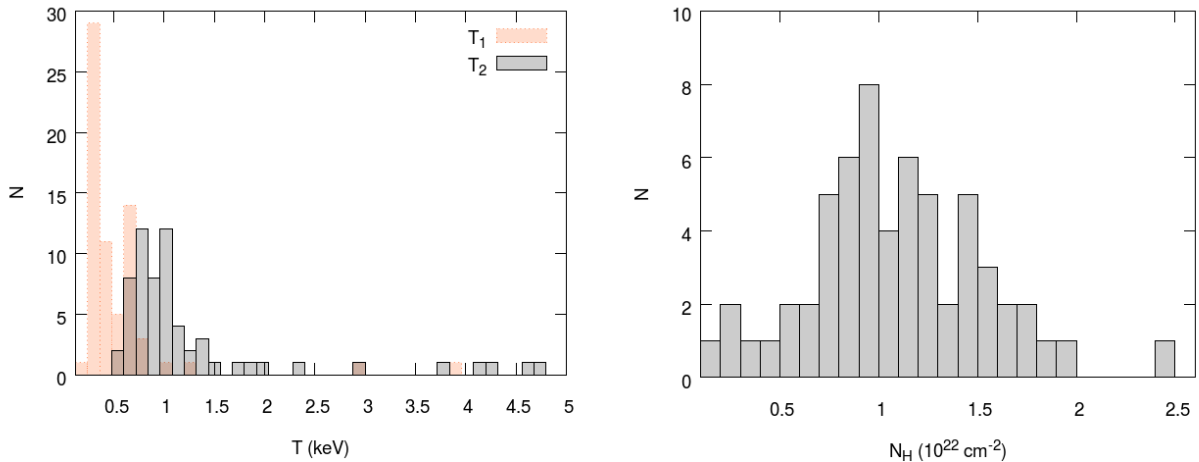


**Fig. 6.** *Left panel:* distribution of *mekal* model temperatures, where  $T_1$  is the temperature of the external, colder gas component and  $T_2$  is the temperature of the internal, hotter gas component, for the CGII sample. *Right panel:* distribution of absorbing column densities associated with the inner, hotter gas component, for the CGII sample.

and IC 2810 (SE) were fit with a single *mekal* component in the 0.4–2 keV range, and NGC 7752/3 (NE) and ESO 440-IG058 (N) were fit with a single *mekal* component in the full 2–7 keV range. These sources are not included in the histograms shown in Fig. 6, or in the averages described previously.

#### 4.4.2. Hard band (2–7 keV) fitting

In the hard X-ray band, where the emission from hot interstellar gas and young stars significantly decreases, X-ray binaries dominate the emission in the absence of an AGN. Their emission can be fit by a simple power-law. The photon index,  $\Gamma$ , is the slope of a power-law model that describes a photon spectrum, defined as  $dN/dE \propto E^{-\Gamma}$  photons  $\text{cm}^{-2} \text{s}^{-1} \text{keV}^{-1}$ . Derived values for  $\Gamma$  for all sources in the CGII sample are listed in Table A.2.

This fit was only performed for galaxies that had at least 20 cts in the 2–7 keV range. Galaxies with a lower count number were fit while imposing a fixed power-law photon index of 2 (average spectral slope found for a sample of local starburst galaxies, Ranalli et al. 2003), leaving only the model normalization as a free parameter. This limit was set in order to obtain meaningful constraints for the spectral slope. It is lower than the one fixed for the CGI sample (50 cts) since many of the sources in the current sample are much fainter, as expected given their lower IR luminosities.

A few objects within the sample show a clear, steep flux increase at energies  $\geq 3$ –4 keV (see, e.g., MCG–03–34–064 in Fig. C.1), which is a sign of the presence of an absorbed AGN (see, e.g., Turner & Miller 2009). In such cases, which all have a count number higher than 20 cts, we fit an absorbed power-law imposing a fixed photon index of 1.8 (a typically expected value for the photon index of an AGN, see, e.g., Nandra & Pounds 1994). This left the absorbing column density,  $N_H$ , as a free parameter. This model was preferred when the fit yielded values  $N_H \geq 10^{23} \text{ cm}^{-2}$ , and it was statistically better than a simple power-law fit. In such cases, we classified the source as an absorbed AGN.

A few sources in the sample (NGC 5331 (N), IRAS F16399–0937 (S), ESO 550–IG025 (S), MCG+12–02–001 (W), CGCG 049–057, UGC 02238, NGC 4418, and ESO 343–IG013 (N) and (S)) are clearly best-fit with a single power-law in the full 0.4–7 keV band, and the  $\Gamma$  parameter shown in Table A.2 corresponds to that fit.

#### 4.4.3. Iron $K\alpha$ lines

The Fe  $K\alpha$  line is a frequently used reliable diagnostic of heavily obscured AGN. As we described in Sect. 4.3, we used it as one of our X-ray AGN selection criteria. The cold iron line seen in some of the CGII sources was fit with a Gaussian model centered at 6.4 keV. Six sources in the CGII sample have such a line fit with a significance above  $2\sigma$ , which is the threshold we set to consider a detection.

A more conservative and frequently used threshold to consider a line as detected in the data is a  $3\sigma$  significance. If we had imposed this more restrictive criterion, only NGC 1068 and MCG–01–34–064 would have detected Fe  $K\alpha$  lines in the sample. The threshold was lowered because of the low signal-to-noise ratio for all sources in the CGII sample. However, we note that lowering it to  $2\sigma$  does not change the fraction of selected AGN within the sample, as all sources with a line detection also meet other selection criteria. We still consider the presence of this line at  $2\sigma$  to be relevant information, which can give support to other AGN determinations, and therefore included it in the analysis.

Parameters of the fit for these six sources are shown in Table 6, including the line energy, intensity, and equivalent width with respect to the continuum. The detection of these lines has been previously reported based on other X-ray observations (Koyama et al. 1989; Band et al. 1990; Mazzarella et al. 2012; Gilli et al. 1999; Levenson et al. 2002; Ricci et al. 2014; Risaliti et al. 2009).

#### 4.5. X-ray luminosities and correlation with $L_{\text{IR}}$

Figure 7 shows the distribution of derived luminosities in the soft and hard band, presented in Table A.1, compared with that of those obtained for the CGI sample of Iwasawa et al. (2011). For CGII, the distributions peak at  $\log(L_{\text{SX}}) \sim 40.6 \text{ erg s}^{-1}$  and  $\log(L_{\text{HX}}) \sim 40.9 \text{ erg s}^{-1}$ , which is slightly lower than the peak of both bands for CGI sample, at  $\log(L_{\text{X}}) \sim 41.1 \text{ erg s}^{-1}$ . The median logarithmic values for the soft- and hard-band luminosities are listed in Table 7. CGII has lower X-ray luminosity values than CGI, as expected, reflecting a correlation between IR and X-ray luminosity that is seen in both the CGI and CGII samples (see Figs. 8 and 9).

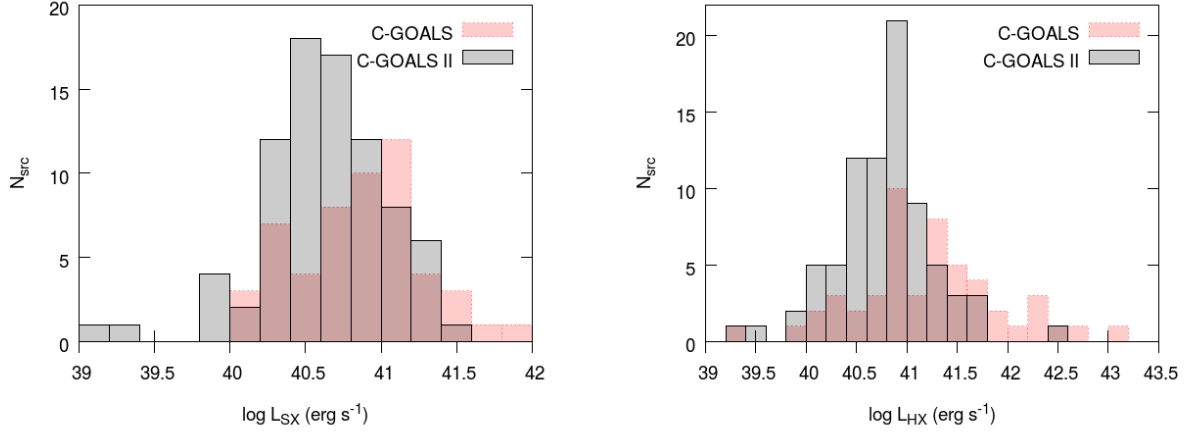


**Fig. 7.** Distributions of soft-band X-ray luminosity, 0.5–2 keV (*left panel*), and hard-band X-ray luminosity, 2–10 keV (*right panel*), for the individual galaxies of CGI and CGII.

**Table 7.** Statistical X-ray properties of the sample.

|  | CGI              | CGII             | C-GOALS          |
|--|------------------|------------------|------------------|
| $\log(L_{\text{SX}})$                  | $40.9 \pm 0.3$   | $40.6 \pm 0.2$   | $40.8 \pm 0.4$   |
| $\log(L_{\text{HX}})$                  | $41.2 \pm 1.7$   | $40.8 \pm 0.8$   | $40.9 \pm 0.6$   |
| $\log(L_{\text{SX}}/L_{\text{IR}})$    | $-4.53 \pm 0.34$ | $-4.16 \pm 0.42$ | $-4.26 \pm 0.48$ |
| $\log(L_{\text{HX}}/L_{\text{IR}})$    | $-4.40 \pm 0.63$ | $-4.04 \pm 0.48$ | $-4.17 \pm 0.59$ |
| $\log(L_{\text{SX}}/L_{\text{IR}})^*$  | $-4.6 \pm 0.1$   | $-4.18 \pm 0.35$ | $-4.26 \pm 0.45$ |
| $\log(L_{\text{HX}}/L_{\text{IR}})^*$  | $-4.5 \pm 0.1$   | $-4.18 \pm 0.37$ | $-4.23 \pm 0.54$ |
| $\log(L_{\text{SX}}/L_{\text{FIR}})^*$ | $-4.44 \pm 0.45$ | $-3.82 \pm 0.32$ | $-3.96 \pm 0.47$ |
| $\log(L_{\text{HX}}/L_{\text{FIR}})^*$ | $-4.22 \pm 0.52$ | $-3.81 \pm 0.45$ | $-3.96 \pm 0.52$ |

**Notes.** Median values of the distribution of soft-band and hard X-ray luminosities; and the distributions of the ratios of X-ray to IR luminosities for the C-GOALS I, C-GOALS II and full C-GOALS sample. <sup>(\*)</sup>AGN removed from the sample.

The origin of this correlation is in the presence of star formation in the galaxies. FIR luminosity measurements detect the energy absorbed by the dust of the interstellar medium from young, bright stars; and thus are a good estimator of the total star formation rate (SFR; e.g., Kennicutt 1998). In galaxies with a considerable amount of star formation, such as starburst galaxies, emission in other wavelengths can also be related to young and massive stars, such as X-ray luminosity (e.g., X-ray binaries emission and supernova remnants, SNRs). Therefore, it has been suggested that if a good correlation between X-ray luminosity and IR luminosity exists in galaxies, the SFR can be directly inferred from the X-ray luminosity. Compatible correlations have been found in previous works for local star-forming galaxies with IR luminosities lower than those of LIRGS (e.g., Ranalli et al. 2003; Grimm et al. 2003; Mineo et al. 2014).

Figure 8 shows the X-ray luminosity as a function of the IRAS IR luminosity. The data show a moderate correlation, with a typical spread of more than one order of magnitude when only sources without detected X-ray AGN presence (open squares) are considered. Sources that contain X-ray AGN typically lie above the trend, adding scatter to the correlation. Sources with multiple components are separated into their respective contributions, and plotted separately, as it has been shown that when they are plotted summed into one single source, the correlation becomes less clear (Iwasawa et al. 2009). Their total (8–1000)  $\mu\text{m}$  IRAS luminosity, as in Table 1, is separated into

the different contributions using the percentages indicated in Table 3.

As we found in the CGI galaxies, X-ray selected AGN tend to be more luminous in X-rays than the rest of the sample, especially in the hard band. However, the values for  $\log(L_{\text{X}}/L_{\text{IR}})$  are higher for the CGII sample than for CGI, as listed in Table 7. This result means that while our sample is less bright both in X-ray and in IR than the CGI sample, we find a higher relative X-ray to IR luminosity. Removing X-ray selected AGN from both samples gives lower ratios, which we also list.

Comparing these average values to the  $\log(L_{\text{X}}/L_{\text{IR}}) \sim -3.7$  found by Ranalli et al. (2003) for local star-forming galaxies with lower SFR, we find a large discrepancy. However, their IR luminosity does not include the 1–40  $\mu\text{m}$  range, which may contribute a non-negligible amount of power, in particular for IR-warm AGN-dominated systems. Therefore a direct comparison needs to introduce a correction. Furthermore, only at radio and FIR wavelengths are the most intense starbursts transparent (e.g., Condon 1992), so that from their detected flux the SFR can be accurately estimated.

IR luminosities derived by Ranalli et al. (2003), hereafter  $L_{\text{FIR}}$ , follow the expression

$$L_{\text{FIR}} = 1.26 \times 10^{-11} (2.58 S_{60\mu} + S_{100\mu}) \text{ erg s}^{-1} \text{ cm}^{-2}, \quad (1)$$

from Helou et al. (1985).

We used this expression to derive  $L_{\text{FIR}}$  for all non-AGN objects in the CGI and CGII samples, again accounting for the contribution of multiple components following Table 3. As listed in Table 7,  $\log(L_{\text{X}}/L_{\text{FIR}})$  is similar to  $-3.7$  for the CGII objects, but not for the galaxies in CGI. A direct comparison between the distribution followed by objects analyzed by Ranalli et al. (2003), as well as their derived correlation, and GOALS objects is shown in Fig. 9.

The best-fit correlations derived by Ranalli et al. (2003) are

$$\log(L_{\text{SX}}) = (0.87 \pm 0.08) \log(F_{\text{FIR}}) + 2.0 \pm 3.7 \quad (2)$$

$$\log(L_{\text{HX}}) = (1.08 \pm 0.09) \log(F_{\text{FIR}}) - 7.1 \pm 4.2 \quad (3)$$

which correspond to the blue dotted lines plotted in Fig. 9.

Galaxies in the GOALS sample with  $L_{\text{FIR}} \lesssim 8 \times 10^{10} L_{\odot}$  follow Eqs. (2) and (3), but those with higher  $L_{\text{IR}}$  have a systematically lower X-ray luminosity than predicted.

This behavior suggests that a better fit would be obtained with a quadratic relation in log scale. Using the least-squares

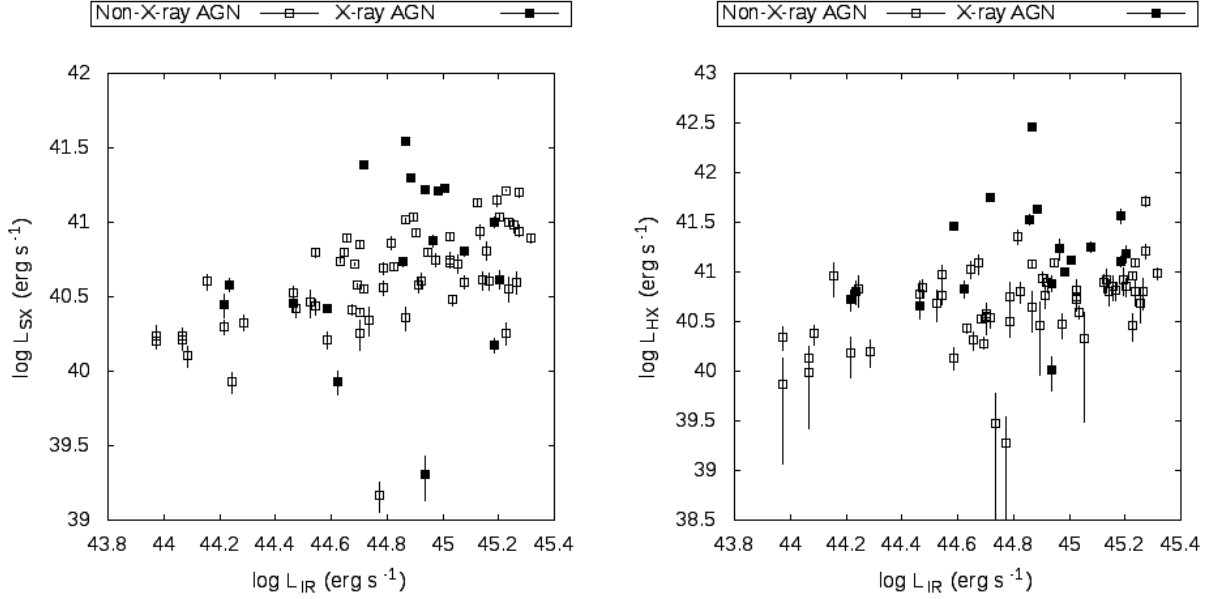


**Fig. 8.** Plots of soft (*left panel*, 0.5–2 keV) and hard (*right panel*, 2–10 keV) X-ray luminosity vs. IR luminosity, where the X-ray luminosity is corrected only for Galactic absorption. X-ray selected AGN, shown in Table 5, are shown in black. When multiple objects are present in a source, their IR luminosity is divided, as shown in Table 3.

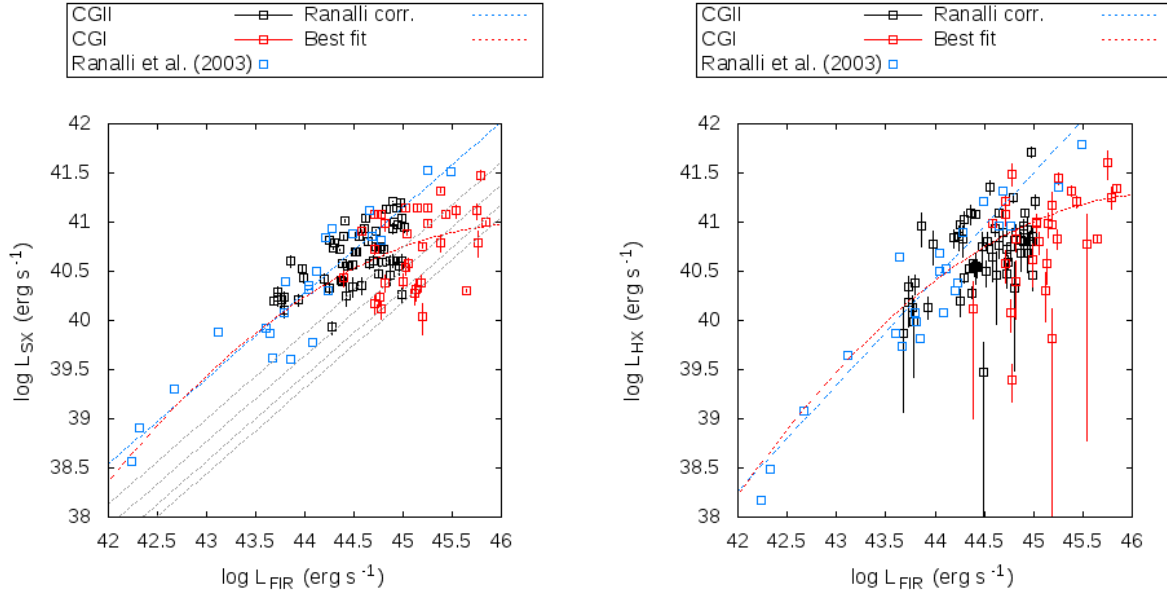


**Fig. 9.** Plots of soft (*left panel*, 0.5–2 keV) and hard (*right panel*, 2–10 keV) X-ray luminosity versus FIR luminosity derived as in Eq. (1), where the X-ray luminosity is corrected only for Galactic absorption. Data used by Ranalli et al. (2003), along with their derived correlation, are shown in blue. CGI and CGII data (for galaxies without an AGN) are plotted in red and black squares respectively. When multiple objects are present in a source, their IR luminosity is divided as shown in Table 3. All sources containing AGN, as listed in Table 5 or classified as AGN by Iwasawa et al. (2011) have been removed both from the plot and from the fits. The red, dashed line shows our best quadratic fit for the C-GOALS + Ranalli et al. (2003) data. Grey, dashed lines (*left panel*) show theoretical lines of obscuration for  $N_{\text{H}} = 0.5, 1.0, 2.0, 5.0 \times 10^{22} \text{ cm}^{-2}$ , as described in Sect. 4.5.

method, we obtain a best fit for the C-GOALS + Ranalli et al. (2003) data:

$$\log(L_{\text{SX}}) = (-0.17 \pm 0.04)x^2 + (15 \pm 2)x + (-263 \pm 8) \quad (4)$$

$$\log(L_{\text{HX}}) = (-0.17 \pm 0.06)x^2 + (15.2 \pm 2)x + (-169 \pm 10) \quad (5)$$

where  $x = \log(L_{\text{FIR}})$ . This fit is plotted as a red dashed line in Fig. 9. Below FIR luminosities of  $\sim 3 \times 10^{44} \text{ erg s}^{-1}$  (i.e.,  $\sim 8 \times 10^{10} L_{\odot}$ ), the quadratic fit overlaps the linear correlation. Above this value, the X-ray luminosity increases far more slowly with FIR luminosity. This effect is stronger in soft X-rays. We note that when we fit a single power-law to

**Table 8.** Half-light radius

| No. | Galaxy              | $R_{\text{H}}^{\text{SX}} (")$ | $R_{\text{H}}^{\text{SX}} (\text{kpc})$ | No. | Galaxy             | $R_{\text{H}}^{\text{SX}} (")$ | $R_{\text{H}}^{\text{SX}} (\text{kpc})$ |
|-----|---------------------|--------------------------------|---|-----|--------------------|--------------------------------|---|
| 45  | UGC 08387           | 2.4                            | 1.3                                     | 104 | NGC 7771           | 3.0                            | 0.9                                     |
| 47  | CGCG 436–030        | 2.6                            | 1.7                                     | 104 | NGC 7770           | 3.7                            | 1.1                                     |
| 49  | NGC 0695            | 3.7                            | 2.5                                     | 105 | NGC 7592 (E)       | 3.1                            | 1.6                                     |
| 50  | CGCG 043–099        | 1.2                            | 1.0                                     | 105 | NGC 7592 (W)       | 0.9                            | 0.5                                     |
| 51  | MCG+07–23–019       | 4.3                            | 3.3                                     | 106 | NGC 6286           | 7.2                            | 3.0                                     |
| 52  | NGC 6670 (E)        | 3.0                            | 1.9                                     | 106 | NGC 6285           | 1.7                            | 0.7                                     |
| 52  | NGC 6670 (W)        | 4.0                            | 2.5                                     | 107 | NGC 4922 (N)       | <0.5                           | <0.3                                    |
| 53  | UGC 02369 (S)       | 1.5                            | 1.0                                     | 110 | NGC 3110           | 9.0                            | 3.5                                     |
| 54  | NGC 1614            | 1.4                            | 0.5                                     | 114 | NGC 0232           | 1.5                            | 0.7                                     |
| 56  | NGC 5331 (N)        | 2.1                            | 1.6                                     | 117 | MCG+08–18–013(E)   | 2.3                            | 1.3                                     |
| 56  | NGC 5331 (S)        | 3.0                            | 2.3                                     | 120 | CGCG 049–057       | 1.1                            | 0.3                                     |
| 57  | IRAS F06076–2139(N) | 0.7                            | 0.6                                     | 121 | NGC 1068           | 7.8                            | 0.6                                     |
| 57  | IRAS F06076–2139(S) | –                              | –                                       | 123 | UGC 02238          | 4.0                            | 1.8                                     |
| 60  | IC 2810(NW)         | 1.2                            | 0.9                                     | 127 | MCG–03–34–064      | <0.5                           | <0.2                                    |
| 60  | IC 2810 (SE)        | 0.7                            | 0.5                                     | 134 | ESO 350–IG038      | 2.4                            | 1.0                                     |
| 63  | IRAS 18090+0130 (E) | 2.4                            | 1.6                                     | 136 | MCG –01–60–022     | 4.6                            | 2.2                                     |
| 63  | IRAS 18090+0130(W)  | <0.5                           | <0.3                                    | 141 | IC 0564            | 8.0                            | 3.6                                     |
| 64  | III Zw 035 (S)      | 1.2                            | 0.7                                     | 141 | IC 0563            | 8.1                            | 3.6                                     |
| 65  | NGC 3256            | 7.7                            | 1.5                                     | 142 | NGC 5135           | 2.1                            | 0.6                                     |
| 67  | IRAS F16399–0937(N) | 3.5                            | 2.2                                     | 144 | IC 0860            | 6.0                            | 1.7                                     |
| 67  | IRAS F16399–0937(S) | 5.3                            | 3.3                                     | 147 | IC 5179            | 14.6                           | 3.6                                     |
| 68  | IRAS F16164–0746    | 1.5                            | 0.9                                     | 148 | CGCG 465–012       | 4.6                            | 2.1                                     |
| 69  | IC 4687             | 3.5                            | 1.4                                     | 157 | MCG–02–33–099      | 1.3                            | 0.5                                     |
| 69  | IC 4686             | <0.5                           | <0.2                                    | 157 | MCG–02–33–098      | 1.2                            | 0.5                                     |
| 69  | IC 4689             | 3.5                            | 1.4                                     | 163 | NGC 4418           | 2.7                            | 0.5                                     |
| 71  | NGC 2623            | 1.0                            | 0.4                                     | 169 | ESO 343–IG013 (N)  | 1.2                            | 0.5                                     |
| 72  | IC 5298             | <0.5                           | <0.3                                    | 169 | ESO 343–IG013 (S)  | 5.7                            | 2.4                                     |
| 73  | IRAS 20351+2521     | 4.0                            | 2.9                                     | 170 | NGC 2146           | 15.5                           | 1.3                                     |
| 75  | NGC 6090 (NE)       | 1.6                            | 1.1                                     | 174 | NGC 5653           | 9.0                            | 2.6                                     |
| 75  | NGC6090 (SW)        | 1.4                            | 0.9                                     | 178 | NGC 4194           | 4.2                            | 0.9                                     |
| 79  | NGC 5256 (NE)       | 0.8                            | 0.5                                     | 179 | NGC 7591           | 0.8                            | 0.3                                     |
| 79  | NGC 5256 (SW)       | 2.2                            | 1.4                                     | 182 | NGC 0023           | 3.2                            | 1.0                                     |
| 80  | IRAS F03359+1523(E) | 1.9                            | 1.4                                     | 188 | NGC 7552           | 3.2                            | 0.4                                     |
| 81  | ESO 550–IG025 (N)   | 2.2                            | 1.4                                     | 191 | ESO 420–G013       | 1.0                            | 0.2                                     |
| 81  | ESO 550–IG025 (S)   | 1.0                            | 0.7                                     | 194 | ESO 432–IG006 (NE) | 2.3                            | 0.8                                     |
| 82  | NGC 0034            | 1.3                            | 0.5                                     | 194 | ESO 432–IG006 (SW) | 2.5                            | 0.9                                     |
| 83  | MCG+12–02–001 (E)   | 2.1                            | 0.7                                     | 195 | NGC 1961           | 8.4                            | 2.4                                     |
| 83  | MCG+12–02–001 (W)   | 2.3                            | 0.8                                     | 196 | NGC 7752/3 (NE)    | 0.8                            | 0.3                                     |
| 85  | IRAS F17138–1017    | 2.8                            | 1.1                                     | 196 | NGC 7752/3 (SW)    | 5.6                            | 2.0                                     |
| 95  | ESO 440–IG058 (N)   | 0.6                            | 0.3                                     | 198 | NGC 1365           | 7.0                            | 0.6                                     |
| 95  | ESO 440–IG058 (S)   | 3.8                            | 2.1                                     | 199 | NGC 3221           | 13.2                           | 4.2                                     |
| 100 | NGC 7130            | <0.5                           | <0.2                                    | 201 | NGC 0838           | 5.1                            | 1.3                                     |

**Notes.** Radius up to which half of the source counts in the 0.5–2 keV band are emitted, for the 84 galaxies analyzed within the CGII sample.

the full data sample, we did not recover a relation that was compatible, within the errors, with Eq. (2). A power-law fit also yielded a larger  $\chi^2$  value than the fits given by Eqs. (4) and (5).

As soft X-rays are easily absorbed by moderate column densities, we show the effect that obscuration could have on the Ranalli et al. (2003) correlation. In order to do so, we took an average spectrum that is characteristic of the galaxies within our sample: a double-component *mekal* model with temperatures  $T_1 = 0.38$  and  $T_2 = 0.97$ , the median values derived from our soft X-ray analysis. According to our model, the inner component of  $T = T_2$  can have considerable absorption, and fitting yields values in the range  $N_{\text{H}} = 0.1\text{--}2.5 \times 10^{22} \text{ cm}^{-2}$ . We assumed different column densities,  $N_{\text{H}} = 0.5, 1.0, 2.0, 5.0 \times 10^{22} \text{ cm}^{-2}$ , and absorbed the hotter component. We used the

model to calculate the decrease in flux caused by the different column densities, and considering that the linear correlation derived by Ranalli et al. (2003) has no intrinsic absorption, we plot the “absorbed” equivalent correlations in Fig. 9.  $N_{\text{H}} = 5.0 \times 10^{22} \text{ cm}^{-2}$  absorbs more than 99% of the emission of the inner component in the 0.5–2 keV range, meaning that higher column densities would result in no change in the emission, that is, only the emission of the outer, unabsorbed component remains.

#### 4.6. Radial profiles

Radial profiles for all sources (except for IRAS F06076–2139 (S), for which not enough counts are detected in the *Chandra* data) were characterized in two different ways. In the first

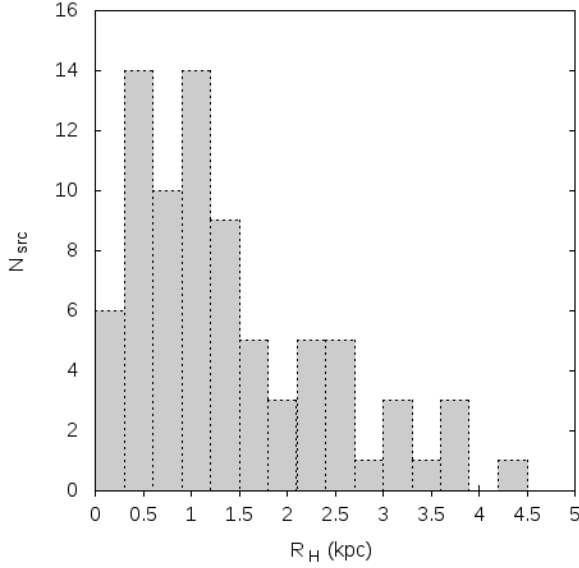


**Fig. 10.** Histogram of half-light radii for the sources in the CGII sample.

method, we computed the soft X-ray half-light radius ( $R_H^{SX}$ ) for the 0.5–2 keV band as the radius within which half of the total number of counts is emitted. In the second method, surface brightness profiles were computed and provided in Appendix B, also shown in Fig. 2 for NGC 2146. These profiles were computed in the soft 0.5–2 keV band, shown as open squares, and the hard 2–7 keV band, shown as filled squares.

Profiles were centered using the hard X-ray peak that corresponds to the nucleus of the galaxy, which typically corresponds to the near-infrared nucleus. When no clear central emission in the (2–7) keV band was detected, the profiles were centered using IR images. For all galaxies whose radial profiles were centered using IR images, a comment has been added in Appendix A.

The values for  $R_H^{SX}$ , both in arcsec and in kpc, are provided in Table 8. While this value can give an idea of the size of the central more intensely emitting region of a galaxy, we note that for sources without an extensive diffuse emission (e.g., NGC 3221, which is mostly composed of point-sources), it might not have a physical meaning. Other sources show non-axisymmetric morphology, most likely associated with extended starburst winds (e.g., UGC 08387, NGC 6286 (SE), NGC 2146, NGC 4194, NGC 1365, and NGC 0838). See Appendix B for detailed images of the morphology of the X-ray emission in all sources

Because of the pixel size of the *Chandra* CCD, the smallest radius within which counts can be computed is limited to  $0.5''$ . Very compact sources can have more than half of their detected counts within this region, making the estimation of  $R_H^{SX}$  impossible. This is the case for six of our sources, for which an upper limit is provided. It would also be the case for the vast majority of sources when the hard band emission were considered, which is the reason we do not provide values of  $R_H^{HX}$ .

Figure 10 shows a histogram of all half-light radii presented in Table 8. Sources with only upper limits derived are included, as they all fall below  $R_H^{SX} = 0.3$  kpc, which is the bin size. The distribution of  $R_H^{SX}$  has a median of  $1.0 \pm 0.1$  kpc, with an interquartile range of 0.5–1.9 kpc. This shows that most sources

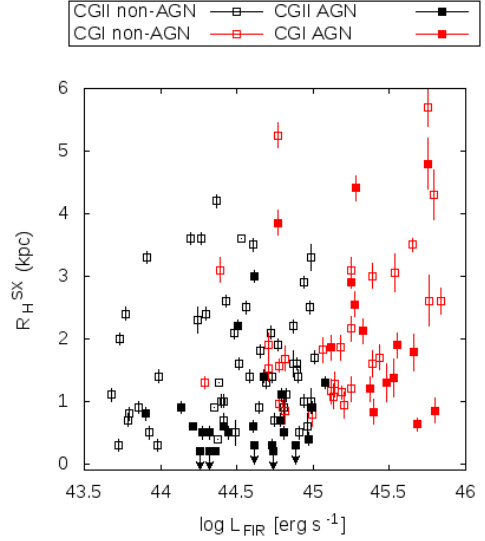


**Fig. 11.** Half-light radius as a function of FIR luminosity (as in Eq. (1)) for galaxies within the CGII (black) and CGI (red) sample. Sources without an AGN are plotted as open squares, while sources with an AGN are plotted as filled squares.

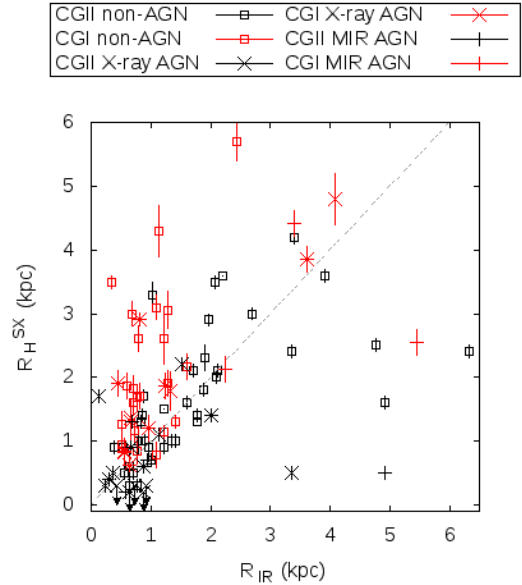


**Fig. 12.** Soft X-ray half-light radius as a function of  $70 \mu\text{m}$  FIR radius, taken from Díaz-Santos et al. (2017). CGI data are shown in red, and CGII data in black. X-ray selected AGN and MIR selected AGN (as specified in Table 5) are plotted separately. The dashed line shows  $R_{IR} = R_H^{SX}$ , and is not a fit to the data. Eleven systems within the whole C-GOALS sample are resolved into individual galaxies in X-rays but not at  $70 \mu\text{m}$ , and are thus not plotted.

within CGII have a compact X-ray distribution, with half of the emission being generated within the inner  $\sim 1$  kpc. VLA 33 GHz studies of the 22 brightest LIRGs and ULIRGs in the C-GOALS sample find half-light radii below 1.7 kpc for all sources, meaning that the emission is also compact in other wavelengths (Barcos-Muñoz et al. 2017).

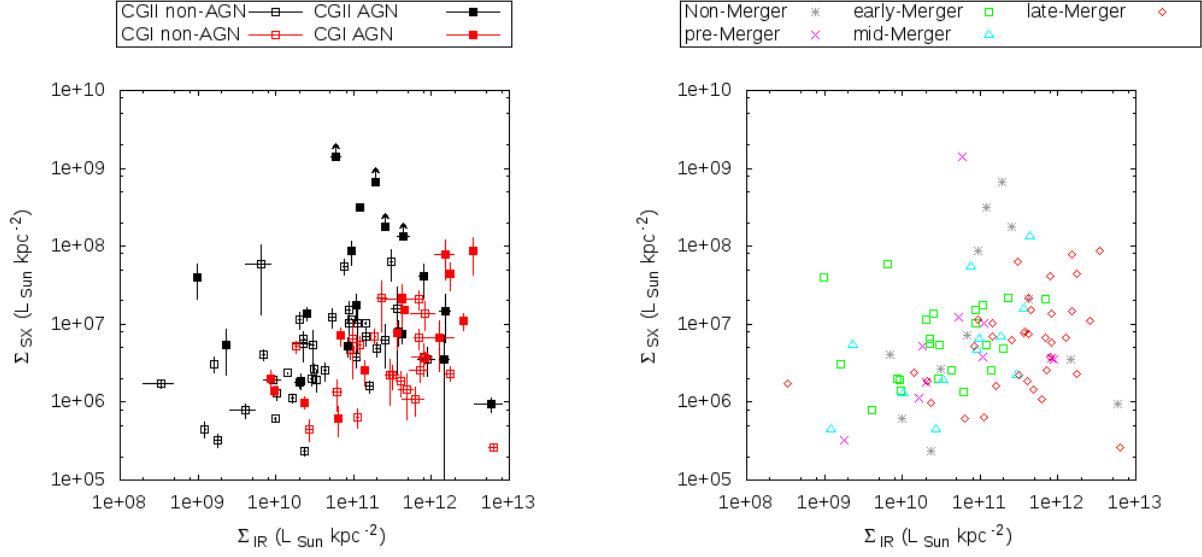


**Fig. 13.** Plots of X-ray luminosity surface density vs. IR luminosity surface density. *Left panel:* red data correspond to CGI sources, and black data corresponds to CGII sources. AGN are highlighted as filled symbols. *Right panel:* sources in the full C-GOALS sample are plotted as different symbols according to merger stage, as derived by Stierwalt et al. (2013). 11 systems within the whole C-GOALS sample are resolved into individual galaxies in X-rays but not at  $70\mu\text{m}$ , and are thus not plotted.

All values of  $R_{\text{H}}^{\text{SX}}$  are upper limits, as any amount of obscuration in the sources (likely important in most, as seen in Fig. 9), which is concentrated in the inner regions, will result in an apparent decrease of compactness.

Figure 11 shows the distribution of half-light radii as a function of the FIR luminosity. The size of the most intensely X-ray emitting region shows no clear correlation with the overall IR luminosity, although CGI sources tend to have higher X-ray radii. Within the CGII sample, sources that contain an AGN, as listed in Table 5, plotted as filled squares, tend to be compact.  $(83 \pm 7)\%$  of them have  $R_{\text{H}}^{\text{SX}} \leq 1$  kpc. This is in agreement with previous results from a study of the extended MIR emission in GOALS using *Spitzer*/IRS spectroscopy, where it was found that progressively more AGN-dominated galaxies tend to show more compact MIR emission (Díaz-Santos et al. 2010).

Figure 12 shows a comparison between  $R_{\text{H}}^{\text{SX}}$  and the IR radius at  $70\mu\text{m}$  taken from Díaz-Santos et al. (2017) for all C-GOALS sources. Most sources in the sample are placed close to the  $R_{\text{IR}} = R_{\text{H}}^{\text{SX}}$  line. CGI sources tend to have a larger X-ray half-light radius for a given characteristic IR radius than CGII sources.

Outliers with very compact soft X-ray emission but a large IR radius are X-ray selected AGN ESO 343–IG013 (N) and IR selected AGN NGC 7592 (W). Both sources show clear strong hard X-ray peaks in the nucleus (see images in Appendix B). Another extreme outlier is IRAS F12112+0305, with  $R_{\text{H}}^{\text{SX}} = 5.7 \pm 0.3$  kpc but much more compact IR emission.

#### 4.7. Luminosity surface density

Using the luminosities listed in Table A.1 and the  $R_{\text{H}}^{\text{SX}}$  in Table 8, we derived luminosity surface densities for all sources in the C-GOALS sample, as  $\Sigma_{\text{SX}} = L_{\text{SX}}/\pi(R_{\text{H}}^{\text{SX}})^2$ .  $\Sigma_{\text{IR}}$  is derived using  $70\mu\text{m}$  radii from Díaz-Santos et al. (2017).

Figure 13 shows  $\Sigma_{\text{SX}}$  as a function of  $\Sigma_{\text{IR}}$ . The X-ray surface density tends to increase with IR surface density, although the correlation is broader than the one existing between luminosities.

**Table 9.** Merger stage.

|                    | CGI | CGII | C-GOALS |
|--------------------|-----|------|---------|
| Non-merger         | 4%  | 18%  | 12%     |
| Pre-merger         | 4%  | 14%  | 10%     |
| early-stage merger | 30% | 31%  | 30%     |
| mid-stage merger   | 17% | 18%  | 18%     |
| late-stage merger  | 44% | 18%  | 27%     |

**Notes.** Percentage of sources classified as different merger stages by Stierwalt et al. (2013) for the C-GOALS I, C-GOALS II and full C-GOALS sample.

The left plot highlights AGN as filled symbols and separates the CGI and CGII samples. CGI sources, brighter in the IR, tend to have lower  $\Sigma_{\text{SX}}$  for a given  $\Sigma_{\text{IR}}$ . Within a given sample, sources with AGN tend to have a larger  $\Sigma_{\text{SX}}$ , which is to be expected because they are both brighter in X-rays and also more compact. Figure 13 also shows, on the right, the same figure but highlighting the merger stage of the sources in the sample. Information on the merger stage is taken from Stierwalt et al. (2013), derived from visual inspection of IRAC  $3.6\mu\text{m}$  (Channel 1) images. Classification is non-merger, pre-merger (galaxy pairs prior to a first encounter), early-stage merger (post first-encounter with galaxy disks still symmetric and intact, but with signs of tidal tails), mid-stage merger (showing amorphous disks, tidal tails, and other signs of merger activity), and late-stage merger (two nuclei in a common envelope). Sources in late-stage mergers tend to have higher  $\Sigma_{\text{IR}}$ , but lower  $\Sigma_{\text{SX}}$  for the same  $\Sigma_{\text{IR}}$ .

The percentages of merger stages in the sample are listed in Table 9. Many CGI sources are late mergers, hence their higher IR luminosity. This is also visible in Fig. 13, as CGI and late mergers have the same behavior with respect to the rest of the sources in the sample.

## 5. Discussion

### 5.1. X-ray to IR luminosity relation

The X-ray to IR luminosity (or SFR) correlation has been studied in numerous previous works (e.g., Fabbiano & Trinchieri 1985; Fabbiano et al. 1988; Fabbiano 1989; Bauer et al. 2002; Grimm et al. 2003; Ranalli et al. 2003; Gilfanov et al. 2004; Persic & Rephaeli 2007; Mineo et al. 2014). For soft X-rays, it originates in starburst-wind shock-heated gas. For hard X-rays (2–10 keV), the relation is thought to originate in high mass X-ray binaries (HMXB), which are end products of star formation. At low SFRs, that is, for local starburst galaxies with  $L_{\text{IR}} \ll 10^{11} L_{\odot}$ , low-mass X-ray binaries (LMXBs) can significantly contribute to the X-ray luminosity. The luminosity from LMXBs correlates with galaxy stellar mass ( $M_{\star}$ ), and this dependence must be considered, along with the contribution of SFR (e.g., Colbert et al. 2004; Gilfanov 2004; Lehmer et al. 2008, 2010).

Figure 9 shows a comparison between C-GOALS data and the correlation derived by Ranalli et al. (2003) for a sample of nearby starbursting galaxies. Works that include the LMXB contribution at low luminosities show a slight decrease in the slope at the high-luminosity end. Therefore, their correlation can be used as a point-of-reference against which to plot the LIRG and ULIRG data, although a rigorous comparison would require including all previously mentioned works and is beyond the scope of this work.

It is clear that at higher IR luminosities the correlation breaks down in an apparent deficit of X-ray flux, more extreme in the 0.5–2 keV band. This has been observed since the inclusion of the C-GOALS ULIRGs and high-luminosity LIRGs into the described correlations (e.g., Iwasawa et al. 2009, 2011; Lehmer et al. 2010). The inclusion of our CGII data provides more information on the transition between low-IR-luminosity galaxies and ULIRGs.

This underluminosity, or X-ray quietness, is explained in many works as an effect of obscuration. LIRGs and ULIRGs have extremely high concentrations of gas and dust in their inner regions, resulting in compact starbursts. High gas column densities can easily absorb soft X-rays, and in the most extreme cases, even hard X-rays.

Galaxies in the CGII sample, which are less IR-luminous than those in the CGI sample, are generally found in less-advanced mergers (see Table 9). The concentrations of gas and dust in the inner regions of the galaxies are higher in the more advanced mergers (e.g., Ricci et al. 2017), implying that the contribution of obscuration is stronger at higher IR luminosities. From an IR point of view, Díaz-Santos et al. (2010) observed that late-stage mergers are much more compact, which also indicates larger column densities.

#### 5.1.1. Soft X-ray faintness

As shown in Fig. 9, the obscuring column densities necessary to dim the soft X-ray emission in most of the sources are compatible with those derived from the two-component model, plotted in Fig. 6 and listed in Table A.2. The derived values of  $N_{\text{H}}$  are lower limits, as any gas phase with higher obscuration contributes less significantly to the X-ray emission, or is even completely absorbed, and therefore cannot be fit.

Our spectral model is based on the existence of two distinct phases in the galaxy interstellar medium (ISM). Emission is likely to come from a complex phase-continuum of gas, and thus individual estimates of properties based on the spectral fitting

should be taken with caution (see, e.g., Strickland & Stevens 2000, for a discussion). However, the simple two-phase model is the most complex we can fit given our data, and it shows that the column densities can at least explain the data.

Figure 13 shows lower  $\Sigma_{\text{SX}}$  for CGI galaxies, which reflects both their X-ray faintness and larger soft X-ray sizes (Fig. 12). We defined the size of the emission as the half-light radius, meaning that larger sizes indicate a less compact source. This implies that the faintness most likely originates in the center of the source. As CGI galaxies are in more advanced merger stages and should have higher column densities, this is likely to be an effect of obscuration. Another likely contribution to the larger soft X-ray sizes are the strongest starbursts in CGI galaxies, which generate larger soft X-ray nebulae.

We note that the *Chandra* resolution is much better than that of *Spitzer*, which should be taken into account in any direct comparison between characteristic sizes or luminosity surface densities. Higher resolution should imply a tendency toward deriving higher compactness, while Fig. 12 shows the opposite: X-ray sizes are generally similar, or even larger than IR sizes. However, we do not know what the IR emission would look like at similar resolutions. This difference between the datasets could explain the presence of outliers below the  $R_{\text{IR}} = R_{\text{H}}^{\text{SX}}$  line, and add to the dispersion of the data. Future observations with the *James Webb* Space Telescope (JWST) would allow for better comparison.

In conclusion, the soft X-ray faintness, and therefore the quadratic best-fit curve given by Eq. (4), can be explained through obscuration, as the necessary column densities are present in the galaxies within the C-GOALS sample.

#### 5.1.2. Hard X-ray faintness

Attributing to extinction the observed faintness in hard X-rays requires much higher gas column densities. While it is clear that more IR-luminous sources (i.e., late-stage mergers) are generally more heavily obscured (e.g., Ricci et al. 2017, for a GOALS subsample), the most extreme sources are  $\sim 1$ – $2$  dex below the correlation shown in Fig. 9. This implies that between  $\sim 90$ – $99\%$  of the central starburst region must be covered in medium that is dense enough to suppress even hard X-rays. To obscure the emission in the 2–8 keV band in which *Chandra* is sensitive, the necessary column densities would be of the order of  $\sim 10^{24} \text{ cm}^{-2}$ . Sources in the sample that are undetected by *NuSTAR* (Ricci et al. 2017) would require even higher column densities, of the order of  $\sim 10^{25} \text{ cm}^{-2}$ .

In order to explain the observed faintness, regions of sizes of the order of the  $R_{\text{H}}^{\text{SX}}$  listed in Table 8 would need to be covered in the high  $N_{\text{H}}$  we described. A column density of  $10^{25} \text{ cm}^{-2}$  could imply  $H_2$  masses of the order of  $\sim 10^{10}$ – $10^{11} M_{\odot}$  for a nuclear star-forming region of 500 pc of radius. It is unclear if such high gas masses are truly concentrated in the inner regions of ULIRGs in the GOALS sample, and thus if this “self-absorbed starburst” scenario is feasible.

To distinguish the origin of the faintness, Iwasawa et al. (2009) stacked spectra of non-AGN sources in CGI, recovering a high-ionization Fe K feature. This feature can be explained by the presence of an internally shocked, hot bubble that is produced by thermalizing the energy of supernovae and stellar winds (e.g., Chevalier & Clegg 1985), which, in contrast to the SNe and HMXB emission, could be visible through the obscuring material. With high SFRs, the luminosity and the spectra with strong Fe  $\text{XXV}$  line can be reproduced (e.g., Iwasawa et al. 2005, for Arp 220). This high-ionization line could also originate

from low-density gas that is photoionized by a hidden AGN (e.g., Antonucci & Miller 1985; Krolik & Kallman 1987), and it has been observed as the dominant Fe K feature in some Compton-thick AGN (e.g., Nandra & Iwasawa 2007; Braito et al. 2009).

Therefore, another explanation for the X-ray faintness could be the presence of a completely obscured AGN in the nucleus of these galaxies. This AGN would contribute to the IR emission, but would escape X-ray detection. While the column densities needed to cover the AGN are as high as those needed to self-absorb a starburst, the obscured region would be much smaller. This would imply much lower masses, that are easily found in the nuclei of GOALS galaxies. The scenario of hidden AGN versus extremely compact starburst has been previously discussed for some of the C-GOALS sources that show a higher X-ray faintness. Cases such as Arp 220 (e.g., Scoville et al. 2017; Barcos-Muñoz et al. 2018) or NGC 4418 (e.g., Costagliola et al. 2013, 2015) are compatible with both scenarios. However, it is worth noting that the hidden-AGN scenario requires the presence of an AGN with significant IR emission in order to explain the X-ray faintness, which means that it is probably unlikely that MIR determinations would systematically fail to pick up their signature.

Díaz-Santos et al. (2017) suggested from interpretation of *Herschel* FIR data on the full GOALS sample that the fraction of young, massive stars per star-forming region in ULIRGs might be higher than expected. This does not imply a change in the initial mass function, but the presence of very young star-forming regions, in which most massive stars still have not disappeared (age younger than a few Myr; Inami et al. 2013). In such a case, the massive stars can contribute to the IR emission, but the number of HMXB and SNe associated with the region will be low, as they are end-products of the star formation. This would result in a lower-than-expected X-ray luminosity for a given IR luminosity. Furthermore, in such a scenario, the winds of very massive stars could generate the hot gas that explains the Fe XXV line, without the need of invoking extreme obscuration over a large population of HMXB.

In order to truly understand the origin of the X-ray faintness, further observations are needed that provide information on the obscuration within the sources (e.g., ALMA or *NuSTAR* observations), or on the unobscured SFRs (e.g., through radio observations).

## 5.2. AGN and double AGN fraction

In Sect. 4.3 we have shown that  $(38 \pm 6)\%$  of the systems (24 of 63) within CGII contain an AGN,  $(31 \pm 5)\%$  (26 of 84) of individual galaxies being classified as AGN, according to MIR and/or X-ray criteria. This fraction can be compared to the  $(50 \pm 7)\%$  of the systems, or  $(38 \pm 7)\%$  (21 of 55) of the analyzed individual galaxies classified by Iwasawa et al. (2011) when analyzing the more IR-luminous objects in the CGI sample. This result may indicate a slight increase of AGN presence with IR luminosity, although the fractions in the two samples are compatible within the statistical errors. Although the increase of the AGN fraction as a function of luminosity found here is not statistically significant, it is consistent with previous findings in optical and IR spectroscopy (e.g., Veilleux et al. 1995; Kim et al. 1995; Yuan et al. 2010; Stierwalt et al. 2013).

Double AGN are detected in two interacting systems, NGC 5256 and ESO 432-IG006, of the 30 multiple systems analyzed here  $(7 \pm 4)\%$ . In the C-GOALS sample, one double AGN system, NGC 6240, was detected out of 24 multiple systems that were analyzed  $(4 \pm 4)\%$ .

Theoretical estimates derived from merger simulations performed by Capelo et al. (2017), which took into account observational effects (e.g., observation angle, distance dimming of X-ray luminosity, and obscuration of gas surrounding central BH), have concluded that in a sample of major mergers hosting at least one AGN, the fraction of dual AGN should be  $\sim 20\text{--}30\%$ . Koss et al. (2012) studied a sample of 167 nearby ( $z < 0.05$ ) X-ray selected AGN and found a fraction of dual AGN in multiple systems of 19.5%. When separated into major pairs (mass ratio  $\geq 0.25$ ) and minor pairs, they found 37.1% and 4.8% respectively. Other studies (e.g., Ellison et al. 2011; Satyapal et al. 2017) found a statistical excess of dual AGN that decreased with galaxy separation. Therefore, dual AGN activation is more likely in advanced merger stages.

Within CGI and CGII, the fraction of double AGN in systems that host at least one AGN is  $(11 \pm 10)\%$  (1 of 9) and  $(29 \pm 14)\%$  (2 of 7) respectively. The fraction found in CGII falls well within the ranges found in the two previously described works, while the dual AGN fraction in CGI is just barely compatible within the errors. Moreover, CGI galaxies are generally found in more advanced merger stages (see Table 9), meaning that according to predictions, their dual AGN fraction should be closer to the mentioned 37.1%, and not to the lower 20%.

The lack of dual AGN in the CGI sample could be explained with heavy obscuration, which is expected to be important for these sources, as discussed in the previous section. Compton-thick ( $N_{\text{H}} > 1.5 \times 10^{24} \text{ cm}^{-2}$ ) AGN may be completely obscured in our *Chandra* data (e.g., Mrk 273, Iwasawa 2018), and their scattered continuum or Fe  $K_{\alpha}$  lines too faint to be detected. MIR criteria can be effective in such cases, even though they may also miss the most heavily buried AGN (e.g., Snyder et al. 2013). Recent simulations by Blecha et al. (2018) found that much of the AGN lifetime is still undetected with common MIR selection criteria, even in the late stages of gas-rich major mergers. This effect is incremented for AGN that do not contribute significantly to the bolometric luminosity, especially when considering that the presence of a strong starburst can help dilute the AGN signature. Figure 5 shows up to 19 of the 32 X-ray selected AGN in C-GOALS that contribute less than 20% to the bolometric luminosity, most of which are missed by MIR selection criteria (see Table 5).

Another likely contribution to the low fraction of dual AGN found in CGI comes from the inability to resolve individual nuclei in a late-stage merger. Many CGI galaxies are found in such a stage. While *Chandra* has a high spatial resolution ( $\sim 0.5''$ ), very closely interacting nuclei, with separations of the order of  $\lesssim 200\text{--}300$  pc, would remain unresolved in our sample. *Spitzer* data, also used in this work for the MIR AGN selection, have a much lower resolution, and would not resolve double AGN with even further separations.

However, as our sample sizes are small and therefore the statistical errors large, we cannot make any strong statements regarding a decreasing trend of the double AGN presence with IR luminosity.

## 6. Conclusions

We analyzed *Chandra*-ACIS data for a sample of 63 LIRGs and ULIRGs, composed of 84 individual galaxies (CGII). These galaxies are a low-IR-luminosity subsample of GOALS, a complete flux-limited sample of the  $60 \mu\text{m}$  selected, bright galaxies in the local Universe ( $z < 0.08$ ). Arcsecond-resolution images, spectra, and radial surface brightness profiles were presented. We compared the observations with *Spitzer* and *Herschel* data

to contrast their X-ray and IR properties. We also compared our results to those found by Iwasawa et al. (2011) for the high-IR-luminosity subsample of GOALS (CGI). We summarize our main findings below.

- Objects with an AGN signature represent  $(31 \pm 5)\%$  of the CGII sample, compared to the  $(38 \pm 7)\%$  reported for the CGI sample. Double AGN are detected in two interacting systems, implying that the fraction of double AGN in systems that host at least one AGN is  $(29 \pm 14)\%$ , in contrast to the  $(11 \pm 10)\%$  found for the CGI sample.
- 19 of 32 of the X-ray selected AGN in the full C-GOALS sample (CGI+CGII) are not energetically significant, contributing less than 20% to the bolometric luminosity of the galaxy, according to MIR determinations.
- The brightest LIRGs, at  $L_{\text{FIR}} > 8 \times 10^{10} L_{\odot}$ , show a hard X-ray faintness with respect to the luminosities predicted by correlations found for nearby star-forming galaxies. This behavior is accentuated for the CGI ULIRGs. Possible explanations for the sources with most extreme deviations include a self-absorbed starburst, an obscured AGN, or the presence of extremely young star-forming regions.
- The extended soft X-ray emission shows a spectrum that is consistent with thermal emission from a two-phase gas, with an inner, hotter and more heavily obscured component, and an outer, colder and unobscured component.
- According to our modeling, an obscuration of the inner component in the range of  $N_{\text{H}} = 1-5 \times 10^{22} \text{ cm}^{-2}$  can explain the soft X-ray faintness for the vast majority of the sources.
- Most sources within CGII have a compact soft X-ray morphology.  $(50 \pm 8)\%$  of the sources generate half of the emission within the inner  $\sim 1$  kpc. This behavior is accentuated for AGN, with  $(83 \pm 7)\%$  of the sources with a half-light radius below  $\sim 1$  kpc.
- CGI sources are, in comparison, less compact, which is most likely an effect of obscuration in the inner regions.
- Most sources in CGII have similar soft X-ray and MIR sizes, although there is important dispersion in this relation.

*Acknowledgements.* We thank the anonymous referee for helpful comments and suggestions. We acknowledge support by the Spanish Ministerio de Economía y Competitividad (MINECO/FEDER, UE) under grants AYA2013-47447-C3-1-P and MDM-2014-0369 of ICCUB (Unidad de Excelencia “María de Maeztu”). N.T.A. acknowledges support from MINECO through FPU14/04887 grant. T.D.-S. acknowledges support from ALMA-CONICYT project 31130005 and FONDECYT regular project 1151239. G.C.P. acknowledges support from the University of Florida. This work was conducted in part at the Aspen Center for Physics, which is supported by NSF grant PHY-1607611; V.U., G.C.P., D.B.S., A.M.M., T.D.-S. and A.S.E. thank the Center for its hospitality during the Astrophysics of Massive Black Holes Mergers workshop in June and July 2018. The scientific results reported in this article are based on observations made by *Chandra* X-ray Observatory, and has made use of the NASA/IPAC Extragalactic Database (NED), which is operated by the Jet Propulsion Laboratory, California Institute of Technology under contract with NASA. We acknowledge the use of the software packages CIAO and HEASoft.

## References

Alam, S., Albareti, F. D., Allende Prieto, C., et al. 2015, *ApJS*, 219, 12  
 Alonso-Herrero, A., Pereira-Santaella, M., Rieke, G. H., & Rigopoulou, D. 2012, *ApJ*, 744, 2  
 Antonucci, R. R. J., & Miller, J. S. 1985, *ApJ*, 297, 621  
 Armus, L., Mazzarella, J. M., Evans, A. S., et al. 2009, *PASP*, 121, 559  
 Atek, H., Kunth, D., Hayes, M., Östlin, G., & Mas-Hesse, J. M. 2008, *A&A*, 488, 491  
 Baan, W. A., & Klöckner, H.-R. 2006, *A&A*, 449, 559  
 Band, D. L., Klein, R. I., Castor, J. I., & Nash, J. K. 1990, *ApJ*, 362, 90  
 Barcos-Muñoz, L., Leroy, A. K., Evans, A. S., et al. 2017, *ApJ*, 843, 117  
 Barcos-Muñoz, L., Aalto, S., Thompson, T. A., et al. 2018, *ApJ*, 853, L28

Bauer, F. E., Alexander, D. M., Brandt, W. N., et al. 2002, *AJ*, 124, 2351  
 Blackburn, J. K. 1995, in *Astronomical Data Analysis Software and Systems IV*, eds. R. A. Shaw, H. E. Payne, & J. J. E. Hayes, *ASP Conf. Ser.*, 77, 367  
 Blecha, L., Snyder, G. F., Satyapal, S., & Ellison, S. L. 2018, *MNRAS*, 478, 3056  
 Braito, V., Reeves, J. N., Della Ceca, R., et al. 2009, *A&A*, 504, 53  
 Brightman, M., & Nandra, K. 2011, *MNRAS*, 413, 1206  
 Capelo, P. R., Dotti, M., Volonteri, M., et al. 2017, *MNRAS*, 469, 4437  
 Casey, C. M., Narayanan, D., & Cooray, A. 2014, *Phys. Rep.*, 541, 45  
 Chapman, J. M., Staveley-Smith, L., Axon, D. J., et al. 1990, *MNRAS*, 244, 281  
 Chevalier, R. A., & Clegg, A. W. 1985, *Nature*, 317, 44  
 Chu, J. K., Sanders, D. B., Larson, K. L., et al. 2017, *ApJS*, 229, 25  
 Clemens, M. S., Vega, O., Bressan, A., et al. 2008, *A&A*, 477, 95  
 Colbert, E. J. M., Heckman, T. M., Ptak, A. F., Strickland, D. K., & Weaver, K. A. 2004, *ApJ*, 602, 231  
 Condon, J. J. 1992, *ARA&A*, 30, 575  
 Corbett, E. A., Norris, R. P., Heisler, C. A., et al. 2002, *ApJ*, 564, 650  
 Costagliola, F., Aalto, S., Sakamoto, K., et al. 2013, *A&A*, 556, A66  
 Costagliola, F., Sakamoto, K., Muller, S., et al. 2015, *A&A*, 582, A91  
 Del Moro, A., Alexander, D. M., Bauer, F. E., et al. 2016, *MNRAS*, 456, 2105  
 Di Matteo, T., Springel, V., & Hernquist, L. 2005, *Nature*, 433, 604  
 Díaz-Santos, T., Charmandaris, V., Armus, L., et al. 2010, *ApJ*, 723, 993  
 Díaz-Santos, T., Armus, L., Charmandaris, V., et al. 2017, *ApJ*, 846, 32  
 Dopita, M. A., Pereira, M., Kewley, L. J., & Capaccioni, M. 2002, *ApJS*, 143, 47  
 Dudik, R. P., Satyapal, S., & Marcu, D. 2009, *ApJ*, 691, 1501  
 Ellison, S. L., Patton, D. R., Mendel, J. T., & Scudder, J. M. 2011, *MNRAS*, 418, 2043  
 Evans, A. S., Vavilkin, T., Pizagno, J., et al. 2008, *ApJ*, 675, L69  
 Fabbiano, G. 1989, *ARA&A*, 27, 87  
 Fabbiano, G., & Trinchieri, G. 1985, *ApJ*, 296, 430  
 Fabbiano, G., Gioia, I. M., & Trinchieri, G. 1988, *ApJ*, 324, 749  
 Fabbiano, G., Baldi, A., King, A. R., et al. 2004, *ApJ*, 605, L21  
 Falstad, N., González-Alfonso, E., Aalto, S., et al. 2015, *A&A*, 580, A52  
 Franceschini, A., Braito, V., Persic, M., et al. 2003, *MNRAS*, 343, 1181  
 Fruscione, A., McDowell, J. C., Allen, G. E., et al. 2006, in *SPIE Conf. Ser.*, *Proc. SPIE*, 6270, 62701V  
 Garmire, G. P., Bautz, M. W., Ford, P. G., Nousek, J. A., & Ricker, Jr., G. R. 2003, in *X-Ray and Gamma-Ray Telescopes and Instruments for Astronomy*, eds. J. E. Truemper, & H. D. Tananbaum, *Proc. SPIE*, 4851, 28  
 Gilfanov, M. 2004, *MNRAS*, 349, 146  
 Gilfanov, M., Grimm, H.-J., & Sunyaev, R. 2004, *Nucl. Phys. B Proc. Suppl.*, 132, 369  
 Gilli, R., Comastri, A., Brunetti, G., & Setti, G. 1999, *New Astron.*, 4, 45  
 Goldader, J. D., Joseph, R. D., Doyon, R., & Sanders, D. B. 1997, *ApJS*, 108, 449  
 Grimm, H.-J., Gilfanov, M., & Sunyaev, R. 2003, *MNRAS*, 339, 793  
 Haan, S., Surace, J. A., Armus, L., et al. 2011, *AJ*, 141, 100  
 Hattori, T., Yoshida, M., Ohtani, H., et al. 2004, *AJ*, 127, 736  
 Helou, G., Soifer, B. T., & Rowan-Robinson, M. 1985, *ApJ*, 298, L7  
 Hernquist, L. 1989, *Nature*, 340, 687  
 Hill, T. L., Heisler, C. A., Norris, R. P., Reynolds, J. E., & Hunstead, R. W. 2001, *AJ*, 121, 128  
 Hinshaw, G., Weiland, J. L., Hill, R. S., et al. 2009, *ApJS*, 180, 225  
 Hopkins, P. F., Bundy, K., Murray, N., et al. 2009, *MNRAS*, 398, 898  
 Hopkins, P. F., Hernquist, L., Cox, T. J., et al. 2005, *ApJ*, 630, 705  
 Howell, J. H., Mazzarella, J. M., Chan, B. H. P., et al. 2007, *AJ*, 134, 2086  
 Hutchings, J. B., Lo, E., Neff, S. G., Stanford, S. A., & Unger, S. W. 1990, *AJ*, 100, 60  
 Inami, H., Armus, L., Charmandaris, V., et al. 2013, *ApJ*, 777, 156  
 Inui, T., Matsumoto, H., Tsuru, T. G., et al. 2005, *PASJ*, 57, 135  
 Iwasawa, K., Sanders, D. B., Evans, A. S., et al. 2005, *MNRAS*, 357, 565  
 Iwasawa, K., Sanders, D. B., Evans, A. S., et al. 2009, *ApJ*, 695, L103  
 Iwasawa, K., Sanders, D. B., Teng, S. H., et al. 2011, *A&A*, 529, A106  
 Iwasawa, K., U, V., Mazzarella, J. M., et al. 2018, *A&A*, 611, A71  
 Joy, M., & Harvey, P. M. 1987, *ApJ*, 315, 480  
 Kaaret, P., & Alonso-Herrero, A. 2008, *ApJ*, 682, 1020  
 Kaastra, J. 1992, *An X-Ray Spectral Code for Optically Thin Plasmas (Internal SRON-Leiden Report, updated version 2.0)*  
 Kalberla, P. M. W., Burton, W. B., Hartmann, D., et al. 2005, *A&A*, 440, 775  
 Kennicutt, Jr., R. C. 1998, *ApJ*, 498, 541  
 Kewley, L. J., Dopita, M. A., Sutherland, R. S., Heisler, C. A., & Trevena, J. 2001, *ApJ*, 556, 121  
 Kewley, L. J., Groves, B., Kauffmann, G., & Heckman, T. 2006, *MNRAS*, 372, 961  
 Kim, D.-C., Sanders, D. B., Veilleux, S., Mazzarella, J. M., & Soifer, B. T. 1995, *ApJS*, 98, 129  
 Kocevski, D. D., Brightman, M., Nandra, K., et al. 2015, *ApJ*, 814, 104  
 Koss, M., Mushotzky, R., Treister, E., et al. 2012, *ApJ*, 746, L22

- Koyama, K., Inoue, H., Tanaka, Y., et al. 1989, *PASJ*, 41, 731
- Kreckel, K., Armus, L., Groves, B., et al. 2014, *ApJ*, 790, 26
- Krolik, J. H., & Kallman, T. R. 1987, *ApJ*, 320, L5
- Kunth, D., Leitherer, C., Mas-Hesse, J. M., Östlin, G., & Petrosian, A. 2003, *ApJ*, 597, 263
- Kuo, C.-Y., Lim, J., Tang, Y.-W., & Ho, P. T. P. 2008, *ApJ*, 679, 1047
- Lahuis, F., Spoon, H. W. W., Tielens, A. G. G. M., et al. 2007, *ApJ*, 659, 296
- Lanzuisi, G., Ranalli, P., Georgantopoulos, I., et al. 2015, *A&A*, 573, A137
- Larson, K. L., Sanders, D. B., Barnes, J. E., et al. 2016, *ApJ*, 825, 128
- Lehmer, B. D., Brandt, W. N., Alexander, D. M., et al. 2008, *ApJ*, 681, 1163
- Lehmer, B. D., Alexander, D. M., Bauer, F. E., et al. 2010, *ApJ*, 724, 559
- Levenson, N. A., Krolik, J. H., Życki, P. T., et al. 2002, *ApJ*, 573, L81
- Levenson, N. A., Weaver, K. A., Heckman, T. M., Awaki, H., & Terashima, Y. 2005, *ApJ*, 618, 167
- Liedahl, D. A., Osterheld, A. L., & Goldstein, W. H. 1995, *ApJ*, 438, L115
- Lipovetsky, V. A., Neizvestny, S. I., & Neizvestnaya, O. M. 1988, *Soobshcheniya Spetsial'noj Astrofizicheskoy Observatorii*, 55, 5
- Lira, P., Ward, M., Zezas, A., Alonso-Herrero, A., & Ueno, S. 2002, *MNRAS*, 330, 259
- Lonsdale, C. J., Smith, H. J., & Lonsdale, C. J. 1993, *ApJ*, 405, L9
- Luangtip, W., Roberts, T. P., Mineo, S., et al. 2015, *MNRAS*, 446, 470
- Magdziarz, P., & Zdziarski, A. A. 1995, *MNRAS*, 273, 837
- Maia, M. A. G., Suzuki, J. A., da Costa, L. N., Willmer, C. N. A., & Rite, C. 1996, *A&AS*, 117, 487
- Maiolino, R., Comastri, A., Gilli, R., et al. 2003, *MNRAS*, 344, L59
- Mazzarella, J. M., Iwasawa, K., Vavilkin, T., et al. 2012, *AJ*, 144, 125
- Meléndez, M., Heckman, T. M., Martínez-Paredes, M., Kraemer, S. B., & Mendoza, C. 2014, *MNRAS*, 443, 1358
- Mewe, R., Gronenschild, E. H. B. M., & van den Oord, G. H. J. 1985, *A&AS*, 62, 197
- Mineo, S., Gilfanov, M., Lehmer, B. D., Morrison, G. E., & Sunyaev, R. 2014, *MNRAS*, 437, 1698
- Mirabel, I. F., & Sanders, D. B. 1988, *ApJ*, 335, 104
- Moorwood, A. F. M., & Oliva, E. 1994, *ApJ*, 429, 602
- Mould, J. R., Huchra, J. P., Freedman, W. L., et al. 2000, *ApJ*, 529, 786
- Mudd, D., Mathur, S., Guainazzi, M., et al. 2014, *ApJ*, 787, 40
- Nandra, K., & Iwasawa, K. 2007, *MNRAS*, 382, L1
- Nandra, K., & Pounds, K. A. 1994, *MNRAS*, 268, 405
- Norris, R. P., & Forbes, D. A. 1995, *ApJ*, 446, 594
- Oda, S., Ueda, Y., Tanimoto, A., & Ricci, C. 2018, *ApJ*, 855, 79
- O'Sullivan, E., Zezas, A., Vrtilik, J. M., et al. 2014, *ApJ*, 793, 73
- Parra, R., Conway, J. E., Aalto, S., et al. 2010, *ApJ*, 720, 555
- Pereira-Santaella, M., Alonso-Herrero, A., Colina, L., et al. 2015a, *A&A*, 577, A78
- Pereira-Santaella, M., Colina, L., Alonso-Herrero, A., et al. 2015b, *MNRAS*, 454, 3679
- Persic, M., & Rephaeli, Y. 2007, *A&A*, 463, 481
- Petric, A. O., Armus, L., Howell, J., et al. 2011, *ApJ*, 730, 28
- Ptak, A., Heckman, T., Levenson, N. A., Weaver, K., & Strickland, D. 2003, *ApJ*, 592, 782
- Ranalli, P., Comastri, A., & Setti, G. 2003, *A&A*, 399, 39
- Ricci, C., Ueda, Y., Paltani, S., et al. 2014, *MNRAS*, 441, 3622
- Ricci, C., Bauer, F. E., Treister, E., et al. 2016, *ApJ*, 819, 4
- Ricci, C., Bauer, F. E., Treister, E., et al. 2017, *MNRAS*, 468, 1273
- Risaliti, G., Gilli, R., Maiolino, R., & Salvati, M. 2000, *A&A*, 357, 13
- Risaliti, G., Elvis, M., Fabbiano, G., Baldi, A., & Zezas, A. 2005, *ApJ*, 623, L93
- Risaliti, G., Elvis, M., Fabbiano, G., et al. 2007, *ApJ*, 659, L111
- Risaliti, G., Miniutti, G., Elvis, M., et al. 2009, *ApJ*, 696, 160
- Romero-Cañizales, C., Pérez-Torres, M. A., Alberdi, A., et al. 2012, *A&A*, 543, A72
- Romero-Cañizales, C., Alberdi, A., Ricci, C., et al. 2017, *MNRAS*, 467, 2504
- Roussel, H., Helou, G., Beck, R., et al. 2003, *ApJ*, 593, 733
- Rudnick, G., Rix, H.-W., & Kennicutt, Jr., R. C. 2000, *ApJ*, 538, 569
- Sales, D. A., Robinson, A., Axon, D. J., et al. 2015, *ApJ*, 799, 25
- Sanders, D. B. 1999, *Ap&SS*, 266, 331
- Sanders, D. B., Soifer, B. T., Elias, J. H., et al. 1988, *ApJ*, 325, 74
- Sanders, D. B., Mazzarella, J. M., Kim, D.-C., Surace, J. A., & Soifer, B. T. 2003, *AJ*, 126, 1607
- Satyapal, S., Ellison, S. L., McAlpine, W., et al. 2014, *MNRAS*, 441, 1297
- Satyapal, S., Secrest, N. J., Ricci, C., et al. 2017, *ApJ*, 848, 126
- Scoville, N., Murchikova, L., Walter, F., et al. 2017, *ApJ*, 836, 66
- Shalyapina, L. V., Moiseev, A. V., Yakovleva, V. A., Hagen-Thorn, V. A., & Burenkov, A. N. 2004, *Astron. Lett.*, 30, 1
- Shu, X. W., Wang, J. X., Jiang, P., Fan, L. L., & Wang, T. G. 2007, *ApJ*, 657, 167
- Silverman, J. D., Kampczyk, P., Jahnke, K., et al. 2011, *ApJ*, 743, 2
- Singh, V., Risaliti, G., Braito, V., & Shastri, P. 2012, *MNRAS*, 419, 2089
- Smith, D. A., Herter, T., Haynes, M. P., Beichman, C. A., & Gautier, III., T. N. 1996, *ApJS*, 104, 217
- Snyder, G. F., Hayward, C. C., Sajina, A., et al. 2013, *ApJ*, 768, 168
- Stierwalt, S., Armus, L., Surace, J. A., et al. 2013, *ApJS*, 206, 1
- Strickland, D. K., & Stevens, I. R. 2000, *MNRAS*, 314, 511
- Surace, J. A., Sanders, D. B., & Mazzarella, J. M. 2004, *AJ*, 127, 3235
- Teng, S. H., & Veilleux, S. 2010, *ApJ*, 725, 1848
- Teng, S. H., Wilson, A. S., Veilleux, S., et al. 2005, *ApJ*, 633, 664
- Terashima, Y., Hirata, Y., Awaki, H., et al. 2015, *ApJ*, 814, 11
- Turner, T. J., & Miller, L. 2009, *A&ARv*, 17, 47
- Turner, M. J. L., Reeves, J. N., Ponman, T. J., et al. 2001, *A&A*, 365, L110
- Valiante, E., Lutz, D., Sturm, E., Genzel, R., & Chapin, E. L. 2009, *ApJ*, 701, 1814
- Vega, O., Clemens, M. S., Bressan, A., et al. 2008, *A&A*, 484, 631
- Veilleux, S., Kim, D.-C., Sanders, D. B., Mazzarella, J. M., & Soifer, B. T. 1995, *ApJS*, 98, 171
- Veilleux, S., Kim, D.-C., & Sanders, D. B. 1999, *ApJ*, 522, 113
- Veilleux, S., Rupke, D. S. N., Kim, D.-C., et al. 2009, *ApJS*, 182, 628
- Wang, J., Fabbiano, G., Elvis, M., et al. 2009, *ApJ*, 694, 718
- Weisskopf, M. C., Tananbaum, H. D., Van Speybroeck, L. P., & O'Dell, S. L. 2000, in *X-Ray Optics, Instruments, and Missions III*, eds. J. E. Truemper, & B. Aschenbach, *Proc. SPIE*, 4012, 2
- West, R. M. 1976, *A&A*, 46, 327
- Xu, C. K., Cao, C., Lu, N., et al. 2015, *ApJ*, 799, 11
- Yeghiazaryan, A. A., Nazaryan, T. A., & Hakobyan, A. A. 2016, *A&A*, 37, A1
- Yuan, T.-T., Kewley, L. J., & Sanders, D. B. 2010, *ApJ*, 709, 884
- Zhou, Z.-M., Wu, H., Huang, L., et al. 2014, *Res. Astron. Astrophys.*, 14, 1393
- Zink, E. C., Lester, D. F., Doppmann, G., & Harvey, P. M. 2000, *ApJS*, 131, 413

## Appendix A: Notes on individual objects

Table A.1. X-ray spectral properties for the sample.

| No. | Galaxy              | SX<br>(1)     | HX<br>(2)    | HR<br>(3)    | $F_{\text{SX}}$<br>(4) | $F_{\text{HX}}$<br>(5) | $L_{\text{SX}}$<br>(6) | $L_{\text{HX}}$<br>(7) | SX/IR<br>(8) | HX/IR<br>(9) |
|-----|---------------------|---------------|--------------|--------------|------------------------|------------------------|------------------------|------------------------|--------------|--------------|
| 45  | UGC 08387           | 15.47 ± 1.06  | 4.28 ± 0.59  | -0.57 ± 0.04 | 5.29                   | 5.57                   | 7.79                   | 9.71                   | -4.44        | -4.33        |
| 47  | CGCG 436-030        | 9.01 ± 0.84   | 3.18 ± 0.54  | -0.48 ± 0.04 | 3.78                   | 5.48                   | 8.75                   | 16.07                  | -4.33        | -4.07        |
| 49  | NGC 0695            | 15.58 ± 1.06  | 5.59 ± 0.66  | -0.47 ± 0.03 | 6.00                   | 11.63                  | 15.78                  | 51.19                  | -4.08        | -3.57        |
| 50  | CGCG 043-099        | 2.60 ± 0.44   | 0.92 ± 0.32  | -0.48 ± 0.09 | 1.07                   | 1.35                   | 3.98                   | 6.39                   | -4.67        | -4.46        |
| 51  | MCG+07-23-019       | 8.51 ± 0.45   | 1.17 ± 0.24  | -0.76 ± 0.04 | 3.55                   | 1.93                   | 10.91                  | 7.10                   | -4.17        | -4.35        |
| 52  | NGC 6670 (E)        | 5.76 ± 0.64   | 1.21 ± 0.35  | -0.65 ± 0.08 | 2.58                   | 2.15                   | 5.60                   | 5.56                   | -4.27        | -4.27        |
| 52  | NGC 6670 (W)        | 7.21 ± 0.72   | 2.93 ± 0.50  | -0.42 ± 0.04 | 3.31                   | 6.18                   | 7.24                   | 22.73                  | -3.95        | -3.45        |
| 53  | UGC 02369 (S)       | 11.16 ± 1.14  | 1.30 ± 0.48  | -0.79 ± 0.08 | 3.71                   | 1.71                   | 9.53                   | 4.90                   | -4.28        | -4.57        |
| 54  | NGC 1614            | 38.57 ± 1.59  | 12.19 ± 0.91 | -0.52 ± 0.02 | 16.62                  | 18.51                  | 10.03                  | 12.36                  | -4.23        | -4.14        |
| 56  | NGC 5331 (N)        | 1.79 ± 0.38   | 0.73 ± 0.26  | -0.42 ± 0.10 | 0.95                   | 1.31                   | 2.89                   | 4.86                   | -4.06        | -3.84        |
| 56  | NGC 5331 (S)        | 4.37 ± 0.59   | 1.36 ± 0.36  | -0.53 ± 0.07 | 2.13                   | 1.97                   | 6.46                   | 7.10                   | -4.35        | -4.30        |
| 57  | IRAS F06076-2139(N) | 1.96 ± 0.37   | 0.97 ± 0.27  | -0.34 ± 0.08 | 0.93                   | 1.48                   | 3.60                   | 6.26                   | -4.68        | -4.44        |
| 57  | IRAS F06076-2139(S) | 0.37 ± 0.17   | 0.35 ± 0.17  | -0.03 ± 0.17 | -(a)                   | -(a)                   | -(a)                   | -(a)                   | -(a)         | -(a)         |
| 60  | IC 2810(NW)         | 3.61 ± 0.50   | 0.18 ± 0.15  | -0.91 ± 0.13 | 1.67                   | 0.55                   | 4.27                   | 2.10                   | -4.33        | -4.73        |
| 60  | IC 2810 (SE)        | 1.75 ± 0.39   | 0.12 ± 0.19  | -0.87 ± 0.22 | 0.70                   | 0.01                   | 2.20                   | 0.30                   | -4.39        | -5.26        |
| 63  | IRAS 18090+0130 (E) | 4.01 ± 0.55   | 1.27 ± 0.36  | -0.52 ± 0.08 | 1.59                   | 2.50                   | 4.08                   | 6.39                   | -4.53        | -4.34        |
| 63  | IRAS 18090+0130(W)  | 1.08 ± 0.30   | 0.33 ± 0.23  | -0.54 ± 0.18 | -(a)                   | -(a)                   | -(a)                   | -(a)                   | -(a)         | -(a)         |
| 64  | III Zw 035 (N)      | 2.34 ± 0.41   | 0.84 ± 0.26  | -0.47 ± 0.09 | 0.96                   | 1.32                   | 1.81                   | 2.89                   | -4.97        | -4.76        |
| 65  | NGC 3256            | 263.36 ± 3.28 | 28.62 ± 1.67 | -0.80 ± 0.01 | 77.43                  | 43.02                  | 16.29                  | 9.21                   | -4.01        | -4.26        |
| 67  | IRAS F16399-0937(N) | 4.02 ± 0.53   | 1.6 ± 0.34   | -0.43 ± 0.06 | 1.79                   | 2.52                   | 4.03                   | 6.45                   | -4.56        | -4.36        |
| 67  | IRAS F16399-0937(S) | 2.06 ± 0.38   | 1.25 ± 0.31  | -0.24 ± 0.07 | 1.00                   | 2.07                   | 2.79                   | 5.30                   | -3.77        | -3.49        |
| 68  | IRAS F16164-0746    | 3.91 ± 0.55   | 2.8 ± 0.52   | -0.17 ± 0.04 | 1.84                   | 6.61                   | 4.12                   | 15.38                  | -4.59        | -4.02        |
| 69  | IC 4687             | 20.68 ± 1.21  | 4.27 ± 0.59  | -0.66 ± 0.04 | 8.60                   | 5.97                   | 7.97                   | 5.30                   | -4.11        | -4.30        |
| 69  | IC 4686             | 4.87 ± 0.59   | 0.90 ± 0.28  | -0.69 ± 0.09 | 2.07                   | 1.49                   | 2.12                   | 1.56                   | -3.95        | -4.09        |
| 69  | IC 4689             | 5.17 ± 0.63   | 0.00 ± 0.21  | -1.00 ± 0.14 | 2.45                   | -(a)                   | 2.72                   | -(a)                   | -4.11        | -(a)         |
| 71  | NGC 2623            | 4.79 ± 0.52   | 3.85 ± 0.49  | -0.11 ± 0.02 | 1.74                   | 7.93                   | 1.49                   | 12.85                  | -5.01        | -4.08        |
| 72  | IC 5298             | 11.76 ± 0.92  | 3.31 ± 0.56  | -0.56 ± 0.04 | 5.17                   | 9.66                   | 10.03                  | 36.65                  | -4.18        | -3.62        |
| 73  | IRAS 20351+2521     | 9.14 ± 0.89   | 1.69 ± 0.52  | -0.69 ± 0.07 | 3.93                   | 2.55                   | 14.02                  | 8.33                   | -4.05        | -4.27        |
| 75  | NGC 6090 (NE)       | 16.71 ± 1.07  | 1.84 ± 0.37  | -0.80 ± 0.05 | 5.89                   | 2.88                   | 13.63                  | 7.81                   | -3.99        | -4.23        |
| 75  | NGC6090 (SW)        | 4.68 ± 0.57   | 0.56 ± 0.21  | -0.79 ± 0.10 | 1.71                   | 3.11                   | 4.00                   | 9.01                   | -3.55        | -3.20        |
| 79  | NGC 5256 (NE)       | 32.39 ± 1.31  | 7.97 ± 0.69  | -0.60 ± 0.02 | 11.62                  | 18.06                  | 24.23                  | 55.81                  | -3.33        | -2.97        |
| 79  | NGC 5256 (SW)       | 20.47 ± 1.02  | 1.7 ± 0.32   | -0.85 ± 0.04 | 7.98                   | 3.30                   | 16.56                  | 7.72                   | -3.72        | -4.05        |
| 80  | IRAS F03359+1523(E) | 5.92 ± 0.67   | 1.41 ± 0.38  | -0.62 ± 0.07 | 2.22                   | 2.30                   | 8.68                   | 8.32                   | -4.20        | -4.21        |
| 81  | ESO 550-IG025 (N)   | 2.23 ± 0.41   | 0.55 ± 0.24  | -0.60 ± 0.12 | 0.73                   | 1.17                   | 1.78                   | 3.58                   | -4.51        | -4.22        |
| 81  | ESO 550-IG025 (S)   | 1.55 ± 0.35   | 0.76 ± 0.26  | -0.34 ± 0.10 | 0.69                   | 1.51                   | 1.65                   | 4.29                   | -4.46        | -4.16        |
| 82  | NGC 0034            | 15.58 ± 1.08  | 6.68 ± 0.76  | -0.40 ± 0.03 | 7.23                   | 12.97                  | 6.40                   | 17.78                  | -4.27        | -3.83        |
| 83  | MCG+12-02-001 (E)   | 11.12 ± 0.89  | 3.77 ± 0.53  | -0.49 ± 0.04 | 4.66                   | 5.59                   | 3.01                   | 3.93                   | -4.56        | -4.44        |
| 83  | MCG+12-02-001 (W)   | 3.02 ± 0.46   | 1.49 ± 0.34  | -0.34 ± 0.06 | 1.29                   | 2.92                   | 1.26                   | 2.39                   | -3.98        | -3.71        |
| 85  | IRAS F17138-1017    | 7.84 ± 0.76   | 6.19 ± 0.71  | -0.12 ± 0.02 | 3.67                   | 12.68                  | 3.94                   | 17.64                  | -4.48        | -3.83        |
| 95  | ESO 440-IG058 (N)   | 2.12 ± 0.38   | 1.02 ± 0.27  | -0.35 ± 0.08 | 0.99                   | 1.27                   | 1.72                   | 2.22                   | -3.74        | -3.63        |
| 95  | ESO 440-IG058 (S)   | 7.16 ± 0.70   | 0.97 ± 0.28  | -0.76 ± 0.08 | 3.40                   | 1.53                   | 5.60                   | 2.97                   | -4.23        | -4.50        |
| 100 | NGC 7130            | 78.11 ± 1.44  | 8 ± 0.53     | -0.81 ± 0.01 | 25.37                  | 13.28                  | 16.89                  | 13.29                  | -3.78        | -3.88        |
| 104 | NGC 7771            | 33.16 ± 1.54  | 12.55 ± 1.14 | -0.45 ± 0.02 | 12.87                  | 20.19                  | 6.26                   | 12.35                  | -4.15        | -3.85        |
| 104 | NGC 7770            | 8.08 ± 0.73   | 0.34 ± 0.29  | -0.92 ± 0.09 | 3.15                   | 1.27                   | 1.59                   | 0.74                   | -3.77        | -4.11        |
| 105 | NGC 7592 (E)        | 8.42 ± 0.76   | 1.11 ± 0.32  | -0.77 ± 0.07 | 3.35                   | 1.80                   | 4.94                   | 3.13                   | -4.09        | -4.29        |
| 105 | NGC 7592 (W)        | 11.29 ± 0.88  | 2.04 ± 0.41  | -0.69 ± 0.05 | 4.21                   | 3.15                   | 6.23                   | 5.87                   | -3.75        | -3.78        |
| 106 | NGC 6285            | 5.04 ± 0.64   | 0.45 ± 0.33  | -0.83 ± 0.12 | 1.94                   | 0.85                   | 1.73                   | 0.97                   | -3.83        | -4.08        |
| 106 | NGC 6286            | 32.15 ± 1.64  | 1.27 ± 0.87  | -0.92 ± 0.05 | 11.96                  | 2.58                   | 10.93                  | 2.92                   | -3.86        | -4.43        |

**Notes.** Column (1): background corrected count rate in the 0.5–2 keV band in units of  $10^{-3}$  ct  $s^{-1}$ . Column (2): background corrected count rate in the 2–7 keV band in units of  $10^{-3}$  ct  $s^{-1}$ . Column (3): X-ray colour as defined by  $HR = (H - S)/(H + S)$ . Column (4): observed 0.5–2 keV band flux in units of  $10^{14}$  erg  $s^{-1}$   $cm^{-2}$ . Column (5): observed 2–7 keV band flux in units of  $10^{14}$  erg  $s^{-1}$   $cm^{-2}$ . Column (6): 0.5–2 keV band luminosity corrected for Galactic absorption in units of  $10^{40}$  erg  $s^{-1}$ . Column (7): 2–10 keV band luminosity corrected for Galactic absorption in units of  $10^{40}$  erg  $s^{-1}$ . Column (8): logarithmic luminosity ratio of the 0.5–2 keV and 8–1000  $\mu$ m bands. Column (9): logarithmic luminosity ratio of the 2–10 keV and 8–1000  $\mu$ m bands. <sup>(a)</sup> Missing values due to inability to fit X-ray spectra, not enough source counts.

Table A.1. continued.

| No. | Galaxy             | SX<br>(1)      | HX<br>(2)     | HR<br>(3)    | $F_{\text{SX}}$<br>(4) | $F_{\text{HX}}$<br>(5) | $L_{\text{SX}}$<br>(6) | $L_{\text{HX}}$<br>(7) | SX/IR<br>(8) | HX/IR<br>(9) |
|-----|--------------------|----------------|---------------|--------------|------------------------|------------------------|------------------------|------------------------|--------------|--------------|
| 107 | NGC 4922 (N)       | 10.93 ± 0.97   | 2.73 ± 0.62   | -0.60 ± 0.05 | 5.00                   | 5.93                   | 7.49                   | 17.28                  | -4.09        | -3.73        |
| 110 | NGC 3110           | 21.92 ± 1.28   | 4.73 ± 0.77   | -0.65 ± 0.04 | 10.32                  | 8.40                   | 8.54                   | 8.70                   | -3.98        | -3.97        |
| 114 | NGC 0232           | 10.91 ± 0.91   | 2.19 ± 0.55   | -0.67 ± 0.06 | 4.85                   | 4.34                   | 5.37                   | 6.58                   | -4.29        | -4.21        |
| 117 | MCG+08-18-013(E)   | 5.27 ± 0.67    | 2.1 ± 0.45    | -0.43 ± 0.06 | 2.43                   | 3.56                   | 4.07                   | 7.84                   | -4.32        | -4.03        |
| 120 | CGCG 049-057       | 0.83 ± 0.28    | 0.76 ± 0.29   | -0.04 ± 0.09 | 0.37                   | 1.26                   | 0.20                   | 1.02                   | -5.63        | -4.93        |
| 121 | NGC 1068           | 1975.11 ± 6.58 | 150.27 ± 2.03 | -0.86 ± 0.00 | 503.35                 | 223.51                 | 16.31                  | 10.15                  | -3.77        | -3.98        |
| 123 | UGC 02238          | 6.94 ± 0.74    | 1.94 ± 0.52   | -0.56 ± 0.06 | 2.89                   | 4.33                   | 3.77                   | 5.88                   | -4.34        | -4.15        |
| 127 | MCG-03-34-064      | 95.67 ± 3.73   | 49.5 ± 2.75   | -0.32 ± 0.01 | 37.92                  | 158.12                 | 35.11                  | 289.53                 | -3.32        | -2.40        |
| 134 | ESO 350-IG038      | 26.85 ± 0.73   | 6.38 ± 0.43   | -0.62 ± 0.02 | 10.38                  | 10.03                  | 10.34                  | 12.12                  | -3.85        | -3.78        |
| 136 | MCG-01-60-022      | 10.52 ± 0.84   | 6.7 ± 0.78    | -0.22 ± 0.02 | 4.30                   | 16.83                  | 5.42                   | 33.62                  | -4.12        | -3.33        |
| 141 | IC 0564            | 7.14 ± 0.77    | 2.45 ± 0.53   | -0.50 ± 0.06 | 3.61                   | 5.18                   | 3.73                   | 9.29                   | -3.97        | -3.57        |
| 141 | IC 0563            | 4.93 ± 0.64    | 2.36 ± 0.57   | -0.34 ± 0.05 | 2.56                   | 4.74                   | 2.64                   | 6.90                   | -4.05        | -3.63        |
| 142 | NGC 5135           | 123.31 ± 2.14  | 12.39 ± 0.9   | -0.82 ± 0.01 | 39.38                  | 26.95                  | 19.69                  | 42.37                  | -3.59        | -3.26        |
| 144 | IC 0860            | 0.68 ± 0.26    | 0.37 ± 0.27   | -0.29 ± 0.17 | -(a)                   | -(a)                   | -(a)                   | -(a)                   | -(a)         | -(a)         |
| 147 | IC 5179            | 39.74 ± 2.14   | 6.71 ± 1.62   | -0.71 ± 0.04 | 15.51                  | 14.38                  | 4.99                   | 6.35                   | -4.13        | -4.02        |
| 148 | CGCG 465-012       | 7.13 ± 0.77    | 1.52 ± 0.58   | -0.65 ± 0.08 | 2.63                   | 4.01                   | 3.65                   | 5.64                   | -4.22        | -4.04        |
| 163 | NGC 4418           | 2.63 ± 0.59    | 0.38 ± 0.32   | -0.75 ± 0.18 | 0.87                   | 0.91                   | 0.15                   | 0.19                   | -5.61        | -5.50        |
| 157 | MCG-02-33-098      | 2.97 ± 0.46    | 0.77 ± 0.26   | -0.59 ± 0.10 | 1.39                   | 1.21                   | 1.11                   | 1.16                   | -4.31        | -3.41        |
| 157 | MCG-02-33-099      | 4.42 ± 0.56    | 1.32 ± 0.33   | -0.54 ± 0.07 | 2.19                   | 2.25                   | 1.76                   | 2.15                   | -4.37        | -4.44        |
| 169 | ESO 343-IG013 (N)  | 2.02 ± 0.38    | 2.05 ± 0.38   | 0.01 ± 0.05  | 0.91                   | 4.45                   | 0.85                   | 6.74                   | -4.70        | -3.80        |
| 169 | ESO 343-IG013 (S)  | 3.15 ± 0.47    | 1.02 ± 0.3    | -0.51 ± 0.08 | 1.67                   | 1.24                   | 1.62                   | 1.36                   | -3.86        | -3.93        |
| 170 | NGC 2146           | 170.25 ± 4.38  | 43.74 ± 2.47  | -0.59 ± 0.01 | 59.70                  | 75.77                  | 2.50                   | 3.76                   | -4.31        | -4.13        |
| 174 | NGC 5653           | 20.26 ± 1.20   | 3.18 ± 0.7    | -0.73 ± 0.04 | 8.00                   | 5.37                   | 3.59                   | 3.44                   | -4.16        | -4.18        |
| 178 | NGC 4194           | 59.99 ± 1.33   | 7.91 ± 0.57   | -0.77 ± 0.02 | 22.87                  | 12.40                  | 5.23                   | 3.37                   | -3.97        | -4.16        |
| 179 | NGC 7591           | 4.29 ± 1.01    | 1.09 ± 0.74   | -0.59 ± 0.17 | -(a)                   | -(a)                   | -(a)                   | -(a)                   | -(a)         | -(a)         |
| 182 | NGC 0023           | 34.84 ± 1.45   | 3.88 ± 0.77   | -0.80 ± 0.03 | 12.89                  | 6.04                   | 7.12                   | 3.47                   | -3.85        | -4.17        |
| 188 | NGC 7552           | 148.31 ± 5.56  | 15.63 ± 2.09  | -0.81 ± 0.03 | 55.45                  | 24.24                  | 3.76                   | 1.92                   | -4.12        | -4.41        |
| 191 | ESO 420-G013       | 56.94 ± 2.19   | 4.17 ± 0.83   | -0.86 ± 0.03 | 23.59                  | 5.81                   | 7.86                   | 2.04                   | -3.76        | -4.34        |
| 194 | ESO 432-IG006 (NE) | 8.09 ± 0.76    | 1.75 ± 0.48   | -0.64 ± 0.06 | 3.69                   | 4.46                   | 3.82                   | 6.41                   | -3.65        | -3.43        |
| 194 | ESO 432-IG006 (SW) | 6.04 ± 0.66    | 1.81 ± 0.46   | -0.54 ± 0.06 | 2.79                   | 4.03                   | 2.87                   | 4.53                   | -4.01        | -3.81        |
| 195 | NGC 1961           | 17.55 ± 0.89   | 4.48 ± 0.83   | -0.59 ± 0.03 | 12.45                  | 15.65                  | 6.22                   | 10.63                  | -3.85        | -3.62        |
| 196 | NGC 7753           | 15.00 ± 1.65   | 4.43 ± 1.67   | -0.54 ± 0.07 | 4.52                   | 7.75                   | 3.36                   | 5.88                   | -3.94        | -3.70        |
| 196 | NGC 7752           | 7.18 ± 0.83    | 1.21 ± 0.53   | -0.71 ± 0.09 | 2.72                   | 1.83                   | 1.97                   | 1.53                   | -3.92        | -4.03        |
| 198 | NGC 1365           | 177.35 ± 3.63  | 121.5 ± 2.95  | -0.19 ± 0.00 | 66.03                  | 374.52                 | 2.62                   | 28.89                  | -4.17        | -3.12        |
| 199 | NGC 3221           | 12.47 ± 1.08   | 4.53 ± 1.02   | -0.47 ± 0.04 | 4.87                   | 12.20                  | 2.59                   | 12.26                  | -4.26        | -3.59        |
| 201 | NGC 0838           | 30.31 ± 0.75   | 3.91 ± 0.39   | -0.77 ± 0.02 | 14.91                  | 6.50                   | 5.50                   | 2.70                   | -3.89        | -4.20        |

**Table A.2.** X-ray spectral parameters for the sample.

| No. | Galaxy              | $\Gamma_{\text{H}}$<br>(1)          | $N_{\text{H}}$<br>(2)                  | $T_1$<br>(3)                           | $T_2$<br>(4)                            | $N_{\text{H}}$<br>(5)                  |
|-----|---------------------|-------------------------------------|--|--|---|--|
| 45  | UGC 08387           | 2.4 <sup>+0.6</sup> <sub>-0.5</sub> |  | 0.35 <sup>+0.29</sup> <sub>-0.13</sub> | 0.72 <sup>+0.21</sup> <sub>-0.14</sub>  | 1.09 <sup>+0.21</sup> <sub>-0.21</sub> |
| 47  | CGCG 436–030        | 1.7 <sup>+0.6</sup> <sub>-0.6</sub> |  | 0.68 <sup>+0.12</sup> <sub>-0.07</sub> | 1.42 <sup>+0.4</sup> <sub>-0.33</sub>   | 1.5 <sup>+0.62</sup> <sub>-0.42</sub>  |
| 49  | NGC 0695            | 0.4 <sup>+0.4</sup> <sub>-0.4</sub> |  | 0.36 <sup>+0.10</sup> <sub>-0.04</sub> | 1.06 <sup>+0.16</sup> <sub>-0.12</sub>  | 1.25 <sup>+0.2</sup> <sub>-0.18</sub>  |
| 50  | CGCG 043–099        | 2.0                                 |  | 0.75 <sup>+0.59</sup> <sub>-0.53</sub> | 1.46 <sup>+78.44</sup> <sub>-0.99</sub> | 0.98 <sup>+0.98</sup> <sub>-0.98</sub> |
| 51  | MCG+07–23–019       | 2.2 <sup>+0.8</sup> <sub>-0.7</sub> |  | 0.51 <sup>+0.07</sup> <sub>-0.04</sub> | 1.03 <sup>+0.27</sup> <sub>-0.15</sub>  | 1.36 <sup>+0.28</sup> <sub>-0.23</sub> |
| 52  | NGC 6670 (E)        | 2.0                                 |  | 0.46 <sup>+0.11</sup> <sub>-0.08</sub> | 0.90 <sup>+0.16</sup> <sub>-0.51</sub>  | 1.87 <sup>+0.42</sup> <sub>-0.31</sub> |
| 52  | NGC 6670 (W)        | 0.5 <sup>+0.5</sup> <sub>-0.6</sub> |  | 0.29 <sup>+0.06</sup> <sub>-0.06</sub> | 0.55 <sup>+0.11</sup> <sub>-0.13</sub>  | 1.15 <sup>+0.39</sup> <sub>-0.26</sub> |
| 53  | UGC 02369 (S)       | 2.0                                 |  | 0.54 <sup>+0.15</sup> <sub>-0.15</sub> | 1.12 <sup>+0.23</sup> <sub>-0.23</sub>  | 0.78 <sup>+0.27</sup> <sub>-0.27</sub> |
| 54  | NGC 1614            | 2.4 <sup>+0.3</sup> <sub>-0.2</sub> |  | 0.63 <sup>+0.06</sup> <sub>-0.05</sub> | 1.12 <sup>+0.16</sup> <sub>-0.08</sub>  | 1.57 <sup>+0.13</sup> <sub>-0.18</sub> |
| 56  | NGC 5331 (N)        | 2.1 <sup>+0.7</sup> <sub>-0.6</sub> |  | –(a)                                   | –(a)                                    | –(a)                                   |
| 56  | NGC 5331 (S)        | 2.2 <sup>+0.8</sup> <sub>-1.0</sub> |  | 0.33 <sup>+0.07</sup> <sub>-0.05</sub> | 1.37 <sup>+78.53</sup> <sub>-0.42</sub> | 1.18 <sup>+0.57</sup> <sub>-1.14</sub> |
| 57  | IRAS F06076–2139(N) | 2.0                                 |  | 0.27 <sup>+0.39</sup> <sub>-0.10</sub> | 0.90 <sup>+0.84</sup> <sub>-0.34</sub>  | 0.84 <sup>+0.64</sup> <sub>-0.82</sub> |
| 57  | IRAS F06076–2139(S) | –(d)                                |  | –(d)                                   | –(d)                                    | –(d)                                   |
| 60  | IC 2810(NW)         | 2.0                                 |  | 0.44 <sup>+0.07</sup> <sub>-0.07</sub> | 1.14 <sup>+0.27</sup> <sub>-0.17</sub>  | 0.93 <sup>+0.19</sup> <sub>-0.2</sub>  |
| 60  | IC 2810 (SE)        | 2.0                                 |  | 1.23 <sup>+0.27</sup> <sub>-0.27</sub> | –(b)                                    | –(b)                                   |
| 63  | IRAS 18090+0130 (E) | 2.7 <sup>+1.0</sup> <sub>-1.0</sub> |  | 0.70 <sup>+0.36</sup> <sub>-0.52</sub> | 4.18 <sup>+14.52</sup> <sub>-1.54</sub> | 0.39 <sup>+0.56</sup> <sub>-0.39</sub> |
| 63  | IRAS 18090+0130(W)  | –(d)                                |  | –(d)                                   | –(d)                                    | –(d)                                   |
| 64  | III Zw 035 (N)      | 2.0                                 |  | 0.63 <sup>+0.19</sup> <sub>-0.32</sub> | 1.06 <sup>+0.37</sup> <sub>-0.29</sub>  | 2.44 <sup>+1.3</sup> <sub>-0.77</sub>  |
| 65  | NGC 3256            | 2.6 <sup>+0.2</sup> <sub>-0.2</sub> |  | 0.40 <sup>+0.02</sup> <sub>-0.01</sub> | 0.84 <sup>+0.026</sup> <sub>-0.03</sub> | 1.04 <sup>+0.03</sup> <sub>-0.02</sub> |
| 67  | IRAS F16399–0937(N) | 1.6 <sup>+1.2</sup> <sub>-1.2</sub> |  | 0.33 <sup>+0.77</sup> <sub>-0.15</sub> | 0.97 <sup>+0.20</sup> <sub>-0.23</sub>  | 1.44 <sup>+3.64</sup> <sub>-0.39</sub> |
| 67  | IRAS F16399–0937(S) | 1.8 <sup>+0.3</sup> <sub>-0.3</sub> |  | –(a)                                   | –(a)                                    | –(a)                                   |
| 68  | IRAS F16164–0746    | 2.8 <sup>+1.4</sup> <sub>-1.5</sub> |  | 0.71 <sup>+0.40</sup> <sub>-0.71</sub> | 0.90 <sup>+0.24</sup> <sub>-0.27</sub>  | 1.68 <sup>+0.73</sup> <sub>-0.55</sub> |
| 69  | IC 4687             | 3.4 <sup>+0.3</sup> <sub>-0.5</sub> |  | 0.96 <sup>+0.11</sup> <sub>-0.14</sub> | 5.84 <sup>+23.86</sup> <sub>-2.61</sub> | 0.17 <sup>+0.11</sup> <sub>-0.08</sub> |
| 69  | IC 4686             | 2.0                                 |  | 0.49 <sup>+0.15</sup> <sub>-0.19</sub> | 1.11 <sup>+0.66</sup> <sub>-0.17</sub>  | 1.58 <sup>+0.38</sup> <sub>-0.48</sub> |
| 69  | IC 4689             | 2.0                                 |  | 0.34 <sup>+0.12</sup> <sub>-0.08</sub> | –(b)                                    | –(b)                                   |
| 71  | NGC 2623            | 0.3 <sup>+0.4</sup> <sub>-0.4</sub> |  | 0.66 <sup>+0.28</sup> <sub>-0.28</sub> | 4.45 <sup>+75.45</sup> <sub>-2.22</sub> | 0.35 <sup>+0.34</sup> <sub>-0.23</sub> |
| 72  | IC 5298             | 1.8                                 | 4.80 <sup>+1.45</sup> <sub>-1.34</sub> | 0.63 <sup>+0.16</sup> <sub>-0.49</sub> | 0.76 <sup>+0.22</sup> <sub>-0.15</sub>  | 1.43 <sup>+0.48</sup> <sub>-0.39</sub> |
| 73  | IRAS 20351+2521     | 2.3 <sup>+1.7</sup> <sub>-1.9</sub> |  | 0.60 <sup>+0.08</sup> <sub>-0.11</sub> | 1.37 <sup>+0.91</sup> <sub>-0.45</sub>  | 1.03 <sup>+0.51</sup> <sub>-0.57</sub> |
| 75  | NGC 6090 (NE)       | 2.4 <sup>+0.7</sup> <sub>-0.6</sub> |  | 0.66 <sup>+0.07</sup> <sub>-0.05</sub> | 1.20 <sup>+0.21</sup> <sub>-0.16</sub>  | 1.18 <sup>+0.28</sup> <sub>-0.25</sub> |
| 75  | NGC6090 (SW)        | 2.0                                 |  | 0.35 <sup>+0.25</sup> <sub>-0.09</sub> | 0.71 <sup>+0.39</sup> <sub>-0.39</sub>  | 1.72 <sup>+3.04</sup> <sub>-0.41</sub> |
| 79  | NGC 5256 (NE)       | 1.8                                 | 0.72 <sup>+0.18</sup> <sub>-0.17</sub> | 0.29 <sup>+0.02</sup> <sub>-0.02</sub> | 0.82 <sup>+0.22</sup> <sub>-0.08</sub>  | 0.96 <sup>+0.11</sup> <sub>-0.11</sub> |
| 79  | NGC 5256 (SW)       | 2.3 <sup>+1.1</sup> <sub>-0.9</sub> |  | 0.24 <sup>+0.02</sup> <sub>-0.05</sub> | 0.74 <sup>+0.08</sup> <sub>-0.08</sub>  | 0.63 <sup>+0.1</sup> <sub>-0.1</sub>   |
| 80  | IRAS F03359+1523(E) | 2.0                                 |  | 0.45 <sup>+0.40</sup> <sub>-0.16</sub> | 4.63 <sup>+75.27</sup> <sub>-3.69</sub> | 0.25 <sup>+1.28</sup> <sub>-0.25</sub> |
| 81  | ESO 550–IG025 (N)   | 2.0                                 |  | 0.78 <sup>+0.34</sup> <sub>-0.27</sub> | 2.38 <sup>+6.07</sup> <sub>-0.95</sub>  | 0.83 <sup>+3.84</sup> <sub>-0.83</sub> |
| 81  | ESO 550–IG025 (S)   | 1.6 <sup>+0.5</sup> <sub>-0.5</sub> |  | –(a)                                   | –(a)                                    | –(a)                                   |
| 82  | NGC 0034            | 1.8                                 | 1.05 <sup>+0.73</sup> <sub>-0.71</sub> | 0.38 <sup>+0.06</sup> <sub>-0.05</sub> | 1.74 <sup>+0.62</sup> <sub>-0.34</sub>  | 0.79 <sup>+0.3</sup> <sub>-0.32</sub>  |
| 83  | MCG+12–02–001 (E)   | 2.3 <sup>+0.4</sup> <sub>-0.4</sub> |  | 0.71 <sup>+0.14</sup> <sub>-0.12</sub> | 1.21 <sup>+0.15</sup> <sub>-0.22</sub>  | 1.3 <sup>+0.23</sup> <sub>-0.18</sub>  |
| 83  | MCG+12–02–001 (W)   | 1.7 <sup>+0.3</sup> <sub>-0.3</sub> |  | –(a)                                   | –(a)                                    | –(a)                                   |
| 85  | IRAS F17138–1017    | 1.1 <sup>+0.3</sup> <sub>-0.3</sub> |  | 0.31 <sup>+0.17</sup> <sub>-0.07</sub> | 1.00 <sup>+0.14</sup> <sub>-0.13</sub>  | 1.71 <sup>+0.27</sup> <sub>-0.24</sub> |
| 95  | ESO 440–IG058 (N)   | –(c)                                |  | 3.91 <sup>+8.85</sup> <sub>-1.63</sub> | –(c)                                    | –(c)                                   |
| 95  | ESO 440–IG058 (S)   | 2.0                                 |  | 0.25 <sup>+0.08</sup> <sub>-0.07</sub> | 0.77 <sup>+0.14</sup> <sub>-0.09</sub>  | 0.81 <sup>+0.17</sup> <sub>-0.16</sub> |
| 100 | NGC 7130            | 1.8                                 | 3.47 <sup>+1.40</sup> <sub>-1.84</sub> | 0.30 <sup>+0.01</sup> <sub>-0.01</sub> | 0.78 <sup>+0.04</sup> <sub>-0.03</sub>  | 0.89 <sup>+0.04</sup> <sub>-0.05</sub> |
| 104 | NGC 7771            | 1.6 <sup>+0.3</sup> <sub>-0.3</sub> |  | 0.52 <sup>+0.08</sup> <sub>-0.04</sub> | 1.04 <sup>+0.16</sup> <sub>-0.09</sub>  | 1.7 <sup>+0.21</sup> <sub>-0.18</sub>  |
| 104 | NGC 7770            | 2.0                                 |  | 0.36 <sup>+0.06</sup> <sub>-0.04</sub> | 1.07 <sup>+0.25</sup> <sub>-0.24</sub>  | 1.1 <sup>+0.43</sup> <sub>-0.32</sub>  |
| 105 | NGC 7592 (E)        | 2.0                                 |  | 0.31 <sup>+0.04</sup> <sub>-0.06</sub> | 0.72 <sup>+0.14</sup> <sub>-0.11</sub>  | 1.22 <sup>+0.3</sup> <sub>-0.26</sub>  |
| 105 | NGC 7592 (W)        | 1.6 <sup>+0.7</sup> <sub>-0.8</sub> |  | 0.36 <sup>+0.30</sup> <sub>-0.12</sub> | 0.75 <sup>+0.42</sup> <sub>-0.27</sub>  | 1.35 <sup>+0.98</sup> <sub>-0.54</sub> |
| 106 | NGC 6285            | 2.0                                 |  | 2.96 <sup>+3.74</sup> <sub>-1.00</sub> | –(b)                                    | –(b)                                   |
| 106 | NGC 6286            | 2.0                                 |  | 0.37 <sup>+0.05</sup> <sub>-0.08</sub> | 0.78 <sup>+0.13</sup> <sub>-0.16</sub>  | 0.57 <sup>+0.13</sup> <sub>-0.13</sub> |

**Notes.** Column (1): Spectral power-law slope in the 2–7 keV range. Column (2): Obscuring column density for galaxies with an absorbed AGN model fit in the 2–7 keV range, in units of  $10^{23} \text{ cm}^{-2}$ . Column (3): external *mekal* model temperature. Column (4): Internal, absorbed *mekal* model temperature. Column (5): Obscuring column density associated with the internal *mekal* model, in units of  $10^{22} \text{ cm}^{-2}$ . (a) Full spectrum fitted with a single power-law. (b) Soft band spectrum fitted with a single *mekal* component. (c) Full spectrum fitted with a single *mekal* component. (d) No fit. Values without errors are imposed, as described in Sect. 4.4.2. Errors reported correspond to  $1\sigma$  for one parameter of interest, leaving 5 parameters free.

Table A.2. continued.

| No. | Galaxy             | $\Gamma_{\text{H}}$<br>(1)          | $N_{\text{H}}$<br>(2)                  | $T_1$<br>(3)                            | $T_2$<br>(4)                            | $N_{\text{H}}$<br>(5)                  |
|-----|--------------------|-------------------------------------|--|---|---|--|
| 107 | NGC 4922 (N)       | 1.8                                 | 2.94 <sup>+1.41</sup> <sub>-1.15</sub> | 0.60 <sup>+0.10</sup> <sub>-0.35</sub>  | 0.58 <sup>+0.16</sup> <sub>-0.08</sub>  | 1.34 <sup>+2.04</sup> <sub>-0.35</sub> |
| 110 | NGC 3110           | 1.7 <sup>+0.5</sup> <sub>-0.5</sub> |  | 0.34 <sup>+0.06</sup> <sub>-0.03</sub>  | 0.89 <sup>+0.09</sup> <sub>-0.10</sub>  | 0.95 <sup>+0.17</sup> <sub>-0.14</sub> |
| 114 | NGC 0232           | 1.6 <sup>+0.7</sup> <sub>-0.6</sub> |  | 0.37 <sup>+0.13</sup> <sub>-0.08</sub>  | 0.91 <sup>+0.12</sup> <sub>-0.11</sub>  | 0.77 <sup>+0.16</sup> <sub>-0.18</sub> |
| 117 | MCG+08-18-013(E)   | 1.8 <sup>+0.8</sup> <sub>-0.8</sub> |  | 0.43 <sup>+2.16</sup> <sub>-0.33</sub>  | 2.93 <sup>+8.25</sup> <sub>-1.45</sub>  | 0.63 <sup>+0.84</sup> <sub>-0.6</sub>  |
| 120 | CGCG 049-057       | 1.0 <sup>+0.7</sup> <sub>-0.6</sub> |  | —(a)                                    | —(a)                                    | —(a)                                   |
| 121 | NGC 1068           | 2.0 <sup>+0.1</sup> <sub>-0.1</sub> |  | 0.23 <sup>+0.00</sup> <sub>-0.00</sub>  | 0.66 <sup>+0.01</sup> <sub>-0.00</sub>  | 0.77 <sup>+0.01</sup> <sub>-0.01</sub> |
| 123 | UGC 02238          | 1.8 <sup>+0.2</sup> <sub>-0.2</sub> |  | —(a)                                    | —(a)                                    | —(a)                                   |
| 127 | MCG-03-34-064      | 1.8                                 | 5.02 <sup>+0.40</sup> <sub>-0.39</sub> | 0.28 <sup>+0.02</sup> <sub>-0.02</sub>  | 1.02 <sup>+0.07</sup> <sub>-0.06</sub>  | 0.9 <sup>+0.1</sup> <sub>-0.09</sub>   |
| 134 | ESO 350-IG038      | 2.0 <sup>+0.2</sup> <sub>-0.2</sub> |  | 0.33 <sup>+0.02</sup> <sub>-0.01</sub>  | 0.97 <sup>+0.04</sup> <sub>-0.05</sub>  | 1.19 <sup>+0.07</sup> <sub>-0.07</sub> |
| 136 | MCG-01-60-022      | 1.8                                 | 1.10 <sup>+0.27</sup> <sub>-0.25</sub> | 0.30 <sup>+0.09</sup> <sub>-0.07</sub>  | 0.68 <sup>+0.06</sup> <sub>-0.10</sub>  | 1.08 <sup>+0.21</sup> <sub>-0.18</sub> |
| 141 | IC 0564            | 0.7 <sup>+0.9</sup> <sub>-0.8</sub> |  | 0.29 <sup>+0.07</sup> <sub>-0.06</sub>  | 0.56 <sup>+0.12</sup> <sub>-0.08</sub>  | 1.42 <sup>+0.31</sup> <sub>-0.32</sub> |
| 141 | IC 0563            | 1.5 <sup>+0.6</sup> <sub>-0.6</sub> |  | 0.65 <sup>+0.06</sup> <sub>-0.07</sub>  | 1.93 <sup>+7.97</sup> <sub>-0.74</sub>  | 3.28 <sup>+2.34</sup> <sub>-2.73</sub> |
| 142 | NGC 5135           | 2.0                                 |  | 0.25 <sup>+0.02</sup> <sub>-0.02</sub>  | 0.68 <sup>+0.09</sup> <sub>-0.04</sub>  | 0.73 <sup>+0.06</sup> <sub>-0.06</sub> |
| 144 | IC 0860            | —(d)                                |  | —(d)                                    | —(d)                                    | —(d)                                   |
| 147 | IC 5179            | 1.6 <sup>+0.5</sup> <sub>-0.5</sub> |  | 0.67 <sup>+0.06</sup> <sub>-0.05</sub>  | 4.28 <sup>+2.38</sup> <sub>-1.12</sub>  | 0.01 <sup>+0.04</sup> <sub>-0.01</sub> |
| 148 | CGCG 465-012       | 2.0 <sup>+0.9</sup> <sub>-1.1</sub> |  | 0.38 <sup>+0.22</sup> <sub>-0.12</sub>  | 3.75 <sup>+12.13</sup> <sub>-2.15</sub> | 0.44 <sup>+0.76</sup> <sub>-0.37</sub> |
| 157 | MCG-02-33-098      | 2.0                                 |  | 0.32 <sup>+0.38</sup> <sub>-0.08</sub>  | 0.99 <sup>+0.36</sup> <sub>-0.22</sub>  | 1.42 <sup>+0.49</sup> <sub>-0.35</sub> |
| 157 | MCG-02-33-099      | 2.0                                 |  | 0.25 <sup>+0.05</sup> <sub>-0.04</sub>  | 1.02 <sup>+0.38</sup> <sub>-0.17</sub>  | 1.25 <sup>+0.28</sup> <sub>-0.31</sub> |
| 163 | NGC 4418           | 1.9 <sup>+0.5</sup> <sub>-0.5</sub> |  | —(a)                                    | —(a)                                    | —(a)                                   |
| 169 | ESO 343-IG013 (N)  | 0.9 <sup>+0.3</sup> <sub>-0.3</sub> |  | —(a)                                    | —(a)                                    | —(a)                                   |
| 169 | ESO 343-IG013 (S)  | 2.2 <sup>+0.3</sup> <sub>-0.4</sub> |  | —(a)                                    | —(a)                                    | —(a)                                   |
| 170 | NGC 2146           | 1.7 <sup>+0.2</sup> <sub>-0.2</sub> |  | 0.38 <sup>+0.03</sup> <sub>-0.02</sub>  | 0.72 <sup>+0.06</sup> <sub>-0.05</sub>  | 1.18 <sup>+0.07</sup> <sub>-0.07</sub> |
| 174 | NGC 5653           | 1.4 <sup>+0.8</sup> <sub>-0.9</sub> |  | 0.32 <sup>+0.03</sup> <sub>-0.02</sub>  | 0.80 <sup>+0.15</sup> <sub>-0.12</sub>  | 0.96 <sup>+0.18</sup> <sub>-0.14</sub> |
| 178 | NGC 4194           | 2.3 <sup>+0.3</sup> <sub>-0.3</sub> |  | 0.34 <sup>+0.01</sup> <sub>-0.01</sub>  | 0.87 <sup>+0.1</sup> <sub>-0.04</sub>   | 0.87 <sup>+0.06</sup> <sub>-0.06</sub> |
| 179 | NGC 7591           | —(d)                                |  | —(d)                                    | —(d)                                    | —(d)                                   |
| 182 | NGC 0023           | 3.0 <sup>+0.6</sup> <sub>-0.7</sub> |  | 0.30 <sup>+0.04</sup> <sub>-0.07</sub>  | 0.84 <sup>+0.05</sup> <sub>-0.07</sub>  | 0.69 <sup>+0.12</sup> <sub>-0.06</sub> |
| 188 | NGC 7552           | 2.4 <sup>+0.4</sup> <sub>-0.4</sub> |  | 0.49 <sup>+0.04</sup> <sub>-0.05</sub>  | 0.87 <sup>+0.1</sup> <sub>-0.11</sub>   | 1.23 <sup>+0.15</sup> <sub>-0.13</sub> |
| 191 | ESO 420-G013       | 2.9 <sup>+0.4</sup> <sub>-0.3</sub> |  | 0.25 <sup>+0.01</sup> <sub>-0.02</sub>  | 0.77 <sup>+0.06</sup> <sub>-0.09</sub>  | 0.58 <sup>+0.09</sup> <sub>-0.09</sub> |
| 194 | ESO 432-IG006 (NE) | 1.8                                 | 4.32 <sup>+1.96</sup> <sub>-1.78</sub> | 0.65 <sup>+0.10</sup> <sub>-0.14</sub>  | 0.73 <sup>+0.89</sup> <sub>-0.51</sub>  | 1.99 <sup>+6.05</sup> <sub>-0.97</sub> |
| 194 | ESO 432-IG006 (SW) | 1.8                                 | 1.22 <sup>+0.76</sup> <sub>-0.81</sub> | 0.27 <sup>+0.17</sup> <sub>-0.07</sub>  | 0.75 <sup>+0.35</sup> <sub>-0.15</sub>  | 0.96 <sup>+0.25</sup> <sub>-0.2</sub>  |
| 195 | NGC 1961           | 1.0 <sup>+0.4</sup> <sub>-0.3</sub> |  | 0.64 <sup>+0.04</sup> <sub>-0.04</sub>  | 4.70 <sup>+5.6</sup> <sub>-1.74</sub>   | 0.23 <sup>+0.25</sup> <sub>-0.15</sub> |
| 196 | NGC 7753           | —(c)                                |  | 6.48 <sup>+19.82</sup> <sub>-2.70</sub> | —(c)                                    | —(c)                                   |
| 196 | NGC 7752           | 2.0                                 |  | 0.49 <sup>+0.12</sup> <sub>-0.16</sub>  | 0.70 <sup>+0.28</sup> <sub>-0.12</sub>  | 1.46 <sup>+0.49</sup> <sub>-0.47</sub> |
| 198 | NGC 1365           | 1.8                                 | 3.42 <sup>+0.13</sup> <sub>-0.13</sub> | 0.33 <sup>+0.01</sup> <sub>-0.01</sub>  | 0.96 <sup>+0.04</sup> <sub>-0.05</sub>  | 0.94 <sup>+0.06</sup> <sub>-0.06</sub> |
| 199 | NGC 3221           | 0.3 <sup>+0.6</sup> <sub>-0.6</sub> |  | 0.43 <sup>+0.16</sup> <sub>-0.09</sub>  | 0.70 <sup>+0.15</sup> <sub>-0.10</sub>  | 1.44 <sup>+0.3</sup> <sub>-0.18</sub>  |
| 201 | NGC 0838           | 2.5 <sup>+0.3</sup> <sub>-0.3</sub> |  | 0.36 <sup>+0.02</sup> <sub>-0.03</sub>  | 1.03 <sup>+0.05</sup> <sub>-0.06</sub>  | 0.87 <sup>+0.07</sup> <sub>-0.07</sub> |

[45] *UGC 08387*. This source meets our [Ne v]  $14.32\ \mu\text{m}$  line selection criterion, and is thus classified as an AGN, although there is no hint of its presence in the X-ray *Chandra* data. As described in [Iwasawa et al. \(2011\)](#), a soft X-ray nebulae extends perpendicular to the plane of the galaxy; this is most likely associated with a galactic-scale outflow.

Previous evidence of the AGN has come from detection of compact radio sources at milli-arcsecond resolution (e.g., [Lonsdale et al. 1993](#); [Parra et al. 2010](#)), which [Romero-Cañizales et al. \(2012\)](#) attributed to various supernovae in coexistence with a low-luminosity AGN. Using VLBI data, [Romero-Cañizales et al. \(2017\)](#) provided evidence for a parsec-scale radio jet.

[47] *CGCG 436–030*. This galaxy shows three bright X-ray peaks in the soft band; only the central peak corresponds to a hard-band peak. The other two peaks, placed following the spiral arm structure in the optical images, most likely correspond to star-forming regions.

The DSS image faintly shows a bridge of material between the galaxy and a fainter galaxy  $\sim 1'$  to the east, with which it seem to be interacting ([Mirabel & Sanders 1988](#); [Zink et al. 2000](#)). This other galaxy is not detected in the *Chandra* X-ray or the MIPS data, and is only visible in near-infrared observations such as the longest-wavelength IRAC channels. Therefore, we have not considered any contribution to the IRAS flux originating from this nearby companion.

[49] *NGC 0695*. This source has a rather flat spectrum in the 0.4–7 keV range. There is considerable extended emission in the soft band, and both bands present a very intense emission from the central region.

[51] *MCG+07–23–019*. This ring galaxy is composed of an elongated main body with double components separated by  $\sim 5''$  ( $\sim 4$  kpc) and an oval ring with a diameter of  $16''$  to the west of the main body ([Hattori et al. 2004](#)). As has been suggested by JHKL-band mapping, the nucleus of the galaxy lies between the two optical components and is heavily obscured in optical images ([Joy & Harvey 1987](#)). *Chandra* data show clear emission coming from the elongated disk of the galaxy. The X-ray emission is more intense in the center, and unobscured in the hard and soft bands. Extended soft X-ray emission around the nucleus partly follows the oval ring, most likely tracing star formation.

[52] *NGC 6670*. This closely interacting merger is composed of two sources, NGC 6670A (or East) and NGC 6670B (or West), separated  $\sim 0.5'$ . Both galaxies contribute to the IRAS flux ([Chu et al. 2017](#)), with the western component being slightly brighter.

X-ray emission from the eastern component is mostly observed in the soft band and is concentrated around the nucleus. The western source, however, shows extended diffuse emission, particularly along the plane of the galaxy. The emission near the center is more intense in the hard and soft band at both sides of the nucleus. This morphology suggests high absorption in the innermost region. The spectrum is also suggestive of a hard excess, and a simple power-law fit results in a photon index of  $\Gamma = 0.5 \pm 0.5$ . Fitting an absorbed power-law of fixed photon index  $\Gamma = 1.8$  results in a moderate absorbing column density of  $N_{\text{H}} \sim 4 \times 10^{22}\ \text{cm}^{-2}$ , and no significant improvement on the fit. The X-ray luminosity of the source is  $L_{\text{X}} \sim 10^{41}\ \text{cm}^{-2}$ . The excess at  $\sim 6.4$  keV, if interpreted as a possible Fe K $\alpha$  line, is not significant to the  $1\sigma$  level.

*XMM-Newton* data for both sources, resolved, in this double system were analyzed by [Mudd et al. \(2014\)](#), with no hint of an AGN presence detected. However, their short exposure implied a detection of  $\sim 100$  cts per source, which lower than the counts detected in our *Chandra* data.

We consider that even though we cannot rule out the possibility of the western source containing an AGN, we have no strong evidence to claim its presence.

[53] *UGC 02369*. This double system, separated by  $\sim 0.4'$ , is clearly dominated in X-rays by the southern component, which, as shown in Table 3, is also responsible for  $\sim 98\%$  of the IR emission. Because the contribution to the IRAS flux originating in the northern galaxy is negligible, we do not present any results for this component. An X-ray analysis would not be possible either, as only  $\sim 5$  cts are detected for this source.

The southern source is compact in X-rays, with emission coming both from the nucleus and from a star-forming region in the spiral arm, in the south in the soft and hard bands.

[54] *NGC 1614*. This source has been classified as a possible obscured AGN through X-ray spectroscopy ([Risaliti et al. 2000](#)), although VLBI studies with a sensitivity limit of 0.9 mJy do not detect a compact radio core in it ([Hill et al. 2001](#)). Recent studies in subarcsecond MIR observations do not completely rule out a possible (weak) AGN scenario, but they constrain the nuclear luminosity to  $< 5\%$  of the overall bolometric luminosity of the galaxy ([Pereira-Santaella et al. 2015b](#)). ALMA observations do not detect the nucleus in either the CO (6–5) line emission or in the  $435\ \mu\text{m}$  continuum, ruling out a Compton-thick AGN with relatively high confidence ([Xu et al. 2015](#)).

This source also does not meet any of our AGN selection criteria either, and we do not see any signs of AGN presence in the *Chandra* spectrum.

Emission in the hard and soft band is peaked in the nucleus, and the soft-band emission also shows elongated extension in the E–W direction, as opposed to the optical edge-on disk, which is elongated toward the N–S direction. Intense star formation, very compact in the nucleus, is the most likely origin of the X-ray emission.

[56] *NGC 5331*. Both galaxies in this system, separated by  $\sim 0.4'$ , contribute to the IRAS flux, although the southern component is responsible for  $\sim 80\%$  of the emission, as shown in Table 3. However, since their X-ray luminosity is similar, the northern galaxy has a much higher logarithmic ratio (HX/IR) =  $-3.84$  (as defined in Table A.1). This value is close to the expected ratio given the correlation derived by [Ranalli et al. \(2003\)](#), but higher than the characteristic X-ray faintness of the GOALS sample.

[57] *IRAS F06076–2139*. This closely interacting merger is clearly dominated by the northern source in IR and X-rays. However, with only  $\sim 10$  cts, the southern source meets our HR criterion for AGN selection (HR =  $-0.03 \pm 0.17$ ). The spectrum also shows an increase in flux toward higher energies, despite the significant error bars. Only the hardness ratio is computed as part of the analysis of this source, because of the low number of counts. For the same reason, a radial profile is not provided for this component.

The northern source comes close to meeting the same AGN selection criteria, with HR =  $-0.34 \pm 0.08$ . The spectrum might indicate an excess in the hard band, although an absorbed power-law fit with a fixed photon index of 1.8 yields a column density of only  $N_{\text{H}} \sim 1.9 \times 10^{22}\ \text{cm}^{-2}$ . With a full-band X-ray luminosity of  $L_{\text{X}} \sim 10^{41}\ \text{erg s}^{-1}$ , and fitting statistics also favoring a non-absorbed power-law, we opt not to consider this source an AGN.

[60] *IC 2810*. Both galaxies in this system, separated by  $\sim 1.1'$ , contribute to the IRAS flux as shown in Table 3, with the north-western source contributing  $\sim 70\%$  of the IR luminosity.

[63] *IRAS 18090+0130*. Both galaxies in this system, separated by  $\sim 1.3'$ , contribute to the IRAS flux, with the eastern component being responsible for  $\sim 80\%$  of the emission. The western

component has a low X-ray flux and not enough counts to provide reliable data for any analysis further than computing a hardness ratio.

[64] *III Zw 035*. This closely interacting double system is completely unresolved in the *Herschel* and MIPS images we used to derive the contribution of each galaxy into the IRAS source, as shown in Table 3. However, Chapman et al. (1990) reported that the majority of the radio continuum (and also probably FIR) emission originates in the northern galaxy. High angular resolution radio continuum observations from (Barcos-Muñoz et al. 2017) indicate that the northern component is the most compact source of the brightest and closest ULIRGs from the GOALS sample, while the authors did not detect the southern component at 33 GHz. The IRAC channel 1–4 images (at 3.6, 4.5, 5.8 and 8.0  $\mu\text{m}$ ) show that the northern source clearly dominates and the southern source fades with increasing wavelength. Thus, we assign a contribution to the IRAS flux of 100% to the northern source.

Because of the lack of IRAS flux originating in the southern component, we do not present results for its X-ray analysis in this work, and we did not consider it a source within our sample. The total X-ray counts for this galaxy are  $\sim 25$  cts in the full 0.5–7 keV range, which does not allow for a detailed X-ray analysis either, although a simple power-law fit gives an estimated  $L_X \sim 2 \times 10^{40} \text{ erg s}^{-1}$ . However, while the soft-band X-ray flux is dominated by the northern source, the hard-band X-ray flux is very similar for both, and the southern source is optically classified as a Seyfert 2 (Yuan et al. 2010). It is then possible that the northern source is responsible for the high IRAS flux, most likely having a burst of star formation, while the NIR and MIR contribution from the southern source might be due to an AGN.

[65] *NGC 3256*. This source is assumed to be in an advanced merger stage, with a northern brighter component (the central peak) and a southern component at about  $\sim 10''$ , elongated in the E–W direction. The possibility of this being a merging obscured companion galaxy was first suggested by Moorwood & Oliva (1994), and radio observations by Norris & Forbes (1995) supported this theory by detecting two equally bright knots. However, high-resolution MIR imaging shows that the northern peak is  $\sim 20$  times brighter than the southern region, suggesting that most of the star formation in the galaxy originates there (Lira et al. 2002). The authors also found the northern peak to be brighter in X-rays in *Chandra* data. The images shown in this work mark the two hard-band peaks reported by them, the southern clearly falling in an obscured region, with dimmer soft-band emission.

The very advanced merger stage of this source makes it hard to determine how much of the surrounding extended emission was initially associated with any of the cores. Therefore, we analyzed it as a single source in order to avoid introducing errors into the determination of its IR and X-ray emission.

[67] *IRAS F16399–0937*. This closely interacting pair is unresolved in *Herschel* and MIPS data, although Haan et al. (2011) derived that most of the MIR emission ( $>90\%$ ) comes from the northern source. We used this value to correct for the fraction contributed to the IRAS flux by each galaxy.

The northern source shows two intense hard X-ray peaks, both corresponding to soft X-ray emitting regions, the more southern of which is the nucleus. The other, as well as the less-intense knots seen in both sources, probably correspond to star-forming regions. The spectrum of this source shows an excess at  $>4$  keV, with a few hard counts coming from the nuclear region. Fitting an absorbed power-law with a photon index of 1.8 yields an absorbing column density of  $N_{\text{H}} \sim 2 \times 10^{23} \text{ cm}^{-2}$ , although an unabsorbed power-law of photon index  $\sim 1.6$  is an equally good

fit. With a net count number of  $\sim 23$  cts, we cannot confidently classify this source as an AGN.

Sales et al. (2015) also considered the possibility that the northern source might contain an embedded AGN, fitting the 0.435–500  $\mu\text{m}$  SED with a model that includes an AGN torus component. The fit suggests an AGN with bolometric luminosity  $L_{\text{bol}} \sim 10^{44} \text{ erg s}^{-1}$ , although the spectrum is also consistent with shocks ( $v \sim 100\text{--}200 \text{ km s}^{-1}$ ). This bolometric luminosity would imply a fraction  $L_X^{\text{AGN}} \sim 10^{42} - 10^{43} \text{ erg s}^{-1}$ , much higher than the  $L_X = 10^{41} \text{ erg s}^{-1}$  detected in the *Chandra* data.

The southern source does not have a clear center in X-rays or MIR and FIR, and so the center for the radial profile was determined using the brightest region in the optical HST image. Because the source is clearly elongated, annuli centered on the eastern edge will include photons from the northern source, and to avoid interference, we removed it from the computation of radial profiles. This component meets our HR AGN selection criterion, although the image in Appendix B shows that no strong hard X-ray peak comes from the nucleus of the source; the origin of the hard counts is concentrated in two point-sources west of the nucleus. Therefore, we did not classify this source as an AGN.

[68] *IRAS F16164–0746*. This source meets two of our AGN selection criteria, the HR and the [Ne v] line, and is also classified as an optical Seyfert 2 in Yuan et al. (2010). The X-ray source is elongated in the soft band, in the direction perpendicular to the disk of the galaxy, which could be interpreted as an outflow. There is also a secondary point source  $\sim 3''$  from the nucleus, in the soft and hard band, without any obvious overlap with a star-forming knot. With an associated X-ray luminosity in the 2–10 keV range of  $\sim 3 \times 10^{40} \text{ erg s}^{-1}$ , it could be classified as a ULX.

[69] *IC 4686/7*. This source is part of a triple merger system, formed by IC 4687 in the north, which closely interacts with the central galaxy, IC 4686, at  $\sim 0.5'$ , and IC 4689  $\sim 1'$  south of IC 4686 (West 1976). All three galaxies contribute more than 10% to the IRAS flux (Chu et al. 2017), and were therefore analyzed here.

[71] *NGC 2623*. With a spectrum that clearly raises toward higher energies, giving a hardness ratio of  $\text{HR} = -0.11 \pm 0.02$ , and also meeting the [Ne v] line criterion, this source is classified as an AGN. This source has been classified as an AGN previously in radio (Lonsdale et al. 1993) and X-rays (Maiolino et al. 2003).

Optical HST images show extended tidal tails, approximately 20–25 kpc in length, with a southern region rich in bright star clusters (Evans et al. 2008), although no X-ray emission is detected with *Chandra* in the region.

[72] *IC 5298*. This source is a clear absorbed AGN. It is visible in the *Chandra* spectrum presented here, and through *XMM-Newton* data analysis. When a photon index of 1.8 is assumed, a column density of  $N_{\text{H}} \sim 4 \times 10^{23}$  is obtained when data from both telescopes are used. A faint line at 6.4 keV is visible in the *Chandra* data, with a significance lower than  $1\sigma$ . The line can be confirmed with a significance of  $\sim 2\sigma$  from *XMM-Newton* EPIC data, with a fit that is also consistent with the derived absorbing column density. The AGN diagnostics is also confirmed through the [Ne v] line and the optical S2 classification (Veilleux et al. 1995).

[73] *IRAS 20351+2521*. This galaxy shows strong central emission in X-rays, originating in the nucleus, with extended emission and point-sources along the spiral arms that trace star-forming knots.

[75] *NGC 6090*. This closely interacting system is completely unresolved in *Herschel* and MIPS data. Therefore, we resorted to

the analysis performed by [Hattori et al. \(2004\)](#) to derive the contribution of each component to the IRAS flux listed in Table 3.

The northeastern source shows hard-band diffuse emission corresponding to the optical central region of the galaxy, and a peak  $\sim 3''$  north of the center. It corresponds to a particularly bright region in the optical and IR in one of the spiral arms.

The sources interact so closely that the radial profiles interfere with each other past 4–5'' from each nucleus, and have therefore been limited to this radius.

[79] *NGC 5256*. This closely interacting system is surrounded by diffuse soft-band emission in X-rays, part of which extends toward the northern direction, following a blue tidal stream seen in optical images. Between the two sources, a slightly curved excess is visible, which can be interpreted as a shock between colliding winds from both galaxies (see [Mazzarella et al. 2012](#)). This excess is the reason that the radial profile in Appendix B for the NE source shows an increase in soft-band surface brightness with distance at 5–6''.

This source has been detected in the [Ne v] line at kiloparsec scales, meeting our AGN selection criteria. However, because the two nuclei are located very close to each other, it is not possible to know which (or if both) is responsible for this emission. The two optical classifications we used ([Veilleux et al. 1995](#); [Yuan et al. 2010](#)) mark the NE source as a Seyfert 2, and the SW source as LINER or composite. However, [Mazzarella et al. \(2012\)](#) reported the opposite optical classification for the sources: the NE source as LINER and the SW source as a Seyfert 2 galaxy.

Based on the X-ray spectra, the NE source can be best fit with an absorbed AGN model, fixing a spectral index of 1.8 and obtaining a column density of  $N_{\text{H}} \sim 8 \times 10^{22} \text{ cm}^{-2}$ , which is interpreted as a mildly absorbed AGN.

The SW source shows an excess that can be fit as an iron 6.4 keV line with a confidence of  $\sim 2.1\sigma$ , which meets one of our X-ray AGN selection criteria.

As reported by [Mazzarella et al. \(2012\)](#), *XMM-Newton* EPIC data only marginally resolve the two sources, and the spectrum is presented for the whole system. However, given the spectra resolved by *Chandra*, the iron line seen in the EPIC data most likely originates in the southwestern source. Their combined analysis also results in a Compton-thick classification of the south-western source.

[80] *IRAS F03359+1523*. Only one of the two sources in this system is observed in X-rays, the eastern source, with an elongated morphology that corresponds to the length of the edge-on disk in the optical data. The sources are unresolved in the *Herschel* data, and only one source is visible in the MIPS data, which is centered at the position of the eastern source. It is not possible to confirm whether this is due to lack of resolution, or if the western source does not contribute to the MIPS flux. However, from observing the IRAC images from channel 1 through 4 (at 3.6, 4.5, 5.8 and 8.0  $\mu\text{m}$ ), it is possible to see that the eastern source clearly dominates and the western source fades with increasing wavelength. [Goldader et al. \(1997\)](#) also described that only one source (believed to be the eastern source) is prominent at radio wavelengths. This, together with the complete lack of X-ray emission originating in this companion source, leads us to believe that the western galaxy does not contribute to the IRAS flux.

Another source, prominent in radio wavelengths, lies  $\sim 1.5'$  to the south of IRAS F03359+1523. [Clemens et al. \(2008\)](#) used NVSS radio data to extrapolate that this nearby galaxy could be responsible for about  $\sim 50\%$  of the IRAS flux. However, images at 8 and 24 microns show a weak source that fades completely at

70 micron, leading us to believe that its contribution to the FIR luminosity is most likely negligible.

[81] *ESO 550-IG025*. Both sources in this system, with a separation of  $\sim 0.3'$ , contribute to the IRAS flux. The southern source has a rather flat spectrum, which is partly due to the contribution of the hard X-ray peak placed at about  $\sim 4''$  west of the nucleus. This source cannot be easily interpreted as the X-ray counterpart to any star-forming regions in the galaxy. If it is associated with this galaxy, its X-ray luminosity in the 2–10 keV range is of  $\sim 3 \times 10^{40} \text{ erg s}^{-1}$ , implying it could be classified as a ULX.

[82] *NGC 0034*. This source, optically classified as a Seyfert 2 (e.g., [Veilleux et al. 1999](#); [Yuan et al. 2010](#)), has an X-ray spectrum that shows a hard band excess. Fitting an absorbed AGN with a fixed photon index of 1.8 gives an absorbing column density of  $N_{\text{H}} \sim 1 \times 10^{23} \text{ cm}^{-2}$ . Previous analyses of *XMM-Newton* data confirmed an AGN, either through marginal detection of the Fe K $\alpha$  line or by modeling an absorption or reflection component (e.g., [Shu et al. 2007](#); [Brightman & Nandra 2011](#)).

[Ricci et al. \(2017\)](#) used joint data from *Chandra*, *XMM-Newton*, and *NuSTAR* and found a clear Fe K $\alpha$  feature at  $6.48_{-0.05}^{+0.06} \text{ keV}$ . Their spectral analysis shows a heavily obscured AGN with a column density of  $N_{\text{H}} = 5.3 \pm 1.1 \times 10^{23} \text{ cm}^{-2}$ . Their results certainly confirm the AGN, and their derived column density differs from the one derived with only *Chandra*, most likely because *Chandra* has much lower sensitivity at high energies.

[83] *MCG+12-02-001*. We consider this system to be composed of three individual sources: a northern component and a main pair, separated by  $\sim 0.3'$ . The western source in the pair is considered an individual galaxy in close interaction with the eastern source, although it may also be an extended star-forming region. The X-ray peak at its center together with its X-ray luminosities of  $L_{\text{SX}} = 1.3 \times 10^{40} \text{ erg s}^{-1}$  and  $L_{\text{HX}} = 2.4 \times 10^{40} \text{ erg s}^{-1}$ , which are comparable to those of the eastern galaxy, mean that this whole system likely is a triple.

The northern source does not contribute to the IRAS flux ([Díaz-Santos et al. 2010](#)), as specified in Table 3, and therefore was not analyzed. It is detected with *Chandra*, with  $\sim 9$  cts in the full 0.5–7 keV range.

[85] *IRAS F17138-1017*. This source has a rather flat spectrum in X-rays, with a flux that slightly increases toward higher energies. It meets the HR criterion for AGN selection, although no [Ne v] line is observed. Fitting with an absorbed AGN model, fixing a spectral index of 1.8, a low column density of  $N_{\text{H}} \sim 2 \times 10^{22} \text{ cm}^{-2}$  is obtained.

Morphologically, *Chandra* data show a soft X-ray deficit at the optical center of the galaxy, that could be caused by absorption. The hard X-ray image does not show a clear emission peak, but a rather homogeneous flux around a larger circular region. X-ray contours in the HST image show very prominent dust lanes close to the nucleus of the galaxy, to which the obtained column density could belong. These dust lanes are most likely absorbing an important part of the soft-band X-ray emission, and might be responsible for the hardness of the spectrum. Based on this and the clear lack of observation of a hard-band peak in the nucleus, we opt not to classify this source as an AGN.

[Ricci et al. \(2017\)](#) fit a combined *Chandra* and *NuSTAR* spectrum with a simple power-law model, obtaining a photon index of  $\sim 1.1$ , which is harder than the typical X-ray emission expected of a star-forming region, but still consistent with this hypothesis.

The hard-band X-ray luminosity of  $L_{\text{HX}} \sim 1.8 \times 10^{41} \text{ erg s}^{-1}$  we derive is high, but not incompatible with being caused by a

strong starburst, as this source falls within the uncertainties of the correlation derived by [Ranalli et al. \(2003\)](#).

[95] *ESO 440–IG058*. Both galaxies, with an angular separation of  $\sim 2'$ , contribute to the IRAS flux in this source, although the southern component dominates at almost  $\sim 90\%$  ([Díaz-Santos et al. 2010](#)). Soft X-ray emission from the southern component is extended. This is most likely an outflow with its origin in a starburst wind.

[100] *NGC 7130*. This galaxy shows clear extended emission in soft X-rays around a strong peak that follows the disk of the face-on optical galaxy, tracing the spiral arms. The spectrum shows a hard excess due to absorption and an iron 6.4 keV line at high energies, which could be due to absorption in the soft band, or due to reflection. A reflection component fitting, using a *pexrav* model ([Magdziarz & Zdziarski 1995](#)) results in an iron line with an equivalent width of  $\sim 0.6$  keV, which is too low for a reflection-originated line. Therefore, our data favor an absorption model, which, when a photon index of 1.8 is imposed, results in a column density of  $N_{\text{H}} = 3 \times 10^{23} \text{ cm}^{-2}$  and an iron line equivalent width of 0.8 keV, that is detected with a significance of  $\sim 2.5\sigma$ .

Based only on the *Chandra* data, we find it difficult to distinguish between this scenario and a Compton-thick source with an imposed photon index of  $\Gamma = 0.0$ , as modeled by [Levenson et al. \(2005\)](#). [Ricci et al. \(2017\)](#) confirmed the Compton-thick AGN using a combined analysis with *NuSTAR* data.

[104] *NGC 7771*. This galaxy is part of an interacting quartet of galaxies, along with close companion *NGC 7770* at an angular distance of  $\sim 1.1'$ , *NGC 7771A* at  $\sim 2.8'$ , and *NGC 7769* at  $\sim 5.4'$  (e.g., [Yeghiazaryan et al. 2016](#)).

About 90% of the IRAS flux originates in *NGC 7771*, with *NGC 7770* being responsible for the remaining  $\sim 10\%$  and *NGC 7769* being resolved as a separate source by IRAS. *NGC 7771A* is faint in the IR, remaining undetected at  $8 \mu\text{m}$  and above. There is no detection for this small component in the *Chandra* data either.

Of the many point sources seen along the disk of *NGC 7771*, [Luangtip et al. \(2015\)](#) classify  $4_{-0}^{+4}$  as ULXs.

[105] *NGC 7592*. This source is a closely interacting triple system, formed by two main IR and X-ray sources (East and West) and a smaller southern source. This third source, seen in the optical SDSS images, is undetected in X-rays, and does not contribute to the IRAS flux either.

There is unresolved detection of the [Ne v] line for this triple source that meets our AGN selection criterion. However, as the western source is classified as an optical Seyfert 2, it is likely that it is the origin of the IR line. The spectrum of the western source shows an excess between 6–7 keV, originating in the nucleus, that can be fitted as a Gaussian line with an energy of  $6.7_{-0.3}^{+0.1}$  keV. The significance of this line is at the  $1\sigma$  level, and thus we did not use this hint as a selection criterion. Given the uncertainties, however, a 6.4 keV line cannot be ruled out completely, especially when combined with the continuum.

The western source presents very compact X-ray emission, as derived from its radial profile, compared to its extended IR emission (as plotted in Fig. 12).

[106] *NGC 6286*. This source interacts with *NGC 6285*,  $\sim 1.5'$  to the northwest, showing very extended tidal disruption features. Both sources contribute to the IRAS flux ([Chu et al. 2017](#)).

The X-ray spectrum of *NGC 6286* shows hard excess emission above 5 keV. With fewer than 20 cts in the 5–8 keV range, the excess is difficult to fit as an absorbed AGN using only *Chandra* data. MIR studies find possible hints of an AGN (e.g., [Vega et al. 2008](#); [Dudik et al. 2009](#)), which are confirmed by hard X-ray *NuSTAR* observations. [Ricci et al. \(2016\)](#) found compelling evidence

of a Compton-thick, low-luminosity AGN ( $N_{\text{H}} \simeq (0.95–1.32) \times 10^{24} \text{ cm}^{-2}$ ). We thus classify this source as an AGN.

This galaxy shows a very extended soft X-ray emission, spreading perpendicular to the optical edge-on disk up to a distance of  $\sim 5–7$  kpc, depending on the direction. A super-wind outflow generated by a strong starburst has been suggested by [Shalyapina et al. \(2004\)](#) through detection of an increase of  $[\text{NII}]\lambda 6583/H_{\alpha}$  ratios, and an emission nebula extending up to  $\sim 9$  kpc from the galactic plane.

[107] *NGC 4922*. This system contains two galaxies, separated by distance of  $\sim 0.4'$ ; the northern source is brighter in both X-rays and IR ([Díaz-Santos et al. 2010](#)). The southern source contributes  $\sim 1\%$  of the IRAS flux, and therefore its analysis is not included in this work. With only  $\sim 40$  cts, all in the 0.4–2 keV range, it is also a weak X-ray source. Another source (*2MASX J13012200+2920231*) lies  $\sim 1.7'$  to the north, which is undetected at  $8 \mu\text{m}$  and above, and most likely does not contribute to the IRAS flux.

The northern source is selected as an AGN through the [Ne v] line, and the pair (unresolved) is also classified as a Seyfert 2 in [Yuan et al. \(2010\)](#). Our X-ray analysis also classifies it as an absorbed AGN, with a column density of  $N_{\text{H}} \sim 3 \times 10^{23} \text{ cm}^{-2}$  when the photon index is fixed to 1.8. An iron 6.4 keV line is faintly visible, although only at a significance of about  $1\sigma$ .

[Ricci et al. \(2017\)](#) analyzed *NuSTAR* observations and based on their similar *Chandra* results concluded that the source detected at high energies must correspond to *NGC 4922* (N), because the companion is not detected in the 2–7 keV range. They detected a prominent Fe K $\alpha$  line at  $6.48_{-0.07}^{+0.07}$  keV, and found that the source is Compton-thick, with  $N_{\text{H}} \geq 4.27 \times 10^{24} \text{ cm}^{-2}$ ; this is more than one order of magnitude higher than our best *Chandra* fit.

[110] *NGC 3110*. This source interacts with nearby galaxy *MCG–01–26–013* at its southwest, separated by  $\sim 1.8'$ , which is not detected in X-rays in the *Chandra* data. Both sources contribute to the IRAS flux, although  $\sim 90\%$  of the IR emission has its origin in *NGC 3110* ([Díaz-Santos et al. 2010](#)). The companion galaxy is not analyzed because it has no significant X-ray emission and low IR luminosity, although the IRAS flux associated with *NGC 3110* is corrected for the pair's contribution.

This source has diffuse soft X-ray emission along the spiral arms, which also contain strong hard X-ray peaks that are most likely associated with star-forming knots. The nucleus of the galaxy, however, does not show peaked emission in the 2–7 keV band. Because of this particular morphology, HST optical and IRAC channel 1 images were used to center the derived radial profiles.

[114] *NGC 0232*. This source is paired with *NGC 0235*, at a distance of  $\sim 2'$ , which is a known Seyfert 2 galaxy. Despite having previously been classified as non-interacting, a faint tidal bridge has been observed to connect the two galaxies ([Dopita et al. 2002](#)). *NGC 0235* has two nuclei and is classified as a minor interaction ([Larson et al. 2016](#)). However, as this companion galaxy is resolved by IRAS ([Surace et al. 2004](#)) as an individual source, we did not include it in our analysis.

[117] *MCG+08–18–013*. This galaxy is paired with *MCG+08–18–012* at  $\sim 1'$  to its west. *MCG+08–18–013* is clearly dominant in the IR and the origin of the IRAS flux ([Chu et al. 2017](#)). This component's X-ray emission originates from two point sources close to the nucleus of the galaxy, one of which is bright in soft-band X-rays, and could be associated with a star-forming region, and the other in hard-band X-rays. We consider this hard-band peak to originate from the nucleus of the galaxy, and used it to center the radial profiles.

*MCG+08–18–013* is undetected in X-rays and therefore not included in the analysis.

[120] *CGCG 049–057*. This source, despite only having a total of  $\sim 30$  cts in the 0.5–7 keV band of the available *Chandra* observation, has a hardness ratio of  $HR = -0.04 \pm 0.09$ , and so meets one of the X-ray AGN selection criteria. The spectrum of the source shows, despite the large error bars, a tendency to rising flux toward higher energies. The X-ray image in the 2–7 keV band shows about  $\sim 5$  cts originating from the innermost region of the source, and thus we classified it as an AGN.

Baan & Klöckner (2006) also classified it as an AGN based on radio observations. Although optical and MIR observations (e.g., Veilleux et al. 1995; Stierwalt et al. 2013; Meléndez et al. 2014) classified it as a starburst, *Herschel* spectroscopic data analyzed by Falstad et al. (2015) showed very high column densities in the nucleus ( $N_{\text{H}} = 0.3\text{--}1.0 \times 10^{25} \text{ cm}^{-2}$ ), meaning that a Compton-thick AGN could be present. This would explain the X-ray weakness we observe, which has previously been reported by Lehmer et al. (2010).

[121] *NGC 1068*. This well-known AGN meets our selection criteria in all bands: Seyfert 2 in both of the used optical classifications, presence of the [Ne v] line in IR, and clear detection of the Fe K $\alpha$  line at 6.4 keV in X-rays with a significance of  $\sim 3.6\sigma$ . The equivalent width of the 6.2  $\mu\text{m}$  PAH feature is not presented in Stierwalt et al. (2013) because the spectrograph was saturated. Howell et al. (2007) analyzed PAH and warm dust emission in NGC 1068 in detail. Their 6.2  $\mu\text{m}$  images are saturated within the inner  $r \sim 500$  pc, although they measure an equivalent width of the PAH feature immediately outside the region of saturation of  $\sim 0.1$ . This suggests that the value of the equivalent width might drop below 0.1 farther in.

Diffuse X-ray emission is clearly observed in this source, following the optical spiral arms and star-forming regions. In order to outline all features, X-ray contours to a low enough level were necessary, which also resulted in the clear contours around the saturated feature that diagonally crosses the image.

Individual point sources can be seen spread throughout the galaxy disk in the soft and hard bands; they most likely correspond to X-ray binaries. We note that we did not mark them as hard X-ray peaks in the image in Appendix B because they are numerous and clearly do not originate from a region near the nucleus of the galaxy. None of these point sources were removed in order to derive radial profiles. Luangtip et al. (2015) classified three of them as ULXs.

[123] *UGC 02238*. This source presents a rather diffuse emission, showing three main X-ray peaks near the nucleus, only one of which (the westernmost) is also peaked in the 2–7 keV band. However, as shown by the contours over the IRAC channel 1 image, this region is outside of the galaxy nucleus. We consider this emission to most likely originate from different intense starburst regions because no clear hard-band central peak is visible. Optical and IR imaging data show a highly disturbed disk and tidal tails, and classify this galaxy as a post-merger stage (e.g., Smith et al. 1996; Larson et al. 2016), which is consistent with the described X-ray morphology.

We fit the overall X-ray 0.5–7 keV emission of this galaxy with a single power-law. Attempts to fit a one or two component *mekal* model produced unsatisfactory results. Two strong point sources can be seen in the 2–7 keV band image presented in Appendix B, which, if associated with the galaxy, would be classified as ULXs. The point-source at the easternmost edge of the disk of the galaxy would have an estimated luminosity of  $\sim 4 \times 10^{40} \text{ erg s}^{-1}$ , and the strong point-source immediately south of the nucleus of the galaxy would be emitting  $\sim 1 \times 10^{40} \text{ erg s}^{-1}$  in the 2–10 keV range. However, the very low number of counts means that these are very rough estimates.

[127] *MCG-03-34-064*. This source has a northeastern companion at  $\sim 1.8'$ , MCG-03-34-063, which is responsible for about  $\sim 25\%$  of the IRAS flux (Chu et al. 2017). The analysis of this companion source is not included in this work because it is undetected in the *Chandra* data. A correction to the IR luminosity for the contribution of MCG-02-34-063 has been considered for this source.

MCG-03-34-064 presents a very peaked central emission in all X-ray bands and is a clear absorbed AGN, as seen from the spectrum. Fitting with a fixed photon index of 1.8 yields an absorbing column density of  $N_{\text{H}} \sim 5 \times 10^{23} \text{ cm}^{-2}$ . The iron K $\alpha$  line at 6.4 keV is detected, with a  $\sim 3\sigma$  significance. With an  $HR = -0.32 \pm 0.01$  our other X-ray AGN selection criterion is almost also met.

Ricci et al. (2017) performed a *NuSTAR* analysis of this source, combined with *XMM-Newton* EPIC data, and derived an absorbing column density of  $N_{\text{H}} = 5.42^{+0.07}_{-0.09} \times 10^{23} \text{ cm}^{-2}$ , which is compatible with our derived result within the errors. They also detected the Fe K $\alpha$  line and a Gaussian line at  $6.62^{+0.01}_{-0.01}$  keV with  $EW \sim 0.2$  keV, that is not detected in the *Chandra* data.

This source also meets the [Ne v] line and 6.2  $\mu\text{m}$  PAH feature AGN selection criteria. Yuan et al. (2010) classified it as a star-forming galaxy, although other works classified it as a Seyfert galaxy (e.g. Lipovetsky et al. 1988; Corbett et al. 2002). [134] *ESO 350-IG038*. This galaxy presents three main star-forming condensations (Kunth et al. 2003; Atek et al. 2008). Only two of these knots, the eastern and western, are clearly resolved as X-ray sources in the *Chandra* data, both presenting peaked emission in the soft and hard bands. The region is surrounded by diffuse, soft X-ray emission. These knots, separated by  $\sim 4''$ , are analyzed together as the X-ray source corresponding to the IRAS source, and not separated as two individual galaxies, as there is no clear evidence of them being individual galaxy nuclei in a state of a closely interacting merger.

[136] *MCG-01-60-022*. This source is near galaxies MCG-01-60-021 and Mrk 0399, at  $\sim 4.4'$  interacting with the former (e.g., Dopita et al. 2002), connected through thin and long tidal bridges. The two nearby galaxies are undetected in the *Chandra* data, and are detected together as another IRAS source, resolved from MCG-01-60-022 (Díaz-Santos et al. 2010).

This source presents diffuse soft-band emission that surrounds the central X-ray peak, which has its origin in an absorbed AGN. This source meets the HR X-ray criterion, and spectral fitting of an absorbed power-law with a fixed photon index of 1.8 yields an absorbing column density of  $N_{\text{H}} \sim 1 \times 10^{23} \text{ cm}^{-2}$ .

[141] *IC 0563/4*. This source is a double system, composed of IC 0564 in the north and IC 0563 in the south, separated by  $\sim 1.6'$ . Both contribute similarly to the IRAS flux and to the overall X-ray luminosity. Morphologically, the two galaxies have faint emission that originates in the nucleus and various point-sources spread throughout the spiral disks.

IC 0563 has a hardness ratio of  $-0.34 \pm 0.05$ , which exceeds our AGN selection threshold. However, the origin of the hardness (also seen as an excess at 3–5 keV in the spectrum shown in Fig. C.1) is not the nucleus of the galaxy, but a point-source located north of it. If the source is associated with the galaxy, with a roughly estimated luminosity of  $\sim 3 \times 10^{40} \text{ erg s}^{-1}$ , it could be classified as a ULX. Interestingly, the point-source spectrum shows a faint line at  $\sim 1.50 \pm 0.03$  keV, with a significance of  $\sim 2\sigma$ . If this source is a ULX within the galaxy, this excess cannot be easily explained as an emission line. If this source is a background quasar for which we detect a redshifted 6.4 keV iron line, a high  $z \sim 3.3$  would be necessary. If it were an object at  $z = 3.3$ , the X-ray spectrum would suggest that its origin is in

reflected light from a Compton-thick AGN. This scenario, however, leads to an unreasonably luminous quasar.

Similarly, IC 0564 shows a spectrum with a high flux at high energies, although the error bars are significant, which is also emitted by a northern point-source. With a roughly estimated luminosity of  $\sim 3 \times 10^{40}$  erg s $^{-1}$ , it might also be classified as a ULX if it is associated with the galaxy.

Both point-sources are marked with green crosses in the images shown in Appendix B.

[142] *NGC 5135*. This galaxy is classified as an optical Seyfert 2 (e.g. Yuan et al. 2010), and meets our IR [Ne v] line criterion for AGN selection (Petric et al. 2011).

It shows an excess in hard X-rays, with a Fe  $K_{\alpha}$  line at 6.4 keV with a  $\sim 2.9\sigma$  significance, which could be the result of either absorption or a reflection component. Fitting an absorbed power-law with fixed photon index of 1.8 yields an absorbing column density of  $N_{\text{H}} \sim 4 \times 10^{23}$  cm $^{-2}$ , which is not large enough to produce the equivalent width of the iron line of  $EW \sim 0.9$  keV obtained through the same model. Fitting a *pxravn* model (Magdziarz & Zdziarski 1995) with a fixed photon index of 2.0 yields a plausible  $EW \sim 1.1$  keV, which means that our data favor a reflection-dominated AGN. *Suzaku* observations extending up to 50 keV allow a better estimate of the absorbing column density,  $\sim 2.5 \times 10^{24}$  cm $^{-2}$ , classifying this source as Compton-thick and providing a good estimate of the strength of the reflection component (Singh et al. 2012).

Morphologically, this source presents a very extended soft-band emission, with two central X-ray peaks that are visible only when the smoothing in the image is set to 0.5'' or less. The northern peak is responsible for the iron emission line, which indicates that it is associated with the nucleus of the galaxy. The southern peak is brighter in the 0.5–2 keV band, and most likely associated with a star-formation region. Of the many point-sources seen in the full band image, up to  $6_{-2}^{+1}$  are classified as ULXs (Luangtip et al. 2015).

[144] *IC 0860*. With only  $\sim 25$  cts, no X-ray analysis beyond the calculation of the HR and the extraction of the radial profile has been performed for this source. However, despite the low count-rate, this galaxy is classified as an AGN with a value of  $HR = -0.29 \pm 0.17$ . The spectrum we obtained also shows a rising tendency toward higher energies. However, because of the small number of counts detected, the classification of this X-ray source remains ambiguous.

[147] *IC 5179*. This galaxy shows dim soft-band extended emission near the nucleus and many X-ray point-sources spread throughout the optical disk, which most likely correspond to X-ray binaries,  $8_{-3}^{+0}$  of which are classified as ULXs (Luangtip et al. 2015). These sources cause the radial profile to seem rather irregular, especially in hard band (see Appendix B).

[148] *CGCG 465–012*. This galaxy is paired with UGC 02894 at its northwest, at a distance of  $\sim 4.2'$ , which is resolved as a separate source by IRAS.

CGCG 465–012 shows diffuse soft X-ray emission throughout its optical disk, concentrated in the nucleus and in a northeastern region  $\sim 5''$  from it, most likely a star-forming region. The hard-band emission is very dim and not peaked.

[157] *MCG–02–33–098/9*. This system is composed of two very closely interacting galaxies (separated by  $\sim 14''$ ), with the western one contributing  $\sim 70\%$  of the IRAS flux (Díaz-Santos et al. 2010). Two nearby galaxies, at  $\sim 0.7'$  northwest and  $\sim 2'$  southeast, most likely do not contribute to the IRAS flux, as they are not detected in MIR wavelengths.

Terashima et al. (2015), using *XMM-Newton EPIC-PN* data, reported the detection of a faint iron line at 6.97 keV. The *Chan-*

*dra* spectrum of MCG–02–33–098 shows a slight increase at  $\sim 7$  keV, which is not significant enough to claim the presence of an excess.

[163] *NGC 4418*. This galaxy is paired with MCG+00–32–013 at its southeast, at a distance of  $\sim 3'$ . Using IR photometry, it can be determined that more than 99% of the IRAS flux originates in NGC 4418 (Chu et al. 2017), therefore this nearby galaxy was not considered in the analysis. It also meets our PAH EW selection criteria (Stierwalt et al. 2013), and thus we classified it as AGN, despite the current debate regarding its nature.

Only two central peaks can be seen in the *Chandra* data; the eastern peak is brighter in the hard band, and thus was used to center the radial profiles. However, this source is known as a possible candidate for containing a heavily obscured AGN, and it is possible that we resolved the non-absorbed emission at either side of the nucleus. While some studies in radio and IR seemed to favor a compact starburst as a central source (e.g., Roussel et al. 2003; Lahuis et al. 2007), it is at least clear that the nucleus is extremely Compton-thick and could host either an AGN or a starburst of obscuration as extreme as the one in Arp 220 (see Costagliola et al. 2013, 2015, and references therein).

[169] *ESO 343–IG013*. Both galaxies in this closely interacting merger, separated by only  $\sim 0.2'$ , contribute to the IRAS flux, with the northern component dominant in both IR (Díaz-Santos et al. 2010) and X-rays.

The X-ray emission is diffuse in the southern source and between sources. The northern source shows a bright X-ray peak in the soft and hard bands, which meets one of our AGN selection criteria, having  $HR = 0.01 \pm 0.05$ . The X-ray spectrum of this component also shows an increase in flux toward higher energies.

The radial profile of the southern source has been centered using the brightest peak in optical and IR images, which corresponds to the dimmer X-ray peak of the 0.5–7 keV image shown in Appendix B. The northern source presents very compact X-ray emission, as derived from its radial profile, compared to its extended IR emission (as plotted in Fig. 12).

[170] *NGC 2146*. This galaxy, most likely a post-merger object (Hutchings et al. 1990), shows very extended soft-band X-ray emission in the direction perpendicular to the plane of the optical disk, originating in a super-wind driven by the central starburst (see Kreckel et al. 2014). The hard-band emission is limited to the region encompassed by the galaxy disk, which presents a lack of soft-band emission. This lack is most likely a result of absorption in the plane of the galaxy. The radial profiles have been centered using the brightest peak in the NIR IRAC channel 1 image.

A detailed *Chandra* analysis of point sources in the galaxy, including seven ULXs, and the extended emission, can be found in Inui et al. (2005).

[174] *NGC 5653*. This source presents a diffuse X-ray emission along the spiral arms seen in the optical images, with a bright X-ray knot at a distance of  $\sim 15''$  from the nucleus. This knot falls on one of the spiral arms and appears very blue in optical images; it also is the strongest X-ray and IR source in the galaxy (Díaz-Santos et al. 2010). It could be argued that this source is a second galaxy, that merges with the larger NGC 5653. This source has been classified as a lopsided galaxy (Rudnick et al. 2000), which is usually assumed to be an indicator of weak tidal interaction. However, as we have no clear evidence of this and do not see a central point-source in hard X-rays, we opt to consider it a particularly active star-forming region. Luangtip et al. (2015) found  $1 \pm 1$  ULXs in this source.

The NIR IRAC channel 1 image was used to centre the radial profile, due to the difficulty of finding a clear nucleus in the X-ray data.

[178] *NGC 4194*. This source, commonly known as the Medusa, is the result of a merger with very particular tidal features, as seen in optical images. The X-ray morphology of the source is also particular, showing a very extended emission in soft X-rays, especially toward the northwest, most likely indicative of a strong starburst-driven wind. Luangtip et al. (2015) find  $1 \pm 1$  ULXs in this source, while a detailed study of all X-ray point sources was performed by Kaaret & Alonso-Herrero (2008).

[179] *NGC 7591*. This galaxy interacts with PGC 214933, at  $\sim 1.8'$  southwest; and a dimmer galaxy lying  $\sim 3.6'$  to the east is detected in HI (Kuo et al. 2008). PGC 214933 contributes  $\sim 6\%$  of the IRAS flux (Chu et al. 2017), and is undetected in the *Chandra* data.

With only  $\sim 26$  cts in the 0.5–7 keV band, no X-ray analysis beyond the calculation of the HR and the extraction of the radial profile has been performed for NGC 7591.

NGC 7591 is the only source in our sample that is optically classified as a Seyfert 2 galaxy (Yuan et al. 2010), while being classified as a LINER by Veilleux et al. (1999), and does not meet any of our AGN selection criteria. The contribution of an AGN component to the bolometric luminosity of the galaxy, as estimated by (Díaz-Santos et al. 2017), is low:  $AGN_{bol} = 0.09 \pm 0.02$ . With a flux estimation using the CIAO tool *srcflux*, the obtained luminosity of this source in the 0.5–7 keV band is  $L_X = 2.5^{+1.8}_{-1.3} \times 10^{40}$  erg s $^{-1}$ . This X-ray luminosity is low for an AGN, and only possible for this type of source if is Compton-thick. Even though we cannot rule out this possibility, we consider that a single optical classification as Seyfert 2 is not a strong enough criterion to classify this source as an AGN.

[182] *NGC 0023*. This source is paired with NGC 0026, at a distance of  $\sim 9.2'$  (Hattori et al. 2004), which is far enough to guarantee no contribution to the IRAS flux.

This source shows central extended emission surrounding the nucleus, which is not a strongly peaked hard X-ray source. The source spectrum shows a lack of emission at  $>3$  keV and a small excess at higher energies, which is not significant enough indicate an AGN. Luangtip et al. (2015) classified  $2 \pm 2$  of the galaxy's point sources as ULXs.

[188] *NGC 7552*. This source shows extended soft-band X-ray emission in the inner region of the galaxy, surrounded by numerous point-sources, which most likely correspond to X-ray binaries. Of these,  $2^{+3}_{-1}$  are classified as ULXs (Luangtip et al. 2015).

[191] *ESO 420-G013*. This source meets our IR [Ne v] line criterion for AGN selection, and shows a slight excess at around 6.4 keV, which is not significant enough in the *Chandra* data to confirm the presence of an X-ray AGN. Although Yuan et al. (2010) classified is as HII dominated, other optical classifications have previously pointed toward a Seyfert nature (e.g., Maia et al. 1996)

[194] *ESO 432-IG006*. The two galaxies in this system, separated by  $\sim 0.5'$ , contribute similarly to the IRAS flux, and have significant X-ray emission. They also present signs of an absorbed AGN. Fitting such a model, with a fixed photon index of 1.8, on the northeastern source yields an absorbing column density of  $N_H \sim 4 \times 10^{23}$  cm $^{-2}$ ; and on the south-western source it yields  $N_H \sim 1 \times 10^{23}$  cm $^{-2}$ .

[195] *NGC 1961*. Most of the X-ray emission of this source is concentrated on the nucleus, with a few point sources spread throughout the spiral arms. Another emission peak is found in a region about  $\sim 20''$  west of the nucleus. It is unclear whether this source truly overlaps with emission regions in IR images (IRAC channels 1–4, MIPS24/70), or has no counterpart.

The spectrum presented in Fig. C.1 includes the full region, and the hard X-ray excess originates in this outer source.

Therefore, we see no spectral traces of the presence of an AGN.

[196] *NGC 7752/3*. This double system is composed of NGC 7752 to the southwest and NGC 7753  $\sim 2'$  to the northeast, the latter being the dominant source in the IRAS flux (Chu et al. 2017).

X-ray emission in the northeastern source is point-like in the nucleus, with a few other point sources spread throughout the galaxy spiral arms. The X-ray best spectral fit for this source was performed using a single *mekal* component for the full spectrum, but no fit is truly satisfactory.

The southwestern source presents much more diffuse emission, with no clear central point source. The most concentrated emission in the soft band comes from a region just west of the IR nucleus of the galaxy, which is the one we used to center the radial profile. This region seems to correspond to a slight increase in IR emission in the IRAC channel 1 image, which means that it is most likely a star-forming region. (Kewley et al. 2001, 2006) used optical diagnostic diagrams to classify this source either as an AGN or the composite of AGN and starburst (Zhou et al. 2014; Pereira-Santaella et al. 2015a), although we see no X-ray signs of activity.

[198] *NGC 1365*. This very bright source meets all three of our X-ray AGN selection criteria, with  $HR = -0.19 \pm 0.00$ , an absorbing column density of  $N_H \sim 3 \times 10^{23}$  cm $^{-2}$  when fitting an absorbed AGN model with fixed photon index of 1.8, and a 6.4 keV iron  $K_\alpha$  line at a significance of  $\sim 2.9\sigma$ . This galaxy hosts a very well-known AGN, with frequent dramatic spectral variability (e.g., Risaliti et al. 2005, 2007) that is attributable to variations in the column density along the line of sight.

The *Chandra* data show bright and extended diffuse emission in soft band, spreading along the central region of the galaxy, and a strong central point source (see, e.g., Wang et al. 2009). Luangtip et al. (2015) found  $6^{+2}_{-1}$  ULXs in this galaxy. We have chosen to show only the central emission in the galaxy in Appendix B and not the open spiral arms around it, in order to better distinguish the X-ray morphology of the region of interest.

[199] *NGC 3221*. This source consists mostly of point-like sources scattered along the optical edge-on disk of the galaxy,  $6^{+0}_{-1}$  of which are classified as ULXs (Luangtip et al. 2015). The hard-band spectrum can be fit with a power law of index  $\Gamma = 0.3 \pm 0.6$ , with the nucleus being a stronger hard X-ray source than the other point sources. Even though such a flat spectrum could be indicative of an obscured AGN, fitting an absorbed power-law with a fixed photon index of 1.8 yields an absorbing column density of only  $N_H \sim 5 \times 10^{22}$  cm $^{-2}$ . We conclude that we cannot confirm the presence of an absorbed AGN, even though we cannot rule out the possibility either.

[201] *NGC 0838*. This galaxy is in a complex system. NGC 0839 is placed  $\sim 2.4'$  to the south-east, and the center of the closely interacting system formed by NGC 0833 and NGC 0835 is found at  $\sim 4'$  to its west. IRAS resolves three of these four sources; NGC 0833/0835 interact too closely to derive their fluxes separately. However, because NGC 0838 is resolved, we did not include the rest of the components of the complex system in this work.

Oda et al. (2018) analyzed 3–50 keV *NuSTAR* data of this compact group. NGC 0838 is not detected above 8 keV, showing no evidence of an obscured AGN. The conclusion that NGC 0838 is a starburst-dominated galaxy is also reached in the detailed works by O'Sullivan et al. (2014), Turner et al. (2001).

This source is very bright in X-rays and has a complex morphology of diffuse soft-band emission surrounding the nucleus, a clear example of a strong starburst wind. Of the point sources,  $2^{+1}_{-0}$  are classified as ULXs (Luangtip et al. 2015).

Appendix B: Observations

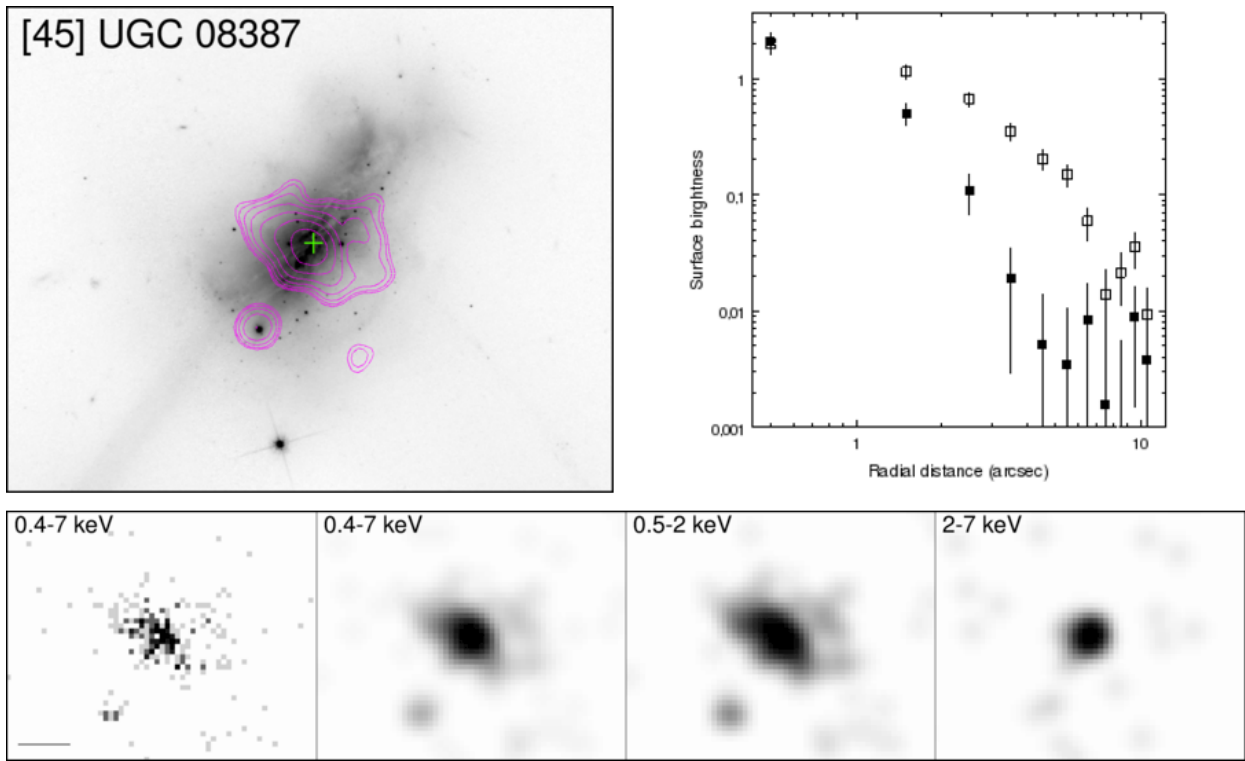


Fig. B.1. Overlay on HST-ACS F814W. Contours: Interval 1.

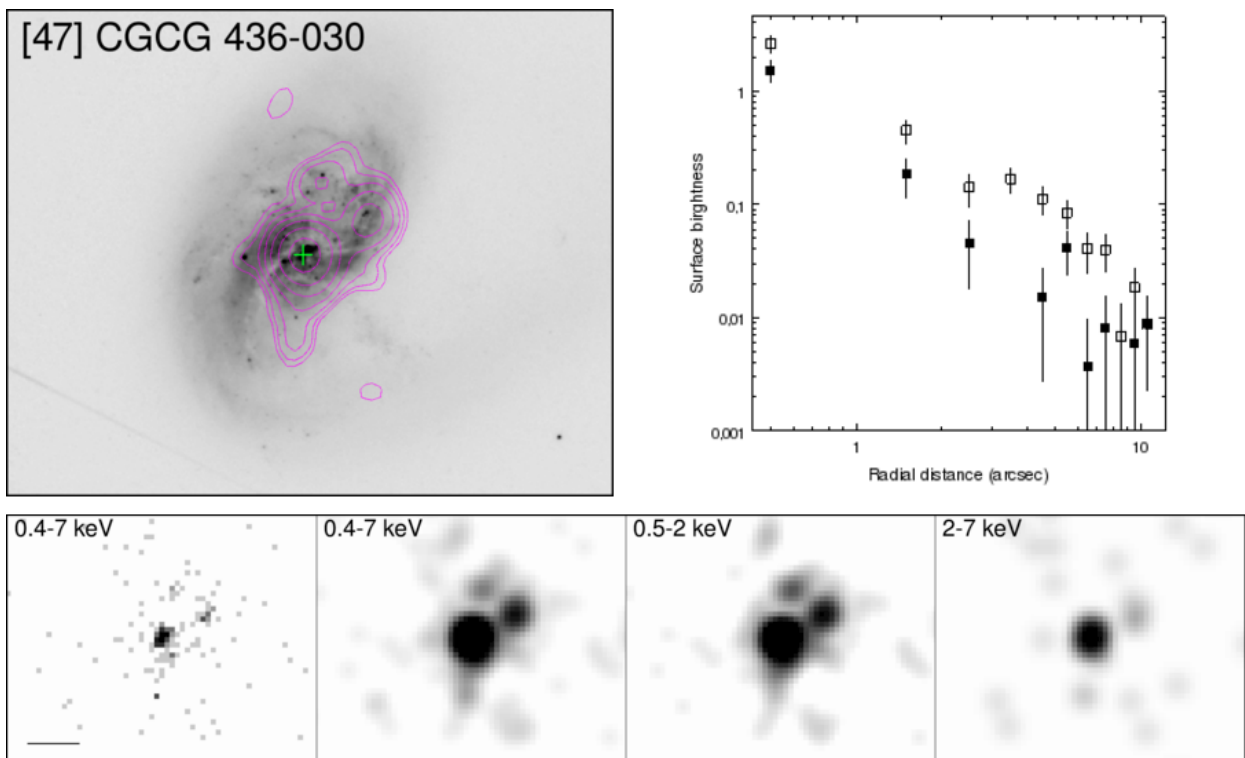


Fig. B.2. Overlay on HST-ACS F814W. Contours: Interval 1.

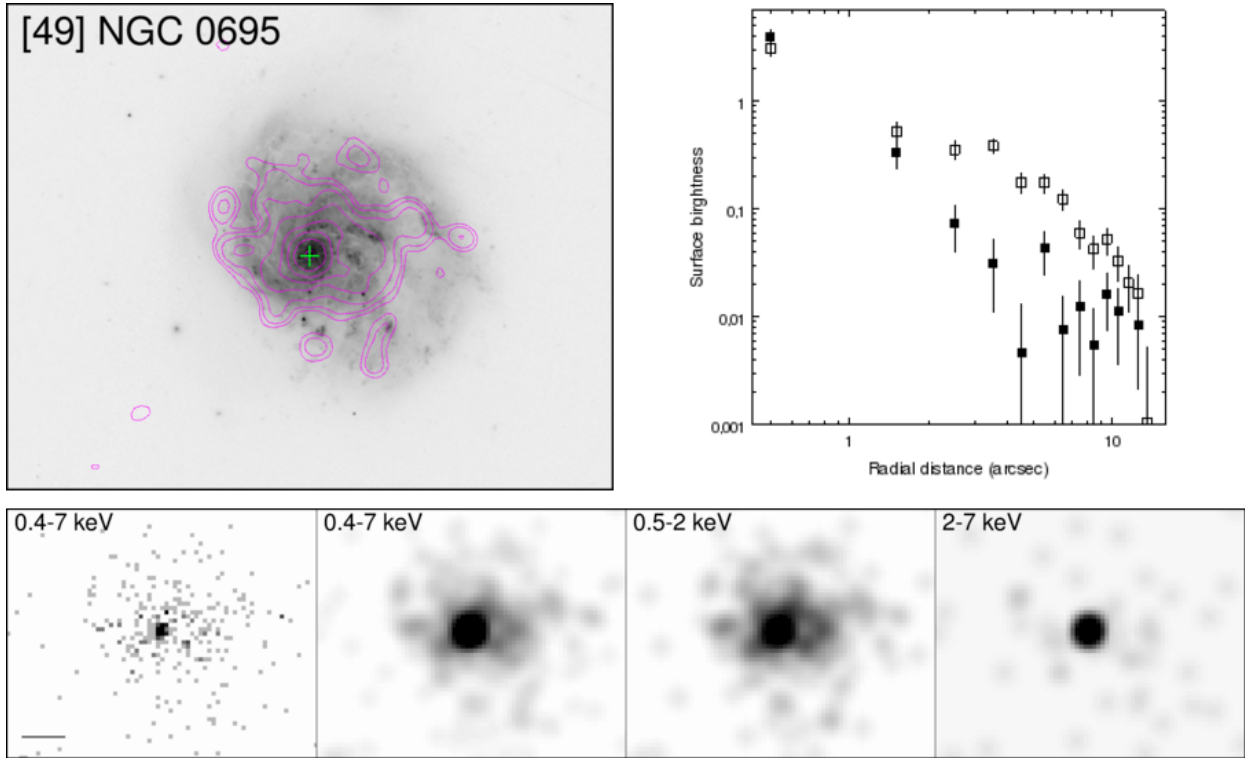


Fig. B.3. Overlay on HST-ACS F814W. Contours: Interval 1.

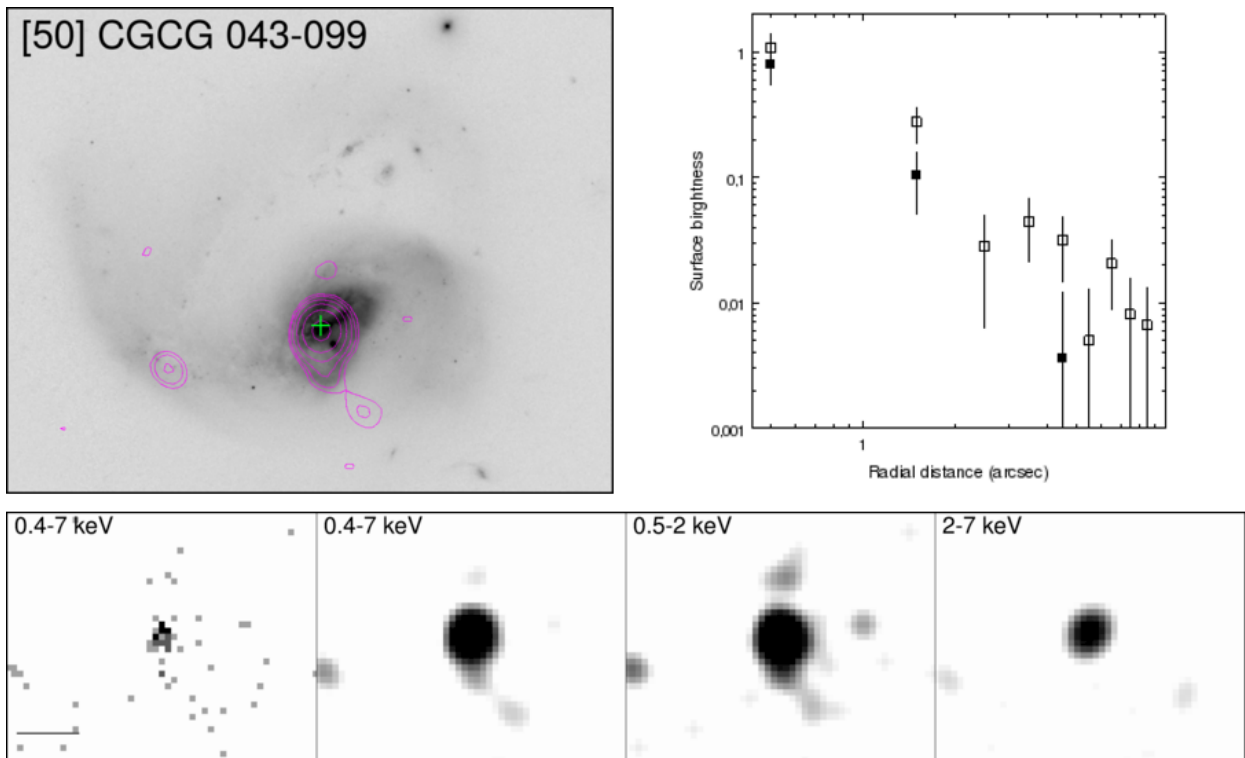
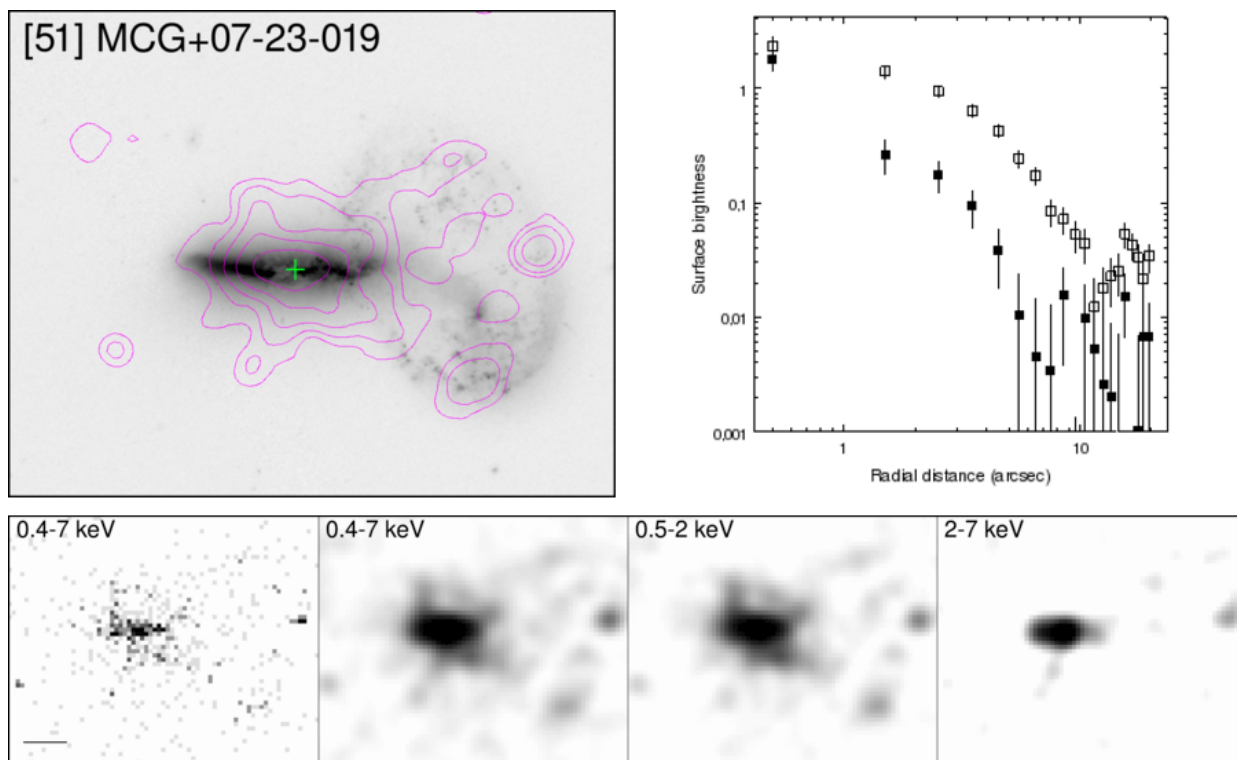
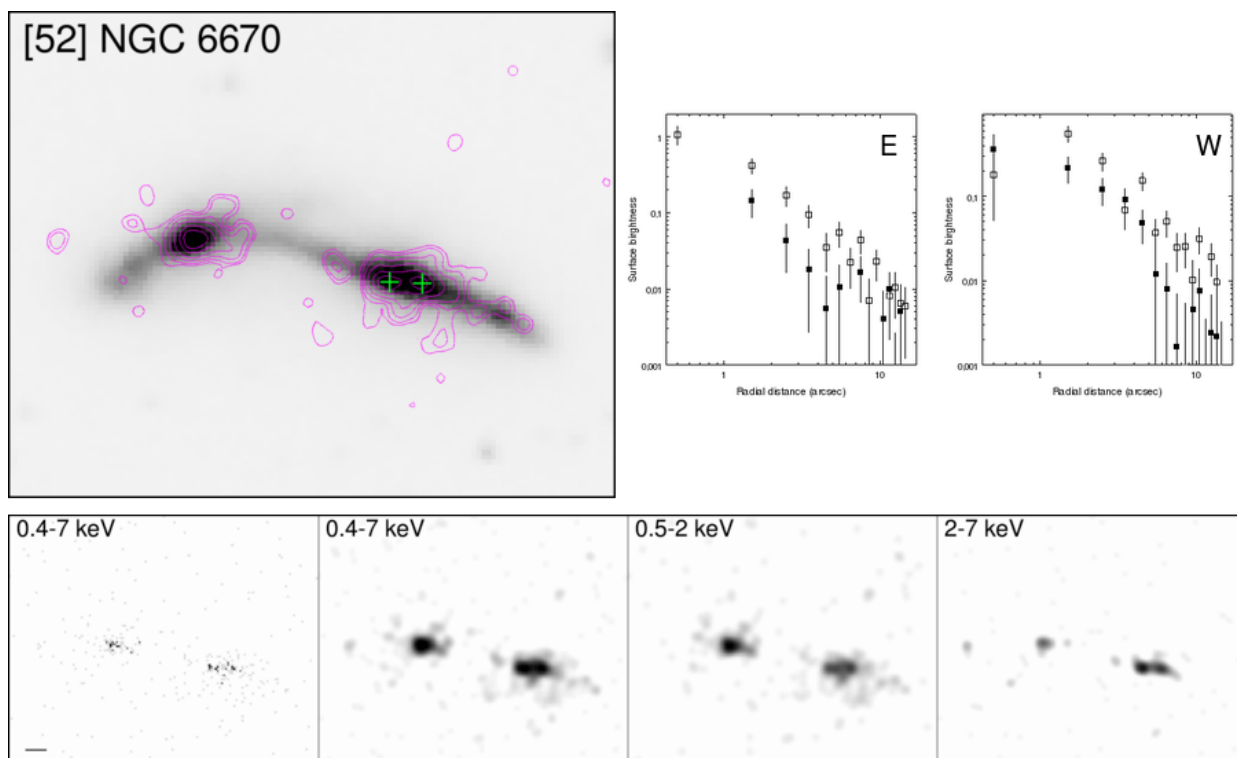


Fig. B.4. Overlay on HST-ACS F814W. Contours: Interval 1.



**Fig. B.5.** *Overlay on HST-ACS F814W. Contours: Interval 3.*



**Fig. B.6.** *Overlay on HST-ACS F814W. Contours: Interval 1.*

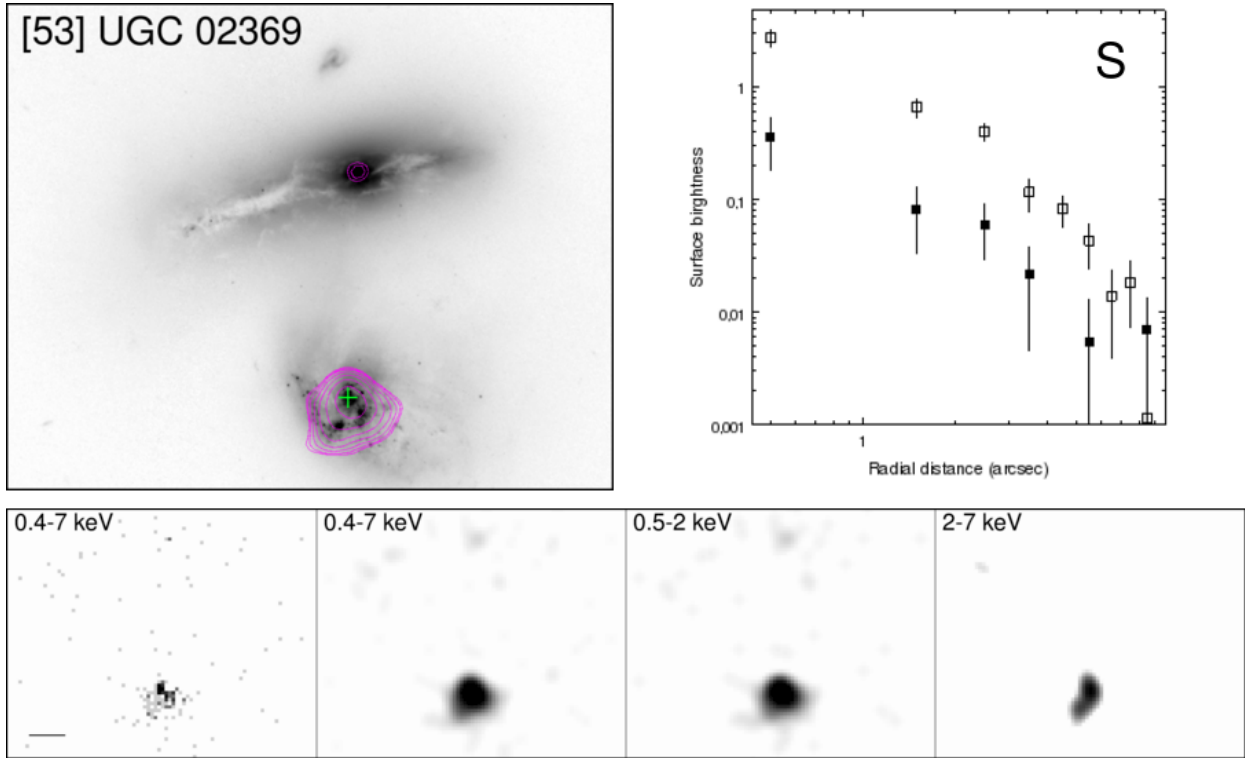


Fig. B.7. Overlay on HST-ACS F814W. Contours: Interval 4.

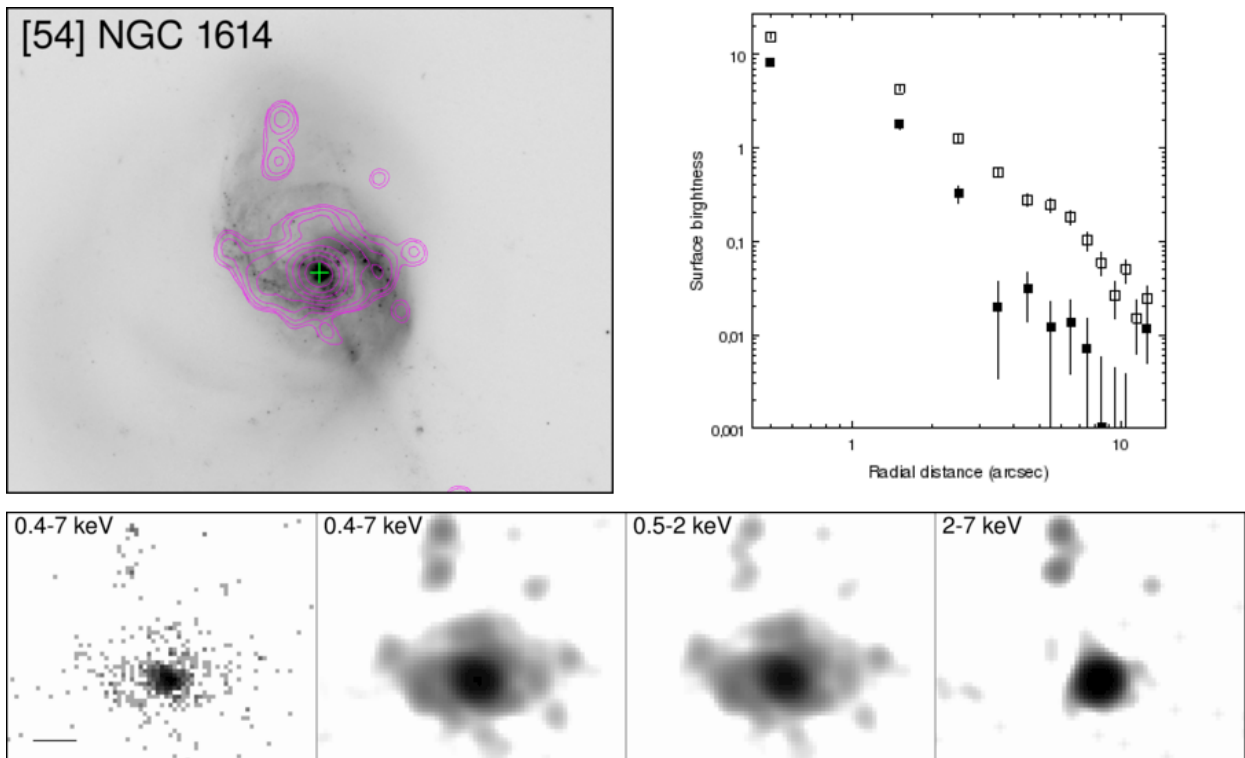


Fig. B.8. Overlay on HST-ACS F814W. Contours: Interval 1.

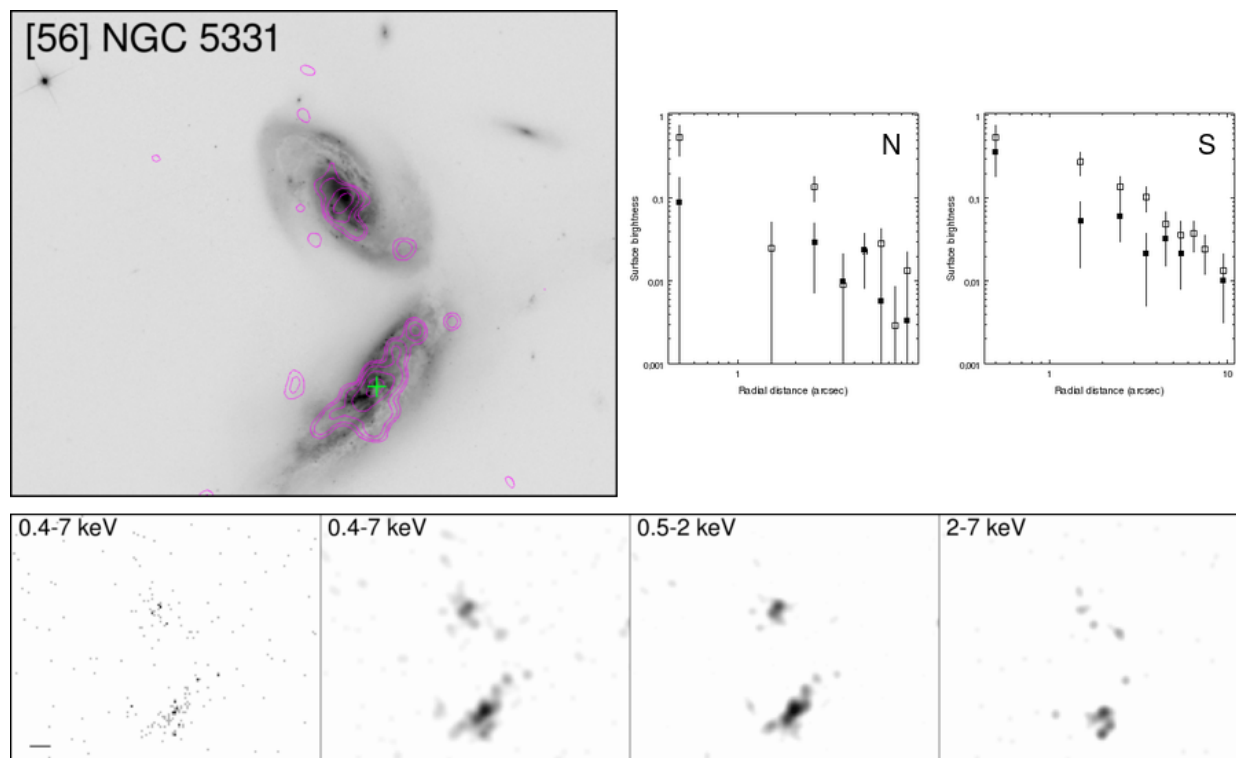


Fig. B.9. Overlay on HST-ACS F814W. Contours: Interval 2.

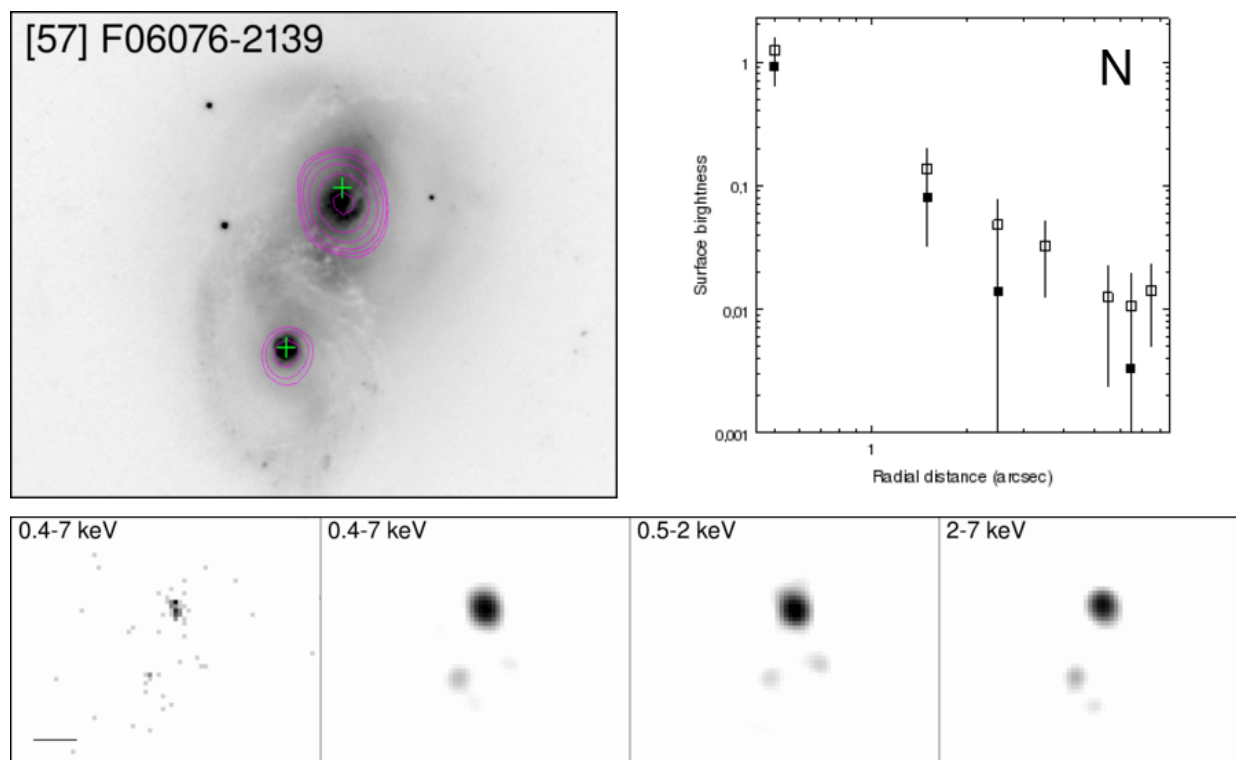
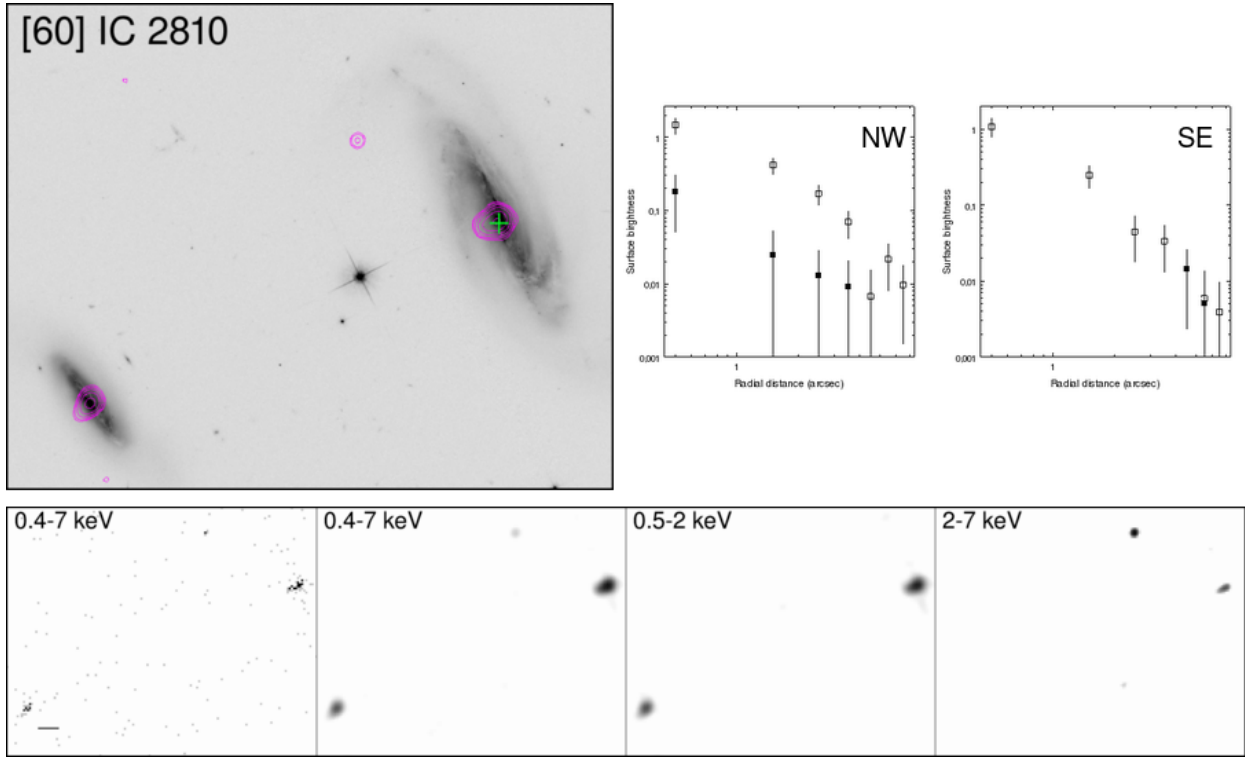
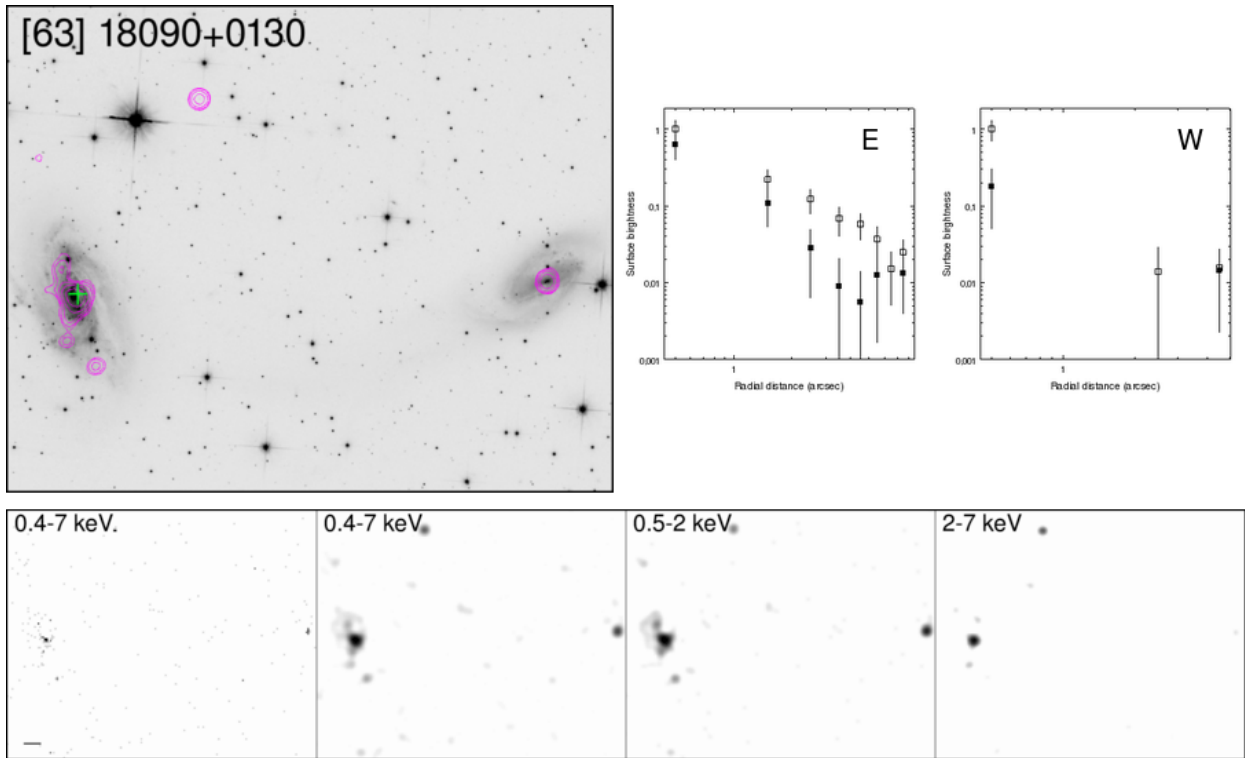


Fig. B.10. Overlay on HST-ACS F814W. Contours: Interval 1.



**Fig. B.11.** *Overlay on HST-ACS F814W. Contours: Interval 1.*



**Fig. B.12.** *Overlay on HST-ACS F814W. Contours: Interval 1.*

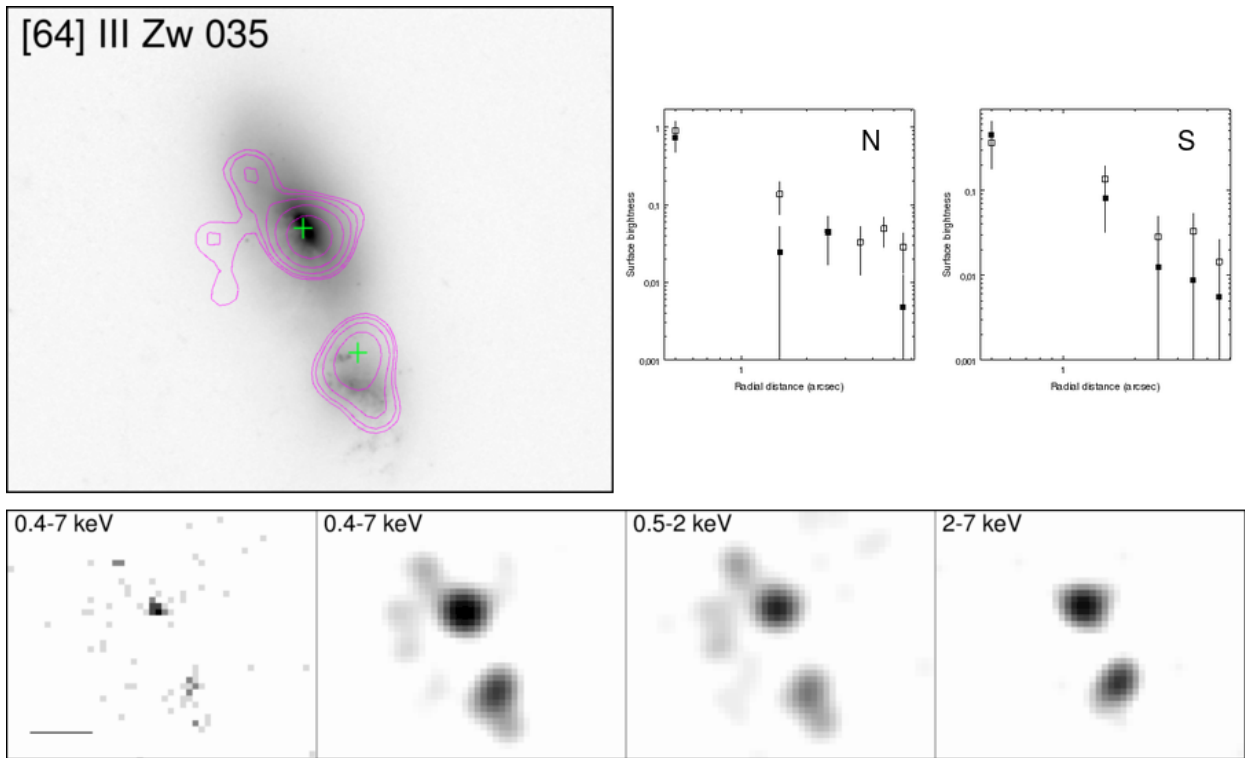


**Fig. B.13.** *Overlay on HST-ACS F814W. Contours: Interval 1.*

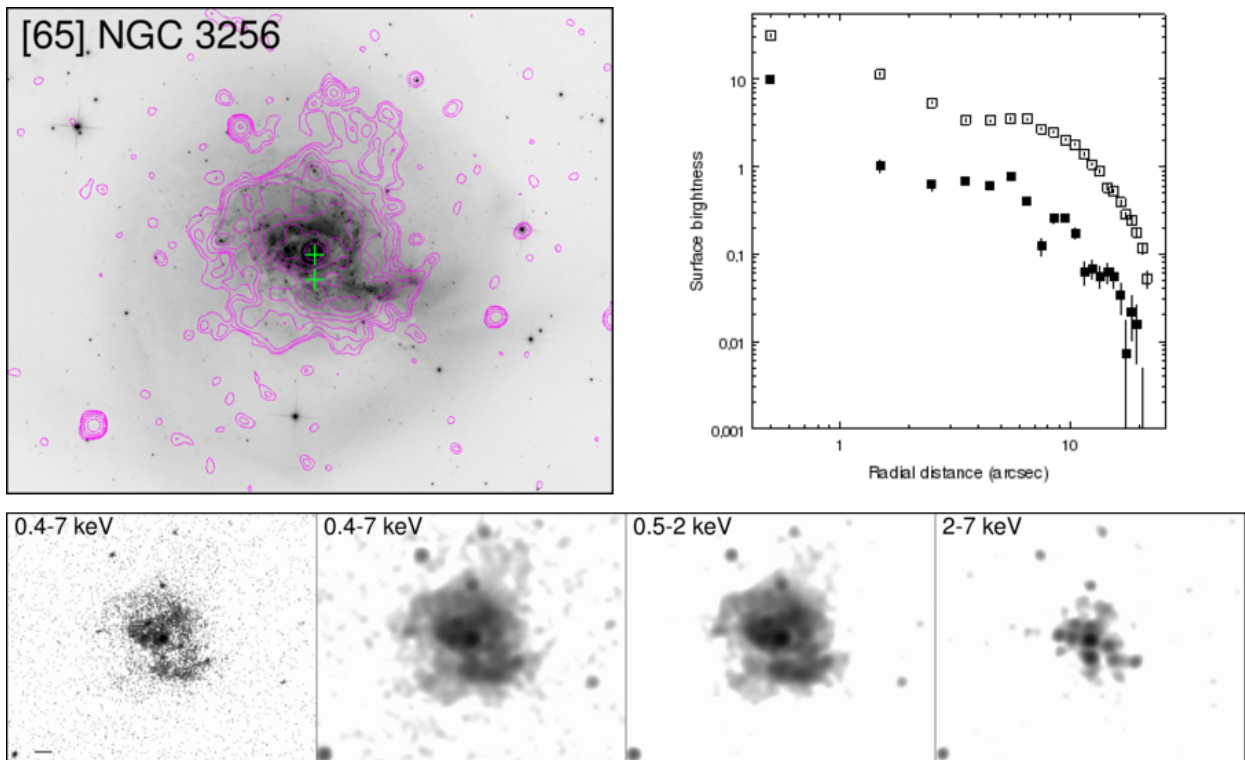


**Fig. B.14.** *Overlay on HST-ACS F814W. Contours: Interval 1.*

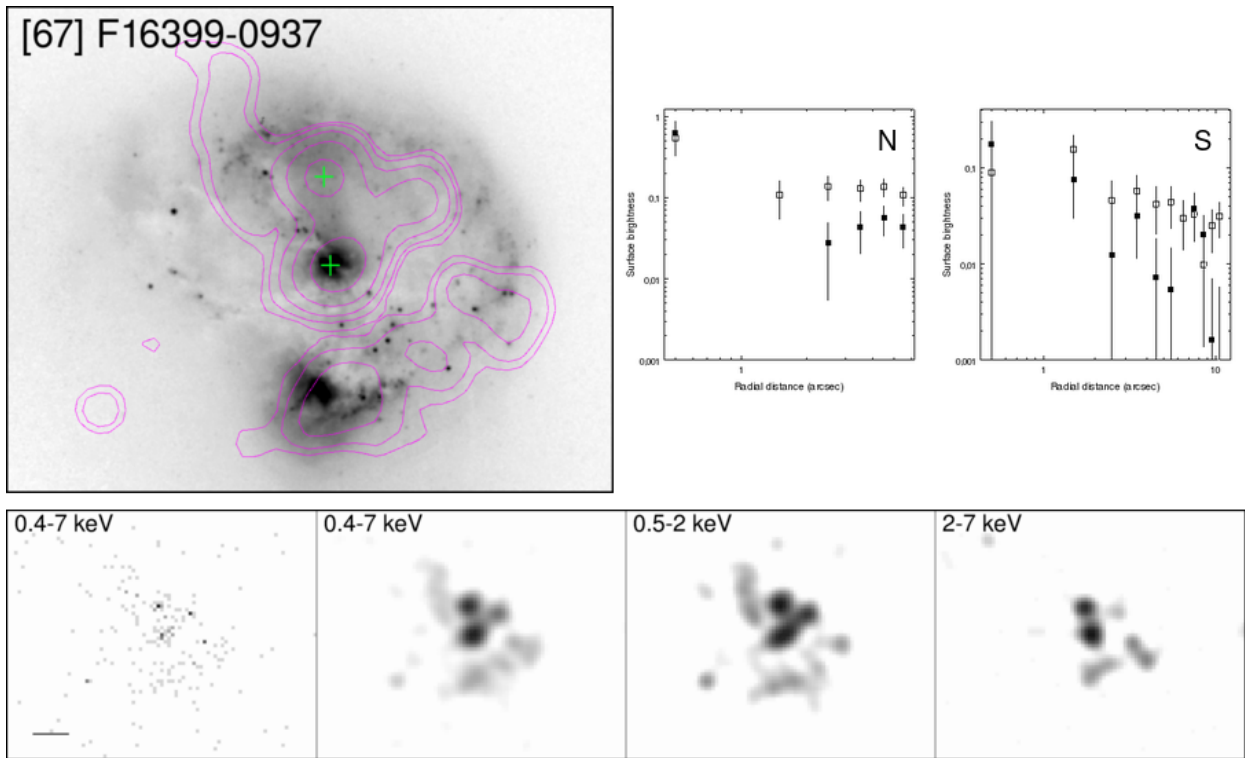


**Fig. B.15.** *Overlay on HST-ACS F814W. Contours: Interval 1.*

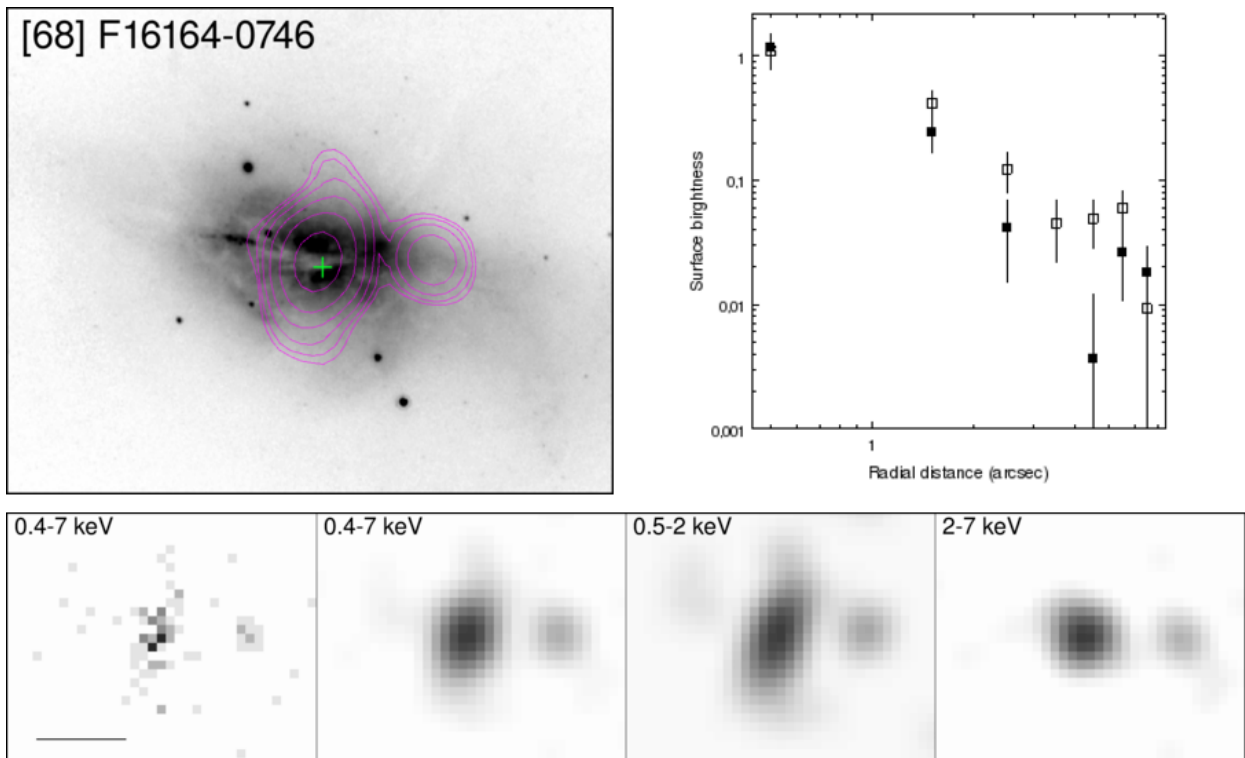


**Fig. B.16.** *Overlay on HST-ACS F814W. Contours: Interval 1.*

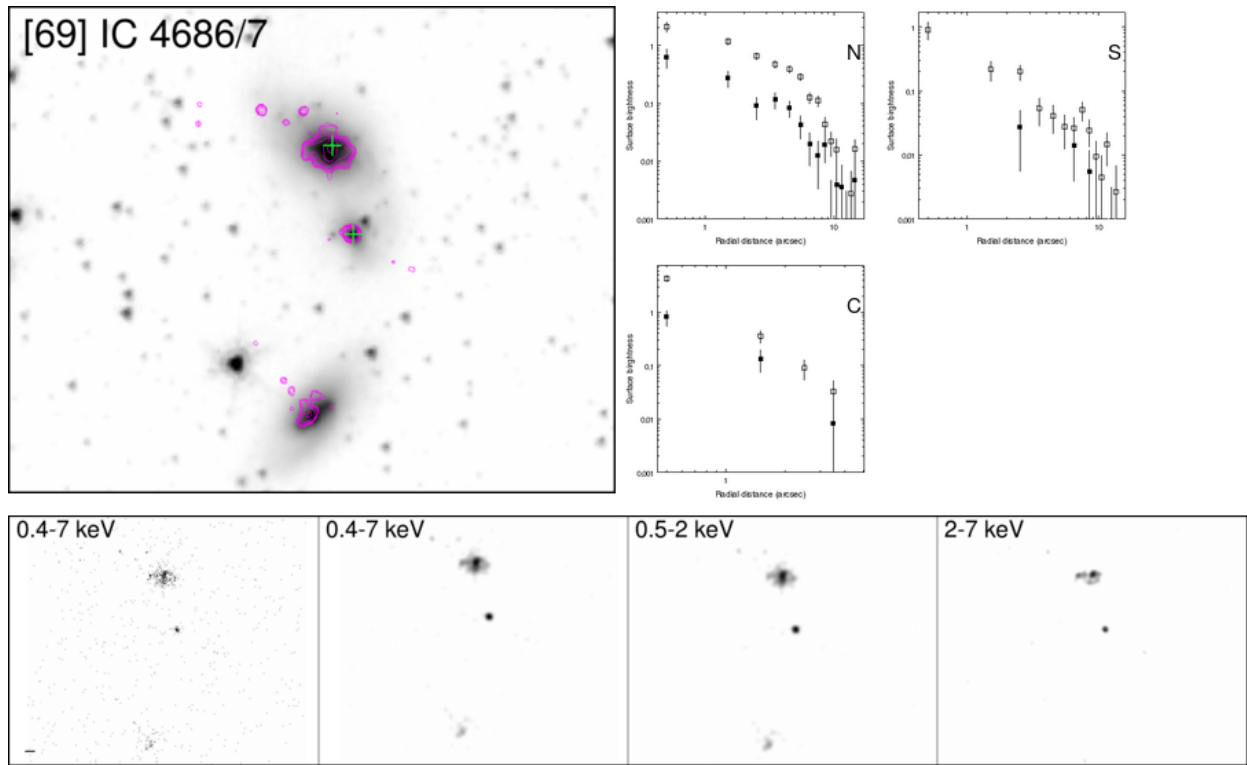


Fig. B.17. Overlay on HST-ACS F814W. Contours: Interval 1.

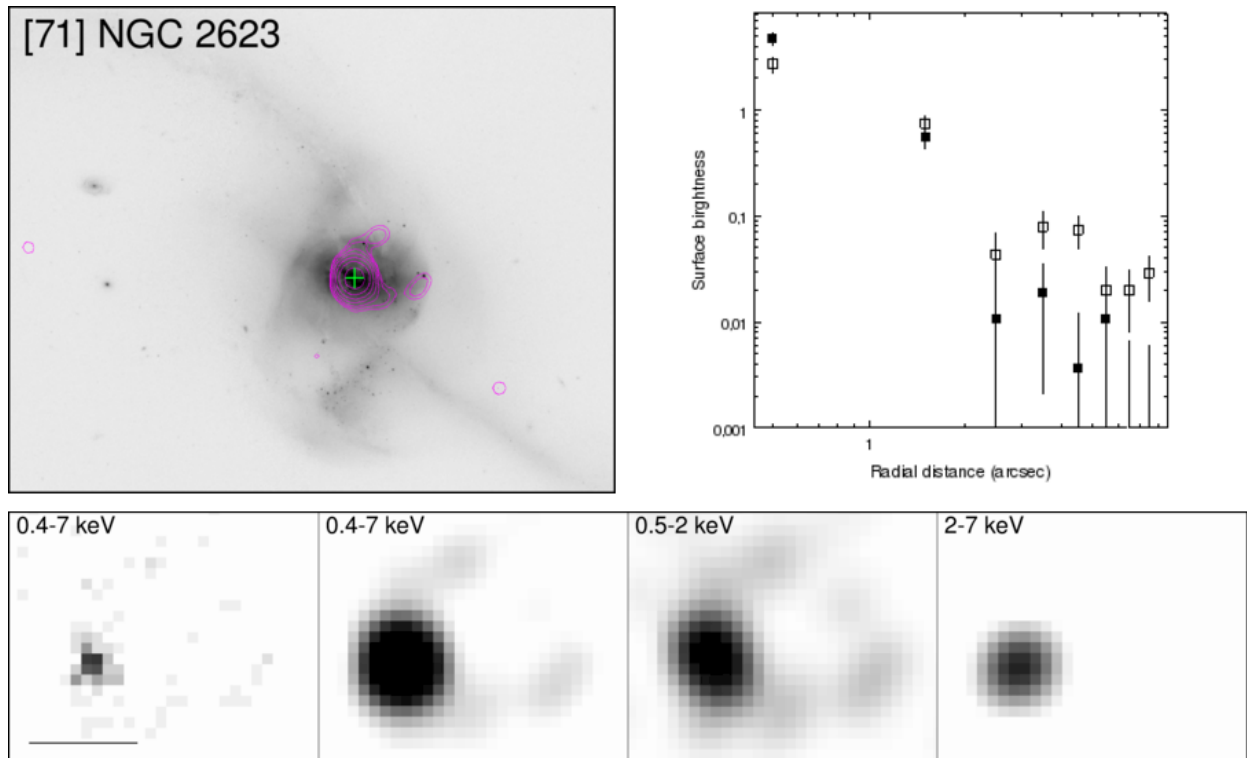
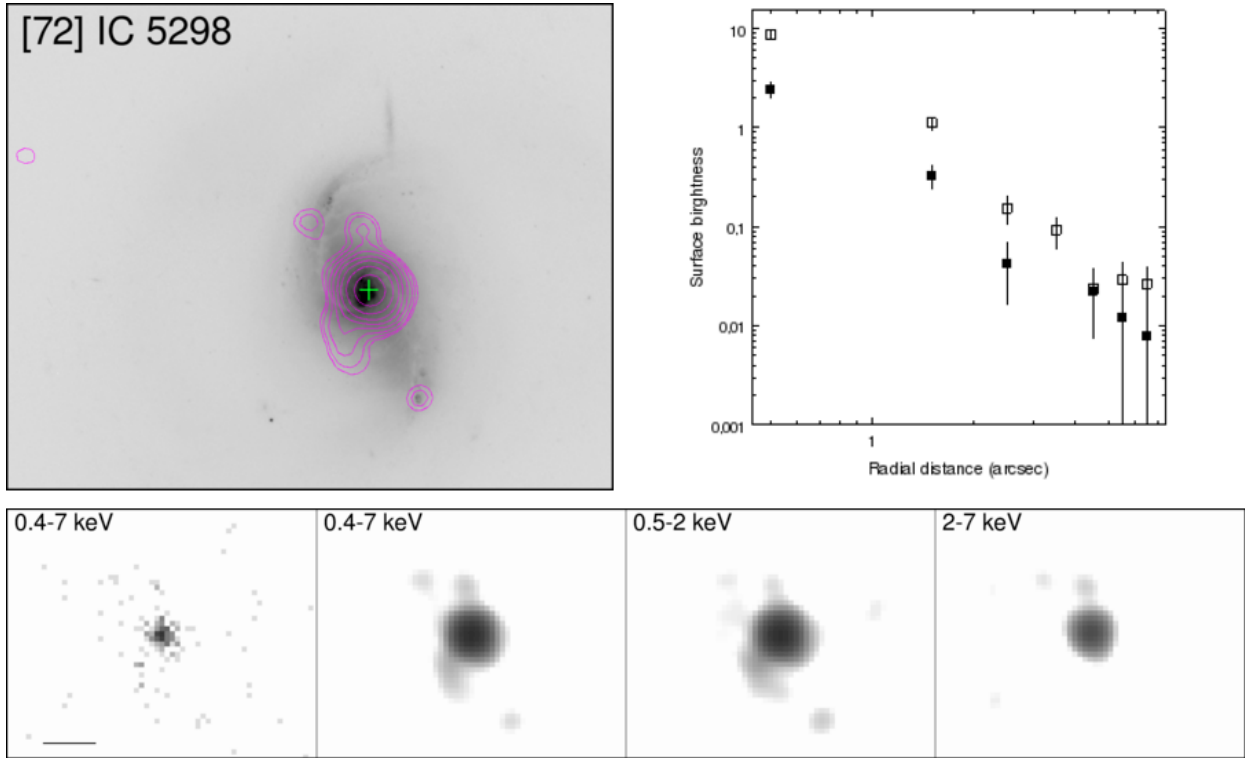
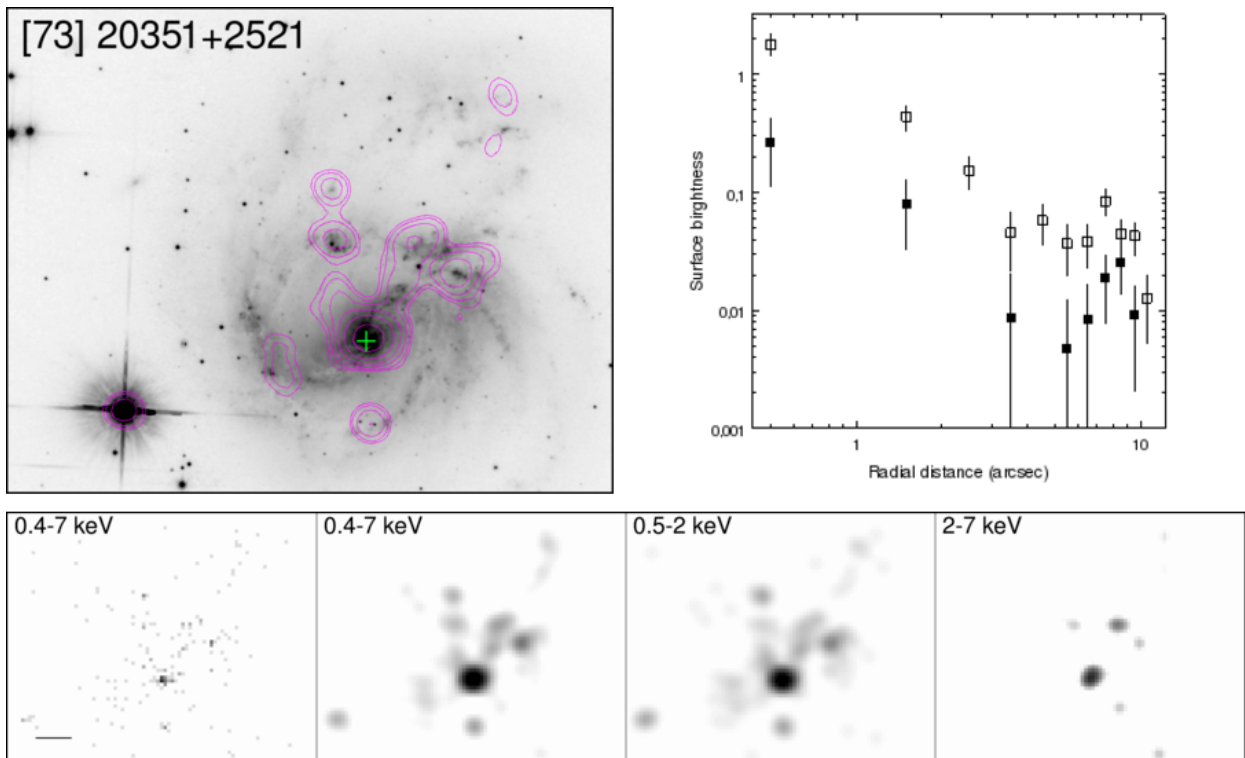


Fig. B.18. Overlay on HST-ACS F814W. Contours: Interval 1.



**Fig. B.19.** *Overlay on HST-ACS F814W. Contours: Interval 1.*



**Fig. B.20.** *Overlay on HST-ACS F814W. Contours: Interval 1.*

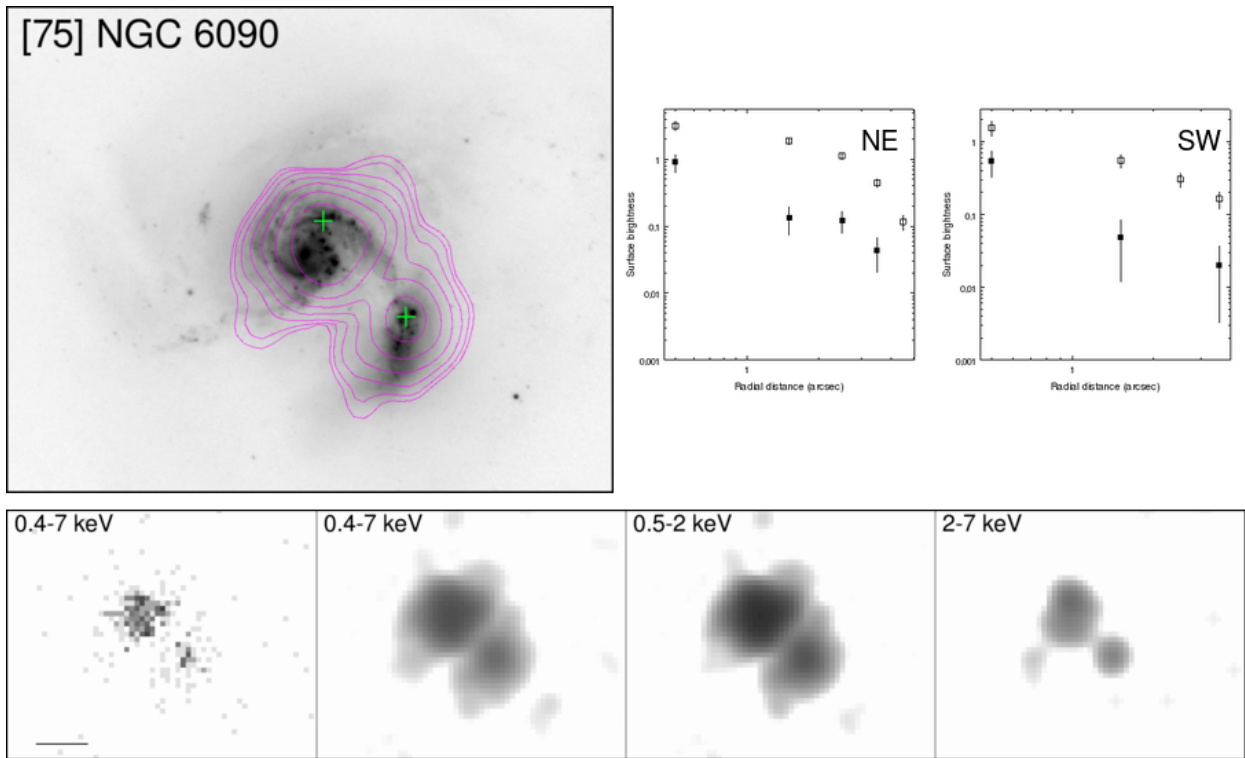


**Fig. B.21.** *Overlay on HST-ACS F814W. Contours: Interval 1.*

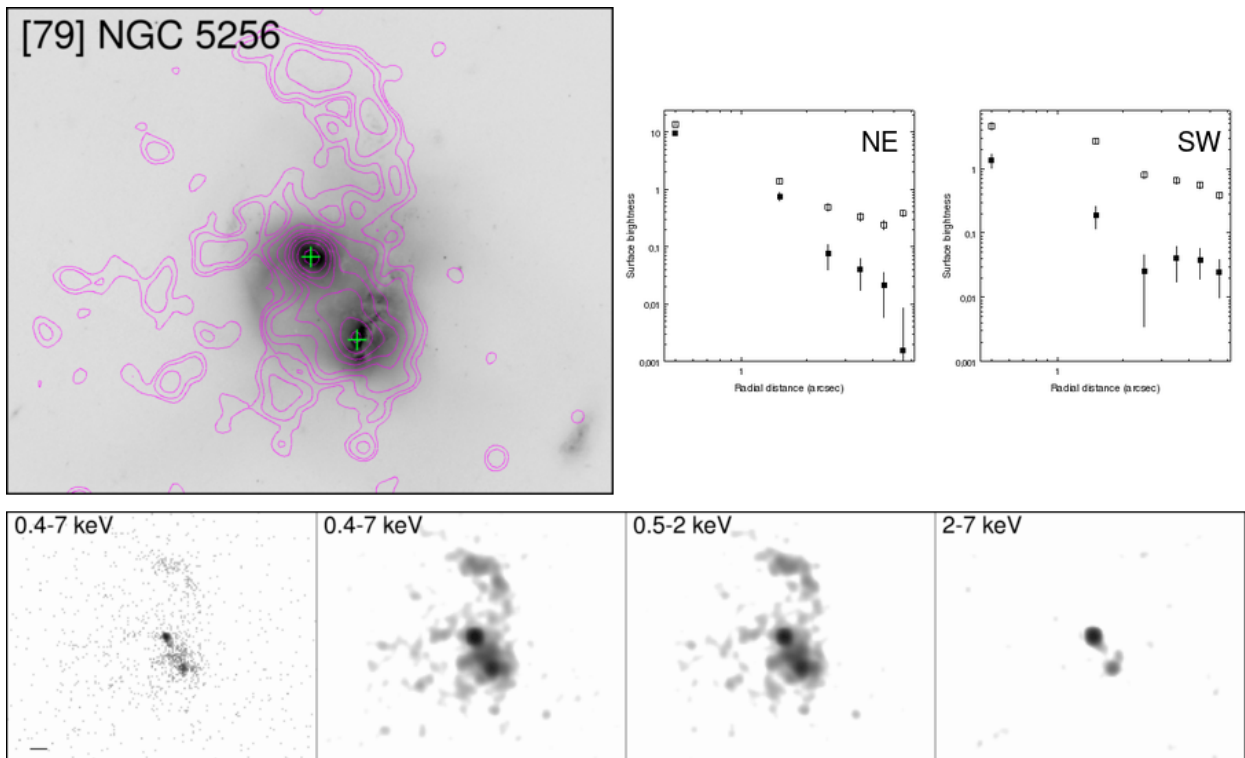


**Fig. B.22.** *Overlay on HST-ACS F814W. Contours: Interval 2.*

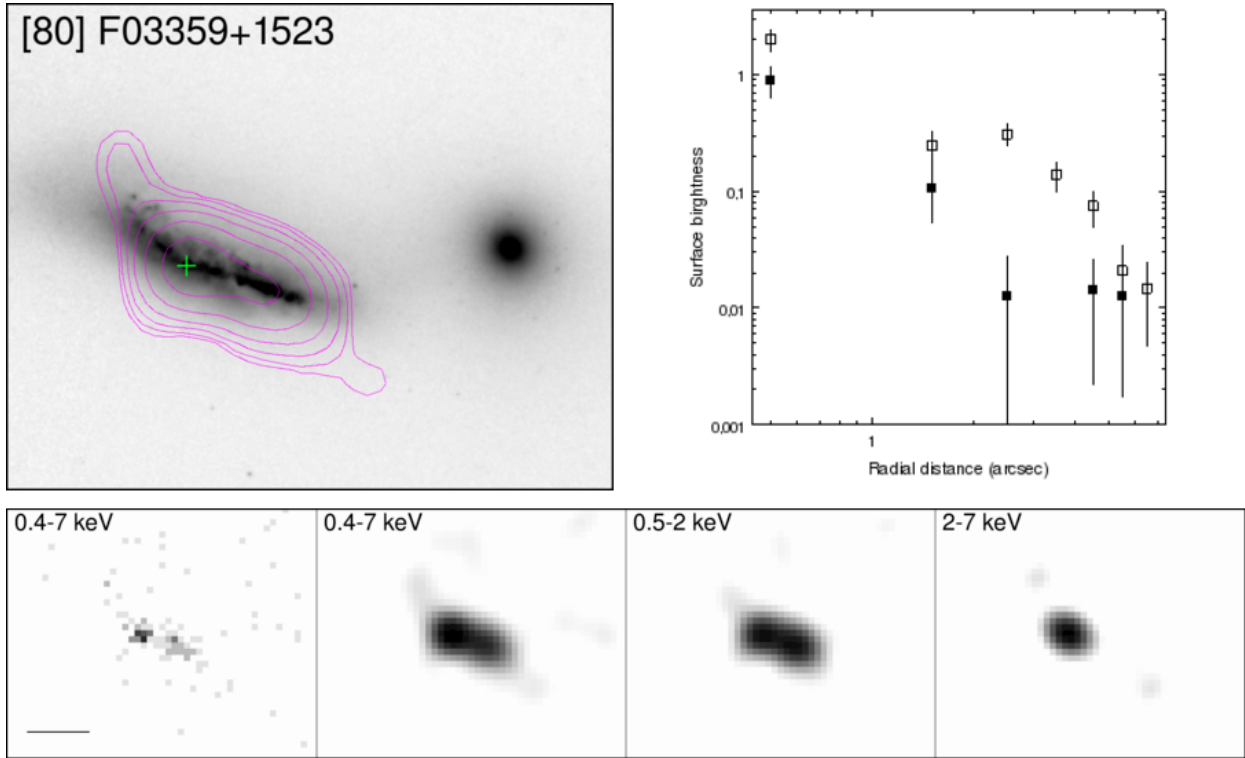


Fig. B.23. Overlay on HST-ACS F814W. Contours: Interval 1.

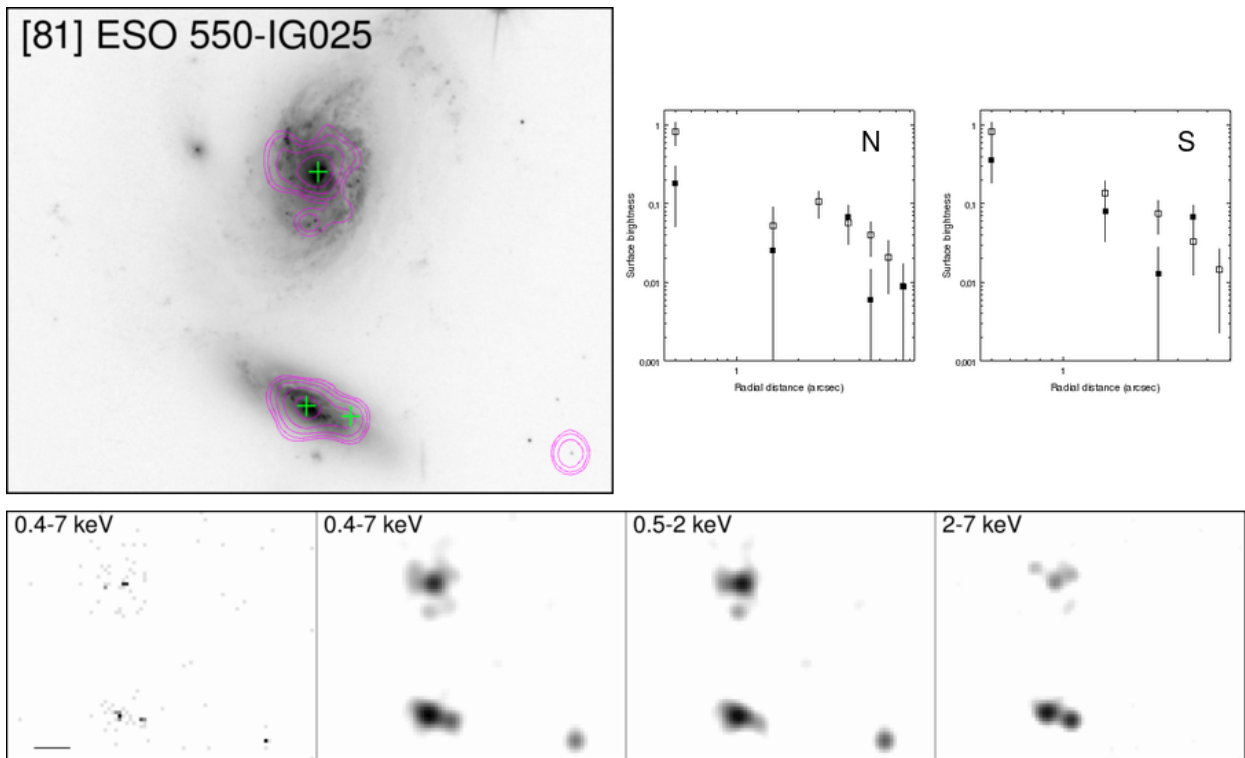


Fig. B.24. Overlay on HST-ACS F814W. Contours: Interval 1.

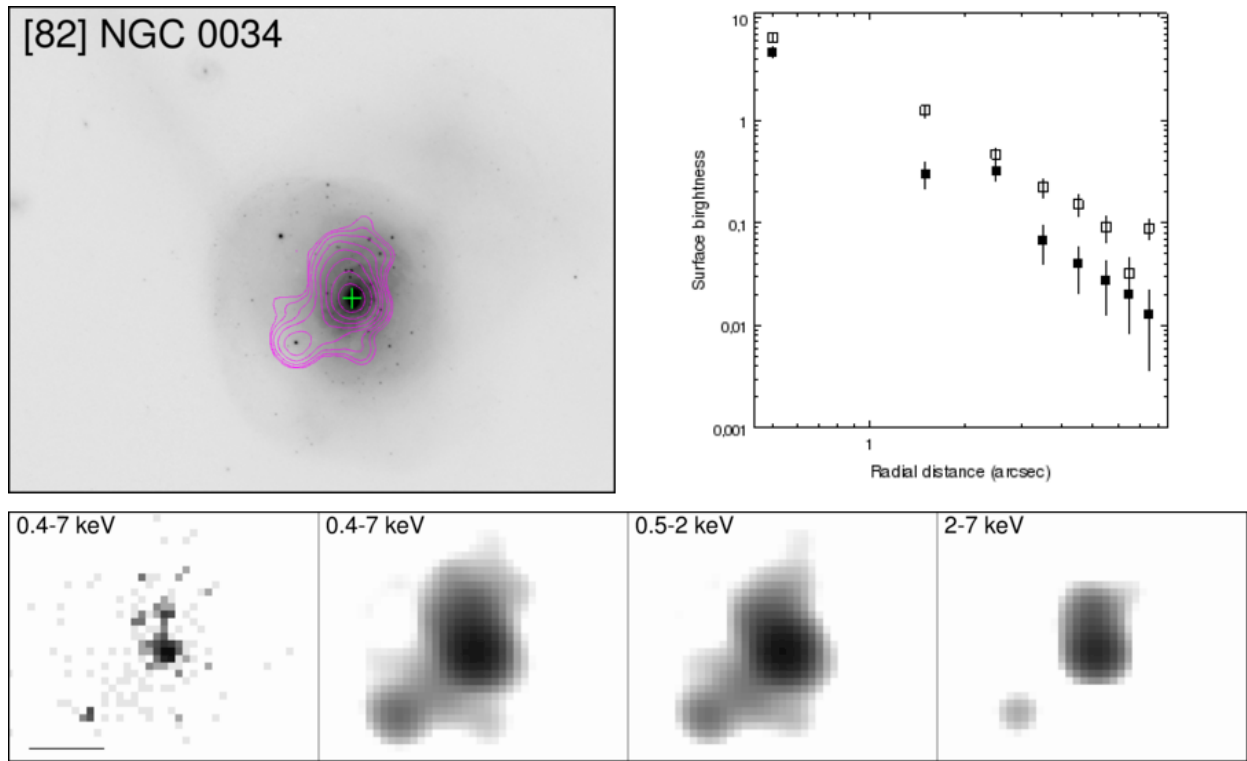


Fig. B.25. Overlay on HST-ACS F814W. Contours: Interval 1.

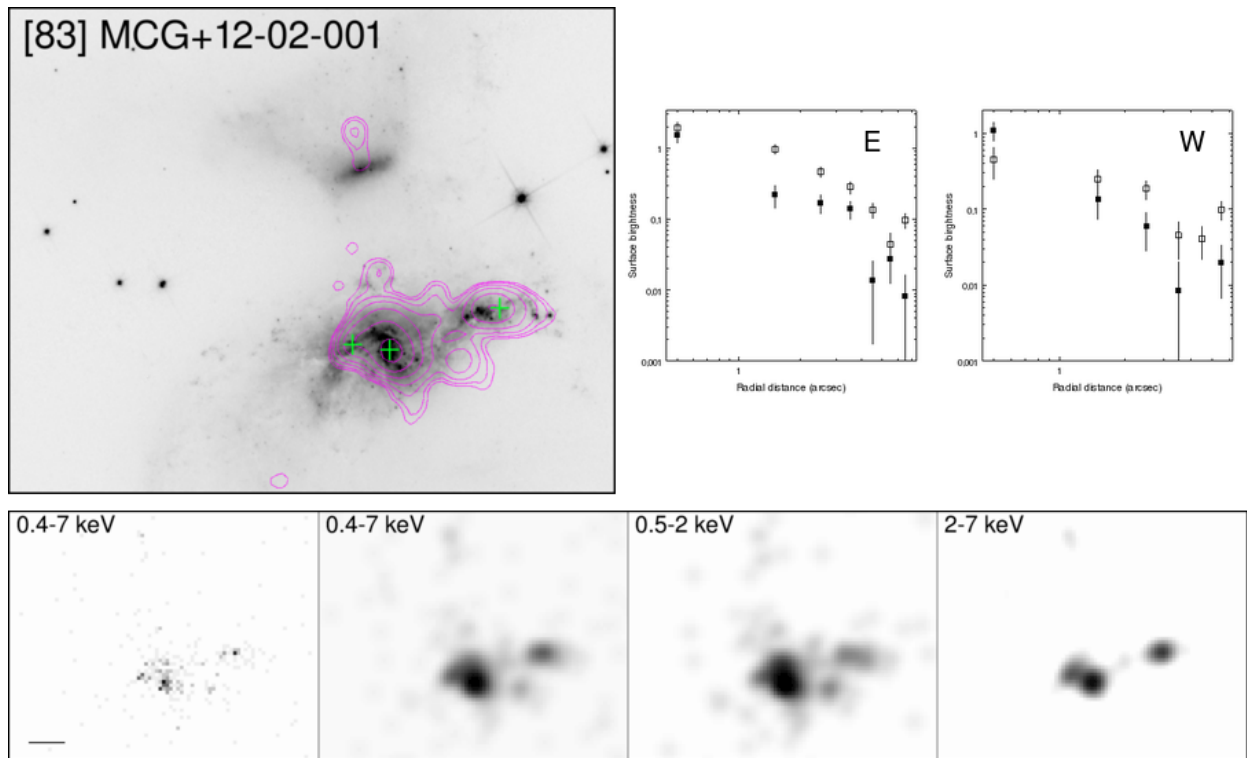
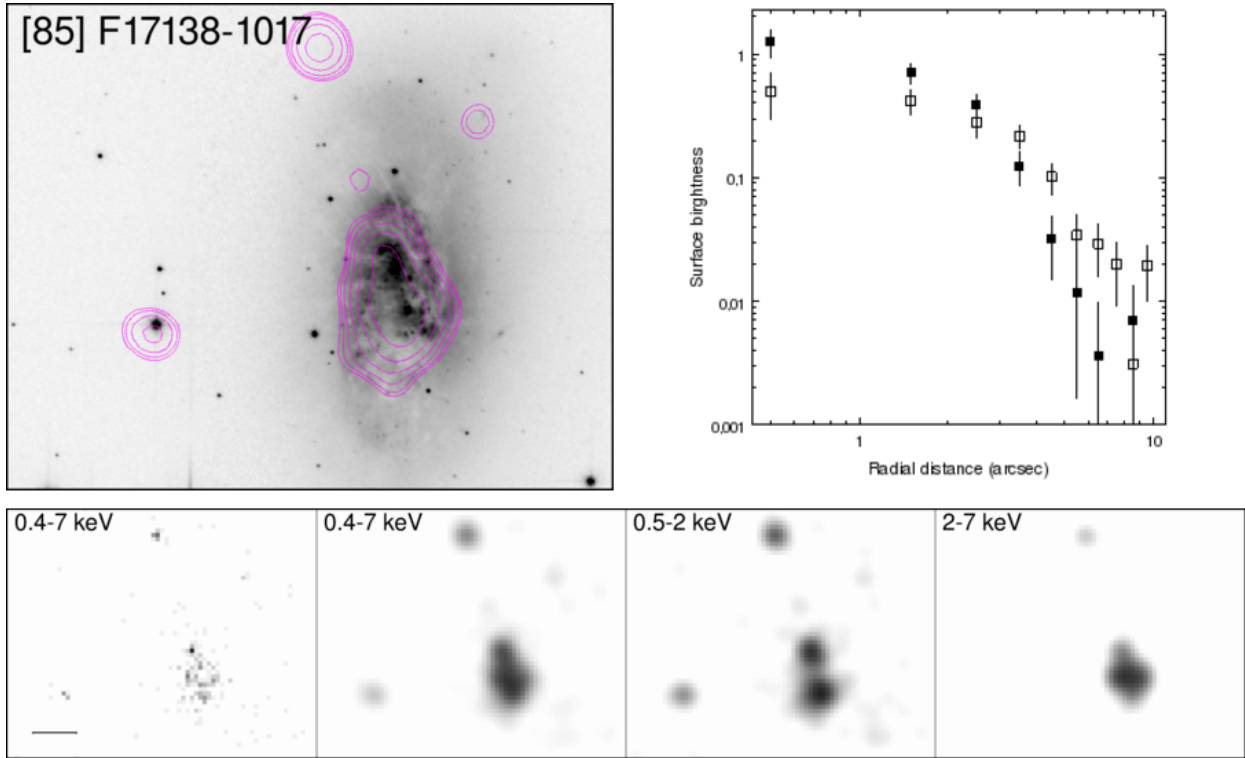
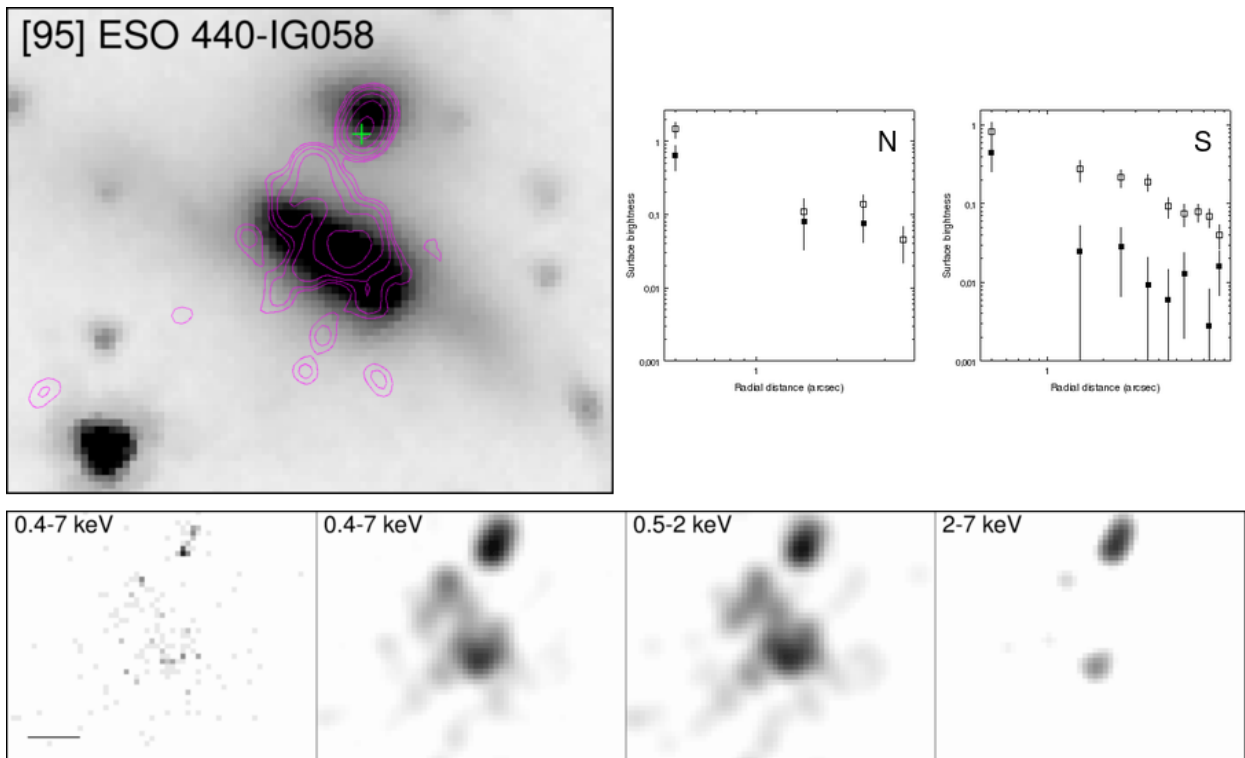


Fig. B.26. Overlay on HST-ACS F814W. Contours: Interval 1.



**Fig. B.27.** Overlay on HST-ACS F814W. Contours: Interval 1.



**Fig. B.28.** Overlay on IRAC channel 1. Contours: Interval 2.

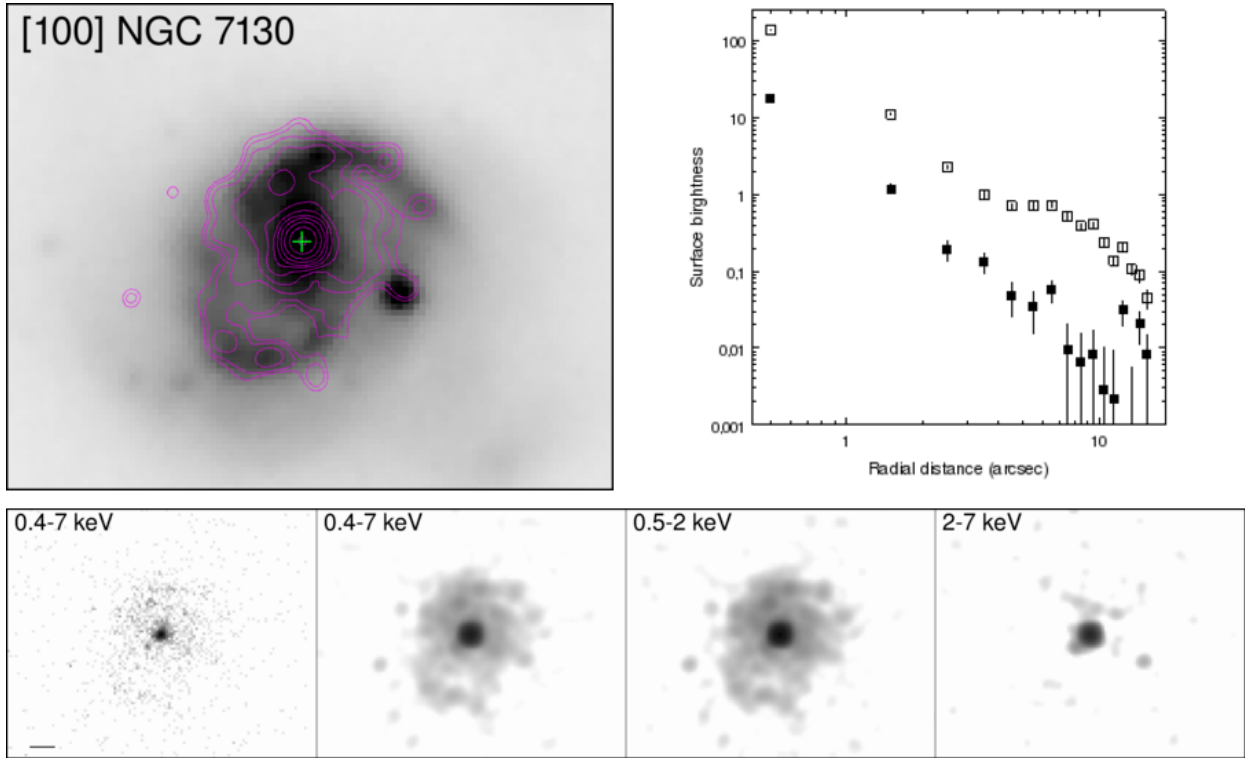


**Fig. B.29.** *Overlay on IRAC channel 1. Contours: Interval 1.*

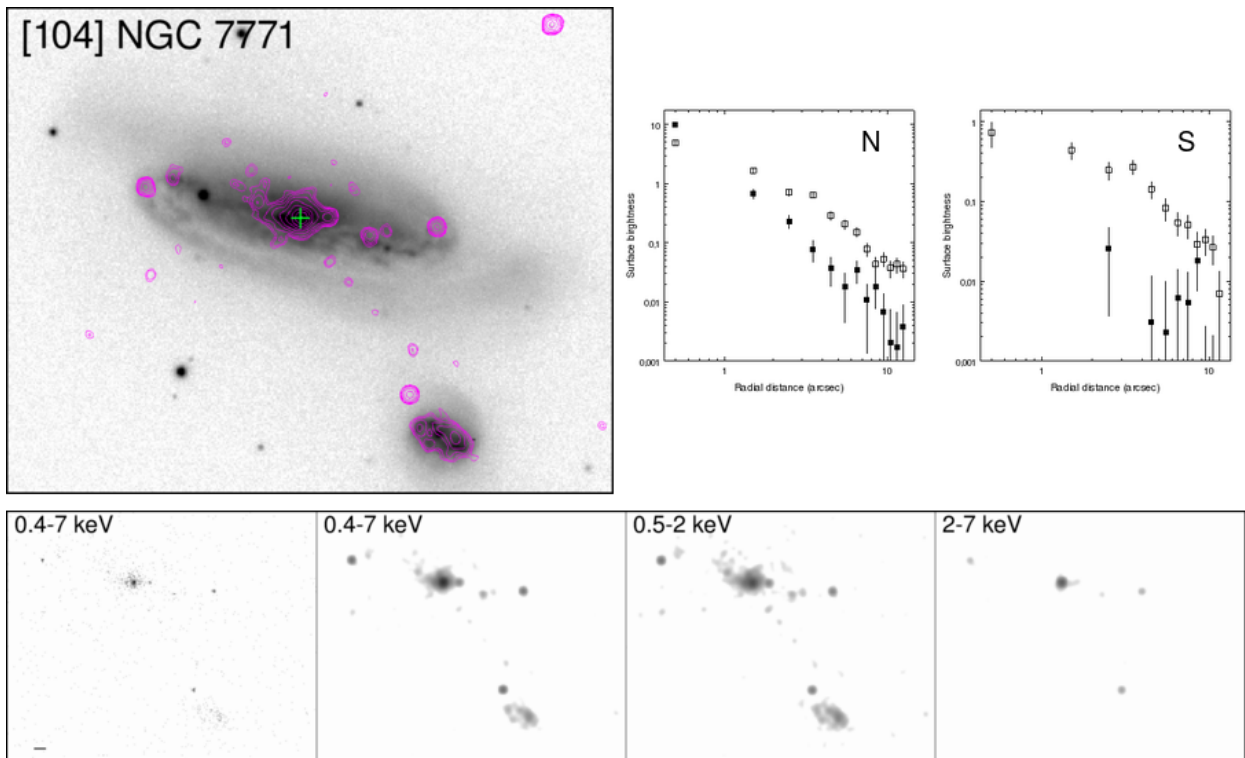


**Fig. B.30.** *Overlay on SDSS DR-12 *i*-band. Contours: Interval 1.*

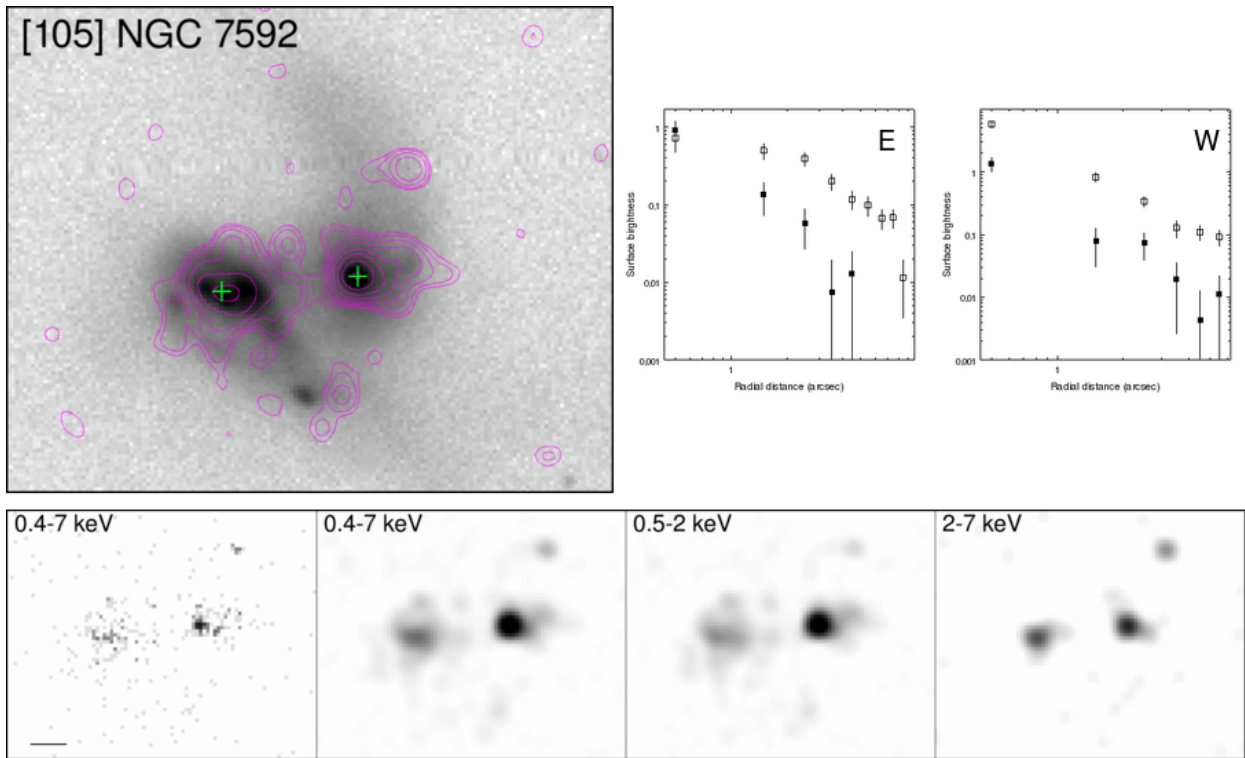


**Fig. B.31.** *Overlay on SDSS DR-12 i-band. Contours: Interval 2.*

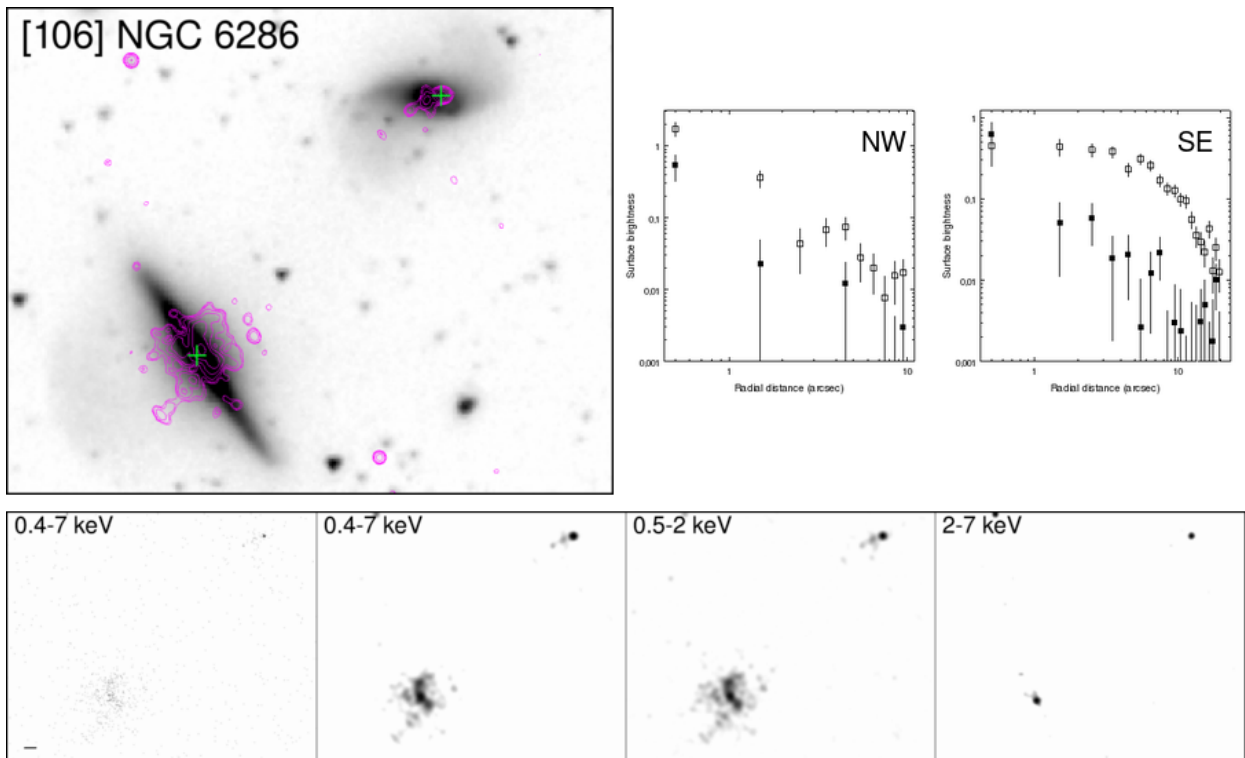


**Fig. B.32.** *Overlay on IRAC channel 1. Contours: Interval 1.*

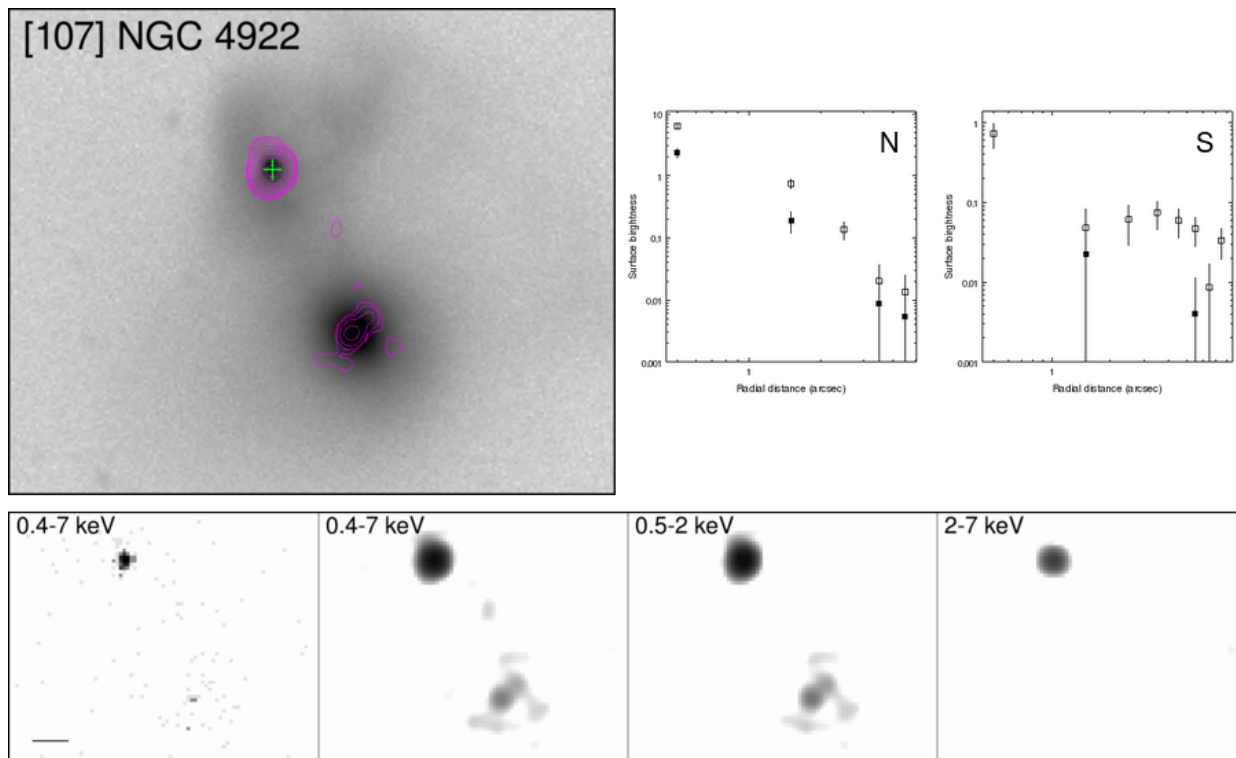


Fig. B.33. Overlay on SDSS DR-12 *i*-band. Contours: Interval 1.

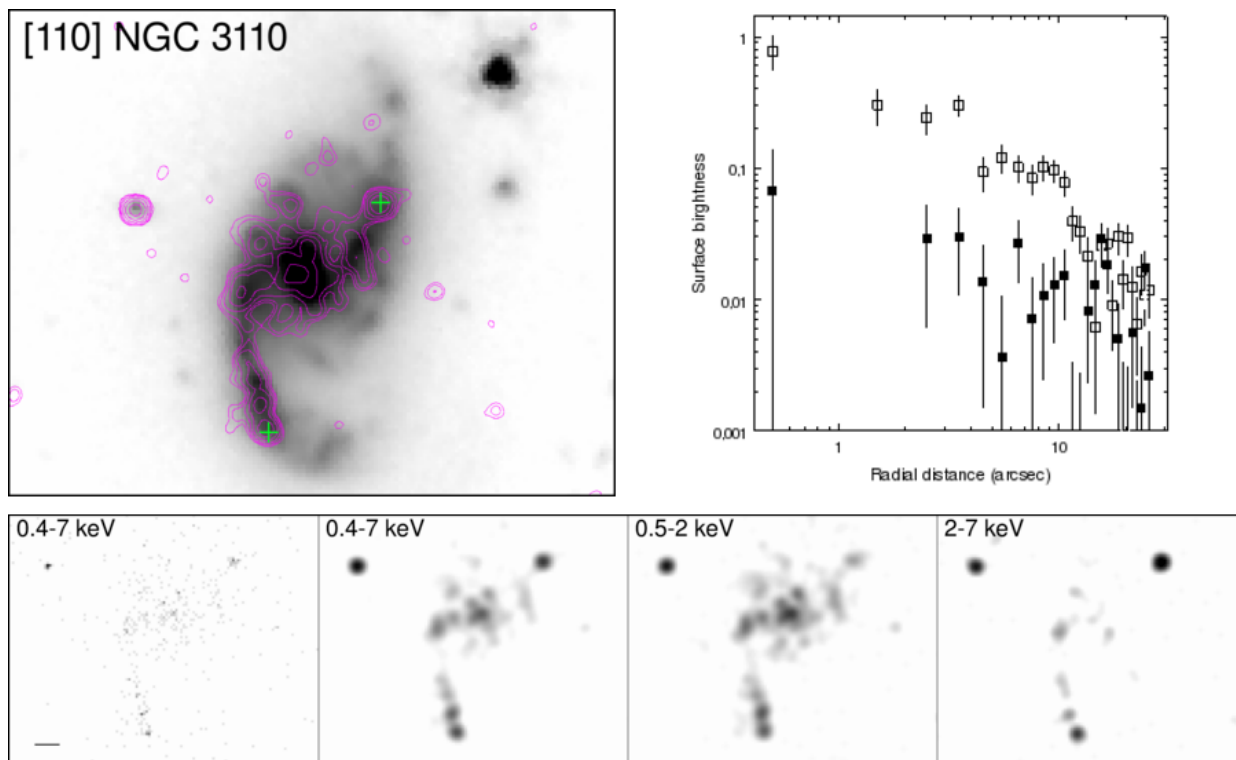


Fig. B.34. Overlay on IRAC channel 1. Contours: Interval 2.

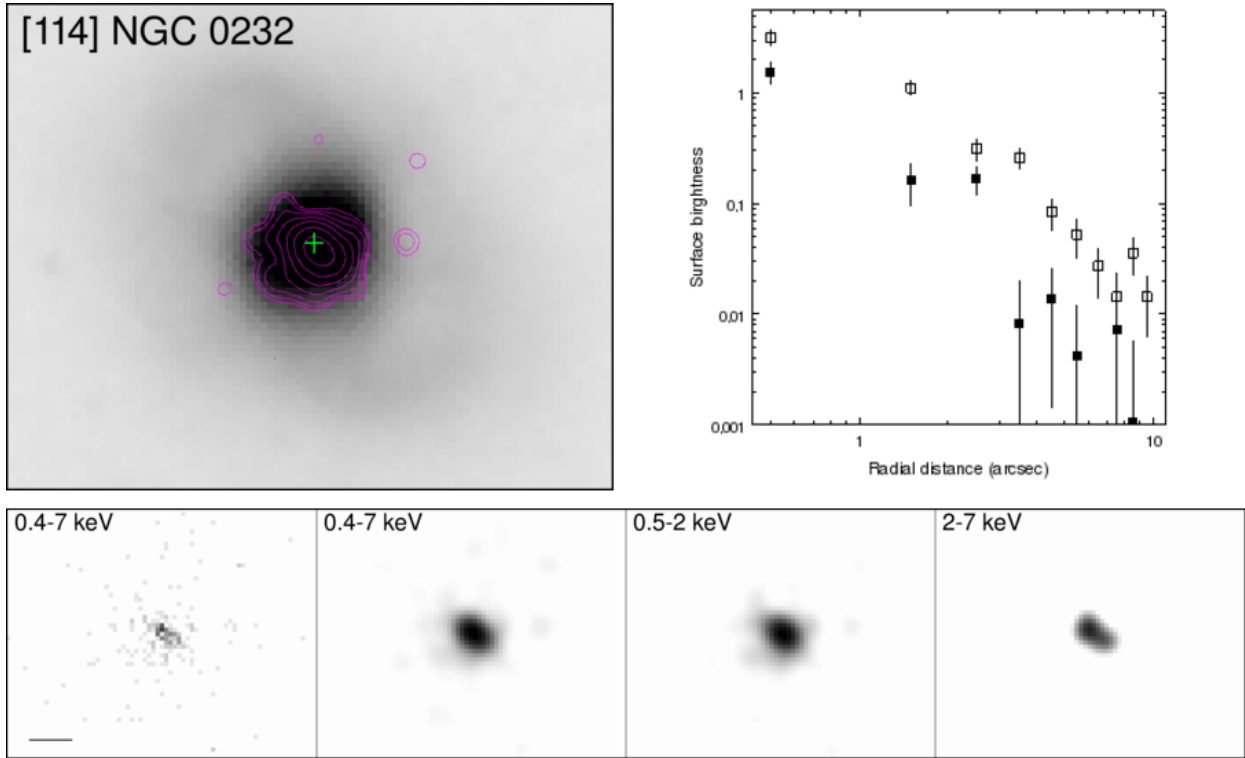


Fig. B.35. Overlay on IRAC channel 1. Contours: Interval 1.

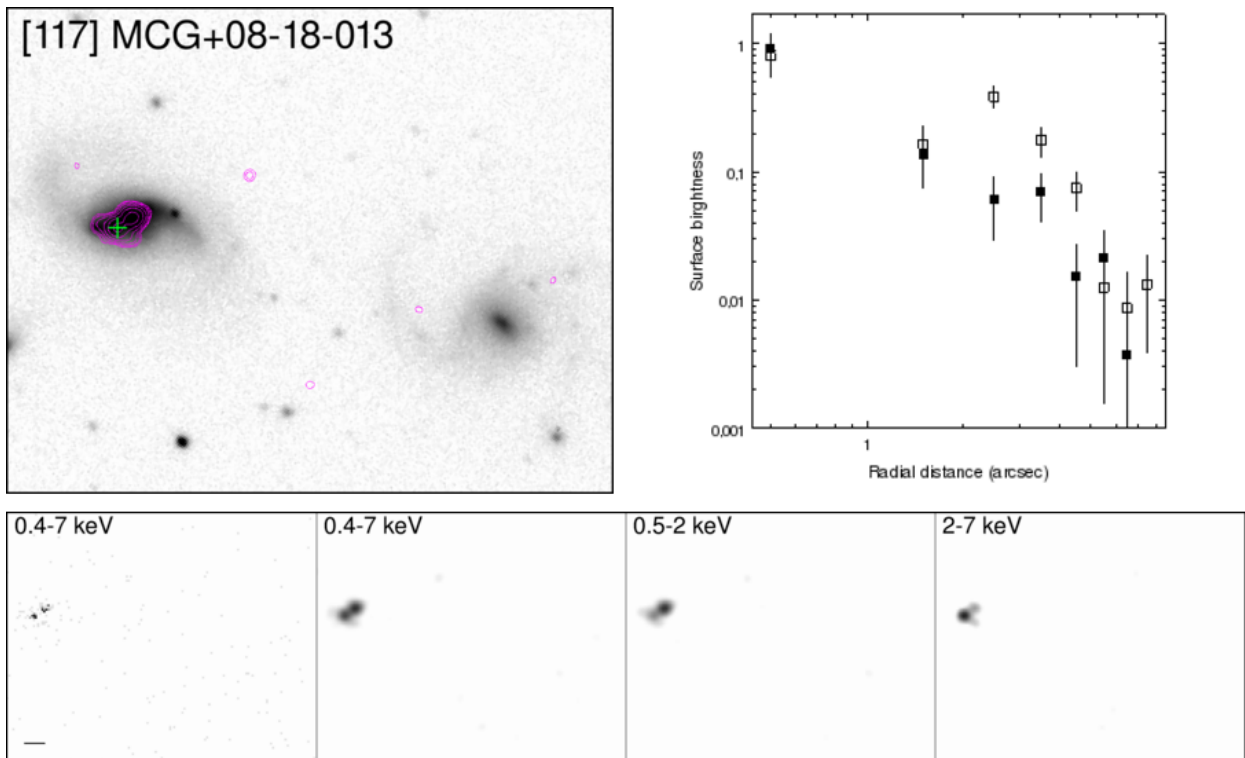
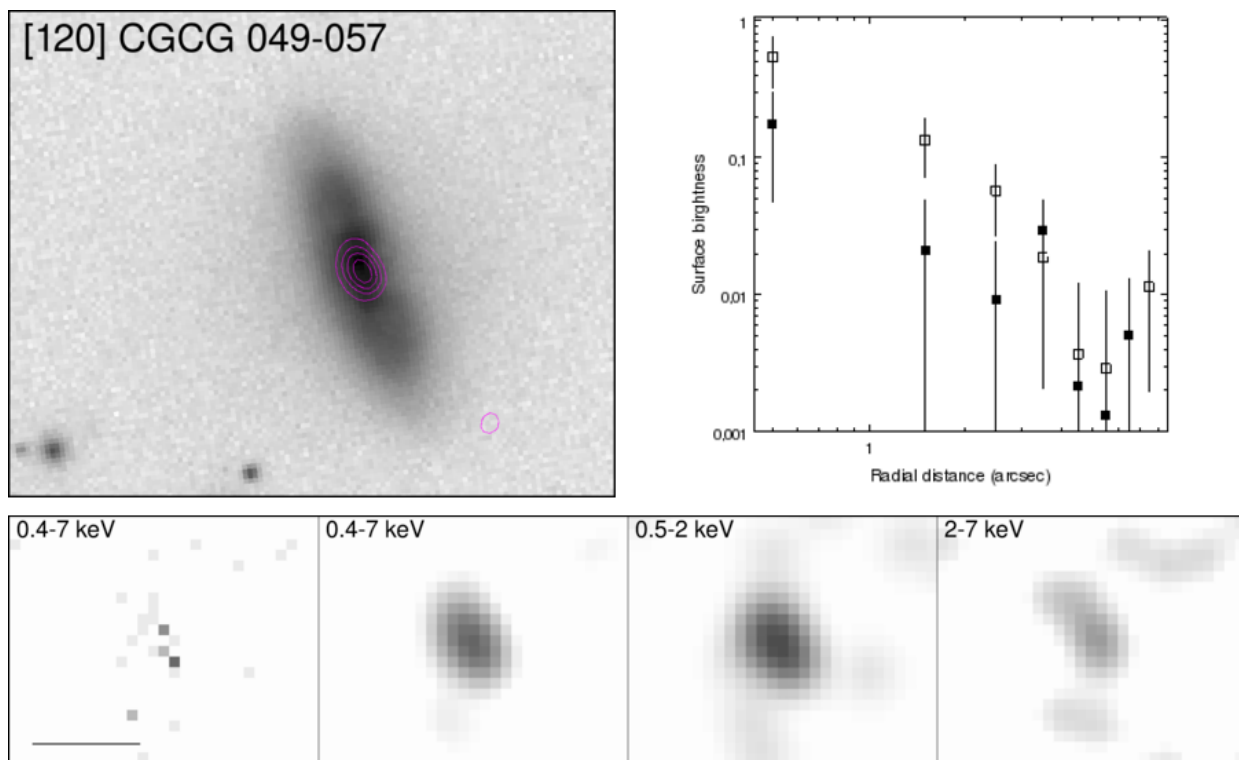
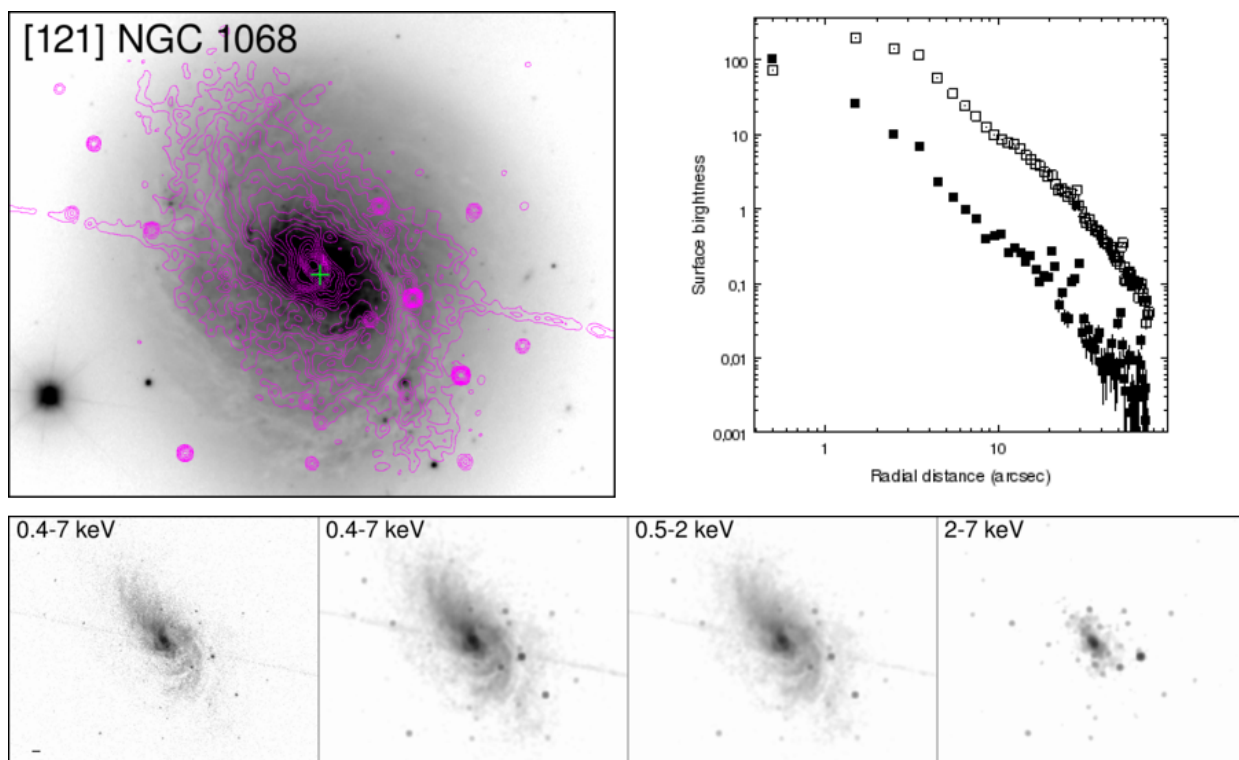


Fig. B.36. Overlay on SDSS DR-12 *i*-band. Contours: Interval 1.



**Fig. B.37.** *Overlay on SDSS DR-12 i-band. Contours: Custom.*



**Fig. B.38.** *Overlay on SDSS DR-12 i-band. Contours: Custom.*

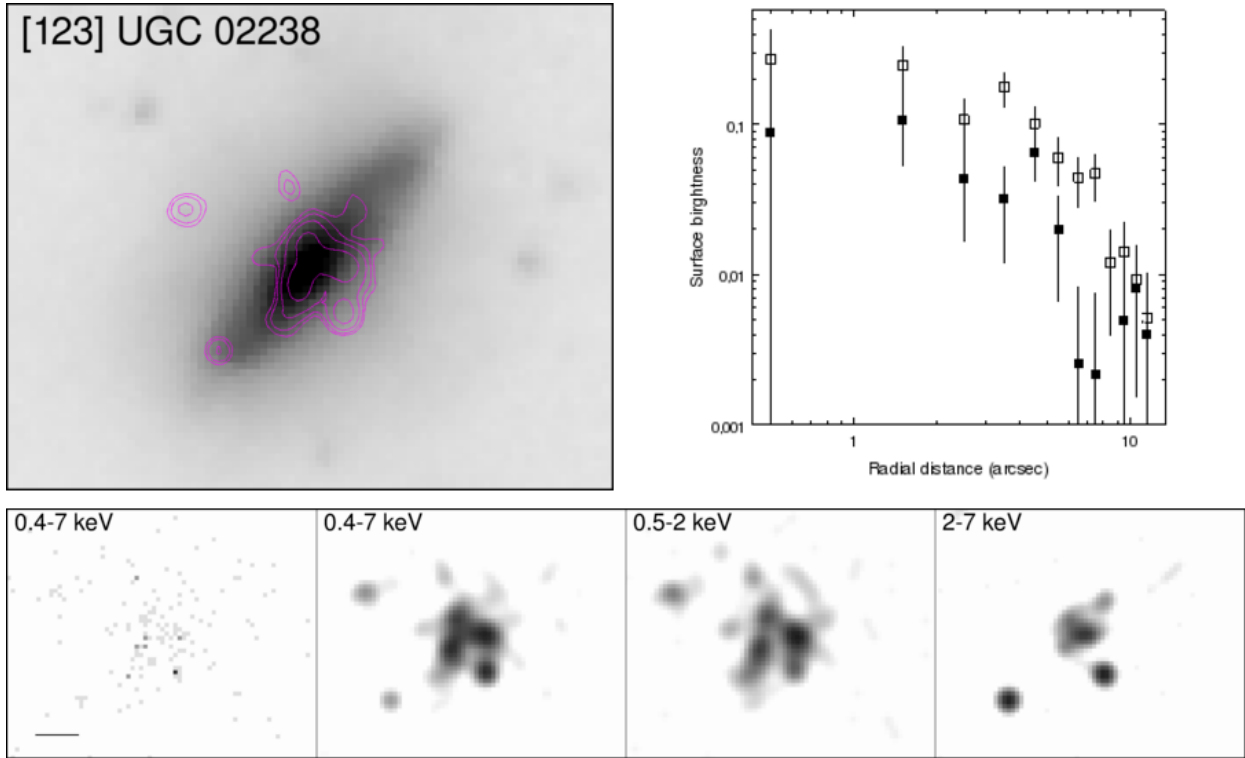


Fig. B.39. Overlay on IRAC channel 1. Contours: Interval 1.

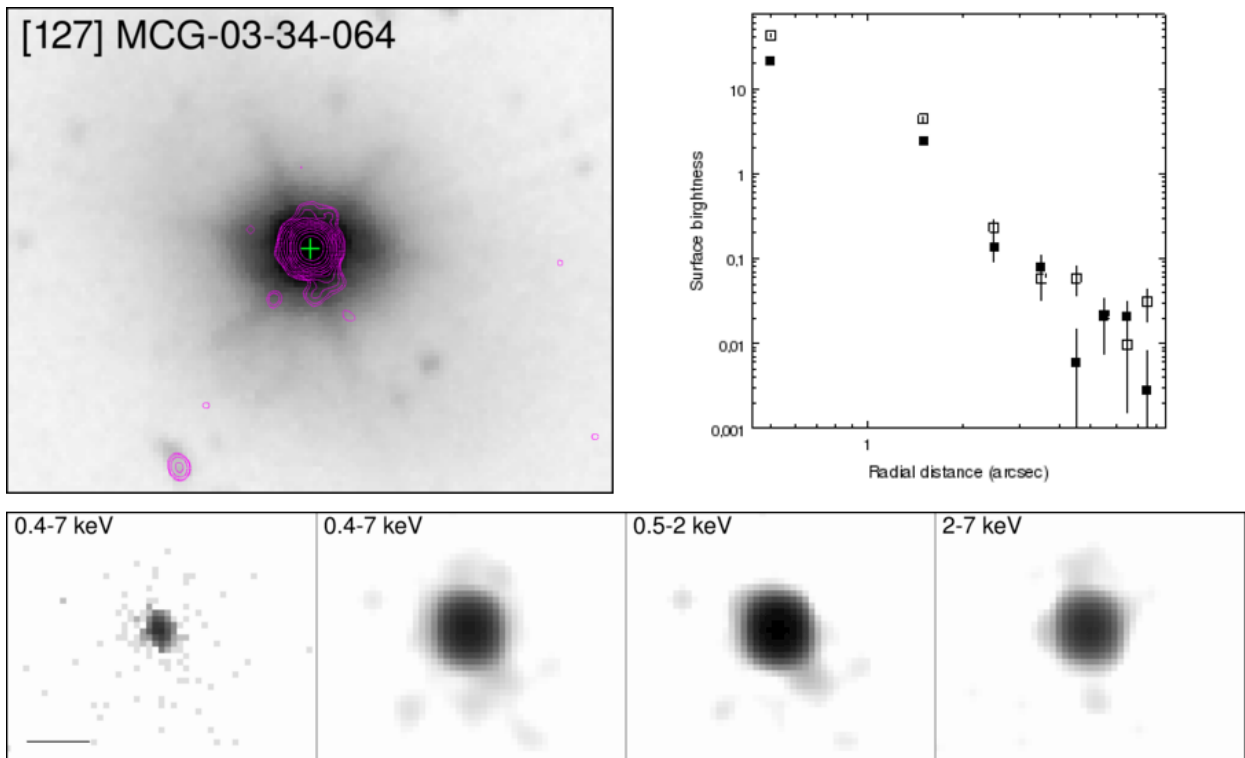
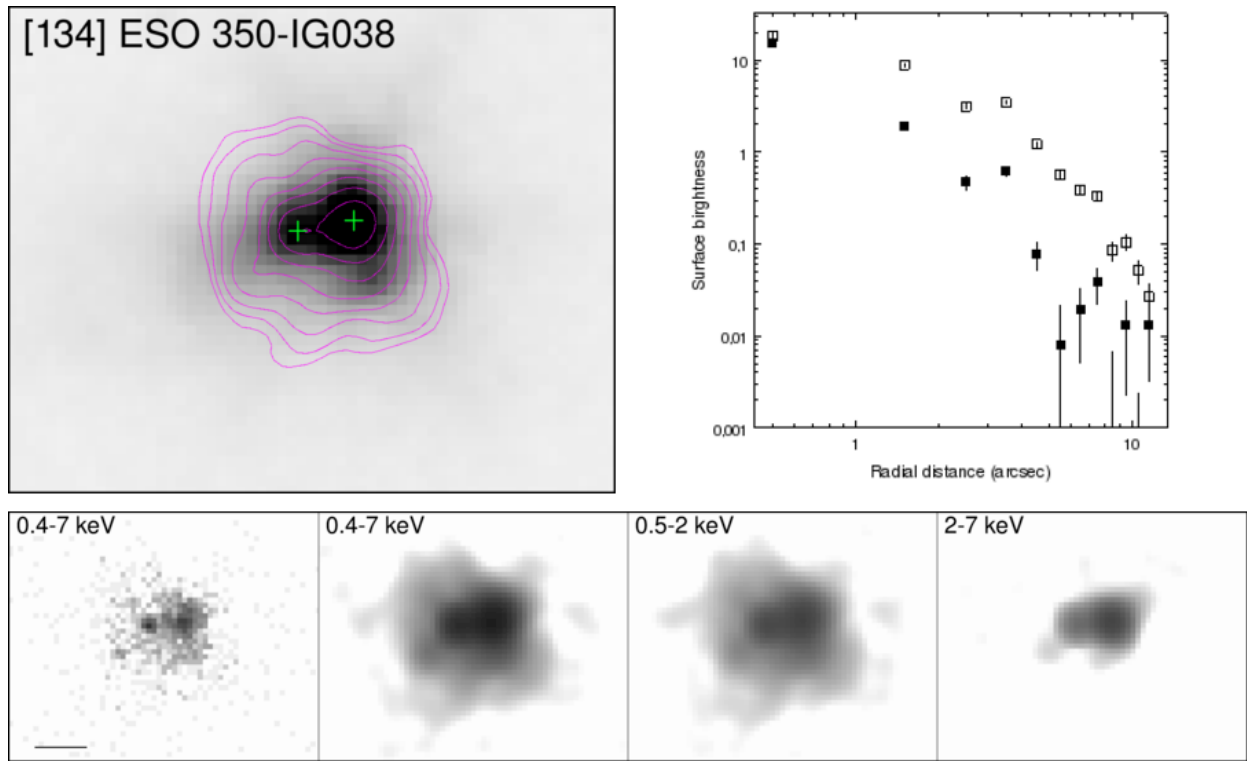
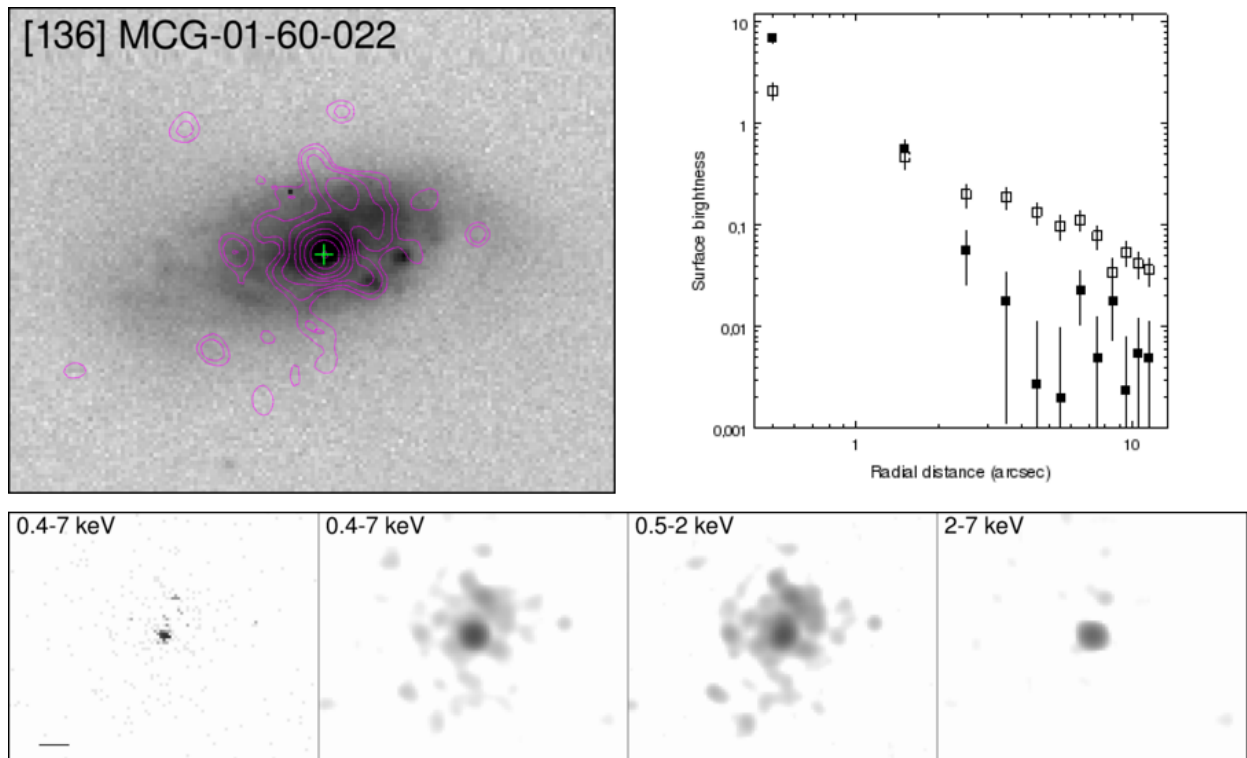


Fig. B.40. Overlay on IRAC channel 1. Contours: Interval 4.



**Fig. B.41.** *Overlay on IRAC channel 1. Contours: Interval 2.*



**Fig. B.42.** *Overlay on SDSS DR-12 i-band. Contours: Interval 2.*

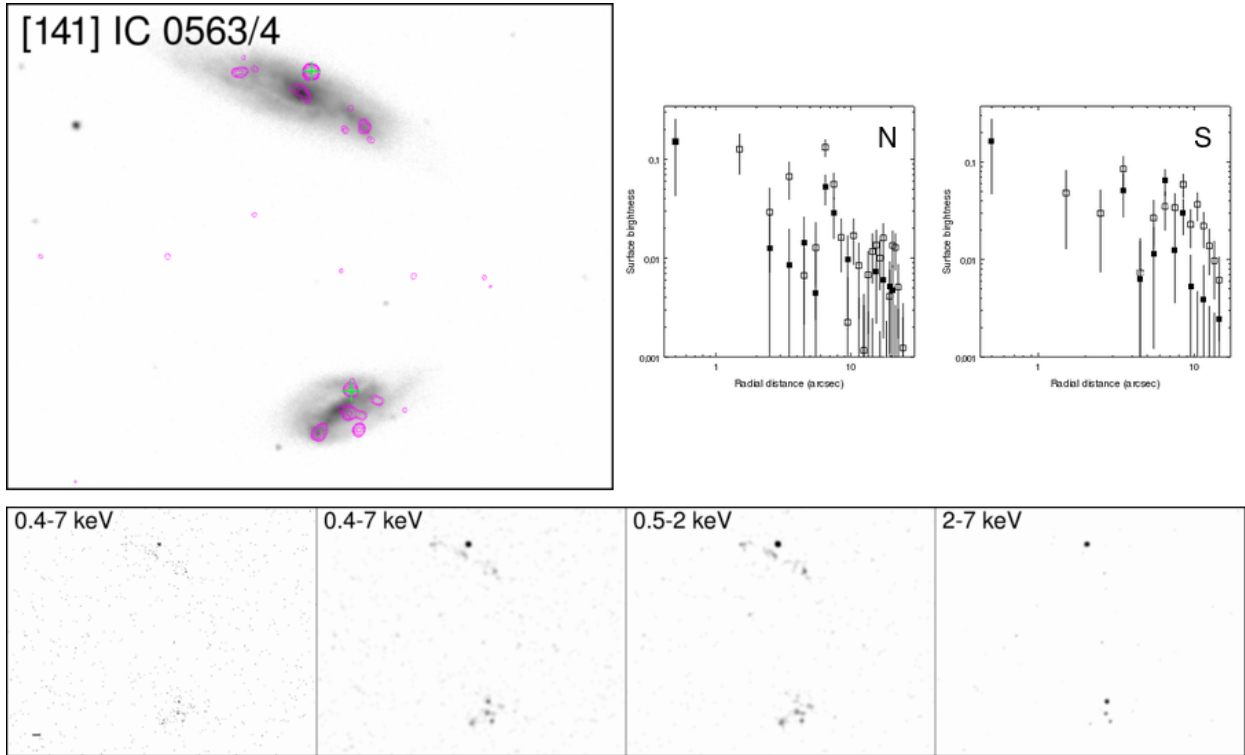


Fig. B.43. Overlay on SDSS DR-12 *i*-band. Contours: Interval 1.

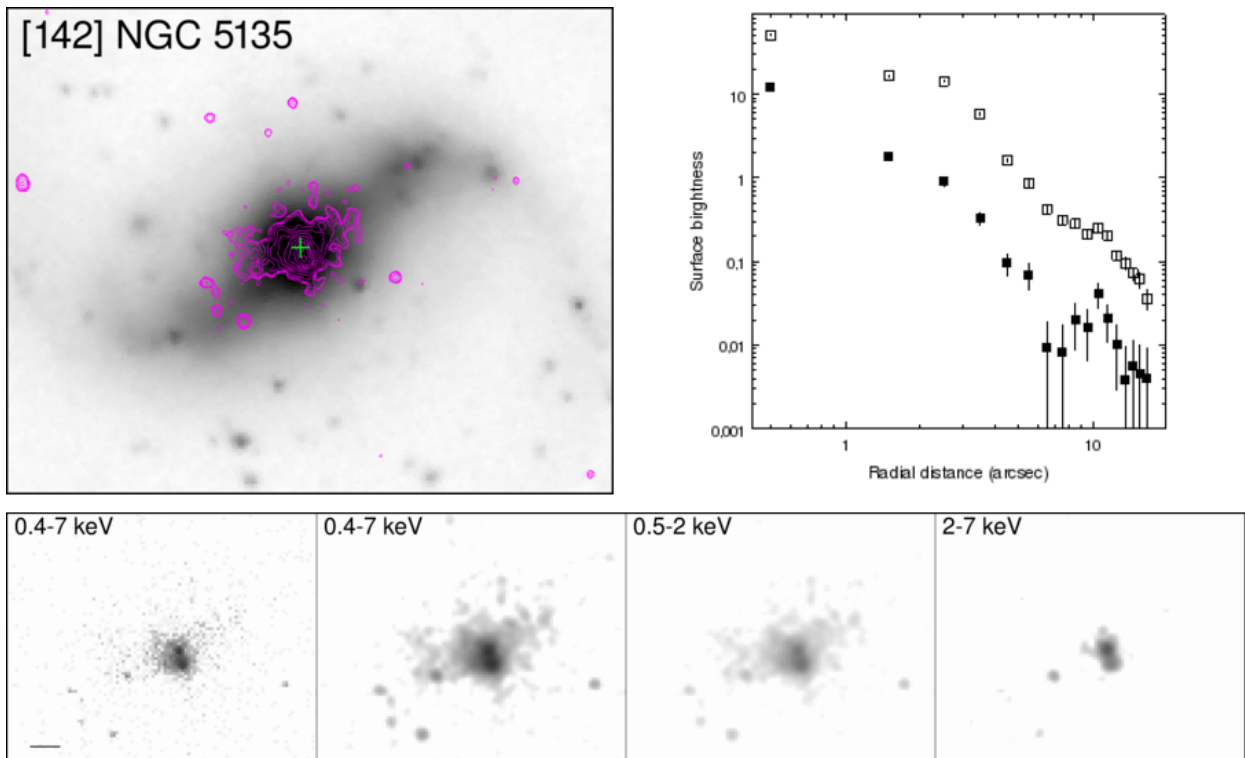


Fig. B.44. Overlay on IRAC channel 1. Contours: Custom.

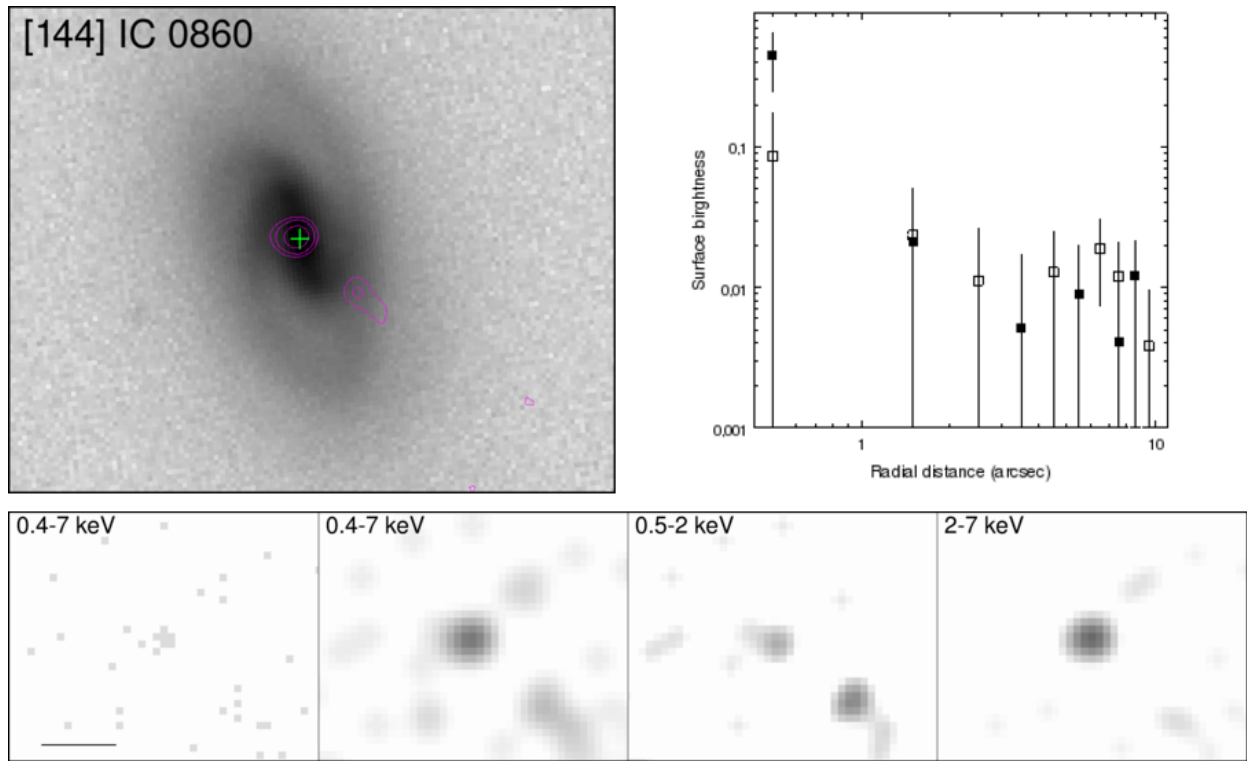


Fig. B.45. Overlay on SDSS DR-12 *i*-band. Contours: Interval 2.

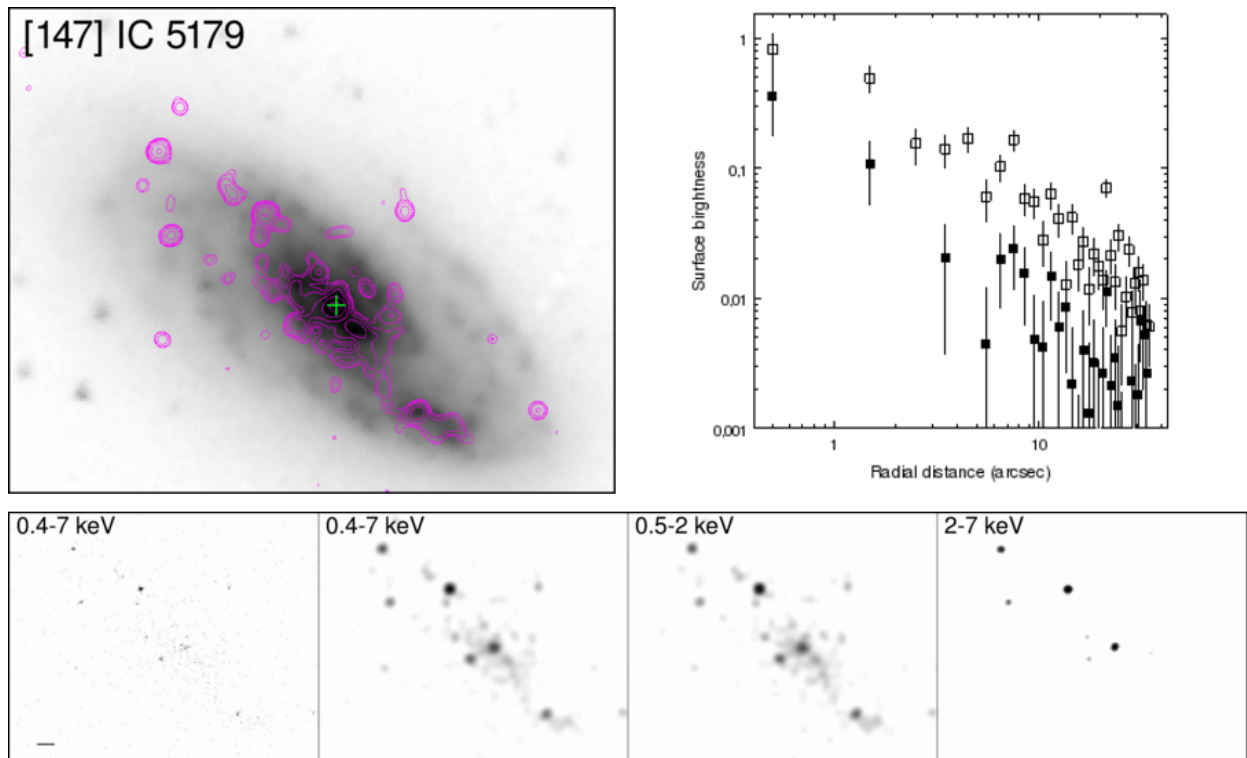


Fig. B.46. Overlay on IRAC channel 1. Contours: Interval 1.

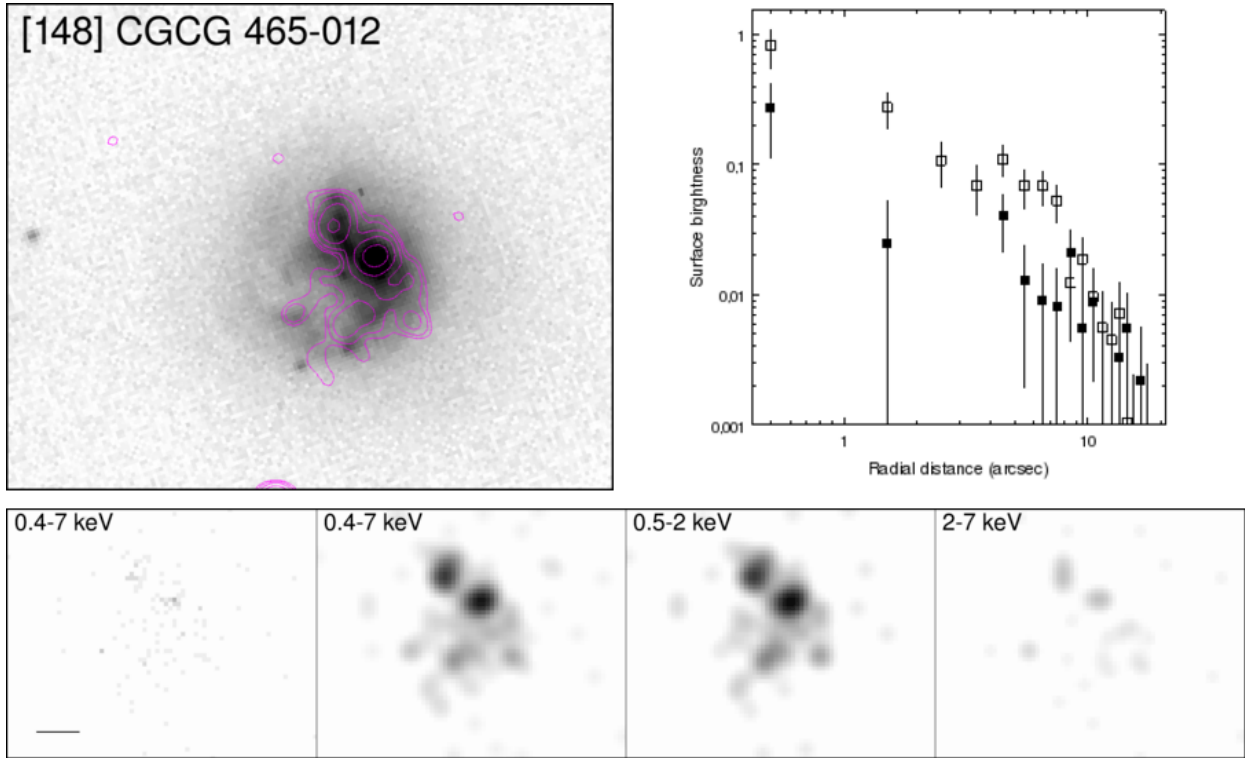


Fig. B.47. Overlay on SDSS DR-12 *i*-band. Contours: Interval 2.

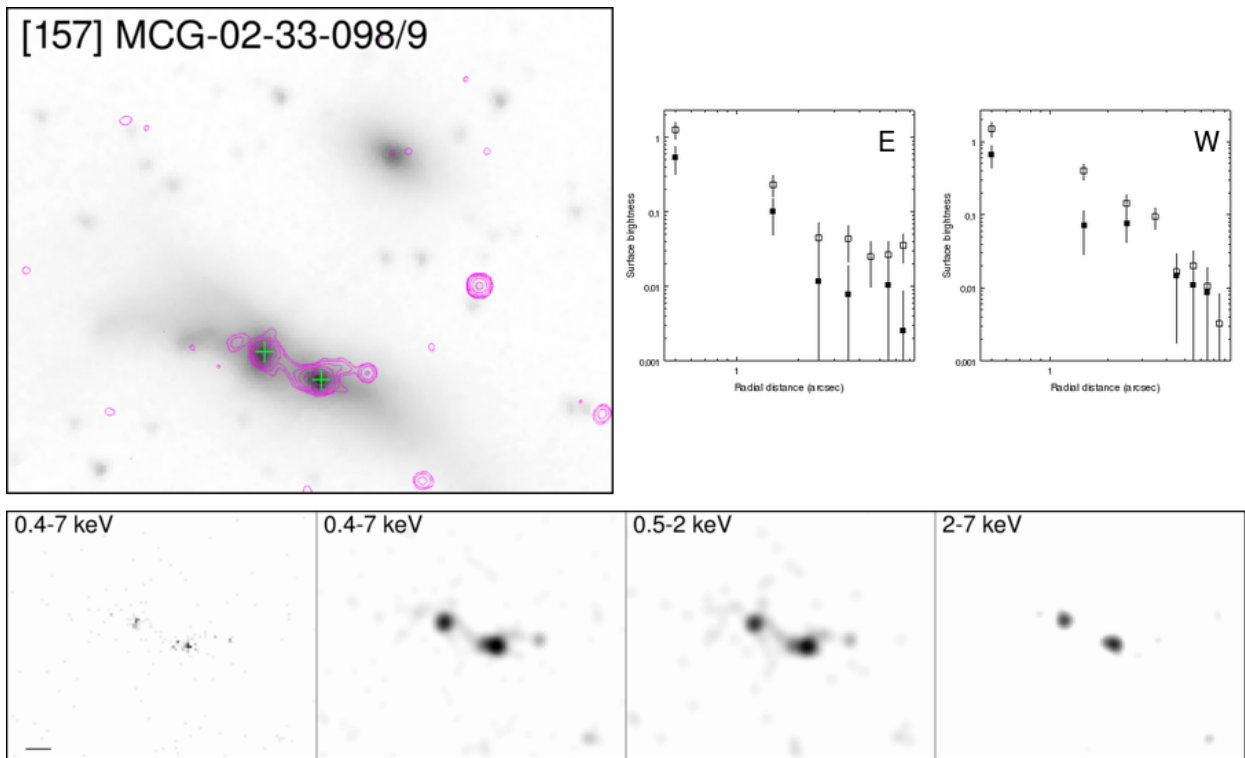


Fig. B.48. Overlay on IRAC channel 1. Contours: Interval 1.

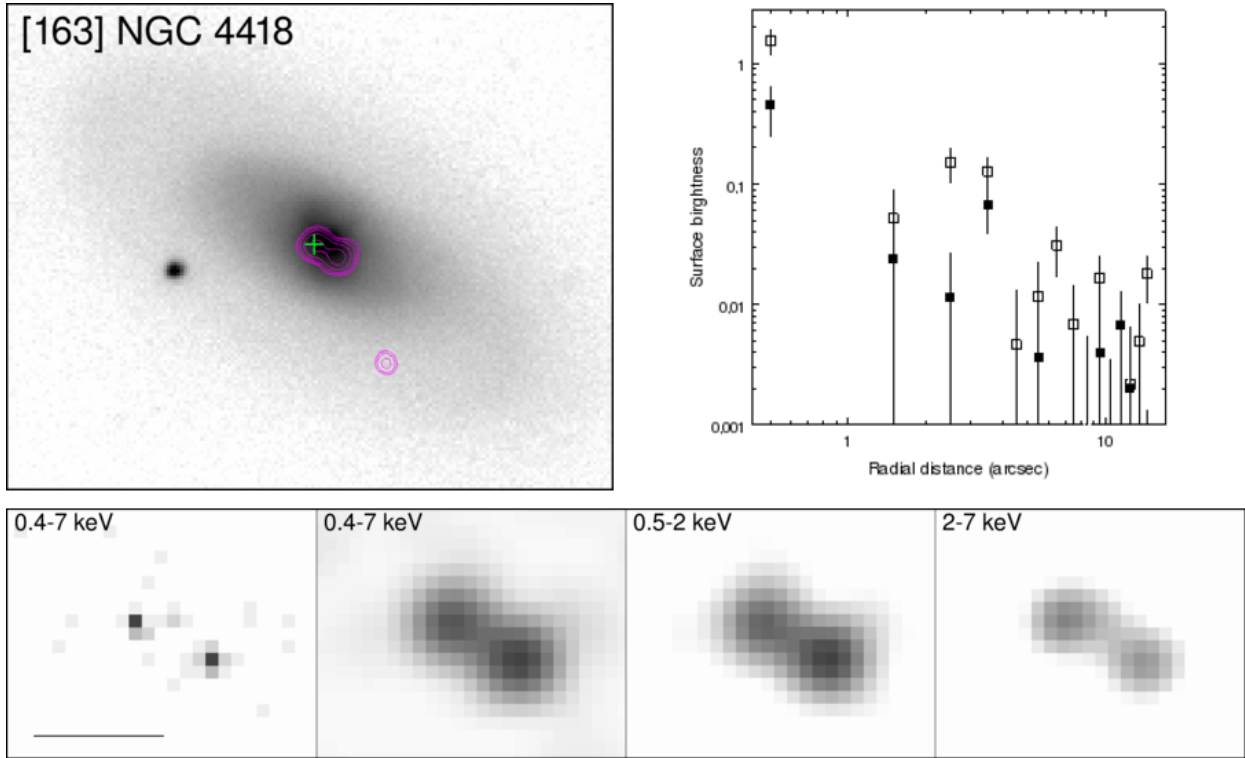


Fig. B.49. Overlay on SDSS DR-12 *i*-band. Contours: Interval 1.

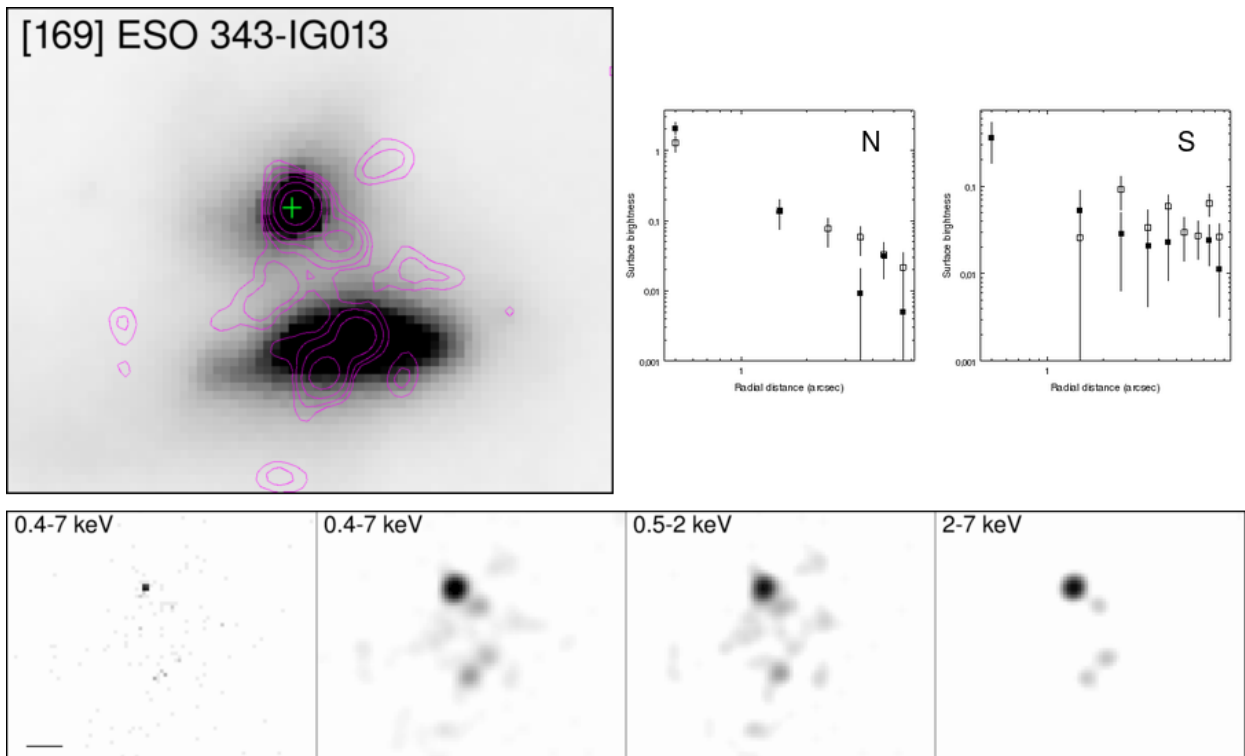
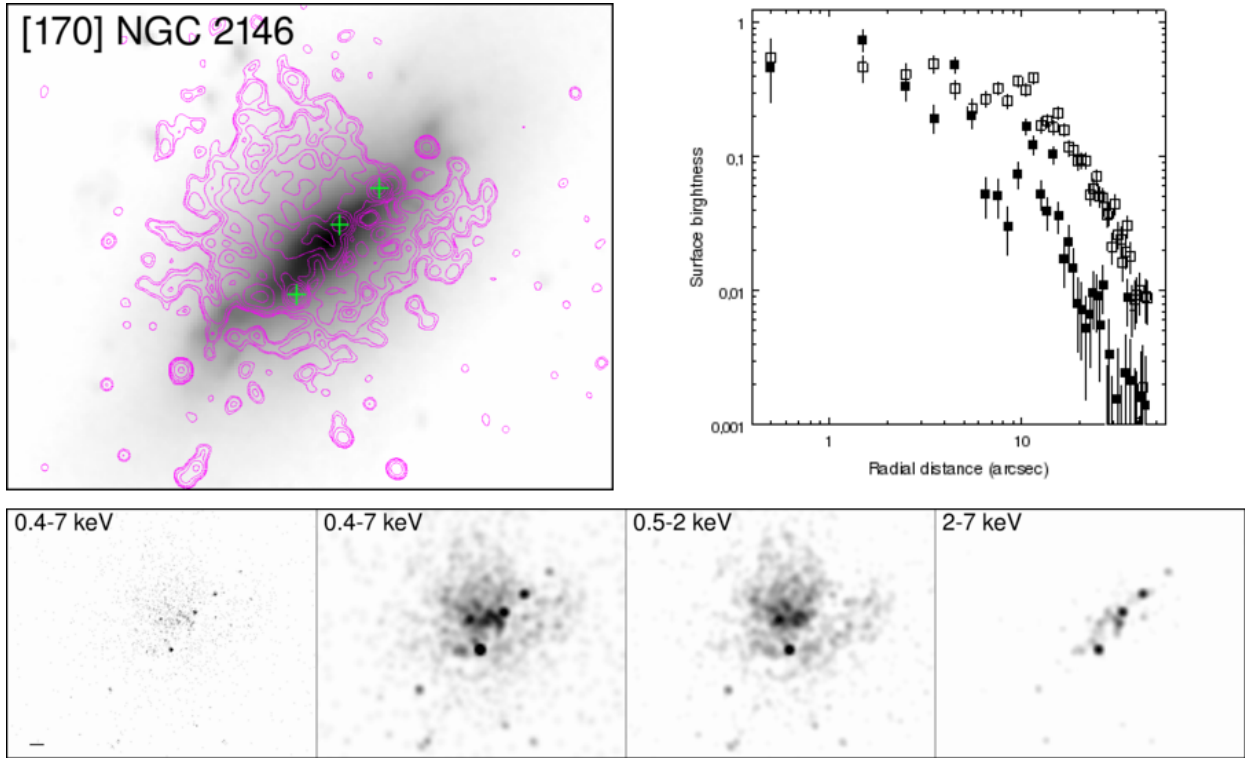
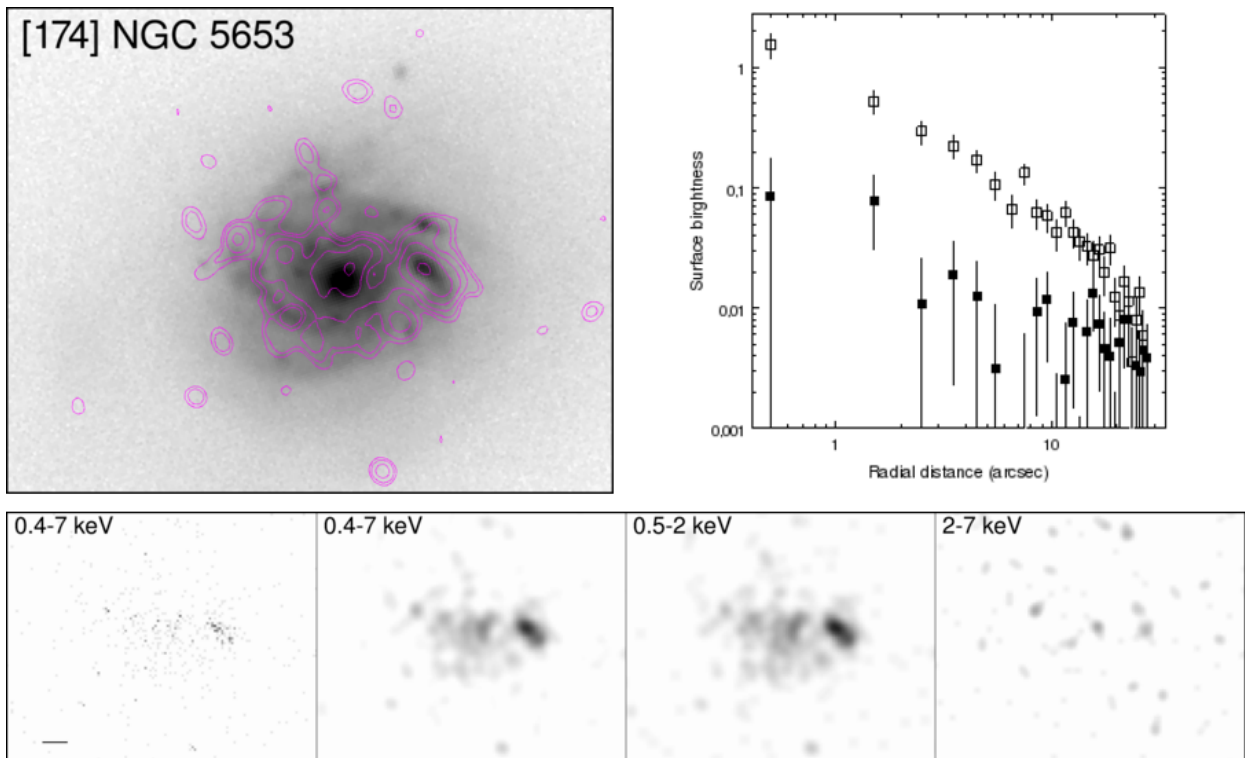


Fig. B.50. Overlay on IRAC channel 1. Contours: Interval 2.



**Fig. B.51.** *Overlay on IRAC channel 1. Contours: Interval 1.*



**Fig. B.52.** *Overlay on SDSS DR-12 i-band. Contours: Interval 2.*

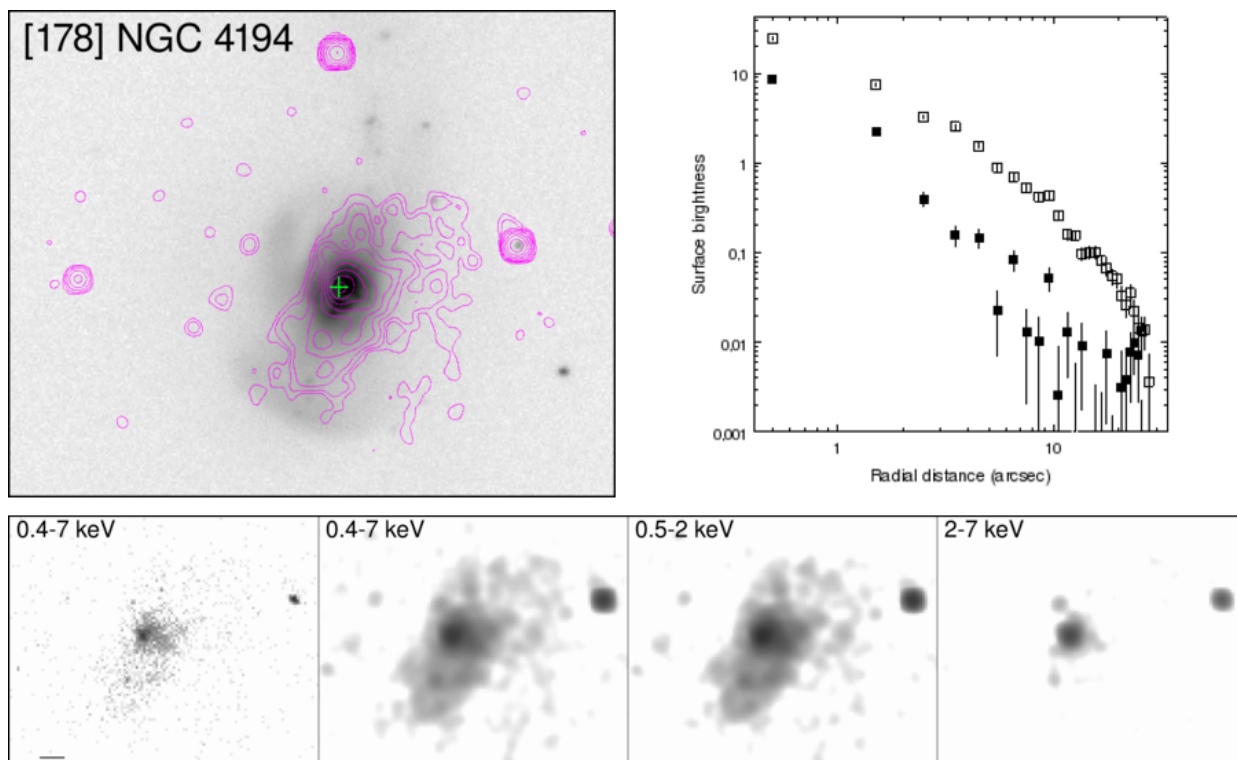


**Fig. B.53.** *Overlay on SDSS DR-12 i-band. Contours: Interval 1.*

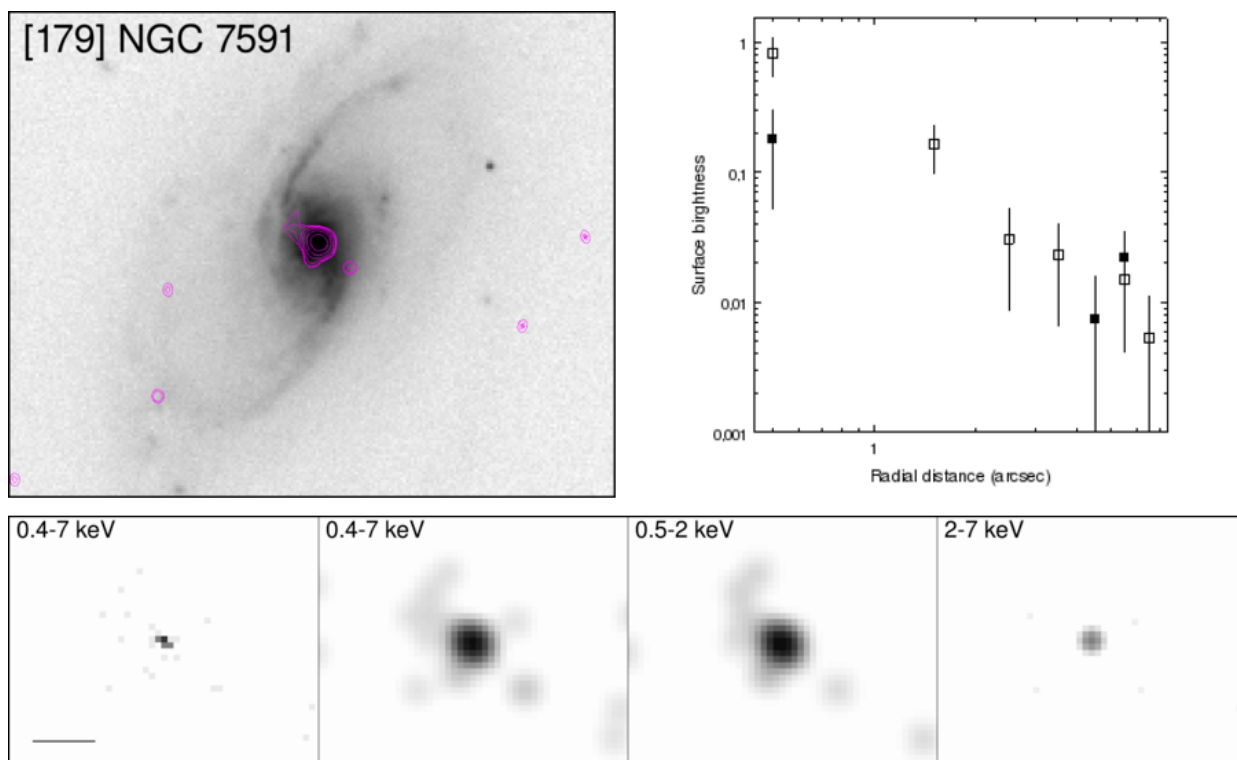


**Fig. B.54.** *Overlay on SDSS DR-12 i-band. Contours: Interval 4.*

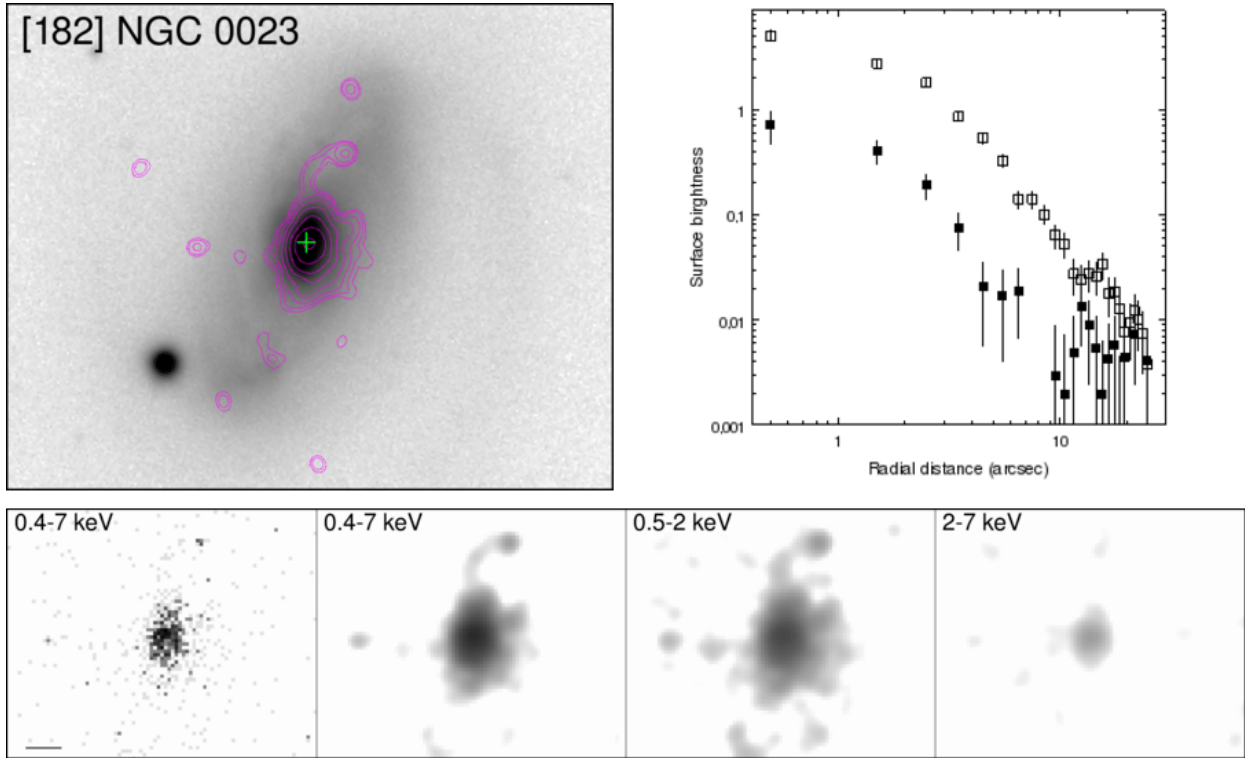


Fig. B.55. Overlay on SDSS DR-12 *i*-band. Contours: Interval 1.

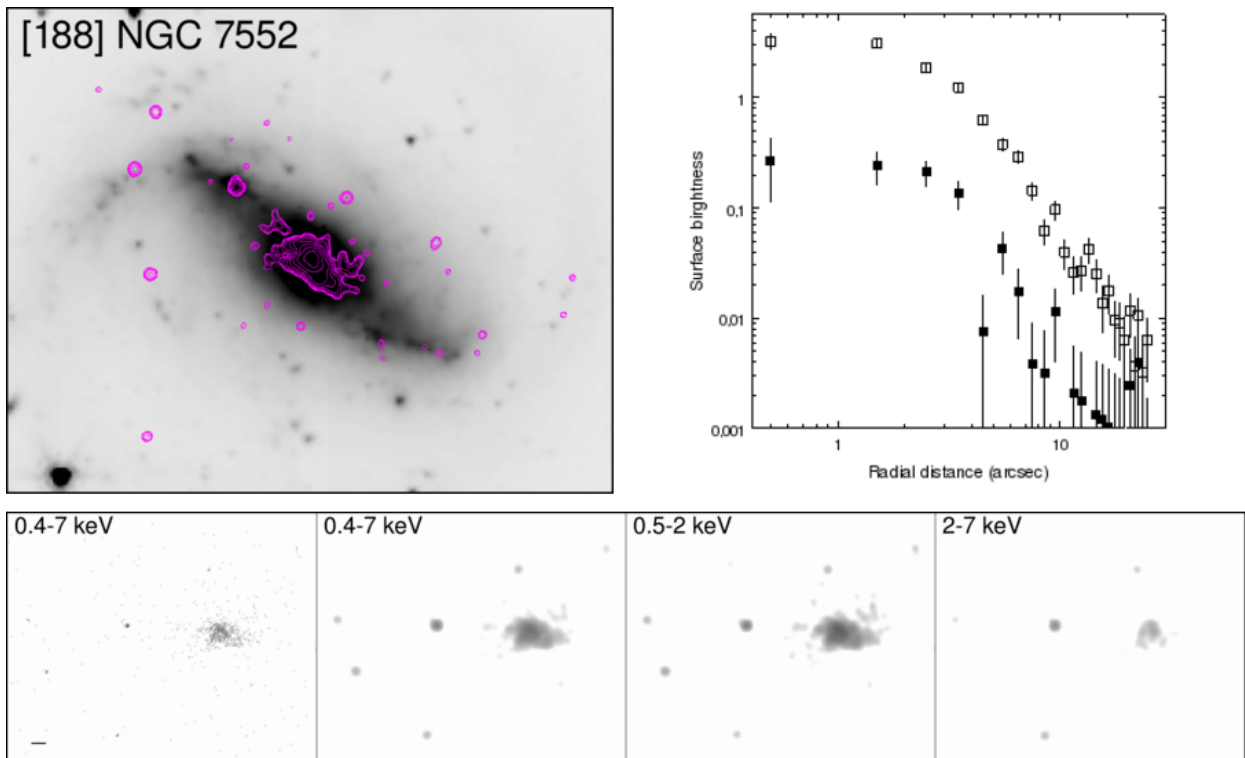


Fig. B.56. Overlay on IRAC channel 1. Contours: Interval 4.

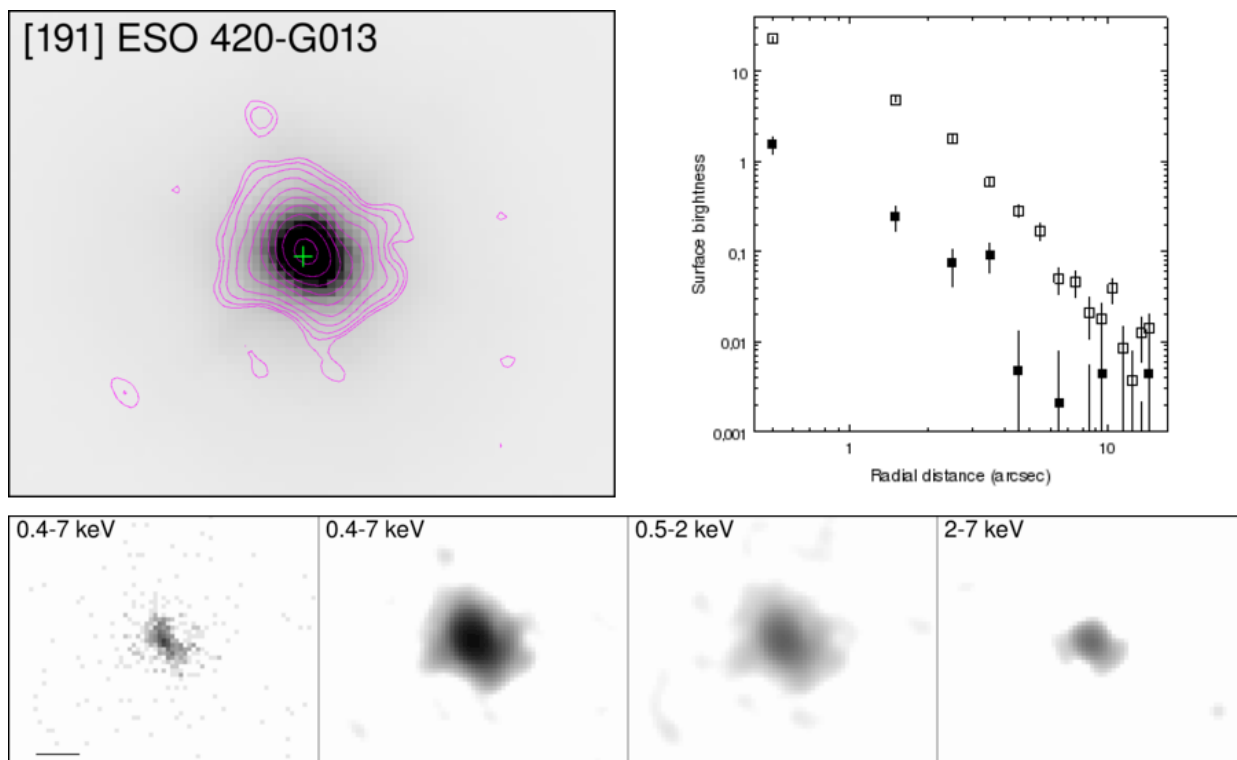


Fig. B.57. Overlay on IRAC channel 1. Contours: Interval 1.

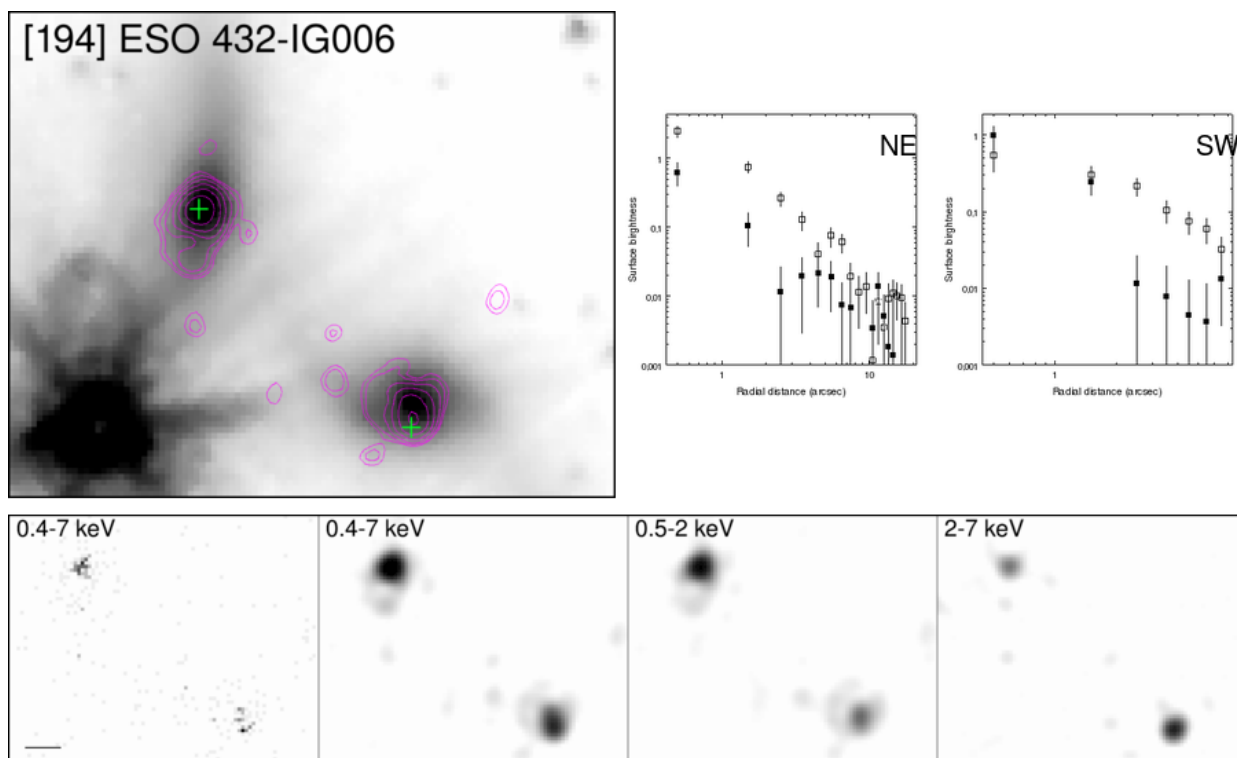


Fig. B.58. Overlay on IRAC channel 1. Contours: Interval 1.

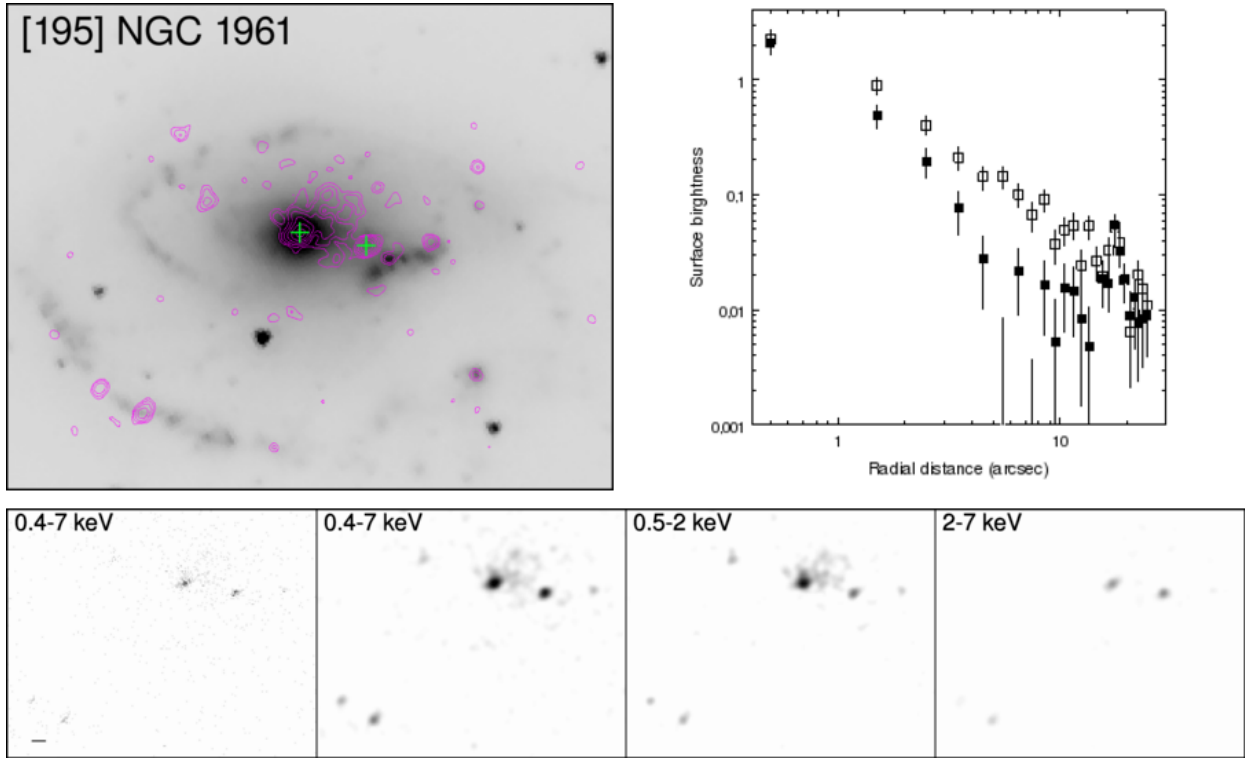


Fig. B.59. Overlay on IRAC channel 1. Contours: Interval 3

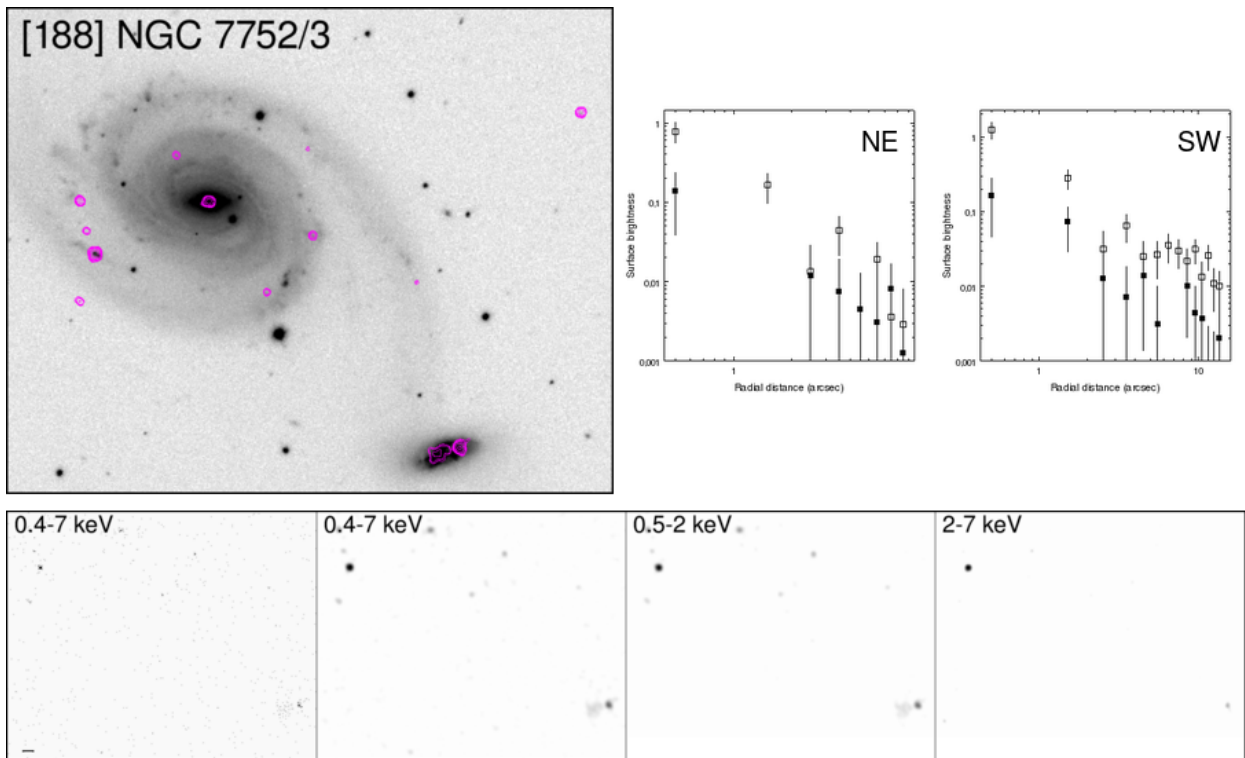
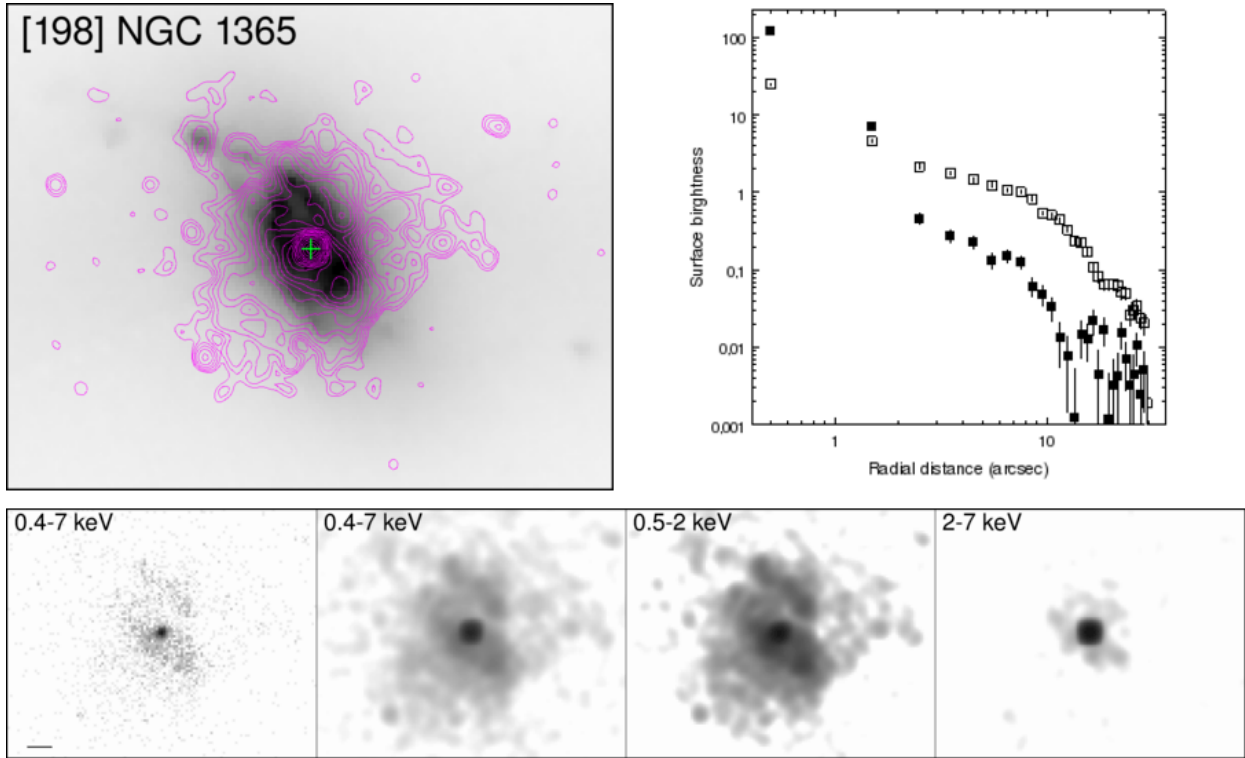
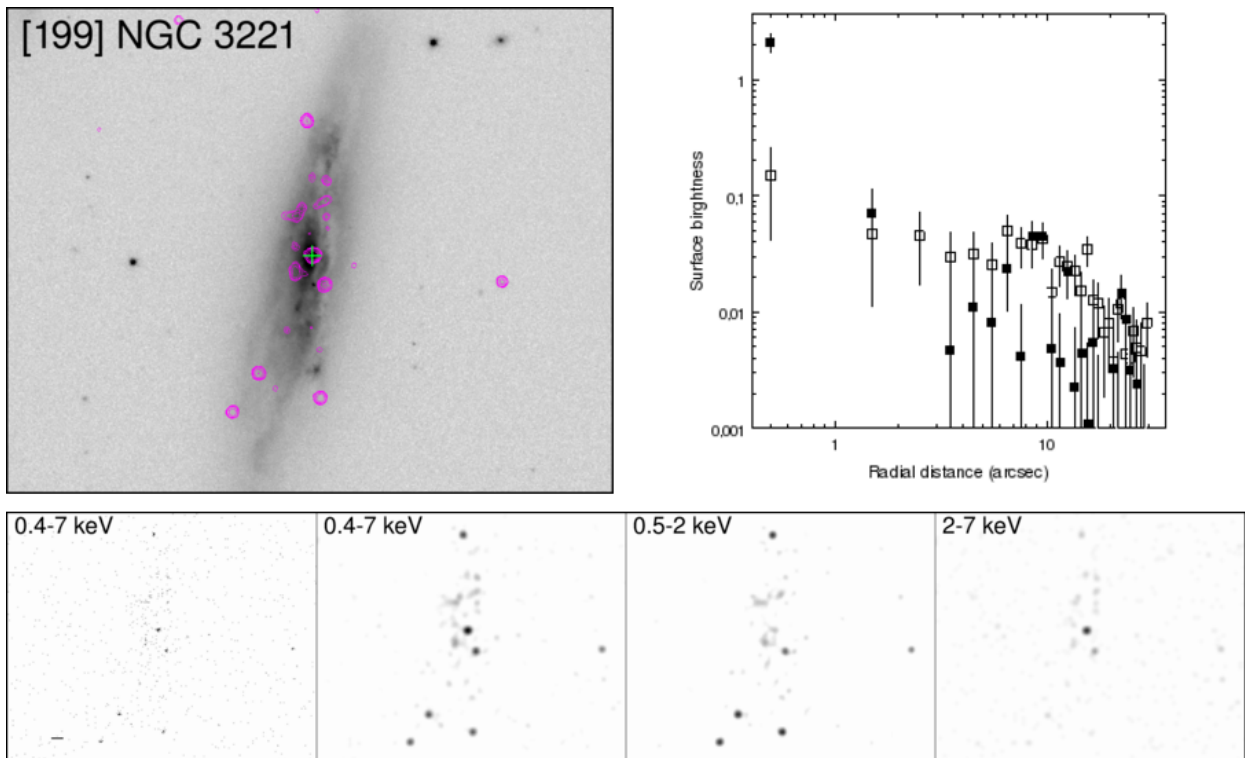


Fig. B.60. Overlay on SDSS DR-12 *i*-band. Contours: Interval 4.



**Fig. B.61.** *Overlay on IRAC channel 1. Contours: Custom.*



**Fig. B.62.** *Overlay on SDSS DR-12 i-band. Contours: Interval 1.*

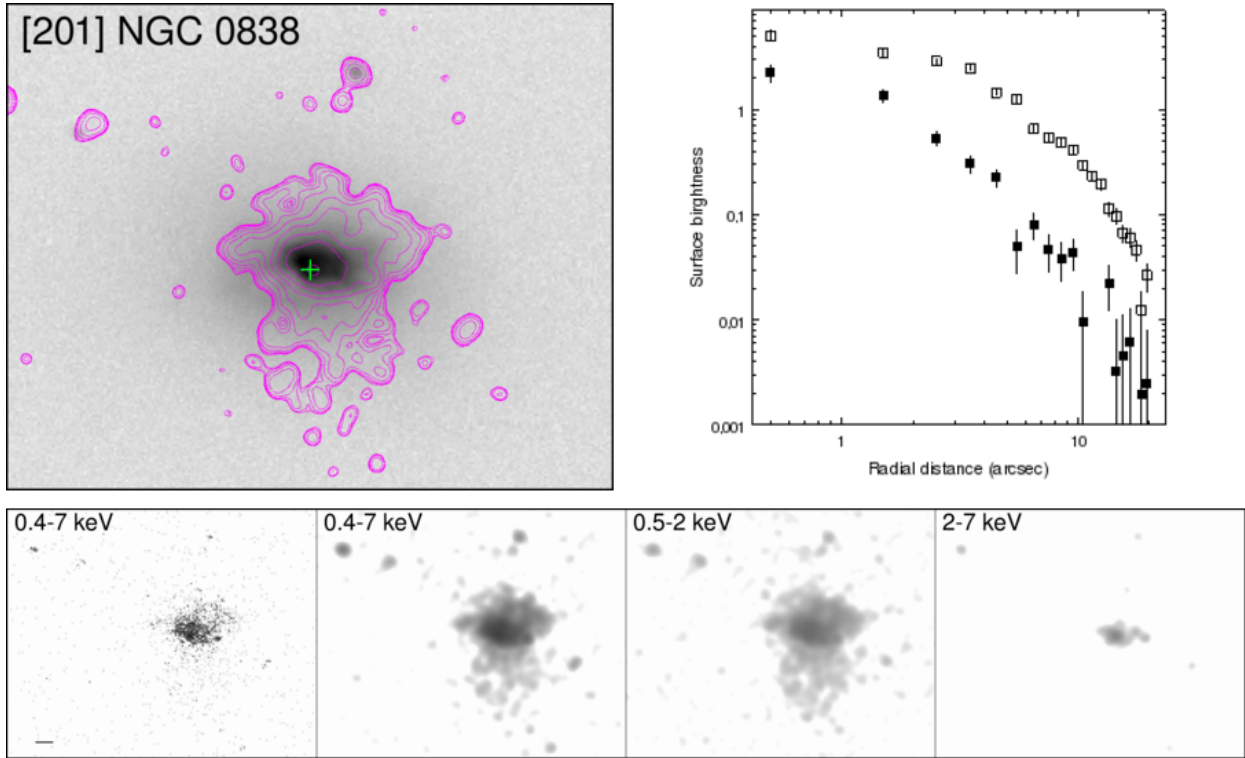


**Fig. B.63.** *Overlay on SDSS DR-12 i-band. Contours: Custom.*

Appendix C: X-ray spectra

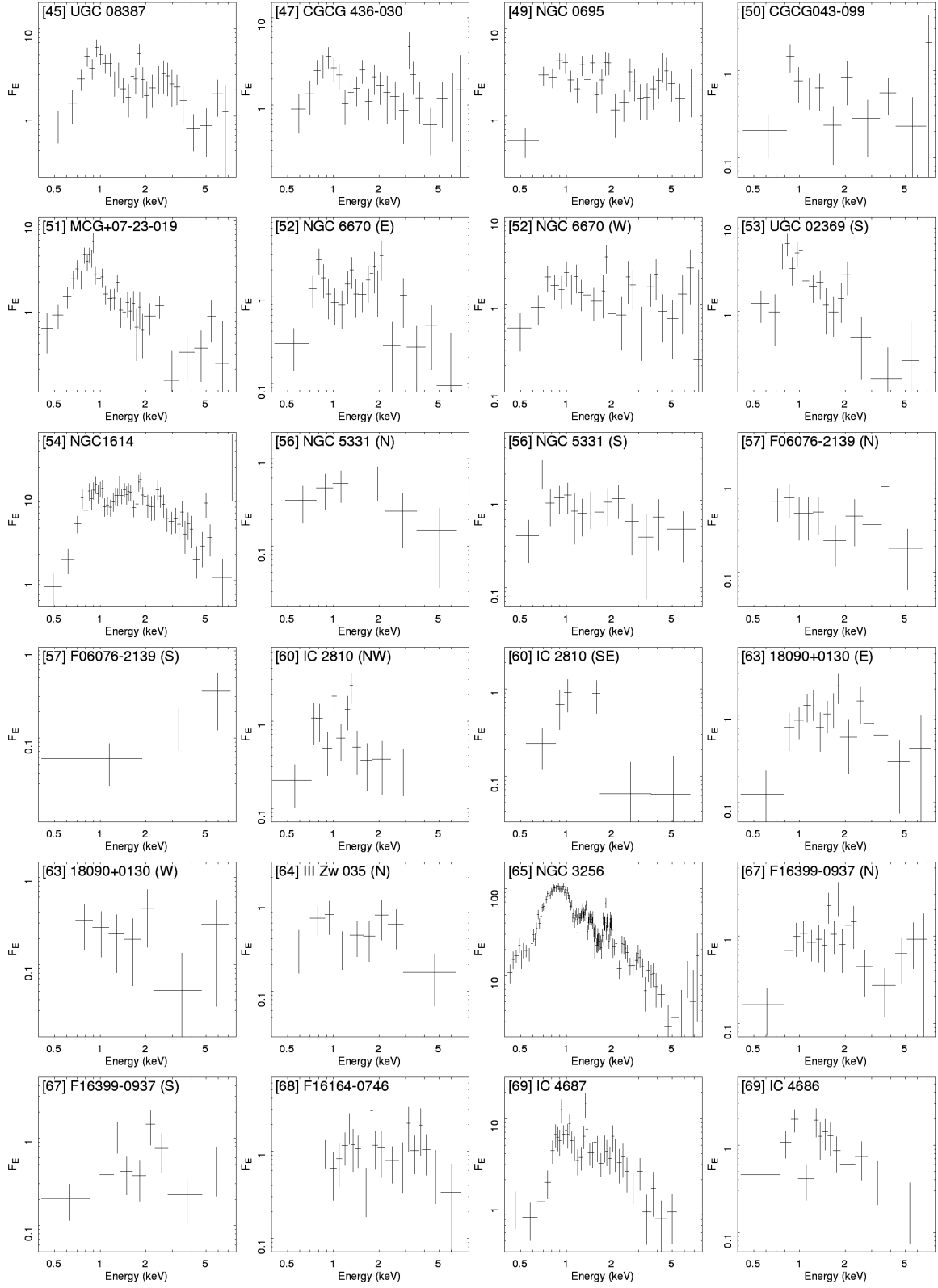


**Fig. C.1.** X-ray flux density spectra for the 84 individual galaxies of CGII, obtained from the *Chandra* ACIS. Flux density in units of  $10^{-14} \text{ erg s}^{-1} \text{ cm}^{-2} \text{ keV}^{-1}$ .

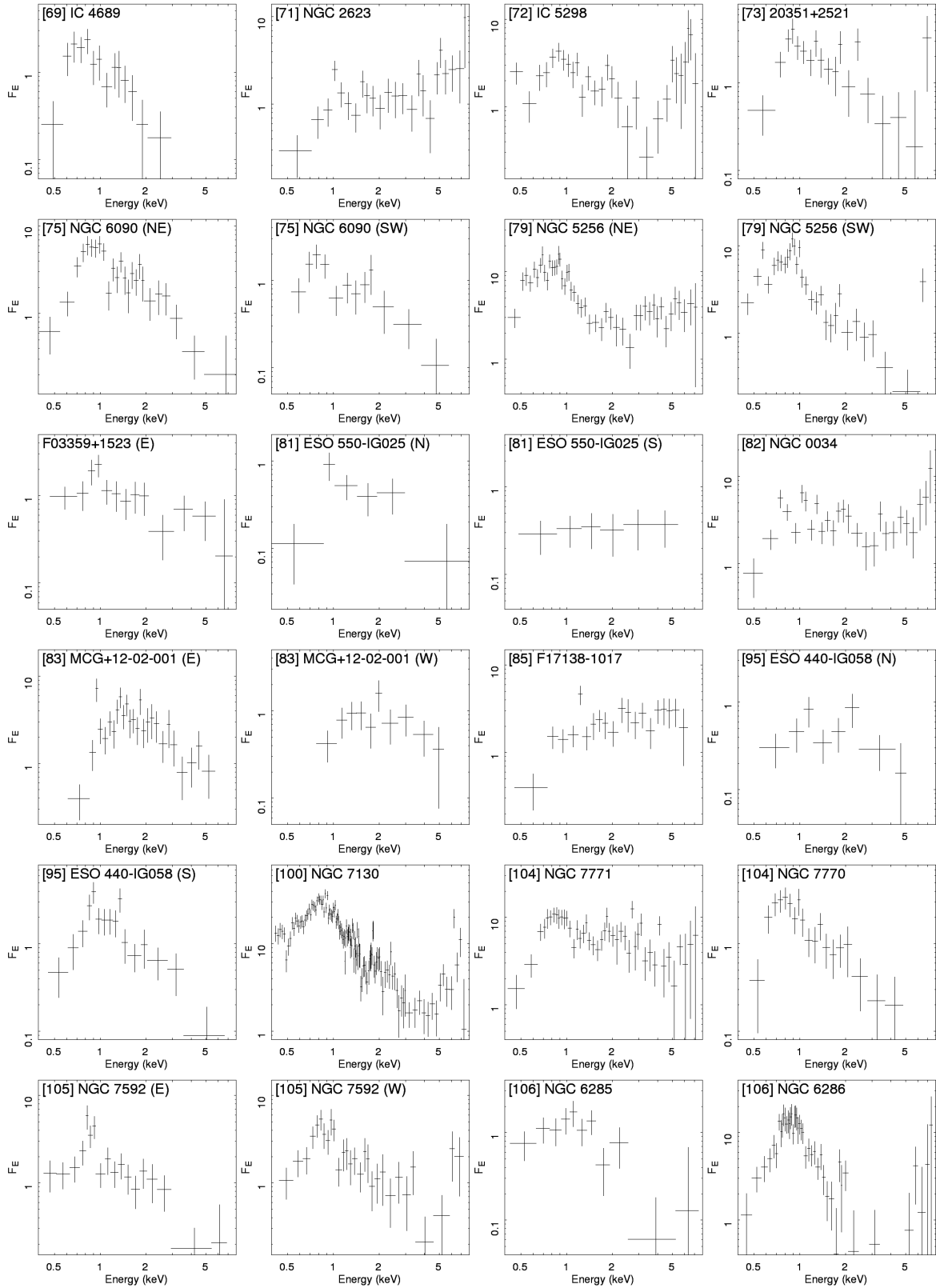


Fig. C.1. continued.

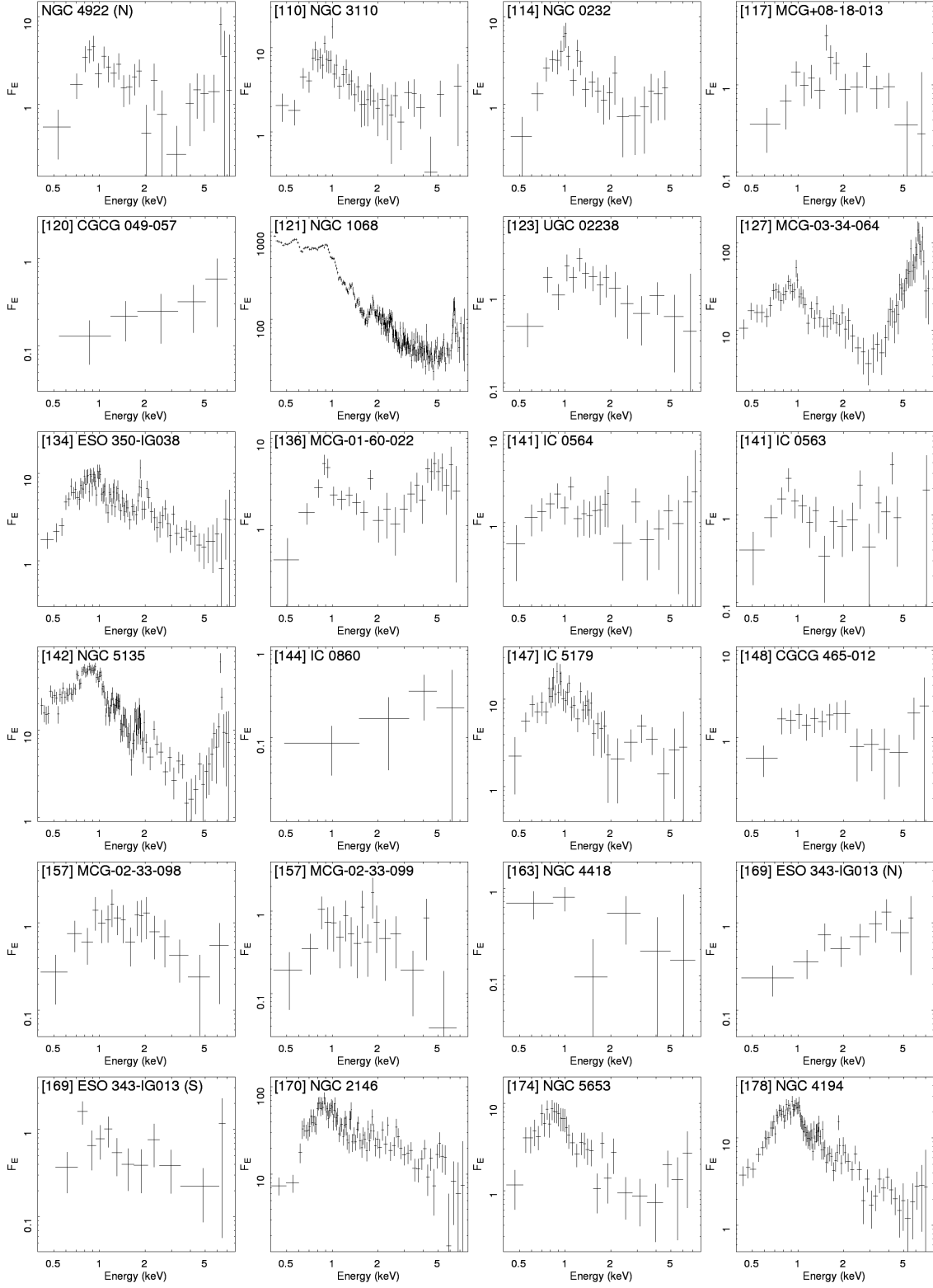


Fig. C.1: continued.

Fig. C.1. continued.

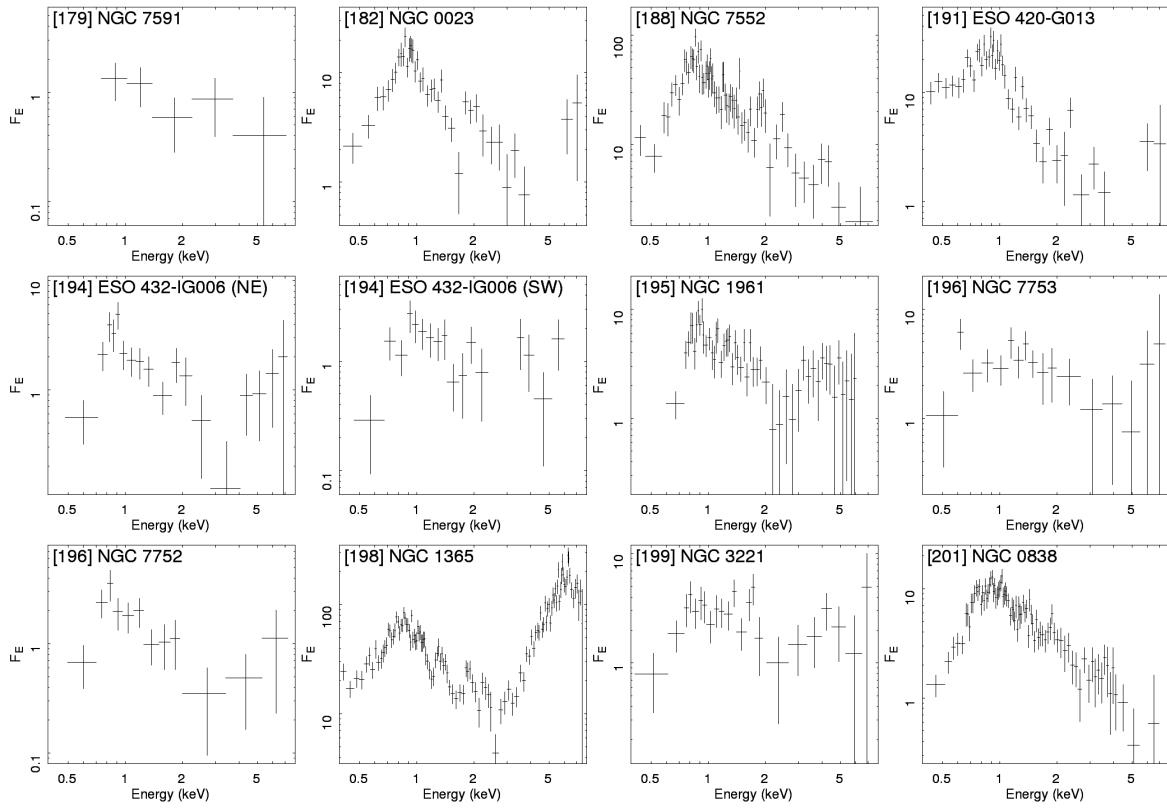


Fig. C.1. continued.

Part II

INTERACTION OF AGN JETS WITH STELLAR  
POPULATIONS



## COLLECTIVE NON-THERMAL EMISSION FROM AN EXTRAGALACTIC JET INTERACTING WITH STARS

---

In this chapter we present our work "Collective non-thermal emission from an extragalactic jet interacting with stars" (Vieyro, Torres-Albà, and Bosch-Ramon, 2017), in which we estimate the jet mass-loading and non-thermal emission caused by populations of stars. We model the winds of stars with high mass-loss rates; OB stars in LIRGs and red giants in elliptical galaxies. We estimate the likelihood of their presence having a dynamical impact on the jet and compute the SED of the emission that results from their interaction.



# Collective non-thermal emission from an extragalactic jet interacting with stars

Florencia L. Vieyro, Núria Torres-Albà, and Valentí Bosch-Ramon

Departament de Física Quàntica i Astrofísica, Institut de Ciències del Cosmos (ICC), Universitat de Barcelona (IEEC-UB),  
Martí i Franquès 1, 08028 Barcelona, Spain  
e-mail: fvieyro@fqa.ub.edu

Received 22 December 2016 / Accepted 29 March 2017

## ABSTRACT

**Context.** The central regions of galaxies are complex environments, rich in evolved and/or massive stars. For galaxies hosting an active galactic nucleus (AGN) with jets, the interaction of the jets with the winds of the stars within can lead to particle acceleration, and to extended high-energy emitting regions.

**Aims.** We compute the non-thermal emission produced by the jet flow shocked by stellar winds on the jet scale, far from the jet-star direct interaction region.

**Methods.** First, prescriptions for the winds of the relevant stellar populations in different types of galaxies are obtained. The scenarios adopted include galaxies with their central regions dominated by old or young stellar populations, and with jets of different power. Then, we estimate the available energy to accelerate particles in the jet shock, and compute the transport and energy evolution of the accelerated electrons, plus their synchrotron and inverse Compton emission, in the shocked flow along the jet.

**Results.** A significant fraction of the jet energy,  $\sim 0.1$ – $10\%$ , can potentially be available for the particles accelerated in jet-wind shocks in the studied cases. The non-thermal particles can produce most of the high-energy radiation on jet scales, far from the jet shock region. This high-energy emission will be strongly enhanced in jets aligned with the line of sight due to Doppler boosting effects.

**Conclusions.** The interaction of relativistic jets with stellar winds may contribute significantly to the persistent high-energy emission in some AGNs with jets. However, in the particular case of M 87, this component seems too low to explain the observed gamma-ray fluxes.

**Key words.** radiation mechanisms: non-thermal – galaxies: active – galaxies: nuclei – galaxies: jets

## 1. Introduction

Active galactic nuclei (AGN) are composed of a supermassive black hole that accretes material from the inner region of the galaxy host. Some AGN are associated with the production of collimated relativistic outflows or jets (e.g., Begelman et al. 1984). These jets propagate through complex environments, rich in stars, dust, gas, clouds, and even stellar clusters. It is very likely, then, that extragalactic jets interact with the obstacles present in the central region of galaxies. These interactions can affect the jet dynamically on different scales (e.g., Blandford & Koenigl 1979; Wang et al. 2000; Sutherland & Bicknell 2007; Jeyakumar 2009). For instance, the penetration of stars with strong winds inside the jet has been proposed as a possible mechanism for jet mass-loading and deceleration (e.g., Komissarov 1994; Bowman et al. 1996; Hubbard & Blackman 2006; Perucho et al. 2014).

In addition to jet dynamical effects, the presence of stars inside the jet can also lead to the generation of high-energy emission. The interaction of a relativistic jet with a powerful stellar wind produces a double bow-shock structure. The shock in the jet flow is a potential site of particle acceleration, and can contribute to the jet non-thermal emission. There have been several works exploring the gamma-ray emission, in the form of both steady radiation and transient events, due to jet-obstacle interactions (e.g., Dar & Laor 1997; Bednarek & Protheroe 1997; Beall & Bednarek 1999; Araudo et al. 2010), and in particular, due to jet-star interactions

(Barkov et al. 2010; Araudo et al. 2013; Bednarek & Banasiński 2015; de la Cita et al. 2016; Banasiński et al. 2016). There is also some direct and indirect evidence of jet-star interactions and jet mass-load by stellar winds (e.g., Müller et al. 2014; Wykes et al. 2013, 2015, and references therein).

Recent numerical simulations have shown that: (i) the effective surface of the shock induced by an obstacle is larger than the obstacle section, increasing the conversion of kinetic energy into internal energy; and (ii) Doppler boosting has to be taken into account even for standing shocks (Bosch-Ramon 2015; de la Cita et al. 2016). In addition, it has been found that for jet-star interactions taking place at relatively large distances from the central source, say  $\gtrsim$ pc-scale, accelerated particles are not strongly cooled close to the shock. In fact, the non-thermal particles can cover distances similar to the jet height without significant energy loss (Bednarek & Banasiński 2015; de la Cita et al. 2016). Regarding the most likely radiation mechanisms, in the jet's innermost regions, hadronic processes cannot be discarded, but in general leptonic emission, namely synchrotron and inverse Compton (IC), will be more efficient in less extreme environments (see Barkov et al. 2012b,a; Khangulyan et al. 2013, for related discussions).

In this work, we study the collective, steady, leptonic, high-energy radiation resulting from the interaction of an AGN jet with different stellar populations. We compute the non-thermal radiation produced at the scale of the jet, and do not consider in detail the radiation component originated on the smaller

scales of the jet-wind interaction structure. The jet-wind interaction region was investigated for individual interactions in [de la Cita et al. \(2016\)](#), its emission being roughly generalized for many encounters for the radio galaxy M 87 in [Bosch-Ramon \(2015\)](#). A detailed study of the extended jet emission as the result of the stellar population in the radiogalaxy Centarus A was conducted by [Wykes et al. \(2015\)](#). This study mostly focused on the presence of red giant stars in the host galaxy.

Here, we aim at analyzing the relevance of the jet-scale high-energy emission contribution for different types of galaxy hosts, namely characterized either by old or young stellar components. Our treatment of the problem includes relativistic beaming and accounts for the effective increase in the shock area, which are effects that were not taken into account before when computing the contribution to high-energy emission from collective jet-star interactions on jet scales. We disregard, at this stage, the effects of strong anisotropy in the stellar spatial distribution at the galaxy center, which may influence the number of available stars interacting with the jet.

The article is organized as follows: in Sect. 2, the stellar populations in the central regions of two types of galaxy are characterized; Sect. 3 contains a description of the jet model; in Sect. 4, we outline the properties of three different galaxy hosts; Sect. 5 presents an estimate of the apparent non-thermal emission for the galaxies studied; whereas Sect. 6 presents accurate calculations of the transport of relativistic electrons along the jet, and a computation of their high-energy emission. The results are presented in Sect. 7, and the conclusions in Sect. 8.

## 2. Characterization of the stellar populations interacting with AGN jets

This work is one of the first approximations to the problem of large-scale emission from jet-star interactions (see also [Bednarek & Banasiński 2015](#); [Wykes et al. 2015](#)), and for this reason two different scenarios are adopted for the types of AGN galaxy host studied: a star-forming galaxy with a dense disk of molecular gas surrounding the nucleus in which the star formation rate (SFR;  $\dot{M}_{\text{SFR}}$ ) is very high; and a massive galaxy with an old stellar population distributed in a bulge. More detailed studies of specific sources, or a mixed galaxy with a large population of evolved stars plus a high SFR, are left for future work.

### 2.1. Effect on the non-thermal energy budget

We characterize the stellar populations inside the jet to obtain the luminosity injected in the form of accelerated particles at the jet-star interactions. This non-thermal luminosity can be estimated as

$$L_{\text{NT}} = \int \int \eta_{\text{NT}} L_j \left\langle \frac{S_s(m, t)}{S_j} \right\rangle n_s(m, z) dm dz, \quad (1)$$

where  $\eta_{\text{NT}}$  is the fraction of jet energy that crosses the effective interaction area  $S_s$  that is converted into non-thermal particle energy,  $L_j$  the jet luminosity,  $n_s(m, z)$  the (assumed stationary) stellar number density,  $m$  the stellar mass,  $z$  the jet height,  $t$  the time, and  $\frac{S_s(m, t)}{S_j}$  (or  $\langle \frac{S_s(m, t)}{S_j} \rangle$ ) the (time average of the) fraction of jet area intercepted by one stellar interaction.

One can integrate over the height of the jet the quantity:

$$\sigma_T = \int \int \left\langle \frac{S_s(m)}{S_j} \right\rangle n_s(m, z) dm dz. \quad (2)$$

If the value of  $\sigma_T$  is much higher than 1, it can be an indicator that the interaction is dynamically relevant for the jet, as all its section will be shaded by collisions with stars and their winds. In addition,  $\sigma_T \gg 1$  would mean that the jet-star collisions should take place in the wake of (many) other collisions further upstream of the jet.

When the jet interacts with a stellar wind, a double bow-shock is generated. The stagnation point is defined as the point where the wind and jet ram pressures are equal, and is located at a distance  $R_s$  from the star. This can define a section for the interaction with the jet,  $S_s = \pi R_s^2$ . However, it has been shown using hydrodynamical simulations that kinetic energy is converted into internal energy at larger distances from the star. This implies that the dynamical interaction is effective significantly farther from the star than  $R_s$  with respect to kinetic energy dissipation, increasing the effective area of the shock by a factor  $A = 10\text{--}100$  ([Bosch-Ramon 2015](#)). The pressures at the stagnation point for the stellar wind and for the jet are:

$$P_s = \rho v_w^2 = \frac{\dot{M} v_w}{4 \pi R_s^2}, \quad P_j \simeq \frac{L_j}{c S_j}, \quad (3)$$

respectively, where  $c$  is the speed of light,  $\dot{M}$  the stellar mass-loss rate, and  $v_w$  the stellar wind speed. At the stagnation point,  $P_s = P_j$ , thus

$$\frac{S_s(m, t)}{S_j} = \frac{A \pi R_s^2(m, t)}{\pi R_j^2} = \frac{A c \dot{M}(m, t) v_w(m, t)}{4 L_j}. \quad (4)$$

Consequently, for  $\sigma_T < 1$ , the non-thermal luminosity injected into the jet depends on the stellar density, wind velocity and mass-loss rate, that is, it does not depend on the jet power. The stars with high momentum rates ( $\dot{M} v_w$ ) are the most relevant for the interaction. Therefore, we focus here on high-mass stars for high-SFR AGN galaxies, and post-main sequence low-mass stars for massive AGN host galaxies with an old stellar population; for simplicity, both groups are modeled as main sequence OB stars, and red giants at different stages of evolution, respectively. Therefore, particularly high mass-loss phases of stars (supergiant, Wolf-Rayet, luminous blue variable, asymptotic giant branch) are not considered as they would be relatively rare, despite their impact being possibly dominant should they interact with the jet not far from its base.

### 2.2. OB stars in star-forming galaxies

Massive star-forming galaxies, such as ultra-luminous and luminous infrared galaxies (ULIRGs and LIRGs), can have SFR of hundreds to a thousand solar masses per year (e.g., [Sanders & Mirabel 1996](#)). Studies of nearby ULIRGs have shown that these galaxies tend to concentrate most of the star formation in inner circumnuclear disks, of a few hundreds of parsec in radius and approximately a hundred parsec in height (e.g., [Medling et al. 2014](#)). In such disks, the SFR can be as high as a few hundred solar masses per year (e.g., [Downes & Solomon 1998](#); [Teng et al. 2014](#)). We consider here that the stellar population interacting with the jet is composed of young OB stars, being formed at the high rates typical of U/LIRGs, and distributed homogeneously in a circumnuclear disk.

#### 2.2.1. Stellar number density

The number of stars being formed per unit of mass, time and volume ( $V$ ) is  $\phi(m, r, t)$ , which actually does not depend on location

(i.e., radius  $r$  from the galaxy centre in spherical coordinates) for a homogeneous spatial distribution. Assuming that the SFR is constant in time (see Araudo et al. 2013), a homogeneous spatial distribution of stars within the disk, and a power-law dependence on the mass,  $\phi(m, r, t)$  can be expressed as:

$$\phi = K \left( \frac{m}{M_\odot} \right)^{-x}, \quad (5)$$

where  $x \sim 2.3$  in the  $0.1 \leq m/M_\odot \leq 120$  range considered (Salpeter 1955; Kroupa 2001), and  $K$  is a normalization constant with units  $[K] = M_\odot^{-1} \text{ yr}^{-1} \text{ pc}^{-3}$ . The star formation rate is  $\dot{M}_{\text{SFR}} = \iint \phi m \, dm \, dV$ :

$$\dot{M}_{\text{SFR}} = K \pi R_d^2 h_d \int_{0.1 M_\odot}^{120 M_\odot} \left( \frac{m}{M_\odot} \right)^{-x+1} dm, \quad (6)$$

where  $R_d$  is the stellar disk radius and  $h_d$  the total disk thickness. Along with  $\dot{M}_{\text{SFR}}$ , these quantities can be known for a given galaxy; thus, the constant  $K$  can be obtained.

As stars are being born, they accumulate in the galaxy. For stars of masses such that  $t < t_{\text{life}}$ , where  $t_{\text{life}}$  is the stellar lifetime, the density of stars is

$$n_s(m) = \int_0^t \phi(t', m) dt' \approx \phi(t=0) \cdot t. \quad (7)$$

For  $t > t_{\text{life}}$ , the massive stars have started to die, and the distribution becomes steeper than  $-2.3$ . Then, the stellar density becomes  $n_s(m) = \phi(m, t=0) \cdot t_{\text{life}}(m)$ , with

$$t_{\text{life}}(m) = 10^a \left( \frac{m}{M_\odot} \right)^{-b} \text{ yr}. \quad (8)$$

We consider  $a = 9.9$ ,  $b = 2.9$  in the range  $1.25 \leq m/M_\odot \leq 3$ ;  $a = 9.6$ ,  $b = 2.4$  in  $3 \leq m/M_\odot \leq 7$ ;  $a = 9.1$ ,  $b = 1.8$  in  $7 \leq m/M_\odot \leq 15$ ;  $a = 8.0$ ,  $b = 0.8$  in  $15 \leq m/M_\odot \leq 60$ ; and  $t_{\text{life}} \approx 0.004 \text{ Gyr}$  at  $m > 60 M_\odot$  (Ekström et al. 2012).

### 2.2.2. Mass-loss rate and wind speed

To estimate  $S_s(m)$ , assumed constant in time for an OB main sequence star, it is necessary to know  $\dot{M}$  and  $v_w$ . We follow the prescriptions in Vink et al. (2000) derived for OB stars. For O stars ( $16 \leq m/M_\odot \leq 120$ ),

$$\begin{aligned} \log \dot{M}(m) = & -6.7 + 2.2 \log(L_s/10^5 L_\odot) - 1.3 \log(m/30 M_\odot) \\ & - 1.2 \log\left(\frac{v_w/v_{\text{esc}}}{2}\right) + 0.9 \log(T_{\text{eff}}/40\,000 \text{ K}) \\ & - 10.9 [\log(T_{\text{eff}}/40\,000 \text{ K})]^2 + 0.85 \log(Z/Z_\odot), \end{aligned} \quad (9)$$

where  $L_s$ ,  $T_{\text{eff}}$ , and  $Z$  are the luminosity, effective temperature, and metallicity of the star, respectively. The terminal wind velocity of the stars in this range is  $v_w \approx 2.6 v_{\text{esc}}$ .

For B stars ( $2 \lesssim m/M_\odot \leq 16$ ),

$$\begin{aligned} \log \dot{M}(m) = & -6.7 + 2.2 \log(L_s/10^5 L_\odot) - 1.3 \log(m/30 M_\odot) \\ & - 1.6 \log\left(\frac{v_w/v_{\text{esc}}}{2}\right) + 1.1 \log(T_{\text{eff}}/20\,000 \text{ K}) \\ & + 0.85 \log(Z/Z_\odot). \end{aligned} \quad (10)$$

The terminal wind velocity of the stars in this range is  $v_w \approx 1.3 v_{\text{esc}}$  for  $T_{\text{eff}} > 12\,500 \text{ K}$ , and it drops to  $v_w \approx 0.7 v_{\text{esc}}$  for  $T_{\text{eff}} < 12\,500 \text{ K}$  (Lamers et al. 1995).

Simple dependencies of the parameters with the stellar mass are assumed:  $L_s \propto m^{3.5}$  in the  $2 \leq m/M_\odot \leq 50$  range,  $L_s \propto m$  in the  $50 \leq m/M_\odot \leq 120$  range,  $R_s \propto m^{0.6}$ , and  $T_{\text{eff}} = \left( \frac{L_s}{4\pi\sigma R_s^2} \right)^{1/4}$ .

Metallicity was measured by Huo et al. (2004) in the central regions of some nearby ULIRGs, among them one of the objects studied in this work, Mrk 231, obtaining values of  $Z \approx Z_\odot$ . We assume here solar metallicity for ULIRG-type galaxies, which implies that the last term in Eqs. (9) and (10) does not contribute to the mass loss of their stars. It would have a significant impact, however, when deriving mass-loss rates for massive stars in environments significantly metal-poorer than our own galaxy (e.g., ULIRGs at  $z \sim 2-3$ ).

The prescriptions given above do not account for two known discrepancies between theoretical and observational mass-loss rates: clumping, and the weak-wind problem. Wind-clumping refers to density inhomogeneities in the stellar wind, and not considering them causes an overestimation of the mass-loss rates that can amount to factors of 2 to 10, depending on the specific diagnostics used to derive the observational values (Puls et al. 2008). Analytical models need to be corrected by the square root of the Clumping factor ( $\dot{M}_{\text{cl}} = \dot{M} \cdot f_{\text{cl}}^{-1/2}$ ) before being adjusted to observational data. Comparisons with the Vink et al. (2000) model, which does not account for clumping, find discrepancies between the theoretical model and empirically derived mass-loss rates of a factor 2–3 lower (e.g., Šurlan et al. 2013; Sundqvist et al. 2011; Smith 2014). Puls et al. (2008) suggest a maximum correction for theoretical models of a factor of 2. In order to be conservative, we reduce the mass-loss rate values given by Eqs. (9) and (10) by a factor of 3.

The weak-wind problem refers to the fact that empirically derived mass-loss rates for late O-early B-type stars might be a factor 10–100 lower than theoretically expected. The first statistically relevant evidence was provided by Chlebowski & Garmany (1991), and was confirmed by many later studies using UV line diagnostics (see Puls et al. 2008, and references therein). However, later results show that the weak-wind problem is reduced or eliminated when taking into account a hotter component of the wind, as the wind is not weak, but its bulk is only detectable in X-rays (e.g., Huenemoerder et al. 2012). Still, a reduction of a factor of 3 in the mass-loss rates of massive O-types to account for clumping, and a reduction of a factor of 10 for late O-early B-type stars to account for both clumping and weak winds, is suggested in a review by Smith (2014).

When applying Eqs. (9) and (10), we correct by a factor of 3 for clumping, and leave the weak-wind problem uncorrected due to the still unknown optimal reduction factor. However, as seen in Fig. 1, where a quantity  $\propto m \times dL_{\text{NT}}/dm$  is shown, stars with masses below  $40 M_\odot$  do not contribute significantly to the non-thermal luminosity; and the weak-wind problem would start to be significant for stars of spectral type O7–O8, which have masses of  $\sim 25-28 M_\odot$  (Smith 2014). Therefore, for this study, correcting for weak winds becomes unnecessary.

Following the given prescriptions and assumed dependencies, the mass-loss rate depends only on the mass. One can compute a weighted average over the mass that is independent of the SFR or the physical characteristics of a particular galaxy. This is valid as long as enough stars of a given mass are present to be treated as a continuum distribution to the needed degree of

accuracy. The average mass-loss rate is

$$\langle \dot{M} \rangle = \frac{\int \dot{M}(m)n_s(m)dm}{\int n_s(m)dm} = 3.4 \times 10^{-9} M_\odot \text{ yr}^{-1}, \quad (11)$$

in the considered  $2 \leq m/M_\odot \leq 120$  range. Following the same procedure, a mass-averaged wind momentum can be derived:  $\langle \dot{M}v_w \rangle = 9.0 \times 10^{25} \text{ g cm s}^{-2}$ .

The total number of stars with masses  $\geq 40 M_\odot$  within the jet, for any given galaxy is

$$N_{\text{OB}} = 13 \left( \frac{\dot{M}_{\text{SFR}}}{100 M_\odot \text{ yr}^{-1}} \right) \left( \frac{h_d}{100 \text{ pc}} \right)^2 \left( \frac{300 \text{ pc}}{R_d} \right)^2 \left( \frac{\theta}{0.1} \right)^2, \quad (12)$$

where  $\theta$  is the jet opening angle. Despite the fact that we adopt the continuum distribution assumption here, this result shows that it is only marginally valid.

### 2.3. Red giants in elliptical galaxies

Elliptical galaxies have in general very low SFRs, and therefore do not have a significant population of young OB stars that can interact with the jet. However, red giants can have high mass-loss rates, in the range of  $\sim 10^{-10} - 10^{-5} M_\odot \text{ yr}^{-1}$  (Reimers 1975), and are abundant in this type of galaxies.

In the characterization of elliptical galaxies we assume the red giants to be distributed in an inner spherical bulge, with a density that decays as a power-law with the radial distance from the galaxy center. We also assume that there is no on-going star formation.

#### 2.3.1. Stellar number density

Knowing the mass profile of any particular elliptical galaxy, we can estimate the total mass of stars contained inside the bulge ( $M_T$ ). Then we use the Salpeter initial mass function (IMF) and normalize it to the total mass of stars:

$$M_T = K \frac{4}{3} \pi R_b^3 \int_{0.1 M_\odot}^{m_2} \left( \frac{m}{M_\odot} \right)^{-x+1} dm, \quad (13)$$

with  $x = -2.3$ , and where  $R_b$  is the radius of the spherical bulge, and  $m_2$  the mass of the stars in the galaxy exiting the red giant phase in the lifetime of the galaxy, that is, the largest stellar mass available.

Knowing the lifetime of a galaxy ( $t_{\text{gal}}$ ), the red giants in the galaxy are those with masses between  $m_1$  and  $m_2$ , with  $m_1 = m(t_{\text{lifetime}} = t_{\text{gal}})$  being the mass of the stars entering the red giant phase at a time equal to the age of the galaxy, and  $m_2 = m(t_{\text{lifetime}} = t_{\text{gal}} - t_{\text{rg}})$  being the mass of the stars which entered the red giant phase exactly one red-giant lifetime before. We assume the lifetime of a red giant to be  $\sim 5\%$  of the main sequence lifetime, and thus fix  $t_{\text{rg}} = 0.05 t_{\text{gal}}$ . We note that this approach assumes that all stars have been formed a time  $t_{\text{gal}}$  ago, that is star formation extended in time is not considered. Some stars may have formed later, which would enter the red giant phase at  $t_{\text{gal}}$  with higher masses, and would then lose more mass in the red giant phase.

Since the lifetime of a galaxy is much larger than the lifetime of a red giant,  $m_1$  and  $m_2$  will be very similar. For a lifetime similar to that of the Milky Way, these masses are  $\approx 0.83 M_\odot$ . Then, we obtain the total number of red giants as:

$$N_T = K \frac{4}{3} \pi R_b^3 \int_{m_1}^{m_2} \left( \frac{m}{M_\odot} \right)^{-x} dm. \quad (14)$$

Since all the red giants have very similar masses, and the total number of them is given by Eq. (14), together with the fact that their mass-loss rate and wind velocities are mass-independent (see Sect. 2.3.2), there is no need to maintain a mass dependency on the number density. However, in this case, since we are considering a large and spherical bulge, there is a decay of the density with radial distance/jet height ( $z$ ), that is,  $n_s(z) \propto N_T/z^\xi$ . We assume this dependence to be a power law, and consider two values for the index  $\xi$ :  $\xi = 1$ , which is the stellar index estimated for M 87 (derived from Gebhardt & Thomas 2009), and  $\xi = 2$  for comparison.

#### 2.3.2. Mass-loss rate and wind speed

The mass-loss rate of a red giant depends on its luminosity and radius, following:

$$\dot{M} = 4 \times 10^{-13} \left( \frac{L}{L_\odot} \right) \left( \frac{g_\odot}{g} \right) \left( \frac{R_\odot}{R} \right) M_\odot \text{ yr}^{-1}, \quad (15)$$

where  $g$  is the stellar surface gravity (Reimers 1975). As a red giant evolves, more hydrogen from the  $H$ -burning shell surrounding the core turns into helium, increasing the mass of the  $He$ -core, and the stellar radius and luminosity. Therefore, the mass-loss rate has a time dependence for a red giant star.

Joss et al. (1987) provide a fit, based on numerical models, to the core mass-luminosity relation for red giants with core masses in the range of  $0.17 M_\odot \leq m_c \leq 1.4 M_\odot$ :

$$L(m_c) \simeq \frac{10^{5.3} \mu^6}{1 + 10^{0.4} \mu^4 + 10^{0.5} \mu^5} L_\odot, \quad \mu \equiv \frac{m_c}{M_\odot}, \quad (16)$$

and a fit to the core mass-radius relation in the same range:

$$R(m_c) \simeq \frac{3.7 \times 10^3 \mu^4}{1 + \mu^3 1.75 \mu^4} R_\odot. \quad (17)$$

As all the red giant stars in the galaxy have a very similar mass, we consider them all to have the same initial core mass, and consequently the exact same mass-loss rate as a function of time. The time dependence can be introduced when considering that the dominant energy source in red giants is the p-p chain, with a  $\sim 0.7\%$  efficiency, and the  $He$ -core mass increases as hydrogen burns into helium according to (Syer & Ulmer 1999):

$$L(m_c) \simeq 0.007 M_\odot c^2 \dot{\mu}. \quad (18)$$

The core-mass range considered in this work is  $0.17 - 0.43 M_\odot$ : starting with an initial core mass that corresponds to the lower limit of the range for which Eqs. (16) and (17) are fitted, and stopping at a value for which the radius, mass-loss and lifetime of the red giant are reasonable ( $R_f \sim 110 R_\odot$ ,  $\dot{M}_f \sim 5 \times 10^{-8} M_\odot \text{ yr}^{-1}$  and  $t_{\text{rg}} \sim 7.3 \times 10^8 \text{ yr}$ ). These values are limited by the considered initial mass of the star, as the sum of the final core mass and total mass lost cannot exceed it. Unlike with OB stars, Eq. (15) does not include a metallicity dependence. Red giants are assumed here to lose along their lifetime all the mass that does not go into the core, independently of metallicity, and therefore the final average mass-loss rate is the same regardless of the specific effects of metallicity on the  $\dot{M}(t)$ -curve.

Wind speeds of red giants are relatively low, typically  $\leq 10^7 \text{ cm s}^{-1}$  (e.g., Crowley 2006; Espey & Crowley 2008). In this work we take, for simplicity,  $v_w = 10^7 \text{ cm s}^{-1}$ , considering it constant during the star evolution.

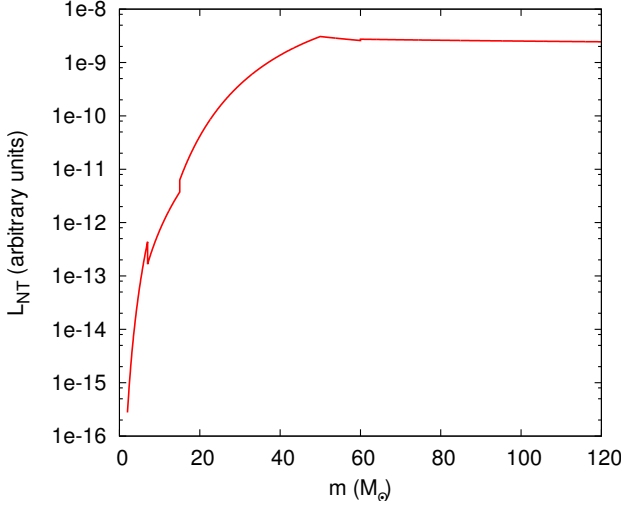


**Fig. 1.** Contribution to the non-thermal luminosity injected into the jet through stellar interactions for different stellar masses of OB stars.

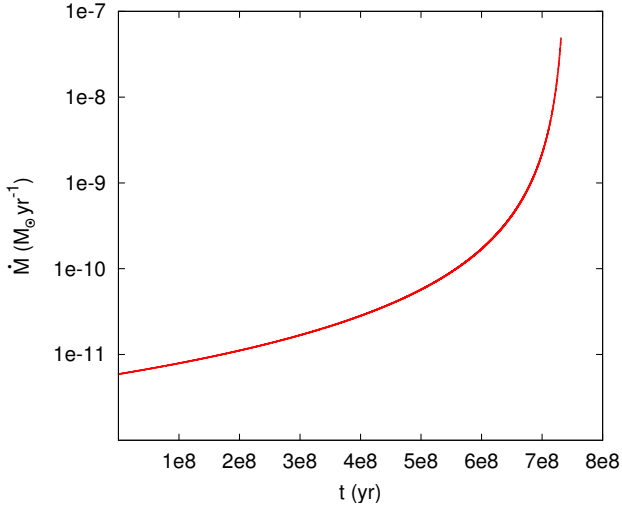


**Fig. 2.** Mass-loss rate as a function of time for a red giant with a core mass ranging from  $0.17 M_{\odot}$  to  $0.43 M_{\odot}$ , in a lifetime of  $\sim 7.3 \times 10^8$  yr.

As seen in Fig. 2, the latter stages of the life of a red giant ( $\sim 0.01 t_{\text{rg}}$ , which means,  $\sim 1\%$  of red giants within the jet) contribute most significantly to the mass-loss rate and, therefore, to the injected non-thermal luminosity. For Eqs. (1) and (4), as the mass-loss rate and wind speed are mass-independent, they can both be used as constants if  $\langle \dot{M} \rangle$  is time-averaged:

$$\langle \dot{M} \rangle = \frac{\int \dot{M}(t) dt}{t_{\text{rg}}} = 5.7 \times 10^{-10} M_{\odot} \text{ yr}^{-1}. \quad (19)$$

Then, taking the considered constant value for the wind speed, we obtain an average wind momentum of  $\langle \dot{M} v_w \rangle = 3.6 \times 10^{23} \text{ g cm s}^{-2}$ .

### 3. Jet model

We adopt a jet with a conical geometry, that is, a constant opening angle  $\theta$ , which is launched at a distance  $z_0$  above the supermassive black hole in the center of the galaxy. The radius of the

jet is a function of the distance  $z$  to the black hole:

$$R_j(z) = \theta z. \quad (20)$$

Assuming equipartition between the magnetic field and the jet total energy density, the magnetic field in the jet base would be

$$\frac{B_0^2}{8\pi} = \frac{1}{2} \frac{L_j}{\pi R_j(z_0)^2 c}, \quad (21)$$

where  $B_0 = B(z_0)$ . The magnetic field decreases with  $z$  according to

$$B(z) = B_0 \left( \frac{z_0}{z} \right)^m, \quad (22)$$

with  $1 \leq m \leq 2$ , depending on the topology of the magnetic field.

Polarization angles from blazars are found to be either nearly transverse or nearly parallel to the jet axis; this dualism is consistent with magnetic fields that are intrinsically oblique, but the observed directions are altered by relativistic effects (Marscher et al. 2002). For toroidal and poloidal fields comparable in the jet frame, since  $B_{\phi}/B_z \geq \Gamma$ , a relativistic jet would be dominated by the toroidal magnetic field in the observer frame (Lyutikov et al. 2004).

In this work, we parametrize the magnetic pressure through a fraction  $\zeta_{\text{eq}}$  of the equipartition value. Also, in most cases the magnetic field is assumed to be predominantly perpendicular to the flow motion, so we adopt  $m = 1$  (Spruit 2010). Therefore, in the flow frame one obtains

$$B'_{\phi}(z) = \frac{1}{\Gamma z} \sqrt{\frac{4\zeta_{\text{eq}} L_j}{\theta^2 c}}, \quad (23)$$

where  $\Gamma$  is the jet bulk Lorentz factor, which is considered to be constant. We consider two cases:  $\zeta_{\text{eq}} = 1$ , which means that  $B(z)$  is in equipartition, and  $\zeta_{\text{eq}} = 10^{-2}$  as an example of a magnetic field below equipartition. In the case where we consider a dominant poloidal field,  $m = 2$  (see Sect. 7; a poloidal magnetic field decays faster than a toroidal field with  $z$ ), we take into account that it remains invariant between the observer and jet frames, that is  $B_z(z) = B'_z(z)$ .

## 4. Galaxy hosts

The prescriptions described in Sect. 2 and the jet model described in Sect. 3 are applied to specific galaxy types to estimate the contribution of jet-star interactions to high-energy radiation in realistic contexts.

### 4.1. Elliptical galaxy: M87

As a fiducial elliptical galaxy, we consider the case of M87. The galaxy bulge has a radius of  $\sim 40''$  (Harris et al. 1999), which corresponds to  $R_b \sim 3.1$  kpc. Knowing the bulge size, we estimate the total mass contained within it from Gebhardt & Thomas (2009), and determine the total number of red giants using Eqs. (13) and (14). The number of red giants within the bulge is  $\approx 1.3 \times 10^9$ .

The jet in M87 has a luminosity of  $L_j = 10^{44} \text{ erg s}^{-1}$  (Owen et al. 2000), an inclination angle of  $20^\circ$  (Acciari et al. 2009), and an opening angle of  $\sim 0.1$  rad (Biretta & Meisenheimer 1993; Doeleman et al. 2012). Taking this aperture, the number of red giants within the jet would be  $\sim 3.2 \times 10^6$ .

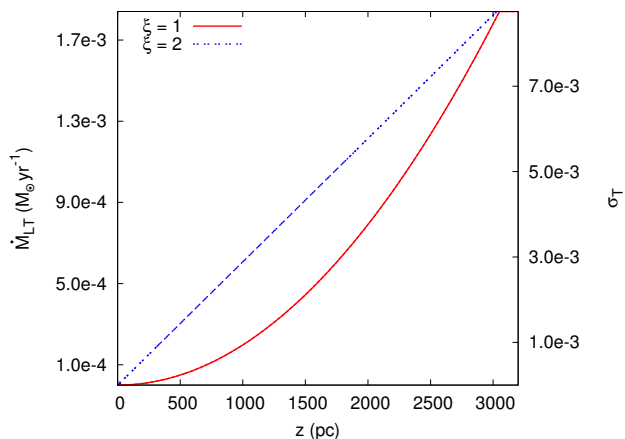


**Fig. 3.** Total mass loaded into the jet (left axis), and total fraction of jet surface intercepted by stellar interactions (right axis), as a function of jet height, for  $\xi = 1$  and 2, in M87.

Radio lobes detected by Owen et al. (2000) show that the emission in M87 comes from a region within  $\sim 40$  kpc. The jet remains undisturbed and collimated only for a few kpc, where it is relativistic, with a Lorentz factor of  $\Gamma \sim 2\text{--}3$  (Biretta et al. 1995). Thus, here we focus on an extension of  $z_{\text{max}} = 5$  kpc and adopt a Lorentz factor of  $\Gamma = 3$ .

We plot in Fig. 3 the total loaded mass rate and the total surface of interaction as defined in Eq. (2). At the total bulge height, we obtain ratios  $\Gamma \dot{M}c^2/L_j \sim 3$  and  $\sigma_T \sim 0.01$ , which mean that wind mass-load and subsequent jet slow down is likely important in the jet of M87 on kpc scales. On the other hand, only 1% of the jet section is covered by interactions, which may mean that the loaded mass is confined only to relatively small regions of the jet. However, given the unstable nature of jet-wind interactions and the subsequent loaded matter evolution (see, e.g., Bosch-Ramon et al. 2012; de la Cita et al. 2016), plus the complex dynamic pattern arising from such an inhomogeneous configuration, it seems more likely that the loaded wind material will effectively spread all over the jet. It is worth noting that both the number of stars within the jet and the jet mass-load estimates derived here are similar to those found by Wykes et al. (2013, 2015) for the radiogalaxy Centaurus A.

#### 4.2. Starburst galaxies: Mrk 231 and 3C 273

We study two sets of parameters describing star-forming galaxies: One is considered to be a local Universe galaxy with a weak jet and a very high SFR, for which we take the particular case of Mrk 231. The other starburst is the powerful quasar 3C 273.

Mrk 231: the jet in Mrk 231 has a luminosity of  $L_j = 10^{43}$  erg s $^{-1}$  (Reynolds et al. 2009). There is evidence supporting a jet viewed nearly along the line of sight, with an inclination  $i < 14^\circ$  and a high Lorentz factor (e.g., Reynolds et al. 2009; Davies et al. 2004); we adopt  $i = 10^\circ$ , and a Lorentz factor of  $\Gamma = 6$ . The size of the collimated radio source is estimated at  $\sim 70$  pc (Taylor et al. 1999), and its opening angle  $\theta = 0.1$ .

The stellar disk of Mrk 231 has a total thickness of 23 pc and a radius of  $\sim 300$  pc, and a nuclear SFR of  $\sim 100\text{--}350 M_\odot \text{ yr}^{-1}$  (Downes & Solomon 1998; Teng et al. 2014). We take here the limit value of  $350 M_\odot \text{ yr}^{-1}$ .

The total mass rate loaded inside the jet of Mrk 231 by stars and the total surface of interaction, as defined in Eq. (2), are

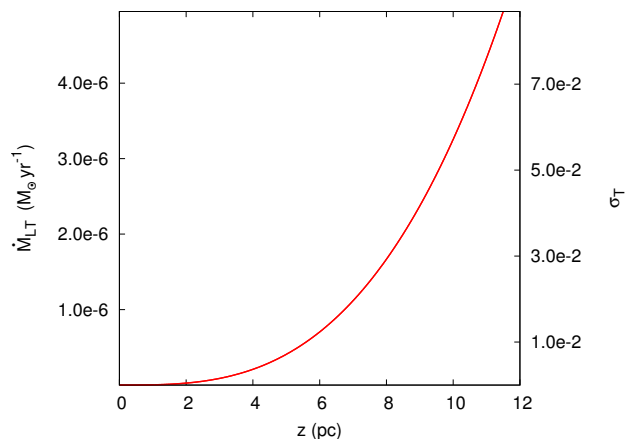


**Fig. 4.** Total mass rate loaded into the jet (left axis), and total fraction of jet surface intercepted by stellar interactions (right axis), as a function of jet height for Mrk 231.

plotted in Fig. 4 as a function of jet height. At the total jet height, we have ratios  $\Gamma \dot{M}c^2/L_j \approx 0.17$  and  $\sigma_T \approx 0.09$ . Unlike the case of M87, the jet of Mrk 231 seems to be only slightly mass-loaded and slowed down by the winds of massive stars, but in this case the loaded matter will spread inside the jet more efficiently due to a higher  $\sigma_T$ -value.

The source 3C 273, located at  $z = 0.158$ , is one of the brightest and closest quasars. The jet luminosity is  $L_j \sim 10^{46}$  erg s $^{-1}$  (e.g., Stawarz 2004; Ghisellini et al. 2010; although lower intrinsic luminosities of  $\sim 4 \times 10^{44}$  erg s $^{-1}$  were recently estimated by Punsly & Kharb 2016). VLBI observations show a small-scale radio jet, whose components are characterized by apparent superluminal motions, indicating a jet close to the line of sight. In addition, radio observations also reveal a large-scale jet, that extends up to tenths of kpc (Conway et al. 1981). The viewing angle of the larger jet, however, seems to differ from the one of the inner jet by  $\sim 20^\circ$  (Stawarz 2004). Thus, we study the emission produced in the inner jet.

Superluminal motions are found up to a distance of hundreds of pc (Davis et al. 1991); we consider that the jet extends up to a distance comparable to the stellar disk radius, that is  $z_{\text{max}} = R_d$ .

This source is highly variable at all wavelengths; a precessing inner jet (Abraham & Romero 1999) and a double helix inside the jet (Lobanov 2009) have been suggested as responsible for the radio variability. Since we do not attempt to model the multi-wavelength emission of the source nor its variability, we consider average values for the inclination angle and the Lorentz factor, adopting  $i = 6^\circ$  and  $\Gamma = 10$  respectively (Jorstad et al. 2005).

With an infrared luminosity of  $\log(L_{\text{IR}}/L_\odot) = 12.73$  (Kim & Sanders 1998), 3C 273 is classified as a ULIRG. For the stellar disk properties, we take a total thickness of 100 pc (average value for nearby ULIRGs in Medling et al. 2014), and a radius of 300 pc as in Mrk 231. SFR estimations for this object are  $50\text{--}150 M_\odot \text{ yr}^{-1}$  (Farrah et al. 2013), and  $129 M_\odot \text{ yr}^{-1}$  (Zhang et al. 2016), for the whole galaxy. As in this type of object, most of the star formation originates in the inner regions; we assume a SFR of  $\sim 100 M_\odot \text{ yr}^{-1}$  to be concentrated in the molecular disk. At the total jet height, we have ratios  $\Gamma \dot{M}c^2/L_j \sim 10^{-3}$  and  $\sigma_T \sim 4 \times 10^{-4}$ , as seen in Fig. 5. Therefore, mass-load and the dynamical effects induced by stellar winds are likely minor in this source.

**Table 1.** Main parameters of the model.

| Parameters   | 3C 273    | Mrk 231   | M 87      |
|--|-----------|-----------|-----------|
| $d$ : distance [Mpc]                                     | 730       | 180       | 16        |
| SRF: star formation rate [ $M_{\odot} \text{ yr}^{-1}$ ] | 100       | 350       | –         |
| $h_d$ : stellar disk thickness [pc]                      | 100       | 23        | –         |
| $R_d$ : stellar disk radius [pc]                         | 300       | 300       | 3100*     |
| $L_c$ : jet power [ $\text{erg s}^{-1}$ ]                | $10^{46}$ | $10^{43}$ | $10^{44}$ |
| $z_{\text{max}}$ : jet height [pc]                       | 300       | 70        | 5000      |
| $\Gamma$ : Lorentz factor                                | 10        | 6         | 3         |
| $\theta$ : opening angle [rad]                           | 0.1       | 0.1       | 0.1       |
| $i$ : inclination [ $^{\circ}$ ]                         | 6         | 10        | 20        |

**Notes.** References for all parameter values are given in Sect. 4. Distances are taken from NED as of March 2017. (\*) Radius of the galactic bulge. The stars in M 87 are assumed to be spherically distributed.

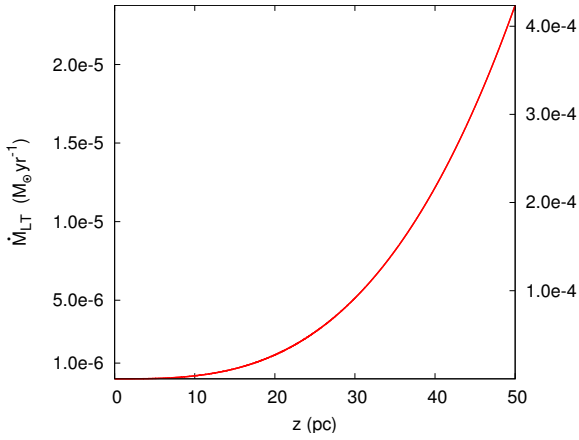


**Fig. 5.** Total mass rate loaded into the jet (left axis), and total fraction of jet surface intercepted by stellar interactions (right axis), as a function of jet height for 3C 273.

Table 1 lists all the relevant parameter values of the model and the sources.

## 5. Radiated non-thermal power

Assuming that IC losses dominate, one can easily estimate the apparent luminosity of the high-energy emission expected from the interaction of a given AGN jet with the population of stars in the host galaxy. The radiative efficiency of the shocked fluid can be approximated as:

$$f_{\text{rad}}(E, z) = \frac{t_{\text{rad}}^{-1}}{t_{\text{rad}}^{-1} + t_{\text{nrad}}^{-1}}. \quad (24)$$

where  $t_{\text{nrad}}^{-1}$  accounts for the non-radiative losses (e.g., adiabatic losses, particle advection), and  $t_{\text{rad}}^{-1}$  accounts only for IC losses in the Thomson regime<sup>1</sup>:

$$t_{\text{IC,T}}^{-1} = \frac{4c\sigma_{\text{T}}}{3} \frac{E}{(m_e c^2)^2} \omega_{\text{ph}}. \quad (25)$$

The luminosity density generated only by the red giants in the galaxy is comparable to the one generated by the whole stellar population in the bulge (derived from Gebhardt & Thomas

<sup>1</sup> However, these losses could be associated as well to synchrotron losses under a magnetic field of equivalent energy density to the dominant photon field.

2009). Here we consider as target photons for IC interactions those emitted by the whole red giant population. Given that other photon fields produced in the galaxy or its central region can be present, the radiative efficiency derived is rather conservative. The photon energy density at a given  $z$ -value is estimated as:

$$\omega_{\text{ph}}(z) = \int \frac{L_s(m)n_s(m, z)}{4\pi c(z^2 + r^2 - 2rz \cos \theta)} dm dV. \quad (26)$$

In the case of M 87,  $L_s(m)$  should be replaced by  $\langle L_s \rangle$ , the time averaged red giant luminosity.

The apparent non-thermal luminosity per unit volume at height  $z$  due to jet-star interactions is then:

$$\frac{dL_{\text{NT}}^{\text{app}}(z)}{dV} = \eta_{\text{NT}} L_j f_{\text{rad}}(z) \frac{\delta_j^4}{\Gamma_j^2} \int \left\langle \frac{S_s(m, z)}{S_j(z)} \right\rangle n_s(z, m) dm, \quad (27)$$

where  $n_s(z, m)$  is the density of stars, and  $\delta_j$  is the Doppler boosting factor, given by

$$\delta_j = \frac{1}{\Gamma(1 - \beta_j \cos i)}, \quad (28)$$

where  $i$  is the inclination, that is, the angle between the jet axis and the line of sight. Notice that Eq. (26) is the photon energy density in the laboratory frame; in the jet frame, it is enhanced by a factor  $\sim \Gamma_j^2$  (whereas the IC target photon energy is enhanced by  $\sim \Gamma_j$ ). We note, however, that  $f_{\text{rad}}$  is an invariant quantity. As mentioned in Sect. 2, the effective area of the shock is larger than the one defined by the stagnation distance; we adopt here  $A = 100$  (Bosch-Ramon 2015). The total radiative output is computed integrating Eq. (27) over the jet volume.

We estimate the apparent non-thermal radiative output at a reference energy of  $E'_{\text{IC}} = (m_e c^2)^2 / kT_s \Gamma$ , where  $E'_{\text{IC}}$  is approximately the maximum of the IC cross-section in the flow frame around the Thomson-Klein-Nishina (KN) transition. In the case of M 87, we obtain  $L_{\text{NT}}^{\text{app}} \approx 5 \times 10^{-3} \eta_{\text{NT}} L_j$  at  $E'_c \approx 250$  GeV, for both values of the index of the stellar density. For Mrk 231, the apparent non-thermal luminosity is  $L_{\text{NT}}^{\text{app}} \approx 7 \times 10^{-2} \eta_{\text{NT}} L_j$  at  $E'_{\text{IC}} \approx 10$  GeV, whereas for 3C 273, it is lower than the jet luminosity,  $L_{\text{NT}} \approx 7 \times 10^{-4} \eta_{\text{NT}} L_j$ , with the same  $E'_{\text{IC}}$ . In Sect. 8 we discuss how reliable these estimates are.

## 6. Non-thermal processes

As shown in Sect. 5,  $L_{\text{NT}}^{\text{app}}$  can easily reach  $\sim 1\%$  of the jet luminosity. In this section we study the non-thermal processes in more detail, and compute the synchrotron and IC spectral energy distributions (SEDs).

### 6.1. Energy losses

We consider that particles lose energy by synchrotron radiation, IC interactions, and adiabatic cooling. We calculate the cooling rates in the flow frame. The cooling rate for synchrotron radiation is given by:

$$t_{\text{synchr}}^{-1}(E', z) = \frac{4}{3} \frac{c\sigma_T}{(m_e c^2)^2} \frac{B'^2(z)}{8\pi} E', \quad (29)$$

and adiabatic losses can be estimated as:

$$t_{\text{ad}}^{-1}(E', z) = \frac{2}{3} \frac{\Gamma c}{z}. \quad (30)$$

There are several radiation fields that can provide targets to IC interactions: locally produced radiation, as synchrotron emission (synchrotron self-Compton, SSC), and external photon fields, such as the radiation from the stars in the galaxy, infrared (IR) photons from dense regions, or the cosmic microwave background (CMB).

In particular, IR photons have been considered in the starburst galaxies. The IR luminosity of the star-forming disk in Mrk 231 is estimated in  $L_{\text{IR}} = 3 \times 10^{12} L_{\odot} \text{ erg s}^{-1}$ ; for the ULIRG 3C 273, we consider an IR luminosity of  $L_{\text{IR}} = 5.4 \times 10^{12} L_{\odot} \text{ erg s}^{-1}$  (both from Sanders et al. 1988). We model the IR fields as gray bodies with a temperature of  $\sim 200$  K. In the case of M 87, the starlight and CMB photons are the most relevant targets (Hardcastle & Croston 2011); thus, we include CMB photons for this source. The extragalactic background light (EBL) energy density is, however, at least a factor 30 below the CMB (Cooray 2016); we therefore do not consider the EBL as an additional target.

In addition, 3C 273 shows an excess in the optical/UV emission, likely the result of an accretion disk or reprocessing of radiation from a hot corona. The coronal emission is also observed on X-rays at  $E \lesssim 30$  keV (Madsen et al. 2015). The size of the accretion flow is estimated in 0.02–0.05 pc (Chidiac et al. 2016). As a result, its photon energy density is deboosted when seen from the jet. Moreover, the scattering probability for IC interactions is reduced a factor  $(1 - \beta \cos \theta)^2 \sim 10^{-16}$ . We consider, then, that this component does not provide a relevant target for our study.

The energy density of synchrotron photons is  $10^{-4}$ – $10^{-3}$  times lower than the magnetic energy density in  $z_{\text{max}}$  for both values of the magnetic field, for the three sources. Then, SSC have turned out to be irrelevant in our scenario, as expected given the large scales involved. In the timescale analysis, we focus on scales  $\sim z_{\text{max}}$  as in most of the cases explored here the largest scales are radiatively dominant.

The maximum energy that electrons can attain depends on the energy loss/gain balance. The acceleration rate is assumed to be:

$$t_{\text{acc}}^{-1}(E', z) = \eta \frac{ecB'(z)}{E'}, \quad (31)$$

where  $\eta = (v/c)^2/2\pi$  and it approaches 0.1 as  $v \rightarrow c$  (we follow the same approach as in de la Cita et al. 2016, further details are provided there).

Figure 6 shows the cooling rate at  $z_{\text{max}}$ , together with the acceleration rate for the starburst galaxies, for the sub-equipartition value of the magnetic field. Figure 7 shows the cooling rate at  $z_{\text{max}}$  for M 87, both for  $B = B_{\text{eq}}$  and  $B = 10^{-1} B_{\text{eq}}$ , in the case of the stellar index  $\xi = 1$ . Similar results (not shown here) to those presented in Fig. 7 are obtained when considering the stellar index  $\xi = 2$ .

In all the explored cases, the maximum electron energy is determined either by synchrotron losses or diffusion out of the accelerator (i.e., the jet-star direct interaction region).

### 6.2. Particle injection

We adopt an injection function, in units of particles per time and energy unit for a jet height interval  $dz$ , given by

$$dQ(E', z) = Q_0(z) E'^{-\alpha} \exp(-E'/E'_{\text{max}}(z)), \quad (32)$$

where the injection index is taken as  $\alpha = 2$ , characteristic of diffusive acceleration mechanisms. The normalization function  $Q_0(z)$  depends on the available non-thermal energy, quantified by Eq. (1). Since the particle energy in the flow frame is  $E'_{\text{NT}} = E_{\text{NT}}/\Gamma$ , and the cell crossing time in the flow frame is  $\Gamma$  times longer,  $dQ(E', z)$  can be normalized through

$$\int_{E'_{\text{min}}}^{E'_{\text{max}}} dE' E' dQ(E', z) \approx \frac{1}{\Gamma^2} dL_{\text{NT}}(z), \quad (33)$$

where  $dL_{\text{NT}}(z)$  is the non-thermal injected luminosity within the jet height interval  $dz$ . The transport equation of electrons is solved following the approach described in de la Cita et al. (2016).

Figure 8 shows electron energy distributions at different heights obtained for M 87 in the case  $\xi = 1$ . For the equipartition magnetic field, the effect of synchrotron cooling is clearly seen in the particle spectra; notice also that particles are able to achieve higher energies at higher  $z$ . Since the diffusion and acceleration rates vary with  $z$  in the same way, the maximum energy is constant along the jet. The non-thermal fraction  $\eta_{\text{NT}}$  has been fixed to 0.1 as a reference value to compute the emission.

### 6.3. Spectral energy distributions

Once the electron energy distribution is known, we can compute in the flow frame the synchrotron and the IC photon rate per energy unit produced within each height interval  $dz$ :  $d\dot{N}'_{\gamma}(E'_{\gamma}, z)$ , and the whole jet SED:

$$E'_{\gamma} L'_{\gamma}(E'_{\gamma}) = \int_{z_{\text{min}}}^{z_{\text{max}}} \int_{E'_{\gamma\text{min}}}^{E'_{\gamma\text{max}}} dE'_{\gamma} E'_{\gamma} d\dot{N}'_{\gamma}(E'_{\gamma}, z), \quad (34)$$

where  $E'_{\gamma}$  is the gamma-ray photon energy in the flow frame.

As mentioned above, particles propagate far from the jet-star interaction region, and reach jet scale regions before cooling down significantly. There, particles are advected with the jet velocity, close to  $c$ , which implies that Doppler boosting must be taken into account (Bosch-Ramon 2015). In the observer frame, the SED is enhanced according to (Lind & Blandford 1985):

$$E_{\gamma} L_{\gamma}(E_{\gamma}) = \delta_j^4 E'_{\gamma} L'_{\gamma}(E'_{\gamma}), \quad (35)$$

where  $E_{\gamma} = \delta_j E'_{\gamma}$ , and  $\delta_j$  is given by Eq. (28).

## 7. Results

Figure 9 shows the contribution to the non-thermal luminosity by jet-star interactions on jet scales for the starburst galaxies 3C 273 (top panel) and Mrk 231 (bottom panel). For reference, the panels show the sensitivity of three gamma-ray instruments: MAGIC (operating; above 100 GeV), CTA (forthcoming; above  $\sim 30$  GeV), and Fermi (operating;  $\sim 0.1$ –100 GeV).

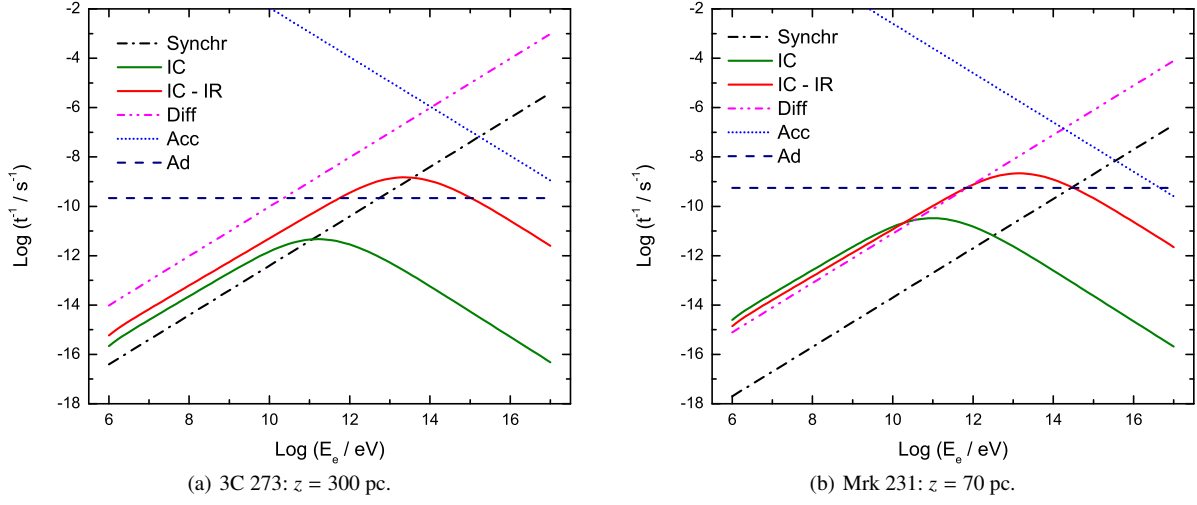


**Fig. 6.** Energy losses at  $z_{\max}$  for the star-forming galaxies in the low- $B$  case.

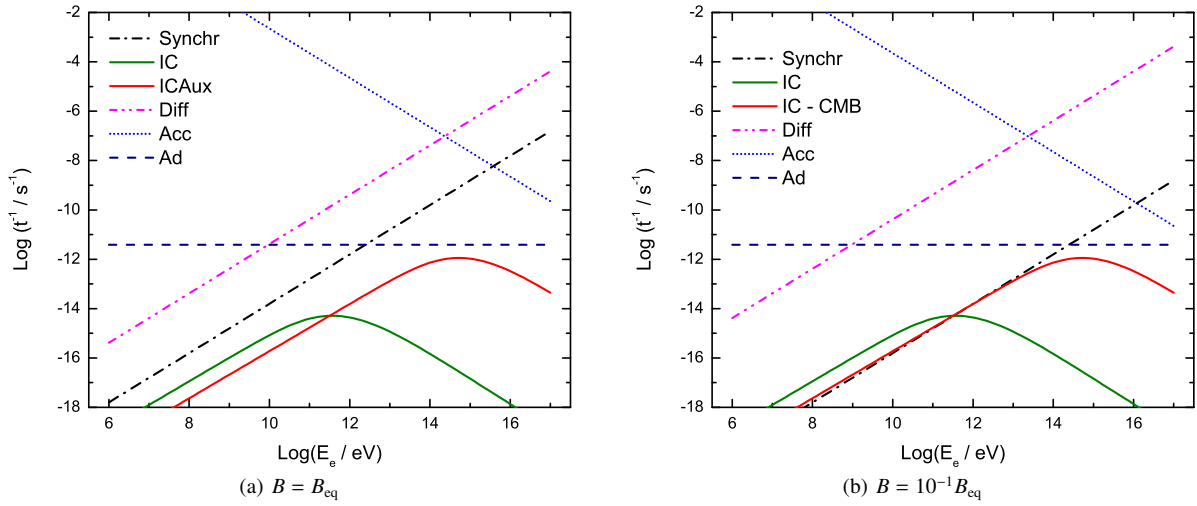


**Fig. 7.** Energy losses at  $z_{\max} = 5$  kpc for M87, in the case  $\xi = 1$ .

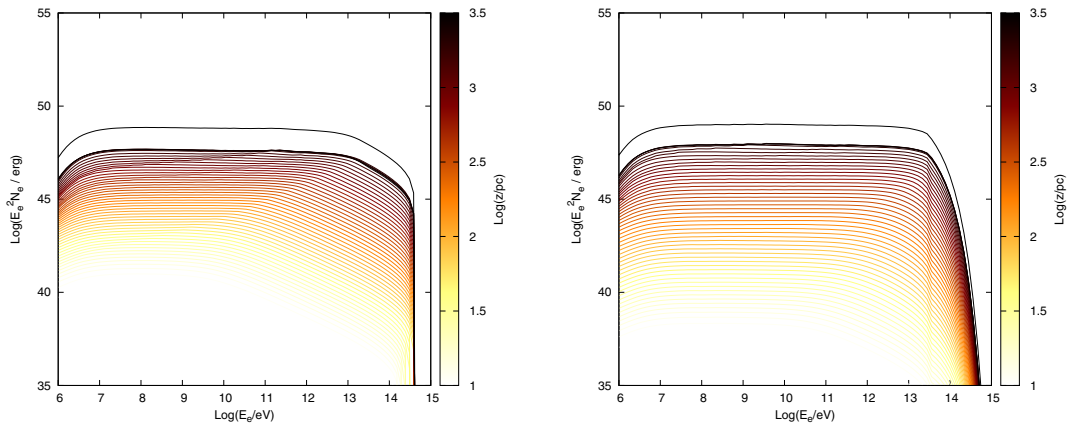


**Fig. 8.** Electron energy distribution at different  $z$  for M87, in the case  $\xi = 1$ . *Left panel* is for  $B = B_{\text{eq}}$ , and *right panel* for  $B = 10^{-1} B_{\text{eq}}$ . The black line on top is the integrated distribution.

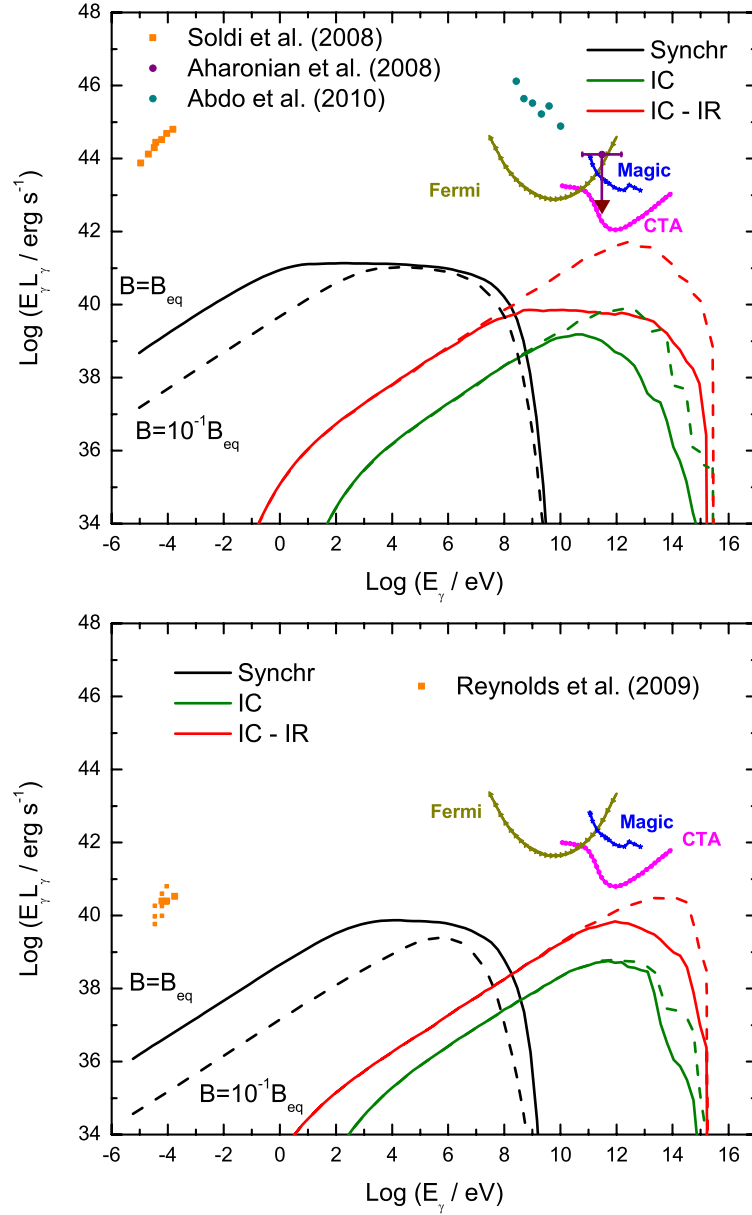


**Fig. 9.** SEDs of the synchrotron and IC emission for the starburst galaxies. *The top panel* corresponds to 3C 273, and *the bottom panel* to Mrk 231. In both panels, solid lines correspond to a magnetic field in equipartition with the jet ram pressure, and dashed lines to the case below equipartition. Radio data for both sources are also presented, along with *Fermi* detection and HESS upper limits for 3C 273.

Radio data of 3C 273 and Mrk 231 are also presented in Fig. 9 (Steenbrugge et al. 2010; Soldi et al. 2008). In the case of Mrk 231, the radio data were taken between 1996 and 2006, a year in which an intense radio flare was detected (this highly variable radio emission is associated with AGN activity; Reynolds et al. 2009). The predicted radio fluxes are well below the typical observed fluxes from Mrk 231 and 3C 273.

For 3C 273, we also show gamma-ray emission detected by *Fermi* during a quiescent state in 2009 (Abdo et al. 2010), and upper limits to TeV emission by HESS (Aharonian et al. 2008). The source is also prominent at X-ray frequencies, although a high percentage in this band comes from a hot corona/disk.

Nevertheless, the emission from the interactions studied here does not contribute significantly in X-rays.

In Fig. 10 we show the contribution to the non-thermal luminosity of M 87 by jet-star interactions on jet scales for the different slopes of the stellar density (top panel), and the two fractions of the equipartition parameter (bottom panel). The figure also shows the sensitivity of the gamma-ray instruments listed above. The data taken by *Fermi* correspond to a quiescent state of M 87, since during a period of ten months there was no evidence of a flare (Abdo et al. 2009). Between 2005 and 2007, the MAGIC collaboration collected more than 100 h of observations of M 87 in a persistent low-emission state (i.e., no flaring

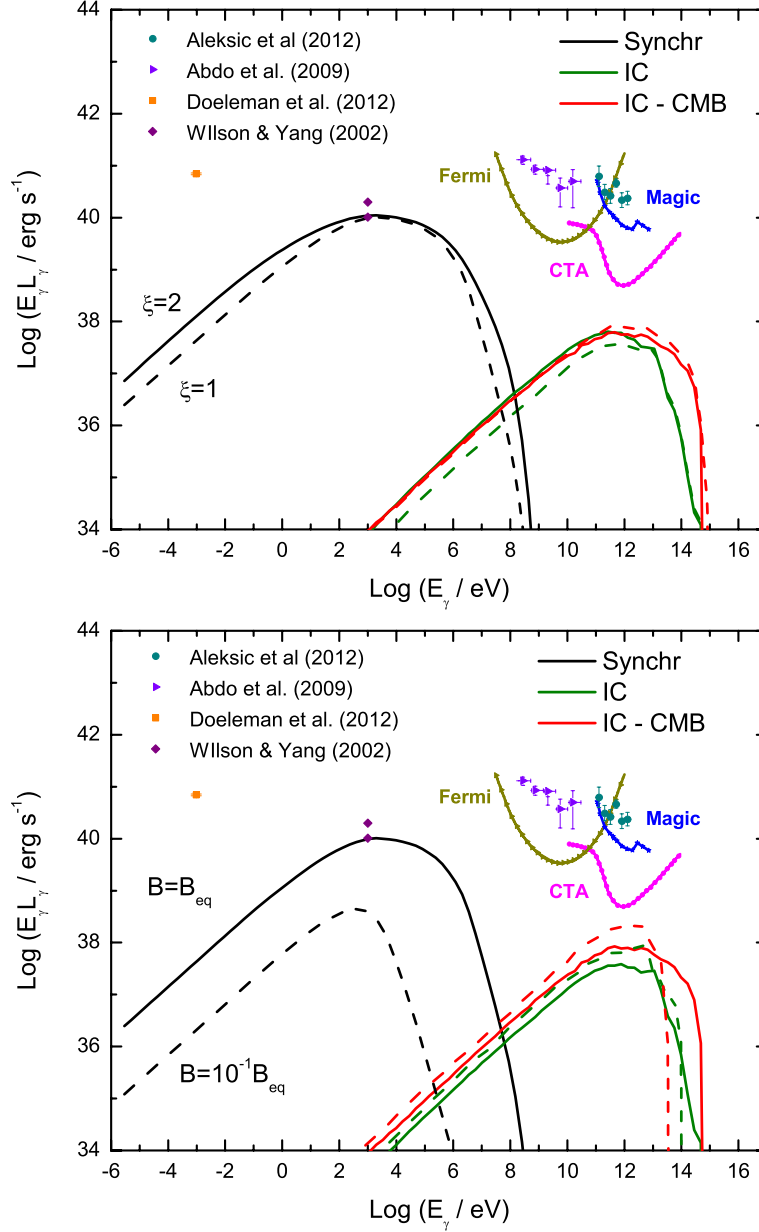


**Fig. 10.** SEDs for the jet of M87. *The top panel* shows the SEDs obtained using the two stellar indexes. *The bottom panel* corresponds to a stellar index of  $\xi = 1$ , and both equipartition and below-equipartition magnetic fields. Sensitivities of gamma-ray detectors are also included, together with the detection by MAGIC (Aleksić et al. 2012) and Fermi (Abdo et al. 2009) of M87 during the source steady state.

events; Aleksić et al. 2012). Both data sets can be used simultaneously, as suggested in Aleksić et al. (2012). The radio luminosity for M87 is from Doeleman et al. (2012). As in the case of Mrk 231 and 3C 273, there is no conflict between the predicted radio emission and the typical observed fluxes from these sources.

The inner jet of M87 ( $\lesssim 3$  kpc) displays a structure made up of several knots, which can be resolved at radio and optical wavelengths. There is also X-ray emission associated to these knots, but it is slightly shifted upstream with respect to the optical peak (Marshall et al. 2002). In addition, the X-ray spectra

from the core and the brightest knots (those close to the nucleus) are similar, and the core flux is larger than those predicted by accretion flow models (Wilson & Yang 2002). All this seems to indicate that an inner jet might contribute (if not dominate) to the X-ray emission. The X-ray fluxes measured close to the nucleus of M87, and in the knot A of the jet, imply luminosities of  $\sim 10^{40}$  erg  $\text{s}^{-1}$  at 1 keV (Wilson & Yang 2002; Marshall et al. 2002). These are similar to the predicted synchrotron luminosity for a magnetic field in equipartition with the jet kinetic power. However, the emission obtained from our model is expected to be diffuse, and unable to reproduce the structure seen in the jet of

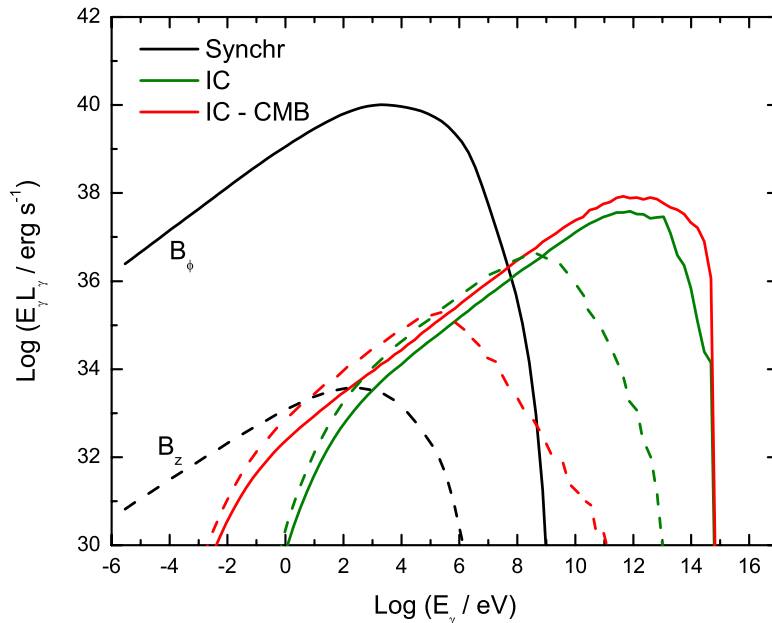


**Fig. 11.** SEDs for the jet of M 87 in the case of  $\xi = 1$ , produced by the different components of the magnetic fields: poloidal (dashed lines) and toroidal (solid lines).

M 87. This suggests two possibilities in our scenario: that a magnetic field below equipartition is a more realistic assumption, or that the acceleration efficiency is lower than the one adopted here.

At TeV energies, the contribution to the luminosity from IC against the CMB is comparable with that against starlight, in agreement with previous results (Hardcastle & Croston 2011).

Although significant transverse components of the magnetic field are found along the jet in M 87 (specially in the bright knots), the projected magnetic field lies mostly along the jet (Owen et al. 1989). We thus consider a case with a dominant poloidal component. Figure 11 shows the SEDs obtained for M 87 using different configurations of the magnetic field (equipartition values).

It is worth noting that our jet models miss jet regions larger than those explored where electrons may still radiate through IC in the CMB. This could be particularly relevant for M 87 and its disrupted jet regions beyond a few kpc, as its kpc-scale jet emission is already little enhanced by Doppler boosting. A similar effect occurs for 3C 273, where a kpc-scale jet seems to have a larger inclination with respect to the line of sight, hence reducing the Doppler enhancement.

## 8. Discussion and summary

In this work, we compute the SEDs of the non-thermal radiation produced by the interaction of extragalactic jets with stars on jet scales. We study two types of galaxy hosts: starburst versus massive elliptical AGN, exemplified by three objects: Mrk 231 and 3C 273 versus M 87; for each one, the stellar populations have been characterized.

For a star-forming galaxy with a high SFR such as Mrk 231, the luminosity in gamma rays computed numerically can be as high as  $\sim 10 \eta_{\text{NT}}\%$  of the jet luminosity ( $\sim 1 \eta_{\text{NT}}\%$  for 3C 273) as long as the magnetic field is a fraction  $\lesssim 10^{-2}$  of the equipartition

value. In that case, the radiation is mostly produced at TeV energies. In all the studied cases, the radiation comes mainly from the largest scales of the emitter, meaning 100 pc scales for the starbursts, and kpc scales for M 87. In M 87, as Doppler boosting effects are minor, the non-thermal luminosity reaches only  $\sim 0.1 \eta_{\text{NT}}\%$  of the jet luminosity. This illustrates the great importance of jet speed and orientation. In addition, the section covered by the stellar winds is smaller than in the case of Mrk 231; not so with respect to 3C 273, but the latter has a much more powerful jet (in addition to the strongest Doppler boosting of the three studied cases). For equipartition fields, unlike Mrk 231 and 3C 273, the synchrotron radiation efficiency in M 87 may be significantly higher than for the IC emission, with synchrotron photons reaching 0.1–1 GeV energies, but most of the emission being released in X-rays. We remark that such high fluxes, expected to be smoothly spatially distributed in our model, are in contradiction with the structured X-ray luminosity observed in the nucleus and knots in M 87. Another important difference between M 87 and the starburst galaxies is the more diluted target photon fields in the former, as seen when comparing the IC cooling rates in Figs. 6 and 7. The available non-thermal-to-jet luminosity ratios obtained in this work range  $L_{\text{NT}}/L_j \sim 10^{-3} - 10^{-1}$ . These ratios are rather significant, although it is worth pointing out that a defect of stars in the jet directions would proportionally affect  $L_{\text{NT}}/L_j$ .

Despite M 87 being potentially detectable by CTA for  $\eta_{\text{NT}} \rightarrow 1$ , it seems unlikely that the interactions of its jets with stars on jet scales will contribute significantly to the persistent gamma-ray emission already detected from this source. It does not seem feasible either, given the limitations in angular resolution, to disentangle a putatively detectable, jet-star interaction kpc-scale radiation from other emitting regions of the galaxy center. For the two starburst AGNs studied, in particular for 3C 273, a detection is possible if the magnetic field is well below equipartition and the acceleration is efficient. Even Mrk 231 might be detectable with CTA for  $\eta_{\text{NT}} \rightarrow 1$ . Nevertheless, the

detectability of these sources ultimately depends on unknown parameters, namely  $\eta_{\text{NT}}$ , and  $\alpha$ , the latter determining whether gamma rays will be an important radiation channel. Slightly more optimistic Doppler boosting parameters would also significantly improve the detectability of these sources. In summary, the non-thermal emission from jet-star interactions on large scales may represent a non-negligible (persistent) contribution to gamma rays, although the uncertainties are high, and more accurate studies, source-specific or population-based, are still needed to better determine the role of the process at high energies, and constrain the values of the free parameters.

It is worth comparing the global large-scale emission, and the emission emitted locally (close to the interaction region), which has not been calculated in this work (see de la Cita et al. 2016). To this end, one can compare the radiative efficiency (Eq. (24)) at the jet scale to that at the jet-star interaction scale. For a region where escape losses dominate radiative losses,  $f_{\text{rad}} \sim t_{\text{rad}}^{-1}/t_{\text{esc}}^{-1} \propto l_c w_{\text{ph}}$ , where  $l_c$  and  $w_{\text{ph}}$  are a characteristic emitter length and the characteristic target photon energy density, respectively. At large scales,  $l_c \sim z$ , and a prescription for  $w_{\text{ph}}$  is given in Sects. 5 and 6.1. Locally, we can approximate  $l_c \sim 10 R_s(z)$ , and  $w_{\text{ph}} \sim L_s/4\pi c(3R_s(z))^2$ . The interactions of the jet with the most evolved red giants, and with massive stars with  $m \gtrsim 40 M_\odot$ , dominate the non-thermal activity; we consider  $\dot{M} = 10^{-7} M_\odot \text{ yr}^{-1}$  and  $L_s = 100 L_\odot$  in the case of red giants, and  $\dot{M} = 2 \times 10^{-6} M_\odot \text{ yr}^{-1}$ ,  $v_w = 10^8 \text{ cm s}^{-1}$  and  $L_s = 5 \times 10^4 L_\odot$  for massive stars. The temperature of the target photon field also affects the cooling distance of electrons, and has to be included in the analysis; roughly:  $f_{\text{rad}}^{\text{glob}}/f_{\text{rad}}^{\text{local}} \propto T_{\text{local}}/T_{\text{glob}}$ . Differences in Doppler boosting between the global and the local scales are neglected.

For 3C 273, one obtains:

$$\frac{f_{\text{rad}}^{\text{glob}}}{f_{\text{rad}}^{\text{local}}} \sim 1 \left( \frac{z}{\text{pc}} \right), \quad (36)$$

hence at hundred-pc scale the global IR IC component largely dominates, whereas the global stellar IC component is comparable with the local one. Something similar happens for Mrk 231. For M 87, on the other hand, one obtains:

$$\begin{aligned} \frac{f_{\text{rad}}^{\text{glob}}}{f_{\text{rad}}^{\text{local}}} &\approx 2 \times 10^{-3} \left( \frac{z}{\text{pc}} \right), \quad \text{for } \xi = 1, \\ \frac{f_{\text{rad}}^{\text{glob}}}{f_{\text{rad}}^{\text{local}}} &\approx 3, \quad \forall z \quad \text{for } \xi = 2; \end{aligned} \quad (37)$$

now, the radiative roles of global CMB and stellar components are comparable, and the temperatures of the dominant target fields are also similar for both the global (taking only red giants) and the local components. Therefore, the global contribution on kpc scales should dominate small-scale contributions for both index values. We recall that the comparison is very crude, and the uncertainty is probably order-of-magnitude. Nevertheless, the result indicates that the few-kpc scale jet emission from jet-star interactions may easily overcome that from the interaction regions themselves.

The analytic prescription to estimate the apparent luminosity given by Eq. (27), considering only IC interactions with stellar photons, yields values approximately ten times higher than those derived numerically (almost a hundred times higher for M 87). This is somewhat expected, given the crude approximation to compute the radiation efficiency: the actual IC cooling rate at the Thomson-KN transition is slightly below the adopted

simple value, and the electrons with lower and higher energies radiate with lower efficiencies. In the Thomson approximation, and for  $\alpha = 2$ , the energy dependence of efficiency already yields an overestimate of the analytical prediction by a factor of  $\ln(E'_{\text{IC}}/E'_{\text{min}}) \sim 10$ . Therefore, we remark that using the analytical prescription to estimate the gamma-ray luminosity from the jet-star interactions is overestimating its value by approximately a factor of 10.

*Acknowledgements.* We thank the anonymous referee for helpful comments and suggestions. We acknowledge support from the Spanish Ministerio de Economía y Competitividad (MINECO/FEDER, UE) under grants AYA2013-47447-C3-1-P, AYA2016-76012-C3-1-P, with partial support from the European Regional Development Fund (ERDF/FEDER), MDM-2014-0369 of ICCUB (Unidad de Excelencia “María de Maeztu”), and the Catalan DEC grant 2014 SGR 86. F.L.V is also supported by the Argentine Agency CONICET (PIP 2014-00338). N.T.A. acknowledges support from MINECO through FPU14/04887 grant. V.B.-R. also acknowledges financial support from MINECO and European Social Funds through a Ramón y Cajal fellowship. This research has been supported by the Marie Curie Career Integration Grant 321520.

## References

- Abdo, A. A., Ackermann, M., Ajello, M., et al. 2009, *ApJ*, **707**, 55  
 Abdo, A. A., Ackermann, M., Ajello, M., et al. 2010, *ApJ*, **714**, L73  
 Abraham, Z., & Romero, G. E. 1999, *A&A*, **344**, 61  
 Acciari, V. A., Aliu, E., Arlen, T., et al. 2009, *Science*, **325**, 444  
 Aharonian, F., Akhperjanian, A. G., Barres de Almeida, U., et al. 2008, *A&A*, **478**, 387  
 Aleksić, J., Alvarez, E. A., Antonelli, L. A., et al. 2012, *A&A*, **544**, A96  
 Araudo, A. T., Bosch-Ramon, V., & Romero, G. E. 2010, *A&A*, **522**, A97  
 Araudo, A. T., Bosch-Ramon, V., & Romero, G. E. 2013, *MNRAS*, **436**, 3626  
 Banasiński, P., Bednarek, W., & Sitarek, J. 2016, *MNRAS*, **463**, L26  
 Barkov, M. V., Aharonian, F. A., & Bosch-Ramon, V. 2010, *ApJ*, **724**, 1517  
 Barkov, M. V., Aharonian, F. A., Bogovalov, S. V., Kelner, S. R., & Khangulyan, D. 2012a, *ApJ*, **749**, 119  
 Barkov, M. V., Bosch-Ramon, V., & Aharonian, F. A. 2012b, *ApJ*, **755**, 170  
 Beall, J. H., & Bednarek, W. 1999, *ApJ*, **510**, 188  
 Bednarek, W., & Banasiński, P. 2015, *ApJ*, **807**, 168  
 Bednarek, W., & Protheroe, R. J. 1997, *MNRAS*, **287**, L9  
 Begelman, M. C., Blandford, R. D., & Rees, M. J. 1984, *Rev. Mod. Phys.*, **56**, 255  
 Biretta, J. A., & Meisenheimer, K. 1993, in *Jets in Extragalactic Radio Sources*, eds. H.-J. Röser & K. Meisenheimer (Berlin: Springer Verlag), Lect. Notes Phys., 421, 159  
 Biretta, J. A., Zhou, F., & Owen, F. N. 1995, *ApJ*, **447**, 582  
 Blandford, R. D., & Königl, A. 1979, *Astrophys. Lett.*, **20**, 15  
 Bosch-Ramon, V. 2015, *A&A*, **575**, A109  
 Bosch-Ramon, V., Perucho, M., & Barkov, M. V. 2012, *A&A*, **539**, A69  
 Bowman, M., Leahy, J. P., & Komisarov, S. S. 1996, *MNRAS*, **279**, 899  
 Chidiac, C., Rani, B., Krichbaum, T. P., et al. 2016, *A&A*, **590**, A61  
 Chlebowski, T., & Garmy, C. D. 1991, *ApJ*, **368**, 241  
 Conway, R. G., Davis, R. J., Foley, A. R., & Ray, T. P. 1981, *Nature*, **294**, 540  
 Cooray, A. 2016, *Royal Society Open Science*, **3**, 150555  
 Crowley, C. 2006, Ph.D. Thesis, School of Physics, Trinity College Dublin, Dublin 2, Ireland  
 Dar, A., & Laor, A. 1997, *ApJ*, **478**, L5  
 Davies, R. I., Tacconi, L. J., & Genzel, R. 2004, *ApJ*, **613**, 781  
 Davis, R. J., Muxlow, T. W. B., & Unwin, S. C. 1991, *Nature*, **354**, 374  
 de la Cita, V. M., Bosch-Ramon, V., Paredes-Fortuny, X., Khangulyan, D., & Perucho, M. 2016, *A&A*, **591**, A15  
 Doeleman, S. S., Fish, V. L., Schenck, D. E., et al. 2012, *Science*, **338**, 355  
 Downes, D., & Solomon, P. M. 1998, *ApJ*, **507**, 615  
 Ekström, S., Georgy, C., Eggenberger, P., et al. 2012, *A&A*, **537**, A146  
 Espey, B. R., & Crowley, C. 2008, in *RS Ophiuchi (2006) and the Recurrent Nova Phenomenon*, eds. A. Evans, M. F. Bode, T. J. O’Brien, & M. J. Darnley, ASP Conf. Ser., 401, 166  
 Farrah, D., Lebouteller, V., Spoon, H. W. W., et al. 2013, *ApJ*, **776**, 38  
 Gebhardt, K., & Thomas, J. 2009, *ApJ*, **700**, 1690  
 Ghisellini, G., Tavecchio, F., Foschini, L., et al. 2010, *MNRAS*, **402**, 497  
 Hardcastle, M. J., & Croston, J. H. 2011, *MNRAS*, **415**, 133  
 Harris, D. E., Biretta, J. A., & Junor, W. 1999, in *The Radio Galaxy Messier 87*, eds. H.-J. Röser, & K. Meisenheimer (Berlin: Springer Verlag), Lect. Notes Phys., 530, 100

- Hubbard, A., & Blackman, E. G. 2006, *MNRAS*, **371**, 1717
- Huenemoerder, D. P., Oskinova, L. M., Ignace, R., et al. 2012, *ApJ*, **756**, L34
- Huo, Z. Y., Xia, X. Y., Xue, S. J., Mao, S., & Deng, Z. G. 2004, *ApJ*, **611**, 208
- Jeyakumar, S. 2009, *Astron. Nachr.*, **330**, 287
- Jorstad, S. G., Marscher, A. P., Lister, M. L., et al. 2005, *AJ*, **130**, 1418
- Joss, P. C., Rappaport, S., & Lewis, W. 1987, *ApJ*, **319**, 180
- Khangulyan, D. V., Barkov, M. V., Bosch-Ramon, V., Aharonian, F. A., & Dorodnitsyn, A. V. 2013, *ApJ*, **774**, 113
- Kim, D.-C., & Sanders, D. B. 1998, *ApJS*, **119**, 41
- Komissarov, S. S. 1994, *MNRAS*, **269**, 394
- Kroupa, P. 2001, *MNRAS*, **322**, 231
- Lamers, H. J. G. L. M., Snow, T. P., & Lindholm, D. M. 1995, *ApJ*, **455**, 269
- Lind, K. R., & Blandford, R. D. 1985, *ApJ*, **295**, 358
- Lobanov, A. P. 2009, in *Approaching Micro-Arcsecond Resolution with VSOP-2: Astrophysics and Technologies*, eds. Y. Hagiwara, E. Fomalont, M. Tsuboi, & M. Yasuhiro, ASP Conf. Ser., 402, 189
- Lyutikov, M., Pariev, V., & Gabuzda, D. 2004, *BAAS*, **36**, 912
- Madsen, K. K., Fürst, F., Walton, D. J., et al. 2015, *ApJ*, **812**, 14
- Marscher, A. P., Jorstad, S. G., Mattox, J. R., & Wehrle, A. E. 2002, *ApJ*, **577**, 85
- Marshall, H. L., Miller, B. P., Davis, D. S., et al. 2002, *ApJ*, **564**, 683
- Medling, A. M., U, V., Guedes, J., et al. 2014, *ApJ*, **784**, 70
- Müller, C., Kadler, M., Ojha, R., et al. 2014, *A&A*, **569**, A115
- Owen, F. N., Hardee, P. E., & Cornwell, T. J. 1989, *ApJ*, **340**, 698
- Owen, F. N., Eilek, J. A., & Kassim, N. E. 2000, *ApJ*, **543**, 611
- Perucho, M., Martí, J. M., Laing, R. A., & Hardee, P. E. 2014, *MNRAS*, **441**, 1488
- Puls, J., Vink, J. S., & Najarro, F. 2008, *A&ARv*, **16**, 209
- Punsly, B., & Kharb, P. 2016, *ApJ*, **833**, 57
- Reimers, D. 1975, *Mem. Soc. R. Sci. Liège*, **8**, 369
- Reynolds, C., Punsly, B., Kharb, P., O'Dea, C. P., & Wrobel, J. 2009, *ApJ*, **706**, 851
- Salpeter, E. E. 1955, *ApJ*, **121**, 161
- Sanders, D. B., & Mirabel, I. F. 1996, *ARA&A*, **34**, 749
- Sanders, D. B., Soifer, B. T., Elias, J. H., et al. 1988, *ApJ*, **325**, 74
- Smith, N. 2014, *ARA&A*, **52**, 487
- Soldi, S., Türler, M., Paltani, S., et al. 2008, *A&A*, **486**, 411
- Spruit, H. C. 2010, in *The Jet Paradigm*, ed. T. Belloni (Berlin: Springer Verlag), Lect. Notes Phys., 794, 233
- Stawarz, Ł. 2004, *ApJ*, **613**, 119
- Steenbrugge, K. C., Heywood, I., & Blundell, K. M. 2010, *MNRAS*, **401**, 67
- Sundqvist, J. O., Puls, J., Feldmeier, A., & Owocki, S. P. 2011, *A&A*, **528**, A64
- Sutherland, R. S., & Bicknell, G. V. 2007, *ApJS*, **173**, 37
- Syer, D., & Ulmer, A. 1999, *MNRAS*, **306**, 35
- Taylor, G. B., Silver, C. S., Ulvestad, J. S., & Carilli, C. L. 1999, *ApJ*, **519**, 185
- Teng, S. H., Brandt, W. N., Harrison, F. A., et al. 2014, *ApJ*, **785**, 19
- Şurlan, B., Hamann, W.-R., Aret, A., et al. 2013, *A&A*, **559**, A130
- Vink, J. S., de Koter, A., & Lamers, H. J. G. L. M. 2000, *A&A*, **362**, 295
- Wang, Z., Wiita, P. J., & Hooda, J. S. 2000, *ApJ*, **534**, 201
- Wilson, A. S., & Yang, Y. 2002, *ApJ*, **568**, 133
- Wykes, S., Croston, J. H., Hardcastle, M. J., et al. 2013, *A&A*, **558**, A19
- Wykes, S., Hardcastle, M. J., Karakas, A. I., & Vink, J. S. 2015, *MNRAS*, **447**, 1001
- Zhang, Z., Shi, Y., Rieke, G. H., et al. 2016, *ApJ*, **819**, L27

## GAMMA RAYS FROM RED GIANT WIND BUBBLES ENTERING THE JETS OF ELLIPTICAL HOST BLAZARS

---

In this chapter we present our work "Gamma rays from red giant wind bubbles entering the jets of elliptical host blazars" (Torres-Albà and Bosch-Ramon, 2019), in which we estimate the gamma-ray emission produced in the interaction between an AGN jet and red giant stars as they penetrate it. We use a semi-analytical approach to describe the dynamical evolution of the material they introduce into the jet, and compare it to results from simulations.



# Gamma rays from red giant wind bubbles entering the jets of elliptical host blazars

Núria Torres-Albà and Valentí Bosch-Ramon

Departament de Física Quàntica i Astrofísica, Institut de Ciències del Cosmos (ICC), Universitat de Barcelona (IEEC-UB), Martí i Franquès 1, 08028 Barcelona, Spain  
e-mail: ntorres@fqa.ub.edu

Received 21 June 2018 / Accepted 29 January 2019

## ABSTRACT

*Context.* Blazars in elliptical hosts have a population of red giants surrounding their jet. These stars can carry large wind-blown bubbles into the jets, leading to gamma-ray emission through bubble-jet interactions.

*Aims.* We study the interaction dynamics and the gamma-ray emission produced when the bubbles formed by red giant winds penetrate the jet of a blazar in an elliptical galaxy.

*Methods.* First, we characterized the masses and penetration rates of the red giant wind bubbles that enter the jet. Then, the dynamical evolution of these bubbles under the jet impact was analysed analytically and numerically, and the radiation losses of the particles accelerated in the interaction were characterised. Finally, the synchrotron and the inverse Compton contributions above  $\sim 100$  MeV were estimated under different jet magnetic fields, powers, and Lorentz factors.

*Results.* We find that an analytical dynamical model is a reasonable approximation for the red giant wind bubble-jet interaction. The radiation produced by these wind bubbles interacting with a jet can have a duty cycle of up to  $\sim 1$ . For realistic magnetic fields, gamma rays could be detectable from sources within the local universe, preferentially from those with high Lorentz factors ( $\sim 10$ ), and this could be a relatively common phenomenon for these sources. For magnetic fields in equipartition with the jet power, and high acceleration rates, synchrotron gamma rays may be detectable even for modest Lorentz factors ( $\sim 3$ ), but with a much lower duty cycle.

*Conclusions.* Blazars in elliptical galaxies within the local universe can produce detectable transient or persistent gamma-ray emission from red giant wind bubbles entering their jets.

**Key words.** radiation mechanisms: non-thermal – galaxies: active – galaxies: nuclei – galaxies: jets

## 1. Introduction

Supermassive black holes, present in the innermost regions of galaxies, may accrete the material surrounding them, becoming active galactic nuclei (AGN). Some AGN produce collimated relativistic outflows, or jets (e.g. Begelman et al. 1984), which propagate through the host galaxy. This propagation will inevitably lead to the jet interacting with a variety of obstacles including stars, gas, and dense clouds. These interactions may affect the jet dynamically (e.g. Blandford & Koenigl 1979; Wang et al. 2000; Sutherland & Bicknell 2007). In particular, stars with high mass-loss rates may load the jet with enough matter to result in deceleration (e.g. Komissarov 1994; Bowman et al. 1996; Hubbard & Blackman 2006; Bosch-Ramon et al. 2012; Perucho et al. 2014, 2017).

The winds of stars interacting with AGN jets produce a double bow-shock structure in which particles can be accelerated to relativistic energies, possibly contributing to the jet's total non-thermal emission. Several works have explored this interaction and the resulting emission, both in the case of steady radiation and transient events (e.g. Bednarek & Protheroe 1997; Barkov et al. 2010, 2012; Khangulyan et al. 2013; Araudo et al. 2013; Bednarek & Banasiński 2015; Wykes et al. 2015; Bosch-Ramon 2015; de la Cita et al. 2016; Vieyro et al. 2017), with results that often point towards possible detectability for nearby sources.

Previous works have considered persistent emission being generated from a whole population of stars, though in all cases

they focus on the interaction that occurs within the jet once the star has already penetrated (Araudo et al. 2013; Wykes et al. 2015; Bosch-Ramon 2015; Vieyro et al. 2017). We refer to this stage of interaction as “steady state”.

In this work, we focus on the possible mass-loading and emission generated at the moment when stars penetrate the jet, and the latter interacts with large “bubbles” of material formed by the collision between the stellar wind and the interstellar medium. Perucho et al. (2017) inferred possible significant non-thermal emission and mass-loading from this early stage in jet-star interaction, using 2D and 3D simulations of one single star with heavy mass loss. We use semi-analytical prescriptions to estimate if this is the case for a whole population of stars within a galaxy.

We focus here on the study of blazar sources, as Doppler boosting is an important factor in enhancing the resulting emission. We consider only low-luminosity sources (i.e.  $L_j = 10^{43} - 10^{45}$  erg s $^{-1}$ ), more abundant in the local universe. As recent studies show that the preferred hosts of blazars are late-type galaxies (e.g. Scarpa et al. 2000; Nilsson et al. 2003; Falomo et al. 2014; Olguín-Iglesias et al. 2016), we model the red giant population within an elliptical bulge. A mostly phenomenological approach is adopted (with the exception of an illustrative numerical simulation), based on specific source knowledge and reference parameter values, as a first simplified step to explore the outcome of the wind bubble and jet interaction.

The paper is organized as follows. A description of the prescriptions used to characterize the stellar population is given in

Sect. 2. In Sect. 3, the properties of the stellar bubbles outside and immediately after penetrating the jet are described. The bubble evolution within the jet is described through analytical estimates and compared with simulation results in Sect. 4. Then, the non-thermal emission generated by bubble-jet interactions is estimated in Sect. 5. Finally, the discussion is presented in Sect. 6.

## 2. Characterization of the stellar population in an elliptical galaxy

Elliptical galaxies contain large populations of red giants, which can have high mass-loss rates, in the range of  $\dot{M} \sim 10^{-10} - 10^{-5} M_{\odot} \text{ yr}^{-1}$  (Reimers 1975). We model the red giant population of any elliptical galaxy by taking as reference values those of M87, as its proximity allows for a precise study.

### 2.1. Stellar number density, mass-loss rate, and wind speed

Assuming a Kroupa initial mass function (IMF), and normalizing it to the total mass of stars ( $M_{\text{T}}$ ), we can estimate the number of stars within the bulge. We take as index for the IMF  $x_1 = -1.3$  for  $0.1 M_{\odot} < M < 0.5 M_{\odot}$  and  $x_2 = -2.3$  for  $0.5 M_{\odot} < M < m_2$  (Kroupa 2001), where  $m_2$  is the mass of the stars exiting the red giant phase (i.e. the most massive stars present; see below). We estimate the total stellar mass adopting that contained within the galactic bulge in M87 (Gebhardt & Thomas 2009), knowing that the radius is  $\sim 40''$  (Harris et al. 1999), corresponding to a bulge radius of  $R_{\text{b}} \sim 3.1$  kpc, which we consider spherical.

From this point on, we follow the calculations in Vieyro et al. (2017) to derive the mass of the red giants in the bulge of the galaxy assuming that all stars formed at the birth of the galaxy (i.e. no star formation extended in time), which yields  $\sim 0.83 M_{\odot}$ , and their number, which is  $N_{\text{T}} \sim 1.3 \times 10^9$ . From Gebhardt & Thomas (2009), we derive that the decay of the density with radial distance/jet height ( $z$ ) can be approximated by  $n_{\text{s}}(z) \propto N_{\text{T}}/z$  in the considered inner  $\sim 40''$ .

We derive the mass-loss rate and wind speed of the red giant population exactly as in Vieyro et al. (2017) for the particular case of M87. The result is a mass-loss rate that increases rapidly with the age of the red giant. Stars are thus modelled as a distribution that depends both on height and red-giant age (i.e. how deep into the red giant phase the star is),  $n_{\text{s}}(z, t_{\text{RG}})$ . For simplicity, we consider a stellar wind of  $v_{\text{w}} = 10^7 \text{ cm s}^{-1}$  (Crowley 2006; Espey & Crowley 2008), and consider it constant during its evolution.

### 2.2. Orbital velocities and penetration rate

In order to study the collective emission and mass-loading generated by the whole population of stars as they penetrate the jet, we need to determine the frequency at which these events occur, that is, the penetration rate ( $PR$ ). Knowing the orbital velocities of stars, one can estimate the penetration rate into the jet for the distance interval ( $z, z + dz$ ) as  $dP(z, t_{\text{RG}}) \approx n_{\text{s}}(z, t_{\text{RG}})v_{\text{orb}}(z)R_{\text{j}}(z)dz$  (Khagulyan et al. 2013), where  $R_{\text{j}}$  is the jet radius.

At low  $z$  the stellar orbital movement is dominated by the central supermassive black hole, and thus stars orbit it following a Keplerian motion, with  $v_{\text{orb}} = \sqrt{GM_{\text{BH}}/z}$ . The gravitational influence of the black hole is dominant within a radius, or jet height,  $z_{\text{g}} = GM_{\text{BH}}/\sigma^2$ , where  $\sigma$  is the stellar velocity dispersion of the bulge. At larger  $z$ , we consider the stars to move within the bulge at a constant velocity  $\sigma$ .

For the black-hole mass, we use the value derived by Gebhardt et al. (2011),  $6.6 \pm 0.4 \times 10^9 M_{\odot}$ . Dispersion veloc-

ity measurements decrease from  $\sigma \sim 480 \text{ km s}^{-1}$  near the nucleus (where the supermassive black hole is dominant) to  $\sigma \sim 320 \text{ km s}^{-1}$  at  $\sim 40''$  (Gebhardt et al. 2011). We take the average value of  $\sigma(z)$ ,  $\sigma = 360 \text{ km s}^{-1}$ , as the constant velocity for stars within the bulge, which gives  $z_{\text{g}} = 220 \text{ pc}$  ( $\sim 2.5''$ ).

## 3. Interaction with the jet

### 3.1. Stars outside the jet

As a star moves outside the jet, the ram pressure generated by its stellar wind is in equilibrium with all external pressures, meaning

$$P_{\text{w}}(\dot{M}) = \rho_{\text{w}}(\dot{M})v_{\text{w}}^2 = P_{\text{ext}}. \quad (1)$$

The external pressures are given by the interstellar medium (ISM) thermal pressure  $P_{\text{ISM}} \approx 10^{-12} \text{ erg cm}^{-2}$ , and the orbital motion of the star through this medium, or ‘‘orbital (ram) pressure’’, is given by

$$P_{\text{orb}}(z) = \rho_{\text{ISM}}v_{\text{orb}}(z)^2, \quad (2)$$

where  $\rho_{\text{ISM}}$  is the ISM density. We fix the ISM density taking one hydrogen atom per  $\text{cm}^3$ , a typical value in the central regions of elliptical galaxies (Tan et al. 2008), throughout the entire bulge.

As the star approaches the jet, the jet lateral pressure  $P_{\text{lat}}$  may be larger than the pressures generated by the movement within the ISM:

$$P_{\text{lat}}(z) = L_{\text{j}}/c\pi z^2\Gamma_{\text{j}}^2, \quad (3)$$

where  $L_{\text{j}}$  and  $\Gamma_{\text{j}}$  are the jet luminosity and Lorentz factor, respectively (Bosch-Ramon & Barkov 2016). Therefore, in close proximity with the jet,

$$P_{\text{ext}} = \max(P_{\text{lat}}, P_{\text{ISM}} + P_{\text{orb}}). \quad (4)$$

We call  $R_{\text{out}}$  the distance from a star at which pressure equilibrium is reached outside the jet. At this distance, the colliding pressures generate a double bow shock in which both stellar-wind material and interstellar material are accumulated. This shocked layer surrounds the star in a bullet-like shape, with material gathering in the direction of the stellar movement toward the jet, and eventually escaping in the opposite direction.

We approximate this shocked region as a sphere of radius  $R_{\text{out}}$ , in which an amount of material of mass  $M_{\text{out}}$  is contained, which can be estimated as

$$R_{\text{out}}^2 = \frac{\dot{M}v_{\text{w}}}{4\pi p_{\text{ext}}}, \quad M_{\text{out}} = 4\pi R_{\text{out}}^3 \rho_{\text{w}}(R_{\text{out}}). \quad (5)$$

We do not consider the mass accumulated within the shocked layer, which would be of the order of  $(v_{\text{w}}/v_{\text{orb}})^2 M_{\text{out}} \lesssim 0.1 M_{\text{out}}$ .

The dominant pressure component for most of the considered jet range is  $P_{\text{orb}}$ , with  $P_{\text{lat}}$  being of comparable value at the base of the jet.

### 3.2. Stars penetrating the jet

As a star begins to penetrate the jet, the most external layers of the bubble it carries are hit by the jet ram pressure. This results in a shock that starts to propagate through those layers with a speed  $c_{\text{s}} \approx \sqrt{L_{\text{j}}/S_{\text{j}}c\rho_{\text{w}}(R)}$ . If the speed at which the shock propagates is sufficiently slow (i.e. the bubble is dense enough), part of the bubble material will penetrate the jet along with the star before

the shock reaches the stagnation radius,  $R_s$ . This will happen for all layers for which

$$c_s(R_{\text{in}}) < v_{\text{orb}}, \quad R_{\text{in}}^2 = \frac{v_{\text{orb}}^2 \dot{M}}{4\pi v_w P_j}, \quad (6)$$

where  $P_j$  is the jet pressure. This means layers with  $R > R_{\text{in}}$  will be expelled before the star fully penetrates the jet, and lost at the jet contact discontinuity (CD), while all layers within  $R_{\text{in}}$ , with mass  $M_{\text{in}} = 4\pi R_{\text{in}}^3 \rho_w(R_{\text{in}})$ , will manage to penetrate.

Once inside the jet, the shock will continue to propagate in the wind until it reaches the stagnation radius  $R_s$ , the distance from the star where the wind and jet ram pressures are equal. There, a double bow shock is formed in which particles can be accelerated up to relativistic energies. In this work, we refer to this emission as steady state emission (e.g. Vieyro et al. 2017), as the jet-wind interaction process is continuous while the stars are inside the jet<sup>1</sup>.

Stellar material contained in the range  $R_s - R_{\text{in}}$  is expelled within the jet as a blob (Bosch-Ramon et al. 2012; Perucho et al. 2017). The typical initial sizes of the bubbles, compared with the jet radius, are shown in Fig. 1 for a red giant of average mass-loss rate ( $\dot{M} = 5.7 \times 10^{-10} M_{\odot} \text{yr}^{-1}$ ), and for the red giant mass-loss rate that generates the dominant events ( $\dot{M}_{\text{dom}} = 1.4 \times 10^{-8} M_{\odot} \text{yr}^{-1}$ , as calculated in Sect. 5.2).

For the particular set of parameters used to plot Fig. 1, above  $z \sim 400$  pc the size of the bubble inside the jet is shown as larger than the size of the bubble outside the jet. In such a case, the material introduced into the jet would be that contained within  $R_s - R_{\text{out}}$ . Another possibility, for a different set of parameters, is that  $R_s$  is larger than  $R_{\text{in}}$ , but smaller than  $R_{\text{out}}$ . In such a case, the star would lose any outer layers in the CD, and once inside the jet, the stellar wind termination region would expand up to the stagnation radius.

Figure 1 shows the mass contained in the bubble outside and right after penetrating the jet, for the average and the event-dominant mass-loss rates. The jet is loaded with the external matter brought by the bubbles expelled by stars at penetration, though this mass-load rate is much lower than the jet  $\dot{M}_{\text{jet}} = L_j / \Gamma_j c^2$ , and therefore unlikely to result in a dynamical effect on the jet.

As has been studied for example by Wykes et al. (2015) and Vieyro et al. (2017), a population of high-mass stars in starburst galaxies can interact strongly with the jet. Young OB stars have stronger winds than red giants, with higher mass-loss rates and speeds. However, these stars have such fast winds that  $v_w > v_{\text{orb}}$ . Following Eq. (5), when that condition is met,  $R_s > R_{\text{in}}$ . Therefore, the star penetrates the jet and the size of the interaction region surrounding the star actually increases, with no significant external material introduced into the jet.

#### 4. Bubble evolution within the jet

We consider a jet that initially expands with a conical geometry, launched close to the supermassive black hole in the centre of the galaxy. We consider that the jet recollimates, which we model as the jet becoming cylindrical:

$$R_j(z) = \begin{cases} \theta z, & \text{if } z < z_{\text{eq}} \\ \text{Const}, & \text{if } z \geq z_{\text{eq}} \end{cases}, \quad (7)$$

when its pressure becomes equal to that of the ISM.

<sup>1</sup> Instabilities produced at the jet-wind interaction region may actually lead to individual star-jet interaction variability (de la Cita et al. 2016).

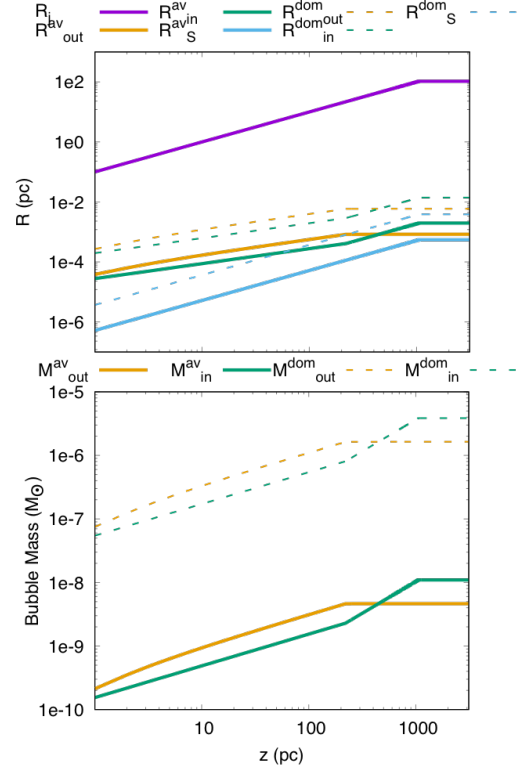


**Fig. 1.** *Top panel:* radius of bubbles outside the jet (yellow), right after penetrating the jet (green) and at stagnation (blue) compared to the radius of the jet, as a function of jet height. *Bottom panel:* mass within bubbles of radius  $R_{\text{out}}$  (yellow), and  $R_{\text{in}}$  (green), as a function of jet height. Parameters used are  $L_j = 10^{44} \text{erg s}^{-1}$ ,  $\Gamma_j = 10$  and the orbital values given in Sect. 2.2. Values for both a red giant of average mass-loss rate (solid line) and a red giant that generates the dominant events (dashed line, see Sect. 5.2) are plotted.

After the star penetrates the jet and a bubble of stellar material is expelled, this bubble evolves as a result of the interaction with the jet. We have adopted the analytical modelling of the evolution of a blob impacted by a jet developed by Barkov et al. (2010, 2012) and Khangulyan et al. (2013; for previous numerical simulations of this process, see e.g. Bosch-Ramon et al. 2012; Perucho et al. 2017).

The shock produced by the impact of the jet ram pressure causes the material of the bubble to heat up, quickly expand, and accelerate, resulting in the bubble reaching relativistic speeds. This acceleration occurs on timescales of

$$t_{\text{acc}} \simeq \begin{cases} z_0 / \beta c, & \text{if } D < 1 \\ z_0 / D \beta c, & \text{if } D > 1 \end{cases}, \quad D \equiv \frac{P_{j,0} \pi R_b^2 z_0}{4c^2 M_b \Gamma_j^3}, \quad (8)$$

where  $D$  is a dimensionless parameter related to the jet luminosity and Lorentz factor and the mass of the bubble,  $R_b$  is the radius of the bubble after acceleration (see e.g. Barkov et al. 2012), and any subindex “0” refers to the value at  $z_0$ , the height at which the star penetrates. The value  $D$  actually gives a comparison between bubble and jet mass on scales of  $z_0$ ; that is, if  $D > 1$  ( $< 1$ ), the jet will (not) effectively accelerate the blob before it covers a distance  $\sim z_0$ . After the blob is accelerated, it is carried downstream (likely at least partially disrupted) until jet termination, at a height  $H$  and at a speed  $\sim \beta c$ , thus on a timescale  $t_{\text{esc}} \sim (H - z_0) / \beta c$ .

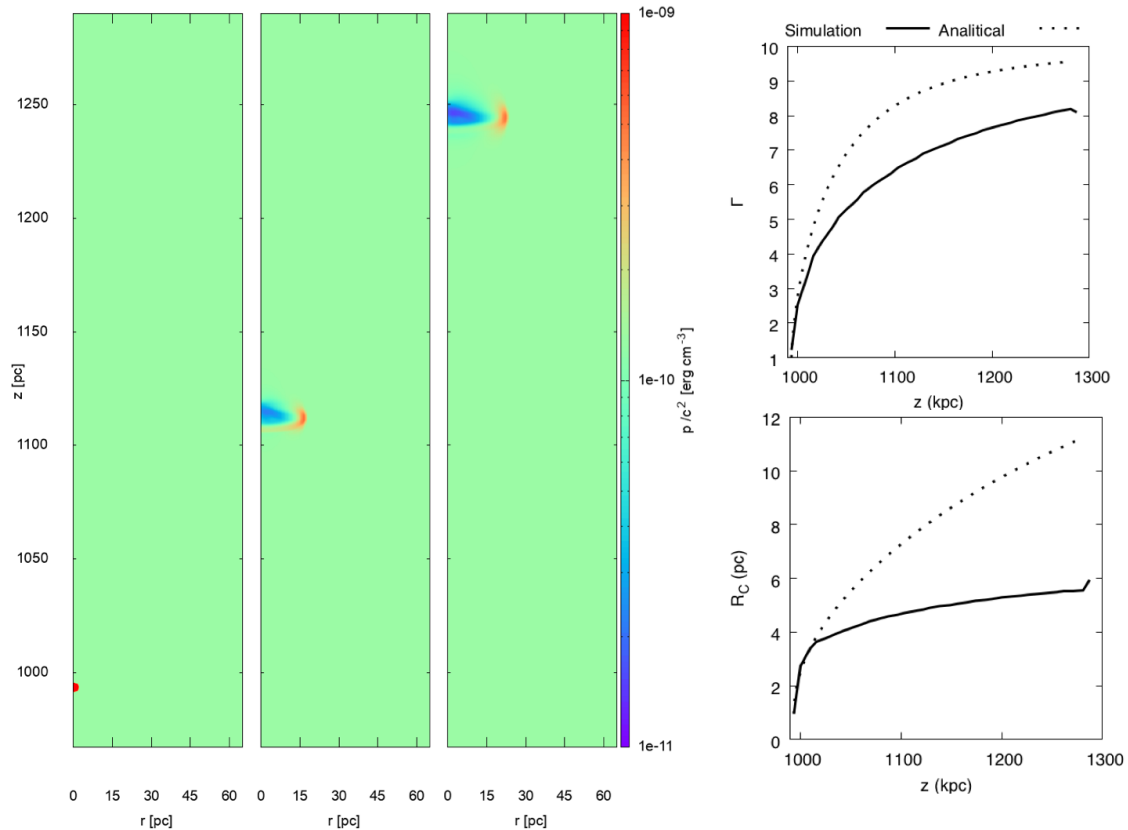


**Fig. 2.** *Left panel:* density maps obtained from a hydrodynamic simulation of the interaction between the jet and the penetrating bubble. Three snapshots are taken  $\sim 0.4$ , 400 and 950 yr after penetration to illustrate bubble evolution. *Right panels:* bubble Lorentz factor/bubble radius as a function of jet height as calculated through the analytical estimate (dotted line) of Barkov et al. (2010, 2012), used to derive all results presented in this work, and compared to those obtained through our simulations (solid line).

This analytical approximation to the bubble evolution within the jet, which we use to calculate the results presented in Sect. 5, can be compared to results obtained through numerical simulations. For that, we simulate here the bubble-jet interaction solving numerically the equations of relativistic hydrodynamics (RHD) assuming axisymmetry, a gas with constant adiabatic index  $\bar{\gamma} = 4/3$ , and a dynamically negligible magnetic field. The RHD equations are solved using the Marquina flux formula (Donat & Marquina 1996; Donat et al. 1998); further details on the code can be found in de la Cita et al. (2016).

The resolution of the calculations is 1000 cells in the vertical direction, the  $z$ -axis, and 200 in the radial direction, the  $r$ -axis. Those numbers of cells correspond to a physical range of  $z_{\text{grid}} = 1000\text{--}1300$  pc and  $r_{\text{grid}} = 0\text{--}65$  pc. The number of cells was chosen such that the results did not change significantly when going to higher resolution. The boundary conditions were set to inflow at  $z_{\text{grid}} = 0$  with parallel stream lines (the jet is re-collimated), reflection at  $r_{\text{grid}} = 0$ , and outflow in the remaining boundaries.

Figure 2 shows three density maps, illustrative snapshots of a simulation of the jet-bubble interaction at  $\sim 0.4$ , 400, and 950 yr after bubble penetration inside the jet. Initial properties are:  $L_j = 10^{44}$  erg s $^{-1}$ ,  $\Gamma_j = 10$ ,  $M_b = 2 \times 10^{-6} M_\odot$ , and  $r_{b,0} = 1.5$  pc. The simulation starts once the cloud has already expanded significantly, moving with a Lorentz factor of 2, in the relativistic regime (e.g. Barkov et al. 2012; Khangulyan et al. 2013). We

focus only on the relativistic regime, as starting from its actual initial radius would require  $10^2\text{--}100^2$  times more cells and thus huge computing costs. As seen in the figure, the shocked bubble evolves upstream of the jet; most of the bubble expansion occurs at early times, and despite partial disruption the structure keeps its integrity.

In Fig. 2 we also plot the bubble radius and Lorentz factor as a function of jet height obtained from the simulation, and compare it to the results of the analytical calculation. The simulated evolution is slightly slower than analytically predicted. We note, however, that while the Lorentz factor of the bubble in the simulation reaches a value of  $\sim 8$ , it should eventually reach the jet Lorentz factor at higher  $z$ . The chosen duration of the simulation of  $\sim 1000$  yr was adopted as a trade-off between a moderated computational time and illustrative effectiveness.

A noticeable difference in Fig. 2 between simulated and analytical results is bubble radius, computed as the mass-averaged cylindrical radius to facilitate comparison. The radius evolves more slowly in the simulation, reaching a final value of a factor  $\lesssim 2$  smaller than the analytical estimate. We expect nevertheless more convergence at larger  $z$  values.

We show thus that the analytical first-order approximation to the bubble evolution used in this work, adopted to derive the results presented in Table 1, is reasonably accurate in the relativistic regime. While instabilities might be important, once the shocked bubble reaches relativistic speeds, its evolution is similar

**Table 1.** Results.

| $L_j$ (erg s <sup>-1</sup> )                        | 10 <sup>43</sup>     | 10 <sup>44</sup>     | 10 <sup>45</sup>     | 10 <sup>43</sup>     | 10 <sup>44</sup>     | 10 <sup>45</sup>     |
|---|----------------------|----------------------|----------------------|----------------------|----------------------|----------------------|
| $\Gamma$  | 3                    | 3                    | 3                    | 10                   | 10                   | 10                   |
| Inverse Compton: $E'_e = E'_{IC}$ , $B = 0.1B_{eq}$ |                      |                      |                      |                      |                      |                      |
| $L_{st}$ (erg s <sup>-1</sup> )                     | $6.5 \times 10^{39}$ | $1.7 \times 10^{40}$ | $1.7 \times 10^{40}$ | $2.5 \times 10^{39}$ | $6.9 \times 10^{39}$ | $1.8 \times 10^{40}$ |
| $L_{pop}$ (erg s <sup>-1</sup> )                    | $1.1 \times 10^{38}$ | $6.5 \times 10^{38}$ | $8.4 \times 10^{38}$ | $3.7 \times 10^{40}$ | $4.7 \times 10^{40}$ | $3.4 \times 10^{40}$ |
| $L_{dom}$ (erg s <sup>-1</sup> )                    | $1.4 \times 10^{38}$ | $8.8 \times 10^{37}$ | $5.5 \times 10^{37}$ | $3.5 \times 10^{40}$ | $3.1 \times 10^{40}$ | $2.5 \times 10^{40}$ |
| $\langle M_b \rangle (M_\odot)$                     | $1.6 \times 10^{-6}$ | $1.7 \times 10^{-6}$ | $1.5 \times 10^{-6}$ | $1.7 \times 10^{-6}$ | $1.7 \times 10^{-6}$ | $1.5 \times 10^{-6}$ |
| $\langle z_0 \rangle$ (kpc)                         | 0.33                 | 1.0                  | 1.6                  | 0.67                 | 1.1                  | 1.6                  |
| $PR$ (yr <sup>-1</sup> )                            | $8.3 \times 10^{-3}$ | $2.6 \times 10^{-2}$ | $4.0 \times 10^{-2}$ | $8.6 \times 10^{-3}$ | $2.7 \times 10^{-2}$ | $4.0 \times 10^{-2}$ |
| $t_{obs}$ (yr)                                      | 54                   | 170                  | 270                  | 40                   | 33                   | 24                   |
| Synchrotron: $E'_e = E'_{Sy}$ , $B = B_{eq}$        |                      |                      |                      |                      |                      |                      |
| $L_{st}$ (erg s <sup>-1</sup> )                     | $7.5 \times 10^{41}$ | $1.9 \times 10^{42}$ | $1.9 \times 10^{42}$ | $1.3 \times 10^{41}$ | $7.4 \times 10^{41}$ | $2.5 \times 10^{42}$ |
| $L_{pop}$ (erg s <sup>-1</sup> )                    | $1.4 \times 10^{40}$ | $4.0 \times 10^{40}$ | $6.7 \times 10^{40}$ | $1.1 \times 10^{42}$ | $2.0 \times 10^{42}$ | $2.5 \times 10^{42}$ |
| $L_{peak}$ (erg s <sup>-1</sup> )                   | $5.8 \times 10^{41}$ | $5.8 \times 10^{42}$ | $5.8 \times 10^{43}$ | $6.3 \times 10^{42}$ | $6.3 \times 10^{43}$ | $6.4 \times 10^{44}$ |
| $\langle M_b \rangle (M_\odot)$                     | $1.5 \times 10^{-6}$ | $1.7 \times 10^{-6}$ | $1.6 \times 10^{-6}$ | $1.7 \times 10^{-6}$ | $1.7 \times 10^{-6}$ | $1.6 \times 10^{-6}$ |
| $\langle z_0 \rangle$ (kpc)                         | 0.26                 | 0.88                 | 1.9                  | 0.91                 | 1.3                  | 1.9                  |
| $PR$ (yr <sup>-1</sup> )                            | $5.7 \times 10^{-3}$ | $2.0 \times 10^{-2}$ | $3.8 \times 10^{-2}$ | $7.4 \times 10^{-3}$ | $2.3 \times 10^{-2}$ | $3.4 \times 10^{-2}$ |
| $t_{peak}$ (yr)                                     | 1.3                  | 0.14                 | 0.014                | 4.8                  | 0.48                 | 0.046                |
| Synchrotron: $E'_e = E'_{Sy}$ , $B = B_{min}$       |                      |                      |                      |                      |                      |                      |
| $B_{min}$ ( $B_{eq}$ )                              | 0.02                 | 0.01                 | 0.01                 | 0.04                 | 0.03                 | 0.02                 |
| $L_{pop}$ (erg s <sup>-1</sup> )                    | $2.1 \times 10^{40}$ | $6.0 \times 10^{40}$ | $1.4 \times 10^{41}$ | $1.7 \times 10^{42}$ | $1.8 \times 10^{42}$ | $1.4 \times 10^{42}$ |
| $L_{dom}$ (erg s <sup>-1</sup> )                    | $6.9 \times 10^{40}$ | $2.1 \times 10^{40}$ | $4.3 \times 10^{40}$ | $1.8 \times 10^{42}$ | $1.1 \times 10^{42}$ | $1.9 \times 10^{42}$ |
| $t_{obs}$ (yr)                                      | 13                   | 45                   | 32                   | 38                   | 65                   | 10                   |

**Notes.** Results for the emission of the whole population of red giants interacting with the jet in steady state ( $L_{st}$ ) and through injecting bubbles at penetration ( $L_{pop}$ ), respectively;  $L_{dom}$  is the luminosity of the typical bubble event that dominates the aforementioned emission, and below it the characteristics of this event are given. For six different jet configurations, we list all results in three cases: inverse Compton emission of electrons with energy  $E'_{IC}$  for  $B = 0.1B_{eq}$ , and synchrotron emission at 100 MeV for  $B_{eq}$  and  $B_{min}$ . The non-listed characteristics of the dominant event in the case of synchrotron emission with  $B_{min}$  are the same as those of the emission with  $B_{eq}$ , for each jet configuration. All the luminosities and energies scale with  $\eta/0.1 \leq 10$ . The luminosities and times are as seen by the observer.

to the analytic predictions, even if disrupted as a filamentary fragmented structure mixed with shocked jet material. The reason is that the transversal expansion of the shocked bubble material is slowed down in the laboratory frame by flow-frame time dilation, and in the longitudinal direction by very similar bottom and the top speeds of the shocked structure in the laboratory frame.

Therefore, from the simulation results, we find it reasonable at this stage to adopt a final constant bubble radius, and a final bubble speed close to that of the jet if  $D > 1$ . For the bubbles that dominate the non-thermal emission (see Sect. 5.2), this condition is fulfilled.

A more complete simulation, including earlier and later stages of the bubble evolution, is planned for future work.

## 5. Radiated non-thermal power

Particles are assumed to be efficiently accelerated at the interaction between the jet and the bubble. The non-thermal energy contained in these particles is uncertain, although we focus here on the case in which the energy budget is significant and detectable radiation may be produced. The specific acceleration mechanism is not considered, and it is just assumed that some fraction of the shocked jet luminosity goes to non-thermal particles.

### 5.1. Energy losses

We assume that electrons (and positrons) are the dominant non-thermal emitting particles. Accelerated protons may also be

present in the jet, although on the scales of interest significant radiation losses are not expected for these particles (see however, e.g. Aharonian 2000). For electrons, we considered the radiative losses via inverse Compton (IC) and synchrotron emission. Regarding non-radiative losses, we considered adiabatic losses for the conical jet, and none after recollimation (but escape when the bubble reaches  $H$ ).

We computed the IC losses as in Bosch-Ramon & Khangulyan (2009; see also Khangulyan et al. 2014). Their approximation is valid for a Planck distribution of target photons of temperature  $T$ , and must be renormalized to the energy density of the considered target photon field. We consider the photon field in an elliptical galaxy as derived by Vieyro et al. (2017).

We also considered synchrotron losses (e.g. Longair 1981) when taking  $B = B_{eq}$ , a magnetic field of equivalent energy density to that of the jet, meaning

$$\frac{B_0^2}{4\pi} = \frac{L_j}{\pi R_j(z_0)^2 c}, \quad (9)$$

with the field depending on height as

$$B(z) = B_0 \left( \frac{z_0}{z} \right)^2, \quad (10)$$

where  $B_0 = B(z_0)$ . We discuss the effects on the synchrotron radiation of considering a lower magnetic field in Sect. 5.2.3.

### 5.2. Radiation

For all combinations of  $L_j = 10^{43}$ ,  $10^{44}$ ,  $10^{45}$ , and  $\Gamma_j = 3$ ,  $10$ , we computed the average luminosity of the whole population of bubbles penetrating the jet (as seen by the observer),  $L_{\text{pop}}$ . Results are presented in Table 1. All parameters except for jet luminosity,  $L_j$ , and Lorentz factor,  $\Gamma_j$ , are fixed as described in Sects. 2 and 3.

We evaluated the emitted non-thermal radiation at two characteristic electron energies: first, for IC emission, at the Thompson-Klein Nishina transition energy, at  $E'_{\text{IC}} = (m_e c^2)^2 / kT\Gamma$ , where the maximum of IC emission is expected for reasonable electron energy distributions, falling in the gigaelectronvolt-Teraelectronvolt range; secondly, for synchrotron emission, for the electrons that generate synchrotron 100 MeV photons as seen by the observer, at  $E'_{\text{Sy}}$ .

We assumed that at most a fraction  $\eta$  of the energy acquired by jet acceleration can be radiated<sup>2</sup>, fixed to 0.1 throughout this work. From first principles, it is not possible to derive the value of  $\eta$ , but the adopted choice maximizes the predicted gamma-ray emission without assuming a full non-thermal conversion of the available energy. All the predicted luminosities thus scale with  $\eta/0.1 \leq 10$ .

We estimated the typical properties of the bubbles that contribute the most to the overall luminosity as

$$\langle A \rangle = \frac{\int A(z, t_{\text{RG}}) L_{\text{pop}}(z, t_{\text{RG}}) dz dt_{\text{RG}}}{L_{\text{pop}}(z, t_{\text{RG}}) dz dt_{\text{RG}}}, \quad (11)$$

where  $A$  denotes the quantity we are interested in evaluating (i.e.  $M_b$  and  $z_0$ ). We refer to events with these properties as the ‘‘dominant’’ events, and list their characteristics in Table 1. Their penetration rate (i.e. rate at which events occur) along with peak luminosity of the event,  $L_{\text{dom}}$  or  $L_{\text{peak}}$ , and typical duration of the peak,  $t_{\text{obs}}$  or  $t_{\text{peak}}$ , are also listed. We note that  $L_{\text{dom}}$  is the average luminosity of a dominant event along its evolution within the jet; in reality, the luminosity is a function of jet height (see Eq. (13)), larger at  $z_0$ , where the star penetrates, and becomes progressively dimmer as the radiative cooling efficiency diminishes.

We also compared the emission generated through this interaction mechanism to that generated in steady state,  $L_{\text{st}}$ , by the same population of red giants (see Sect. 3). The apparent non-thermal luminosity per unit volume at a height  $z$  due to jet-star interactions in steady state is

$$\frac{dL_{\text{st}}(z)}{dV} = \eta L_j F_{\text{rad}}(z) \frac{\delta_j^3}{\Gamma_j^3} \int \left\langle \frac{S_s(z, t)}{S_j(z)} \right\rangle n_s(z, t) dt, \quad (12)$$

where  $\langle S_s(m, t)/S_j \rangle$  is the time-averaged fraction of jet area intercepted by one stellar interaction.

#### 5.2.1. Inverse Compton emission

At electron energies  $E'_{\text{IC}}$ , for all jet parameters considered,  $t'_{\text{IC}} \sim 10^{12} - 10^{13}$  s. This is much larger than the characteristic acceleration time of any considered bubble, typically in the range  $t'_{\text{acc}} \sim 10^6 - 10^9$  s. Therefore, the IC emission at the energy of interest will last until long after the bubble has been accelerated.

As the bubble propagates downstream in the jet, the former radiates an IC luminosity  $L'_{\text{b,IC}} \sim E'_{\text{b,max}}/t'_{\text{IC}}(z)$  in the flow frame, where  $E'_b$  is the total energy emitted by one single bubble in the same frame during its evolution

<sup>2</sup> The bubble acquires in the laboratory frame an energy  $\sim \Gamma_j M_b c^2$  due to jet acceleration.

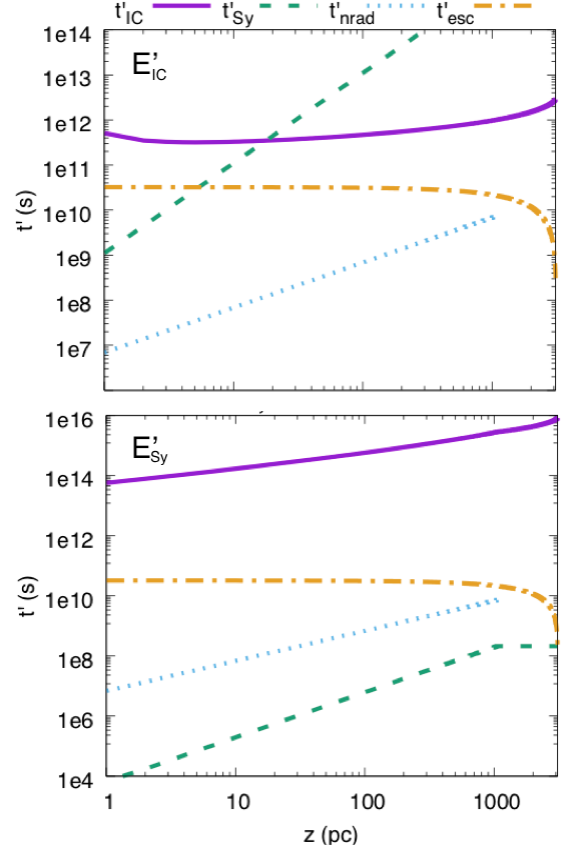


**Fig. 3.** Inverse Compton and synchrotron loss times for a jet with  $L_j = 10^{44}$  erg s<sup>-1</sup>,  $\Gamma_j = 10$ , and (top panel)  $B = 0.1B_{\text{eq}}$ , evaluated at  $E'_{\text{IC}}$ ; (bottom panel)  $B = B_{\text{eq}}$ , evaluated at  $E'_{\text{Sy}}$ . The time for the bubble to reach the jet termination height, and the time of adiabatic losses, are also plotted.

$$E'_b(M_b, z_0) = \int_{z_0}^{z_{\text{max}}} \eta \frac{M_b c^2}{t'_{\text{IC}}(z) \Gamma \beta c} dz; \quad (13)$$

$z_{\text{max}}$  is the maximum height the bubble reaches before losing all energy, or the jet maximum height,  $H$ . This approximation implicitly assumes that the energy distribution of the non-thermal electrons is  $\propto E^{-2}$  (see Sect. 6.2).

Characteristic times for energy losses evaluated at  $E'_{\text{IC}}$ , as well as  $t_{\text{esc}}$ , are plotted in Fig. 3. The energy losses are dominated by adiabatic expansion up to the jet recollimation point. At higher  $z$ , the shortest timescale is  $t'_{\text{esc}}$ , meaning the bubbles exit the jet before emitting (mostly through IC) all of their available energy.

We note that, contrary to the study of synchrotron gamma-ray emission below, IC energy losses are computed taking  $B = 0.1B_{\text{eq}}$ , which is a reasonable value for a jet with power dominated by its kinetic energy. However, since the energy losses at  $E'_{\text{IC}}$  are dominated by non-radiative processes, considering more (or less) intense magnetic fields does not significantly affect the results.

We can estimate the luminosity detected by an observer, generated by the whole bubble population, averaged in time as

$$L_{\text{pop}} = \delta_j^3 \int_{z_{\text{BH}}}^H E'_b(m, z) PR(m, z) dm dz, \quad (14)$$

where  $\delta_j$  is the Doppler boosting factor. This is a valid description as long as there is more than one dominant bubble simultaneously emitting<sup>3</sup>, meaning that the source duty cycle is larger than 1. In addition, the emission generated by the whole population,  $L_{\text{pop}}$ , as seen by the observer will be larger than the emission produced by one single, dominant event,  $L_{\text{dom}}$ .

The predicted apparent luminosities of the IC emission are a few times  $10^{40}$  erg s<sup>-1</sup>. These values are of the order of the steady state emission generated by the whole stellar population within the jet.

### 5.2.2. Synchrotron emission

If we evaluate the energy losses at  $E'_{\text{Sy}}$ ,  $t'_{\text{Sy}}$  is dominant at all heights for  $B' = B'_{\text{eq}}$  (see Fig. 3). The synchrotron emission is so intense that the characteristic emission time is lower than the acceleration time of the bubble,  $t'_{\text{acc}}$ . Therefore, electrons of energy  $E'_{\text{Sy}}$  immediately radiate via synchrotron emission the energy acquired via particle acceleration triggered by the jet-bubble interaction. Electrons in the flow frame are accelerated at a rate  $\xi q B' c$ , where  $\xi$ , a free parameter representing the acceleration efficiency, is fixed to 0.1. Such an efficiency is sufficient to produce observable 100 MeV synchrotron photons, although for  $\xi$  well below 0.1 synchrotron emission would not reach gamma-ray energies (X-rays of luminosities similar to those of IC in Table 1 could still be produced).

Synchrotron 100 MeV photons are produced when a single bubble enters the jet and is accelerated, following a flare-like lightcurve (see Barkov et al. 2012). From Khangulyan et al. (2013), the apparent total energy emitted by a bubble in the synchrotron fast cooling regime is:

$$E_{\text{b}}(M_{\text{b}}, z) = \eta F_{\text{rad}} \bar{F}_{\text{e}} M_{\text{b}} c^2 \delta_j^3, \quad (15)$$

where we take  $\bar{F}_{\text{e}} = 0.2$  (Barkov et al. 2010), and  $F_{\text{rad}}$  is the efficiency with which the particle loses energy through synchrotron radiation. Doppler boosting is already accounted for in Eq. (15) for the energy radiated by one single bubble.

Unlike in the case of the IC emission, synchrotron  $L_{\text{peak}}$  is 1–3 orders of magnitude higher than the average luminosity  $L_{\text{pop}}$ , with

$$L_{\text{peak}}(M_{\text{b}}, z) = \eta F_{\text{rad}} c F_{\text{e,max}} P_0 \delta_j^2 \pi r_{\text{b}}^2, \quad (16)$$

where we take  $F_{\text{e,max}} = 0.4$  (Barkov et al. 2010), and  $r_{\text{b}}$  is the radius of the bubble once it has expanded and reached relativistic velocities (Khangulyan et al. 2013). The apparent duration of this intense emission can be roughly estimated as  $t_{\text{peak}} = E_{\text{b}}/L_{\text{b}}$ , which shows that the emission is highly variable, like intense, short flares occurring a few times per century or millennia.

For the high  $\xi$  adopted, the synchrotron 100 MeV emission could reach luminosities of  $\sim 10^{44}$  erg s<sup>-1</sup> for the most powerful jets considered, even under low jet Lorentz factors. As the emission is intense but short, we would have duty cycles of  $PR \cdot t_{\text{obs}} \sim 10^{-4} - 10^{-2}$ , depending on  $L_j$  and  $\Gamma_j$ .

<sup>3</sup> The Doppler-boosted luminosity of one single bubble is  $L_{\text{b}}^{\text{app}} = \delta^4 L'_{\text{b}}$ . If more than one star is within the jet emitting at different heights, the photons emitted by the distribution of sources at the same time in  $K'$  are not observed simultaneously in  $K$ , leading to  $\delta^4 \rightarrow \delta^3/\Gamma$  (see Sikora et al. 1997). Thus, if insufficient events take place at the same time, the apparent luminosity of the whole population can be reduced to that of one single bubble.

### 5.2.3. Synchrotron emission at low magnetic fields

Synchrotron emission at  $\sim 100$  MeV is highly dependent on the value of the magnetic field: high magnetic fields yield an intense emission radiated in a very short amount of time, yielding a low duty cycle.

In order to maximize the duty cycle, we take the lowest possible value of the magnetic field,  $B = B_{\text{min}}$ , for which electrons with  $E'_{\text{Sy}}$  still cool more efficiently through synchrotron emission than through non-radiative losses. Looking at Fig. 3, this would result in values of  $t'_{\text{Sy}}$  just below  $t'_{\text{ad}}$  and/or  $t'_{\text{esc}}$ . The obtained magnetic field values,  $B_{\text{min}}$ , are listed in Table 1. For these values of  $B$ , luminosity is up to  $\sim 10^{42}$  erg s<sup>-1</sup>, but the duty cycle can be increased up to  $PR \cdot t_{\text{obs}} > 1$ .

We note that in this case with  $B = B_{\text{min}}$ ,  $t'_{\text{Sy}} > t'_{\text{acc}}$ , meaning that the synchrotron emission is computed as described in Sect. 5.2.1, that is, as is done for inverse Compton radiation.

## 6. Discussion

The dynamical evolution of a bubble of stellar material expelled within the jet is semi-quantitatively well-described by the analytical estimates used in Sect. 4, and only differs from simulations by a moderate numerical factor. Our numerical estimates on gamma-ray energy production are not significantly affected by these differences as long as the bubble Lorentz factor eventually reaches  $\sim \Gamma_j$ . Only in the case of intense Synchrotron emission at high magnetic fields, could there be a small reduction of luminosity, of a factor of a few, if indeed the bubble radius were overestimated in the long run.

Results presented in Table 1 indicate that the emission generated by stars penetrating the jet can be relatively persistent at high energies, through either inverse Compton or through synchrotron emission in the case of low magnetic fields. With large magnetic fields, emission at 100 MeV could be dominated by bright and infrequent events on top of the persistent, lower IC radiation.

The steady state emission of the whole population is unlikely to be detectable. We note that the similar values of  $L_{\text{st}}$  for all the explored jet configurations are due to the fact that it does not strongly depend on either  $\Gamma_j$  or  $L_j$ . The small differences are due to jet geometry, which influences the amount of stars within the jet (e.g. a jet of  $L_j = 10^{43}$  erg s<sup>-1</sup> recollimates at low heights), or due to differences in  $F_{\text{rad}}$  (e.g. under high  $B$  values, for  $L_j = 10^{45}$  the impact of synchrotron losses on electrons at  $E'_{\text{IC}}$  is noticeable).

Inverse Compton emission of the bubbles at  $E'_{\text{IC}}$  seems difficult to detect for the explored jet configurations unless  $\eta \rightarrow 1$ , or for a very nearby source. This is because non-radiative losses, or even synchrotron losses, dominate the process.

Synchrotron emission at  $E'_{\text{Sy}}$  with high magnetic fields can result in bright, detectable flares, although the high luminosity implies a short duration. If we consider lower magnetic fields, persistent emission can be achieved, and luminosities of the order of  $10^{42}$  erg s<sup>-1</sup> for  $\Gamma_j = 10$ .

There are some factors that may easily increase the radiation in the scenario studied here. For instance, for significantly lower values of  $\rho_{\text{ISM}}$  at  $z \sim \text{kpc}$ , say  $\gtrsim 0.1$  cm<sup>-3</sup>, the emission energetics would grow by a factor of several due to the associated larger bubble mass (see Sect. 3.2), limited now by  $M_{\text{in}}$  (see Fig. 1). Furthermore, a younger, more massive red giant population, or the sporadic presence of an asymptotic giant branch (AGB) star within the jet, could also enhance the expected emission.

### 6.1. Younger red giant populations and AGB stars

Our results show that the emission produced by wind bubbles as they penetrate the jet is generally dominated by the most evolved stars within our modelled population (with  $\dot{M} \sim 1.4 \times 10^{-8} M_{\odot} \text{yr}^{-1}$ ). The mass of the bubbles scales with mass-loss rate as  $\propto \dot{M}^{3/2}$ , and the luminosity emitted by the bubble interacting with the jet is proportional to its mass (except for the case of synchrotron emission of 100 MeV photons at  $B_{\text{eq}}$ ). Therefore, our results are scalable with mass-loss rate.

If we had a population of red giants of  $M_{\text{RG}} = 1.5 M_{\odot}$  with a total mass comparable to that of the Galaxy, it would imply an increase of luminosity of a factor of  $\sim 20$  in the case of low-B synchrotron emission, and of a factor of  $\sim 60$  in the case of Inverse Compton emission. In the case of high-B emission, emission depends on the final radius of the bubble, and it would increase by a factor of  $\sim 6$ . In all cases, considering these less abundant stars would lead to a decrease of event occurrences of  $\sim 0.4$ .

We note that in the rare occasion an AGB star penetrates an AGN jet, its wind bubble can inject into the latter up to  $\sim 10^{-2} M_{\odot}$ . This could potentially lead to a long duration event with IC luminosity  $\sim 10^{44} \text{erg s}^{-1}$ .

### 6.2. Caveats of the radiation estimates

In this work we estimate the energy radiated by accelerated particles at a given energy,  $E'_{\text{IC, sy}}$ , where the maximum of emission is expected to be. In assuming that all the available energy that goes into particle acceleration is radiated or lost at the mentioned energy, we are overestimating the overall emission. Depending on the energy distribution of the particles, this simple approximation can differ from a more precise calculation. In the case of inverse Compton emission, we expect this overestimation to be of a factor of a few, and in the case of synchrotron emission, of up to one order of magnitude (Vieyro et al. 2017, and in prep.). This has to be taken into account when reading the luminosities in Table 1. The approximations adopted are valid for electron energy distributions  $\propto E^2$ , typical for astrophysical sources. Harder electron distributions would still lead to similar results to those obtained but for very extreme cases, while steeper distributions would imply an even higher overestimate of the gamma-ray luminosity.

The radiation estimates were focused on gamma rays and a broad band study would require more detailed modelling. Nevertheless, it is worth exploring in the future the radio and X-ray synchrotron emission in the jet-bubble interactions.

## 7. Summary

In this work we have studied the gamma-ray emission produced when the bubbles formed by red giant winds penetrate the jet of a blazar in an elliptical galaxy, and described their dynamical evolution both analytically and through one illustrative simulation. We have shown that the analytical approximation is reasonably accurate at the present stage in the relativistic regime. We have found that the gamma rays produced by the red giant wind bubbles interacting with jets may reach detectable levels if Lorentz factors are high, non-thermal particles are generated very efficiently, and particle acceleration takes place at very high rates (to produce synchrotron 100 MeV photons). This predicted emission could be higher under the presence of an important population of younger red giants, in the rare event an AGB star enters the jet, or for relatively low values of  $\rho_{\text{ISM}}$ . Unless  $B = B_{\text{eq}}$ , duty

cycles are not far below one, and in some cases, a few dominant bubbles could contribute simultaneously to the gamma-ray emission. For  $B = B_{\text{eq}}$ , short bright synchrotron 100 MeV flares may be detected, with year or sub-year scale duration. Most of the known blazars in the local universe are hosted by elliptical galaxies. Therefore, provided that electrons are efficiently accelerated in bubble-jet interactions, it is plausible that some persistent or transient gamma-ray emission detected from the nearest blazars could originate in events like those described here.

*Acknowledgements.* We want to thank the anonymous referee for constructive and useful comments. We acknowledge support by the Spanish Ministerio de Economía y Competitividad (MINECO/FEDER, UE) under grants AYA2013-47447-C3-1-P, AYA2016-76012-C3-1-P, with partial support by the European Regional Development Fund (ERDF/FEDER), MDM-2014-0369 of ICCUB (Unidad de Excelencia “María de Maeztu”), and the Catalan DEC grant 2017 SGR 643. N.T.A. acknowledges support from MINECO through FPU14/04887 grant.

## References

- Aharonian, F. A. 2000, *New Astron.*, **5**, 377
- Araudo, A. T., Bosch-Ramon, V., & Romero, G. E. 2013, *MNRAS*, **436**, 3626
- Barkov, M. V., Aharonian, F. A., & Bosch-Ramon, V. 2010, *ApJ*, **724**, 1517
- Barkov, M. V., Aharonian, F. A., Bogovalov, S. V., Kelner, S. R., & Khangulyan, D. 2012, *ApJ*, **749**, 119
- Bednarek, W., & Banasiński, P. 2015, *ApJ*, **807**, 168
- Bednarek, W., & Protheroe, R. J. 1997, *MNRAS*, **287**, L9
- Begelman, M. C., Blandford, R. D., & Rees, M. J. 1984, *Rev. Mod. Phys.*, **56**, 255
- Blandford, R. D., & Koenigl, A. 1979, *Astrophys. Lett.*, **20**, 15
- Bosch-Ramon, V. 2015, *A&A*, **575**, A109
- Bosch-Ramon, V., & Barkov, M. V. 2016, *A&A*, **590**, A119
- Bosch-Ramon, V., & Khangulyan, D. 2009, *Int. J. Mod. Phys. D*, **18**, 347
- Bosch-Ramon, V., Perucho, M., & Barkov, M. V. 2012, *A&A*, **539**, A69
- Bowman, M., Leahy, J. P., & Komissarov, S. S. 1996, *MNRAS*, **279**, 899
- Crowley, C. 2006, PhD Thesis, School of Physics, Trinity College Dublin, Dublin 2, Ireland
- de la Cita, V. M., Bosch-Ramon, V., Paredes-Fortuny, X., Khangulyan, D., & Perucho, M. 2016, *A&A*, **591**, A15
- Donat, R., & Marquina, A. 1996, *J. Comput. Phys.*, **125**, 42
- Donat, R., Font, J. A., Ibáñez, J. M. I., & Marquina, A. 1998, *J. Comput. Phys.*, **146**, 58
- Espey, B. R., & Crowley, C. 2008, *ASP Conf. Ser.*, **401**, 166
- Falomo, R., Pian, E., & Treves, A. 2014, *A&ARv*, **22**, 73
- Gebhardt, K., & Thomas, J. 2009, *ApJ*, **700**, 1690
- Gebhardt, K., Adams, J., Richstone, D., et al. 2011, *ApJ*, **729**, 119
- Harris, D. E., Biretta, J. A., & Junor, W. 1999, *Lect. Notes Phys.*, **530**, 100
- Hubbard, A., & Blackman, E. G. 2006, *MNRAS*, **371**, 1717
- Khangulyan, D. V., Barkov, M. V., Bosch-Ramon, V., Aharonian, F. A., & Dorodnitsyn, A. V. 2013, *ApJ*, **774**, 113
- Khangulyan, D., Aharonian, F. A., & Kelner, S. R. 2014, *ApJ*, **783**, 100
- Komissarov, S. S. 1994, *MNRAS*, **269**, 394
- Kroupa, P. 2001, *MNRAS*, **322**, 231
- Longair, M. S. 1981, *High Energy Astrophysics* (Cambridge and New York: Cambridge University Press)
- Nilsson, K., Pursimo, T., Heidt, J., et al. 2003, *A&A*, **400**, 95
- Oluín-Iglesias, A., León-Tavares, J., Kotilainen, J. K., et al. 2016, *MNRAS*, **460**, 3202
- Perucho, M., Martí, J. M., Laing, R. A., & Hardee, P. E. 2014, *MNRAS*, **441**, 1488
- Perucho, M., Bosch-Ramon, V., & Barkov, M. V. 2017, *A&A*, **606**, A40
- Reimers, D. 1975, *Mem. Soc. R. Sci. Liege*, **8**, 369
- Scarpa, R., Urry, C. M., Padovani, P., Calzetti, D., & O’Dowd, M. 2000, *ApJ*, **544**, 258
- Sikora, M., Madejski, G., Moderski, R., & Poutanen, J. 1997, *ApJ*, **484**, 108
- Sutherland, R. S., & Bicknell, G. V. 2007, *ApJS*, **173**, 37
- Tan, J. C., Beuther, H., Walter, F., & Blackman, E. G. 2008, *ApJ*, **689**, 775
- Vieyro, F. L., Torres-Albà, N., & Bosch-Ramon, V. 2017, *A&A*, **604**, A57
- Wang, Z., Wiita, P. J., & Hooda, J. S. 2000, *ApJ*, **534**, 201
- Wykes, S., Harcastle, M. J., Karakas, A. I., & Vink, J. S. 2015, *MNRAS*, **447**, 1001

### Part III

## INTERACTION OF AGN JETS WITH A SNR



## NON-THERMAL EMISSION RESULTING FROM A SUPERNOVA EXPLOSION INSIDE AN EXTRAGALACTIC JET

---

In this chapter we present our work "Non-thermal emission resulting from a supernova explosion inside an extragalactic jet" (Vieyro, Bosch-Ramon, and Torres-Albà, 2019), in which we estimate the emission produced by the explosion of a core-collapse supernova inside the jet of a galaxy with significant star formation. We compute the lightcurve of the emission as the supernova remnant moves through the jet, as well as the SED at the expected maximum of emission. We include simulations to illustrate the dynamical evolution of the interaction.



# Non-thermal emission resulting from a supernova explosion inside an extragalactic jet

F. L. Vieyro<sup>1,2</sup>, V. Bosch-Ramon<sup>2</sup>, and N. Torres-Albà<sup>2</sup>

<sup>1</sup> Instituto Argentino de Radioastronomía (IAR, CCT La Plata, CONICET; CICPBA), C.C.5, 1984 Villa Elisa, Buenos Aires, Argentina

e-mail: [fvieyro@iar.unlp.edu.ar](mailto:fvieyro@iar.unlp.edu.ar)

<sup>2</sup> Departament de Física Quàntica i Astrofísica, Institut de Ciències del Cosmos (ICC), Universitat de Barcelona (IEEC-UB), Martí i Franquès 1, 08028 Barcelona, Spain

Received 28 April 2018 / Accepted 11 January 2019

## ABSTRACT

**Context.** Core-collapse supernovae are found in galaxies with ongoing star-formation. In a starburst galaxy hosting an active galactic nucleus with a relativistic jet, supernovae can take place inside the jet. The collision of the supernova ejecta with the jet flow is expected to lead to the formation of an interaction region, in which particles can be accelerated and produce high-energy emission.

**Aims.** We study the non-thermal radiation produced by electrons accelerated as a result of a supernova explosion inside the jet of an active galactic nucleus within a star-forming galaxy.

**Methods.** We first analyzed the dynamical evolution of the supernova ejecta impacted by the jet. Then, we explored the parameter space using simple prescriptions for the observed gamma-ray lightcurve. Finally, the synchrotron and the inverse Compton spectral energy distributions for two types of sources, a radio galaxy and a powerful blazar, are computed.

**Results.** For a radio galaxy, the interaction between a supernova and a jet of power  $\sim 10^{43} - 10^{44}$  erg s<sup>-1</sup> can produce apparent gamma-ray luminosities of  $\sim 10^{42} - 10^{43}$  erg s<sup>-1</sup>, with an event duty cycle of supernova remnant interacting with the jet close to one for one galaxy. For a blazar with a powerful jet of  $\sim 10^{46}$  erg s<sup>-1</sup>, the jet-supernova ejecta interaction could produce apparent gamma-ray luminosities of  $\sim 10^{43} - 10^{44}$  erg s<sup>-1</sup>, but with a much lower duty cycle.

**Conclusions.** The interaction of supernovae with misaligned jets of moderate power can be relatively frequent, and can result in steady gamma-ray emission potentially detectable for sources in the local universe. For powerful blazars much farther away, the emission would be steady as well, and it might be detectable under very efficient acceleration, but the events would be rather infrequent.

**Key words.** radiation mechanisms: non-thermal – galaxies: active – galaxies: nuclei – galaxies: jets

## 1. Introduction

Active galactic nuclei (AGNs) are composed of a supermassive black hole accreting material from the central region of its galaxy host. In order for the black hole to be active, dust, gas, and matter must be available for accretion. One way to enhance accretion is through galaxy mergers (Stockton 1982). At the same time, galaxy interactions or mergers can stimulate nuclear star formation (Toomre & Toomre 1972).

Although galaxies hosting AGNs can be of different types, they tend to be massive galaxies ( $M > 10^{10} M_{\odot}$ ) with younger stellar populations than average (Kauffmann et al. 2003). Several studies have shown that luminous AGN hosts are likely to have higher star-formation rates (SFRs) than normal galaxies (e.g., Kauffmann et al. 2003; Shao et al. 2010); but it may also be the case for low or moderate luminosity AGNs, as suggested by Hickox et al. (2014), Gürkan et al. (2015). There is growing evidence supporting a close connection between nuclear starbursts and AGNs (e.g., Alexander & Hickox 2012). For example, AGN surveys show that the fraction of galaxies hosting AGNs is significantly lower for red galaxies (quiescent, composed mainly of old stars) than for blue (star-forming) galaxies (Wang et al. 2017).

Given the large amount of dust released in supernova (SN) explosions, these events were proposed as a possible mechanism to link starburst phenomena and AGN feedback

(Ishibashi & Fabian 2016). Type Ia SNe are the only type of SNe found in old, elliptical galaxies. These are thermonuclear explosions associated either to an accreting white dwarf in a binary system, or to the merger of two white dwarfs (e.g., Maoz et al. 2014). On the other hand, in star-forming galaxies, a high rate of core-collapse SNe resulting from the explosions of massive, short-lived stars is expected (Kelly & Kirshner 2012).

Since high SFRs favor the occurrence of core-collapse SNe, one cannot neglect the possibility of a core-collapse SN taking place inside the jet of a radio-loud AGN. The resulting interaction, with the SN ejecta playing the role of a dynamical obstacle, may lead to detectable non-thermal radiation: When a jet interacts with an obstacle (e.g., clouds, stars with strong winds), a bow-shaped structure forms in the collision region of the two fluids. Particles can be accelerated up to relativistic energies in this region, and produce high-energy emission. The interaction between relativistic jets and obstacles has been explored in several works. Many of these works focused on studying the dynamical effects that the interaction can have on the jet (e.g., Komissarov 1994; Hubbard & Blackman 2006; Perucho et al. 2014, 2017); others were devoted to study the radiative effects, as gamma-ray flares (e.g., Barkov et al. 2010, 2012a; Bosch-Ramon et al. 2012; Banasiński et al. 2016), or steady high-energy emission (e.g., Araudo et al. 2010, 2013; Bednarek & Protheroe 1997;

Bosch-Ramon 2015; Bednarek & Banasiński 2015; Wykes et al. 2015; de la Cita et al. 2016; Vieyro et al. 2017). Star-jet interactions were also proposed to explain the rapid-variability observed in some powerful blazars (e.g., Barkov et al. 2012b; Khangulyan et al. 2013; Aharonian et al. 2017).

In the present work, we have considered the dynamics and radiation of an AGN jet interacting with a SN. At first, the explosion is not halted by the jet presence until the SN ejecta becomes diluted enough. Then, when the SN ejecta reaches a size similar to the stagnation radius, that is, when the SN ejecta and jet ram pressures balance each other, the SN ejecta expansion is significantly slowed down by the jet impact in all directions but downstream the jet. From that point on, the evolution of the supernova remnant (SNR) is strongly affected by the jet impact. The possibility of supernova-AGN jet interaction has been previously explored for instance by Blandford & Koenigl (1979), who considered the prospect of such an interaction being the cause of the knots observed in the jet of the galaxy M87. In addition, Bednarek (1999) discussed the possibility of very efficient particle acceleration due to the interaction of an AGN jet with a SN shell. In that work, the SN was assumed to be within or close enough to the jet for the interaction to be significant, although the dynamical evolution of the interaction and the associated gamma-ray emission were not computed.

This article is organized as follows: in Sect. 2, the dynamical evolution of a SN ejecta accelerated by a jet is described using a simple model; this model is complemented in the Appendix with hydrodynamical simulations. In Sect. 3, we explore the jet parameter space, and study the outcomes of different scenarios using a simple prescription for the gamma-ray lightcurve. In Sect. 4 we compute the spectral energy distributions (SEDs) resulting from the electrons accelerated in the jet-SN ejecta interaction; we explore two cases: a nearby radio galaxy, and a more distant and powerful blazar. We discuss the adopted model and its results in Sect. 5, and close with the conclusions in Sect. 6.

## 2. Dynamical evolution

The dynamical evolution of an obstacle, for example, a cloud of gas, inside a jet has been extensively studied in several works. The impact of the jet causes a transfer of momentum and the consequent acceleration of the cloud. In addition, it produces a shock wave that propagates through the cloud, compressing and heating it up. The heated material suffers a lateral expansion occurring approximately at the speed of sound. The cloud also forms an elongated tail in the downstream direction as a result of the pressure gradient caused by the impact of the jet. Kelvin–Helmholtz instabilities will start striping material from the cloud downstream. Rayleigh–Taylor instabilities can also develop at the cloud surface directly impacted by the jet, given the acceleration exerted by the jet on the cloud. Eventually, the instabilities should lead to the disruption of the cloud, mixing the latter with the jet flow.

The above description is rather simplified; in reality it is far more complex. Numerical studies show that for quite homogeneous clouds, the cross section can grow significantly before the cloud total disruption (Bosch-Ramon et al. 2012). This takes longer than the time it takes the shock to cross the cloud (e.g., Cooper et al. 2009; Pittard et al. 2010), and the (initial) acceleration timescale of the cloud (Bosch-Ramon et al. 2012). Radiative cooling, accompanied by subsequent cloud disruption, has been shown to significantly extend in time the obstacle role of a cloud impacted by a supersonic, non-relativistic wind (Cooper et al. 2009). On the other hand, relativistic simulations still show

efficient expansion and acceleration of the cloud despite its disruption and radiative cooling (Perucho et al. 2017). The evolution can also be altered by additional factors, such as magnetic fields or thermal conduction, that are not taken into account in this work (e.g., Klein et al. 1994; Fragile et al. 2005).

For the acceleration of the cloud, we have based our study on Barkov et al. (2012a). In that work, the authors describe a model for the acceleration of a cloud, in the present case the SN ejecta, pushed by a magnetically-dominated jet. Here, we studied the dynamical evolution in the case of a purely hydrodynamical jet, since on the jet scales of interest most of the jet magnetic energy is expected to have been already transferred to kinetic energy.

We refer to the laboratory and the SN ejecta reference frame  $K$  and  $K'$ , respectively. For a relativistic jet with negligible thermal pressure, the momentum flux of the jet in  $K'$  is:

$$f' = \Gamma_{\text{rel}}^2 \beta_{\text{rel}}^2 \rho_j h_j c^2, \quad (1)$$

where  $h_j = 1 + \hat{\gamma} \epsilon_j$  is the jet enthalpy,  $\hat{\gamma}$  the adiabatic index (4/3 and 5/3 for a relativistic and a non-relativistic ideal, monoatomic adiabatic gas, respectively), and  $\beta_{\text{rel}} = (\beta_j - \beta_c)/(1 - \beta_j \beta_c)$  the relative velocity between the jet and SN ejecta in  $c$  units, which have velocities  $\beta_j$  and  $\beta_c$  in  $K$ , respectively. The jet momentum flux in  $K$ ,  $f$ , relates to  $f'$  through:

$$f' = \left(1 - \frac{\beta_c}{\beta_j}\right)^2 \Gamma_c^2 f. \quad (2)$$

where  $\Gamma_c$  is the Lorentz factor of the cloud.

The SN ejecta momentum increases due to the acceleration caused by the jet in its direction of motion. The equation of motion is (Barkov et al. 2012a):

$$\frac{d\Gamma_c}{dt} = \frac{\pi r_c^2 \beta_c}{M_c c} f', \quad (3)$$

which, combined with Eq. (2), results in:

$$\frac{d\Gamma_c}{dt} = \frac{\pi r_c^2 \beta_c}{M_c c} \left(1 - \frac{\beta_c}{\beta_j}\right)^2 \Gamma_c^2 f \approx \frac{L_j}{M_c c^2} \left(\frac{r_c}{r_j(z)}\right)^2 \left(1 - \frac{\beta_c}{\beta_j}\right)^2 \Gamma_c^2 \beta_c, \quad (4)$$

where  $L_j = \pi r_j^2 \Gamma_j^2 \beta_j \rho_j h_j c^2$  ( $\approx \pi r_j^2 f c$  for  $\Gamma_j \gg 1$ ) is the jet power (including rest mass).

The jet is assumed to be conical, that is, with a constant opening angle  $\theta$ , where the radius of the jet is a function of the distance  $z$  to the black hole:  $r_j(z) \approx \theta z$ . We adopt a jet Lorentz factor of  $\Gamma_j = 10$  and an opening angle of  $\theta = 1/\Gamma_j$ .

The time lasted by the event as seen by the observer relates to the time in the laboratory frame  $t$  as

$$t_{\text{obs}}(z) = \int_{z_0}^z (1 - \beta_c \cos i) dt = \int_{z_0}^z (1 - \beta_c \cos i) \frac{dz}{\beta_c c}, \quad (5)$$

where  $i$  is the angle between the jet axis and the line of sight.

The impact of the jet, in addition to transferring kinetic energy, heats up the SN ejecta as well. The SN ejecta is in pressure balance with the shocked jet flow that is pushing, with the pressure at the contact region being  $\sim f'$ . Since initially the jet flow is strongly supersonic in  $K'$ ,  $f'$  is larger than the jet lateral total pressure, and the jet-SN ejecta pressure balance leads to the above mentioned fast SN ejecta expansion, fueled by the jet-transferred heat.

The expansion of the SN ejecta enhances the interaction with the jet, favoring the acceleration of the former, and also its disruption. As already noted, simulations show that the (deformed)

SN ejecta expansion and acceleration can continue for some time (Bosch-Ramon et al. 2012; Perucho et al. 2017; see also the Appendix). If the SN ejecta achieves a relativistic regime, which is the case for a powerful jet, its expansion in the laboratory frame is slowed down: (i) in the jet direction, by the relatively small velocity difference between different parts of the SN ejecta; (ii) in the direction perpendicular to the jet, relativistic time dilation in the flow frame leads to a slow expansion. We note that the lateral pressure of the shocked jet fluid, which passes around the SN ejecta, may contribute to confine the SN ejecta, slowing its expansion down to some extent (not considered here but at the end of the expansion; see below). These effects combined allow the SN ejecta to keep some integrity even when close to total disruption, extending the time needed for fully mixing with the jet flow and the traveled distance inside the jet in the laboratory frame. For weak jets, the SN ejecta accelerates at a low rate, and it is expected to cover a longer distance inside the jet before its disruption (Khanguyan et al. 2013). These predictions are supported by results presented in the appendix, where we show the results of an axisymmetric, relativistic hydrodynamical simulation of an interaction between the SN ejecta and a relatively weak jet. Based on these results, and on the above discussion for the powerful jet case, we have assumed for simplicity here that most of the SN ejecta mass remains in causal contact with the jet contact surface, effectively evolving as a roughly spherical cloud, with its radius increasing as

$$r_c(t) = R_0 + \int \frac{c_s dt}{\Gamma_c(t)}, \quad (6)$$

where  $R_0$  is the initial SN ejecta radius, and

$$c_s^2 = \frac{\hat{\gamma} P_c}{h_c \rho_c} \quad (7)$$

is the SN ejecta sound speed squared, with  $h_c$  being the specific enthalpy of the SN ejecta, and  $P_c$  its pressure. In the present context,  $R_0$  is determined through balancing its pressure and  $f'$ . This condition can be written as

$$[P_c = f'] \sim \left[ \frac{3E_0}{10\pi R_0^3} = \frac{L_j}{c\pi r_j(z)^2} \right], \quad (8)$$

where  $E_0$  is the total energy of the SN ejecta, adopted as the standard isotropic SN luminosity of  $E_0 = 10^{51}$  erg. For simplicity, we adopted a reference SN ejecta mass value of  $M_c = 10 M_\odot$ . We note that, since  $\beta_c \sim 0$  at the beginning of the interaction, we use  $f' = f$  in Eq. (8).

**Applicability of the dynamical model.** When the SN ejecta has expanded significantly, its pressure can become smaller than the jet lateral pressure, taken here one hundredth of  $f$  as a fiducial value. Its exact value does not have a strong impact on the results as long as the jet is highly supersonic in  $K$ . Once the SN ejecta pressure is equal to the jet lateral pressure, the SN ejecta evolves more smoothly with the jet flow. From that point on, we assumed that the jet energy and momentum transferred to the SN ejecta become small, and therefore neglect any further acceleration of particles.

When the SN ejecta covers the whole jet section, its expansion rate is assumed to be the same as that of the jet, i.e.,  $r_c \sim r_j$ , with the jet flow at the interaction location moving with the SN ejecta. This is a reasonable assumption to zeroth order, as long as the jet external medium is much denser than the jet itself, which is expected for a jet on the galactic disk scales, as the denser

medium inertia encapsulates the jet shocked flow (see Sect. 5). An accurate account of this situation can show complex features in the jet and SN ejecta hydrodynamics; this requires a numerical study, and a detailed account of such a process is out of the scope of this work (see the appendix for a simulation with a simple gas model).

### 3. General study

#### 3.1. Simplified model

The galaxy host is assumed to be a starburst with a high SFR ( $M_{\text{SFR}}$ ) and a disk geometry. We considered that the starburst has an IR luminosity of  $L_{\text{IR}} = 10^{12} L_\odot$  (e.g., an ultraluminous infrared galaxy, ULIRG, Sanders et al. 1988). The stellar and IR fields are modeled as gray bodies with characteristic temperatures of  $T_s = 30000$  K and  $T_{\text{IR}} = 200$  K, respectively (Vieyro et al. 2017).

There are three important free parameters in the model,  $L_j$ ,  $\Gamma_j$ , and  $i$ . Throughout this work, we consider the jet Lorentz factor to be constant; in particular, we adopt  $\Gamma_j = 10$ , which is a common value in AGNs (e.g., Jorstad et al. 2017). Moderate variations around this value do not affect significantly the results of the model for jets with modest power, but the effect would be important for powerful blazars (see Sect. 5.4). The parameter space of the jet luminosity and inclination can be studied adopting a simplified model of the apparent non-thermal luminosity. The limitations of this simplified model are discussed in Sect. 5.

We considered that the SN explosion takes place at a height  $z_0$  inside the jet. We fix  $z_0 \sim 50$  pc, as these are roughly the scales at which it is more likely that a SN explosion will occur within the jet, for the adopted star-forming disk. For smaller  $z_0$ , the jet volume is much smaller; for larger  $z_0$ , in the disk periphery and beyond, star formation is suppressed.

Inside the jet, the shocked SN ejecta acceleration and evolution results in an evolution of the jet energy flux dissipated at the jet-SN ejecta interaction surface in  $K'$ . This dissipated energy flux of the jet can be taken as a proxy of the energy flux injected into non-thermal particles. The corresponding power injected into non-thermal particles at  $z$ , due to the jet-SN ejecta interaction, can be expressed in  $K'$  as:

$$L'_{\text{NT}}(z) = \eta_{\text{NT}} \pi r_c^2 \beta_{\text{rel}} \Gamma_{\text{rel}} (\Gamma_{\text{rel}} h_j - 1) \rho_j c^3, \quad (9)$$

where the constant  $\eta_{\text{NT}}$  is the fraction of jet energy that impacts the SN ejecta and is converted into non-thermal energy. We note that the rest-mass energy has been removed to derive  $L'_{\text{NT}}$ . A reference value of 0.1 has been adopted for  $\eta_{\text{NT}}$  in this work; high enough so significant radiation is predicted, but well below the upper-limit of 1 (see Sect. 5.5).

Only a fraction of the energy that is injected in non-thermal particles is channeled into radiation. This fraction is quantified with the radiative efficiency  $\xi'_{\text{IC/sync}}(E', z)$ , which in  $K'$  can be estimated as

$$\xi'_{\text{IC/sync}}(E', z) = \frac{t'^{-1}_{\text{IC/sync}}}{t'^{-1}_{\text{rad}} + t'^{-1}_{\text{nrad}}}, \quad (10)$$

where  $t'^{-1}_{\text{nrad}}$  accounts for the non-radiative losses in  $K'$  (e.g., adiabatic losses and particle advection, of similar scale; see Vieyro et al. 2017), and  $t'^{-1}_{\text{rad}} = t'^{-1}_{\text{IC}} + t'^{-1}_{\text{sync}}$  for synchrotron and IC losses in  $K'$ . The emitted energy in  $K'$  is, then,  $L'_{\text{intr}} = L'_{\text{NT}}(z) \xi'_{\text{IC/sync}}(E', z)$ .

The intrinsic luminosity should be corrected by Doppler boosting. The IC and synchrotron lightcurves of the radiation as seen by the observer can be estimated as

$$L_{\text{IC/sync}}^{\text{app}}(t_{\text{obs}}) = \delta_c(z)^4 L'_{\text{intr}} = \delta_c(z)^4 L'_{\text{NT}}(z) \xi'_{\text{IC/sync}}(E, z), \quad (11)$$

where  $\delta_c$  is the Doppler boosting factor of the emitting flow:

$$\delta_c = \frac{1}{\Gamma_c(1 - \beta_c \cos i)}, \quad (12)$$

and  $t_{\text{obs}}$  is related to  $z$  through Eq. (5). Equation (11) is valid as long as the accelerated particles follow an energy distribution similar to  $\propto E^{-2}$ , meaning that the energy is equally distributed among different energy scales (see also Sect. 4).

We have focussed here on electrons (and positrons) as radiating particles, and synchrotron and IC as radiative processes, as they emit the most efficiently in the regions of interest. Previous works considered also hadronic emission close to or at the jet base (e.g., Barkov et al. 2010, 2012b).

We derived the magnetic field to compute synchrotron emission assuming that the total magnetic energy density is a fraction  $\zeta_{\text{eq}}$  of the jet energy density. For a magnetic field predominantly perpendicular to the flow motion (e.g., toroidal), in  $K'$  one obtains:

$$B'_{\phi}(z) \approx \frac{1}{\Gamma_c z} \sqrt{\frac{4\zeta_{\text{eq}} L_j}{\theta^2 c}}. \quad (13)$$

An equipartition magnetic field,  $\zeta_{\text{eq}} = 1$ , would imply in our convention that the jet energy density is equally divided between magnetic and particle energy density. Throughout the article we adopt  $\zeta_{\text{eq}} = 10^{-2}$  (except when otherwise indicated), which results in a magnetic field 10 times below the equipartition value, as estimated in some extragalactic jets (Hardcastle 2011).

We consider as main target photons for IC interactions the infrared (IR) field associated with starburst galaxies (Vieyro et al. 2017), and compute the IC cooling rate using the full Klein–Nishina cross section (Khagulyan et al. 2014) and following the target treatment described in Dermer & Schlickeiser (1993).

To obtain the lightcurves of IC emission, we calculate  $L_{\text{IC}}^{\text{app}}$  at a reference energy of  $E'_{\text{IC}} = (m_e c^2)^2 / k T_{\text{IR}} \Gamma_c$ , where  $E'_{\text{IC}}$  is approximately at the maximum of the IC cross section in  $K'$  for (quasi)head-on IC interactions, around the transition from the Thomson to the Klein–Nishina regime.

### 3.2. Results of the simplified model

In Fig. 1, we show the evolution of the SN ejecta Lorentz factor for blazar-like sources (i.e.,  $i = 0^\circ$ ), for different values of jet power,  $\Gamma_j = 10$  and  $z_0 = 50$  pc. The more powerful the jet, the shorter the time it takes for the SN ejecta to be accelerated to a higher Lorentz factor; it reaches a relativistic regime before covering the whole jet section only for the most powerful jets ( $L_j = 10^{46} - 10^{47}$  erg s $^{-1}$ ). We recall that, for all the cases studied,  $\eta_{\text{NT}} = 0.1$ .

In all cases, the SN ejecta expands and eventually covers the whole jet cross section. After this point, the dynamical model becomes less suitable to describe the evolution of the SN ejecta, hence in the figure we show this evolution phase using dashed lines (see Sect. 5 for a discussion of the validity of the model).

In Fig. 2, we show the approximated IC lightcurve in gamma rays, as seen by the observer, for  $L_j = 10^{43} - 10^{44}$  erg s $^{-1}$  and different inclination angles. For intermediate inclinations, say

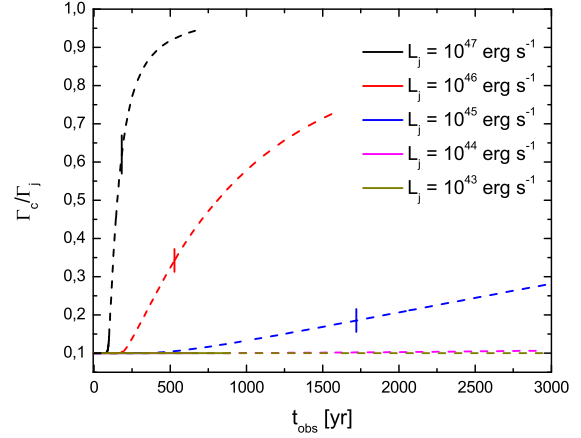


**Fig. 1.** Evolution of the SN ejecta Lorentz factor for different jet powers, for  $i = 0^\circ$ . The vertical ticks mark the point where the SN ejecta crosses 1 kpc. The lines become dashed when the SN ejecta covers the whole jet section.

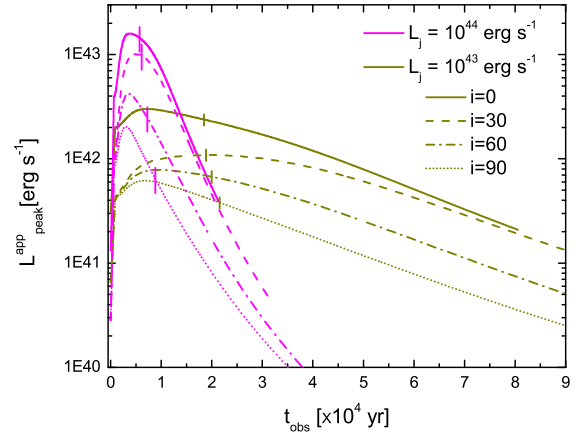


**Fig. 2.** Gamma-ray IC lightcurves computed for different inclination angles. As in Fig. 1, the vertical bars indicate the point where the SN reaches 1 kpc.

$i = 30^\circ$ , the apparent luminosities are above  $10^{42}$  and  $10^{41}$  erg s $^{-1}$ , during an observed period of  $\sim 10^4$  and  $\sim 10^5$  yr, for  $L_j = 10^{44}$  and  $10^{43}$  erg s $^{-1}$ , respectively. For completeness, the lightcurves show the SN ejecta propagating until it reaches  $z = 25$  kpc. Nevertheless, the jet properties can change significantly on kpc scales (e.g., the jets may be already disrupted in weak, FRI-type jets), and our prescription for the SN ejecta evolution may be far from correct in those regions. Therefore, effective jet–SN ejecta interaction may be reliable up to  $z \lesssim 10$  kpc, and in fact results beyond  $z \sim 1$  kpc (indicated in the figures by vertical ticks) should be taken with caution.

For the most powerful jets,  $L_j \geq 10^{45}$  erg s $^{-1}$ , synchrotron self-Compton (SSC) is the main mechanism of gamma-ray emission and for such process the semi-analytical approach described in Sect. 3.1 is no longer valid. For these jets, however, the approach is still valid for, and worth applying to, the synchrotron gamma-ray emission, which may reach  $\geq 100$  MeV as seen by the observer. The critical synchrotron energy can be estimated as

$$E_c = \zeta 236 \text{ MeV } \delta_c, \quad (14)$$

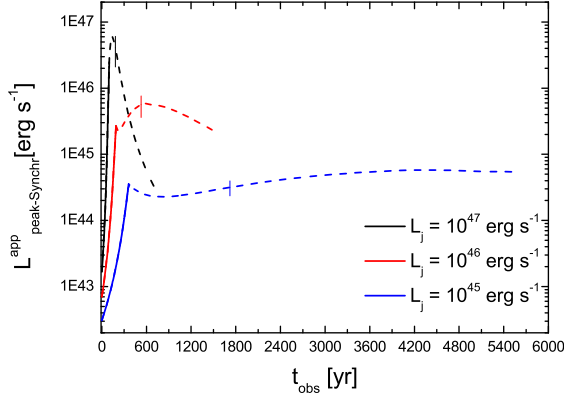


**Fig. 3.** Gamma-ray synchrotron lightcurves for powerful jets with  $i = 0^\circ$ . As in Fig. 1, the solid-to-dashed transition indicates the moment the SN ejecta covers the jet section, and the vertical bars show the point where the SN crosses 1 kpc.

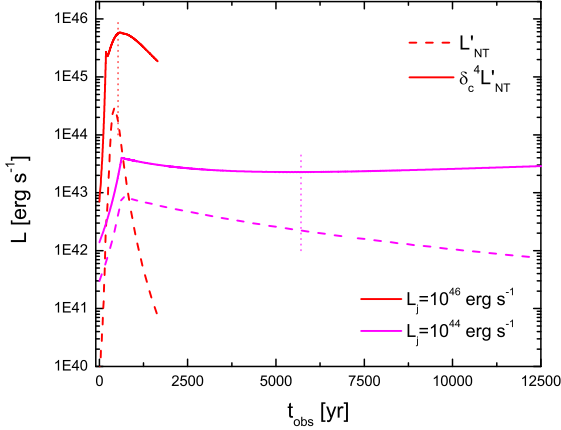


**Fig. 4.** Luminosity injected into non-thermal particles in  $K'$ ,  $L'_{\text{NT}}$  (dashed lines), and corrected by Doppler boosting,  $L'_{\text{NT}}\delta_c^4$  (solid lines), for  $L_j = 10^{44}-10^{46} \text{ erg s}^{-1}$ , and  $i = 0^\circ$ . The vertical bars show the point where the SN ejecta crosses 1 kpc.

where  $\varsigma < 1$ , determines the particle acceleration rate  $\dot{E} = \varsigma q B c$ , and typically is not well constrained. For values of  $\varsigma \gtrsim 1/\delta_c$ , the critical energy can reach values of  $\sim 100 \text{ MeV}$  as seen by the observer. Figure 3 shows the synchrotron lightcurves for the powerful jets; we consider blazar-like sources, since high  $\delta_c$  values are necessary to obtain photons of  $100 \text{ MeV}$  as seen by the observer. As in Fig. 2, the evolution is computed until  $z = 25 \text{ kpc}$ , and the vertical bars mark the moment when the jet crosses 1 kpc. It can be seen that for these jets, the synchrotron radiation could dominate the gamma-ray emission in the *Fermi* energy range. As mentioned in Sect. 3.1, we have adopted  $\zeta_{\text{eq}} = 10^{-2}$ ; since synchrotron losses are dominant for high energy electrons, the luminosities obtained at  $\sim 100 \text{ MeV}$  are similar for  $\zeta_{\text{eq}} = 10^{-4}-1$ .

In Fig. 4 we compare the power injected into non-thermal particles in the fluid frame,  $L'_{\text{NT}}$ , and corrected by Doppler boosting,  $L'_{\text{NT}}\delta_c^4$ , for  $L_j = 10^{44} \text{ erg s}^{-1}$  (IC lightcurve) and  $L_j = 10^{46} \text{ erg s}^{-1}$  (synchrotron lightcurve). In both cases, the rapid rise in the luminosity at the beginning of the event is caused by the increase of the flux injected into non-thermal particles (given by Eq. (9)). The SN ejecta reaches low Lorentz factors for the

**Table 1.** Main parameters of the model.

| Parameters                              | Radio galaxy | Blazar    |
|---|--------------|-----------|
| $L$ : jet power ( $\text{erg s}^{-1}$ ) | $10^{44}$    | $10^{47}$ |
| $\Gamma_j$ : jet Lorentz factor         | 10           | 10        |
| $i$ : inclination angle                 | 60           | 0         |
| $z$ : redshift                          | 0.026        | 1         |

weakest jets (at least within 1 kpc, as can be seen in Fig. 1), thus Doppler boosting is not strong, and it only moderately increases the luminosity, as seen by the observer. For the strongest jets ( $\gtrsim 10^{45} \text{ erg s}^{-1}$ ), Doppler boosting is more relevant throughout the interaction. The higher peak luminosities and slower decay in  $L'_{\text{NT}}\delta_c^4$  are the result of Doppler boosting in all the cases.

In Barkov et al. (2012a), the characteristic effective timescale of the interaction, that is the time during which the SN ejecta-jet interaction intensity is strong enough for effective particle acceleration to occur, can be roughly estimated as

$$\Delta t \sim 10^3 \left( \frac{\Gamma_j}{10} \right) \left( \frac{L_j}{10^{46} \text{ erg s}^{-1}} \right)^{-1} \left( \frac{M_c}{10 M_\odot} \right) \text{ yr.} \quad (15)$$

This expression is valid once the SN ejecta covers the complete jet section, which occurs early in all the cases studied here. This is in agreement with the results shown in Fig. 3 for powerful jets. For weaker jets, the slow acceleration of the SN ejecta renders Eq. (15) not suitable to estimate  $\Delta t$ .

#### 4. Spectral energy distributions

As illustrative cases, the synchrotron and IC SEDs are computed at the time when the SN ejecta covers the jet section for two cases: a nearby radio galaxy with an intermediate jet power, and a powerful blazar at higher redshift. Both galaxies are considered to host a nuclear starburst as described in Sect. 3. We considered the radio galaxy to be located in the local universe at a distance  $d = 100 \text{ Mpc}$  ( $z \approx 0.026$ , for  $H_0 = 70 \text{ km s}^{-1} \text{ Mpc}^{-1}$ ,  $\Omega_\Lambda = 0.7$ , and  $\Omega_M = 0.3$ ), with a jet power  $L_j = 10^{44} \text{ erg s}^{-1}$ , and an inclination angle  $i = 60^\circ$ . On the other hand, the more powerful blazar is considered to be located at  $z = 1$  (equivalent to a luminosity distance of  $6.6 \text{ Gpc}$ ), hosting a powerful jet with  $L_j = 10^{47} \text{ erg s}^{-1}$  pointing toward the observer. Table 1 lists all the relevant parameter values of the model and the sources.

In order to compute the SEDs, we assume an injection rate of non-thermal particles in  $K'$  following an energy distribution of the form:

$$Q'(E', z) = Q_0(z) E' - \alpha \exp(-E'/E'_{\text{max}}(z)), \quad (16)$$

where  $\alpha = 2$  is taken as a fiducial value, typical for efficient accelerators, and characteristic of diffusive acceleration mechanisms. Functions  $Q$  much softer in energy would lead to gamma-ray emission much more difficult to detect, whereas harder  $Q$  would slightly increase the gamma-ray output. The value of  $E'_{\text{max}}$ , determining the maximum particle energy, has been derived as in Vieyro et al. (2017). The total non-thermal luminosity injected is:

$$\int Q'(E', z) E' dE' = L'_{\text{NT}}(z). \quad (17)$$

For each  $z$  value, the transport equation in steady state is solved for an homogeneous emitter (one-zone), which has the following

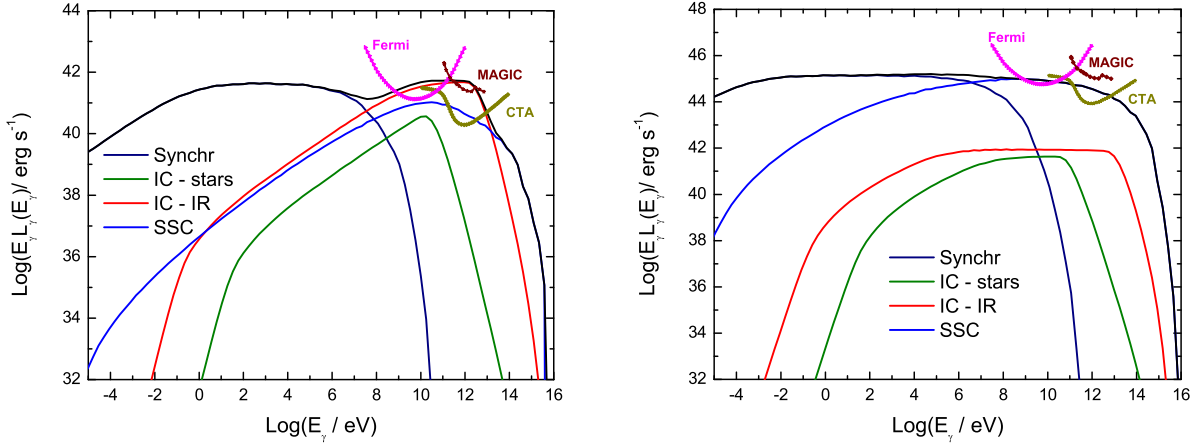


**Fig. 5.** Synchrotron and IC SEDs for the radio galaxy (*left*) and the blazar (*right*) cases, together with the sensitivities of different gamma-ray instruments (*Fermi* -pink-, presently operating Cherenkov telescopes -brown-, CTA -green-), at  $z = 51.3$  and  $55.3$  pc, respectively.

semi-analytical solution:

$$N'(E', z) = \frac{1}{|\dot{E}'(E', z)|} \int_{E'}^{E'_{\max}} Q'(E^*, z) dE^*, \quad (18)$$

where  $|\dot{E}'(E', z)| = E' t'^{-1}_{\text{rad+rad}}(E', z)$  accounts for the radiative and the non-radiative electron energy losses (Vieyro et al. 2017). We consider three different target fields for IC interactions: the radiation from the stars in the galaxy, IR photons associated with the starburst, and synchrotron emission (for SSC). The SSC calculations are correct as long as IC losses of synchrotron targets are not dominant. Although for powerful jets SSC is the main mechanism for gamma-ray emission (as shown in Fig. 5), it is not the dominant radiative loss mechanism.

Figure 5 shows the computed SEDs obtained for the radio galaxy (left panel) and the blazar (right panel), together with the sensitivities of the *Fermi* observatory, MAGIC, as an example of current imaging air Cherenkov telescopes (IACTs), and the future Cherenkov Telescope Array (CTA). These SEDs correspond to the moment when the SN ejecta covers the whole jet section (see the solid-to-dashed line transition in Fig. 1). For the radio galaxy this occurs at  $z = 51.3$  pc, when the SN ejecta has a Lorentz factor of only  $\Gamma_c = 1.0003$ , whereas for the blazar, the Lorentz factor is  $\Gamma_c = 1.43$ , at  $z = 55.3$  pc. Although the peak in the lightcurves is predicted to be somewhat later in both cases (as seen, for example, in Fig. 3 for the blazar case), we compute the SEDs when  $r_c$  equals  $r_j$  because, up to this point, the semi-analytical treatment for the SN ejecta evolution is reasonably accurate. Nevertheless, the difference in the luminosity levels in the lightcurves between the moment when  $r_c = r_j$ , and their maxima, is only a factor of approximately two to three. Gamma-ray absorption effects are important above 10 TeV and have not been computed for the SEDs, but they are discussed in Sect. 4.2 below.

#### 4.1. Main observational characteristics

The radio galaxy case yields the most optimistic predictions for detection, as its IC emission may be detectable by *Fermi* and current IACTs, for the adopted parameter values. In the blazar case, the synchrotron losses are dominant, causing a significant decrease in the gamma-ray IC luminosity. This effect, together with the large distances involved (say  $z \sim 1$ ), makes the jet-SN

ejecta interactions difficult to detect from very powerful blazars with current instruments, but potentially detectable by CTA in the future. We note that a blazar of intermediate power, say  $L_j \sim 10^{44}$  erg s $^{-1}$ , would present a similar SED to the one of the radio galaxy (Fig. 5, left panel), with a higher normalization due to beaming effects. This case could be easily detected in the local universe, although this kind of source is rare with respect to sources of equal power with misaligned jets.

Very bright (or weak) radio sources may be evidence of the presence of high (low) magnetic fields, and can be used to constrain the  $\zeta_{\text{eq}}$  parameter. Low X-ray fluxes may also be an indicator of a very low magnetic fields. These comparison between bands may be difficult for weak radio and X-ray emission as it could be easily masked by other persistently emitting regions.

We can compare our predictions on different wavelengths with the steady emission detected from sources with similar characteristics to those of the two examples studied here. For instance, the well known quasar 3C 273 has a jet close to the line of sight with an estimated power of  $L_j \sim 10^{46}$  erg s $^{-1}$ . The host galaxy is classified as an ULIRG, implying high SFR and IR luminosity. The gamma-ray luminosity observed by *Fermi* during a quiescent state in 2009 (Abdo et al. 2010) is  $L_{1-10\text{GeV}} \gtrsim 10^{45}$  erg s $^{-1}$ , comparable to the blazar case (right panel of Fig. 5). For the adopted value of  $\zeta_{\text{eq}} = 10^{-2}$ , the radio fluxes obtained are also similar to the typical observed fluxes from 3C 273, whereas in X-rays intrinsic jet emission, or even an accretion disk (as the one in 3C 273), could hide the radiation from a jet-SN ejecta interaction. In the radio galaxy case we take M87 as reference. This galaxy has a jet of  $L_j \sim 10^{44}$  erg s $^{-1}$ , with an inclination angle of  $i = 20^\circ$ . The detected radio luminosity is of  $L_{230\text{GHz}} \sim 7 \times 10^{40}$  erg s $^{-1}$  (Doeleman et al. 2012), similar to the one obtained here. In the  $\sim$ GeV range we also obtained fluxes comparable to those observed in the steady state of M87. In X-rays, however, our predictions are greater than the fluxes of M87; this could be alleviated by reducing  $\zeta_{\text{eq}}$ , which would affect also the predicted radio luminosity, or adopting a much lower value for  $\zeta$  (the acceleration rate efficiency).

The observer luminosities predicted in this work for jet-SN ejecta interactions are comparable to those already observed in steady sources, and particular spectral shapes cannot be predicted from a purely phenomenological particle acceleration model (one may say that typical acceleration spectra render

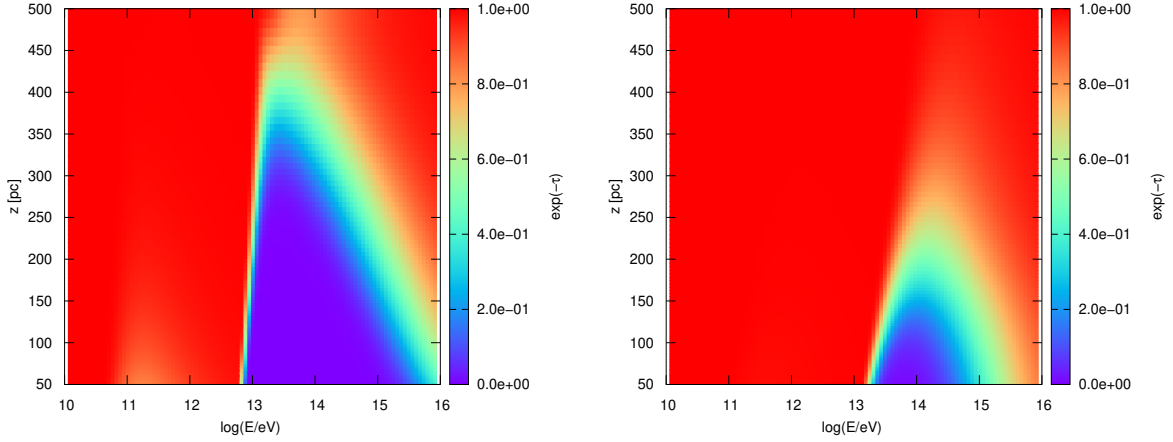


**Fig. 6.** Absorption maps in the IR and OB star radiation fields, for the radio galaxy (*left panel*) and the blazar (*right panel*).

typical radiation spectra). The magnetic field strength is also difficult to assess from first principles, adding more freedom to the spectral outcome of synchrotron and IC. In addition, the long timescales involved imply that the predicted lightcurves cannot be distinguished from intrinsic jet persistent emission. We can state, however, that SN ejecta are arguably the largest effective internal obstacles that AGN jets can encounter. Anything as massive, such as a compact molecular cloud, will be too diluted to fully enter the jet, whereas smaller objects such as stars and their winds can hardly cover a whole jet but in rare occasions: a large wind momentum rate plus a weak jet; lighter obstacles will produce also shorter events. Finally, for relatively nearby sources, radio VLBI could be used to resolve the obstacle, and discriminate different scenarios. For instance, Müller et al. (2014) found evidence of jet-obstacle interaction (probably with a star) in Centaurus A (see also Snios et al. 2019). A detailed case-by-case study, rich in observational information (not very common), is needed to ascertain whether a particular source persistent activity may be associated to a jet-SN ejecta interaction.

#### 4.2. Gamma-ray absorption

Gamma-ray absorption cannot be neglected in the explored scenario in the IR and UV fields of the starburst. Figure 6 shows maps of gamma-ray opacity, associated to  $e^{\pm}$  pair creation in the IR and OB star radiation fields, for the radio galaxy (left panel) and the blazar (right panel) cases. Absorption above  $\sim 10$  TeV is due to the IR field of the starburst. OB star emission affects mostly gamma rays of energies  $\geq 100$  GeV.

The IR absorption can be roughly estimated by  $\tau_{\gamma\gamma} \sim 0.2\sigma_{\text{T}}n_{\text{IR}}R_{\text{d}}$ , where  $n_{\text{IR}} = L_{\text{IR}}/\pi R_{\text{d}}^2 c(2.7kT_{\text{IR}})$ . For the values adopted in Sect. 3.1, we obtain  $\tau_{\gamma\gamma} \sim 80$ . This implies that all the emission at energies  $\geq 10$  TeV should be absorbed when the SN is within or close to the starburst disk, which is the case for the considered events around their maxima. This absorption would lead to pair creation in the jet surroundings, with a subsequent secondary synchrotron and IR-target IC emission. Given the complex structure of the jet-SN ejecta interaction region, it is difficult to assess the anisotropy level of the secondary radiation, as some pairs may get boosted if injected in the unshocked jet, while others would get isotropized in the surroundings. We speculate that, in the blazar scenario, this secondary emission may be minor with respect to the overall beamed emission, whereas for

radio galaxies this contribution may be more important (see, e.g., Inoue 2011).

The UV field of OB stars, unlike the IR field, has a considerably lower impact. The optical depth takes now values of  $\lesssim 10^{-2}$  for the radio galaxy, and even lower for the blazar case. This absorption should lead to secondary pairs emitting at  $\sim 10$  GeV energies, although their contribution would probably be minor.

## 5. Discussion

In this work, we studied the interaction of a relativistic jet with a SNR and its radiative consequences. First, we estimated in a simplified manner the observed gamma-ray luminosity evolution expected from this interaction. We then calculated, with more detail, the SED expected for a radio galaxy at  $d = 100$  Mpc and a blazar at  $z = 1$ . We discuss below some of the assumptions adopted in this work.

### 5.1. Model comparison

In Fig. 7 we compare the luminosity evolution obtained using the simplified treatment given by Eq. (11) and the luminosity computed as described in Sect. 4. The plot corresponds to jets with  $L_{\text{j}} = 10^{43}-10^{44}$  erg s $^{-1}$ ,  $i = 60^{\circ}$  and  $\zeta_{\text{eq}} = 10^{-2}$ . We have also included a comparison for a more powerful jet, of  $L_{\text{j}} = 10^{46}$  erg s $^{-1}$  and  $i = 0^{\circ}$ , for which we considered a well below equipartition magnetic field,  $B = 10^{-3}B_{\text{eq}}$ , in order for the external IC to dominate the emission over SSC. For the less powerful, non-blazar jets, the simple analysis predicts the emission rather accurately; for the powerful blazar, the simple prescription overestimates the luminosity by approximately an order of magnitude (as found already in Vieyro et al. 2017). The discrepancy of the synchrotron emission around  $\sim 100$  MeV predicted for blazar-sources by the two approaches (not shown in the figure) is higher than for the IC emission; during the peak of the event, however, we obtain the same difference of  $\sim 0.1$ .

### 5.2. Nature of the emitting flow

The assumptions that the emitter moves with the SN ejecta and has its size are in fact assumptions whose validity depends on the scenario. When the SN ejecta is slow, it efficiently acquires momentum, but not energy, while for a faster and

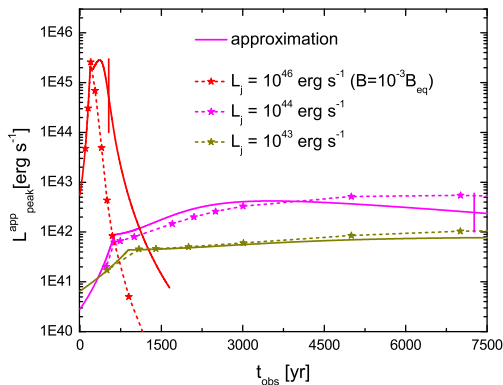


**Fig. 7.** Comparison between the gamma-ray lightcurves obtained with the simplified prescription (solid curve) and the more detailed treatment (dashed curve; stars indicate the points where the luminosity was computed). We consider  $i = 60^\circ$  and  $\zeta_{\text{eq}} = 10^{-2}$  for  $L_j = 10^{43}$  and  $10^{44} \text{ erg s}^{-1}$ , and  $i = 0^\circ$  and  $\zeta_{\text{eq}} = 10^{-6}$  for  $L_j = 10^{46} \text{ erg s}^{-1}$ . The vertical ticks indicate the moment the SN reaches 1 kpc (for  $L_j = 10^{43} \text{ erg s}^{-1}$  this takes place at  $t_{\text{obs}} \sim 1.8 \times 10^4 \text{ yr}$ , hence it is not shown in the plot).

diluted SN ejecta the energy transfer becomes more efficient (see Barkov et al. 2010, for a discussion of the energy transfer phases). Therefore, for a slow SN ejecta with a radius smaller than that of the jet, the shocked jet flow can be far more efficient at dissipating jet power in the form of non-thermal particles than within the SN ejecta. The emission from this quasi-stationary flow will be beamed, which would not be the case for an emitter moving with the SN ejecta. On the other hand, in the sub-relativistic regime, the emitter is expected to be larger than the SN ejecta due to the extended oblique shock farther downstream (Bosch-Ramon 2015). Thus, the predicted radiation luminosity is affected by these unaccounted factors: beaming from a quasi-stationary flow, and a larger dissipation region.

When the SN ejecta becomes relativistic, the energy transferred from the jet to the shocked jet flow and to the SN ejecta becomes similar, and thus the latter may become a significant emitter in addition to the shocked jet flow. Both the shocked jet flow and the SN ejecta will still have different Doppler boosting patterns until  $\Gamma_c \rightarrow \Gamma_j$ , point at which particle acceleration should become very weak or null.

Despite the qualitative differences, in the context of phenomenological modeling the model and most of the parameter values are basically the same regardless of the actual emitting flow: the shocked jet flow or the SN ejecta. The magnetic field values may otherwise differ in both regions.

In the scenario we studied, the radius of the SN ejecta tends to the jet radius. If the SN ejecta covers the whole jet section well before  $\Gamma_c \rightarrow \Gamma_j$ , the shocked jet flow is still the most significant emitter, but it will move at the same velocity as the SN ejecta as long as the shocked jet flow is encapsulated by the external medium around the SN ejecta (see the following discussion and the Appendix).

### 5.3. A jet covered by the SN ejecta

As mentioned in Sect. 2 the shape of the SN ejecta impacted by the jet grows sideways and forms an elongated tail along the jet direction. The ability of the SN ejecta to intercept jet energy is the most important factor in our study, and this depends exclusively on the size of the SN ejecta perpendicular to the jet. The

lateral expansion of the SN ejecta near the surface impacted by the jet is expected to be fast. Here, for simplicity, we assumed that this expansion takes place at the sound speed, and that the density evolves as if the SN ejecta were spherical. SN ejecta disruption, plus some lateral pressure exerted by the shocked jet, makes this approximation less accurate. However, as discussed in the Appendix, the evolution of the main parameters obtained with the semi-analytical approach does not deviate significantly from the results of axisymmetric, relativistic hydrodynamical simulations<sup>1</sup>.

Expansion leads the SN ejecta to cover the whole jet section. At that point, we assume that the SN ejecta is confined by the jet walls and expands at the same rate as the conical jet. For a jet propagating in vacuum this approximation would be wrong, since nothing would prevent the SN ejecta to expand further. However, extragalactic jets usually propagate in media much denser than the jet itself, in particular when crossing their host galaxies. Thus, the dense external medium, heated and compressed by the SN ejecta when  $r_c \gtrsim r_j$ , strongly slows down its expansion with its large inertia. At most, the speed of the lateral expansion of the SN ejecta should be that of the Sedov-Taylor phase, with  $\dot{R}_{\text{c,st}} \sim (L_j/\rho_{\text{ISM}})^{1/5} t^{-2/5}$ . For most cases, after just  $\sim 100 \text{ yr}$ ,  $\dot{R}_{\text{c,st}}$  already becomes lower than  $\theta\beta_j c$ , meaning that the SN ejecta and the jet do eventually expand at roughly the same rate. Such a situation is likely to prevent the SN ejecta from expanding sideways beyond the jet. If  $\Gamma_c \rightarrow \Gamma_j$ , this situation may not have such a strong impact on the jet global structure, although the medium-SN ejecta interaction could slow down the latter. For slow or slowed-down SN ejecta, the braked jet should become disrupted at the  $z$  of the interaction with the SN ejecta, and shocked jet material flowing backwards may strongly affect jet propagation even far upstream, filling a lobe-like structure. The SN ejecta should also get disrupted by the jet impact, although at a slower rate, at least when the SN ejecta density is still higher than the jet density (e.g., Bosch-Ramon et al. 2012; see also the appendix).

Some of the effects discussed can be found in the complementary simulation presented in the Appendix. An accurate treatment of this scenario, combining detailed hydrodynamical simulations and precise radiation calculations, is left for future work.

### 5.4. Varying $\Gamma_j$ and $M_c$

The jet Lorentz factor adopted in this work,  $\Gamma_j = 10$ , was taken as a reference value for illustrative purposes, but adopting  $\Gamma_j = 5$  does not have a significant impact on the results for the weakest jets. We note that the velocity of the jet is likely non uniform through the section of the latter. The jet is expected to develop a shear layer as a transition region to the external medium. In addition, it has been proposed that the jet could consist of a light, ultra-relativistic, electron-positron pair plasma central spine, and a hadronic, heavier and slower outer layer, resulting from the Blandford-Znajek and Blandford-Payne processes (e.g., Xie et al. 2012; Ghisellini et al. 2005 and references therein). A non-uniform velocity profile with jet radius may not have a major impact in the explored scenario: the SN ejecta completely covers the jet before getting relativistic speeds, and thus the effect of any radial profile of the jet properties should tend to get smoothed out over the jet-SN ejecta contact surface.

<sup>1</sup> We note here the complexities and uncertainties related to implementing an accurate numerical approach, which makes a semi-analytical treatment valuable for exploring several cases.

In any case, a non-homogeneous jet thrust and energy flux is likely to affect the SN ejecta evolution (e.g., enhancing instability growth), which is worth of a devoted future numerical study.

We also considered the impact of a less massive SN ejecta, adopting  $M_c = 1 M_\odot$ . The main difference obtained in this case is the duration of the events, which become approximately ten times shorter than for  $M_c = 10 M_\odot$ , for the same  $L_j$ -value; the lightcurve peak luminosities are, on the other hand, similar.

### 5.5. Impact of $\eta_{\text{NT}}$

An additional free parameter of the model is the acceleration efficiency  $\eta_{\text{NT}}$ . Here we have adopted a constant value of 0.1 throughout the paper. This parameter at present can only be constrained observationally, with a range as wide as  $\eta_{\text{NT}} = 0-1$ , and its value may also change as the properties of the jet-SN ejecta contact region evolve. Here, our results simply scale linearly with  $\eta_{\text{NT}}$ , and any change in the efficiency linearly affects the predicted luminosities. We note that additional acceleration sites may be present as well, as for instance: the more oblique region of the jet-SN ejecta shock present when  $r_c \ll r_j$  and  $\Gamma_c \ll \Gamma_j$ ; or the region encompassing the SN-ejecta, the jet termination, and the external medium when  $r_c \gtrsim r_j$ . Here, we have considered only the jet-SN ejecta interaction region with section  $\sim \pi r_c^2$ .

### 5.6. Duty cycle

To determine how frequent the jet-SN ejecta interactions are in an AGN hosting a central disk-like starburst, one can estimate the SN rate expected in this type of galaxy. Stars with initial masses  $M > 8 M_\odot$  end their life as core-collapse SN (Matzner & McKee 1999); the upper limit on the progenitor mass is not clearly determined, but there is evidence that massive stars, with  $M \gtrsim 20 M_\odot$ , collapse into a black hole, failing in produce a SN (Smartt 2015). We considered an initial mass function  $\phi(m) \propto m^{-\alpha}$ , where  $\alpha = 0.3$  for  $0.01 \leq m/M_\odot < 0.08$ ,  $\alpha = 1.8$  for  $0.1 \leq m/M_\odot < 0.5$ ,  $\alpha = 2.7$  for  $0.5 \leq m/M_\odot < 1$ , and  $\alpha = 2.3$  for  $m/M_\odot \geq 1$  (Kroupa 2001). Assuming a constant SFR, the core-collapse SN rate can be estimated according to (Mattila & Meikle 2001):

$$R_{\text{SN}} = \dot{M}_{\text{SFR}} \frac{\int_{8 M_\odot}^{20 M_\odot} \phi(m) dm}{\int_{0.1 M_\odot}^{120 M_\odot} m \phi(m) dm}. \quad (19)$$

For  $\dot{M}_{\text{SFR}} = 100 M_\odot \text{ yr}^{-1}$ , the SN rate in the starburst disk results in  $\sim 70$  SN per century.

For a starburst disk with radius  $R_d = 300 \text{ pc}$  and total thickness  $h_d = 100 \text{ pc}$ , only  $\sim 0.01\%$  of these SNe will take place inside the jet with the adopted geometry. As discussed in Sect. 3.2, for a jet power  $L_j \sim 10^{43}-10^{44} \text{ erg s}^{-1}$ , a non-blazar source (say  $i \sim 30^\circ$ ), and  $\eta_{\text{NT}} = 0.1$ , the interaction could result in a gamma-ray luminosity  $\gtrsim 10^{41}-10^{42} \text{ erg s}^{-1}$  for periods of  $\sim 10^4 \text{ yr}$ . This implies that for a single radio galaxy, the duty cycle of core-collapse SNe exploding within the jet should be approximately one. These gamma-ray luminosities may be detectable by *Fermi* and current IACTs, and in the future by CTA, for sources up to a few hundreds of Mpc, perhaps even further away for a more extreme choice of parameter values (e.g.,  $\eta_{\text{NT}} \rightarrow 1$ ). In addition, provided the high duty cycle, several of these sources in the sky may be simultaneously producing gamma rays due to jet-SN ejecta interactions.

Regarding blazar type sources, the most powerful ones, say  $L_j \sim 10^{47} \text{ erg s}^{-1}$ , may be detectable at  $z \sim 1$  in the future by

CTA. However, the brief nature of such events, with a lightcurve peak duration  $\sim 100 \text{ yr}$  and a duty cycle per source of  $\sim 1\%$ , and the scarcity of objects, would imply a low frequency of occurrence.

As future work, we plan to study the statistics of starburst AGN with jet-SN ejecta interactions. In addition, Type Ia SNe can also occur in non star-forming galaxies, which are much more numerous than galaxies hosting starbursts. The interaction between a jet of an AGN and a Type Ia SN should also be studied, as many AGN are massive elliptical galaxies with jets. This study is also work under way.

## 6. Conclusions

In galaxies with high SFRs and jets of moderate power, the duty cycle of the interaction of the jet with SNe could be close to unity. This implies a rather steady gamma-ray luminosity that may be detectable, perhaps by *Fermi* and current IACTs, and more likely by the future instrument CTA, for sources in the local universe. Since there are several nearby galaxies with the characteristics assumed in this work, jet-SN ejecta emission could be responsible for some of the radio galaxies and relatively weak blazars detected as persistent gamma-ray sources. Blazars with powerful jets, not common in the local universe, might be still detectable at farther distances due to the expected higher luminosities, although the shorter duration of the events and scarce object numbers make their detection more unlikely.

*Acknowledgements.* We want to thank an anonymous referee for his/her useful comments that helped to improve the manuscript. This work was supported by the Spanish Ministerio de Economía y Competitividad (MINECO/FEDER, UE) under grants AYA2013-47447-C3-1-P and AYA2016-76012-C3-1-P with partial support by the European Regional Development Fund (ERDF/FEDER), MDM-2014-0369 of ICCUB (Unidad de Excelencia “María de Maeztu”), and the Catalan DEC grant 2014 SGR 86. F.L.V acknowledges support from the Argentine Agency CONICET (PIP 2014-00338). N.T.A. acknowledges support from MINECO through FPU14/04887 grant.

## References

- Abdo, A. A., Ackermann, M., Ajello, M., et al. 2010, *ApJ*, 714, L73  
 Aharonian, F. A., Barkov, M. V., & Khangulyan, D. 2017, *ApJ*, 841, 61  
 Alexander, D. M., & Hickox, R. C. 2012, *New Astron. Rev.*, 56, 93  
 Araudo, A. T., Bosch-Ramon, V., & Romero, G. E. 2010, *A&A*, 522, A97  
 Araudo, A. T., Bosch-Ramon, V., & Romero, G. E. 2013, *MNRAS*, 436, 3626  
 Banasiński, P., Bednarek, W., & Sitarek, J. 2016, *MNRAS*, 463, L26  
 Barkov, M. V., Aharonian, F. A., & Bosch-Ramon, V. 2010, *ApJ*, 724, 1517  
 Barkov, M. V., Aharonian, F. A., Bogovalov, S. V., Kelner, S. R., & Khangulyan, D. 2012a, *ApJ*, 749, 119  
 Barkov, M. V., Bosch-Ramon, V., & Aharonian, F. A. 2012b, *ApJ*, 755, 170  
 Bednarek, W. 1999, in *Plasma Turbulence and Energetic Particles in Astrophysics*, eds. M. Ostrowski, & R. Schlickeiser, 360  
 Bednarek, W., & Banasiński, P. 2015, *ApJ*, 807, 168  
 Bednarek, W., & Protheroe, R. J. 1997, *MNRAS*, 287, L9  
 Blandford, R. D., & Koehnig, A. 1979, *Astrophys. Lett.*, 20, 15  
 Bosch-Ramon, V. 2015, *A&A*, 575, A109  
 Bosch-Ramon, V., Perucho, M., & Barkov, M. V. 2012, *A&A*, 539, A69  
 Cooper, J. L., Bicknell, G. V., Sutherland, R. S., & Bland-Hawthorn, J. 2009, *ApJ*, 703, 330  
 de la Cita, V. M., Bosch-Ramon, V., Paredes-Fortuny, X., Khangulyan, D., & Perucho, M. 2016, *A&A*, 591, A15  
 de la Cita, V. M., del Palacio, S., Bosch-Ramon, V., et al. 2017, *A&A*, 604, A39  
 Dermer, C. D., & Schlickeiser, R. 1993, *ApJ*, 416, 458  
 Doelman, S. S., Fish, V. L., Schenck, D. E., et al. 2012, *Science*, 338, 355  
 Donat, R., & Marquina, A. 1996, *J. Comput. Phys.*, 125, 42  
 Donat, R., Font, J. A., Ibáñez, J. M., & Marquina, A. 1998, *J. Comput. Phys.*, 146, 58  
 Fragile, P. C., Anninos, P., Gustafson, K., & Murray, S. D. 2005, *ApJ*, 619, 327  
 Ghisellini, G., Tavecchio, F., & Chiaberge, M. 2005, *A&A*, 432, 401  
 Gürkan, G., Hardcastle, M. J., Jarvis, M. J., et al. 2015, *MNRAS*, 452, 3776  
 Hardcastle, M. J. 2011, *Science*, 332, 429

- Hickox, R. C., Mullaney, J. R., Alexander, D. M., et al. 2014, *ApJ*, 782, 9
- Hubbard, A., & Blackman, E. G. 2006, *MNRAS*, 371, 1717
- Inoue, Y. 2011, *ApJ*, 728, 11
- Ishibashi, W., & Fabian, A. C. 2016, *MNRAS*, 463, 1291
- Jorstad, S. G., Marscher, A. P., Morozova, D. A., et al. 2017, *ApJ*, 846, 98
- Kauffmann, G., Heckman, T. M., Tremonti, C., et al. 2003, *MNRAS*, 346, 1055
- Kelly, P. L., & Kirshner, R. P. 2012, *ApJ*, 759, 107
- Khangulyan, D. V., Barkov, M. V., Bosch-Ramon, V., Aharonian, F. A., & Dorodnitsyn, A. V. 2013, *ApJ*, 774, 113
- Khangulyan, D., Aharonian, F. A., & Kelner, S. R. 2014, *ApJ*, 783, 100
- Klein, R. I., McKee, C. F., & Colella, P. 1994, *ApJ*, 420, 213
- Komissarov, S. S. 1994, *MNRAS*, 269, 394
- Kroupa, P. 2001, *MNRAS*, 322, 231
- Maoz, D., Mannucci, F., & Nelemans, G. 2014, *ARA&A*, 52, 107
- Mattila, S., & Meikle, W. P. S. 2001, *MNRAS*, 324, 325
- Matzner, C. D., & McKee, C. F. 1999, *ApJ*, 510, 379
- Mignone, A., & Bodo, G. 2005, *MNRAS*, 364, 126
- Müller, C., Kadler, M., Ojha, R., et al. 2014, *A&A*, 569, A115
- Perucho, M., Martí, J. M., Laing, R. A., & Hardee, P. E. 2014, *MNRAS*, 441, 1488
- Perucho, M., Bosch-Ramon, V., & Barkov, M. V. 2017, *A&A*, 606, A40
- Pittard, J. M., Hartquist, T. W., & Falle, S. A. E. G. 2010, *MNRAS*, 405, 821
- Sanders, D. B., Soifer, B. T., Elias, J. H., et al. 1988, *ApJ*, 325, 74
- Shao, L., Lutz, D., Nordon, R., et al. 2010, *A&A*, 518, L26
- Smartt, S. J. 2015, *PASA*, 32, e016
- Snios, B., Wykes, S., Nulsen, P.E.J., et al. 2019, *ApJ*, 871, 248
- Stockton, A. 1982, *ApJ*, 257, 33
- Toomre, A., & Toomre, J. 1972, *ApJ*, 178, 623
- Vieyro, F. L., Torres-Albà, N., & Bosch-Ramon, V. 2017, *A&A*, 604, A57
- Wang, T., Elbaz, D., Alexander, D. M., et al. 2017, *A&A*, 601, A63
- Wykes, S., Hardcastle, M. J., Karakas, A. I., & Vink, J. S. 2015, *MNRAS*, 447, 1001
- Xie, W., Lei, W.-H., Zou, Y.-C., et al. 2012, *Res. Astron. Astrophys.*, 12, 817

## Appendix A: Two-dimensional hydrodynamical simulations

To quantify the precision of the semi-analytic model used to describe the evolution of a SN ejecta accelerated by the jet (see Sect. 2), we have performed axisymmetric, relativistic hydrodynamical (RHD) simulations in two dimensions of the interaction between a jet and a spherical cloud. We have considered a jet of negligible thermal pressure (1% of the jet ram pressure),  $L_j = 10^{45} \text{ erg s}^{-1}$ , and  $\Gamma_j = 10$ , and a uniform cloud at rest of  $10 M_\odot$ , initial radius  $R_c = 1.25 \times 10^{18} \text{ cm}$  (12.5 cells), and in pressure balance with the jet ram pressure (see Sect. 2). At the considered interaction location, the magnetic field was assumed to be dynamically negligible. The code that solved the RHD equations was the same as in [de la Cita et al. \(2017\)](#): third order in space ([Mignone & Bodo 2005](#)); second order in time; and using the Marquina flux formula ([Donat & Marquina 1996](#); [Donat et al. 1998](#)). The adiabatic index of the gas was fixed to  $4/3$ , corresponding to an ideal, monoatomic relativistic gas.

The grid adopted consisted of a uniform grid with 150 cells between  $r_0^{\text{grid}} = 0$  and  $r_{\text{max}}^{\text{grid}} = 1.5 \times 10^{19} \text{ cm}$  in the  $r$ -direction, and 300 cells between  $z_0^{\text{grid}} = 1.48 \times 10^{20}$  and  $z_{\text{max}}^{\text{grid}} = 1.78 \times 10^{20} \text{ cm}$  in the  $z$ -direction. An extended grid was added with 150 cells in the  $r$ -direction, from  $r_{\text{max}}^{\text{grid}} = 1.5 \times 10^{19}$  and  $r_{\text{max}}^{\text{grid}} \approx 10^{20} \text{ cm}$ , and with 200 cells in the  $z$ -direction, from  $z_{\text{max}}^{\text{grid}} = 1.78 \times 10^{20}$  and  $z_{\text{max}}^{\text{grid}} \approx 4.2 \times 10^{20} \text{ cm}$ . The resolution was chosen such that no significant differences could be seen in the hydrodynamical results when increasing the resolution.

Inflow conditions (the jet) were imposed at the bottom of the grid, reflection at the axis, and outflow in the remaining grid boundaries. On the scales of the grid, for simplicity we approximated the jet streamlines as radial, and added a smooth but thin shear layer transiting from the jet properties to the external medium properties (radial velocity of  $10^8 \text{ cm s}^{-1}$ , number density  $\approx 1 \text{ cm}^{-3}$ , pressure equal to the jet thermal pressure) at  $\theta \approx 1/\Gamma_j$ .

Figure A.1 shows combined maps of pressure (left) and density (right) at different times, showing the beginning of the interaction (top left), and three intermediate stages:  $t = 592.6 \text{ yr}$  (top right),  $t = 1188.1 \text{ yr}$  (bottom left), and  $t = 1848.9 \text{ yr}$  (bottom right). The plots show some of the effects discussed in Sects. 2 and 3, namely:

1. The SN ejecta completely covers the jet cross section from an early time;
2. Despite disruption, the cloud evolves roughly as a coherent structure (see also the figures shown below) until it has moved significantly further downstream;
3. The cloud does not expand much beyond the jet original radius before its disruption;
4. The jet begins to accelerate the SN material after  $\sim 1000 \text{ yr}$  (similar to what is shown in Fig. 1 for the jet with  $L_j = 10^{45} \text{ erg s}^{-1}$ ), although in fact the simulation acceleration time is a few times longer.

To better illustrate the similarities between the semi-analytical treatment and the numerical simulations, in Fig. A.2 we show the comparison between the evolution of the main parameters of the cloud derived using both approaches. In the left panel we show the evolution of the cloud Lorentz factor; the acceleration of the cloud is reasonably reproduced by the treatment presented in Sect. 2, although, as mentioned above, the acceleration time obtained from the simulation is longer, favoring detectability (the duty cycle discussed in Sect. 5.6 is a conservative estimate if the acceleration time is longer). In the right panel, we have plotted the evolution of the mass-averaged cylindrical radius of the cloud. This parameter differs somewhat from the spherical semi-analytical case, but the differences are small in the long run, and with the jet still being effectively fully covered by the SN ejecta, which means that our approximation should be accurate enough at this stage. A generalization of the simulation to include other cases, and the computation of the radiative outcome, are left for future work.

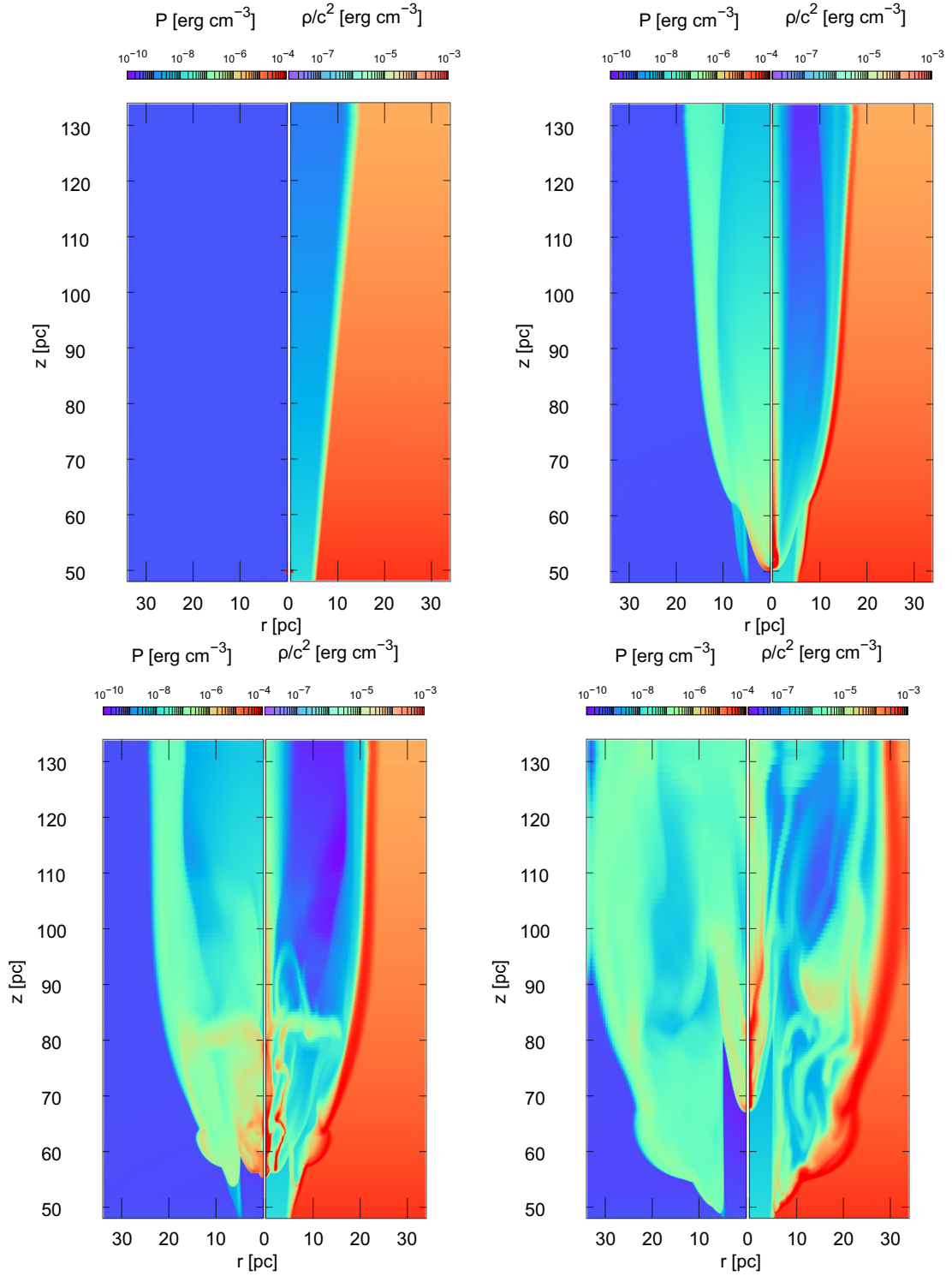


**Fig. A.1.** Combined color maps of a SN material pressure (*left*) and density (*right*) at different times: beginning of the interaction (*top left*),  $t = 592.6$  yr (*top right*),  $t = 1188.1$  yr (*bottom left*), and  $t = 1848.9$  yr (*bottom right*).

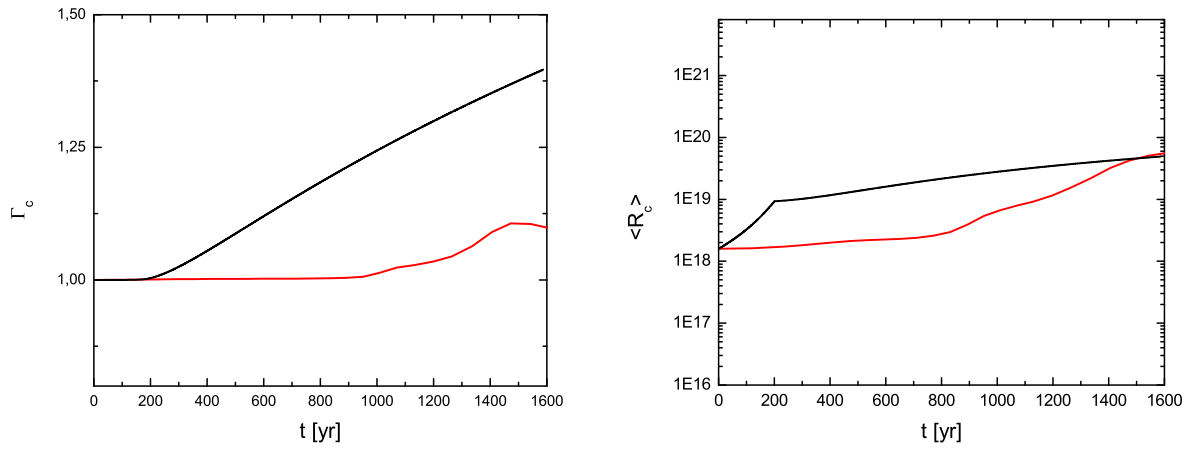


**Fig. A.2.** Comparison between the cloud evolution obtained using the semi-analytical approach (black lines) and the average values evolution obtained in the numerical simulations (red lines) for the Lorentz factor (*left*), and mass-averaged cylindrical radius (*right*). The time shown in these plots is in the laboratory frame.



## TYPE IA SUPERNOVA EXPLOSION INSIDE AN EXTRAGALACTIC JET

---

In this chapter we present our work "Type I a supernova explosion inside an extragalactic jet", which has been sent for publication to A&A. In this work we follow the procedure explained in the previous section, but applied to Type I a supernovae in elliptical galaxies.



# Gamma rays from Type Ia SNe inside jets of elliptical host AGN

N. Torres-Albà<sup>1</sup>, F. L. Vieyro<sup>2</sup>, and V. Bosch-Ramon<sup>1</sup>

<sup>1</sup> Departament de Física Quàntica i Astrofísica, Institut de Ciències del Cosmos (ICC), Universitat de Barcelona (IEEC-UB), Martí i Franquès 1, E08028 Barcelona, Spain

<sup>2</sup> Instituto Argentino de Radioastronomía (IAR, CCT La Plata, CONICET; CICPBA), C.C.5, (1984) Villa Elisa, Buenos Aires, Argentina

June 21, 2019

## ABSTRACT

**Context.** Elliptical galaxies are the preferred hosts of blazars and radio-loud AGN. In addition, type Ia supernovae are frequent in these galaxies and can, in occasion, take place within the relativistic jet. As the supernova ejecta is impacted by the jet, shocks form in which particles can be accelerated up to relativistic energies, leading to non-thermal emission.

**Aims.** We study the dynamical evolution and the non-thermal emission of a type Ia supernova ejecta impacted by the jet of an AGN in an elliptical host.

**Methods.** We used semi-analytical models to describe the dynamics of the interaction between the SN ejecta and the jet. Then, we estimated the lightcurves of the expected high-energy emission for different jet powers. Finally, we computed the synchrotron and IC SEDs for the particular case of M87 and for two blazars, a weak, nearby one, and a powerful one at redshift  $z = 0.5$ .

**Results.** The interaction between the ejecta of a type Ia supernova and the jet of a powerful blazar, with power  $L_j = 10^{47}$  erg s<sup>-1</sup>, could result in steady gamma-ray emission above  $10^{44}$  erg s<sup>-1</sup> for  $3 \times 10^3$  yr. For a jet with power  $L_j = 10^{44}$  erg s<sup>-1</sup>, the steady gamma-ray emission could reach above  $10^{42}$  erg s<sup>-1</sup> for  $\sim 4 \times 10^3$  yr. In particular, this interaction taking place in the radio galaxy M87 could account for the observed X-rays and a significant fraction of its gamma-ray luminosity.

**Conclusions.** The jets of AGN hosted in elliptical galaxies could interact with the ejecta of Type Ia supernovae, resulting in a few sources potentially detectable by MAGIC at  $z \lesssim 0.25$ , and tens with CTA at  $z \lesssim 0.5$ .

**Key words.** Radiation mechanisms: non-thermal – Galaxies: active – Galaxies: nuclei – Galaxies: jets

## 1. Introduction

Active galactic nuclei (AGN) can be found in the nucleus of galaxies as their central supermassive black hole accretes the surrounding material. This process may lead to the production of relativistic, collimated outflows, or jets (Begelman et al. 1984). Since these jets are launched from the innermost regions of the galaxy, they inevitably interact with a variety of different obstacles as they cross the host galaxy.

The interaction between jets and penetrating objects has been previously studied in many different works, both as means of jet deceleration (e.g. Komissarov 1994; Hubbard & Blackman 2006; Perucho et al. 2017) and production of gamma-ray emission. Interaction with individual objects, such as stars or gas clouds, can explain both rapid variability in blazars (e.g. Barkov et al. 2012; Khangulyan et al. 2013; Aharonian et al. 2017), and gamma-ray flares (Barkov et al. 2010; Bosch-Ramon et al. 2012; Banasiński et al. 2016). Interaction with whole populations of obstacles, however, may lead to the production of steady, gamma-ray emission (e.g. Araudo et al. 2010, 2013; Bosch-Ramon 2015; Wykes et al. 2015; Vieyro et al. 2017; Torres-Albà & Bosch-Ramon 2019).

Another obstacle an AGN jet may encounter is the material ejected (i.e. the ejecta) by a supernova (SN) explosion that has taken place within it. Blandford & Koenigl (1979) mentioned this scenario as a possible way to explain the knots of M87, and Bednarek (1999) as a scenario for particle acceleration. More

recently, Vieyro et al. (2019) studied this scenario in detail, in the context of core-collapse SNe in star-forming galaxies, including numerical simulations of the dynamical evolution of the SN ejecta within the jet, and calculations of the potentially associated gamma-ray emission. They concluded that the emission could be detectable both in nearby radio galaxies and powerful blazars at higher redshift.

Whereas AGN surveys show that the fraction of galaxies hosting AGN is significantly lower for elliptical galaxies (quiescent, with no ongoing star formation) than for star-forming ones (Wang et al. 2017), given the higher abundance of inactive elliptical galaxies, the latter tend to be the preferred hosts of radio-loud AGN (e.g. Kotilainen et al. 1998; Falomo et al. 2000; Scarpa et al. 2000; Nilsson et al. 2003; Olguín-Iglesias et al. 2016).

While Vieyro et al. (2019) focused on core-collapse SNe, Type Ia SNe are the only SNe that take place in early-type galaxies with negligible star formation. These SNe are produced in the thermonuclear explosions associated either to an accreting white dwarf in a binary system, or to the merger of two white dwarfs (e.g. Maoz et al. 2014). In this work, we consider a type Ia SN exploding within the jet of an elliptical galaxy, and study its dynamical evolution after being impacted by the jet. At the contact surface between the SN ejecta and the jet, a double bow-shock is generated, in which particles can be accelerated to very high energies, leading to gamma-ray emission.

The article is organized as follows: In Sect. 2, the dynamical evolution of a SN ejecta accelerated by a jet is described using a simple analytical model. Then, in Sect. 3 we explore the

Send offprint requests to: N. Torres-Albà  
e-mail: ntorres@fqa.ub.es

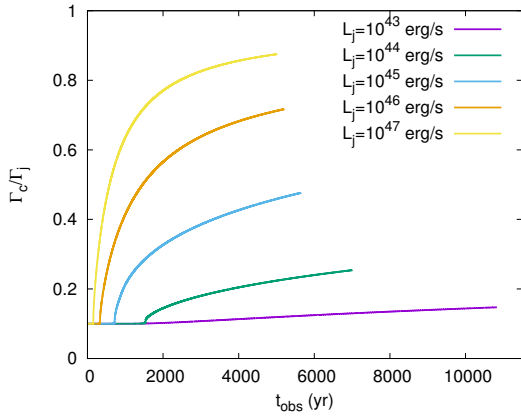


**Fig. 1.** Evolution as a function of observed time of the Lorentz factor of the SN ejecta, for  $i = 0^\circ$  and  $\Gamma_j = 10$ , for different jet powers. The considered evolution ranges from  $z = 1 - 4$  kpc.

jet parameter space, and study the outcomes of different scenarios through computing the gamma-ray lightcurve. In Sect. 4 we compute the spectral energy distributions (SEDs) resulting from the electrons accelerated in the jet-SN ejecta interaction, and in Sect. 5, the event rates and duty cycles for these interactions are computed. Finally, we discuss the adopted model and its results in Sect. 6, and close with the conclusions in Sect. 7.

## 2. Dynamical evolution

After the SN explosion, the ejecta expanding inside the relativistic jet is accelerated through momentum transfer. At some point, a shock wave is produced as the jet impacts the SN ejecta, resulting in heating and expansion of the shocked material.

The detailed semi-analytical approach to describe the dynamical evolution of the ejecta from a core-collapse SN inside an extragalactic jet can be found in Vieyro et al. (2019), based on the theoretical work of Barkov et al. (2010, 2012) and Khangulyan et al. (2013). Vieyro et al. (2019) compared the results of the analytical model to those derived from simulations of the same scenario, reaching the conclusion that the used analytical approximation is valid to describe the evolution of the SN ejecta as long as it reaches at least mildly relativistic speeds, which is the case for the jet configurations studied in this work.

We use the same analytical approximation to describe the acceleration and expansion of the ejecta of a Type Ia SN as it is pushed by the jet. However, in this case, the considered host galaxy is a massive elliptical instead of a starburst, with negligible star formation, in which SNe are expected to be mostly of type Ia. This leads to a few differences in regards to the evolution of the SN ejecta.

To begin with, the typical Type Ia SN ejecta has a lower mass than a core-collapse one, of  $M_c \simeq 1 M_\odot$  (e.g. Scalzo et al. 2014; Wilk et al. 2018). Also, while core-collapse SNe are expected to occur in regions with high star formation, a Type Ia may take place anywhere within the galaxy. We consider that the possible progenitors of the SNe are mostly located within the bulge of the elliptical galaxy, which holds most of its stellar mass, and through which the jet is expected to remain collimated and relativistic (and can thus more efficiently accelerate the SN ejecta). We take as reference values to model a generic bulge of an elliptical host those derived by Gebhardt & Thomas (2009) for M87,

a nearby, well-studied elliptical radio galaxy. That is, a bulge of  $\sim 3$  kpc of radius, which we assume spherical for simplicity. We then consider a SN exploding at a height  $z_0 \sim 1$  kpc, a characteristic height at which we expect events to be frequent, and still low enough for the SN ejecta to travel a large distance within the galaxy.

We take into account that, for the less powerful jets, the pressure of the external medium ( $P_{\text{ISM}}$ ) may be large enough to halt the free expansion of the initially conical jet, forcing it to recollimate and adopt a cylindrical geometry. In particular, we consider  $P_{\text{ISM}} = 10^{-12}$  erg cm $^2$  (see Torres-Albà & Bosch-Ramon 2019).

A SN ejecta expelled at  $z_0 = 1$  kpc within the jet has initially a higher total pressure than the jet. This results in a free expansion of the SN ejecta, which halts once its ram pressure reaches equilibrium with that of the jet. The free expansion phase within the jet lasts longer than in the ISM, given the lower density of the extragalactic jets. For a type Ia SN with the standard energy of  $10^{51}$  erg (Gamezo et al. 2003), and a jet of  $10^{44}$  erg s $^{-1}$ , the equilibrium is achieved at a radius of  $R_0 \sim 6$  pc, 900 yr after the explosion. For a more powerful jet, of  $10^{47}$  erg s $^{-1}$ , the free-expansion phase lasts  $\sim 90$  yr, and the equilibrium radius is  $R_0 \sim 0.6$  pc.

The jet can only affect the evolution of the SN ejecta from the moment their ram pressures balance each other. Then, the SN ejecta is shocked, and expands and accelerates due to the interaction with the jet. As discussed in Vieyro et al. (2019), it can be assumed that the SN ejecta effectively evolves as a roughly spherical cloud, with radius increasing as:

$$r_c(t) = R_0 + \int \frac{c_s dt}{\Gamma_c(t)}, \quad (1)$$

where  $c_s$  is the sound speed of the jet-shocked SN ejecta. The radius increases up to reaching the jet radius, at which point the SN ejecta covers the whole jet section and its expansion rate is assumed to be that of the jet (i.e.  $r_c \sim r_j$ , see Vieyro et al. 2019, for a discussion and simulations of the dynamical evolution and its effects on the jet).

As the SN ejecta expands, it is more efficiently accelerated by the jet due to its larger impact area. The Lorentz factor achieved by the SN ejecta is shown, as a function of the observed time, in Fig. 1.

## 3. Estimation of emitted radiation

We consider jets of different power,  $L_j$ , within an M87-like spherical bulge, as described in Sect. 2. We study the expected, apparent non-thermal luminosity of the interaction adopting a simplified model.

This simplified model assumes that, at every height  $z$ , the interaction of the SN ejecta with the jet results in the generation of non-thermal particles. Expressed in the reference frame of the ejecta,  $K'$ , the luminosity injected into non-thermal particles is:

$$L'_{\text{NT}} = \eta_{\text{NT}} S_c \rho_j \Gamma_{\text{rel}} (\Gamma_{\text{rel}} h - 1) \beta_{\text{rel}} c^3, \quad (2)$$

where  $\eta_{\text{NT}}$  is the fraction of jet energy invested into non-thermal particle acceleration, and  $S_c$  the ejecta section. A fixed value of  $\eta_{\text{NT}} = 0.1$  is considered throughout this work, and all results on expected luminosity are scalable with this value.

As in Vieyro et al. (2019), we focus on acceleration of electrons/positrons, as leptonic radiation processes are the most efficient ones in the regions of interest. The accelerated electrons cool through either radiative (inverse Compton, synchrotron emission) or non-radiative processes (adiabatic losses, particle

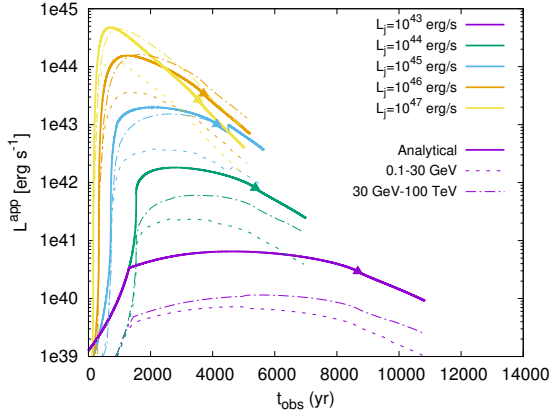


**Fig. 2.** Inverse Compton lightcurves evaluated at electron energy  $E'_e = E'_{IC}$  for different jet powers, for inclination angle  $i = 0^\circ$  and  $\Gamma_j = 10$ . The considered evolution ranges from  $z = 1-4$  kpc, while the triangles mark the 3 kpc passage. The solid line represents the lightcurve calculated through the analytical approximation, while the dashed lines are the same lightcurves calculated through proper integration of the SED in the 0.1 – 30 GeV range, and the dashed-dotted lines are the lightcurves obtained integrating the SED in the 30 GeV–100 TeV range.

advection). For all the cases studied in this work, synchrotron self-Compton losses are negligible in front of the mentioned emission channels.

The observed emission resulting from this cooling is

$$L'_{IC/Sy}(z) = \delta_c^4(z) L'_{NT} \xi'_{IC/Sy}(E_e, z), \quad (3)$$

where  $\delta$  is the Doppler boosting factor, and  $\xi_{IC/Sy}$  is the radiative efficiency of a particular emission channel (see Vieyro et al. 2017). This approximation assumes that the non-thermal energy is at least distributed evenly for different electron energy decades, i.e.  $N(E) \propto E^{-2}$  or harder (as in, e.g., Vieyro et al. 2019). Much softer electron energy distributions would be somehow equivalent to adopting a small value of  $\eta_{NT}$ .

To compute the synchrotron emission, we assume the magnetic energy density to be a certain fraction,  $\zeta_{eq}$ , of the equipartition value (i.e. total magnetic energy density is equal to half the jet energy density). The toroidal magnetic field, considered to be dominant, goes as

$$B'(z) = \frac{1}{\Gamma_c z} \sqrt{\frac{4\zeta_{eq} L_j}{\theta^2 c}} \quad (4)$$

until jet recollimation, at which point it becomes constant.

As main targets for the IC interaction, we consider the radiation field generated by the red-giant population within the bulge of M87, as in Vieyro et al. (2017), which can account for the luminosity of the whole stellar population. We also considered the photon field generated by the accretion disk of the AGN, assuming it has an overall luminosity equal to that of the jet, and concluded that it is negligible at such jet heights, specially when considering Doppler (de)boosting (i.e., the target photons come from ‘behind’ the SN ejecta, with respect to the latter motion).

One can obtain a reasonably accurate approximation for the lightcurves of IC emission, estimating  $L'_{IC}$  as if all the available non-thermal energy (Eq. 2) were emitted by electrons with energy  $E'_{IC} = (m_e c^2)^2 / k T_* \Gamma_c$ . These electrons emit gamma-ray photons at the energy in which the maximum of IC emission is

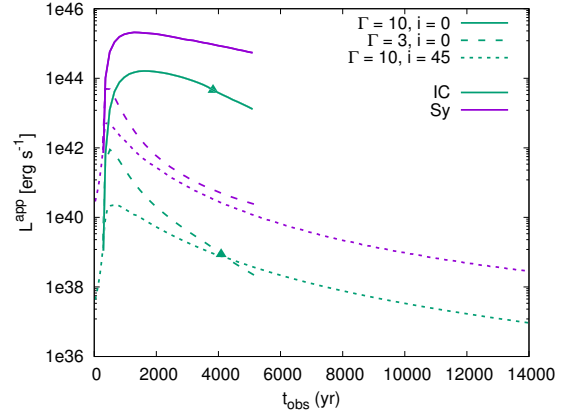


**Fig. 3.** IC (30 GeV – 100 TeV) and synchrotron (0.1 – 100 MeV) lightcurves for a jet of  $L_j = 10^{46}$  erg s $^{-1}$ , comparing the results shown on Fig. 2 with the effects of assuming a lower Lorentz factor or higher inclination angle. The triangles mark the 3 kpc passage, point after which IC emission is slightly overestimated.

expected (as done in Vieyro et al. 2017; Torres-Albà & Bosch-Ramon 2019).

This simple analytical calculation results in the lightcurves plotted in Fig. 2, for different jet powers. The figure also includes a comparison with the lightcurves computed through the proper integration of the spectral energy distribution (SED; see the following section), within two different ranges. The first range, with energies of the emitted photons between 0.1 – 30 GeV, approximately corresponds to the *Fermi* range; and the second, from 30 GeV to 100 TeV, would account for the overall emission in the CTA range.

The analytical approximation differs from the proper calculation of the integrated energy emitted in the CTA range by a factor of  $\sim 6$  at the lowest jet powers, and a factor of  $\lesssim 1.1$  at the highest jet powers. In the *Fermi* range, the integrated calculation is below the analytical approximation by a factor of  $\sim 5-7$  rather consistently.

We note that all lightcurves are plotted until  $t_{obs}(z = 4\text{kpc})$ . However, we model the IC emission using the stellar distribution within a bulge of height 3 kpc, and consider an isotropic photon field. Once the SN ejecta has exited the bulge, photons come with oblique directions towards the accelerated electrons in  $K'$ , and are relativistically less boosted. This implies that the curves past 3 kpc are a slight overestimation.

Figure 3 shows lightcurves for the particular case of a jet with  $L_j = 10^{46}$  erg s $^{-1}$ , but considering a Lorentz factor of  $\Gamma = 3$  or an inclination angle of  $i = 45^\circ$ . The biggest differences between these cases and the  $\Gamma = 10$  blazar are given by the considerable diminishing of the Doppler boosting. As the bubble acceleration keeps on increasing, Doppler boosting is more and more significant at larger  $t_{obs}$ ; therefore, the  $\Gamma = 10$  blazar lightcurve does not fall as quickly as the others. As a result, despite this brightest case being the shortest in observed duration, it is the one that spends the longest time close to its highest luminosity (and, therefore, is likely to be detectable for a longer time). Figure 3 also shows the behaviour of synchrotron emission in the 0.1–100 MeV range, which is much more intense than IC. However, emitted photons only reach 100 MeV in cases of very high particle acceleration efficiency (see SEDs in Sect. 4 for details).

#### 4. Spectral energy distributions

At the peak of the IC emission, as given by the lightcurves in Fig. 2, we calculate the SEDs for the IC and synchrotron emission. We consider three different cases: the particular case of M87, a nearby blazar, and a powerful blazar at higher redshift.

The SEDs are computed as in Vieyro et al. (2019), in particular adopting  $N(E) \propto E^{-2}$ , but considering different target photon fields. The maximum energy achieved by accelerated electrons is defined by the energy loss/gain balance (with losses being dominated by synchrotron emission at the highest electron energies). The acceleration rate is computed as

$$t'_{\text{acc}}(E', z) = \epsilon \frac{eB'(z)c}{E'}, \quad (5)$$

where  $\epsilon \leq 1$  is the acceleration efficiency. In the particular case of  $L_j = 10^{44}$  erg s $^{-1}$ , and at the interaction height of the maximum electron IC emission (i.e. where the SEDs are computed), electrons can achieve energies of

$$E'_{e,\text{max}} \sim 10^{16} \epsilon^{1/2} \text{ eV}, \quad (6)$$

while protons (if present; see Sect. 6.3 for a discussion) would reach

$$E'_{p,\text{max}} \sim 3 \times 10^{19} \epsilon \text{ eV}, \quad (7)$$

since their losses are dominated by either escape of adiabatic expansion.

##### 4.1. M87

For the particular case of M87, we consider a jet with  $L_j = 10^{44}$  erg s $^{-1}$  (Owen et al. 2000), half-opening angle  $\theta = 0.1$  (Biretta & Meisenheimer 1993; Doeleman et al. 2012), Lorentz factor  $\Gamma_j = 3$  (Biretta et al. 1995), inclination  $i = 20^\circ$  (Acciari et al. 2009) and luminosity distance  $D_L = 16$  Mpc (as in NED, as of March 2019).

Figure 4 shows the SEDs resulting from the interaction between the jet and the SN ejecta. The equipartition fraction is taken to be  $\zeta_{\text{eq}} = 10^{-2}$  as per our default value (as is the case for Cen A, Hardcastle et al. 2003), and the  $\zeta_{\text{eq}} = 10^{-4}$  case is included for comparison. In both cases, in order to recover an X-ray emission similar to that detected by Wilson & Yang (2002),  $\epsilon$  must be much lower than 1. The mentioned parameters heavily modify the synchrotron emission, but since IC emission is generated by lower-energy particles, it is hardly affected by changes in the acceleration efficiency or the magnetic field. However, in the extreme case of  $\zeta_{\text{eq}} = 1$ , the synchrotron emission would be intense enough to result in a decrease of a factor  $\sim 2 - 3$  of the peak of IC emission. In such a scenario, X-ray emission would be too high to be compatible with current observations

Our study does not imply that the parameter configuration  $\zeta_{\text{eq}} = 10^{-2}$ ,  $\epsilon = 10^{-6}$  or  $\zeta_{\text{eq}} = 10^{-4}$ ,  $\epsilon = 10^{-4}$  are best-fit parameters for M87. This particular configuration is simply compatible with the observed data, and thus with this interaction taking place within the jet of M87 at the time of observation. If this were the case, it could account for up to  $\sim 30\%$  of the gamma ray emission detected by MAGIC, though in order to explain the remaining emission and in particular the Fermi detection, other processes need to be taking place simultaneously<sup>1</sup>

<sup>1</sup> We note that the radio and X-ray emission shown corresponds solely to that of the brightest knot in the jet; while the gamma-ray emission detected is produced by the sum of the nucleus and the full jet.

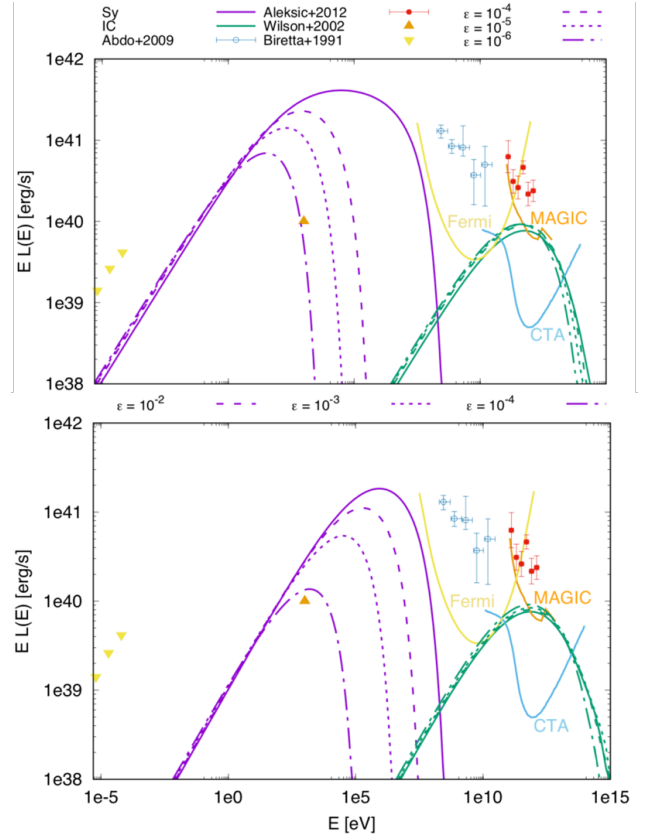


**Fig. 4.** Synchrotron and IC SEDs for M87 and  $\epsilon = 10^{-1}$ , for (top) high magnetic field,  $\zeta_{\text{eq}} = 10^{-2}$  and (bottom) low magnetic field,  $\zeta_{\text{eq}} = 10^{-4}$ . Curves with lower acceleration efficiencies,  $\epsilon$ , are included for comparison. Also plotted are sensitivity curves for Fermi (Ackermann et al. 2012, after 10 years of survey), MAGIC (Aleksić et al. 2016) and CTA (both after 50h of direct observation), as well as MAGIC data from Aleksić et al. (2012), *Fermi* data from Abdo et al. (2009), X-ray data from Wilson & Yang (2002) and radio data from Doeleman et al. (2012). X-ray and radio data both correspond to emission at kpc scales, taken from the brightest knot (knot A) in the jet of M87, and have error bars smaller than the size of the point. The resolution of gamma ray observatories does not allow to disentangle emission from the kpc-scale jet and the nucleus. All data were taken during the source’s low-emission state.

From lightcurve computations, we estimate that emission at a level similar to that reached by the shown SED would last for  $\sim 5000$  yr. Considering a system with the same parameters but  $\Gamma_j = 10$ , which could serve as a model for other nearby radio galaxies, the overall non-thermal luminosity at the peak of emission would be a factor of  $\sim 5$  higher, and the event would remain at maximum brightness a  $\sim 20\%$  longer time.

##### 4.2. Blazar sources

We consider two blazar sources, with jet luminosities  $L_j = 10^{44}$  and  $10^{47}$  erg s $^{-1}$ ,  $\Gamma_j = 10$ ,  $\theta = 0.1$ , in which a Type Ia SN has exploded within the jet. We take as default parameters  $\zeta_{\text{eq}} = 10^{-2}$  and  $\epsilon = 10^{-1}$ . The powerful blazar is placed at a moderate redshift of 0.5, while the less powerful one is placed at 100 Mpc, resulting in the SEDs plotted in Figure 5.

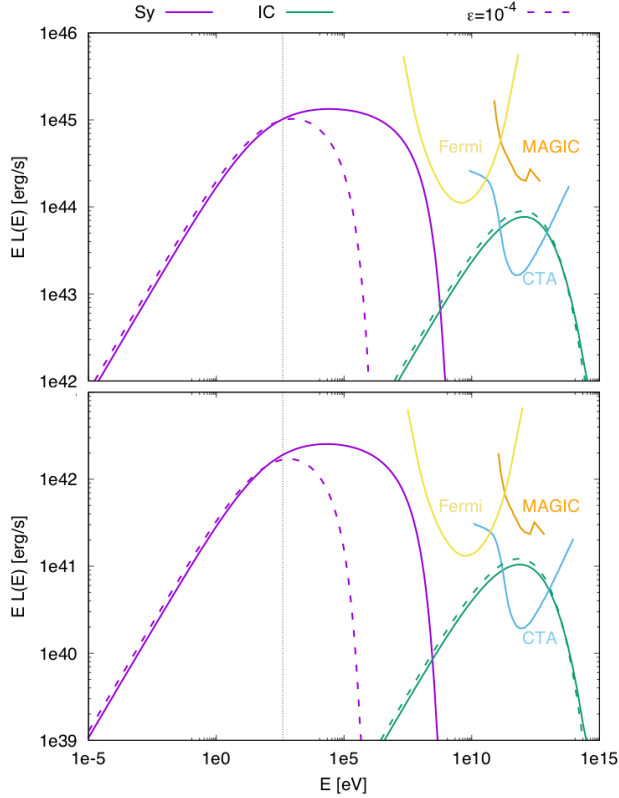


**Fig. 5.** Synchrotron and IC SEDs for a blazar with (*top*)  $L_j = 10^{47}$  erg s $^{-1}$  and at a redshift 0.5 and (*bottom*)  $L_j = 10^{44}$  erg s $^{-1}$  and at a distance of 100 Mpc, for  $\zeta_{\text{eq}} = 0.1$  and  $\epsilon = 10^{-1}, 10^{-4}$ . Also plotted are sensitivity curves for *Fermi* (Ackermann et al. 2012, after 10 years of survey), *MAGIC* (Aleksić et al. 2016) and *CTA* (both after 50h of direct observation). The vertical, dashed line marks  $E = 400$  eV.

The duration of these events, with a luminosity comparable to that shown in the SED, would be of  $t_{\text{obs}} \sim 6000$  yr for  $L_j = 10^{44}$  erg s $^{-1}$  and of  $t_{\text{obs}} \sim 2000$  yr for  $L_j = 10^{47}$  erg s $^{-1}$ .

In the case of blazars, we are not modeling specific sources and therefore we have no direct comparison with observations in order to constraint the parameters. A possible comparison with observational data, however, is obtaining a SED with a shape that is compatible with that of the blazar sequence determined by Ghisellini et al. (2017). The average SED at lower luminosities shows a synchrotron peak at  $\sim 10^{17}$  Hz, which corresponds to  $\sim 400$  eV (dashed, vertical line in Fig. 5). Our model recovers a peak centered near this energy, and an overall similar SED shape, only for lower acceleration efficiencies than initially considered, of  $\epsilon \sim 10^{-4}$ .

## 5. Event rate and duty cycle

### 5.1. Type Ia supernova rate within the jet

Type Ia SN event rate has been extensively studied and has proven to be a difficult quantity to constrain, given that it depends on the evolutionary path of the progenitor system and the nature of the binary companion. Theoretical estimations depend on population models, and yield different results depending on the assumed proportion of SNe coming from systems formed by two white dwarfs, or by a white dwarf and an evolved star (Ruiter

et al. 2009). In order to better constrain these unknowns, the SN rate is generally studied as a function of the stellar mass, star formation rate (SFR), luminosity, and morphology of the galaxy.

We assume an elliptical galaxy with an age of 10 Gyr, and consider that all the stars have been generated at the birth of the galaxy in one single starburst ( $t_{\text{gal}} = 0$ ). These are the same assumptions taken to derive the stellar photon field of the galaxy, used to compute the IC emission. In such a case, a Type Ia SN event rate of

$$r_{\text{SN}} \sim 4 \times 10^{-2} (M_{\text{gal}}/10^{10} M_{\odot})^{-1} (100 \text{ yr})^{-1} \quad (8)$$

is expected (Mannucci et al. 2005; Scannapieco & Bildsten 2005; Maoz & Mannucci 2012). The elliptical galaxy M87, which we use throughout this work as a reference for a typical elliptical, has an estimated stellar mass of  $2 \times 10^{11} M_{\odot}$  within its bulge (Gebhardt & Thomas 2009). This yields a Type Ia SN event rate of  $\sim 0.9 (100 \text{ yr})^{-1}$ , although only a fraction of these will take place inside the jet.

As mentioned in Sect 2, we consider a jet that can recollimate when in pressure equilibrium with the external medium. A jet with  $L_j = 10^{44}$  erg s $^{-1}$  and  $\Gamma_j = 10$  recollimates at a distance of  $\sim 1$  kpc; in this case, the number of SNe taking place within the galaxy bulge and the jet is  $r_{\text{SN}} \sim 2 \times 10^{-4} (100 \text{ yr})^{-1}$ . A jet with  $L_j \geq 10^{45}$  erg s $^{-1}$ , or one with lower luminosity and  $\Gamma_j = 3$ , would not recollimate within the bulge of the galaxy, and thus  $r_{\text{SN}} \sim 2 \times 10^{-3} (100 \text{ yr})^{-1}$ .

However, it is worth mentioning that the pressure profile of the jet environment could be different than assumed. If that were the case, the jet might remain conical up to  $\sim 3$  kpc, or become parabolic, and the duty cycle could be up to a factor of ten higher for weak jets.

### 5.2. Expected number of detectable blazars

The duration of each individual event is given by the lightcurves seen in Fig. 2. For a weak jet, of  $L_j = 10^{44}$  erg s $^{-1}$  and  $\Gamma_j = 10$ , the expected duration of an event is of  $t_{\text{obs}} \approx 10^4$  yr. This implies a duty cycle of  $r_{\text{SN}} \cdot t_{\text{obs}} = 2 \times 10^{-2}$  for each individual elliptical galaxy. Therefore, 2% of the time a SN ejecta should be interacting with these weak jets, if they are hosted in an elliptical galaxy.

Focusing on weak blazars, one could expect to detect events occurring in the local universe (see Fig. 5, bottom panel). The blazar number density peaks at different redshift according to the luminosity. BL Lacs dominate the local luminosity function for  $L_{\gamma}^{\text{obs}} < 10^{46}$  erg s $^{-1}$ ; the average redshift is  $\sim 0.5$ . *MAGIC* could detect such sources up to distances of  $D_L \sim 50$  Mpc, while *CTA* should be able to do so up to redshift  $z \sim 0.1$ . The average number of sources within such volumes is of  $\sim 0.06$  and  $\sim 100$ , respectively; most of these with  $L_{\gamma}^{\text{obs}} \lesssim 10^{45}$  erg s $^{-1}$  (Zeng et al. 2014). This implies that *MAGIC* is most likely unable to detect such sources, while a couple of blazars within the local universe (which present interaction with a Type Ia SN remnant) may be detectable by *CTA* once it is operational.

In the case of powerful jets, event length is shorter, of  $t_{\text{obs}} = 2 \times 10^3$  yr, but since the jets do not recollimate the duty cycle is larger, of  $r_{\text{SN}} \cdot t_{\text{obs}} = 4 \times 10^{-2}$ . FSRQ are the most luminous blazars, with gamma luminosities of  $10^{41} < L_{\gamma}^{\text{obs}} \lesssim 10^{50}$  erg s $^{-1}$ . The number density peaks at  $z \sim 0.8$ , with an average luminosity of  $6 \times 10^{47}$  erg s $^{-1}$ . *MAGIC* could detect such sources up to redshift of  $z \sim 0.25$ , while *CTA* should be able to do so up to  $z \sim 0.5$ . The estimated number of sources within these volumes is approximately  $\sim 100$  and  $\sim 1.2 \times 10^3$ , respectively (Ajello et al.

2012). A 4% of these sources should have detectable gamma-ray emission, as given by Fig. 5 top panel, produced through the interaction between SNe and jets. This implies that about  $\sim 4$  of these sources in the sky could be detectable by MAGIC, and up to  $\sim 50$  by CTA in the near future.

All the estimations presented above consider jets with  $\Gamma_j = 10$ . If we were to consider that all jets have  $\Gamma_j = 3$ , the redshift up to which those sources are detectable would be significantly reduced. Repeating the same procedure, we would obtain that no BL Lacs are present within the small redshift range, and only about  $\sim 5$  FSRQs are (detectable by CTA only). Therefore, given the duty cycle of  $\sim 4\%$ , we expect that most of the time we would not detect a type Ia SN-jet interaction taking place.

### 5.3. Expected number of detectable radio galaxies

The case of radio galaxies is slightly different. Due to the lack of significant Doppler Boosting, the maximum distance at which we can detect the interaction between a Type I SN and an AGN jet is smaller. We consider a radio galaxy with reasonable jet parameters of  $L_j = 10^{44}$  erg s $^{-1}$  and  $i = 45^\circ$ . CTA would detect the jet interacting with a Type I SN up to luminosity distances  $D_L \simeq 30$  Mpc or  $D_L \simeq 50$  Mpc, for  $\Gamma_j = 3$  and 10, respectively. The number of radio galaxies within these volumes is, respectively, 7 and 14 (see catalogue by van Velzen et al. 2012). MAGIC could detect sources up to  $D_L \simeq 16$  Mpc if  $\Gamma_j = 10$ , volume which contains 5 known radio galaxies. For  $\Gamma_j = 3$ , it is likely that we would reach detectable levels only for M87, for which we know the current gamma-ray emission is somewhat above that generated by a SN-jet interaction.

For the SN rate within the jet of a radio galaxy and the event lengths given in Sect. 3, the resulting duty cycle is  $r_{\text{SN}} \cdot t_{\text{obs}} = 10^{-2}$ . This means that, statistically, a 1% of the sources (i.e. at most one detectable radio galaxy) would be hosting one such event at a time.

## 6. Discussion

### 6.1. Blazar detectability

As shown in Figs. 4 and 5, the detectability in gamma-rays of the Type Ia SN interacting with AGN jets is barely influenced by assumptions on the value of the magnetic field (unless it is extremely high), or the efficiency of electron acceleration  $\epsilon$ . As calculated in Sect. 5, we may expect this interaction to be detectable in tens of blazars once CTA is operational.

Currently, the number of persistent blazars detected (correctly identified as such and with known redshift) at TeV energies is 15 at  $z < 0.1$  and 42 at  $z < 0.5$  (from TeVCat, Wakely & Horan 2008, as of 22 April 2019). Therefore, the number of blazar jets interacting with a SN we estimate to be detectable with CTA is of the same order as the number of currently detected VHE blazars. However, CTA will also increase the total number of detected blazar sources. Dubus et al. (2013) estimate that  $\sim 20$  new blazars would be detected with CTA in a 250 h blank survey, while dedicating 50 h to observe each source in the whole *Fermi*/LAT catalogue could result in  $\geq 170$  detections (a 30% of the whole *Fermi* catalogue) with the most favorable array configurations. Thus, regardless of the emitting mechanism, it is likely that many more persistent VHE blazars will be discovered, either serendipitously or through other means. What our study shows is that a non-negligible fraction of these objects may be detected due to their jets interacting with Type Ia SNe.

### 6.2. Interaction of the accelerated SN ejecta with CMB photons

In the interaction between the SN ejecta and the jet, the dominant radiative losses of electrons are synchrotron emission and IC scattering of photons from the stellar population within the galaxy bulge. Inverse Compton scattering with CMB photons is a comparatively inefficient channel. However, as the SN ejecta moves downstream of the jet, both the magnetic field and the stellar photon field weaken.

We consider here an extension of the evolution of the SN remnant within the jet up to distances of  $z = 10$  kpc, and compute the radiative losses through IC upscattering of CMB photons, using the analytical approximation introduced in Sect. 3. In the range of  $z = 4 - 10$  kpc, we consider that the ISM pressure within the galaxy diminishes sufficiently for the jet to expand conically in all cases (i.e. also for the weak, recollimated jets). We present results of the expected IC luminosity for the three cases considered in the previous sections.

For M87, the observed emission could be of  $L_{\text{CMB}} = 5 \times 10^{40}$  erg s $^{-1}$ , and for the  $L_j = 10^{44}$  erg s $^{-1}$  blazar, we can expect  $L_{\text{CMB}} = 2 \times 10^{41}$  erg s $^{-1}$ ; in both cases during  $t_{\text{obs}} \sim 10^4$  yr. The case of the powerful  $L_j = 10^{47}$  erg s $^{-1}$  blazar is slightly different. Since it accelerates the remnant much more efficiently, the shock is weak at such heights, and it reaches a maximum  $L_{\text{CMB}} = 10^{42}$  erg s $^{-1}$  which decays one order of magnitude in about  $t_{\text{obs}} \sim 5000$  yr. Note, however, that the corrections depicted in Fig. 2 should be applied to all derived luminosities.

If the blazars were to have  $\Gamma_j = 3$ , we could expect a similar luminosity for the weak blazar case, though a shorter event; and a much lower luminosity for a powerful blazar, given by the fact that synchrotron losses are still very relevant in this particular scenario.

### 6.3. Hadrons and CR

The same shocks that accelerate electrons could accelerate hadrons present in the source, injected into the jet by the SN itself. At the considered jet heights, the magnetic field is too low for synchrotron emission to be an efficient radiation channel for protons. Similarly, photohadronic production against the diluted star photon field is inefficient, and the low energy of the target photons ( $kT_* \sim 0.3$  eV) requires proton energies that are most likely unfeasible. In the same way,  $pp$  interactions with the matter of the SN ejecta itself are an inefficient radiation mechanism. Given the large cooling times, hadrons lose energy adiabatically and eventually escape the jet, filling the surrounding medium. For instance, they can be carried to the jet termination regions, where they may be reaccelerated and fill the jet lobes. The most energetic hadrons could diffuse into the intergalactic medium.

The expected composition for these cosmic rays is that of the metals produced in a Type Ia SN, consisting mostly of iron-peak elements (Cr-Ni), of which about  $\sim 0.5 - 0.6 M_\odot$  is the iron isotope  $^{56}\text{Fe}$  (Nomoto et al. 1984; Thomas et al. 1998). Since the supernova rate within the jet can range from  $r_{\text{SN}} \sim 2 \times 10^{-5} - 2 \times 10^{-6}$  yr $^{-1}$ , all elliptical galaxies with a jet would be injecting  $\sim 10^{-5} - 10^{-6} M_\odot$  yr $^{-1}$  of iron into the jet lobes; some of this iron could escape in the form of very energetic CR into the IGM.

### 6.4. Observational signatures and constraints

The presence of a SNR within the jet of an AGN would be characterized by the significant enhancement of emission, in the shape of a bow-shock, around the obstacle. While this structure

cannot be resolved in gamma-rays, radio observations of nearby galaxy Centaurus A show a distinct bow-shaped feature, interpreted as the result of the presence of a red-giant star within the jet (Müller et al. 2014). The presence of individual X-ray knots within the inner kiloparsec can also be explained through the presence of a stellar population (Wykes et al. 2015).

A SNR within the jet would have a higher luminosity than one single, or even a population of, AGB stars (Vieyro et al. 2017). Also, the SNR would be expected to cover the whole jet section, unlike the knot generated by one single star. Distinguishing this morphologies, however, would require a high enough resolution to appreciate the size of the interaction region. This is only feasible for nearby sources.

The (multiple) star and the SNR scenarios evolve differently, as stars cross the jet while the SNR moves downstream (see e.g. Snios et al. 2019); however, the dynamical timescales are of thousands of years, not allowing to make this distinction. On the other hand, a significant difference between the two scenarios is in the highest energy CR output. As mentioned above, a SN exploding within the jet results in an average iron production of  $10^{-5} - 10^{-6} M_{\odot} \text{ yr}^{-1}$ . Main sequence and AGB stars within the jet would generate mainly intermediate-mass CR, with  $^{16}\text{O}$ ,  $^{12}\text{C}$  and  $^{14}\text{N}$  as the key isotopes. Their iron output would be of  $10^{-11} - 10^{-8} M_{\odot} \text{ yr}^{-1}$ , depending on population assumptions, per elliptical galaxy (Wykes et al. 2015, derived for Cen A). The composition of CR cannot be ascertained for individual galaxies. However, if jetted elliptical galaxies dominated the CR at the highest energies, one would expect the overall density of iron in those CR to be dominated by SNR exploding within the jets of those galaxies. Currently, the composition of extragalactic CR (ECR) is not well-constrained enough to derive a conclusion; but the iron to proton relative abundances are expected to affect the ECR spectrum (e.g. Allard et al. 2005). In the future, this might be a way to constrain the number of Type Ia SN taking place within the jet.

The acceleration of protons in the interaction between a jet and the SN ejecta can lead to efficient to proton-proton collisions (see e.g. Barkov et al. 2010, in a similar scenario), and the subsequent emission of gamma rays and neutrinos. Therefore, one cannot in principle exclude this scenario to explain the neutrino event detected from TXS 0506+056 (IceCube Collaboration et al. 2018). However, we note that proton-proton radiation will be efficient only very close to the base of the jet. Although the rate of such an event strongly depends on the stellar distribution in the inner pc region, the associated probability may be easily orders of magnitude below those studied here, which correspond to kpc scales.

Possible constraints on the parameters of our model are determined, mostly, by the shape of the synchrotron emission in X-rays. Our model is compatible with this interaction taking place within the jet of M87 when considering low acceleration efficiencies,  $\epsilon \sim 10^{-4} - 10^{-7}$ , depending on the adopted value of the magnetic field. Likewise, the computed blazar SEDs are similar to the blazar sequence of Ghisellini et al. (2017) for  $\epsilon \sim 10^{-4}$ . These values are compatible with previous observational studies, which also show that particle acceleration efficiency in blazars should be low, with derived values of  $\epsilon$  of  $10^{-4.5}$  (Inoue & Takahara 1996),  $\leq 10^{-5}$  (Finke et al. 2008),  $10^{-7}$  (Sato et al. 2008) or  $10^{-5}$  (Inoue & Tanaka 2016).

The strength of the magnetic field is more difficult to constrain comparing with observational data. In this work we have taken  $\zeta_{\text{eq}} = 10^{-2}$  as our default value, based on observations of the jet of Cen A (Hardcastle et al. 2003). As shown in the SED of M87, lower values of the magnetic field would also be

compatible with observations when adopting higher acceleration efficiencies. A magnetic field in equipartition with the jet energy density, however, would be incompatible with X-ray observations.

Despite what Cen A observations tell us about the jet, we must note that the magnetic field within the SN ejecta is not necessarily the same as that of the jet. Our model makes no distinction between the properties of particles accelerated in either shock (i.e., the shocked jet material or the shocked SN ejecta material), and adding more parameters would needlessly complicate the model without improving its constraining power.

## 7. Summary and conclusions

We have studied the dynamical evolution and gamma-ray emission of the ejecta of a Type Ia SN within the jet of an elliptical galaxy. The bulk of the expected emission, according to our model, is produced in X-rays and soft gamma-rays, and VHE gamma rays in the CTA range. We cannot rule out the presence of significant emission in the Fermi range, but it would require a rather extreme acceleration efficiency ( $\eta_{\text{NT}} \lesssim 1$ ). Our results indicate that as many as  $\sim 50$  blazars could be observed up to  $z \simeq 0.5$ , thanks to this interaction taking place within them (if most of the sources have Lorentz factors  $\Gamma_j \sim 10$ ). More locally, we could expect to detect a few BL Lacs, given the same assumption; and, statistically, at most one radio galaxy at a time. If the sources have, in their majority,  $\Gamma_j \sim 3$ , we could expect to not detect even one single event most of the time.

## Acknowledgments

This work was supported by the Spanish Ministerio de Economía y Competitividad (MINECO/FEDER, UE) under grant AYA2016-76012-C3-1-P with partial support by the European Regional Development Fund (ERDF/FEDER), MDM-2014-0369 of ICCUB (Unidad de Excelencia ‘María de Maeztu’), and the Catalan DEC grant 2017 SGR 643. N.T.A. acknowledges support from MINECO through FPU14/04887 grant. F.L.V acknowledges support from the Argentine Agency CONICET (PIP 2014-00338) and the National Agency for Scientific and Technological Promotion (PICT 2017-0898). The NASA/IPAC Extragalactic Database (NED) is operated by the Jet Propulsion Laboratory, California Institute of Technology, under contract with the National Aeronautics and Space Administration. This research has made use of the CTA instrument response functions provided by the CTA Consortium and Observatory, see <http://www.cta-observatory.org/science/cta-performance/> (version prod3b-v1) for more details. This research has made use of the TeVCat online source catalog (<http://tevcat.uchicago.edu>).

## References

- Abdo, A. A., Ackermann, M., Ajello, M., et al. 2009, *ApJ*, 707, 55
- Acciari, V. A., Aliu, E., Arlen, T., et al. 2009, *Science*, 325, 444
- Ackermann, M., Ajello, M., Albert, A., et al. 2012, *The Astrophysical Journal Supplement Series*, 203, 4
- Aharonian, F. A., Barkov, M. V., & Khangulyan, D. 2017, *ApJ*, 841, 61
- Ajello, M., Shaw, M. S., Romani, R. W., et al. 2012, *ApJ*, 751, 108
- Aleksić, J., Alvarez, E. A., Antonelli, L. A., et al. 2012, *A&A*, 544, A96
- Aleksić, J., Ansoldi, S., Antonelli, L. A., et al. 2016, *Astroparticle Physics*, 72, 76
- Allard, D., Parizot, E., Olinto, A. V., Khan, E., & Goriely, S. 2005, *A&A*, 443, L29
- Araudo, A. T., Bosch-Ramon, V., & Romero, G. E. 2010, *A&A*, 522, A97
- Araudo, A. T., Bosch-Ramon, V., & Romero, G. E. 2013, *MNRAS*, 436, 3626

- Banasieński, P., Bednarek, W., & Sitarek, J. 2016, MNRAS, 463, L26
- Barkov, M. V., Aharonian, F. A., & Bosch-Ramon, V. 2010, ApJ, 724, 1517
- Barkov, M. V., Bosch-Ramon, V., & Aharonian, F. A. 2012, ApJ, 755, 170
- Bednarek, W. I. 1999, in Plasma Turbulence and Energetic Particles in Astrophysics, ed. M. Ostrowski & R. Schlickeiser, 360–365
- Begelman, M. C., Blandford, R. D., & Rees, M. J. 1984, Reviews of Modern Physics, 56, 255
- Biretta, J. A. & Meisenheimer, K. 1993, in Lecture Notes in Physics, Berlin Springer Verlag, Vol. 421, Jets in Extragalactic Radio Sources, ed. H.-J. Röser & K. Meisenheimer, 159
- Biretta, J. A., Zhou, F., & Owen, F. N. 1995, ApJ, 447, 582
- Blandford, R. D. & Koehnig, A. 1979, Astrophys. Lett., 20, 15
- Bosch-Ramon, V. 2015, A&A, 575, A109
- Bosch-Ramon, V., Perucho, M., & Barkov, M. V. 2012, A&A, 539, A69
- Doeleman, S. S., Fish, V. L., Schenck, D. E., et al. 2012, Science, 338, 355
- Dubus, G., Contreras, J. L., Funk, S., et al. 2013, Astroparticle Physics, 43, 317
- Falomo, R., Scarpa, R., Treves, A., & Urry, C. M. 2000, ApJ, 542, 731
- Finke, J. D., Dermer, C. D., & Böttcher, M. 2008, ApJ, 686, 181
- Gamezo, V. N., Khokhlov, A. M., Oran, E. S., Chitchekanova, A. Y., & Rosenberg, R. O. 2003, Science, 299, 77
- Gebhardt, K. & Thomas, J. 2009, ApJ, 700, 1690
- Ghisellini, G., Righi, C., Costamante, L., & Tavecchio, F. 2017, MNRAS, 469, 255
- Hardcastle, M. J., Worrall, D. M., Kraft, R. P., et al. 2003, ApJ, 593, 169
- Hubbard, A. & Blackman, E. G. 2006, MNRAS, 371, 1717
- IceCube Collaboration, Aartsen, M. G., Ackermann, M., et al. 2018, Science, 361, 147
- Inoue, S. & Takahara, F. 1996, ApJ, 463, 555
- Inoue, Y. & Tanaka, Y. T. 2016, ApJ, 828, 13
- Khangulyan, D. V., Barkov, M. V., Bosch-Ramon, V., Aharonian, F. A., & Dorodnitsyn, A. V. 2013, ApJ, 774, 113
- Komissarov, S. S. 1994, MNRAS, 269, 394
- Kotilainen, J. K., Falomo, R., & Scarpa, R. 1998, A&A, 332, 503
- Mannucci, F., Della Valle, M., Panagia, N., et al. 2005, A&A, 433, 807
- Maoz, D. & Mannucci, F. 2012, PASA, 29, 447
- Maoz, D., Mannucci, F., & Nelemans, G. 2014, ARA&A, 52, 107
- Müller, C., Kadler, M., Ojha, R., et al. 2014, A&A, 569, A115
- Nilsson, K., Pursimo, T., Heidt, J., et al. 2003, A&A, 400, 95
- Nomoto, K., Thielemann, F. K., & Yokoi, K. 1984, ApJ, 286, 644
- Olguín-Iglesias, A., León-Tavares, J., Kotilainen, J. K., et al. 2016, MNRAS, 460, 3202
- Owen, F. N., Eilek, J. A., & Kassim, N. E. 2000, ApJ, 543, 611
- Perucho, M., Bosch-Ramon, V., & Barkov, M. V. 2017, A&A, 606, A40
- Ruiter, A. J., Belczynski, K., & Fryer, C. 2009, ApJ, 699, 2026
- Sato, R., Kataoka, J., Takahashi, T., et al. 2008, ApJ, 680, L9
- Scalzo, R., Aldering, G., Antilogus, P., et al. 2014, MNRAS, 440, 1498
- Scannapieco, E. & Bildsten, L. 2005, ApJ, 629, L85
- Scarpa, R., Urry, C. M., Falomo, R., Pesce, J. E., & Treves, A. 2000, ApJ, 532, 740
- Snios, B., Wykes, S., Nulsen, P. E. J., et al. 2019, ApJ, 871, 248
- Thomas, D., Greggio, L., & Bender, R. 1998, MNRAS, 296, 119
- Torres-Albà, N. & Bosch-Ramon, V. 2019, arXiv e-prints, arXiv:1902.05008
- van Velzen, S., Falcke, H., Schellart, P., Nierstenhöfer, N., & Kampert, K.-H. 2012, A&A, 544, A18
- Vieyro, F. L., Bosch-Ramon, V., & Torres-Albà, N. 2019, A&A, 622, A175
- Vieyro, F. L., Torres-Albà, N., & Bosch-Ramon, V. 2017, A&A, 604, A57
- Wakely, S. P. & Horan, D. 2008, International Cosmic Ray Conference, 3, 1341
- Wang, T., Elbaz, D., Alexander, D. M., et al. 2017, A&A, 601, A63
- Wilk, K. D., Hillier, D. J., & Dessart, L. 2018, MNRAS, 474, 3187
- Wilson, A. S. & Yang, Y. 2002, ApJ, 568, 133
- Wykes, S., Hardcastle, M. J., Karakas, A. I., & Vink, J. S. 2015, MNRAS, 447, 1001
- Zeng, H., Yan, D., & Zhang, L. 2014, Monthly Notices of the Royal Astronomical Society, 441, 1760

Part IV

IMPACT OF AGN JETS IN REIONIZATION



## AGN JETS VERSUS ACCRETION AS REIONIZATION SOURCES

---

In this chapter we present our work "AGN jets versus accretion as reionization sources", which has been sent for publication to A&A. In this work, we explore the possibility of AGN jets having contributed to the reionization of the Universe through inverse Compton scattering of CMB photons.



# AGN jets versus accretion as reionization sources

Núria Torres-Albà<sup>1</sup>, Valentí Bosch-Ramon<sup>1</sup> and Kazushi Iwasawa<sup>1,2</sup>

<sup>1</sup> Departament de Física Quàntica i Astrofísica, Institut de Ciències del Cosmos (ICC), Universitat de Barcelona (IEEC-UB), Martí i Franquès 1, E08028 Barcelona, Spain

<sup>2</sup> ICREA, Pg. Lluís Companys 23, E-08010 Barcelona, Spain

June 21, 2019

## ABSTRACT

**Context.** Cosmic reionization put an end to the dark ages that came after the recombination era. Observations seem to favor the scenario of massive-star photons generated in low-mass galaxies being responsible for the bulk of reionization and, whereas a possible contribution from AGN accretion disks has been widely considered, they are currently thought to have had a minor role in reionization.

**Aims.** We aim to study the possibility of AGN having contributed to reionization not only through their accretion disks, but also through ionizing photons coming from the AGN jets interacting with the IGM.

**Methods.** We adopt an empirically derived AGN luminosity function at  $z \simeq 6$ , use X-ray observations to correct it for the presence of obscured sources, and estimate the density of jetted AGN. We then use analytical calculations to derive the fraction of jet energy that goes into ionizing photons. Finally, we compute the contribution of AGN jets to the H II volume filling factor at redshifts  $z \simeq 15 - 5$ .

**Results.** We show that the contribution of the AGN jet lobes to the reionization of the Universe at  $z \sim 6$  might have been as high as  $\gtrsim 10\%$  of that of star-forming galaxies, under the most favorable conditions of jetted and obscuration fraction.

**Conclusions.** The contribution of AGN to the reionization, while most likely not dominant, could have been higher than previously assumed, thanks to the radiation originated in the jet lobes.

**Key words.** Radiation mechanisms: non-thermal – Galaxies: active – Galaxies: jets – dark ages, reionization – cosmology: miscellaneous – intergalactic medium

## 1. Introduction

Cosmic reionization represents an important stage in the evolution of the Universe, putting an end to the dark ages that came following the recombination era. Observations indicate that the intergalactic medium (IGM) was completely reionized at redshift  $z \simeq 6$  (e.g. Fan et al. 2006; Pentericci et al. 2014; Tilvi et al. 2014; McGreer et al. 2015). However, the onset and duration of reionization remain uncertain. The latest Planck results (Planck Collaboration et al. 2018) favor a reionization that happened late and fast ( $z = 7.82 \pm 0.71$ ), consistent with it being driven by photons from massive stars in low-mass galaxies (e.g. Robertson et al. 2015), as long as the escape fraction of the ionizing radiation is high enough (e.g. Stark 2016).

In addition to star-forming galaxies, accretion disks of active galactic nuclei (AGN) are also possible sources of ionizing photons at high redshift (e.g. Arons & McCray 1970; Meiksin & Madau 1993). Thus, they have since long been considered possible contributors to reionization (e.g. Grazian et al. 2018), or at least indirect factors in the reionization process (e.g. Seiler et al. 2018; Kakiichi et al. 2018). Such sources, however, are presently thought to play a minor role in the reionization of hydrogen (e.g. Hopkins et al. 2007; Onoue et al. 2017; Parsa et al. 2018; Matsuoka et al. 2018).

Still, accretion might not be the only ionizing radiation source in AGN. In particular, the termination regions of AGN-produced jets are known to be filled with non-thermal electrons (Croston et al. 2018), which cool efficiently through Inverse Compton (IC) and synchrotron radiation. At such large distances from the jet base, and taking into account the high density of the CMB photon field at  $z \simeq 6$ , it is expected that IC would dominate radiative losses, upscattering CMB photons to higher energies (e.g. Wu et al. 2017).

For the brightest blazars, there is evidence to indicate that jets may be as powerful as accretion radiation, if not more (Ghisellini et al. 2014; Sbarrato et al. 2016). Sbarrato et al. (2015) suggest that at  $z \simeq 6$  the jetted fraction of the most powerful AGN might be close to one. Whereas radiation from an accretion disk is easily absorbed by the dense obscuring medium surrounding the AGN, the jet lobes are located in regions free from dense surrounding material. Therefore, if the jetted fraction is high enough, the number of sources that contributed to reionization with photons from their jet lobes might be larger than those contributing with accretion disk photons.

Recently, Bosch-Ramon (2018) explored the possible role of AGN jets and their termination regions in the reionization epoch, using empirically derived black-hole mass functions and assuming a certain duty-cycle and accretion power. The conclusion reached in that work was that jet

Send offprint requests to: N. Torres-Albà  
e-mail: ntorres@fqa.ub.edu

lobes might contribute non-negligibly to the reionization of the Universe at  $z \gtrsim 6$ .

In this work, we carry out a more quantitative study of the impact of AGN jet lobes in reionizing the Universe, expanding it up to significantly higher redshifts. To do that, we improve the estimations of Bosch-Ramon (2018) using recent, empirically derived quasar luminosity functions (LFs) at  $z \simeq 6$ , and correcting them for possible obscured sources. The work is structured as follows: In Sect. 2, we discuss the adopted luminosity functions and how we correct them to account for the presence of obscured sources. In Sect. 3, we compute the fraction of jet power that goes to ionizing radiation. In Sect. 4, we use the obtained results to estimate the contribution of AGN jets to the ionizing photon density at  $z \simeq 6$ , and to the H II volume filling factor in the IGM in the range  $z \simeq 15 - 5$ . Finally, we summarize and discuss our results in Sect. 5.

## 2. Luminosity function

In order to characterize the AGN population at the epoch of reionization we must assume a quasar LF. Various studies have attempted to construct the LF at  $z \sim 6$ , including those based on optical/UV (e.g. Willott et al. 2010b; Onoue et al. 2017; Kulkarni et al. 2018), X-ray (e.g. Parsa et al. 2018; Vito et al. 2018), or radio data (e.g. Caccianiga et al. 2019).

LFs derived from radio studies tend to be inconsistent with X-ray results, finding a lower density of sources as well as different density peaks as a function of redshift (see, e.g. Ajello et al. 2009; Caccianiga et al. 2019). Wu et al. (2017) and Saxena et al. (2017) attribute the low number density of radio sources at  $z > 3$  to quenching of radio emission due to higher densities of the CMB (see also Sect. 5). On the other hand, X-ray studies are also inconsistent with those derived from rest-UV surveys, finding an excess of sources at lower luminosities. This is presumably associated to dust obscuration effects, which are much more important at UV wavelengths. However, the mentioned X-ray and radio LFs cover a broad redshift range, reaching much later times than we are interested in, and are generally derived using smaller source samples. We therefore opt to use the most recent UV results, and correct them for the effects of obscuration. In particular, we use the LF derived in one of the latest and most complete studies (Matsuoka et al. 2018), based on a compilation of rest-UV data (Jiang et al. 2016; Willott et al. 2010b; Matsuoka et al. 2018). Their sample has the advantage of covering a broad luminosity range, but within a narrow  $5.7 < z < 6.5$  redshift range.

To the LF from Matsuoka et al. (2018) we added a correction for the absorbed AGN fraction based on results from Vito et al. (2018), who analyzed X-ray data of AGN in the  $3 < z < 6$  range. They derive an obscured AGN fraction of  $\approx 0.8$  at high X-ray luminosities, as well as a decrease of obscuration at  $L_x < 10^{43}$  erg s $^{-1}$ . Although this decrease goes against the well-established trend that low-luminosity AGN are more frequently obscured than those of higher luminosity (e.g. Lawrence 1991; Ueda et al. 2003; Steffen et al. 2003; Simpson 2005), Vito et al. (2018) attribute this unexpected result to incompleteness of the sample at low luminosities, and thus determine it is unreliable. Based on this, we assumed first a constant obscuration (CO) fraction of 0.8, a value that is compatible with their data in all luminosities in which the sample is complete. The LF we derive

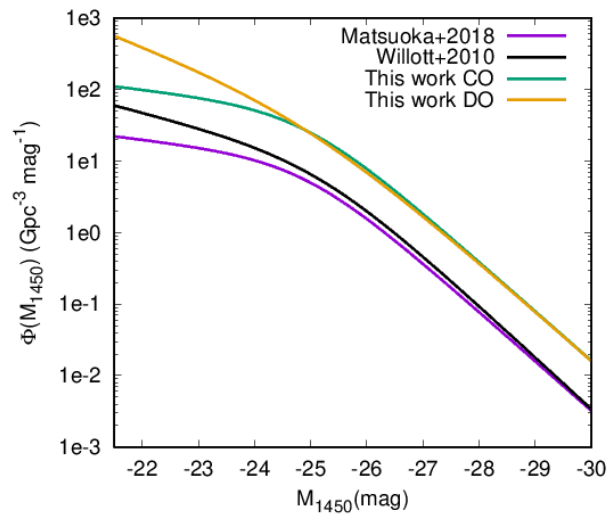


Fig. 1: Luminosity functions derived by Matsuoka et al. (2018); Willott et al. (2010a) compared to those used in this work. The two curves used here are based on that of Matsuoka et al. (2018) and include a constant correction for obscuration (CO), or a differential correction for obscuration (DO).

is:

$$\Phi_{\text{CO}}(M_{1450}) = \frac{\Phi_*}{10^{0.4 * (\alpha_{\text{CO}} + 1)(M - M_*)} + 10^{0.4 * (\beta + 1)(M - M_*)}}, \quad (1)$$

in units of Gpc $^{-3}$  mag $^{-1}$ , where  $\alpha_{\text{CO}} = -1.23$  and  $\beta = -2.73$ ,  $M_* = -24.9$  is the break magnitude, and  $\Phi_* = 5 \times 10.9$  is the normalization corrected for an 80% of obscured sources.

Nevertheless, as mentioned, there could be a trend in the obscured AGN fraction at  $z \sim 6$  to increase at low luminosities, as confirmed by Ueda et al. (2014) for  $z \lesssim 3$ . This would imply that the less luminous sources in the sample adopted by us could have obscured fractions larger than the assumed value of 0.8, which could make our corrected LF conservative at low luminosities. We can account for this effect with a second correction, which we refer to as correction for differential obscuration (DO). Therefore, we consider that 80% of the brightest observed sources, of  $L_{\text{bol}} = 10^{48}$  erg s $^{-1}$ , are obscured and, following the trend derived by Ueda et al. (2014), we then assume that sources three orders of magnitude fainter should be obscured  $\sim 4$  times more often. This yields a second LF,  $\Phi_{\text{DO}}$ , with the same parameters but  $\alpha_{\text{DO}} = -1.76$ .

In Fig. 1, we compare our two LFs, CO and DO, with that originally derived by Matsuoka et al. (2018), and that of Willott et al. (2010a).

For further comparison, we also transformed the magnitude LFs,  $\Phi(M_{1450})$ , to bolometric luminosity using a correction factor of 4.4, as in Willott et al. (2010a) (from Richards et al. 2006). We then transformed this to a black-hole mass function (BHMF,  $\Phi_{\text{BH}}$ ). For this conversion, one must assume an Eddington ratio ( $\lambda_{\text{Edd}} \equiv L_{\text{bol}}/L_{\text{Edd}}$ ). For the sake of consistency, we used observational data taken

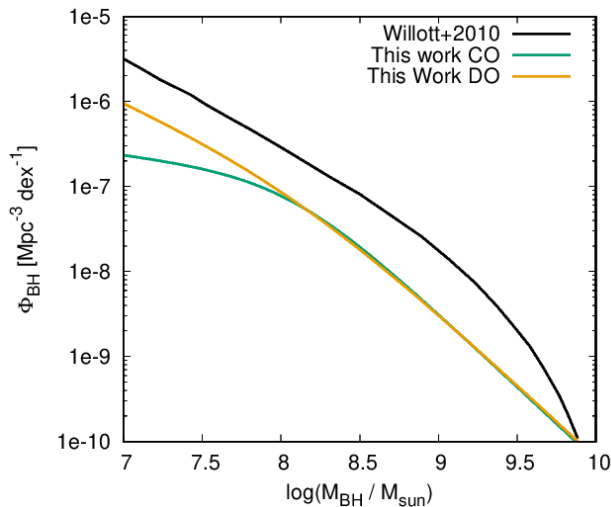


Fig. 2: Black hole mass functions derived from the luminosity functions in Fig. 1, compared to that of Willott et al. (2010a).

from Fig. 3 of Matsuoka et al. (2019), who analyzed the same sample of AGN used to derive our LFs. Using those data, we found an average  $\lambda_{\text{Edd}} = 0.83 \pm 0.12$ , and no significant trend with AGN luminosity or black-hole mass. Averages in all the different luminosity bins taken are compatible, within the errors, with the average value for the whole sample.

In Fig. 2, we compare the BHMFs derived in this work to that of Willott et al. (2010a), used by Bosch-Ramon (2018) to obtain a first estimation of the contribution of AGN jets to reionization. Our BHMFs are lower than that of Willott et al. (2010a), partly due to the fact that we do not account for the presence of quiescent black holes. In this sense, the BHMF from e.g. Willott et al. (2010a) serves as a kind of upper-limit; that is, our BHMFs should not exceed those including quiescent (or weakly accreting) AGN, as they are AGN-BHMFs. Willott et al. (2010a) also used UV data to derive an observational LF, but instead of transforming it into a BHMF, they assumed a Schechter BHMF (hence the noticeably different shape), transformed the BHMF into an LF, and re-fitted it to the data. Other differences arise from small changes on the duty cycle and the assumed value of  $\lambda_{\text{Edd}}$ , and a different correction prescription for obscured sources.

### 3. Ionizing efficiency of jet lobes

The termination regions of AGN jets are expected to inflate lobes on scales  $\sim 100$  kpc, with the lobe pressure potentially dominated by non-thermal electrons. Moreover, the energetics of shocked shells of IGM at  $z \gtrsim 6$  may be dominated by thermal cooling, through free-free continuum and line emission. Due to these factors, a significant fraction of the jet luminosity could be transformed into photons that would ionize, excite and heat the IGM either through direct or indirect (via secondary electrons) interactions (see Bosch-Ramon 2018, and references therein).

We estimated the ionizing power of IC interactions between the relativistic electrons in the lobes, and CMB photons, which are upscattered into H-ionizing photons. We adopted different broad electron energy distributions and assumed a minimum particle energy of  $E_{e,\text{min}} = 1$  MeV. In such a scenario, the energy injected into accelerating electrons in the jet would be turned into ionizing luminosity with an efficiency of  $\approx 30 - 40\%$  for  $p \lesssim 3$  in a (cooled) electron energy distribution  $\propto E^{-p}$  (adopting the energy ratio going to ionization from Shull & van Steenberg 1985). For  $p > 3$ , the efficiency quickly goes down (e.g. 1% for  $p = 4$ ), unless higher values of  $E_{e,\text{min}}$ , even above the minimum electron energy required to produce H-ionizing photons ( $E_{e,\text{min}} \approx 4 \times 10^{-5}$  erg, or a Lorentz factor  $\gamma_{e,\text{min}} \approx 50$ , at  $z \simeq 6$ ), are assumed. If that is the case, then higher efficiencies, of up to  $\sim 40\%$ , can be reached regardless of the value of  $p$ . Note that Wu et al. (2017) adopt  $\gamma_{e,\text{min}} \sim 100$  for their modeling of lobe radio emission in high- $z$  blazars (see sect. 3.2 in Bosch-Ramon 2018).

Bosch-Ramon (2018) described that the shocked IGM shell may be close to radiative. In fact, for a jet lobe suffering strong IC losses, the evolution of the shocked IGM shell formed by a jet with power  $10^{44}$  erg  $\text{s}^{-1}$  (equivalent to a black hole mass  $\simeq 10^6 M_{\odot}$  under our assumptions) would be likely radiative under primordial abundances. A larger, yet relatively small, IGM metallicity, say 1% the solar value, would result in this shell evolution being even more radiative. For such a shocked IGM shell, the expected thermal-to-ionizing luminosity efficiency would be similar to that of IC, as the emission would be likely released in the far UV. However, a proper assessment of the thermal losses of the shocked IGM shell requires a detailed characterization of the jet lobe-IGM interaction (including IC losses), and some knowledge on the medium metallicity.

### 4. Contribution to reionization

The luminosity functions  $\Phi_{CO,DO}(M_{1450})$  can be converted first into functions of luminosity  $L_{1450}$  and then into functions of bolometric luminosity,  $L_{\text{bol}}$ , using the mentioned 4.4 correction factor. We assume that all AGN are jetted, extrapolating the results found by Sbarrato et al. (2015) for the few powerful blazars detected at high redshift at gamma-ray energies. Deviations from this assumption, as well as from the obscured fraction taken in Sect. 2, are included within a parameter  $\epsilon$ . All numerical results presented in this section use an  $\epsilon = 1$ . See a discussion on this assumption in Sect. 5.

It is then necessary to estimate how much energy goes into ionizing radiation as a function of  $L_{\text{bol}}$ . First of all, we must assume a relation between accretion disk luminosity and jet power,  $L_j = \chi L_{\text{bol}}$ . There is evidence of a correlation between the two (e.g. Rawlings & Saunders 1991; Celotti et al. 1997; Ghisellini et al. 2010), and Ghisellini et al. (2014) find that the power of bright relativistic jets tends to be even larger than the luminosity of their accretion disks. We assume a value of  $\chi = 1$ , and again all results on ionizing photon density scale with it.

Following the results from Sect. 3, we assume that a factor  $\xi = 0.3$  of the jet power goes into ionizing radiation, which implies that lobe pressure is dominated by relativistic electrons that can produce H-ionizing photons via IC, and/or the shocked IGM shell is radiative. The H-ionizing

luminosity (comoving) density is then computed as:

$$\dot{\epsilon}_{\text{CO,DO}} = \int \chi \xi \epsilon \Phi_{\text{CO,DO}}(L_{\text{bol}}) L_{\text{bol}} dL_{\text{bol}}. \quad (2)$$

We integrate in the range  $L_{\text{bol}} = 10^{43} - 10^{48}$  erg s<sup>-1</sup>, which corresponds to AGN with black-hole masses in the range  $M_{\text{BH}} \approx 10^5 - 10^{10} M_{\odot}$ . The resulting values are  $\dot{\epsilon}_{\text{CO}} = 4.3 \times 10^{38}$  erg s<sup>-1</sup> Mpc<sup>-3</sup> and  $\dot{\epsilon}_{\text{DO}} = 9.2 \times 10^{38}$  erg s<sup>-1</sup> Mpc<sup>-3</sup>. Considering 13.6 eV per H-ionizing photon, this translates to photon densities of  $\dot{n}_{\text{CO,DO}} = 3.2 \times 10^{49}, 6.8 \times 10^{49}$  s<sup>-1</sup> Mpc<sup>-3</sup>. These results, obtained for  $z = 6$ , can be compared to those derived by Matsuoka et al. (2018) using their LF (uncorrected for absorption), which takes into account only the ionizing photons produced in the accretion disk of the AGN,  $\dot{n}_{\text{disk}} = 6.3 \times 10^{48}$  s<sup>-1</sup> Mpc<sup>-3</sup>.

We can extrapolate our results to higher redshifts. The evolution of the H II volume filling factor in the IGM,  $Q_{\text{HII}}(t)$ , is given by:

$$\frac{dQ_{\text{HII}}}{dt} = \frac{\dot{n}_{\text{ion}}}{\bar{n}_{\text{H}}} - \frac{Q_{\text{HII}}}{\bar{t}_{\text{rec}}}, \quad (3)$$

where  $\bar{n}_{\text{H}}$  and  $\bar{t}_{\text{rec}}$  are the mean hydrogen density and recombination time, respectively (see Madau et al. 1999). To numerically integrate this equation we consider that the IGM is fully neutral at  $z \simeq 15$ , when reionization might have started (Bromm & Yoshida 2011; Dunlop 2013).

The ionizing photon densities necessary to balance recombination (in the ionized IGM, i.e.,  $Q_{\text{HII}} = 1.0$ ) is

$$\dot{n}_{\text{ion}}^{\text{crit}} = 10^{50.0} C_{\text{HII}} \left( \frac{1+z}{7} \right)^3 \text{ s}^{-1} \text{ Mpc}^{-3}, \quad (4)$$

where  $C_{\text{HII}}$  is an effective HII clumping factor (Bolton & Haehnelt 2007), within the range  $C_{\text{HII}} = 1.0 - 5.0$  (Shull et al. 2012). We plotted a comparison between  $\dot{n}_{\text{ion}}^{\text{crit}}$  and our derived  $\dot{n}_{\text{ion}}$  for two cases: assuming  $\dot{n}_{\text{ion}}$  constant with redshift, and assuming it evolves as  $\propto 10^{-0.7z}$  (normalizing using the LF at  $z \sim 6$ ; Matsuoka et al. 2018) in Fig. 3. The figure also includes the evolution of the ionizing photon density generated by star-forming galaxies,  $\dot{n}_{\text{stars}}$  (Robertson et al. 2015); and that generated by AGN disks (Matsuoka et al. 2018). Figure 3 also depicts the evolution of the HII volume filling factor as a function of redshift, including contributions from all the different considered  $\dot{n}_{\text{ion}}$ . The clumping factor used in both plots is  $C_{\text{HII}} = 3.0$ , and varying it in the 1.0 – 5.0 range can lead to relatively small variations (see Matsuoka et al. 2018).

The plot for  $\dot{n}_{\text{ion}}$  shows that star-forming galaxies are enough to fully maintain the IGM ionized at  $z = 6$ . The contribution from AGN disks is likely small, at most of a  $\sim 4\%$ , while AGN jets could contribute with a  $\sim 10\%$  (CO) or  $\sim 20\%$  (DO).

The plot for the  $Q_{\text{HII}}$  evolution shows that, assuming a constant  $\dot{n}_{\text{ion}}$ , the contribution of AGN jets to reionization could be of  $\sim 5\%$  (CO) or  $\sim 10\%$  (DO) at  $z = 6$ , redshift at which the contribution of star-forming galaxies may suffice to fully reionize the IGM. When adopting  $\dot{n}_{\text{ion}}(z) \propto 10^{-0.7z}$ , derived from the  $z$ -evolution of the LF normalization at  $z \lesssim 6$ , one finds that the contribution of AGN to  $Q_{\text{HII}}$  at  $z \sim 6$  would be lower by a factor of  $\sim 3$ .

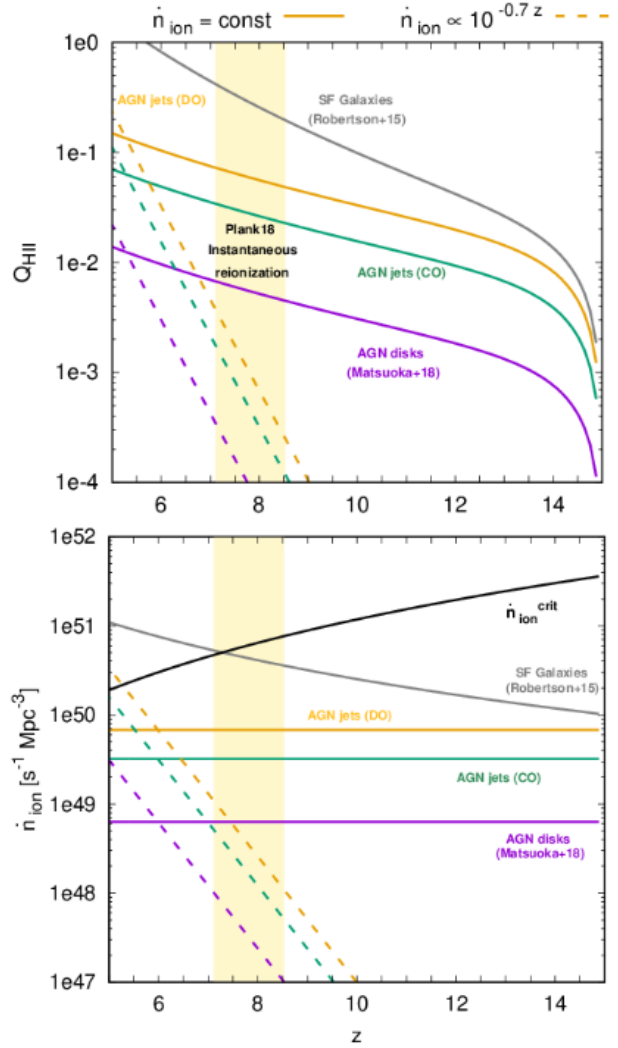


Fig. 3: Evolution of the H II volume filling factor (top) and the ionizing photon density (bottom) as a function of redshift. The plotted contributions are those of AGN disks (Matsuoka et al. 2018), star-forming galaxies (Robertson et al. 2015), and AGN jets (constant obscuration, CO, and differential obscuration, DO), for  $\epsilon = 1$ . The shaded area represents the estimation of the redshift of instantaneous reionization ( $1\sigma$  confidence interval, Planck Collaboration et al. 2018). The solid black line (bottom) represents the critical photon density necessary to keep the IGM ionized.

## 5. Summary and discussion

We have used LFs derived from UV data at  $z \sim 6$  to estimate the contribution of AGN jets to the reionization of the Universe. In order to do this, we have taken the LF of Matsuoka et al. (2018) and corrected it in three different ways to account for the presence of obscured sources. We have considered an obscuration factor constant at all AGN luminosities (CO), fainter sources being more obscured than brighter ones (DO), and an LF with no turnover (NT).

We have estimated that  $\sim 30\%$  of the jet energy of these sources could have turned into ionizing radiation. We have computed the contribution of AGN jet lobes to the ionizing photon density and H II volume filling factor at  $z > 6$ .

### 5.1. Contribution to reionization

The contribution of star-forming galaxies as derived by Robertson et al. (2015) is both dominant and sufficient to reionize the Universe at  $z \simeq 6$ , though this result depends on key assumptions such a large escape fraction of ionizing radiation,  $f_{\text{esc}} \simeq 0.2$ , and the luminosity function extending up to  $M_{\text{UV}} \simeq -13$  (see e.g. Robertson et al. 2015; Stark 2016). Considerable uncertainty remains in the stellar masses of  $z > 6$  galaxies, and there is also the possibility of an accelerated decline in  $\rho_{\text{SFR}}(z > 8)$  (e.g. Oesch et al. 2014), which would reduce their impact on reionization.

The contribution of jets to reionization is difficult to estimate without a precise knowledge of the evolution of the LF normalization at high redshifts (i.e.  $\dot{n}_{\text{ion}}(z)$ ). It might be negligible if one assumes a strong decay with redshift, or it might be as high as  $\gtrsim 10\%$  if it remains constant, the jetted AGN fraction is close to 1 and the fraction of obscured sources is high.

Our results indicate that AGN jet lobes could generate as many as  $\sim 20\%$  of the necessary photons to keep the IGM ionized at  $z = 6$  ( $\dot{n}_{\text{obs}} \sim 7 \times 10^{50} \text{ s}^{-1} \text{ Mpc}^{-3}$ , Madau 2017), well above the  $\sim 4\%$  derived for accretion disks, due to the lack of obscuration effects in the jet lobe scenario.

However, this higher reionization impact requires assuming a number of things. First; either a large relativistic electron pressure in the lobes or radiative shocked IGM shells, or both. Secondly, a jetted AGN fraction of almost 1. And thirdly, that our estimation of the number of obscured sources at  $z \sim 6$  is correct. Again, if these conditions are not met, their contribution becomes negligible.

Asides from this consideration, different approaches to estimate the ionization power of AGN jets can render relatively different results. For instance, using the BHMF derived by Willott et al. (2010a), Bosch-Ramon (2018) derived  $\dot{n}_{\text{ion}} = 1.5 \times 10^{50} \text{ s}^{-1} \text{ Mpc}^{-3}$  in a best-case scenario, a factor of  $\sim 2$  larger than our  $\dot{n}_{\text{DO}}$ . Similarly, considering a higher minimum AGN luminosity (i.e.  $L_{\text{j}} = 10^{45} \text{ erg s}^{-1}$ , equivalent to  $M_{\text{BH}} \simeq 10^7 M_{\odot}$ , which corresponds to the faintest data points in the sample used to derive the LFs) can lead to significant changes. The contribution of both AGN disks and of  $\Phi_{\text{CO}}$  to reionization would vary only in a  $\sim 10\%$ ; and that of  $\Phi_{\text{DO}}$  by a factor of  $\sim 2$ . However, it is unlikely that no AGN of lower luminosities exist, and one must take into account that the contribution of those sources may be significant. Remarkably, changes in  $\alpha$  (in this work,  $\alpha = -1.23, -1.76$ ), the least constrained of the LF parameters, yield very different results.

### 5.2. Jetted fraction and obscured sources

Asides from  $\alpha$ , another important and not fully constrained parameter is the normalization (i.e. total number of sources). The results presented in Sect. 4 all scale linearly with  $\epsilon$ . Our assumption of  $\epsilon = 1$  implies that all AGN at  $z \simeq 6$  are jetted. Sbarrato et al. (2015) analyzed *Swift* data of known  $z > 4$  blazars (i.e. five sources with  $L_{\text{j}} \sim 10^{47} \text{ erg s}^{-1}$ ) and suggested that jetted sources might

be enough to represent all AGN at those redshifts. This conclusion strongly depends on the derived Lorentz factors of the blazars, and the small statistics imply a large uncertainty on the jetted source fraction. Also, whether their results hold for lower luminosity AGN is uncertain.

This  $\epsilon$  should also include possible deviations from the assumed 80% of obscured sources. Whereas Vito et al. (2018) find this value in the  $z = 3 - 6$  range, most of their sources have  $z < 4$ . Maximum obscuration fraction may be expected at  $z \sim 2 - 3$ , at the peak of star-formation in the Universe. Therefore, while Vito et al. (2018) do not observe this trend, a decay of obscuration fraction at  $z \simeq 6$  is possible.

Our results, therefore, all scale with

$$\epsilon = f_{\text{jet}} \left( \frac{1 - f_{\text{obsc}}}{1 - 0.8} \right)^{-1}, \quad (5)$$

where  $f_{\text{jet}}$  and  $f_{\text{obsc}}$  are the jetted and obscured AGN fractions, respectively. If  $\epsilon < 0.2$ , AGN jets would be contributing to reionization less than accretion disks; for example, with  $f_{\text{obsc}} = f_{\text{jet}} = 0.5$ ,  $\epsilon = 0.2$  is already reached.

We note that studies of X-ray binaries show that their jets are produced under certain conditions of accretion (advection dominated), at either very low rates ( $\lambda_{\text{Edd}} \sim 0.1$ ) or very high rates ( $\lambda_{\text{Edd}} \sim 1$ ), and that otherwise disk emission dominates (e.g. Fender et al. 2004). The Eddington ratios of  $z \sim 6$  quasars of Matsuoka et al. (2019) are distributed around the mean value of  $\sim 0.8$ . If the behaviour of SMBH at high- $z$  depended on accretion in a similar manner, the jetted AGN fraction could be low. However, it is unclear whether the behaviour of X-ray binaries can be extrapolated to SMBH at high- $z$ .

We note that the X-ray data of Vito et al. (2018) only extends up to AGN with  $L_{\text{bol}} = 10^{47} \text{ erg s}^{-1}$ , and, despite they do not observe a clear trend with luminosity, assuming  $L_{\text{bol}} = 10^{48} \text{ erg s}^{-1}$  to have an obscured fraction of 0.8 may be an overestimation. However, redoing the calculations excluding the most luminous AGN ( $L_{\text{bol}} = 10^{47} - 10^{48} \text{ erg s}^{-1}$ ) results only in a decrease of  $Q_{\text{HII}}$  of a  $\sim 10\%$  when using  $\Phi_{\text{CO}}$  and a negligible one when using  $\Phi_{\text{DO}}$ .

On another note, the limited sensitivity of the current surveys means that we have no accurate knowledge of the number of low-luminosity AGN at high  $z$ . For instance, intermediate-mass black holes in the center of gas-rich dwarf galaxies may be active at  $z \gtrsim 6$ , as mechanical feedback could shutter both star-formation and AGN activity (e.g. Silk 2017). Also, weakly accreting black holes of any mass could contribute to reionization to some extent, but would pass unnoticed to observations. Finally, the present observational constraints on black-hole past activity (e.g. accreted mass, accretion rate, etc.) do not allow the derivation of strong constraints on the ionizing contribution of AGN jets at very high  $z$  (see Bosch-Ramon 2018, and references therein).

### 5.3. Comparison to AGN accretion

The results shown in Sect. 4 for the contribution of AGN accretion disks to reionization are directly taken from Matsuoka et al. (2018). They do not correct their  $\Phi$  for the presence of obscured sources, as they assume no ionizing radiation can escape them. However, in a jetted source, a

small fraction of ionizing radiation can escape in the direction of the jets (which must be unobscured) and contribute to the ionization of the surrounding medium. This would increase the contribution of disks as

$$\dot{n}_{\text{disk}} = 4(1 + 5\epsilon\rho)\% \quad (6)$$

where  $\rho$  is the escape fraction caused by the drilling of the jets. Setting, for example,  $\rho = 0.1$  and using  $\epsilon = 1$  as done for jets, AGN disks may contribute to  $\dot{n}_{\text{ion}}$  a 6% instead of the 4% mentioned above. This implies that  $\epsilon < 0.2/(1 - \rho)$  makes the contribution of AGN disks more relevant than that of jets, deviating from the minimum  $\epsilon$  given in the previous section if  $\rho$  is large.

#### 5.4. Quenched radio emission

As mentioned in Sect. 2, there is a discrepancy in the LF at different energy bands, with radio LFs, which should account for jetted sources, finding lower densities of AGN at high redshift than those derived at high energies. It is however natural to expect significantly less synchrotron emission with respect to IC emission in the extended jet regions, as the CMB energy density is  $\propto (1+z)^4$ . The reason is that, unless radiation comes from very close to the jet base, synchrotron emission is suppressed at high redshift. This can take place in two different contexts: (i) Non-radiative losses can be dominant (e.g. adiabatic losses due to the jet expansion). Since the photon energy density of the CMB is larger than the energy density of the magnetic field, IC emission can be much brighter than synchrotron emission. To exemplify this, we can consider the particular case of a jet with a total power of  $10^{44}$  erg s $^{-1}$ , a Lorentz factor of 10, Poynting flux equal to a 10% of the matter energy flux, and a half-opening angle of 0.1 rad, at  $z \sim 6$ . In such a case, the synchrotron emission can only overcome the CMB IC luminosity at a distance  $\lesssim 10$  pc from the jet base. The same jet in the local universe could have a synchrotron component brighter than the IC one up to a jet height  $\sim 300$  pc. This effect leads to comparatively stronger IC emission. (ii) IC emission might be so intense that it would dominate over non-radiative losses, with radio electrons losing most of their energy via IC CMB. This effect reduces the radio emission with respect to the case with dominant non-radiative losses. Accounting for these effects, one may easily expect different LF  $z$ -evolutions at different frequencies.

Wu et al. (2017) study this mechanism for radio quenching at  $z > 3$  and conclude that it can efficiently dim the diffuse radio emission from jetted AGN. However, their limited sample does not allow them to confirm whether the mechanism is entirely sufficient to explain the radio-loud AGN deficit at high redshifts.

Finally, it is worth mentioning that, in addition to ionizing the medium, about 10–20% of the energy of jet lobe hard photons may go to heat the IGM at  $z \gtrsim 6$ . An accurate estimate of the level of IGM heating due to jet lobes is beyond the scope of this work, but certainly it should be compatible with the thermal history of the IGM at very high redshift (see, e.g., D’Aloisio et al. 2017; Garaldi et al. 2019).

#### Acknowledgments

We acknowledge support by the Spanish Ministerio de Economía y Competitividad (MINECO/FEDER, UE)

under grant AYA2016-76012-C3-1-P, with partial support by the European Regional Development Fund (ERDF/FEDER), MDM-2014-0369 of ICCUB (Unidad de Excelencia ‘María de Maeztu’), and the Catalan DEC grant 2017 SGR 643. N.T.-A. acknowledges support from MINECO through FPU14/04887 grant.

#### References

- Ajello, M., Costamante, L., Sambruna, R. M., et al. 2009, *ApJ*, 699, 603
- Arons, J. & McCray, R. 1970, *Astrophysical Letters*, 5, 123
- Bolton, J. S. & Haehnelt, M. G. 2007, *MNRAS*, 382, 325
- Bosch-Ramon, V. 2018, *A&A*, 617, L3
- Bromm, V. & Yoshida, N. 2011, *Annual Review of Astronomy and Astrophysics*, 49, 373
- Caccianiga, A., Moretti, A., Belladitta, S., et al. 2019, *MNRAS*, 484, 204
- Celotti, A., Padovani, P., & Ghisellini, G. 1997, *MNRAS*, 286, 415
- Croston, J. H., Ineson, J., & Hardcastle, M. J. 2018, *MNRAS*, 476, 1614
- D’Aloisio, A., Upton Sanderbeck, P. R., McQuinn, M., Trac, H., & Shapiro, P. R. 2017, *MNRAS*, 468, 4691
- Dunlop, J. S. 2013, in *Astrophysics and Space Science Library*, Vol. 396, *The First Galaxies*, ed. T. Wiklind, B. Mobasher, & V. Bromm, 223
- Fan, X., Strauss, M. A., Becker, R. H., et al. 2006, *AJ*, 132, 117
- Fender, R. P., Belloni, T. M., & Gallo, E. 2004, *MNRAS*, 355, 1105
- Garaldi, E., Compostella, M., & Porciani, C. 2019, *MNRAS*, 483, 5301
- Ghisellini, G., Tavecchio, F., Foschini, L., et al. 2010, *MNRAS*, 402, 497
- Ghisellini, G., Tavecchio, F., Maraschi, L., Celotti, A., & Sbarrato, T. 2014, *Nature*, 515, 376
- Grazian, A., Giallongo, E., Boutsia, K., et al. 2018, *A&A*, 613, A44
- Hopkins, P. F., Richards, G. T., & Hernquist, L. 2007, *ApJ*, 654, 731
- Jiang, L., McGreer, I. D., Fan, X., et al. 2016, *ApJ*, 833, 222
- Kakiichi, K., Ellis, R. S., Laporte, N., et al. 2018, *MNRAS*, 479, 43
- Kulkarni, G., Worseck, G., & Hennawi, J. F. 2018, *arXiv e-prints*, arXiv:1807.09774
- Lawrence, A. 1991, *MNRAS*, 252, 586
- Madau, P. 2017, *ApJ*, 851, 50
- Madau, P., Haardt, F., & Rees, M. J. 1999, *ApJ*, 514, 648
- Matsuoka, Y., Onoue, M., Kashikawa, N., et al. 2019, *ApJ*, 872, L2
- Matsuoka, Y., Strauss, M. A., Kashikawa, N., et al. 2018, *ApJ*, 869, 150
- McGreer, I. D., Mesinger, A., & D’Odorico, V. 2015, *MNRAS*, 447, 499
- Meiksin, A. & Madau, P. 1993, *ApJ*, 412, 34
- Oesch, P. A., Bouwens, R. J., Illingworth, G. D., et al. 2014, *ApJ*, 786, 108
- Onoue, M., Kashikawa, N., Willott, C. J., et al. 2017, *ApJ*, 847, L15
- Parsa, S., Dunlop, J. S., & McLure, R. J. 2018, *MNRAS*, 474, 2904
- Pentericci, L., Vanzella, E., Fontana, A., et al. 2014, *ApJ*, 793, 113
- Planck Collaboration, Aghanim, N., Akrami, Y., et al. 2018, *arXiv e-prints*, arXiv:1807.06209
- Rawlings, S. & Saunders, R. 1991, *Nature*, 349, 138
- Richards, G. T., Lacy, M., Storrie-Lombardi, L. J., et al. 2006, *The Astrophysical Journal Supplement Series*, 166, 470
- Robertson, B. E., Ellis, R. S., Furlanetto, S. R., & Dunlop, J. S. 2015, *ApJ*, 802, L19
- Saxena, A., Röttgering, H. J. A., & Rigby, E. E. 2017, *MNRAS*, 469, 4083
- Sbarrato, T., Ghisellini, G., Tagliaferri, G., et al. 2015, *MNRAS*, 446, 2483
- Sbarrato, T., Ghisellini, G., Tagliaferri, G., et al. 2016, *MNRAS*, 462, 1542
- Seiler, J., Hutter, A., Sinha, M., & Croton, D. 2018, *MNRAS*, 480, L33
- Shull, J. M., Harness, A., Trenti, M., & Smith, B. D. 2012, *ApJ*, 747, 100
- Shull, J. M. & van Steenberg, M. E. 1985, *ApJ*, 298, 268
- Silk, J. 2017, *ApJ*, 839, L13
- Simpson, C. 2005, *MNRAS*, 360, 565
- Stark, D. P. 2016, *Annual Review of Astronomy and Astrophysics*, 54, 761
- Steffen, A. T., Barger, A. J., Cowie, L. L., Mushotzky, R. F., & Yang, Y. 2003, *ApJ*, 596, L23
- Tilvi, V., Papovich, C., Finkelstein, S. L., et al. 2014, *ApJ*, 794, 5
- Ueda, Y., Akiyama, M., Hasinger, G., Miyaji, T., & Watson, M. G. 2014, *ApJ*, 786, 104
- Ueda, Y., Akiyama, M., Ohta, K., & Miyaji, T. 2003, *ApJ*, 598, 886
- Vito, F., Brandt, W. N., Yang, G., et al. 2018, *MNRAS*, 473, 2378
- Willott, C. J., Albert, L., Arzoumanian, D., et al. 2010a, *AJ*, 140, 546
- Willott, C. J., Delorme, P., Reylé, C., et al. 2010b, *AJ*, 139, 906
- Wu, J., Ghisellini, G., Hodges-Kluck, E., et al. 2017, *MNRAS*, 468, 109

Part V

SUMMARY OF RESULTS, DISCUSSION AND  
CONCLUSIONS



## SUMMARY, DISCUSSION AND CONCLUSIONS

In this chapter we summarize the results found in the different articles presented in the thesis, as well as the discussion of those results and the reached conclusions. We add to the discussion our prospects for future work.

## 8.1 INFRARED AND X-RAY EMISSION FROM NEARBY LIRGS

In the first part of the thesis we have presented an X-ray analysis of 84 individual galaxies, which are contained within 63 LIRGs of the GOALS sample (CGII). Using *Chandra* data, we have provided arcsecond-resolution images, spectra and radial surface brightness profiles for each object. We have contrasted the derived X-ray properties with IR results obtained through the analysis of *Spitzer* and *Herschel* data. We have also provided a comparison with the IR-brightest U/LIRGs in GOALS (CGI), studied by Iwasawa et al. (2011).

## 8.1.1 AGN detection in the sample

To determine the AGN presence within the sample we have used diagnostic criteria in IR (detection of [Ne v] line, equivalent width of the PAH feature) and X-rays (hardness ratio, detection of Fe K $_{\alpha}$  line, absorption feature).

We have found that the percentage of sources with an AGN in the CGII sample ( $31 \pm 5$  %) is compatible, within the errors, with that found for the CGI sample ( $38 \pm 7$  %). Previous studies have found a significant increase of AGN presence with IR luminosity (e.g. Veilleux et al., 1995; Valiante et al., 2009; Yuan, Kewley, and Sanders, 2010; Alonso-Herrero et al., 2012). We do not recover this result with enough significance, perhaps due to the low statistics of the sample, or because AGN in CGI are efficiently obscured.

We invoke a similar explanation to justify the low percentage of dual AGN in CGI. Simulations by Capelo et al. (2017) and observations by (Koss et al., 2012) indicate that the presence of dual AGN in systems that host at least one AGN is  $\sim 20 - 30\%$ , with an observed 37.1% in major mergers. The fractions we derive for CGI and CGII are  $(11 \pm 10)\%$  and  $(20 \pm 14)\%$ , respectively. While CGII galaxies fall within the expected range, the CGI results are low for a sample in which major mergers predominate.

AGN detection in CGI galaxies could be hindered by obscuration, as IR-brighter sources are expected to have larger quantities of gas

and dust in their inner regions. Another possible explanation is that dual mergers reside in galaxies in which the nuclei are too closely interacting for even *Chandra* to resolve them (and even more so in the case of MIR observations). In the first scenario, future observations with *NuSTAR* (Privon et al., in prep) might find signatures of heavily obscured AGN within the CGI galaxies. In the second scenario, perhaps the angular resolution of JWST (much better than that of *Spitzer* or *Herschel*) will allow for precise IR diagnostics to complement the *Chandra* observations.

Another interesting result, derived from comparison to MIR diagnostics is the high number of X-ray detected AGN which are not energetically significant (contribute to  $< 0.2L_{\text{bol}}$ ) in the sample. 19 out of 32 AGN in the full (CGI+CGII) sample are detected in X-rays and yet completely covered by the starburst emission in IR. This result highlights the potential of X-ray observations for AGN detection in U/LIRGs. Current models of galaxy evolution predominantly assume mergers of galaxies trigger an AGN phase, and there is debate regarding whether they are an essential step in galaxy formation. Therefore, detecting the AGN (even when not energetically dominant) is essential to understand the process of galaxy evolution.

It is possible that the non-dominant AGN detected in these galaxies represent the obscured stage predicted by the evolutionary model of Sanders et al. (1988). Star formation appears to be the dominant source of energy in most of the galaxies, which might imply it quenches itself, perhaps without a significant role of the AGN. The AGN could become more strongly active at a later stage and actively contribute to quenching, or it might just become energetically relevant as a byproduct of the decrease of star formation.

Future work in these aspects will be carried out through analysis of the *NuSTAR* data and, hopefully, through analysis of the 94 systems in GOALS for which *Chandra* data is still unavailable. A contrast between JWST observations and X-ray data is also considered as a future work prospect.

### 8.1.2 IR to X-ray luminosity correlation

We have compared the IR and X-ray luminosities for all sources within the sample. A comparison to an existing correlation, derived by Ranalli, Comastri, and Setti (2003), shows an X-ray faintness in the brightest GOALS galaxies. This effect, already shown by Iwasawa et al. (2011), has generally been attributed to self-obscuration of the starburst (e.g. Lehmer et al., 2010).

We have shown that our spectral model is compatible with obscuration being the cause of the faintness in soft X-rays, as expected.

We estimate that the necessary  $\text{H}_2$  masses to obscure the hard X-ray emission could be of  $\sim 10^{10} - 10^{11} M_{\odot}$  within the inner 500 pc

of the galaxy, in the most extreme cases. While U/LIRGs have large amounts of molecular gas in their nuclei, we want to note that no work individually compares their X-ray faintness to their derived  $\text{H}_2$  masses. Recent  $^{12}\text{CO}$  and  $^{13}\text{CO}$  observations with the IRAM-30m telescope (Herrero-Illana et al. in prep) of 55 GOALS galaxies will provide a sample with which to start this comparison. As future work, we intend to test the self-obscured starburst model using these data. The confirmation or rejection of this hypothesis is particularly interesting, given how alternative explanations may exist for the observed X-ray faintness.

A scenario in which an obscured AGN is responsible for the enhanced IR emission, while remaining undetected in X-rays, was proposed by Iwasawa et al. (2009). Our work shows that most X-ray AGN in the sample are not energetically significant, according to MIR determinations. This scenario, therefore, seems unlikely.

A new hypothesis is the possibility, supported by the work of Díaz-Santos et al. (2017), that the star-forming regions in GOALS galaxies are very young, with not many end-products of stellar evolution (SNRs, X-ray binaries) yet formed. This would imply their reprocessed UV photons could contribute to the IR luminosity, while remaining X-ray faint. Investigating this novel possibility is something we leave for future work.

### 8.1.3 *Soft-band emission*

We have computed radial profiles of the soft X-ray emission for the sources in the sample. We have shown that the characteristic region in which X-ray emission is emitted tends to be similar to the size of the IR emission (although proper comparison would require IR data at a similar resolution to that of *Chandra*). We have also shown that emission tends to be compact, with half the sources in the sample emitting most of their photons in the inner  $\sim 1$  kpc. CGI galaxies have larger soft X-ray radii, which we attribute to an effect of obscuration, or of the greater strength of their winds.

The multiwavelength size comparison also shows sources that deviate strongly from the expected 1:1 relation (e.g. ESO 343-IG013 N, NGC 7592, IRAS F12112+0305). The reason for these deviations is worth investigating in the future, for each individual galaxy. Future JWST observations, with a resolution more similar to that of *Chandra*, will also provide a better comparison for the whole sample.

In order to show the effects of obscuration in soft band we have modeled the spectra in the 0.5 – 2 keV range using a two-phase gas model; with an inner, hotter, obscured component and an external, colder, non-obscured one. We have shown that the model can satisfactorily fit the data, although without being superior to a model with one single phase and an enriched metallicity.

Both effects (multi-phase gas and non-solar metallicity) are expected in the starburst-heated gas of a U/LIRG, and the quality of our data is not enough to allow for a distinction between the two models. As future work, we intend to relate the soft-band emission modeling with the radial profiles in two ranges: 0.5 – 1 keV and 1 – 2 KeV. In this way, we expect to see whether the softer emission (generated by the coldest component of the two-phase model) truly originates in the outer regions of the galaxy.

## 8.2 INTERACTION OF AGN JETS WITH OBSTACLES

In parts II and III of the thesis we have analyzed the interaction of AGN jets with different kinds of obstacles. In our first work, we considered the population of stars always present within the jet, impacting the flow with their stellar winds (which we refer to as "steady-state" interaction), both for star-forming galaxies, and older elliptical galaxies. A second work considered the material that stars accumulate around themselves as they propagate through the ISM (which we refer to as "bubbles"), and is introduced into the jet at the moment stars penetrate it. In our two final works we considered supernova explosions taking place within the jet; core-collapse supernovae in starbursts, and type Ia supernovae in galaxies without significant star formation.

In our analysis we have modeled the populations of stars within the inner regions of both U/LIRGs and elliptical galaxies, in order to characterize their winds, their distribution, and their orbital velocities. We have also estimated supernova rates in these two different types of galaxies, and given predictions regarding the detectability of the events.

We have calculated the dynamical evolution of obstacles within jets using a semi-analytical model, and compared the results to simulations.

We have used a semi-analytical approach to derive the possible non-thermal emission produced in these interactions. We have focused on gamma-ray radiation, but the derived SEDs also show the non-thermal contribution at all wavelengths. Our radiation models are purely leptonic, as these are the most efficient mechanisms at large scales (e.g. Barkov et al., 2012; Barkov, Bosch-Ramon, and Aharonian, 2012; Khangulyan et al., 2013, and also estimations within this thesis). We have also given estimates on the possible dynamical impact of these interactions on the jet.

### 8.2.1 *Non-thermal emission*

The main focus of our work in parts II and III of the thesis has been to determine the relevance of the non-thermal emission produced when stellar populations interact with extragalactic jets in different ways.

Non-thermal emission can be produced through all the mechanisms studied (steady-state, bubbles, and SN explosions), although with different characteristics.

Steady-state emission is moderately faint for the populations and sources modelled in Ch. 3, although for starburst galaxies (if magnetic fields are below equipartition) emission is close to the detectability threshold for CTA. Given how the number of high-mass stars within the jet (see Sect. 8.2.5) and the fraction of energy converted into non-thermal radiation ( $\eta$  in our works) are not well-known, it is possible that some sources could produce detectable emission. For M 87, our modeled radio galaxy, gamma-ray emission is two orders of magnitude below the emission detected by MAGIC. For an equipartition magnetic field, the predicted X-ray emission is comparable to that of knot A (the brightest); but this is likely to be an overestimation, since these intense X-rays are observed only in the knots (and steady-state emission would be diffuse throughout the whole jet).

In this first work, when boosting the observed radiation to account for relativistic effects, we used a Doppler factor of  $\delta^4$  (Eq. 27 in Ch. 3). In fact, it should have been  $\delta^3/\Gamma$ , as explained in Ch. 4 (Eq. 12) and in Sikora et al. (1997). The difference between the two mentioned equations is of a factor  $\sim \Gamma^2$  for small viewing angles, which could imply a large overestimation of the SEDs shown in Ch. 3. However, we have realized that there is a simpler way to estimate the energy available for particle acceleration. In the first work, we estimated the effective area of interaction between the jet and the stars,  $\langle S_s/S_j \rangle$ , as the energy intercepted by the shock is proportional to this quantity. This approach is based on the extrapolation of small-scale simulations performed by de la Cita et al., 2016. However, we could have used the same approach as adopted for wind bubbles, and assume that the non-thermal energy is proportional to the total amount of matter injected into the jet by the stellar winds,  $\Gamma\dot{M}c^2$ . This is true as long as the shocked wind reaches the jet velocity, as assumed in that work. This approach does not rely on as many parameters (and is therefore less error-inducing), and combining it with the correct Doppler boosting, it yields results very similar to those presented in Ch. 3. The conclusions derived there are, therefore, valid.

The case of bubbles introduced by stellar penetration into the jet is slightly different. Due to the high velocity of their winds, OB stars in starburst galaxies do not introduce a significant amount of material within the jets. The emission associated to this phenomenon can therefore be relevant only in elliptical galaxies, which have slow-wind

stars. Gamma-ray emission from this interaction is likely to be detectable only through synchrotron emission at  $\sim 100$  MeV, which implies an efficient acceleration rate of the emitting electrons ( $\epsilon \geq 0.1$ ). Observational results from blazar studies, and the results derived by ourselves in Ch. 6, seem to favour much lower efficiencies (although it does not imply this is necessarily the case in all scenarios). Whether the emission is likely to be persistent or characterized by bright, infrequent events depends solely on the value of the magnetic fields (with lower fields implying slower losses, and therefore longer, steady radiation). This interaction could, however, be relevant at X-ray wavelengths, which are certainly emitted through synchrotron, even for low efficiencies. IC emission is only expected to be detectable if more massive bubbles, of younger red giants, penetrated the jet (see also Sect. 8.2.5).

We note that the steady-state emission in elliptical blazars shown in Ch. 4 was computed using the  $\langle S_s/S_j \rangle$  approach, although with the correct Doppler boosting. Therefore, it is likely underestimated by a factor of a few times  $\Gamma$ . Therefore, it is much more relevant than initially discussed in Ch. 4, and likely to eclipse the bubble-associated emission unless a particularly massive one penetrated the jet.

Supernova explosions within jets are much more infrequent than the previously discussed interactions, but likely to contribute to the non-thermal emission in a significant manner once they occur inside the jet. For galaxies with intense star formation, the emission can be easily detectable at gamma-rays both for radio-galaxies, and for blazars at  $z \sim 1$  (the latter with Fermi and CTA, but not with current Cherenkov arrays). In the case of elliptical galaxies, the interaction is less bright, as it frequently occurs further downstream of the jet, and the mass expelled by type Ia supernovae is also smaller than that of core-collapse supernovae. However, our estimations show that as long as jet Lorentz factors are high enough, tens of cases could be detected by CTA. The SNR events would last for thousands of years, given the slow evolution of the remnant, which brings the duty cycles of this interaction up to a few percent.

### 8.2.2 *Observational distinctions between scenarios*

As discussed in Ch. 6, distinguishing between a particularly massive star interacting with a jet in steady-state and a massive cloud (either a bubble or a SNR) is not easy with the current observational limitations.

For nearby sources, X-ray and radio imaging resolutions might be enough to disentangle morphological signatures of the emission. Unlike stellar populations or wind bubbles, a SNR is expected to cover the jet section for the majority of its interaction with the jet, which al-

lows to rule out single bright knots with a too-small section in nearby radio-galaxies.

Both wind bubbles and SNR are expected to move downstream of the jet, while a star (or group of stars) within the jet would cross it roughly horizontally. The crossing time can be of the order of thousands of years, which means that they would appear as stationary knots in observations. A wind bubble (say, of  $\sim 10^{-6} M_{\odot}$ ) would be accelerated quickly enough to appreciate, in timescales of years, its movement. A SNR, however, is slowly accelerated within the jet for thousands of years, which makes the detection of proper motion hardly possible.

For blazar sources at large distances the distinction between scenarios is further complicated by the lack of resolution. With only the detection of the non-thermal SED, a scenario of strong steady-state emission cannot be distinguished from the presence of a supernova remnant within the jet. A wind bubble could be differentiated, in principle, if massive enough to overshadow the steady-state emission (or the contribution of other wind bubbles), as the emission of the former is expected to fade after a few years.

Distinguishing between emissions would be possible, in principle, from SED fitting in galaxies for which the stellar populations and radiation and magnetic fields were very well determined. Again, this is only possible for nearby sources.

### 8.2.3 Usability of simplified models

One of the important results of this thesis is how it establishes the usability of simplified models to describe phenomena that have a high computational cost if calculated accurately.

Throughout the works in this thesis, we have approximated both the IC and synchrotron gamma-ray emission as if emitted only by electrons of the energy at which emission is strongest. This estimation can give an order-of-magnitude idea of the overall detectability of the emission, while being computationally cost-efficient. However, this approach results in an overestimation of the emission. We show for different scenarios how the accurately-computed IC lightcurve is only a factor of  $\sim 10 - 1$  lower than the simple estimation. In Ch. 5 and 6 we plot these differences, and show that they are very small both for non-blazar sources and for powerful elliptical blazars.

The approximation should be used with more caution when trying to gauge the synchrotron emission. As it generally spans a wide range of frequencies, there is not a narrow peak of emission in the SED, which translates into a larger part of the radiation being emitted at lower wavelengths than those of interest. Also, one should remember that it is unknown whether gamma-ray energies can be reached

through synchrotron processes (since the acceleration efficiency is generally unconstrained, and may be too low).

The simplified model is useful when calculating the emission of multiple, evolving obstacles (as done in Ch. 4), which would be very costly to compute accurately.

Another semi-analytical approximation used in the work is the model for the dynamical evolution of clouds within the jet (from Barkov et al., 2012). In Ch. 4 and 5 we have compared it with results of simulations and concluded that it correctly describes the evolution, although it slightly overestimates the final radius of the bubble and the speed of the acceleration. These effects are increasingly important with larger cloud masses.

Future work in this aspect will include dynamical simulations of the described scenarios, with particular attention to the initial and final stages of the evolution of the clouds within the jet, and their possible dynamical impact (particularly in the case of SNR).

#### 8.2.4 *Jet mass-loading*

The jet is expected to be dynamically affected if enough material can be introduced in it. As estimated in Ch. 3, it is likely that the populations of stars expected to be present within the jets of elliptical galaxies are enough to slow them down on kiloparsec scales. A proper study of this mass-loading, using the population models in this thesis, will be carried out as future work.

From our simple estimations, we are confident to say that wind bubbles from penetrating stars are unlikely to affect the jet dynamically through the loaded mass. It is possible, however, that their repeated and frequent impacts help develop instabilities in the shear layer, which could facilitate the entrainment of external material. This is difficult to ascertain without the use of simulations.

Finally, supernovae explosions within the jet are expected to eventually affect it dynamically. The simulations shown in Ch. 5 do not extend until such large times, but a detailed study of the final stages of the interaction is a future work worth carrying out.

#### 8.2.5 *Modeling of stellar populations*

An accurate modelling of the stellar populations within the galaxy is necessary in order to make accurate predictions of the expected non-thermal emission.

In this thesis, we have used prescriptions which are not strongly dependent on the characteristics of one single source. In this way, our estimations allow us to predict whether the interaction could be relevant, regardless of particular source morphologies. Comparisons

with specific sources should take into account a variety of details that we have left out of our models.

In starburst galaxies, we have imposed star formation in the shape of a disk that overlaps with the jet near its base. It is well known, however, that star formation in U/LIRG disks may be clumpy (e.g. Wilman, Edge, and Johnstone, 2005), or even have the shape of a ring surrounding the central engine (e.g. Xu et al., 2015). It is also possible that the jet or AGN winds quench star formation near the centre (e.g. Dubois et al., 2013; Naab and Ostriker, 2017), resulting in the mentioned ring configurations. Other works suggest that the launching of the jet may induce star-formation instead of quenching it, although most likely emptying the central regions of gas (e.g. Gaibler et al., 2012). The process of jet launching, however, seems to temporarily increase star formation in the nucleus; and the timescales of gas depletion are of a few Myr. There is, therefore, possibilities for this interaction to occur in star-forming galaxies.

It is also possible that massive clusters formed in a knotty area within the ring enter the jet due to their orbital motions. As mentioned in Ch. 3, a number of massive stars (i.e.  $M \gtrsim 40 M_{\odot}$ ) of the order of 10 is enough to produce significant non-thermal emission. Wykes et al. (2015) studied the stellar populations of Centaurs A, and found a star-formation region possibly intersecting the jet. They reached the conclusion that their emission is likely significant.

In elliptical galaxies, the main challenge is determining the ages of the populations of red giants (which determines their mass). In our works, we assumed all stars formed when the galaxy was formed; but this is unlikely. Since galaxies are expected to form after undergoing mergers and bursts of star formation, different populations of stars are expected to coexist in them. "Younger" red giants are more massive, and are expected to have heavier winds. However, due to the known shape of the initial mass function, they are also expected to be less numerous. We expect these younger populations to result in more infrequent, yet brighter events (both for steady-state and bubble interaction), dominating flaring over the persistent emission.

In order to properly estimate the exact characteristics of the emission in a source, one needs a better knowledge of the geometry and the star-formation history of the galaxy. Such precise studies are only possible for nearby galaxies. We expect that, with future observations, we will be able to apply the already developed tools to predict the non-thermal emission in nearby sources.

### 8.3 AGN JETS AS REIONIZATION SOURCES

In part IV of the thesis we have estimated the impact of AGN jets in the reionization of the universe. We have assumed a significant fraction of AGN could be jetted at high redshift. Since the jets are

not covered by large column densities of obscuring material, their emission can escape and interact with the IGM. Then, through IC upscattering of CMB photons (much denser at high redshifts), they could significantly contribute to the production of ionizing radiation.

We have used the AGN LF based on the latest rest-UV data at  $z \sim 6$  and corrected them for the effects of obscuration. With an obscuration fraction of  $f_{\text{obsc}} \sim 0.8$  (Vito et al., 2018) and a jetted fraction of  $f_{\text{jet}} \sim 1$  (Sbarrato et al., 2015), jets could contribute up to a  $\sim 10\%$  to the H II volume filling factor at  $z \sim 6$ .

The data of Vito et al. (2018), however, mostly includes sources in the range  $z = 3 - 4$ . The obscuration fraction could be lower at higher redshifts, but not enough sources have been detected this far to make accurate predictions. Recently, Vito et al. (2019) reported the discovery of the first heavily obscured quasar at  $z > 6$ . The source is part of the program to observe ten  $z > 6$  quasars (Vito et al. in prep), which might offer better constraints on the evolution of obscuration fraction with redshift once it is published.

Whether all (or most) AGN are jetted at high redshift is also not well constrained. Sbarrato et al. (2015) suggest that this might be the case, although their sample is small and contains mostly very bright sources. Our predictions of jet impact on reionization scale as  $\epsilon = f_{\text{jet}} \times 0.2 / (1 - f_{\text{obsc}})$ . Once future observations allow us to better constrain both  $f_{\text{jet}}$  and  $f_{\text{obsc}}$ , our results could be easily used to give an accurate estimation of the importance of jets as reionization sources.

## BIBLIOGRAPHY

---

- Abdo, A. A. et al. (2010). “The Spectral Energy Distribution of Fermi Bright Blazars.” In: *ApJ* 716.1, pp. 30–70. DOI: [10.1088/0004-637X/716/1/30](https://doi.org/10.1088/0004-637X/716/1/30). arXiv: [0912.2040](https://arxiv.org/abs/0912.2040) [astro-ph.CO].
- Acero, F. et al. (2009). “Detection of Gamma Rays from a Starburst Galaxy.” In: *Science* 326.5956, p. 1080. DOI: [10.1126/science.1178826](https://doi.org/10.1126/science.1178826). arXiv: [0909.4651](https://arxiv.org/abs/0909.4651) [astro-ph.HE].
- Aharonian, F. A. (2000). “TeV gamma rays from BL Lac objects due to synchrotron radiation of extremely high energy protons.” In: *New Astronomy* 5.7, pp. 377–395. DOI: [10.1016/S1384-1076\(00\)00039-7](https://doi.org/10.1016/S1384-1076(00)00039-7). arXiv: [astro-ph/0003159](https://arxiv.org/abs/astro-ph/0003159) [astro-ph].
- Alonso-Herrero, Almudena et al. (2012). “Local Luminous Infrared Galaxies. II. Active Galactic Nucleus Activity from Spitzer/Infrared Spectrograph Spectra.” In: *ApJ* 744.1, 2, p. 2. DOI: [10.1088/0004-637X/744/1/2](https://doi.org/10.1088/0004-637X/744/1/2). arXiv: [1109.1372](https://arxiv.org/abs/1109.1372) [astro-ph.CO].
- Antonucci, R. R. J. and J. S. Miller (1985). “Spectropolarimetry and the nature of NGC 1068.” In: *ApJ* 297, pp. 621–632. DOI: [10.1086/163559](https://doi.org/10.1086/163559).
- Antonucci, Robert (1993). “Unified models for active galactic nuclei and quasars.” In: *ARA&A* 31, pp. 473–521. DOI: [10.1146/annurev.aa.31.090193.002353](https://doi.org/10.1146/annurev.aa.31.090193.002353).
- Araudo, A. T., V. Bosch-Ramon, and G. E. Romero (2010). “Gamma rays from cloud penetration at the base of AGN jets.” In: *A&A* 522, A97, A97. DOI: [10.1051/0004-6361/201014660](https://doi.org/10.1051/0004-6361/201014660). arXiv: [1007.2199](https://arxiv.org/abs/1007.2199) [astro-ph.HE].
- (2013). “Gamma-ray emission from massive stars interacting with active galactic nuclei jets.” In: *MNRAS* 436.4, pp. 3626–3639. DOI: [10.1093/mnras/stt1840](https://doi.org/10.1093/mnras/stt1840). arXiv: [1309.7114](https://arxiv.org/abs/1309.7114) [astro-ph.HE].
- Barkov, M. V. et al. (2012). “Rapid TeV Variability in Blazars as a Result of Jet-Star Interaction.” In: *ApJ* 749.2, 119, p. 119. DOI: [10.1088/0004-637X/749/2/119](https://doi.org/10.1088/0004-637X/749/2/119). arXiv: [1012.1787](https://arxiv.org/abs/1012.1787) [astro-ph.HE].
- Barkov, Maxim V., Felix A. Aharonian, and Valentí Bosch-Ramon (2010). “Gamma-ray Flares from Red Giant/Jet Interactions in Active Galactic Nuclei.” In: *ApJ* 724.2, pp. 1517–1523. DOI: [10.1088/0004-637X/724/2/1517](https://doi.org/10.1088/0004-637X/724/2/1517). arXiv: [1005.5252](https://arxiv.org/abs/1005.5252) [astro-ph.HE].
- Barkov, Maxim V., Valentí Bosch-Ramon, and Felix A. Aharonian (2012). “Interpretation of the Flares of M87 at TeV Energies in the Cloud-Jet Interaction Scenario.” In: *ApJ* 755.2, 170, p. 170. DOI: [10.1088/0004-637X/755/2/170](https://doi.org/10.1088/0004-637X/755/2/170). arXiv: [1202.5907](https://arxiv.org/abs/1202.5907) [astro-ph.HE].
- Bednarek, W. and R. J. Protheroe (1997). “Gamma-rays from interactions of stars with active galactic nucleus jets.” In: *MNRAS* 287.3,

- pp. L9–L13. DOI: [10.1093/mnras/287.3.L9](https://doi.org/10.1093/mnras/287.3.L9). arXiv: [astro-ph/9612073](https://arxiv.org/abs/astro-ph/9612073) [astro-ph].
- Bell, A. R. (1978). “The acceleration of cosmic rays in shock fronts - I.” In: *MNRAS* 182, pp. 147–156. DOI: [10.1093/mnras/182.2.147](https://doi.org/10.1093/mnras/182.2.147).
- Bicknell, G. V. (1984). “A model for the surface brightness of a turbulent low mach number jet. I. Theoretical development and application to 3C 31.” In: *ApJ* 286, pp. 68–87. DOI: [10.1086/162577](https://doi.org/10.1086/162577).
- Blandford, R. D. and A. Koenigl (1979). “A Model for the Knots in the M87 Jet.” In: *Astrophysical Letters* 20, p. 15.
- Blandford, R. D. and D. G. Payne (1982). “Hydromagnetic flows from accretion disks and the production of radio jets.” In: *MNRAS* 199, pp. 883–903. DOI: [10.1093/mnras/199.4.883](https://doi.org/10.1093/mnras/199.4.883).
- Blandford, R. D. and R. L. Znajek (1977). “Electromagnetic extraction of energy from Kerr black holes.” In: *MNRAS* 179, pp. 433–456. DOI: [10.1093/mnras/179.3.433](https://doi.org/10.1093/mnras/179.3.433).
- Blandford, Roger and David Eichler (1987). “Particle acceleration at astrophysical shocks: A theory of cosmic ray origin.” In: *Physics Reports* 154.1, pp. 1–75. DOI: [10.1016/0370-1573\(87\)90134-7](https://doi.org/10.1016/0370-1573(87)90134-7).
- Bosch-Ramon, V. (2015). “Non-thermal emission from standing relativistic shocks: an application to red giant winds interacting with AGN jets.” In: *A&A* 575, A109, A109. DOI: [10.1051/0004-6361/201425208](https://doi.org/10.1051/0004-6361/201425208). arXiv: [1501.03118](https://arxiv.org/abs/1501.03118) [astro-ph.HE].
- Böttcher, M. et al. (2013). “Leptonic and Hadronic Modeling of Fermi-detected Blazars.” In: *ApJ* 768.1, 54, p. 54. DOI: [10.1088/0004-637X/768/1/54](https://doi.org/10.1088/0004-637X/768/1/54). arXiv: [1304.0605](https://arxiv.org/abs/1304.0605) [astro-ph.HE].
- Bowman, M., J. P. Leahy, and S. S. Komissarov (1996). “The deceleration of relativistic jets by entrainment.” In: *MNRAS* 279, p. 899. DOI: [10.1093/mnras/279.3.899](https://doi.org/10.1093/mnras/279.3.899).
- Bressan, A., L. Silva, and G. L. Granato (2002). “Far infrared and radio emission in dusty starburst galaxies.” In: *A&A* 392, pp. 377–391. DOI: [10.1051/0004-6361:20020960](https://doi.org/10.1051/0004-6361:20020960). arXiv: [astro-ph/0206029](https://arxiv.org/abs/astro-ph/0206029) [astro-ph].
- Burbidge, G. R. (1956). “On Synchrotron Radiation from Messier 87.” In: *ApJ* 124, p. 416. DOI: [10.1086/146237](https://doi.org/10.1086/146237).
- Capelo, Pedro R. et al. (2017). “A survey of dual active galactic nuclei in simulations of galaxy mergers: frequency and properties.” In: *MNRAS* 469.4, pp. 4437–4454. DOI: [10.1093/mnras/stx1067](https://doi.org/10.1093/mnras/stx1067). arXiv: [1611.09244](https://arxiv.org/abs/1611.09244) [astro-ph.GA].
- Cappi, M. et al. (1999). “Diffuse thermal emission from very hot gas in starburst galaxies.” In: *A&A* 350, pp. 777–790. arXiv: [astro-ph/9908312](https://arxiv.org/abs/astro-ph/9908312) [astro-ph].
- Condon, J. J. (1992). “Radio emission from normal galaxies.” In: *ARA&A* 30, pp. 575–611. DOI: [10.1146/annurev.aa.30.090192.003043](https://doi.org/10.1146/annurev.aa.30.090192.003043).
- Curtis, H. D. (1918). “Descriptions of 762 Nebulae and Clusters Photographed with the Crossley Reflector.” In: *Publications of Lick Observatory* 13, pp. 9–42.

- Dar, Arnon and Ari Laor (1997). "Hadronic Production of TeV Gamma-Ray Flares from Blazars." In: *ApJ* 478.1, pp. L5–L8. DOI: [10.1086/310544](https://doi.org/10.1086/310544). arXiv: [astro-ph/9610252](https://arxiv.org/abs/astro-ph/9610252) [astro-ph].
- De Young, D. S. (1986). "Mass Entrainment in Astrophysical Jets." In: *ApJ* 307, p. 62. DOI: [10.1086/164393](https://doi.org/10.1086/164393).
- De Young, David S. (1993). "On the Relation between Fanaroff-Riley Types I and II Radio Galaxies." In: *ApJ* 405, p. L13. DOI: [10.1086/186754](https://doi.org/10.1086/186754).
- Di Matteo, Tiziana, Volker Springel, and Lars Hernquist (2005). "Energy input from quasars regulates the growth and activity of black holes and their host galaxies." In: *Nature* 433.7026, pp. 604–607. DOI: [10.1038/nature03335](https://doi.org/10.1038/nature03335). arXiv: [astro-ph/0502199](https://arxiv.org/abs/astro-ph/0502199) [astro-ph].
- Díaz-Santos, T. et al. (2017). "A Herschel/PACS Far-infrared Line Emission Survey of Local Luminous Infrared Galaxies." In: *ApJ* 846.1, 32, p. 32. DOI: [10.3847/1538-4357/aa81d7](https://doi.org/10.3847/1538-4357/aa81d7). arXiv: [1705.04326](https://arxiv.org/abs/1705.04326) [astro-ph.GA].
- Díaz Trigo, María et al. (2013). "Baryons in the relativistic jets of the stellar-mass black-hole candidate 4U1630-47." In: *Nature* 504.7479, pp. 260–262. DOI: [10.1038/nature12672](https://doi.org/10.1038/nature12672). arXiv: [1311.5080](https://arxiv.org/abs/1311.5080) [astro-ph.HE].
- Dubois, Yohan et al. (2013). "AGN-driven quenching of star formation: morphological and dynamical implications for early-type galaxies." In: *MNRAS* 433.4, pp. 3297–3313. DOI: [10.1093/mnras/stt997](https://doi.org/10.1093/mnras/stt997). arXiv: [1301.3092](https://arxiv.org/abs/1301.3092) [astro-ph.CO].
- Ebisawa, Ken et al. (1994). "Spectral Evolution of the Bright X-Ray Nova GS 1124-68 (Nova MUSCAE 1991) Observed with GINGA." In: *PASJ* 46, pp. 375–394.
- Efstathiou, A. and M. Rowan-Robinson (1995). "Dusty discs in active galactic nuclei." In: *MNRAS* 273.3, pp. 649–661. DOI: [10.1093/mnras/273.3.649](https://doi.org/10.1093/mnras/273.3.649).
- Fabian, A. C. (2012). "Observational Evidence of Active Galactic Nuclei Feedback." In: *ARA&A* 50, pp. 455–489. DOI: [10.1146/annurev-astro-081811-125521](https://doi.org/10.1146/annurev-astro-081811-125521). arXiv: [1204.4114](https://arxiv.org/abs/1204.4114) [astro-ph.CO].
- Fabian, A. C. et al. (2009). "Broad line emission from iron K- and L-shell transitions in the active galaxy 1H0707-495." In: *Nature* 459.7246, pp. 540–542. DOI: [10.1038/nature08007](https://doi.org/10.1038/nature08007).
- Fanaroff, B. L. and J. M. Riley (1974). "The morphology of extragalactic radio sources of high and low luminosity." In: *MNRAS* 167, 31P–36P. DOI: [10.1093/mnras/167.1.31P](https://doi.org/10.1093/mnras/167.1.31P).
- Gaibler, V. et al. (2012). "Jet-induced star formation in gas-rich galaxies." In: *MNRAS* 425.1, pp. 438–449. DOI: [10.1111/j.1365-2966.2012.21479.x](https://doi.org/10.1111/j.1365-2966.2012.21479.x). arXiv: [1111.4478](https://arxiv.org/abs/1111.4478) [astro-ph.CO].
- Gandhi, P. (2005). "X-ray studies of active galactic nuclei." In: *Asian Journal of Physics* 13, pp. 90–107.
- George, I. M. and A. C. Fabian (1991). "X-ray reflection from cold matter in Active Galactic Nuclei and X-ray binaries." In: *MNRAS* 249, p. 352. DOI: [10.1093/mnras/249.2.352](https://doi.org/10.1093/mnras/249.2.352).

- Ghisellini, G. et al. (2017). "The Fermi blazar sequence." In: *MNRAS* 469.1, pp. 255–266. DOI: [10.1093/mnras/stx806](https://doi.org/10.1093/mnras/stx806). arXiv: [1702.02571](https://arxiv.org/abs/1702.02571) [astro-ph.HE].
- Greenstein, Jesse L. (1963). "Red-Shift of the Unusual Radio Source: 3C 48." In: *Nature* 197.4872, pp. 1041–1042. DOI: [10.1038/1971041a0](https://doi.org/10.1038/1971041a0).
- Hardcastle, M. J. et al. (2003). "Radio and X-Ray Observations of the Jet in Centaurus A." In: *ApJ* 593.1, pp. 169–183. DOI: [10.1086/376519](https://doi.org/10.1086/376519). arXiv: [astro-ph/0304443](https://arxiv.org/abs/astro-ph/0304443) [astro-ph].
- Harrison, Christopher (2014). "Observational constraints on the influence of active galactic nuclei on the evolution of galaxies." PhD thesis. Durham University.
- Harwit, M. and F. Pacini (1975). "Infrared galaxies: evolutionary stages of massive star formation." In: *ApJ* 200, pp. L127–L129. DOI: [10.1086/181913](https://doi.org/10.1086/181913).
- Hopkins, Philip F., Eliot Quataert, and Norman Murray (2012). "Stellar feedback in galaxies and the origin of galaxy-scale winds." In: *MNRAS* 421.4, pp. 3522–3537. DOI: [10.1111/j.1365-2966.2012.20593.x](https://doi.org/10.1111/j.1365-2966.2012.20593.x). arXiv: [1110.4638](https://arxiv.org/abs/1110.4638) [astro-ph.CO].
- Hopkins, Philip F. et al. (2005). "Black Holes in Galaxy Mergers: Evolution of Quasars." In: *ApJ* 630.2, pp. 705–715. DOI: [10.1086/432438](https://doi.org/10.1086/432438). arXiv: [astro-ph/0504190](https://arxiv.org/abs/astro-ph/0504190) [astro-ph].
- Hopkins, Philip F. et al. (2009). "Compact high-redshift galaxies are the cores of the most massive present-day spheroids." In: *MNRAS* 398.2, pp. 898–910. DOI: [10.1111/j.1365-2966.2009.15062.x](https://doi.org/10.1111/j.1365-2966.2009.15062.x). arXiv: [0903.2479](https://arxiv.org/abs/0903.2479) [astro-ph.CO].
- Ishibashi, W. and A. C. Fabian (2016). "AGN-starburst evolutionary connection: a physical interpretation based on radiative feedback." In: *MNRAS* 463.2, pp. 1291–1296. DOI: [10.1093/mnras/stw2063](https://doi.org/10.1093/mnras/stw2063). arXiv: [1609.08963](https://arxiv.org/abs/1609.08963) [astro-ph.GA].
- Iwasawa, K. et al. (2009). "High-Ionization Fe K Emission From Luminous Infrared Galaxies." In: *ApJ* 695.1, pp. L103–L106. DOI: [10.1088/0004-637X/695/1/L103](https://doi.org/10.1088/0004-637X/695/1/L103). arXiv: [0903.1503](https://arxiv.org/abs/0903.1503) [astro-ph.GA].
- Iwasawa, K. et al. (2011). "C-GOALS: Chandra observations of a complete sample of luminous infrared galaxies from the IRAS Revised Bright Galaxy Survey." In: *A&A* 529, A106, A106. DOI: [10.1051/0004-6361/201015264](https://doi.org/10.1051/0004-6361/201015264). arXiv: [1103.2755](https://arxiv.org/abs/1103.2755) [astro-ph.CO].
- Khangulyan, D. V. et al. (2013). "Star-Jet Interactions and Gamma-Ray Outbursts from 3C454.3." In: *ApJ* 774.2, 113, p. 113. DOI: [10.1088/0004-637X/774/2/113](https://doi.org/10.1088/0004-637X/774/2/113). arXiv: [1305.5117](https://arxiv.org/abs/1305.5117) [astro-ph.HE].
- Komissarov, S. S. (1994). "Mass-Loaded Relativistic Jets." In: *MNRAS* 269, p. 394. DOI: [10.1093/mnras/269.2.394](https://doi.org/10.1093/mnras/269.2.394).
- Kormendy, John et al. (2009). "Structure and Formation of Elliptical and Spheroidal Galaxies." In: *ApJS* 182.1, pp. 216–309. DOI: [10.1088/0067-0049/182/1/216](https://doi.org/10.1088/0067-0049/182/1/216). arXiv: [0810.1681](https://arxiv.org/abs/0810.1681) [astro-ph].

- Koss, Michael et al. (2012). "Understanding Dual Active Galactic Nucleus Activation in the nearby Universe." In: *ApJ* 746.2, L22, p. L22. DOI: [10.1088/2041-8205/746/2/L22](https://doi.org/10.1088/2041-8205/746/2/L22). arXiv: [1201.2944](https://arxiv.org/abs/1201.2944) [astro-ph.HE].
- Laing, R. A. and A. H. Bridle (2002). "Dynamical models for jet deceleration in the radio galaxy 3C 31." In: *MNRAS* 336.4, pp. 1161–1180. DOI: [10.1046/j.1365-8711.2002.05873.x](https://doi.org/10.1046/j.1365-8711.2002.05873.x). arXiv: [astro-ph/0207427](https://arxiv.org/abs/astro-ph/0207427) [astro-ph].
- Laor, Ari and Ehud Behar (2008). "On the origin of radio emission in radio-quiet quasars." In: *MNRAS* 390.2, pp. 847–862. DOI: [10.1111/j.1365-2966.2008.13806.x](https://doi.org/10.1111/j.1365-2966.2008.13806.x). arXiv: [0808.0637](https://arxiv.org/abs/0808.0637) [astro-ph].
- Laurent, O. et al. (2000). "Mid-infrared diagnostics to distinguish AGNs from starbursts." In: *A&A* 359, pp. 887–899. arXiv: [astro-ph/0005376](https://arxiv.org/abs/astro-ph/0005376) [astro-ph].
- Lehmer, B. D. et al. (2010). "A Chandra Perspective on Galaxy-wide X-ray Binary Emission and its Correlation with Star Formation Rate and Stellar Mass: New Results from Luminous Infrared Galaxies." In: *ApJ* 724.1, pp. 559–571. DOI: [10.1088/0004-637X/724/1/559](https://doi.org/10.1088/0004-637X/724/1/559). arXiv: [1009.3943](https://arxiv.org/abs/1009.3943) [astro-ph.CO].
- Liang, E. P. T. (1979). "On the hard X-ray emission mechanism of active galactic nuclei sources." In: *ApJ* 231, pp. L111–L114. DOI: [10.1086/183015](https://doi.org/10.1086/183015).
- Liang, E. P. T. and R. H. Price (1977). "Accretion disk coronae and Cygnus X-1." In: *ApJ* 218, pp. 247–252. DOI: [10.1086/155677](https://doi.org/10.1086/155677).
- Lynden-Bell, D. (1969). "Galactic Nuclei as Collapsed Old Quasars." In: *Nature* 223.5207, pp. 690–694. DOI: [10.1038/223690a0](https://doi.org/10.1038/223690a0).
- Marian, V. et al. (2019). "Major mergers are not the dominant trigger for high-accretion AGNs at  $z = 2$ ." In: *arXiv e-prints*, arXiv:1904.00037, arXiv:1904.00037. arXiv: [1904.00037](https://arxiv.org/abs/1904.00037) [astro-ph.GA].
- Mastichiadis, A. and J. G. Kirk (1997). "Variability in the synchrotron self-Compton model of blazar emission." In: *A&A* 320, pp. 19–25. arXiv: [astro-ph/9610058](https://arxiv.org/abs/astro-ph/9610058) [astro-ph].
- Mewe, R., E. H. B. M. Gronenschild, and G. H. J. van den Oord (1985). "Calculated X-radiation from optically thin plasmas. V." In: *A&AS* 62, pp. 197–254.
- Middelberg, Enno and Uwe Bach (2008). "High resolution radio astronomy using very long baseline interferometry." In: *Reports on Progress in Physics* 71.6, 066901, p. 066901. DOI: [10.1088/0034-4885/71/6/066901](https://doi.org/10.1088/0034-4885/71/6/066901). arXiv: [0803.2983](https://arxiv.org/abs/0803.2983) [astro-ph].
- Migliari, Simone, Rob Fender, and Mariano Méndez (2002). "Iron Emission Lines from Extended X-ray Jets in SS 433: Reheating of Atomic Nuclei." In: *Science* 297.5587, pp. 1673–1676. DOI: [10.1126/science.1073660](https://doi.org/10.1126/science.1073660). arXiv: [astro-ph/0209131](https://arxiv.org/abs/astro-ph/0209131) [astro-ph].
- Moorwood, Alan F. M. (1996). "Starburst Galaxies." In: *Space Sci. Rev.* 77.3-4, pp. 303–366. DOI: [10.1007/BF00226226](https://doi.org/10.1007/BF00226226).
- Mücke, A. and R. J. Protheroe (2001). "A proton synchrotron blazar model for flaring in Markarian 501." In: *Astroparticle Physics* 15.1,

- pp. 121–136. DOI: [10.1016/S0927-6505\(00\)00141-9](https://doi.org/10.1016/S0927-6505(00)00141-9). arXiv: [astro-ph/0004052](https://arxiv.org/abs/astro-ph/0004052) [astro-ph].
- Müller, C. et al. (2014). “TANAMI monitoring of Centaurus A: The complex dynamics in the inner parsec of an extragalactic jet.” In: *A&A* 569, A115, A115. DOI: [10.1051/0004-6361/201423948](https://doi.org/10.1051/0004-6361/201423948). arXiv: [1407.0162](https://arxiv.org/abs/1407.0162) [astro-ph.HE].
- Naab, Thorsten and Jeremiah P. Ostriker (2017). “Theoretical Challenges in Galaxy Formation.” In: *ARA&A* 55.1, pp. 59–109. DOI: [10.1146/annurev-astro-081913-040019](https://doi.org/10.1146/annurev-astro-081913-040019). arXiv: [1612.06891](https://arxiv.org/abs/1612.06891) [astro-ph.GA].
- Nandra, K. and K. A. Pounds (1994). “GINGA observations of the X-ray spectra of Seyfert galaxies.” In: *MNRAS* 268, pp. 405–429. DOI: [10.1093/mnras/268.2.405](https://doi.org/10.1093/mnras/268.2.405).
- Ohm, Stefan (2016). “Starburst galaxies as seen by gamma-ray telescopes.” In: *Comptes Rendus Physique* 17.6, pp. 585–593. DOI: [10.1016/j.crhy.2016.04.003](https://doi.org/10.1016/j.crhy.2016.04.003). arXiv: [1601.06386](https://arxiv.org/abs/1601.06386) [astro-ph.HE].
- Padovani, P. et al. (2017). “Active galactic nuclei: what’s in a name?” In: *A&A Rev.* 25.1, 2, p. 2. DOI: [10.1007/s00159-017-0102-9](https://doi.org/10.1007/s00159-017-0102-9). arXiv: [1707.07134](https://arxiv.org/abs/1707.07134) [astro-ph.GA].
- Persic, M. and Y. Rephaeli (2002). “X-ray spectral components of starburst galaxies.” In: *A&A* 382, pp. 843–859. DOI: [10.1051/0004-6361:20011679](https://doi.org/10.1051/0004-6361:20011679). arXiv: [astro-ph/0112030](https://arxiv.org/abs/astro-ph/0112030) [astro-ph].
- Perucho, M., V. Bosch-Ramon, and M. V. Barkov (2017). “Impact of red giant/AGB winds on active galactic nucleus jet propagation.” In: *A&A* 606, A40, A40. DOI: [10.1051/0004-6361/201630117](https://doi.org/10.1051/0004-6361/201630117). arXiv: [1706.06301](https://arxiv.org/abs/1706.06301) [astro-ph.HE].
- Perucho, M. and J. M. Martí (2007). “A numerical simulation of the evolution and fate of a Fanaroff-Riley type I jet. The case of 3C 31.” In: *MNRAS* 382.2, pp. 526–542. DOI: [10.1111/j.1365-2966.2007.12454.x](https://doi.org/10.1111/j.1365-2966.2007.12454.x). arXiv: [0709.1784](https://arxiv.org/abs/0709.1784) [astro-ph].
- Perucho, M. et al. (2014). “On the deceleration of Fanaroff-Riley Class I jets: mass loading by stellar winds.” In: *MNRAS* 441.2, pp. 1488–1503. DOI: [10.1093/mnras/stu676](https://doi.org/10.1093/mnras/stu676). arXiv: [1404.1209](https://arxiv.org/abs/1404.1209) [astro-ph.HE].
- Petrucci, P. O. et al. (2018). “Testing warm Comptonization models for the origin of the soft X-ray excess in AGNs.” In: *A&A* 611, A59, A59. DOI: [10.1051/0004-6361/201731580](https://doi.org/10.1051/0004-6361/201731580). arXiv: [1710.04940](https://arxiv.org/abs/1710.04940) [astro-ph.HE].
- Ranalli, P., A. Comastri, and G. Setti (2003). “The 2–10 keV luminosity as a Star Formation Rate indicator.” In: *A&A* 399, pp. 39–50. DOI: [10.1051/0004-6361:20021600](https://doi.org/10.1051/0004-6361:20021600). arXiv: [astro-ph/0211304](https://arxiv.org/abs/astro-ph/0211304) [astro-ph].
- Romero, Gustavo E. et al. (2017). “Relativistic Jets in Active Galactic Nuclei and Microquasars.” In: *Space Sci. Rev.* 207.1–4, pp. 5–61. DOI: [10.1007/s11214-016-0328-2](https://doi.org/10.1007/s11214-016-0328-2). arXiv: [1611.09507](https://arxiv.org/abs/1611.09507) [astro-ph.HE].

- Róžańska, A. et al. (2015). "Warm and optically thick dissipative coronae above accretion disks." In: *A&A* 580, A77, A77. DOI: [10.1051/0004-6361/201526288](https://doi.org/10.1051/0004-6361/201526288). arXiv: [1504.03160](https://arxiv.org/abs/1504.03160) [astro-ph.GA].
- Rubin, Robert H. (1968). "A Discussion of the Sizes and Excitation of H II Regions." In: *ApJ* 154, p. 391. DOI: [10.1086/149766](https://doi.org/10.1086/149766).
- Salpeter, E. E. (1964). "Accretion of Interstellar Matter by Massive Objects." In: *ApJ* 140, pp. 796–800. DOI: [10.1086/147973](https://doi.org/10.1086/147973).
- Sanders, D. B. (1999). "A New View of Galaxy Evolution from Submillimeter Surveys with SCUBA." In: *Ap&SS* 269, pp. 381–389. DOI: [10.1023/A:1017061400637](https://doi.org/10.1023/A:1017061400637). arXiv: [astro-ph/9910028](https://arxiv.org/abs/astro-ph/9910028) [astro-ph].
- Sanders, D. B. and I. F. Mirabel (1996). "Luminous Infrared Galaxies." In: *ARA&A* 34, p. 749. DOI: [10.1146/annurev.astro.34.1.749](https://doi.org/10.1146/annurev.astro.34.1.749).
- Sanders, D. B. et al. (1988). "Warm Ultraluminous Galaxies in the IRAS Survey: The Transition from Galaxy to Quasar?" In: *ApJ* 328, p. L35. DOI: [10.1086/185155](https://doi.org/10.1086/185155).
- Sbarrato, T. et al. (2015). "Blazar candidates beyond redshift 4 observed by Swift." In: *MNRAS* 446.3, pp. 2483–2489. DOI: [10.1093/mnras/stu2269](https://doi.org/10.1093/mnras/stu2269). arXiv: [1410.0364](https://arxiv.org/abs/1410.0364) [astro-ph.HE].
- Schmidt, M. (1963). "3C 273 : A Star-Like Object with Large Red-Shift." In: *Nature* 197.4872, p. 1040. DOI: [10.1038/1971040a0](https://doi.org/10.1038/1971040a0).
- Seyfert, Carl K. (1943). "Nuclear Emission in Spiral Nebulae." In: *ApJ* 97, p. 28. DOI: [10.1086/144488](https://doi.org/10.1086/144488).
- Shakura, N. I. and R. A. Sunyaev (1973). "Reprint of 1973A&A....24..337S. Black holes in binary systems. Observational appearance." In: *A&A* 500, pp. 33–51.
- Shields, G. A. (1978). "Thermal continuum from accretion disks in quasars." In: *Nature* 272.5655, pp. 706–708. DOI: [10.1038/272706a0](https://doi.org/10.1038/272706a0).
- (1990). "Extragalactic HII regions." In: *ARA&A* 28, pp. 525–560. DOI: [10.1146/annurev.aa.28.090190.002521](https://doi.org/10.1146/annurev.aa.28.090190.002521).
- Shklovskii, I. S. (1961). "Radio Galaxies." In: *Soviet Ast.* 4, p. 885.
- Sikora, Marek et al. (1997). "Learning about Active Galactic Nucleus Jets from Spectral Properties of Blazars." In: *ApJ* 484.1, pp. 108–117. DOI: [10.1086/304305](https://doi.org/10.1086/304305).
- Sikora, Marek et al. (2009). "Constraining Emission Models of Luminous Blazar Sources." In: *ApJ* 704.1, pp. 38–50. DOI: [10.1088/0004-637X/704/1/38](https://doi.org/10.1088/0004-637X/704/1/38). arXiv: [0904.1414](https://arxiv.org/abs/0904.1414) [astro-ph.CO].
- Smith, Harding E. et al. (1998). "The Emergence of a Quasar from the Luminous Infrared Galaxy MRK 231." In: *American Astronomical Society Meeting Abstracts #192*. Vol. 192. American Astronomical Society Meeting Abstracts, p. 11.10.
- Soifer, B. T. et al. (1986). "The Luminosity Function and Space Density of the Most Luminous Galaxies in the IRAS Survey." In: *ApJ* 303, p. L41. DOI: [10.1086/184649](https://doi.org/10.1086/184649).
- Steffen, W. et al. (1997). "Jet-Cloud Interactions and the Brightening of the Narrow-Line Region in Seyfert Galaxies." In: *ApJ* 491.2,

- pp. L73–L76. DOI: [10.1086/311066](https://doi.org/10.1086/311066). arXiv: [astro-ph/9710178](https://arxiv.org/abs/astro-ph/9710178) [astro-ph].
- Stierwalt, S. et al. (2013). “Mid-infrared Properties of Nearby Luminous Infrared Galaxies. I. Spitzer Infrared Spectrograph Spectra for the GOALS Sample.” In: *ApJS* 206.1, 1, p. 1. DOI: [10.1088/0067-0049/206/1/1](https://doi.org/10.1088/0067-0049/206/1/1). arXiv: [1302.4477](https://arxiv.org/abs/1302.4477) [astro-ph.CO].
- Sturm, E. et al. (2002). “Mid-Infrared line diagnostics of active galaxies. A spectroscopic AGN survey with ISO-SWS.” In: *A&A* 393, pp. 821–841. DOI: [10.1051/0004-6361:20021043](https://doi.org/10.1051/0004-6361:20021043). arXiv: [astro-ph/0207381](https://arxiv.org/abs/astro-ph/0207381) [astro-ph].
- Tadhunter, Clive (2008). “An introduction to active galactic nuclei: Classification and unification.” In: *New Astron. Rev.* 52.6, pp. 227–239. DOI: [10.1016/j.newar.2008.06.004](https://doi.org/10.1016/j.newar.2008.06.004).
- Torres-Albà, N. et al. (2018). “C-GOALS. II. Chandra observations of the lower luminosity sample of nearby luminous infrared galaxies in GOALS.” In: *A&A* 620, A140, A140. DOI: [10.1051/0004-6361/201834105](https://doi.org/10.1051/0004-6361/201834105). arXiv: [1810.02371](https://arxiv.org/abs/1810.02371) [astro-ph.GA].
- Torres-Albà, Núria and Valentí Bosch-Ramon (2019). “Gamma rays from red giant wind bubbles entering the jets of elliptical host blazars.” In: *A&A* 623, A91, A91. DOI: [10.1051/0004-6361/201833697](https://doi.org/10.1051/0004-6361/201833697). arXiv: [1902.05008](https://arxiv.org/abs/1902.05008) [astro-ph.HE].
- VERITAS Collaboration et al. (2009). “A connection between star formation activity and cosmic rays in the starburst galaxy M82.” In: *Nature* 462.7274, pp. 770–772. DOI: [10.1038/nature08557](https://doi.org/10.1038/nature08557). arXiv: [0911.0873](https://arxiv.org/abs/0911.0873) [astro-ph.CO].
- Valiante, E. et al. (2009). “A Backward Evolution Model for Infrared Surveys: The Role of AGN- and Color- $L_{\text{TIR}}$  Distributions.” In: *ApJ* 701.2, pp. 1814–1838. DOI: [10.1088/0004-637X/701/2/1814](https://doi.org/10.1088/0004-637X/701/2/1814). arXiv: [0906.4110](https://arxiv.org/abs/0906.4110) [astro-ph.CO].
- Veilleux, S. et al. (1995). “Optical Spectroscopy of Luminous Infrared Galaxies. II. Analysis of the Nuclear and Long-Slit Data.” In: *ApJS* 98, p. 171. DOI: [10.1086/192158](https://doi.org/10.1086/192158).
- Veilleux, Sylvain and Donald E. Osterbrock (1987). “Spectral Classification of Emission-Line Galaxies.” In: *ApJS* 63, p. 295. DOI: [10.1086/191166](https://doi.org/10.1086/191166).
- Vieyro, F. L., V. Bosch-Ramon, and N. Torres-Albà (2019). “Non-thermal emission resulting from a supernova explosion inside an extragalactic jet.” In: *A&A* 622, A175, A175. DOI: [10.1051/0004-6361/201833319](https://doi.org/10.1051/0004-6361/201833319). arXiv: [1901.09003](https://arxiv.org/abs/1901.09003) [astro-ph.HE].
- Vieyro, Florencia L., Núria Torres-Albà, and Valentí Bosch-Ramon (2017). “Collective non-thermal emission from an extragalactic jet interacting with stars.” In: *A&A* 604, A57, A57. DOI: [10.1051/0004-6361/201630333](https://doi.org/10.1051/0004-6361/201630333). arXiv: [1704.01919](https://arxiv.org/abs/1704.01919) [astro-ph.HE].
- Vito, F. et al. (2018). “High-redshift AGN in the Chandra Deep Fields: the obscured fraction and space density of the sub- $L_*$  popula-

- tion." In: *MNRAS* 473.2, pp. 2378–2406. DOI: [10.1093/mnras/stx2486](https://doi.org/10.1093/mnras/stx2486). arXiv: [1709.07892](https://arxiv.org/abs/1709.07892) [astro-ph.GA].
- Vito, Fabio et al. (2019). "Discovery of the first heavily obscured QSO candidate at  $z > 6$  in a close galaxy pair." In: *arXiv e-prints*, arXiv:1906.04241, arXiv:1906.04241. arXiv: [1906.04241](https://arxiv.org/abs/1906.04241) [astro-ph.GA].
- Wang, Y. et al. (2009). "A relativistic mixing-layer model for jets in low-luminosity radio galaxies." In: *MNRAS* 397.2, pp. 1113–1124. DOI: [10.1111/j.1365-2966.2009.15026.x](https://doi.org/10.1111/j.1365-2966.2009.15026.x). arXiv: [0905.2507](https://arxiv.org/abs/0905.2507) [astro-ph.CO].
- Wilman, R. J., A. C. Edge, and R. M. Johnstone (2005). "The nature of the molecular gas system in the core of NGC 1275." In: *MNRAS* 359.2, pp. 755–764. DOI: [10.1111/j.1365-2966.2005.08956.x](https://doi.org/10.1111/j.1365-2966.2005.08956.x). arXiv: [astro-ph/0502537](https://arxiv.org/abs/astro-ph/0502537) [astro-ph].
- Wilson, A. S. and Y. Yang (2002). "Chandra X-Ray Imaging and Spectroscopy of the M87 Jet and Nucleus." In: *ApJ* 568.1, pp. 133–140. DOI: [10.1086/338887](https://doi.org/10.1086/338887). arXiv: [astro-ph/0112097](https://arxiv.org/abs/astro-ph/0112097) [astro-ph].
- Wilson, C. K. and R. E. Rothschild (1983). "Observations of a hard X-ray component in the spectrum of Nova Oph." In: *ApJ* 274, pp. 717–722. DOI: [10.1086/161483](https://doi.org/10.1086/161483).
- Wykes, Sarka et al. (2015). "Internal entrainment and the origin of jet-related broad-band emission in Centaurus A." In: *MNRAS* 447.1, pp. 1001–1013. DOI: [10.1093/mnras/stu2440](https://doi.org/10.1093/mnras/stu2440). arXiv: [1409.5785](https://arxiv.org/abs/1409.5785) [astro-ph.HE].
- Xu, C. K. et al. (2015). "ALMA Observations of Warm Dense Gas in NGC 1614—Breaking of the Star Formation Law in the Central Kiloparsec." In: *ApJ* 799.1, 11, p. 11. DOI: [10.1088/0004-637X/799/1/11](https://doi.org/10.1088/0004-637X/799/1/11). arXiv: [1411.1111](https://arxiv.org/abs/1411.1111) [astro-ph.GA].
- Yuan, T. T., L. J. Kewley, and D. B. Sanders (2010). "The Role of Starburst-Active Galactic Nucleus Composites in Luminous Infrared Galaxy Mergers: Insights from the New Optical Classification Scheme." In: *ApJ* 709.2, pp. 884–911. DOI: [10.1088/0004-637X/709/2/884](https://doi.org/10.1088/0004-637X/709/2/884). arXiv: [0911.3728](https://arxiv.org/abs/0911.3728) [astro-ph.CO].
- Zel'dovich, Ya. B. and I. D. Novikov (1964). "The Radiation of Gravity Waves by Bodies Moving in the Field of a Collapsing Star." In: *Soviet Physics Doklady* 9, p. 246.
- de la Cita, V. M. et al. (2016). "Coupling hydrodynamics and radiation calculations for star-jet interactions in active galactic nuclei." In: *A&A* 591, A15, A15. DOI: [10.1051/0004-6361/201527084](https://doi.org/10.1051/0004-6361/201527084). arXiv: [1604.02070](https://arxiv.org/abs/1604.02070) [astro-ph.HE].

The bibliography printed above refers to citations in the Introduction, individual chapter introductions, Summary and Discussion, and Conclusions. Citations in each individual publication can be found listed within the corresponding publication.



#### COLOPHON

This document was typeset using the typographical look-and-feel classicthesis developed by André Miede. The style was inspired by Robert Bringhurst's seminal book on typography "*The Elements of Typographic Style*".

#### FUNDING ACKNOWLEDGEMENTS

The author acknowledges financial support from Ministerio de Educación, Cultura y Deporte through FPU/04887 grant. We also acknowledge support by the Spanish Ministerio de Economía y Competitividad (MINECO/FEDER, UE) under grant AYA2016-76012-C3-1-P, with partial support by the European Regional Development Fund (ERDF/FEDER), MDM-2014-0369 of ICCUB (Unidad de Excelencia María de Maeztu), and the Catalan DEC grant 2017 SGR 643.